UNIVERSIDAD NACIONAL AUTÓNOMA DE MÉXICO

DOCTORADO EN CIENCIAS BIOMÉDICAS

INSTITUTO DE NEUROBIOLOGÍA

DINÁMICA DE LA ACTIVIDAD POBLACIONAL DE NEURONAS EN LA CORTEZA PREMOTORA DEL PRIMATE DURANTE LA PRODUCCIÓN DE INTERVALOS RÍTMICOS

T E S I S

QUE PARA OPTAR POR EL GRADO DE:

DOCTOR EN CIENCIAS

P R E S E N T A:

JORGE ARTURO GÁMEZ DE LEÓN

DIRECTOR DE TESIS

DR. HUGO MERCHANT NANCY

INSTITUTO DE NEUROBIOLOGÍA

COMITÉ TUTOR

DR. VICTOR HUGO DE LAFUENTE FLORES

INSTITUTO DE NEUROBIOLOGÍA

DR. LUIS LEMUS SANDOVAL

INSTITUTO DE FISIOLOGÍA CELULAR

QUERÉTARO, QRO. MAYO DE 2019.

JURADO

Universidad Nacional Autónoma de México

Instituto de Neurobiología

	Firma
Presidente Dr. José Bargas Díaz	_____
Secretario (tutor) Dr. Hugo Merchant Nancy	_____
Vocal Dr. Ranier Gutiérrez Mendoza	_____
Vocal Dr. Pavel Ernesto Rueda Orozco	_____
Vocal Dr. Roman Rossi Pool	_____

Agradecimientos

A la Dirección General de Estudios de Posgrado de la UNAM y al Doctorado en Ciencias Biomédicas. Número de cuenta: 509003223

Al Consejo Nacional de Ciencia y Tecnología. Número de beca: 339118

Al personal de la Biblioteca del campus UNAM Juriquilla, encabezado por su coordinador el Dr. Francisco Javier Valles Valenzuela.

A las unidades de Videoconferencia del Instituto de Neurobiología y del Instituto de Fisiología Celular, dirigidas por la Psic. María de Lourdes Lara Ayala y por la C. Ana María Escalante Gonzalbo, respectivamente.

Al personal de la Unidad de Enseñanza, a cargo de la M.C. Leonor Casanova Rico.

Al Ing. Luis Prado y a Raúl Paulín por su asistencia técnica.

Al Dr. Hugo Merchant y a todos mis compañeros del laboratorio B-15 con los que he coincidido a lo largo del Posgrado.

Tabla de contenido

Abreviaturas

a.u., unidades arbitrarias

CGBT, CBGT, circuito corteza-ganglios basales-tálamo

CC, condición de continuación

CP, componente principal

DAT, Teoría de atención dinámica

DDM, modelo de deriva-difusión

dPCA, demixed PCA

EEG, electroencefalograma

fMRI, resonancia magnética funcional

IOI, intervalo entre estímulos

M1, corteza motora primaria

MPC, corteza premotora medial

MSE, error cuadrático medio

NSQ, núcleo supraquiasmático

PCA, análisis de componentes principales

PET, tomografías de emisión de positrones

PMdc, corteza premotora medial caudal

PMdr, corteza premotora medial rostral

PMvc, corteza premotora ventral cauda

PMvr, corteza premotora ventral rostral

Pre-SMA, área motora presuplementaria

SC, condición de sincronización

SCT, tarea de sincronización-continuación

SEF, campo ocular suplementario

SI, índice de sorpresa

SMA, área motora suplementaria

SRTT, tarea de tiempo de reacción

ST, tarea de sincronización

STS, surco temporal superior

SVM, máquina de vector de soporte

TDNN, red neuronal de retraso temporal

TIND, datos normalizados al intervalo blanco

UTND, datos normalizados unitarios

GAE, evolución gradual audiomotora

Índice de figuras

Índice de código

Abstract

Encoding time is essential for adapting our motor commands to the demands of the environment. Furthermore, the ability to generate rhythms of different tempos is a characteristic of human musical cognition. Previous studies have identified the medial premotor cortex (MPC) as part of a circuit for perception and production of rhythmic patterns. However, the neuronal population code behind rhythmic tapping remains largely unknown. Hence, we analyzed the extracellular single unit activity of hundreds of MPC (medial premotor cortex) neurons from two monkeys performing a synchronization-continuation task (SCT) synchronizing their movements to a visual metronome. We also trained two monkeys on a visual and auditory synchronization task (ST). Furthermore, one of the monkeys performed a tempo-changing synchronization task (TCST).

We found that the rhythmic synchronization capabilities of monkeys are larger than previously known. The monkeys are capable of predictively adapting their tapping to a tempo-changing visual metronome. On the other hand, the neural population activity in the MPC shows a strong periodic pattern when projected into a low-dimensional state-space during isochronous tapping. Different tempos are encoded by circular trajectories that travel at a constant speed but with different radii. Additionally, the increase in amplitude and variability of the neural trajectories accounted for the scalar property of interval timing. We found that the neural trajectories do not follow the tapping kinematics. In addition, simulations of an evolving sequential pattern of neural activations revealed a relation between the number of neurons and the duration of their activation periods to the properties of the neural state trajectories. Thus, our results support the notion that timing during rhythmic behaviors is encoded in radius of the circular periodic dynamics of MPC neural populations.

Resumen

La codificación del tiempo es esencial para adaptar nuestros comandos motores a las demandas del ambiente. La habilidad de generar ritmos de diferentes *tempos* es una característica de la cognición musical humana. Se sabe que la corteza premotora medial (MPC) es parte del circuito de percepción y producción de ritmos. Sin embargo, el código neuronal que subyace la producción rítmica no se conoce completamente. En este trabajo, analizamos la actividad unitaria extracelular de cientos de neuronas en la MPC de dos monos que realizaron una tarea de sincronización-continuación (SCT) sincronizando sus movimientos a un metrónomo visual. Posteriormente, entrenamos a dos monos en una tarea de sincronización (ST) a metrónomos visuales y auditivos. Además, uno de los monos realizó una tarea donde el metrónomo visual presentaba aceleraciones y desaceleraciones (TCST).

Utilizando la tarea de TCST comprobamos que las capacidades de los monos para la sincronización de ritmos son más grandes de lo que se creía. El mono fue capaz de sincronizar sus movimientos de manera predictiva a un metrónomo visual con variaciones. Por otro lado, el análisis de la actividad neuronal poblacional de la MPC durante la tarea de SCT, mostró que la actividad poblacional presentó un patrón periódico al ser proyectada en un plano fase. Los diferentes intervalos blancos fueron codificados por trayectorias neuronales circulares que viajaron a una velocidad constante, pero con diferentes radios. Además, el incremento en la amplitud y variabilidad de las trayectorias neuronales estuvo correlacionado con la propiedad escalar de la medición de intervalos de tiempo. Encontramos que las trayectorias neuronales no siguen la cinemática del movimiento de los brazos de los monos. Además, realizamos simulaciones de patrones secuenciales de activación de grupos neuronales, los cuales revelaron una relación entre el número de neuronas y la duración de sus periodos de activación con las propiedades de las trayectorias neuronales. Por los tanto, los resultados de este trabajo apoyan la idea de que la medición del tiempo durante la generación de ritmos está codificada en el radio de la dinámica periódica circular de poblaciones neuronales de la MPC.

Introducción

La sincronización a los ritmos es la habilidad de armonizar los movimientos de diferentes partes del cuerpo a un pulso regular o ritmo musical, permitiendo la respuesta síncrona a este pulso durante el baile o la interpretación musical en un conjunto (Hugo Merchant, Grahn, Trainor, Rohrmeier, & Fitch, 2015; Phillips-Silver & Keller, 2012; B. H. Repp, 2005; B. H. Repp & Su, 2013). La habilidad de los humanos para coordinar sus movimientos con una gran precisión temporal y sin embargo mantenerse flexibles a los cambios en el ritmo de la música es una característica de la cognición musical (Mills, van der Steen, Schultz, & Keller, 2015). Existen dos mecanismos principales que determinan la sincronización sensoriomotora: la anticipación temporal y la adaptación (Mills et al., 2015; van der Steen & Keller, 2013). La anticipación temporal es un proceso predictivo donde los mecanismos neuronales extraen información de los patrones regulares de un estímulo para planear y coordinar una secuencia de movimientos (van der Steen & Keller, 2013). Por otro lado, la temporización adaptiva es un proceso reactivo donde la información pasada (Mills et al., 2015) se usa para generar correcciones a partir del error, permitiendo al sujeto responder a variaciones en el tiempo de los estímulos al ajustar la temporización de sus movimientos.

Sin embargo, se desconoce en gran medida el sustrato neuronal que permite la sincronización rítmica. Estudios recientes, han ligado estructuras específicas, tanto corticales como subcorticales, con actividades que requieren una coordinación temporal estricta en la escala de tiempo de los cientos de milisegundos, tales como: ejecutar o escuchar música (Zatorre, Chen, & Penhune, 2007) y la percepción y generación del habla (Wilson, Saygin, Sereno, & Iacoboni, 2004). Existe evidencia de que la capacidad de percibir y estimar el tiempo durante la generación y percepción rítmica emerge de interacciones de un circuito principal distribuido, Corteza -Ganglios Basales-Tálamo (CBGT), con regiones cerebrales específicas que proveen señales necesarias para temporalizar eventos (Hugo Merchant, Harrington, & Meck, 2013a).

Una tarea utilizada para el estudio de movimientos rítmicos en la escala de los cientos de milisegundos es la tarea de sincronización-continuación. Esta tarea consiste de dos fases: durante la fase de sincronización se presentan estímulos visuales o auditivos a intervalos regulares, el sujeto debe presionar un botón de manera intermitente siguiendo los estímulos presentados; en la fase de continuación, el sujeto debe continuar presionando el botón de manera intermitente con el mismo intervalo de tiempo, pero sin la presencia de los estímulos sensoriales. Usando registros extracelulares en la corteza premotora medial (MPC) de monos Rhesus (Macaca mulatta), nuestro grupo ha reportado patrones de actividad neuronal que se modulan con el intervalo producido (Hugo Merchant, Zarco, Pérez, Prado, & Bartolo, 2011). Durante estos experimentos se encontraron diversas poblaciones neuronales que interactúan entre sí, para dar origen a la regulación temporal de las respuestas motoras.

En este trabajo, examino el papel de la dinámica poblacional neuronal de la MPC en la codificación de información temporal. El trabajo se divide en dos enfoques: por un lado en la descripción del comportamiento de los monos durante las tareas rítmicas; mientras que por otro, en el análisis de la dinámica poblacional en el contexto de sistemas dinámicos.

Antecedentes

El tiempo

Los organismos tienen una habilidad extraordinaria para medir el tiempo. Diversas actividades se llevan a cabo a diferentes escalas temporales. La habilidad de estimar el tiempo es esencial para actividades tan diversas como el habla, los deportes, la toma de decisiones, el ciclo sueño-vigilia, etc. Los organismos cuentan con diferentes sistemas que les permiten medir el tiempo en diversas escalas. Sin embargo, todavía no hay un consenso en el funcionamiento de algunos de estos mecanismos. El sustrato neuronal que permite la medición del tiempo en la escala de los cientos de milisegundos es tema de múltiples estudios en la actualidad.

Diferentes escalas del tiempo en los sistemas biológicos

Para medir el tiempo los organismos han desarrollado diferentes sistemas para distintas escalas temporales (ver Figura 1). Existen sistemas altamente especializados como el núcleo supraquiasmático, en la base del hipotálamo, el cuál es el principal reloj de los ciclos circadianos en los mamíferos (Gillette, Martha U., 1991). Este reloj central se encarga de regular la actividad metabólica, hormonal y conductual durante el día (Schibler & Sassone-Corsi, 2002). Así como, de sincronizar a los osciladores periféricos que se encuentran dentro de las células de distintos tejidos. Estos osciladores periféricos se regulan por un mecanismo transcripcional controlado por el asa de señales de los genes Clock/Bmal y Per/Cry (Reppert & Weaver, 2002).

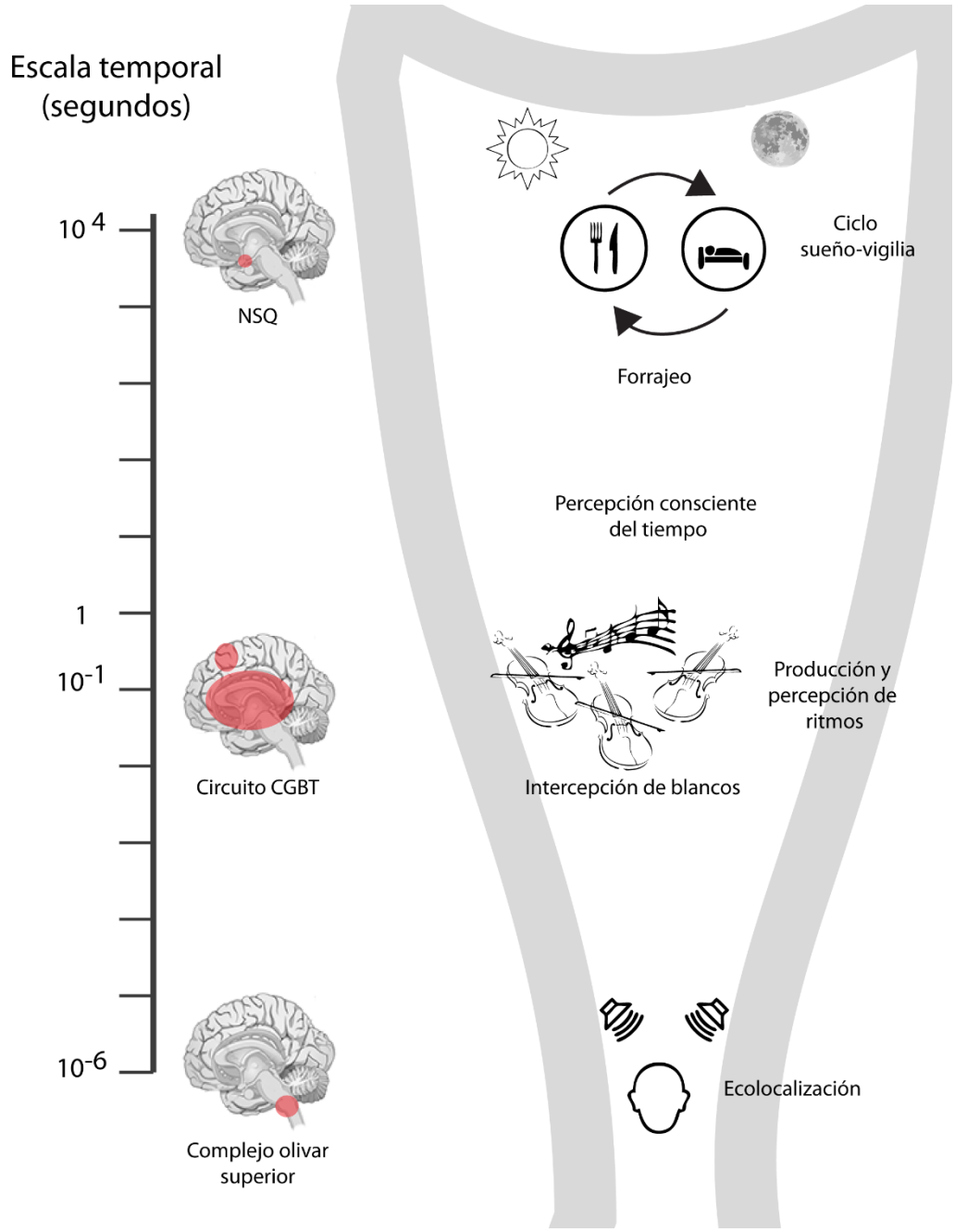

Figura 1 Escalas de tiempo

El tiempo a través de diferentes escalas. Diferentes áreas del cerebro están involucradas en la medición del tiempo a diferentes escalas. En el rango de las horas el núcleo supraquiasmático (NSQ) se considera el reloj principal de los ciclos circadianos como el ciclo sueño-vigilia. Mientras tanto, en la escala de los cientos de milisegundos, se ha propuesto que el circuito corteza-ganglios basales-tálamo (CGBT). En el otro extremo, el complejo olivar superior está involucrado en la detección de diferencias temporales en la escala de los microsegundos en las señales acústicas que son recibidas por las cócleas izquierda y derecha para la localización espacial de los sonidos.

En la escala de decenas de milisegundos hasta los segundos se encuentran una gran variedad de comportamientos complejo tales como la comprensión y producción del habla (Zatorre & Binder, 2000) , calcular el tiempo de contacto para una actividad motora (Hugo Merchant & Georgopoulos, 2006) o sincronizar los movimientos del cuerpo al ritmo de la música (Cross, Hamilton, & Grafton, 2006). El procesamiento temporal en esta escala implica la interacción coordinada de diversas áreas cerebrales como la corteza, el cerebelo, los ganglios basales y el tálamo.

En el otro extremo de la escala temporal, podemos encontrar otro sistema que implica la medición del tiempo en la escala de las fracciones de milisegundos para la localización de la fuente de un sonido. La diferencia del tiempo en el que llega un sonido a ambos oídos es parte de la información usada por el cerebro para estimar la localización de la fuente del sonido (Grothe, Pecka, & McAlpine, 2010), de tal manera que son neuronas del complejo olivar superior en mamíferos, las que miden la diferencia en microsegundos de la activación excitatoria biaural de ambos oídos (Goldberg & Brown, 1969).

Neurofisiología del tiempo en los cientos de milisegundos

Una tarea de temporización puede ser explícita o implícita, siendo la principal diferencia si los sujetos que la realizan deben proveer un estimado evidente de la duración (J. Coull & Nobre, 2008). En tareas de tiempo explicito, estimaciones de la duración del estímulo o del periodo inter-estímulo son provistas por los sujetos de forma de discriminaciones perceptuales o respuestas motoras (J. Coull & Nobre, 2008).Tanto la estimación de la duración de un estímulo, así como le predicción temporal de un evento requieren de una representación métrica del tiempo, donde la temporalización de un evento pueda ser medida en una escala continua. De igual manera, la categorización y discriminación temporal requieren de una representación ordinal del tiempo, donde el tiempo relativo entre una secuencia de eventos se pueda comparar de forma categórica (J. T. Coull, Cheng, & Meck, 2011). En cambio, en el caso del tiempo implícito, la temporalización es un subproducto de tareas con objetivos no relacionados directamente a la medición del tiempo(J. Coull & Nobre, 2008). Donde, sin embargo, los estímulos sensoriales o respuestas motoras se encuentran dentro de un esquema temporal estricto. Aun cuando las acciones se desarrollan en el tiempo, no es indispensable que la información temporal sea representada o regulada de manera explícita. De ahí que la velocidad y duración de una serie de acciones motoras secuenciales pueden no reflejar una temporalización directa, por el contrario puede ser una propiedad emergente de la dinámica compleja del sistema neuromuscular (Ivry, Richard B., 1996).

La complejidad del procesamiento de la información temporal para la percepción, aprendizaje-memoria y el control motor voluntario depende de una red compleja de áreas corticales en los lóbulos parietal y frontal, así como en los ganglios basales y el cerebelo (Hugo Merchant, 2014). Aun cuando no se conoce en su totalidad el mecanismo de medición del tiempo en la escala de los cientos de milisegundos, cada vez hay más evidencia de que el mecanismo central de temporalización es una red distribuida recurrente corteza-ganglios basales-tálamo, así como un conjunto de estructuras contexto dependientes que se reclutan de acuerdo al contexto de la tarea en ejecución (Hugo Merchant, Harrington, & Meck, 2013b). Esta red central se activa durante las tareas de percepción temporal, así como en las de temporalización motora (Schubotz, Friederici, & von Cramon, 2000). Esta red incluye las áreas de la corteza premotora medial (el área motora

suplementaria [SMA] y el área motora pre-suplementaria [pre-SMA]), así como el neoestriado, el globo pálido y el tálamo motor (ver Figura 2). En trabajos anteriores de nuestro laboratorio, por medio de registros en la corteza premotora medial de monos mientras llevaban a cabo una tarea de producción de secuencias de intervalos isócronos, se han encontrado grupos de neuronas cuya actividad está relacionada con la medición del tiempo asociada principalmente a los movimientos realizados durante una tarea de sincronización-continuación (Hugo Merchant et al., 2011). Las neuronas de la MPC están sintonizadas a la duración y el orden secuencial de movimientos rítmicos producidos ya sea en sincronía con un metrónomo o guiados por un ritmo endógeno (tarea de sincronización-continuación), (Crowe, Zarco, Bartolo, & Merchant, 2014; Hugo Merchant, Pérez, et al., 2015a).

Los perfiles de activación de estos circuitos específicos durante la medición de intervalos siguen un patrón progresivo de activación neuronal o *moving bump*, en el que cada neurona presenta un único periodo de actividad durante la progresión y donde este patrón se repite para cada intervalo producido de la secuencia rítmica (Crowe et al., 2014; Hugo Merchant & Bartolo, 2018; Hugo Merchant, Pérez, et al., 2015a). Sin embargo, las células de la MPC codifican al mismo tiempo el intervalo, el orden serial y la fase de la tarea durante la SCT, mostrando perfiles de activación complejos y heterogéneos que hacen difícil entender los mecanismos neuronales relacionados con la tarea.

Ritmos y la tarea sincronización

La tarea de sincronización requiere que los sujetos realicen movimientos siguiendo un ritmo externo, usualmente un metrónomo isócrono. Es un paradigma popular gracias a su simplicidad y larga historia (B. H. Repp, 2005). Los mecanismos básicos de sincronización sensoriomotora son comúnmente estudiados usando esta tarea y sus resultados son particularmente relevantes para la ejecución musical, la danza y los deportes. La tarea de sincronización es un paradigma sencillo. Sin embargo las patrones de respuesta puede ser muy complejos, lo que genera interrogantes sobre los mecanismos involucrados de sincronización y percepción sensorimotora (Thaut, Miller, & Schauer, 1998).

El análisis matemático de la tarea de sincronización debe revelar dos tipos de información: como se controla el tiempo motor y como se sincroniza la temporalización interna con un metrónomo externo (Thaut et al., 1998). Existen dos medidas que son consideradas muy relevantes en la ejecución de la tarea de sincronización: las asincronías y la variabilidad. Las asincronías, que se definen como la diferencia del tiempo entre que el estímulo ocurrió y que se llevó a cabo el movimiento de respuesta, permiten medir la diferencia de fase entre la temporalización interna y el metrónomo externo. Mientras que la variabilidad permite evaluar la estabilidad de la producción rítmica. Se puede utilizar estadística circular para describir las asincronías, calculando una resultante media y la varianza circular para estudiar la sincronización del sujeto con el metrónomo (B. H. Repp, 2005).

En tareas de reproducción rítmica guiada por un metrónomo, los humanos usualmente tienen asincronías promedio negativas, en especial para estímulos auditivos (BrunoH. Repp & Penel, 2004). Lo que significa que están anticipando sus movimientos a la aparición del estímulo. En cambio, los monos han mostrado tener asincronías positivas arriba de 300 milisegundos en una tarea de SCT

(Zarco, Merchant, Prado, & Mendez, 2009). Sin embargo, en un trabajo reciente, se describió como un entrenamiento en el que el mono recibió retroalimentación inmediata sobre el tiempo de su movimiento con respecto al metrónomo en una tarea de sincronización visual, le permitió realizar movimientos con asincronías negativas (Gámez et al., 2018).

El sistema motor cortical

El sistema motor cortical incluye las áreas 4 y 6 de Brodmann las cuales consisten de la corteza motora primaria, así como las áreas premotoras, entre las que se encuentran el área motora suplementaria y pre-suplementaria (S. Geyer, Matelli, Luppino, & Zilles, 2000). En el cerebro del mono, la corteza motora primaria (área 4 de Brodmann) se localiza inmediatamente anterior al surco central. Mientras que las otras áreas motoras (área 6 de Brodmann) se encuentran rostrales a la motora primaria y pueden subdividirse en tres grupos: la corteza premotora medial (áreas F3 y F6), la corteza premotora dorsolateral (áreas F2 y F7) y la corteza premotora ventrolateral (áreas F4 y F5).

Corteza motora primaria

La corteza motora primaria se localiza en el giro pre-central inmediatamente rostral al surco central. Esta corteza es agranular, pues no cuenta con la capa IV cortical (Chouinard & Paus, 2006). La corteza motora primaria está involucrada principalmente en controlar los parámetros cinemáticos y dinámicos de los movimientos voluntarios, mientras que las otras áreas premotoras están más relacionadas con la preparación de los movimientos voluntarios en respuesta a señales externas e internas (Cheney, 1985).

En el siglo XIX Fritsch y Hitzig demostraron que la estimulación eléctrica de áreas específicas de la corteza de diferentes mamíferos anestesiados provocaba movimientos de partes contralaterales de sus cuerpos. Al estimular sitios cercanos de la corteza se generaban movimientos en partes cercanas del cuerpo (Fritsch & Hitzig, 2009). Pero no fue hasta mediados del siglo XX donde por estimulación eléctrica de baja intensidad en la corteza motora primaria se creó un mapa somatotópico de la relación de movimientos con sitios específicos de la corteza(W. Penfield & Rasmussen, 1950; Wilder Penfield & Boldrey, 1937; Woolsey et al., 1952). Se ha comprobado la existencia de este mapa somatotópico, donde la cabeza, las extremidades superiores y las extremidades inferiores tienen representaciones secuenciales y en gran medida segregadas, organizadas desde la parte ventral, lateral y medial respectivamente (Lemon, Roger, 1988). Sin embargo, existe un sobrelape importante entre un área que controla una parte más específica del cuerpo, como puede ser un dedo de una mano, y otros sitios que controlan otras áreas específicas (Schieber, 2001).

La estructura columnar es una característica importante de varias áreas corticales como la corteza visual primaria (Hubel & Wiesel, 1959) y la corteza sensorial (Mountcastle, 1957). Sin embargo, a pesar de que se han hecho diversos intentos de encontrar una estructura espacial en las propiedades funcionales de las neuronas en la corteza motora primaria, no se ha logrado obtener

evidencia contundente de que esta exista aun cuando existen similitudes en la estructura de esta corteza con otras áreas corticales (Hatsopoulos, 2010). Sin embargo, La corteza motora primaria se caracteriza por tener la mayor concentración de neuronas gigantes de Betz. Los axones de la capa V de la corteza motora proyectan, a través del tracto corticoespinal, a la asta ventral de la medula espinal. La mayoría de las fibras corticoespinales decusan en la decusación piramidal. Las fibras corticoespinales hacen conexiones monosinápticas con las neuronas motoras e interneuronas de la medula espinal (Kandel, Schwartz, & Jessell, 1991).

La información de la corteza motora primaria es modulada por información sensorial ascendente, así como por la actividad de otras regiones motoras de la corteza, el cerebelo y los ganglios basales. Mientras los ganglios basales juegan un papel crucial en la toma de decisiones y en el control motor. Por medio de la vía directa, promoviendo el movimiento, y la vía indirecta, inhibiendo patrones motores no deseados (Grillner & Robertson, 2015). El cerebelo por su parte, se encarga de realizar ajustes para adaptar los comandos motores a las condiciones de la musculatura a través del núcleo ventrolateral del tálamo, así como los núcleos motores en el tallo cerebral (Kandel et al., 1991).

Cortezas premotoras

Las cortezas premotoras se dividen en la corteza premotora ventral (PMv), que a su vez se divide en una región caudal (F4) y una rostral (F5); la corteza premotora dorsal (PMd), que de igual manera se subdivide en una región caudal (F2) y otra rostral (F7); y finalmente en la corteza premotora medial, que a su vez se subdivide en el área motora suplementaria propiamente (SMA o F3) y en el área motora pre-suplementaria (pre-SMA o F6) (Mendoza & Merchant, 2014). La mayoría de las cortezas premotoras tienen conexiones directas con M1. Sin embargo, la PMd en su región rostral, así como pre-SMA no cuentan con proyecciones directas a la corteza motora primaria. Los axones del tracto corticoespinal desde la corteza motora primaria y otras áreas premotoras terminan en interneuronas de las láminas intermedias de la espina dorsal (He, Dum, & Strick, 1993). Únicamente la corteza motora primaria tiene neuronas con axones que terminan directamente en neuronas motoras espinales en la parte ventral y lateral del cuerno ventral espinal. M1, PMdc, SMA, PMvc y PMvr tiene conexiones reciprocas con regiones específicas de la corteza parietal, mientras que la pre-SMA y la PMdr reciben conexiones de las cortezas prefrontales. Las cortezas PMdc, SMA, PMvc y PMvr tienen conexiones con M1, a diferencia de la pre-SMA y la PMdr (Mendoza & Merchant, 2014).

La corteza premotora medial (MPC) se encuentra rostral a la corteza motora primaria y principalmente ocupa la superficie mesial del hemisferio (Kandel et al., 1991). Tiene una organización topográfica, aunque no es tan clara como la de M1. La parte caudal de la SMA (SMA propiamente) tiene proyecciones directas a M1 y a la medula espinal, mientras que la parte rostral (pre-SMA) no proyecta directamente a M1, pero recibe proyecciones de la corteza prefrontal y las áreas motoras del cíngulo (Mendoza & Merchant, 2014). Ambas regiones tienen conexiones con las otras áreas premotoras. SMA recibe entrada talámica desde el núcleo VLo y VLm, mientras que pre-SMA recibe entrada talámica desde VApc (Jun Tanji, 1994). Ambas áreas reciben proyecciones disinápticas del núcleo dentado del cerebelo y del segmento interno del globo pálido (Akkal, Dum, & Strick, 2007). Finalmente, ambas áreas proyectan a los ganglios basales. Estudios en humanos y otros primates muestran la importancia de la SMA en tareas motoras que demandan el uso de la

memoria motora, así como en la organización temporal del movimiento, en especial en la realización secuencial de múltiples movimientos (Jun Tanji, 1994). Nuestro grupo he reportado que en el SMA existe una representación del orden secuencial y la estructura temporal de la producción de intervalos temporales durante tareas de sincronización (Hugo Merchant et al., 2011).

Premotora ventral rostral (F5)

La corteza F5 cuenta con una representación de la mano y la boca (Ferrari, Gerbella, Coudé, & Rozzi, 2017; G Rizzolatti et al., 1988). La corteza PMv ha sido asociada con la transformación de la información de un objetivo en el espacio, a la información motora necesaria para alcanzarlo (Kurata & Hoshi, 2002). Se divide en tres regiones F5c, F5p y F5a.

El área F5p contiene neuronas que codifican movimientos de la mano hacia un objetivo, por ejemplo movimientos de aprehensión de un objeto con la mano, además de neuronas que responden a la vista de objetos (Jeannerod, Arbib, Rizzolatti, & Sakata, 1995; Raos, Umiltá, Gallese, & Fogassi, 2004).

El área F5c tiene campos relacionados con el movimiento de la mano y la cara/boca (Gentilucci et al., 1988) . En esta área se describió por primera vez un sistema de neuronas espejo, las cuales incrementan su actividad durante la ejecución de ciertas acciones, así como cuando se observa a alguien más realizando la misma acción (Giacomo Rizzolatti, Fadiga, Gallese, & Fogassi, 1996). Una hipótesis es que este sistema de neuronas espejo es la base de la imitación y la comprensión de las consecuencias de las acciones motoras (Giacomo Rizzolatti, Fogassi, & Gallese, 2001). Se han descrito neuronas espejo que se activan ante acciones dirigidas a un objetivo de la mano/brazo, así como otras neuronas espejo que tienen que ver con movimientos de la boca (Giacomo Rizzolatti & Craighero, 2004).

Finalmente, estudios multimodales de la arquitectura del área F5a muestran que ésta es una región transicional entre F5 y la corteza frontal (Belmalih et al., 2009). El área F5a parece estar especialmente activa durante la aprehensión de objetos tridimensionales guiada por la vista (Theys, Pani, van Loon, Goffin, & Janssen, 2012).

De manera general, el área F5 está conectada con el campo de la mano en la corteza motora primaria, tiene proyecciones al tallo cerebral y a la medula espinal, además de a las áreas parietales AIP, PFG y SII. El circuito AIP-F5 juega un papel crucial en las transformaciones viso-motora para la acción de aprehensión (G. Luppino, Murata, Govoni, & Matelli, 1999) .

Premotora ventral caudal (F4)

La región caudal del área premotora ventral tiene una representación de los movimientos del brazo, cuello, cara y boca (Gentilucci et al., 1988). Esta área está involucrada en la percepción del espacio peri-personal, así como en la transformación de posiciones específicas de este espacio en movimientos del brazo, cuello y orofaciales (Giacomo Rizzolatti, Fogassi, & Gallese, 2002). Las neuronas en esta área se activan durante la ejecución de movimientos motores del brazo dirigidos a un objetivo, tales como movimientos de alcance o el movimiento para llevar algo a la boca, así como durante movimientos orofaciales (Giacomo Rizzolatti et al., 2002). De acuerdo a sus

respuestas sensoriales, las neuronas en F4 se pueden dividir en somatosensoriales, visuales y bimodales (Fogassi et al., 1996). Siendo estás últimas las más abundantes. Los campos receptivos táctiles abarcan áreas amplias y se encuentran asociados a la cara, el brazo y la parte superior del cuerpo. Las neuronas bimodales tienen campos receptivos visuales tridimensionales limitados al espacio peri-personal (Stefan Geyer, Luppino, & Rozzi, 2012). Los campos receptivos visuales de la mayoría de estas neuronas están relacionados con los campos receptivos táctiles y su relación no cambia con la posición de los ojos (Fogassi et al., 1996).

F4 es parte del circuito cortical que incluye área ventral intra-parietal (VIP), el sector intra-parietal del área PE (PEip) y la corteza somatosensorial secundaria (SII) (Giacomo Rizzolatti et al., 2002). El área VIP cuenta con neuronas visuales y bimodales con propiedades funcionales similares a las neuronas de F4. VIP junto con F4 forman el circuito parietofrontal encargado de codificar el espacio peripersonal y en transformar la localización de un objeto en los movimientos necesarios para alcanzarlo.

Premotora dorsal caudal (F2)

El área F2 tiene una representación somato-tópica de la pierna (parte dorsal) y el brazo (parte ventral) (He et al., 1993; Raos, Franchi, Gallese, & Fogassi, 2003). En esta área, se pueden encontrar neuronas que responden a estímulos sensoriales tanto propioceptivos como táctiles y visuales. Utilizando una tarea donde se da una señal de instrucción seguida por una señal de inicio del movimiento después de un periodo de retraso, se encontraron tres grupos de neuronas distribuidos en un gradiente de la zona rostral a la caudal: neuronas que presentan una actividad fásica inmediatamente después de la señal de instrucción; neuronas que muestran actividad sostenida durante el periodo de espera; y neuronas que incrementan su actividad principalmente entre la señal de inicio del movimiento y el movimiento en si (S. Geyer et al., 2000; Johnson, Ferraina, Bianchi, & Caminiti, 1996). Las neuronas relacionadas a la tarea están involucradas en codificar los comandos motores asociados a una señal simbólica, tanto en la ejecución como la observación de la tarea. Esta actividad se ha asociado al ensayo mental de las acciones motoras y sus consecuencias (Cisek & Kalaska, 2004).

La corteza F2 recibe proyecciones de las áreas PEc, PEip, MIP, V6A, (Giuseppe Luppino, Rozzi, Calzavara, & Matelli, 2003; Matelli, Govoni, Galletti, Kutz, & Luppino, 1998). Las áreas parietales conectadas con F2 son parte del sistema parieto-frontal, involucrado en la guía sensorial de los movimientos de alcance del brazo, con neuronas que se activan durante la ejecución de movimientos de alcance y que además son responsivas a estímulos visuales y somatosensoriales (Burnod et al., 1999).

Premotora dorsal rostral (F7)

En humanos, el campo ocular suplementario (SEF) se localiza en la frontera entre F3 y F6. Sin embargo, en los macacos esta área se encuentra en la parte más dorso medial del área F7 (Nachev, Kennard, & Husain, 2008). Las neuronas del SEF responden a estímulos visuales y acústicos, además de que se encuentran activas durante movimientos oculares de seguimiento y sacádicos (Stuphorn, Brown, & Schall, 2010). Se sabe que el SEF está involucrado en codificar movimientos sacádicos relativos a un marco de referencia centrado en el objeto. Aunque las neuronas del SEF no controlan

directamente el inicio de las sácadas, pueden señalizar la producción de errores, la anticipación y la recepción de refuerzo, así como la presencia de conflicto (Stefan Geyer et al., 2012).

El SEF se encuentra fuertemente conectado con el campo ocular frontal (FEF), pero también recibe proyecciones de las áreas dorsales y ventrales de la corteza dorsolateral prefrontal. Además de proyectar al colículo superior, a la región oculomotora del núcleo caudado, al putamen, al tálamo y a núcleos del tallo cerebral (Huerta & Kaas, 1990).

Área motora suplementaria (F3)

El área F3 se encuentra directamente rostral a la representación de la pierna en F1 (ver Figura 2). Por medio de micro estimulación se encontró que el área F3 tiene una organización somatotópica donde la representación de la pierna se encuentra en la región caudal, el brazo en el área central y los movimientos orofaciales en la parte más rostral (G. Luppino, Matelli, Camarda, Gallese, & Rizzolatti, 1991). Los movimientos evocados fueron en su mayoría complejos, involucrando dos o más articulaciones, además de que se requirió una corriente mayor que la necesaria para evocar movimientos en M1 (G. Luppino et al., 1991). Muchas neuronas en F3 tienen características similares a las de F1, con respuestas asociadas al tiempo de inicio de un movimiento y muestran un incremento en su actividad durante la preparación del movimiento. Sin embargo, también se ha descrito que las neuronas de F3 son importantes para la ejecución de secuencias motoras memorizadas, donde neuronas de esta área se activan en relación a secuencias específicas de movimientos aprendidos (Mushiake, Inase, & Tanji, 1991). Además, lesiones de esta área en humanos provocan deficiencias en la habilidad de realizar movimientos secuenciales (Laplane, Talairach, Meininger, Bancaud, & Orgogozo, 1977).

F3 tiene conexión con la corteza cingulada, la región agranular de la corteza insular, las áreas parietales PE, PF, PG, SII, así como con F1 y con las otras premotoras dorsales F2, F7 y ventrales F4 y F5, además de F6 (Giuseppe Luppino, Matelli, Camarda, & Rizzolatti, 1993) . F3 proyecta al putamen y recibe entrada talámica de los núcleos ventral lateral pars oralis (VLo), ventral posterios lateral pars oralis (VPLo) y ventral lateral pars caudalis (VLc), así como de las partes más caudales de VPLo y VLc (Matelli & Luppino, 1996). Siendo F3 parte del circuito motor de los ganglios basales y un circuito cerebelar que se origina en los sectores dorso-rostrales del dentado y el núcleo interpositus (Matelli & Luppino, 1996). De manera global, las conexiones de F3 sugieren que está área está involucrada en el control motor, usando información de la posición de las extremidades para preparar de manera predictiva la estabilización de una referencia postural egocéntrica durante el movimiento (Massion, 1992).

Área motora pre-suplementaria (F6)

El área F6 es la parte rostral de la corteza premotora medial (ver Figura 2). Es difícilmente excitable por microestimulación. Para evocar respuestas motoras se requieren corrientes más altas y trenes de estimulación más largos, que genera movimientos complejos y principalmente restringidos al brazo (G. Luppino et al., 1991). Casi todas las entradas a F6 provienen de áreas pre-rolándicas en especial de las áreas premotoras F7 y F5, la corteza prefrontal (área 46), así como del cíngulo (24c) (Giuseppe Luppino et al., 1993). En comparación con otras cortezas premotoras, las conexiones con el lóbulo parietal son limitadas, con conexiones a las áreas PFG y PG del banco lateral del surco

intraparietal, además de tener conexiones con la ínsula (Giuseppe Luppino et al., 1993). F6 es objetivo de proyecciones talámicas del núcleo ventral anterior pars parvocellularis (VApc), así como del área X de Olszeweski. Por lo tanto, F6 recibe entradas principalmente del llamado circuito "complejo" de los ganglios basales y del circuito cerebelar que se origina en los sectores ventrocaudal del dentado y del núcleo interpositus.

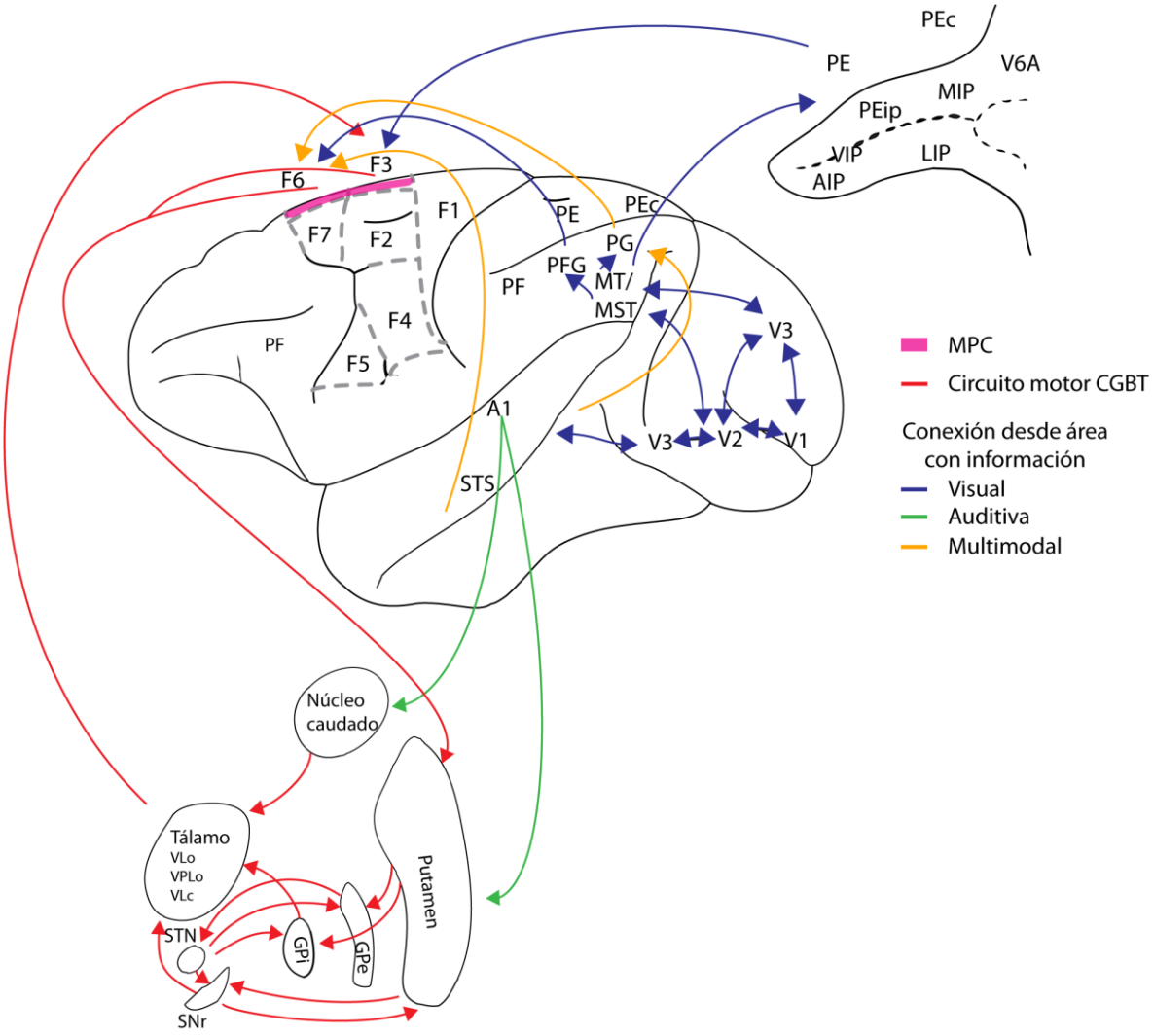

Figura 2 Vista lateral del cerebro del mono Rhesus

Se muestra la localización de la corteza premotora medial (MPC, en magenta), formada por F3 y F6, con respecto a las otras cortezas premotoras (F2, F4, F5, F7) y a la corteza motora primaria (F1) (G. Luppino & Rizzolatti, 2000). En rojo se muestran las conexiones de F3 y F6 con el circuito motor CGBT (Matelli & Luppino, 1996; Mendoza & Merchant, 2014; Nachev et al., 2008), así como algunos posibles caminos del flujo de información visual y auditiva hacia la MPC (flechas azules para áreas con información visual, flechas verdes para áreas con información auditiva y flechas amarillas para áreas con información multimodal) (Jürgens, 1984; Lima, Krishnan, & Scott, 2016; Giuseppe Luppino et al., 1993; Mesulam, Hoesen, Pandya, & Geschwind, 1977).

Se considera que está región tiene que ver con funciones motoras complejas. Se le ha implicado tanto en la ejecución, como en la imaginación de la ejecución de movimientos del brazo, mano y dedos (Decety, Philippon, & Ingvar, 1988; Stephan et al., 1995), generación del lenguaje (Binder

et al., 1997), activación de representaciones motoras durante la percepción e imaginación auditivas (Lima et al., 2016), memoria de trabajo (Petit, Courtney, Ungerleider, & Haxby, 1998), aprendizaje y ejecución de secuencias de movimientos (Sakai et al., 1998; Jun Tanji & Shima, 1994), percepción y categorización temporal (Françoise Macar, Coull, & Vidal, 2006; Mendoza, Méndez, Pérez, Prado, & Merchant, 2018), acciones generadas internamente (Rosenberg-Katz et al., 2012) y actualización de planes motores (Matsuzaka & Tanji, 1996; Shima, Mushiake, Saito, & Tanji, 1996). En la MPC hay neuronas que responden a estímulos auditivos, visuales y táctiles. Ya sea de manera exclusiva a una modalidad o a combinaciones de dos modalidades. Siendo estás últimas las más comunes, en especial para la combinación visual-auditivo (J Tanji & Kurata, 1982). Las latencias medias de respuestas neuronales motoras en la PMC a estímulos es de 128ms para la modalidad visual, 108ms para la modalidad auditiva y 68ms para la modalidad táctil (J Tanji & Kurata, 1982). La latencia de respuestas neuronales motoras asociadas a estímulos es aproximadamente 20 ms más corta en la MPC que en F1 (J Tanji & Kurata, 1982). Con excepción de la información propioceptiva, la información sensorial llega a la PMC sólo de manera indirecta (Jürgens, 1984). La información visual y auditiva pueden llegar a la PMC (ver Figura 2) desde el surco temporal superior (STS), de áreas parietales (PE, PFG y PG), así como de manera indirecta desde otras áreas premotoras y prefrontales (Lima et al., 2016; Giuseppe Luppino et al., 1993).

Estudios de resonancia magnética funcional (fMRI) y tomografías de emisión de positrones (PET) han involucrado a la MPC en un circuito de medición temporal para la percepción y reproducción de intervalos únicos (J. T. Coull, Vidal, Nazarian, & Macar, 2004; F. Macar et al., 2002; Françoise Macar et al., 2006) y rítmicos (Lewis, Wing, Pope, Praamstra, & Miall, 2004). Además, en un estudio en humanos con lesiones unilaterales de la MPC, se encontró que los sujetos presentaban dificultad para generar secuencias rítmicas de memoria (Halsband, Tanji, & Freund, 1993).

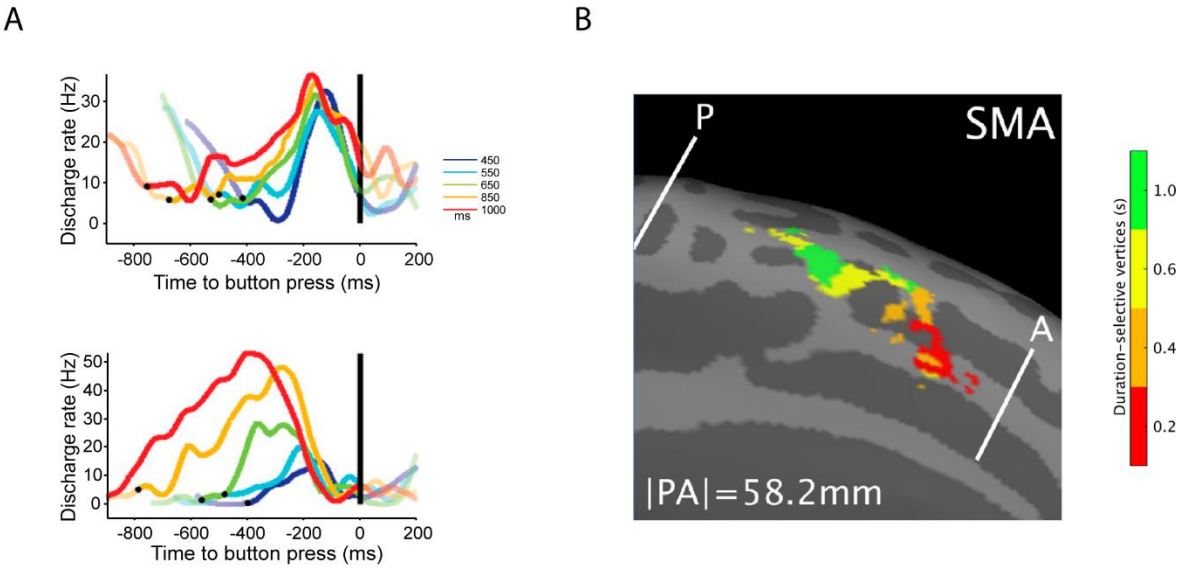

Figura 3 Representación del tiempo en la MPC

***A**, Promedio de la función de densidad de espigas alineada al movimiento siguiente durante una tarea de SCT, para neuronas de tiempo relativo (arriba) y acumuladores de tiempo (abajo). Los colores indican la duración del intervalo blanco. Las neuronas de tiempo relativo disminuyen la pendiente de su actividad con intervalos más largos, mientras que las neuronas acumuladores de tiempo modulan la tasa de disparo máxima que alcanzan con el intervalo blanco (tomado y modificado de Hugo Merchant et al., 2011). **B**, mapa cronotópico en la MPC obtenido con fMRI durante una tarea de*

discriminación temporal. Se muestran los grupos de voxeles proyectados en la superficie del cerebro, clasificados de acuerdo a un procedimiento del "ganador-toma-todo" basado en mapas-t estadísticos, como la respuesta máxima a cada una de las cuatro duraciones del primer estímulo (tomado y modificado de Protopapa et al., 2019).

Por otro lado, registros electrofisiológicos en F6 han demostrado que hay neuronas cuya actividad está relacionada a la medición del tiempo en tareas de producción de intervalos (Hugo Merchant, Pérez, Zarco, & Gámez, 2013; Hugo Merchant et al., 2011; Mita, Mushiake, Shima, Matsuzaka, & Tanji, 2009). Estas neuronas se pueden agrupar de acuerdo a su perfil de activación (ver Figura 3A) durante una tarea de sincronización-continuación como de tiempo relativo, acumuladores de tiempo, así como *swinging cells* (Hugo Merchant et al., 2011). Además, un grupo de neuronas están sintonizadas la duración de los intervalos, presentando una actividad preferente para una duración particular (Hugo Merchant, Pérez, et al., 2013; Mita et al., 2009). Recientemente, en un estudio de fMRI en humanos, donde los sujetos tenían que decidir cual estímulo duraba más entre dos estímulos visuales cuya duración estaba en los cientos de milisegundos, se encontró un mapa cronotópico (ver Figura 3B). Este mapa cubría desde F3 hasta F6, donde las áreas que tenían una actividad preferente para intervalos cortos se encontraban anteriores a las que preferían intervalos largos (Protopapa et al., 2019).

Modelos de la medición del tiempo en la corteza

El tiempo es una dimensión esencial en los modelos de control motor. Sin embargo, no existen muchos modelos de temporización. Uno de los modelos más aceptado por muchos años fue el de un marcapasos central (Gibbon, Malapani, Dale, & Gallistel, 1997). Sin embargo, no se ha encontrado evidencia biológica contundente de la existencia de este circuito (Buonomano & Laje, 2010). En los últimos años ha cobrado fuerza el modelo de un reloj poblacional, donde la información temporal está distribuida en la actividad de un grupo de neuronas que sigue patrones reproducibles.

Modelos de acumulador

Marcapasos central

Este modelo está basado en la existencia de un circuito que funciona como un reloj central, donde este generador de ritmos emite pulsos con regularidad, los cuales son almacenados en un acumulador (Gibbon et al., 1997). El valor del acumulador se almacena en una memoria que puede ser usada para comparar este valor con el tiempo en el que se recibe algún tipo de retroalimentación. En este modelo la propiedad escalar surge de la diferencia entre la comparación entre el valor del acumulador y una muestra que es tomada de una distribución aprendida de duraciones que se presentaron anteriormente. Por lo tanto, el error de acumulación es proporcional a la duración medida (Buhusi & Meck, 2005).

Este modelo tiene la ventaja de tener etapas claramente marcadas: reloj, memoria y decisión. Lo que permite buscar áreas cerebrales asociadas con cada una de estas etapas en específico (Gibbon et al., 1997). También es fácil generar predicciones que se pueden poner a prueba en modelos biológicos, como pueden ser manipulaciones farmacológicas dirigidas a las diferentes fases del modelo (Meck, 1996). Aun cuando el modelo ha tenido éxito estableciendo predicciones, no se ha podido demostrar de manera contundente los mecanismos neurofisiológicos que podrían ser la base de su funcionamiento (Buonomano & Laje, 2010).

Actividad en rampa

Un patrón de actividad de neuronas corticales que codifican de manera robusta información temporal es la actividad en rampa, que puede ser definida como incrementos o decrementos consistentes en la tasa de disparo en el tiempo. Registros en diferentes áreas del cerebro sugieren la existencia de neuronas que representan el tiempo al aumentar o disminuir su actividad en forma de rampa (Reutimann, 2004), está actividad es iniciada por un evento y llega a su pico en el tiempo esperado de un segundo evento. Si se cambia el intervalo entre ambos eventos, la rampa modifica su pendiente para adaptarse al nuevo tiempo. Información temporal precisa puede ser codificada en la pendiente y en la actividad máxima de la rampa, incrementando la variabilidad en intervalos más largos siendo un posible sustrato de la propiedad escalar (Narayanan, 2016).

Existen diversos modelos del posible sustrato de la actividad en rampa. Uno de estos modelos, se enfoca en las propiedades biofísicas de una neurona única. Basado en un asa de retroalimentación positiva entre la tasa de disparo, el flujo de Ca^{2+} hacia el interior de la célula y la activación de una corriente de entrada de Ca^{2+} (Durstewitz, 2003).

Deriva-difusión

En un modelo de deriva-difusión (DDM), existe un acumulador a partir del cual se toman las decisiones al llegar un umbral al del tiempo acumulado más ruido. El valor del acumulador se puede ver como la posición de una partícula en el espacio. Cuando la partícula cruza cierto umbral preestablecido, el comportamiento se ejecuta (Hugo Merchant & Averbeck, 2017).

El modelo del acumulador como una caminata aleatoria con una deriva puede ser descrito como:

$$\varphi(t) = \varphi(t-1) + w\Delta t + \varepsilon(t),$$

Donde la señal $\varphi(t)$ inicia en 0 al empezar a medir el intervalo de tiempo, sirve como una representación interna del tiempo transcurrido y toma un valor máximo de 1 cuando se ha completado el intervalo a medir; $\varepsilon(t)$ es el ruido; w es la tasa de deriva; y Δt es la longitud del paso temporal usado en la simulación (Luzardo, Ludvig, & Rivest, 2013).

En un DDM, una serie de muestras tomadas de una distribución estacionaria se integran en el tiempo generando una trayectoria de caminata aleatoria. Este tipo de modelos se ha considerado como un posible sustrato de la medición de intervalos de tiempo. Donde la respuesta en rampa de

las neuronas es la señal temporal y la actividad neuronal espontánea es considerada la evidencia ruidosa del proceso de acumulación del DDM (Simen, Balci, deSouza, Cohen, & Holmes, 2011). La media de la distribución de la cual fueron tomadas las muestras es la tasa de deriva, mientras que la varianza de la distribución es la tasa de difusión.

Osciladores

Otro modelo está basado en la hipótesis de que la medición del tiempo surge de una serie de elementos poblacionales que oscilan a diferentes frecuencias. Este modelo se basa en neuronas que funcionan como detectores de patrones síncronos entre los diferentes osciladores (Buonomano & Laje, 2010) . Un ejemplo de este modelo de osciladores, se basa en la activación coincidente de neuronas espinosas medianas en los ganglios basales por osciladores neuronales corticales con una actividad rítmica y sincrónica (Salinas & Sejnowski, 2001) . Los osciladores corticales se sincronizan al iniciar un ensayo y oscilan a una frecuencia fija. Cambios que dependen de la experiencia en la transmisión cortico-estriatal son los que permiten a las neuronas en el estriado detectar los patrones de activación de los osciladores corticales cuando hay un evento reforzador como la recompensa o retroalimentación (Salinas & Sejnowski, 2001).

Existen diferentes modelos matemáticos que se pueden usar para representar este modelo. Un posible modelo está descrito por la ecuación diferencial:

$$\frac{dz}{dt} = z(\alpha + i\omega + (\beta + i\delta)|z|^2) + c\ s(t)$$

Donde *z* es una variable compleja que representa las oscilaciones a través del tiempo. Mientras que los parámetros del sistema son: α es un parámetro de bifurcación, β es un parámetro de saturación no lineal, ω es la frecuencia natural en radianes, y δ es el parámetro de sintonización de frecuencia. Mientras que *c*, la fuerza de la conexión, representa la influencia del estímulo en el oscilador (Large & Snyder, 2009).

Señal poblacional

Finalmente, un tercer tipo de modelo se basa en la hipótesis de que el tiempo es una característica emergente de la dinámica de toda red neuronal. De tal manera, que la evolución del estado de la red, donde el estado instantáneo se representa como un vector poblacional con la actividad de cada una de las neuronas de la población, puede ser usado para medir el tiempo por neuronas especializadas, que son las salidas del circuito y que han sido entrenadas para reconoces patrones específicos en la actividad poblacional (Buonomano & Laje, 2010).

El modelo dice que el tiempo es una propiedad emergente de la interacción entre muchas unidades, de tal manera, que es capaz de medir escalas de tiempo mucho mayores que la constante de tiempo de las neuronas individuales (Buonomano & Laje, 2010).

Uno de los primeros modelos poblacionales que se propuso se basó en células de Purkinje del cerebelo. Las cuales miden el tiempo, desde cientos de milisegundos hasta los segundos, al ser sensibles a patrones específicos de la actividad de la población de células granulares (Buonomano & Mauk, 1994).

El cerebro como un sistema dinámico

Un sistema dinámico consiste en un conjunto de variables y una regla que describe su evolución en el tiempo. Las variables se denominan variables de estado, pues representan los diferentes valores que describen el comportamiento del sistema en un estado dado. La evolución del sistema se puede representar como una ecuación diferencial que describe el estado siguiente a partir del estado anterior y las entradas al sistema (Izhikevich, 2007). Además, el sistema dinámico puede ser representado en un espacio fase, que es una representación gráfica de la evolución de los estados que toma el sistema en el tiempo. Si el sistema tiene N variables de estado, su estado fase será de N dimensiones. El estado del sistema en un instante del tiempo corresponderá a un único punto en este espacio (Breakspear, 2017). De tal manera, que un sistema dinámico que puede ser descrito por un vector de variables de estado **x** y una función f que describe su evolución en el tiempo se puede expresar como:

$$\dot{x}_t = f(x_t, parámetros, ruido)$$

Para una gran cantidad de funciones de este tipo existe un conjunto de soluciones especiales de f llamadas atractores (Schoner & Kelso, 1988). Un atractor es estable si todas las soluciones cercanas en el espacio fase convergen en el tiempo a la solución del atractor.

Existen diferentes tipos de atractores, siendo un punto fijo, una constante, el más sencillo. Cuando las soluciones oscilan entre un conjunto de valores se conoce como un atractor de tipo ciclo límite (Boeing, 2016). Además, existen otros tipos de atractores más complejos, como pueden ser los llamados atractores extraños, los cuales aparecen en los sistemas caóticos (Boeing, 2016). En un sistema pueden coexistir diferentes tipos de atractores, lo que se llama multiestabilidad (Feudel, Physics, & Systems, 2008). Se ha propuesto que la multiestabilidad puede ser un mecanismo usado por el sistema nervioso, para representar diferentes objetos de la percepción por una misma red neuronal, la cual sigue una dinámica diferente a partir de una señal de entrada distinta (Feudel et al., 2008).

En lugar de decodificar respuestas neuronales individuales y sus correlatos con parámetros de una tarea, el enfoque del estudio del cerebro como un sistema dinámico busca estudiar la evolución de la actividad neuronal en términos de las reglas por las cuales el estado actual cambia al estado siguiente (Shenoy, Sahani, & Churchland, 2013). Los desarrollos en la tecnología que permiten registros simultáneos de cientos de neuronas, así como el incremento del poder computacional y el desarrollo de algoritmos de análisis avanzados multivariables de la actividad de grandes poblaciones neuronales han posibilitado nuevos análisis desde un marco de trabajo de sistemas dinámicos (Cunningham & Yu, 2014; Shenoy et al., 2013).

El paradigma de sistemas dinámicos establece tres condiciones que debe cumplir un sistema neuronal para poder ser estudiado bajo este paradigma: en primer lugar, las condiciones iniciales del sistema deben determinar en gran medida la subsecuente evolución del mismo; segundo, la actividad de las neuronas no deben estar únicamente relacionadas a las entradas y salidas del sistema, también debe relacionares con el procedimiento que se está llevando a cabo; por último, diferentes procesamientos deben seguir diferentes trayectorias que no se superponen (Pandarinath et al., 2018).

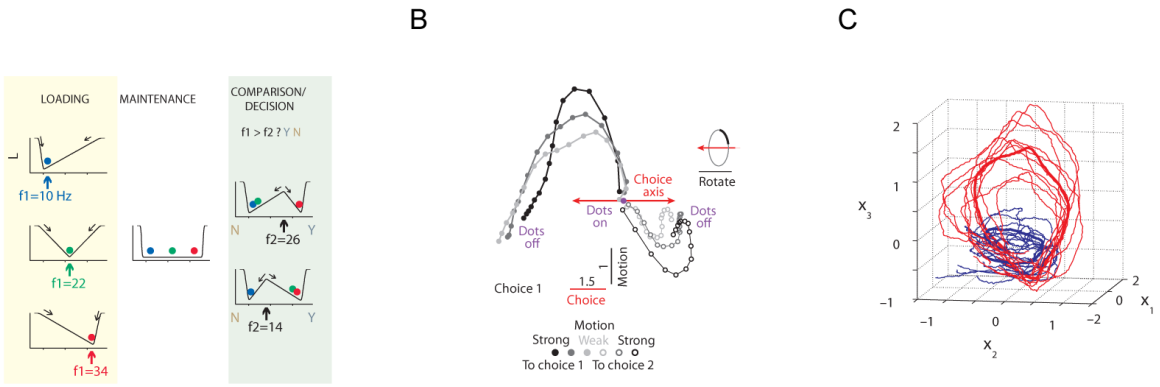

Figura 4 Atractores en sistemas dinámicos de poblaciones neuronales

***A**, algoritmo dinámico de una dimensión para la discriminación de dos estímulos en la corteza prefrontal de monos Rhesus. El valor de la variable de estado (eje horizontal) es usado para representar tanto la memoria del primer estímulo, así como la salida del proceso de decisión. El modelo se basa en un conjunto de atractores fijos que representan la información sensorial y la salida de la decisión (tomado de Machens, Romo, & Brody, 2005). **B**, Dinámica de las respuestas poblacionales en la corteza prefrontal durante una tarea donde monos fueron entrenados a seleccionar e integrar información sensorial ruidosa para la toma de decisiones. Las respuestas en la tarea se representan como puntos en el espacio de estado. El eje horizontal representa las dos posibles respuestas y se comporta como un atractor de línea (tomado de Mante, Sussillo, Shenoy, & Newsome, 2013). **C,** Trayectorias neuronales obtenidas por análisis de factores de la actividad de grupos neuronales en la corteza parietal posterior (PPC) de ratones en una tarea de selección en un laberinto T. Cada línea delgada corresponde a un ensayo individual y las líneas gruesas corresponden a las medias para ensayos correctos, en rojo ensayos en los que el ratón se dirigió hacia la derecha y en azul cuando lo hizo hacia la izquierda. La dinámica poblacional muestra atractores de ciclo límite durante los ensayos (tomado de Harvey, Coen, & Tank, 2012).*

Se ha descrito la dinámica de poblaciones neuronales en diferentes regiones del cerebro bajo distintos paradigmas experimentales, donde se han encontrado dinámicas basadas en diferentes tipos de atractores (ver Figura 4). Por ejemplo, la actividad de neuronas en la corteza prefrontal de monos realizando una tarea de discriminación de un estímulo vibratorio, se puede modelar como una red neuronal de inhibición mutua, donde la memoria de trabajo y el proceso de toma de decisión se comportan como un sistema dinámico con atractores de punto fijo (Machens et al., 2005). En cambio, la actividad poblacional de la corteza prefrontal de monos, durante una tarea de discriminación visual, presenta un proceso dinámico que se desenvuelve a nivel poblacional gobernado por un atractor lineal que representa las opciones entre las que elige el mono (Mante et al., 2013). Mientras tanto, en la corteza parietal posterior se encontró que diferentes secuencias de neuronas se activaban de acuerdo a una decisión perceptual sobre la dirección que tomaba un ratón en un laberinto en T. La dinámica poblacional durante esta tarea estuvo dominada por dos

diferentes atractores de ciclo límite a los que tendía el sistema de acuerdo a la dirección seleccionada por el ratón (Harvey et al., 2012).

En sistemas con una gran cantidad de dimensiones, puede ser difícil interpretar la información y relacionarla a variables específicas. Una técnica comúnmente usada en estos casos es la reducción dimensional. Este método permite determinar las variables latentes existentes en un conjunto de datos multidimensional. Por ejemplo, la reducción dimensional permite proyectar la actividad multidimensional, compuesta por la actividad individual de un grupo de neuronas, a un espacio con un menor número de dimensiones para generar una superficie multidimensional estable o *manifold* (Cunningham & Yu, 2014). De hecho, estudios recientes han reconstruido parámetros claves de diversas tareas conductuales a partir de la información de la dinámica poblacional de estados neuronales sobre una reducción dimensional (Kobak et al., 2016; Murray & Escola, 2017; Rossi-Pool et al., 2017, p.)

Reducción dimensional por análisis de componentes principales (PCA)

La reducción de dimensiones usualmente se aplica en situaciones donde se tienen un cierto número de variables medidas, pero se sospecha que estas variables covarían de acuerdo a un número menor de variables explicativas o variables latentes que no son aparentes en los datos originales (Cunningham & Yu, 2014). La varianza en los datos que no es capturada por las variables latentes se considera ruido. Diversos estudios han utilizado técnicas de reducción dimensional para interpretar como es que las poblaciones de neuronas codifican información, como cambian su actividad durante el aprendizaje o para buscar restricciones causales en la actividad de redes neuronales (Sadtler et al., 2014).

El análisis de componentes principales (PCA) es una técnica de análisis de estadística multivariable para la compresión y la extracción de características de conjuntos de datos (Zhou et al., 2009). PCA busca una combinación lineal de las variables originales de tal manera que las variables derivadas capturen la mayor cantidad de varianza de los datos originales (Zhou et al., 2009). El PCA se puede usar como una técnica efectiva de reducción dimensional, proyectando los datos originales en un nuevo espacio donde los ejes son los vectores propios (*eigenvectors*) de los datos y la magnitud de estos nuevos ejes son los valores propios (*eigenvalues*) (Tipping & Bishop, 1999). Para un conjunto de vectores de datos de *d* dimensiones $\{\boldsymbol{x_n}\}, n \in \{1, \dots, N\}$, los q ejes principales $w_j, j \in \{1, \dots, q\}$, son los ejes ortonormales en los cuales la varianza retenida es máxima. Se puede demostrar que los vectores w_j están dados por los q vectores propios (*eigenvectors*), aquellos asociados a los mayores valores propios λ_j (*eigenvalues*) de la matriz de covarianza de la muestra

$$S = \sum_n \frac{(x_n - \bar{x})(x_n - \bar{x})^T}{N}$$

, donde $\bar{x}$ es la media de la muestra, de tal manera que $Sw_j = \lambda_j w_j$. Los *q* componentes principales del vector observado x_n están dados por el vector $y_n = W^T(x_n - \bar{x})$, donde $W = (w_1, w_2, \dots, w_q)$. Las variables y_j no están correlacionadas de tal manera que la matriz de covarianza $\sum_n \frac{y_n y_n^T}{N}$ es diagonal con elementos λ_j (Tipping & Bishop, 1999).

Por otro lado, se ha propuesto que un modelo de neurona artificial puede utilizar el PCA como una regla de aprendizaje (Oja, 1982a). Donde, usando un modelo sencillo de una neurona artificial:

$$\eta = \sum_{i=1}^{n} \mu_i \xi_i$$

La salida de la neurona (η) está definida como la suma ponderada de sus pesos sinápticos (μ_i) por sus entradas (ξ_i). En este modelo, los pesos sinápticos se ajustan de acuerdo a una **regla Hebbiana de aprendizaje** definida como:

$$\Delta\mu_i = \gamma\eta(t)\xi_i(t),$$

Donde el cambio en el vector de pesos ($\Delta\mu_i$) depende de las entradas (ξ_i) y la salida de la neurona (η), modulada por el coeficiente de plasticidad (γ). Por otro lado, la **regla de aprendizaje de Oja**

$$\Delta\mu_i = \gamma\eta(t)[\xi_i(t) - \eta(t)\mu_i(t)],$$

agrega un término de olvido proporcional ($-\eta(t)\mu_i(t)$) a la **regla Hebbiana de aprendizaje**. Usando **la regla de aprendizaje de Oja**, el vector de pesos converge a uno de los vectores propios de la matriz de covarianza de la entrada (Oja, 1982b). Por lo tanto, la salida de la neurona se convierte en el primer componente principal de los datos de entrada. También se ha demostrado que es posible generalizar esta regla de aprendizaje con un circuito de neuronas paralelas capaces de converger a otros componentes principales (Sanger, 1989).

Trayectorias neuronales

Como se ha visto en secciones previas, un patrón complejo que varía en el tiempo de una población de *n* neuronas puede ser visto como una trayectoria en un espacio neuronal, donde cada neurona es una dimensión en un espacio *n*-dimensional (Buonomano & Laje, 2010). El estudio de la dinámica poblacional se puede llevar a cabo como una descripción de los parámetros geométricos que definen esta trayectoria en el tiempo. Si las trayectorias neuronales generadas siguen un camino que cambia de manera continua y que no se repite, se pueden usar para medir el tiempo (Gouvêa et al., 2015).

Por ejemplo, en la Figura 5A se muestra la actividad de 220 neuronas durante un intervalo temporal de 440ms. Esta actividad ha sido delimitada en 22 bines de tiempo de 20ms cada uno. Utilizando PCA hemos obtenido una matriz de pesos que nos permite proyectar las 220 dimensiones originales de la actividad neuronal original, a un espacio que concentre la varianza de los datos en las primeras dimensiones. En la Figura 5B se muestra la proyección de los datos en cada uno de los primeros tres componentes principales. Cada uno de los bines de 20ms de actividad neuronal corresponde a un punto en cada uno de los componentes principales, por lo tanto, la proyección de los datos mantiene una estructura temporal. Un componente principal representa una dimensión de una variable latente de los datos originales. Se puede utilizar varios componentes principales para generar un espacio multidimensional de *m* dimensiones (ver Figura 5C). En este espacio de *m* dimensiones, la coordenada de cada uno de los bines de tiempo es la mezcla de los *m* valores con los que se

representó ese bin de actividad en *m* componentes principales. Dado que cada uno de los bines está asociado a un tiempo en particular, se puede generar una trayectoria neuronal que muestra la evolución del estado de la población neuronal a través del tiempo. Finalmente, se pueden proyectar otros datos al espacio original obtenido usando PCA, multiplicando la matriz de pesos obtenida en los datos originales por un nuevo conjunto de datos, siempre y cuando la población neuronal sea la misma.

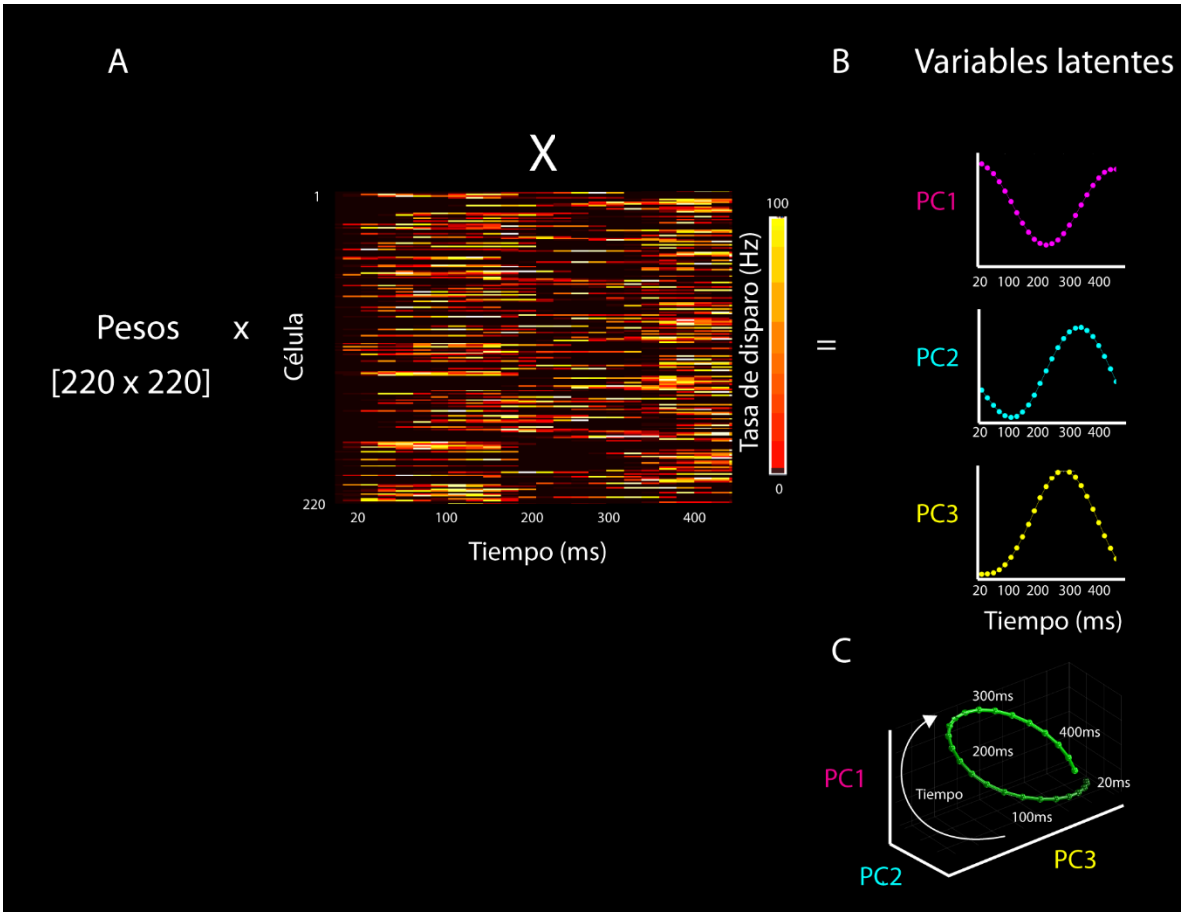

Figura 5 Generación de una trayectoria neuronal

***A**, X representa la actividad neuronal de 220 neuronas durante 22 bines de tiempo de 20ms cada uno. **B,** las variables latentes se obtienen al multiplicar la actividad neuronal X por una matriz de pesos que se obtuvo por PCA. Se muestra la proyección de la actividad X en los primeros tres componentes principales. Cada punto en los componentes principales es equivalente a la actividad de las 220 neuronas en un bin de tiempo. **C,** Se puede construir un espacio de tres dimensiones donde cada eje es uno de los primeros tres componentes principales. Las coordenadas de cada punto en este espacio corresponden al valor proyectado de la actividad neuronal X en cada uno de los tres componentes principales. La estructura temporal de los puntos en el espacio de componentes principales permite crear una trayectoria neuronal que representa la evolución de la actividad neuronal poblacional en el tiempo.*

Justificación

Se desconoce cómo es que el cerebro mide el tiempo transcurrido durante actividades que requieren la estimación del tiempo en la escala de los milisegundos. Sin embargo, en diversos estudios se ha asociado a la Corteza Premotora Medial (MPC) con actividades en esta misma escala temporal. Debido a lo anterior, estudiar la dinámica de la actividad neuronal poblacional en la MPC durante tareas de sincronización nos permitirá comprender mejor los mecanismos de medición del tiempo presentes en la corteza cerebral.

Hipótesis

- La actividad neuronal poblacional se puede representar como una trayectoria reproducible usando el Análisis de Componentes Principales (PCA), en registros de la Corteza Premotora Medial del mono Rhesus (MPC), adquiridos durante tareas de producción rítmica.
- Esta trayectoria tendrá información temporal del intervalo producido por el mono.

Objetivos

- Entrenar dos monos en una tarea de sincronización y de ritmo dinámico.
- Analizar la actividad neuronal poblacional en la MPC de monos Rhesus, durante una tarea de sincronización, utilizando técnicas que permitan registrar la actividad de decenas de neuronas simultáneamente.

Materiales y métodos

Tareas

Tarea de sincronización continuación (SCT)

En la tarea de SCT los monos fueron entrenados para presionar un botón cada vez que un estímulo con un intervalo inter-estímulo constante se les presentaba (Figura 6A). Esto resultó en un ciclo de estímulo-movimiento. Después de cuatro movimientos sincronizados, el estímulo fue suprimido y el mono tenía que continuar realizando movimientos para presionar el botón con la misma duración por tres intervalos adicionales. Los monos recibían recompensa (gotas de jugo) si cada intervalo producido tenía un error menor al 30% del intervalo blanco. El performance de los monos fue mayor al 70% de intervalos correctos. La cantidad jugo que recibían los monos fue proporcional a la longitud del intervalo blanco. Los ensayos se separaban por un tiempo variable de 1.2 a 4s. Los intervalos blancos definidos por un estímulo visual (cuadro rojo de 5cm de lado, presentado por 33ms) o auditivo (ruido blanco con una duración de 33ms), fueron 450, 550,650,850 y 1000ms. Los intervalos blancos se eligieron de manera pseudoaleatoria entre repeticiones. Los monos realizaron cinco repeticiones correctas para cada intervalo blanco.

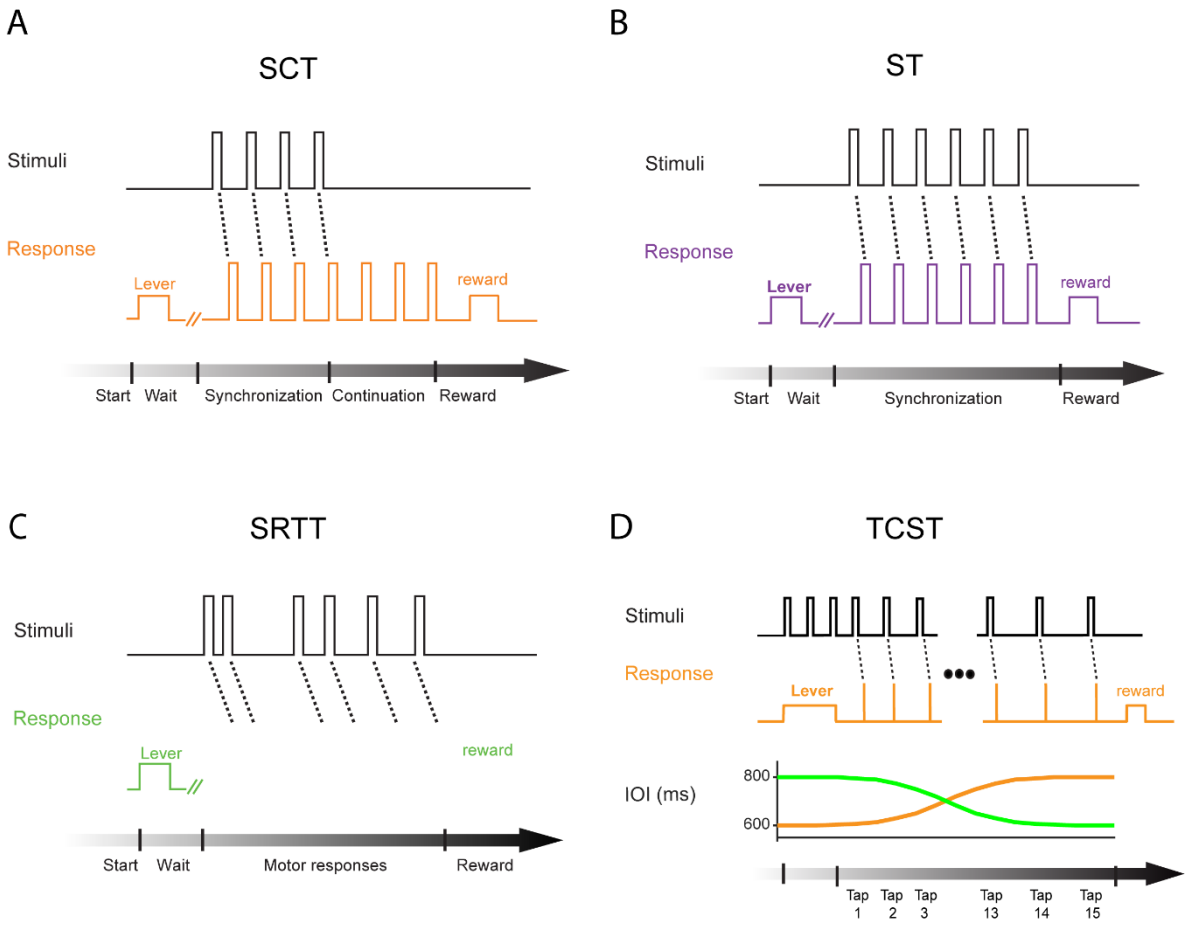

Figura 6. Tareas

***A**, Tarea de sincronización-Continuación (SCT). El ensayo iniciaba cuando el mono ponía su mano en una palanca por un tiempo variable. Después, el metrónomo era presentado y el mono presionaba un botón para producir tres intervalos de una duración determinada siguiendo el estímulo isócrono (fase de sincronización, SC), después de la cual, el animal tenía que continuar haciendo movimientos rítmicos para presionar el botón y producir tres intervalos adicionales sin la guía del metrónomo (fase de continuación, CC). Los ensayos correctos eran recompensados con jugo. Los intervalos instruidos fueron de 450, 550, 650, 850 y 1000ms. **B**, tarea de sincronización (ST). Similar a la fase de sincronización de la SCT, el animal tenía que producir cinco intervalos guiados por un metrónomo visual. Los intervalos instruidos fueron 450, 550, 650, 750, 850 y 950ms. **C**, Tarea de tiempo de reacción (SRTT). Como en la SCT el ensayo iniciaba cuando el mono ponía su mano en una palanca por un tiempo variable. Sin embargo, en esta tarea el mono presionaba el botón después de cada uno de seis estímulos separados por un intervalo inter-estímulo aleatorio, impidiendo que el mono pudiera predecir cuando debía presionar el botón para el siguiente intervalo. **D**, Durante la tarea de sincronización a un ritmo variable (TCST), los sujetos debían presionar el botón 15 veces siguiendo una secuencia de estímulos visuales que contenía cambios en su ritmo de presentación. El intervalo de presentación entre estímulos (IOI) seguía una función sigmoide decreciente (aceleración, 800–600 ms IOIs, línea verde) o creciente (desaceleración, 600–800 ms IOIs, línea naranja).*

[tomado y modificado de Gámez et al., 2019 y Gámez et al., 2018]

Tarea de sincronización (ST)

Los monos fueron entrenados para poner atención en una secuencia de estímulos cortos con un intervalo inter-estímulo constate y a presionar un botón en sincronía con los últimos seis estímulos

(Figura 6B). Al inicio del ensayo, los monos pusieron su mano en un sensor mientras atendían al menos a dos estímulos, después de los cuales podían mover la mano, siendo el objetivo producir seis *taps* en sincronía con los seis pulsos restantes del metrónomo.

Los monos recibían una recompensa (jugo de fruta) si su comportamiento durante el ensayo cumplía con dos condiciones: el intervalo producido no tenía más del 18% de diferencia con el intervalo indicado y si todas las asincronías entre los estímulos y los *taps* eran menores a un umbral (280ms en el mono M01 y 240ms en el mono M02). Los ensayos estaban separados por un tiempo variable aleatorio de 1.2 a 4 segundos. Los intervalos entre estímulos (IOI), 450 o 850 ms, para el estímulo visual (cuadro rojo con lados de 5cm, presentado por 33ms) o auditivo (ruido blanco con una duración de 33ms) fueron presentados en bloques de 30 ensayos para el mono M01 y 60 ensayos para el mono M02. El orden de las cuatro combinaciones de intervalos y modalidades fue aleatorio para cada día. A diferencia de la tarea de SCT, la tarea de ST no incluía una fase de continuación y en su lugar contenía una fase de sincronización perceptual que consistía en esperar tres estímulos sin realizar movimientos del brazo al inicio de cada ensayo. Además, las reglas de recompensa en la tarea ST incluían un umbral de error tanto para la duración del intervalo, así como para la magnitud de la asincronía estímulo-*tap*, mientras que la regla de recompensa para la tarea de SCT solamente toma en cuenta un umbral para la duración del intervalo. Finalmente, durante la ST la cantidad de recompensa que recibía el mono en cada ensayo no dependía del intervalo blanco.

Tarea de ritmo dinámico

Esta tarea requería que el mono presionara un botón siguiendo una secuencia de estímulos visuales con un cambio en el ritmo del metrónomo. Un ensayo consistía en una secuencia de 15 taps donde los intervalos entre estímulo de un metrónomo visual (cuadro verde de 5 cm de lado, presentado por 33ms) seguía una función sigmoidal de manera decreciente (incremento de *tempo,* intervalos entre estímulos de 800-600ms) o ascendente (decremento de *tempo*, intervalos entre estímulos de 600-800ms). La función utilizada para generar los intervalos entre estímulos fue:

$$y = 0.20\left(\frac{1}{1+e^{-1.5(t-4)}}\right)d + I$$

donde *y* es el intervalo blanco, *t* es el tiempo transcurrido del ensayo, *d* es 1 para el metrónomo ascendente y -1 para el metrónomo descendiente e *I* es el intervalo inicial (600ms para el metrónomo ascendente y 800 para el metrónomo descendiente). Los ensayos se organizaron en bloques para la condición de incremento y decremento de *tempo*, cada bloque consistía de 60 ensayos y el orden de los bloques fue aleatorio en cada día. Los ensayos se separaron por un intervalo variable aleatorio de 1.2 a 4s. El ensayo iniciaba con una fase de sincronización perceptual donde el sujeto tenía que mantener su mano en un sensor durante los primeros tres estímulos antes de empezar a presionar el botón. Un ensayo se consideraba correcto cuando los intervalos producidos estaban dentro de un 35% del intervalo blanco y las asincronías eran menores a 250ms (Figura 6D).

Tarea de tiempo de reacción

En la tarea de tiempo de reacción (SRTT) los monos debían presionar un botón cada vez que un estímulo les era presentado, pero en este caso el intervalo inter-estímulo entre cada par de estímulos era aleatorio entre 450, 550, 650, 750, 850 o 950ms. De tal manera que era imposible la temporalización explicita de los *taps* (Figura 6C). Los monos recibían recompensa si el tiempo de respuesta después de cada estímulo estaba dentro de una ventana de 200 a 500ms. El intervalo inter-ensayo fue similar a la tarea ST. Se utilizó un estímulo visual (cuadro blanco con un lado de 5cm, presentado por 33ms) y se recolectaron 30 repeticiones correctas para M01 y 60 repeticiones correctas para M02. En esta tarea la cantidad de recompensa otorgada no dependía de los intervalos blancos presentados.

Sistema de registro

Para las tareas de SCT y SRTT los registros extracelulares se obtuvieron de la MPC de monos usando un sistema de 7 ó 16 microelectrodos (1-3MΩ, Uwe Thomas Recording, Germany, S3) con movimiento independiente. Únicamente los ensayos correctos fueron analizados, debido a la variabilidad adicional en la actividad neuronal durante los diferentes errores que pueden cometer los monos en la tarea. Todas las neuronas aisladas fueron registradas, sin importar su actividad durante la tarea. Los sitios de registro se modificaron para cada sesión. En cada sitio, los potenciales de membrana extracelulares se muestrearon a 40Khz. La actividad de neurona unitaria se extrajo de los registros usando el programa “Plexon off-line sorter” (Plexon, Dallas, TX). En estos registros se analizó la actividad de 1477 neuronas (1074 del mono M01 y 403 del mono M03) que no mostraron cambios significativos en su actividad espontanea durante el periodo de espera de todas las tareas (ANOVA, $p > 0.05$). Además, utilizamos un sistema semicrónico con un electrodo de alta-densidad de silicio, donde se obtuvieron 26 y 41 neuronas registradas de manera simultánea mientras el mono M01 realizaba las tareas de ST y SRTT.

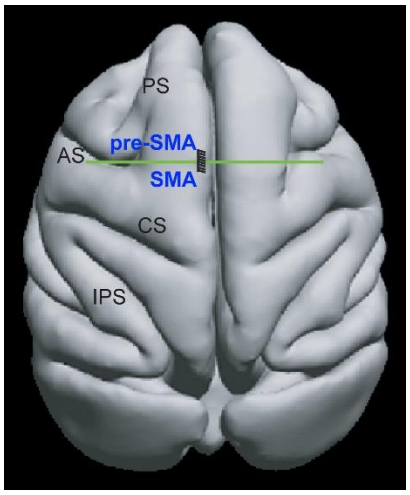

Figura 7 Localización de los electrodos de silicio para los registros en la MPC en el mono M01 durante la tarea de ST

Reconstrucción de la superficie cortical del cerebro del mono M01 y posición de los electrodos de silicio Buszaki-64 sobre la MPC.PS, surco principal; AS, surco arcuato; CS, surco central; pre-SMA, corteza motora pre-suplementaria; SMA, corteza motora suplementaria; IPS, surco intraparietal. La línea verde corresponde a la localización antero-posterior de la rodilla del surco arcuato que divide la pre-SMA de la SMA. Los electrodos de silicio fueron implantados tomando en cuenta esta marca, de tal manera que los 4 shanks más anteriores se localizaron en la pre-SMA, mientras que los 4 shanks posteriores se localizaron en la SMA. Para ver la localización de los registros de los monos 1 y 2 durante la tarea de SCT ver la Fig 1B de Hugo Merchant et al., 2011.

[tomado y modificado de Gámez et al., 2019].

Análisis de trayectorias neuronales

Periodos de activación neuronales

Usamos un análisis de tren de eventos de Poisson para identificar los periodos de activación neuronales dentro de cada intervalo definido por dos *taps* subsecuentes. Este análisis determina que tan improbable es que el número de potenciales de acción en una condición específica sea producto del azar. El número de espigas dentro de una ventana de tiempo se comparó con el número es espigas predichas por la distribución de Poisson derivada de la tasa de disparo media durante el registro completo de la célula. La medida de la improbabilidad fue nombrada Índice de Sorpresa (SI) definido como:

$$SI = -logP$$

Donde P está definida por la ecuación de Poisson:

$$P = e^{-rT} \sum_{i=n}^{\infty} \frac{(rT)^i}{i!}$$

P es la probabilidad de que, dado una tasa de descarga **r,** el tren de espigas para un intervalo producido **T** contenga **n** o más espigas en un ensayo. Por lo tanto, un índice alto de SI indica una baja probabilidad de que una elevación específica en la actividad sea producto del azar. Este análisis asume que un periodo de activación es estadísticamente diferente de la tasa promedio de descarga **r**, considerando que la actividad de la célula sigue un proceso no-homogéneo de Poisson (Perez, Kass, & Merchant, 2013). La detección de los periodos de activación arriba del azar ha sido descrita en otros trabajos (H. Merchant, Battaglia-Mayer, & Georgopoulos, 2001; Hugo Merchant, Pérez, et al., 2015b). Basados en los resultados del análisis de trenes de eventos de Poisson se obtuvo la latencia de respuesta y los periodos de activación para cada célula y para cada combinación de intervalos blanco y órdenes seriales.

Generación de trayectorias

Normalización de eventos temporales

Desarrollamos un algoritmo de normalización del tiempo para alinear los datos neuronales de diferentes tiempos de las respuestas provenientes de distintas sesiones de registro a un mismo marco de referencia. Para cada intervalo entre pares de *taps* consecutivos (*tap* anterior y *tap* siguiente), restamos al tiempo de los eventos ocurridos durante el intervalo (espigas, estímulos y taps) el tiempo del *tap* siguiente. El resultado de la resta lo dividimos entre el intervalo producido. Por lo que los tiempos de los *taps* tomaron valores de menos uno y cero, mientras que los tiempos de los otros eventos quedaron normalizados dentro de este rango. Finalmente, agregamos el número de la secuencia a los tiempos de los eventos. De tal manera, que todos los tiempos de los movimientos, estímulos y espigas tuvieron valores entre cero y siete para un ensayo de SCT:

$$evento\_normalizado = \frac{\left(tiempo_{evento} - tiempo_{tap}\right)}{intervalo_{producido}} + número\_secuencia$$

Por lo tanto, el rango de tiempo de los eventos entre el primero y el último tap de los datos normalizados de un ensayo (UTND) fue el mismo sin importar el intervalo blanco. Además del marco de referencia de tiempo relativo al ensayo, usamos un marco normalizado relativo al intervalo blanco (TIND), el cual era la multiplicación del UTND por el intervalo blanco. Este procedimiento de normalización del tiempo no fue realizado en los registros simultáneos (ver Código 1 y Código 2).

```
%Función timeNormalization
%Descripción:
%  Normaliza el tiempo de espigas, taps y estímulos con respecto al tiempo de
%  los taps. Puede generar datos normalizados de un ensayo (UTND) o datos
%  normalizados relativo al intervalo blanco (TIND)
```

```
%
%Entradas:
%  pSpikes, tiempos de las espigas en arreglo de celdas (intervalos,
%           repeticiones)
%  pMovs, tiempos de los taps en arreglo de celdas (intervalos,
%         repeticiones)
%  pStims, tiempo de los estímulos en arreglo de celdas (intervalos,
%          repeticiones)
%  task, nombre de la tarea (mt [SCT o ST], co [SRTT])
%  normTime, 0 para UTND o 1 para TIND
%Salidas:
%  spikes_w, tiempo de espigas normalizadas en arreglo de celdas (intervalos,
%            repeticiones)
%  movs_w, tiempo de taps normalizados en arreglo de celdas (intervalos,
%          repeticiones)
%  stims_w, tiempo de estímulos normalizados en arreglo de celdas (intervalos,
%           repeticiones)

function [spikes_w,movs_w,stims_w]=timeNormalization(pSpikes,pMovs,pStims,...
                                                     task,normTime)
    %Configuración
    if(~exist('normTime'))
        normTime=0;
    end
    if(task(1)=='m')
        maxTaps=8;

    else
        maxTaps=6;

    end


    neuInts=[];

    %Obtener el número de intervalos y repeticiones
    [totInts,totReps]=size(pSpikes{1});

    %Obtener el intervalo producido promedio para cada ensayo
    for numNeuron=1:length(pSpikes)
        for cInt=1:totInts
            tgtInt{cInt}=[];
            for cRep=1:totReps
                tgtInt{cInt}=horzcat(tgtInt{cInt}, ...
                    pStims{numNeuron}{cInt,cRep}(2:maxTaps-1)- ...
                    pStims{numNeuron}{cInt,cRep}(1:maxTaps-2));
            end
            meanTgtInt{cInt}=mean(tgtInt{cInt},2);
        end
        neuInts=vertcat(neuInts,mean(cell2mat(meanTgtInt)));
    end
    ints=mean(neuInts)/1000;

    %Normaliza el tiempo de los eventos
    for numNeuron=1:length(pSpikes)
        numNeuron
        for cInt=1:totInts
            for cRep=1:totReps
                lastMov=-inf;
                spikes_w{numNeuron}{cInt,cRep}=[];
                movs_w{numNeuron}{cInt,cRep}=[];
                stims_w{numNeuron}{cInt,cRep}=[];
                for nMov=2:maxTaps
                    cMov=pMovs{numNeuron}{cInt,cRep}(nMov);

                    spikes_w{numNeuron}{cInt,cRep}=vertcat( ...
                        spikes_w{numNeuron}{cInt,cRep}, ...
                        alignData(pSpikes{numNeuron}{cInt,cRep}, ...
                        lastMov,cMov)+nMov);
                    movs_w{numNeuron}{cInt,cRep}=vertcat( ...
                        movs_w{numNeuron}{cInt,cRep}, ...
```

```
                        alignData(pMovs{numNeuron}{cInt,cRep}, ...
                        lastMov,cMov)+nMov);
                    stims_w{numNeuron}{cInt,cRep}=vertcat( ...
                        stims_w{numNeuron}{cInt,cRep}, ...
                        alignData(pStims{numNeuron}{cInt,cRep}, ...
                        lastMov,cMov)+nMov);
                    lastMov=cMov;
                end
                %Obtiene TIND
                if(normTime)
                    spikes_w{numNeuron}{cInt,cRep}= ...
                        spikes_w{numNeuron}{cInt,cRep}*ints(cInt);
                    movs_w{numNeuron}{cInt,cRep}= ...
                        movs_w{numNeuron}{cInt,cRep}*ints(cInt);
                    stims_w{numNeuron}{cInt,cRep}= ...
                        stims_w{numNeuron}{cInt,cRep}*ints(cInt);
                end
            end
        end
    end
end
```

Código 1 Función timeNormalization

Función para normalizar el tiempo de espigas, taps y estímulos con respecto al tiempo de los taps. Puede generar datos normalizados de un ensayo (UTND) o datos normalizados relativo al intervalo blanco (TIND).

```
%Función alignData
%Descripción:
%  Normaliza los tiempos de datos entre un intervalo definido por los taps
%  anterior y siguiente
%input:
%  data, tiempos de datos (espigas, taps, estímulos)
%  lastMov, tiempo del tap anterior
%  cMov, tiempo del tap siguiente
%output:
%  alignedData
function alignedData=alignData(data,lastMov,cMov)
    interLength=cMov-lastMov;
    nData=data(find(data>lastMov & data<=cMov ));
    alignedData=(nData-cMov)/interLength;
end
```

Código 2 Función alignData

Función para normalizar los tiempos de datos entre un intervalo definido por los taps anterior y siguiente.

Binarización de datos

Para todos los tipos de datos normalizados y simultáneos binarizamos los datos neuronales calculando la tasa de disparo en ventanas consecutivas de 0.02 unidades (ver Código 3). Para el UTND siempre obtuvimos 50 bines entre cada par de taps para todos los intervalos blancos, mientras que para el TIND y los datos registrados de manera simultánea el número de bines dependió del intervalo blanco del ensayo. Por ejemplo, el número total de bines fue 23 y 50 para ensayos de intervalos blancos de 450 y 1000ms respectivamente. Los datos binarizados de cada neurona fueron divididos por la tasa de descarga máxima de esa neurona durante todas las repeticiones e intervalos blancos del SCT. Finalmente, se realizó una convolución de la tasa de disparo binarizada con un kernel gaussiano (ver Código 4).

```
%Función SDF_bin
```

```
%Descripción:
%Calcula la función de densidad de espigas a partir de los tiempos de disparo
% de una neurona, calculando la tasa de disparo en bines de 20 ms y realizando
%una convolución con un kernel gaussiano
%Entrada:
%   spikes_times                Vector con los tiempos de disparo de la
%                               neurona
%   minT                        Tiempo inicial
%   maxT                        Tiempo final
%   movs                        Tiempo de los taps
%   stims                       Tiempo de los estímulos
%   adjustInterval              Opcional-Ajustar la longitud del kernel
%                               gaussiano a este intervalo
%Salida:
% sdf                           Función de densidad de espigas
% winTimes                      tiempo inicial y final para cada bin
% bws                           longitud de cada bin de tiempo
% winMovs                       número de bin en el que ocurrieron los taps
% winStims                      número de bin en el que ocurrieron los
%                               estímulos
function [ sdf, winTimes,bws,winMovs,winStims ] = SDF_bin( spikes_times, minT, maxT, ...
                                                    movs,stims, adjustInterval )
a=0.02;
b=0.05;
windowLength=0.02;

%Opcional, ajustar kernel gaussiano a intervalo blanco
if(exist('adjustInterval'))
    a=a/adjustInterval;
end

%Calcular limites de bines de tiempo
winTimes=minT:windowLength:maxT;
bws=repmat([windowLength],1,length(winTimes));
winSpikes=[];

count=1;

%Calcular tasa de disparo para cada bin de tiempo
for wt=winTimes
    winSpikes(count)=length(find (spikes_times>=wt & ...
                      spikes_times<wt+windowLength))/windowLength;

    count=count+1;
end

%Calcular convolución con kernel gaussiano
if(length(winSpikes)>0)
    x=[-1*b:a:b];
    k=gausswin(length(x));
    z=conv(winSpikes,k);
    sdf=z(floor(length(k)/2):end-ceil(length(k)/2));
else
    sdf=[];
end

%Calcular bin en el que caen los taps
winMovs=[];
for curMov=movs'
    idxList=find(winTimes>curMov);
    if(numel(idxList)<1)
        idxList(1)=length(winTimes);
    end
    winMovs(end+1)=idxList(1);
end


%Calcular bin en el que caen los estímulos
winStims=[];
for curStim=stims'
    idxList=find(winTimes>curStim);
```

```
    if(numel(idxList)<1)
        idxList(1)=length(winTimes);
    end
    winStims(end+1)=idxList(1);
end
```

Código 3 Función SDF_bin

Función para calcular la función de densidad de espigas a partir de los tiempos de disparo de una neurona, binarizando la tasa de disparo en bines de 20 ms y realizando una convolución con un kernel gaussiano

```
%Función getNeuronsSDF
%Calcula la función de densidad de espigas binearizada para un arreglo de
%neuronas
%Entrada:
% spikes_array(neuron).task{intervalos,repeticiones}  Datos del tiempo
%                                                      de las espigas
% mov_array(neuron).task{intervalos,repeticiones}     Tiempo de los taps
% stim_array(neuron).task{intervalos,repeticiones}    Tiempo de los
%                                                       estímulos
% task                                                Nombre de la tarea
%                                                       (mtv,mta,coa,cov)
% trials                                              Vector con los
%                                                       ensayos por
%                                                       procesar
% intervals                                           Vector con el índice
%                                                      de los intervalos
%                                                      blancos por procesar
% minTime                                             Tiempo de inicio
% Salida:
% cell_data(neuron).task{tar.interval,repetition}  SDF de las neuronas
% cell_bws(neuron).task{tar.interval,repetition}   Duración de las ventanas
%                                                   de tiempo usadas para
%                                                    binarizar los datos
% cell_movs(neuron).task{tar.interval,repetition}  Número de bin en el que
%                                                   ocurrieron los taps
% cell_stims(neuron).task{tar.interval,repetition} Número de bin en el que
%                                                   ocurrieron los
%                                                   estímulos

function               [cell_data,cell_bws,cell_movs,cell_stims]=getNeuronsSDF(spikes_array,
mov_array,stim_array, task, trials, intervals, minTime)
    cell_data={};
    cell_movs={};
    cell_stims={};
    cell_bws={};

    %Selecciona parámetros de acuerdo a la tarea
    if(task(1)=='m')
        maxTaps=8;
        realTaps=7;
        maxStims=7;
    else
        maxTaps=6;
        realTaps=5;
        maxStims=5;
    end

    %Obtiene número de neuronas, intervalos y repeticiones
    numCells=length(spikes_array);
    numIntervals=eval(['size(spikes_array(1).' task ',1)']);
    numTrials=eval(['size(spikes_array(1).' task  ',2)']);
    popMinTime=[];
    popMaxTime=[];

    %Busca el tiempo máximo por intervalo blanco
    maxMovs=[];
```

```
    for interval=intervals
        allMovsTrials=[];
        for cell=1:numCells
            movCell=[eval(['mov_array(cell).' task '{interval,:}'])];
            allMovsTrials=vertcat(allMovsTrials,movCell(1:maxTaps)');
        end
        maxMovs(interval)=mean(allMovsTrials(:,end));
    end

    %Obtiene SDF para cada una de las célulares, intervalos blanco y repeticiones
    for(cellNum=1:numCells)

        row_data=[];
        row_movs=[];
        row_stims=[];
        row_bws=[];
        for trial=trials
            for interval=intervals
                spikes=eval(['spikes_array(cellNum).' task '{interval,trial}']);
                stims=eval(['stim_array(cellNum).' task '{interval,trial}']);
                stims=stims(2:maxStims);
                movs=eval(['mov_array(cellNum).' task '{interval,trial}']);

[sdf_data,~,bws,movs,stims]=SDF_bin(spikes,minTime,maxMovs(interval),movs,stims);
                movs=movs(1:maxTaps);

                row_data=[row_data sdf_data];
                row_movs=[row_movs;movs'];
                row_stims=[row_stims;stims'];
                row_bws=[row_bws;bws'];
            end
        end

        cell_data{end+1}=row_data;
        cell_movs{end+1}=row_movs;
        cell_stims{end+1}=row_stims;
        cell_bws{end+1}=row_bws;
    end
end
```

Código 4 Función getNeuronsSDF

Esta función calcula la función de densidad de espigas binarizada para un arreglo de neuronas

Cálculo de la matriz de coeficientes de componentes principales

Dada una transformación lineal de una matriz X en una matriz Y, de tal manera que la dimensión de Y explica la varianza de los datos originales X en orden descendente. El análisis de componentes principales puede ser descrito como la búsqueda de la matriz P que transforma X en Y de tal manera que:

$$Y = PX$$

Por lo tanto, primero calculamos la matriz P usando la matriz X que incluye todos los ensayos para todos los intervalos blancos y repeticiones para una modalidad de una tarea de nuestra población neuronal UTND (ver Código 5). Usando está P en otros datos garantiza que las mismas transformaciones se aplicaron a los diferentes conjuntos de actividad neuronal. Por lo tanto, usando el marco de referencia UTND evitamos que se sobre o bajo represente la información de diferentes intervalos blancos, debido al número constante de bines para todas las condiciones.

```
%Función getCoeff
%Descripción:
% Obtiene coeficientes de PCA a partir de datos de actividad de un grupo de
% neuronas
%Entradas:
% spikes_arr(neuron).task{tar.interval,repetition}   Tiempos de las espigas
%                                                     de grupo de neuronas
% movs_arr(neuron).task{tar.interval,repetition}     Tiempos de taps
% stims_arr(neuron).task{tar.interval,repetition}    Tiempos de estímulos
% task                                               Nombre de las tareas
% minTime                                            Tiempo de inicio del
%                                                     análisis
%Salidas:
% coeff                                              Coeficientes de PCA
% normVector                                         Vector de
%                                                    normalización de
%                                                    actividad neuronal
% explained                                          Porcentaje de varianza
%                                                     explicada para cada
%                                                     componente principal
function [ coeff,normVector,explained ] = getCoeff( spikes_arr, movs_arr, stims_arr,task,
minTime)

    %Configuración de acuerdo a la tarea
    if(task(1)=='m')
        numTaps=8;
    else
        numTaps=6;
    end

    neuronList=1:size(spikes_arr);

    full_data=[];

    %Obtiene SDF para cada tarea
    for tcount=1:length(task)
        tStr=task{tcount};
        [numIntervals,numTrials]=eval(['size(spikes_arr(1).' tStr ')']);
        int_list=[1:numIntervals];
        reps_list=[1:numTrials];
        [data,bws,movs,stims]=getNeuronsSDF(spikes_arr,movs_arr,stims_arr,...
            tStr,reps_list,int_list,minTime);
        data={data{neuron_list}};
        full_data=horzcat(full_data,cell2mat(data'));
    end

    normVector=max(full_data);

    frData=full_data;

    frData(isnan(frData))=0;

    %Obtiene coeficientes
    covx=cov(frData);
    [coeff,latent,explained]=pcacov(covx);
```

Código 5 Función getCoeff

Esta función obtiene coeficientes de PCA a partir de datos de actividad de un grupo de neuronas

Generando trayectorias neuronales

La información del TIND para cada ensayo de todas las neuronas constituyen las columnas de la matriz X'. Los coeficientes de la matrix P de los componentes principales se multiplicó por la matriz

X’ para transformar los datos neuronales en el espacio de los datos originales Y (ver Código 6). Usar la misma matriz de transformación para cada uno de los ensayos permitió la comparación de las trayectorias de diferentes ensayos y tareas. Una función de suavizado por pesos locales se aplicó a las columnas de la matriz Y. Las primeras tres dimensiones de Y fueron usadas para generar una representación tridimensional de las trayectorias en el tiempo.

```
%Función getTrajectory
%Proyecta datos en nuevo espacio usando la matriz de coeficientes coeff
%Entrada:
% spikes_arr(neuron).task{tar.interval,repetition}  Tiempos de las espigas
%                                                    de grupo de neuronas
% movs_arr(neuron).task{tar.interval,repetition}    Tiempos de taps
% stims_arr(neuron).task{tar.interval,repetition}   Tiempos de estímulos
% task                                              Nombre de las tareas
% minTime                                           Tiempo de inicio del
%                                                    análisis
% coeff                                             Coeficientes para
%                                                   proyectar los datos en
%                                                   nuevo espacio de PCA
%Salida:
% t             Datos proyectados en nuevo espacio (trayectorias)
% movFinal      Bines en los que ocurrieron los taps
% stimsFinal    Bines en los que ocurrieron los estímulos
% neuData       SDF de neuronas tal como se usaron para obtener
%               trayectorias
function [ t, movFinal, stimsFinal, neudata] = getTrajectory (spikes_arr, ...
                        movs_arr, stims_arr,task, minTime, coeff, normVector)

    %Configuración de acuerdo a la tarea
    if(task(1)=='m')
        numTaps=8;
    else
        numTaps=6;
    end
    neuronList=1:size(spikes_arr);

    normalizeDataTrajectory=1;
    substractMean=0;

    %Obtiene número de intervalos y repeticiones de los datos
    [numIntervals,numTrials]=eval(['size(spikes_arr(1).' task ')']);

    for interval=1:numIntervals
        for trial=1:numTrials
            stimTaps=[];

            %Obtiene SDF para cada ensayo
            [dataTrial,bwsTrial,movTrial,stimsTrial]=getNeuronsSDF(spikes_arr,...
                      movs_arr,stims_arr,task,[trial],[interval],minTime);

            dataTrial={dataTrial{neuron_list}};
            bwsTrial={bwsTrial{neuron_list}}
            movTrial={movTrial{neuron_list}};
            stimsTrial={stimsTrial{neuron_list}};

            %Normaliza datos antes de calcular trayectoria
            if(normalizeDataTrajectory)
                dataTrial = bsxfun(@rdivide, cell2mat(dataTrial')', normVector)';
            else
                dataTrial=cell2mat(dataTrial');
            end


            dataTrial(isnan(dataTrial))=0;
            dataTrial(isinf(dataTrial))=0;

            %Guarda SDF del ensayo
            neudata{trial,interval}=dataTrial;
```

```
            if(substractMean==1)
                dataTrial=bsxfun(@minus,dataTrial,mean(dataTrial,2));
            end

            %Calcula trayectoria
            p=(coeff'*dataTrial);

            %Suavizar trayectoria
            col=[];
            for i=1:size(p,1)
                col=horzcat(col,smooth(p(i,:),20,'lowess'));
            end

            t{trial,interval}=col';
            movFinal{trial,interval}=cell2mat(movTrial)';
            stimsFinal{trial,interval}=cell2mat(stimsTrial)';
            bwsFinal{trial,interval}=cell2mat(bwsTrial)';
        end
    end
end
```

Código 6 Función getTrayectory

Función para proyectar datos en nuevo espacio usando la matriz de coeficientes obtenida anteriormente

Amplitud, radio y variabilidad

Los primeros tres PCs explicaron el 10.7, 3.8 y 2.3 porcentaje de varianza. Sin embargo, el PC2 y el PC3 mostraron una fuerte estructura oscilatoria con una diferencia de fase de π/2 radianes durante la SCT. Para estos dos PCs calculamos los centroides de los segmentos de las trayectorias entre dos taps consecutivos. Medimos los radios de los segmentos de la trayectoria en dos dimensiones como la media de las distancias entre el centroide y cada punto perteneciente al segmento de la trayectoria. La variabilidad de la trayectoria fue calculada como la desviación estándar de las distancias euclidianas entre el centroide y cada punto en el segmento de la trayectoria para los seis órdenes seriales (3 para SC y 3 para el CC) para cada intervalo blanco. La variabilidad temporal del comportamiento para cada intervalo blanco fue calculada como la desviación estándar de los intervalos producidos en un ensayo, para los seis elementos de ordenes seriales del SCT (ver Código 7).

```
%Función getTrayectoryStatistics
%Descripción:
% Obtiene estdísticas de las trayectorias (radio [media,sem y sd], variabilidad
% [media,sem y sd] de los radios, perfil de velocidad, velocidad linear y angular)
%Entradas:
% trajectories              Proyección de los datos neuronales en un
%                           espacio de PCA
% dims                      Vector con las dimensiones (componentes principales)
%                           sobre los que se calcularan las estadísticas
% firstTap                  Delimitar el análisis a las trayectorias a
%                           partir de este tap
% lastTap                   Delimitar el análisis a las trayectorias
%                           antes de este tap
%Salidas:
% radius                    Radios
% radius_sem                Error estándar de los radios
% radius_sd                 Desviación estándar de los radios
```

```
% variability               Variabilidad de los radios
% variability_sd            Desviación estándar de la variabilidad
% speed_profile             Perfil de velocidad
% all_radius                Valores crudos de los radios
% all_variability           Valores crudos de la variabilidad de los radios
% speed_lin                 Velocidad linear
% speed_ang                 Velocidad angular

function [radius, radius_sem, radius_sd, variability, ...
          variability_sd,speed_profile,all_radius,all_variability,...
          speed_lin,speed_ang]=getTrajectoryStatistics(trajectories,...
                                                dims, firstTap, lastTap)
    speed_profile={};
    mean_speed={};

    bin_size=0.02; %tamaño de bin de 20ms


    for c_interval=1:num_intervals
        for c_trial=1:num_trials
            taps{c_trial, c_interval}=[60 size(trajectories{c_trial,c_interval},2)];
        end
    end

    %Obtiene número de intervalos y ensayos de los datos
    num_intervals=size(trajectories,2);
    num_trials=size(trajectories,1);

    %Inicializa variables
    all_dists=cell(1,num_intervals);
    all_radius = zeros(num_trials,num_intervals);
    all_variability = zeros(num_trials,num_intervals);

    all_taps_coords=cell(length(dims),1);
    all_taps_coords_mid=cell(length(dims),1);
    figure
    hold on;

    %Obtiene posición de las trayectorias en el tap y en el punto
    %intermedio entre el tap anterior y el siguiente
    for c_interval=1:num_intervals
        mean_dists{c_interval}=[];
    end


    all_taps_dists=[];
    all_mids_dists=[];

    for c_interval=1:num_intervals
        mean_dists{c_interval}=[];
        for c_trial=1:num_trials
            all_dists_new{c_interval,c_trial}=[];
            num_movements=size(taps{c_trial,c_interval},2);

            s_lin{c_trial,c_interval}=[];
            s_ang{c_trial,c_interval}=[];
            s_instant{c_trial,c_interval}=[];

            last_tap=lastTap-1;

            all_rad=[];
            for c_tap=firstTap+1:last_tap

                %Define los puntos de la trayectoria que corresponden al
                %segmento entre el tap actual y el siguiente
                epIni=taps{c_trial,c_interval}(1,c_tap-1);
                epEnd=taps{c_trial,c_interval}(1,c_tap);


                traj_tap=trajectories{c_trial,c_interval}(dims,epEnd);
```

```
                traj_inter=trajectories{c_trial,c_interval}(dims,epIni+fix((epEnd-
epIni)/2));

                ep_data=trajectories{c_trial,c_interval}(dims,epIni:epEnd);

                %Calcula centroide para inter-tap
                mean_ep=mean(ep_data');

                %Obtiene distancia entre centroide y cada punto en la
                %trayectoria
                inter_dists=pdist(vertcat(mean_ep,ep_data'));
                inter_dists=inter_dists(1:size(ep_data,2));
                all_dists_new{c_interval,c_trial}=[all_dists_new{c_interval,c_trial}
inter_dists];
                all_dists{c_interval}=horzcat(all_dists{c_interval},inter_dists);

                %Calcula distancia media para el segmento de la trayectoria
                mean_dists{c_interval}=horzcat( mean_dists{c_interval},mean(inter_dists));


                %Obtiene velocidad angular y lineal para los puntos del
                %segmento de la trayectoria
                for c_bin=1:size(ep_data,2)-1
                    [rad_tap,r_prev]=cart2pol(ep_data(1,c_bin)-mean_ep(1),ep_data(2,c_bin)-
mean_ep(2));
                    [rad_next_tap,r_next]=cart2pol(ep_data(1,c_bin+1)-
mean_ep(1),ep_data(2,c_bin+1)-mean_ep(2));
                    s_instant{c_trial,c_interval}(end+1)=sqrt(((ep_data(1,c_bin)-
mean_ep(1))-(ep_data(1,c_bin+1)-mean_ep(1)))^2 + ...
                                ((ep_data(2,c_bin)-mean_ep(2))-(ep_data(2,c_bin+1)-
mean_ep(2)))^2)/bin_size;


                    all_rad(end+1)=r_next;

s_ang{c_trial,c_interval}(end+1)=abs(angdiff(rad_tap,rad_next_tap))/bin_size;
                    s_lin{c_trial,c_interval}(end+1)=s_ang{c_trial,c_interval}(end)*(r_next-
0);
                end

            end
            all_radius(c_trial,c_interval) = mean(all_dists_new{c_interval,c_trial});
            all_s_ang(c_trial,c_interval)=mean(s_ang{c_trial,c_interval});
            all_s_lin(c_trial,c_interval)=mean(s_lin{c_trial,c_interval});

            %Variabilidad de los radios para el ensayo
            all_variability(c_trial,c_interval) = std(all_dists_new{c_interval,c_trial});

        end
        %perfil de velocidad angular
        speed_profile_ang{c_interval}=mean(vertcat(s_ang{:,c_interval}));

        %perfil de velocidad lineal
        speed_profile_lin{c_interval}=mean(vertcat(s_lin{:,c_interval}));
    end

    %Obtiene estadísticas para los radios
    radius = mean(all_radius);
    radius_sem = std(all_radius)./sqrt(num_movements*num_trials);
    radius_sd = std(all_radius);

    variability = mean(all_variability);
    variability_sd = std(all_variability);

    speed_ang=all_s_ang;
    speed_lin=all_s_lin;

end
```

Código 7 Función getTrayectoryStatistics

Obtiene radio, variabilidad de los radios, perfil de velocidad, velocidad linear y angular de las trayectorias generadas con anticipación.

Decodificador

Entrenamos una red neuronal con retraso temporal (TDNN) para decodificar los intervalos producidos a partir del primer PC de los registros simultáneos de la actividad neuronal durante la ST. La arquitectura de la TDNN tenía una capa de entrada con 20 retrasos temporales y una capa oculta con 10 unidades (ver Figura 8). La capa de salida consistía en una unidad única que fue entrenada para generar un valor de 1 cuando un *tap* ocurría o 0 de otro modo. Entrenamos la red usando un algoritmo de propagación inversa de regularización Bayesiana que minimizaba el error cuadrado medio de la salida. El tiempo de *tap* fue definido como el tiempo del pico de la salida de la red neuronal cuando superaba un umbral de 0.12. Consideramos que un intervalo había sido decodificado correctamente cuando el tiempo decodificado y el del *tap* producido tenían una diferencia menor a 60ms. Usamos una validación cruzada con 5 divisiones para evaluar el comportamiento de la red neuronal (ver Código 8).

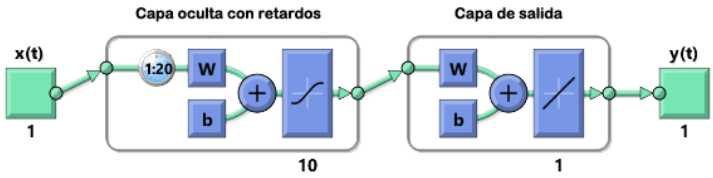

Figura 8 Arquitectura del decodificador basado en una red neuronal con retraso temporal

*Red neuronal con retraso temporal con 20 retrasos de entrada, una capa oculta de 20 unidades y una capa de salida de 1 unidad. **x(t)** es la señal de entrada, mientras que **y(t)** representa la señal de salida. **W** y **b,** son los pesos y el sesgo para cada capa de la red respectivamente. Los valores de **W y b** fueron ajustados usando un algoritmo de propagación inversa de regularización Bayesiana.*

```
%Función trainNeuralNetworkFunction
%Descripción:
% Entrena una red neuronal de retraso temporal (TDNN) para decodificar el
% tiempo de los taps a partir de la proyección de la actividad neuronal
% proyectada en un componente principal.
% Nota: función basada en el código generado por la aplicación Neural Time
% Series de Matlab
%
%Entradas:
% datos    serie de tiempo de datos neuronales proyectados en un componente
%          principal
% m        serie de tiempo con 0 donde no hay tap y 1 donde sí lo hay
%
%Salidas:
% net       objeto de matlab con red neuronal artificial entranada

function [net]=trainNeuralNetwork(datos,objetivo)


X = tonndata(datos,true,false);
T = tonndata(objetivo,true,false);

%Función de entrenamiento Bayesian Regularization backpropagation
trainFcn = 'trainbr';
```

```
%20 retrasos y 10 neuronas en la capa intermedia
inputDelays = 1:20;
hiddenLayerSize = 10;
net = timedelaynet(inputDelays,hiddenLayerSize,trainFcn);

net.input.processFcns = {'removeconstantrows','mapminmax'};
net.output.processFcns = {'removeconstantrows','mapminmax'};

[x,xi,ai,t] = preparets(net,X,T);

%Configuración de división de datos para entrenamiento
net.divideFcn = 'dividerand';
net.divideMode = 'time';
net.divideParam.trainRatio = 70/100;
net.divideParam.valRatio = 15/100;
net.divideParam.testRatio = 15/100;

%Mide el performance con MSE
net.performFcn = 'mse';

%Función para graficar avance
net.plotFcns = {'plotperform','plottrainstate', 'ploterrhist', ...
    'plotregression', 'plotresponse', 'ploterrcorr', 'plotinerrcorr'};

%Entrenar red
[net,tr] = train(net,x,t,xi,ai);

%Evaluar red
y = net(x,xi,ai);
e = gsubtract(t,y);
performance = perform(net,t,y)

% Recalcular performance de entrenamiento y pruebas
trainTargets = gmultiply(t,tr.trainMask);
valTargets = gmultiply(t,tr.valMask);
testTargets = gmultiply(t,tr.testMask);
trainPerformance = perform(net,trainTargets,y);
valPerformance = perform(net,valTargets,y)
testPerformance = perform(net,testTargets,y)


%Eliminar retraso de la red
nets = removedelay(net);
nets.name = [net.name ' - Predict One Step Ahead'];
view(nets)
[xs,xis,ais,ts] = preparets(nets,X,T);
ys = nets(xs,xis,ais);
stepAheadPerformance = perform(nets,ts,ys)
```

Código 8 Función trainNeuralNetwork

Entrena una red neuronal de retraso temporal (TDNN) para decodificar el tiempo de los taps a partir de la proyección de la actividad neuronal proyectada en un componente principal

Clasificador

Para estudiar la relación entre la dinámica de las trayectorias neuronales y el intervalo instruido de la SCT, normalizamos la longitud de cada segmento de los primeros 8 PCs asociados a un intervalo producido para que fuera de 30 bines. Este paso fue necesario para evitar un sesgo asociado a la longitud del segmento (ver Código 9).

```
%Función getFixedResample
% Remuestrea los datos neuronales proyectados en un componente principal,
```

```
% para normalizar el número de bines entre dos taps consecutivos de la trayectoria
%Entrada:
% t             Trayectorias neuronales
% movs          Tiempos de los taps
% totDims       Componente principal máximo al cual se aplicará el remuestreo
% task          Nombre de la tarea de donde provienen los datos
% fixedLength   Número de bines a normalizar
%
%Salida:
% tFix          Trayectorias remustreadas con duración de fixedLength
% newMovs       Número de bin donde se produjeron los taps
%
function [ tFix,newMovs] = getFixedResample( t,movs, totDims,task,fixedLength )

    %Obtiene número de intervalos y repeticiones de los datos de entrada
    totInts=size(t,2);
    totReps=size(t,1);
    if (task(1)=='r')
        intStep=2;
    else
        intStep=1;
    end
    totInt=1;
    for int=1:intStep:totInts
        for rep=1:totReps
            totMovs=size(movs{rep,int},2);
            for dim=1:totDims
                tDimTmp=[];
                meanMov=fix(mean(movs{rep,int}));
                tmovs=[];
                %Se remuestrean los datos para cada segmento de la trayectoria entre cada par
                %de taps
                for m=1:totMovs-1
                    %Agrega valores al inicio y al final de la trayectoria
                    %para minimizar artefactos en estos puntos
                    tOrg=t{rep,int}(dim,meanMov(m):meanMov(m+1)-1);
                    tOrgFix=[repmat(tOrg(1),1,length(tOrg))   tOrg   repmat(   tOrg(end),   1,
length(tOrg))];

                    %Remuestrea la trayectoria
                    tResFix=resample(tOrgFix',fixedLength*3,length(tOrgFix));

                    %Elimina muestras que se agregaron al inicio y al final
                    tRes=tResFix(fixedLength+1:fixedLength*2);
                    tDimTmp=[tDimTmp squeeze(tRes)];
                    tmovs(m)=length(squeeze(tRes));
                end
                newMovs{rep,int}=[1 cumsum(tmovs)+1];
                tFix{rep,totInt,dim}=tDimTmp;
            end
        end
        totInt=totInt+1;
    end
end
```

Código 9 Función getFixedResample

Remuestrea los datos neuronales proyectados en un componente principal, para normalizar el número de bines entre dos taps consecutivos de la trayectoria

Después, aplicamos una segunda capa de PCA' a cada uno de los segmentos originales de la trayectoria neuronal para cada CP de manera independiente. Mantuvimos los primero 3 PC's, pues ellos explicaban el 96% de la varianza. Como resultado, se obtuvo un punto en este nuevo espacio tridimensional para cada segmento de trayectoria de 30 bines. Para evaluar cuales PC tenían más

información acerca de los parámetros de la SCT, llevamos a cabo un procedimiento de clasificación en cada PC usando un algoritmo de máquinas de vectores de soporte (SVM, Cortes & Vapnik, 1995). Cada clasificador fue entrenado 10 veces y se usó una validación cruzada de 5 divisiones (ver Código 10) para evaluar el comportamiento del clasificador (ver Código 11). De esta manera se identificó el PC con más información para cada parámetro de la SCT y se nombró como el "mejor PC".

```
%Función performanceClassifierSVM
%Descripción:
% Entrena tres modelos de SVM sobre el PCA', de las trayectorias neuronales
% normalizadas a 30 bines para todos los intervalos blancos, para
% clasificar los segmentos de trayectoria por intervalo blanco, secuencia y
% fase de la tarea de SCT
%
%Entradas:
% tFixed        Trayectorias normalizadas a 30 bines
% targetDims    Componentes principales a usar para generar el PCA'
% totRepsNN     Número de repeticiones del entrenamiento de los SVMs
%
%Salidas:
% perfEp        Performance del modelo de SVM para secuencia
% perfInt       Performance del modelo de SVM para intervalo blanco
% perfPh        Performance del modelo de SVM para fase
% SVMEp         Modelo de SVM para secuencia
% SVMInt        Modelo de SVM para intervalo
% SVMPh         Modelo de SVM para fase
function         [perfEp,perfInt,perfPh,SVMEp,SVMInt,SVMPh]=performanceClassifierSVM(tFixed,
pcaDims, totRepeticiones)


confPh=[];
confEp=[];
confInt=[];
netPh=[];

totReps=size(tFixed,1);
totInts=size(tFixed,2);
totDataDims=size(tFixed,3);
totTaps=size(tFixed{1,1,1},2);

d=[];
half_d=[];
tartIntReal=[];
tartStimFull=[];

%Objetivo de secuencia para SCT
tartEp=horzcat(repmat([ 1 ]',[1 1]), ...
            repmat([ 2 ]',[1 1]), ...
            repmat([ 3 ]',[1 1]), ...
            repmat([ 4 ]',[1 1]), ...
            repmat([ 5 ]',[1 1]), ...
            repmat([ 6 ]',[1 1]));

tartEpFull=horzcat(tartEp, ...
                tartEp, ...
                tartEp, ...
                tartEp, ...
                tartEp);

%Objetivo de intervalo blanco para SCT
tartIntFull=horzcat( repmat([ 1 ]',[1 6*(totReps)]), ...
                     repmat([ 2 ]',[1 6*(totReps)]), ...
                     repmat([ 3 ]',[1 6*(totReps)]), ...
                     repmat([ 4 ]',[1 6*(totReps)]), ...
```

```
                    repmat([ 5 ]',[1 6*(totReps)]));

%Objetivo de fase para SCT
tartPh=horzcat( repmat([ 1 ]',[1 3]), ...
                repmat([ 2 ]',[1 3]));
tartPhFull=horzcat(tartPh, ...
                   tartPh, ...
                   tartPh, ...
                   tartPh, ...
                   tartPh);
%Inicializaciones
row=1;
col=1;
cEp=[];
cPh=[];
cInt=[];

fSource=[];
cSource=[];
dSource=[];

outClass={};
comb=pcaDims;
finCombs{1}=comb;
dtest=[];
fd=[]
fdtest=[];
dSource=[];

for idTrial=1:totReps
    d=[];
    tTmp=[];
    cSource=[];
    fSource=[];

    for ep=1:totTaps-1
        for cco=comb
            trial=idTrial;
            %Obtener media del intervalo generado
            etTmp=vertcat(tFixed{trial,1,cco}(:,ep)', ...
                tFixed{trial,2,cco}(:,ep)', ...
                tFixed{trial,3,cco}(:,ep)', ...
                tFixed{trial,4,cco}(:,ep)', ...
                tFixed{trial,5,cco}(:,ep)');
            fSource=vertcat({[1 trial ep cco]},{[2 trial ep cco]},{[3 trial ep cco]},{[4 trial
ep cco]},{[5 trial ep cco]});
            tTmp=horzcat(tTmp,etTmp);
            cSource=horzcat(cSource,fSource);
        end
    end
    fd=horzcat(fd,tTmp);
    dSource=horzcat(dSource,cSource);
end

data=reshape(fd',1,[]);
sourceData=reshape(dSource,1,[]);

totDims=length(comb);
waveData=squeeze(reshape(data,size(data,1),30*totDims,[]));
sourceData=squeeze(reshape(sourceData,size(sourceData,1),1*totDims,[]));

%Obtiene nube de puntos de PCA'
[coeffData,scoresData,latentData]=princomp(waveData');
cumVarPCA=cumsum(latentData)./sum(latentData);

redPCAData=[scoresData(:,1) scoresData(:,2) scoresData(:,3) ];

for(rep=1:totRepeticiones)
    targetEp=repmat(tartEpFull, 1, totReps);
    epData=horzcat(redPCAData,targetEp');
```

```
    %Entrena SVM para decodificar secuencia
    [SVMEp{rep}, perfEp{rep}] = trainSVM(epData);

    targetPh=repmat(tartPhFull, 1, totReps);
    phData=horzcat(redPCAData,targetPh');

    %Entrena SVM para decodificar la fase de la tarea
    [SVMPh{rep}, perfPh{rep}] = trainSVM(phData);


    targetInt=tartIntFull;
    intData=horzcat(redPCAData,targetInt');

    %Entrena SVM para decodificar intervalo blanco
    [SVMInt{rep}, perfInt{rep}] = trainSVM(intData);
    c=predict(SVMInt{rep},redPCAData);
    d=waveData;
    s=[redPCAData(:,1),redPCAData(:,2),redPCAData(:,3)];
    ti=targetInt;


end
```

Código 10 Función performanceClassifierSVM

Función para generar tres modelos de SVM sobre el PCA', de las trayectorias neuronales normalizadas a 30 bines para todos los intervalos blancos, para clasificar los segmentos de trayectoria por intervalo blanco, secuencia y fase de la tarea de SCT

```
%Función trainSVM
%Descripción:
%Entrena una máquina de vector de soporte para clasificar una nube de puntos
%tridimensional con respecto a una variable de la tarea de SCT y calcula
%una validación cruzada de 5 iteraciones
%Entradas:
% datasetTable   arreglo donde cada renglón representa el PCA' de
% un segmento de las trayectorias neuronales. Las primeras tres columnas
% contienen las coordenadas tridimensionales del punto en el espacio de los
% valores de los componentes principales (columna 1 - PC1, columna 2
% - PC2, columna 3 - PC3); la cuarta columna contiene el valor de clase de
% la tarea de SCT que define ese segmento de la trayectoria (intervalo,
% secuencia o fase)
%
% Nota: función basada en el código generado por el toolbox de Statistics and
% Machine Learning de Matlab
%Salidas:
% trainedClassifier    Objeto de un clasificador de SVM entrenado
% validationAccuracy   Precisión del modelo entrenado

function [trainedClassifier, validationAccuracy] = trainSVM(datasetTable)

%establecer orden de los datos
datasetTable = table(datasetTable);
datasetTable.Properties.VariableNames = {'column'};
datasetTable.column_1 = datasetTable.column(:,1);
datasetTable.column_2 = datasetTable.column(:,2);
datasetTable.column_3 = datasetTable.column(:,3);
datasetTable.column_4 = datasetTable.column(:,4);
datasetTable.column = [];

predictorNames = {'PC1', 'PC2', 'PC3'};
```

```
predictors = datasetTable(:,predictorNames);
predictors = table2array(varfun(@double, predictors));

response = datasetTable.column_4;

% Entrenar el clasificador
template = templateSVM('KernelFunction', 'linear', 'PolynomialOrder', [], 'KernelScale',
'auto', 'BoxConstraint', 1, 'Standardize', 1);

trainedClassifier = fitcecoc(predictors, response, 'Learners', template, 'Coding',
'onevsone', 'PredictorNames', {'column_1' 'column_2' 'column_3'}, 'ResponseName',
'column_4');

% Calcular validación cruzada de 5 iteraciones
partitionedModel = crossval(trainedClassifier, 'KFold', 5);

% Evaluar modelo
validationAccuracy = 1 - kfoldLoss(partitionedModel, 'LossFun', 'ClassifError');
```

Código 11 Función trainSVM

Entrena una máquina de vector de soporte para clasificar una nube de puntos tridimensional con respecto a una variable de la tarea de SCT y calcula una validación cruzada de 5 iteraciones

Además, para estudiar como afectaba el tamaño de la población neuronal usado para generar el PCA la información contenida en la trayectoria. Se ordenó cada neurona de acuerdo a la magnitud de los pesos del PCA para cada "mejor PC". De manera iterativa eliminamos la actividad del 10% (ver Código 12) de las neuronas con los mayores pesos en el PCA para el "mejor PC" hasta alcanzar el 1% de la población (15 neuronas en total). Finalmente, para cada tamaño de la población, calculamos el PCA de segunda capa en las nuevas trayectorias y la clasificación basada en SVM correspondiente (ver Código 13).

```
%Función zeroNeurons
% Pone en ceros la actividad de una lista de neuronas de los datos crudos
% con los tiempos de las espigas
%Entrada:
% cSpikes               Datos crudos con los tiempos de las espigas de
%                           las neuronas
% neuronsToRemove       Lista de índices de las neuronas a las cuales se
%                       les eliminará su actividad
% task                  Nombre de la tarea sobre la que se trabajará
%
%Salida:
% redSpikes             Datos con los tiempos de las espigas donde se ha
%                       eliminado la actividad de las neuronas seleccionadas
%
function [redSpikes]=zeroNeurons(cSpikes,neuronsToRemove,task)

%Obtener tamaño de los datos
[m,n]=eval(['size(cSpikes(1).' task ')']);

%Eliminar actividad de cada neurona en la lista a remover
for neu=neuronsToRemove
    for x=1:m
        for y=1:n
            eval(['cSpikes(neu).' task '{x,y}=[];']);
        end
    end
end

%Regresa nuevos datos con la actividad de las neuronas eliminadas
```

```
redSpikes=cSpikes;
```

Código 12 Función zeroNeurons

Función para poner en ceros la actividad de una lista de neuronas de los datos crudos con los tiempos de las espigas

```
%Función robustSVM
% Entrena un conjunto de SVM para clasificar intervalo blanco, secuencia y
% fase para una serie de subpoblaciones donde se va eliminando la actividad
% de las neuronas que más participan en un componente principal
%Entrada:
% t                 Trayectorias originales de la actividad neuronal proyectada
%                   en los componentes principales
% bws               Longitud de cada bin de las trayectorias
% movs              Bines en los que ocurrieron los taps
% stims             Bines en los que ocurrieron los estímulos
% neudata           SDF de la actividad neuronal con la que se obutvieron
%                   las trayectorias
% coeff             Matriz de coeficientes utilizada para obtener las
%                   trayectorias originales
% task              Nombre de la tarea
% targetDims        Componentes principales a usar para entrenar los SVMs
% cSpikes           Datos crudos de la actividad neuronal con los tiempos
%                   de las espigas
% cMov              Datos crudos de los tiempos de los taps
% cStim             Datos crudos de los tiempos de los estímulos
%
%Salida:
% cep               Performance del SVM para clasificar la secuencia de la SCT
%                   en cada subpoblación
% cint              Performance del SVM para clasificar el intervalo blanco de la SCT
%                   en cada subpoblación
% cph               Performance del SVM para clasificar la fase de la SCT
%                   en cada subpoblación
% classifierEp      Modelos de SVM para clasificar la secuencia de la SCT
%                   en cada subpoblación
% classifierInt     Modelos de SVM para clasificar el intervalo blanco de la SCT
%                   en cada subpoblación
% classifierPh      Modelos de SVM para clasificar la secuencia de la SCT
%                   en cada subpoblación
% tFinal            Trayectorias neuronales generadas para cada
%                   subpoblación


function [ cep,cint,cph, classifierEp,classifierInt,classifierPh, tFinal] = ...
            robustSVM( t, bws,movs, stims, neudata,coeff, task, ...
            targetDims, cSpikes,cMov,cStim)
    tFinal=[];
    fullNeuronList=[1:length(cSpikes)];


    randList=randperm(size(t{1,1},1));
    sortvalues_arr={};
    orgNeuronList_arr={};
    corrNeurons={};

    %Ordena neuronas por su participación en un PC
    for tDim=1:length(targetDims)
        [sortvalues_arr{tDim},orgNeuronList_arr{tDim}]= ...
            sort((coeff(:,targetDims(tDim))),'descend');
    end
    sortvalues=cell2mat(sortvalues_arr);
    orgNeuronList_arr=cell2mat(orgNeuronList_arr);
    partitions=[100 90 80 70 60 50 40 30 20 10 1];

    for nPart=1:length(partitions)
```

```
        part=partitions(nPart);
        lengthList=size(orgNeuronList_arr,1);
        invPartList=(1-(part/100))*lengthList;

        %Selecciona porcentaje de neuronas a eliminar
        newListArr=orgNeuronList_arr(1:invPartList,:);
        newNeuronList=setdiff(unique(orgNeuronList_arr(:)),newListArr(:));

        if(partitions(nPart)<100)
            %Pone en ceros actividad de neuronas eliminadas
            [redSpikes]=zeroNeurons(cSpikes,setdiff(fullNeuronList,newNeuronList),task);
            [curTrajectory,coefTmp,bwsTmp,curMov,curStim,curNeuData]= ...
                getTrayectory(redSpikes,cMov,cStim,{task},-1,coeff);
            tFinal{nPart,rep}.tr=curTrajectory;
            tFinal{nPart,rep}.neuData=curNeuData;
            tFinal{nPart,rep}.neurons=curNeuData;
            tFinal{nPart,rep}.newNeuronList=newNeuronList;
            tFinal{nPart,rep}.orgNeuronList=orgNeuronList_arr(:);
            tFinal{nPart,rep}.removeNeuronList=newListArr(:);

        else
            curTrajectory=t;
        end

        %Normaliza duración de los segmentos de las trayectorias a 30 bines
        [tf]=getFixedResample(curTrajectory,movs,10,org_task,30);

        %Entrena SVM
        [cep{nPart,rep},cint{nPart,rep},cph{nPart,rep},classifierEp{nPart,rep}, ...
            classifierInt{nPart,rep},classifierPh{nPart,rep}]= ...
            classifierPerformanceSVM(tf,org_task, targetDims,1); %1 repeticion, deberian ser
10

    end
end
```

Código 13 Función robustSVM

Función para entrenar un conjunto de SVM para clasificar el intervalo blanco, secuencia y fase de una serie de subpoblaciones donde se va eliminando de manera iterativa la actividad de las neuronas que más participan en un componente principal

Análisis de la cinemática de los monos durante las tareas

Aplicamos el método de flujo óptico Lucas-Kanade para medir la velocidad del movimiento del brazo del mono durante la tarea de ST. Este método calcula un campo de flujo de los cambios de intensidad entre dos cuadros consecutivos de un video. El video analizada fue grabado con una cámara *Microsoft Kinect for Windows* a 30 cuadros por segundo con una resolución de 640x480 pixeles. El método de flujo óptico fue aplicado a un área más pequeña de 141x141 pixeles del video original, la cual contenía el brazo del mono durante todo el ensayo y ningún otro objeto en movimiento. El vector de velocidad del movimiento del brazo fue calculado para todos los cuadros como la magnitud de la suma de los vectores del campo de flujo cuya magnitud haya sido mayor a un umbral predeterminado. El vector de velocidad fue calculado del primer al último tap de cada ensayo correcto. Reportamos la velocidad como la magnitud del vector de velocidad (ver Código 14).

```
%Función videoOpticFlow
```

```
% Utiliza un modelo de Lucas-Kanade para estimar el flujo óptico en un
% video RGB
%Entrada:
% video1            Objeto video de matlab obtenido usando VideoReader
% iniTime           Tiempo inicial del segmento de video por analizar
% endTime           Tiempo final del segmento de video por analizar
%
%Salida:
% rho               Vector con la magnitud de la suma de vectores por
%                   cuadro de video analizado
%
function [rho] = videoOpticFlow(video1, iniTime, endTime)

    vint=1/video1.FrameRate;
    %Crea objeto para análisis de flujo óptico
    opticFlow = opticalFlowLK('NoiseThreshold',0.0009);

    p_frame=[];
    c=1;



    for cTime=iniTime:vint:endTime
        %Leer cuadro de video
        video1.currentTime=cTime;
        n_frame=rgb2gray(video1.readFrame());
        n_frame=uint8(max(n_frame(:))) - n_frame;

        %Estima cambio con el  último cuadro del video utilizando el modelo
        %de flujo óptico
        flow(c)=estimateFlow(opticFlow, n_frame);

        %Selecciona vectores utilizando un umbral
        gIdx=find(flow(c).Magnitude>1);

        %Convierte la suma de vectores de movimiento en coordenadas polares
        [theta(c),rho(c)]=cart2pol(sum(flow(c).Vx(gIdx)),sum(flow(c).Vy(gIdx)));

        c=c+1;
        p_frame=n_frame;
    end



end
```

Código 14 Función videoOpticFlow

Función para estimar el flujo óptico en un video RGB utilizando un modelo de flujo óptico de Lucas-Kanade.

Posteriormente, el estado cinemático del brazo fue marcado como “en movimiento” cuando el vector de velocidad fue mayor a un umbral y como “en descanso” de otro modo. El algoritmo de marcado consideró un cambio en el estado cinemático cuando el nuevo estado se mantenía por más de 3 cuadros consecutivos (ver Código 15).

```
%Función mov_dwell_analysis
% Analiza el vector de movimiento obtenido con el algoritmo de flujo óptico
% para establecer un vector de movimiento/pausa
%Entrada:
% rho               Arreglo de celdas con
% movs              Tiempo final del segmento de video por analizar
% stims
% fps
%
%Salida:
```

```
% mov_dwell_array   Estructura con los resultados del análisis
%   .dwell          Vector con duración en número de cuadros de la pausa
%   .dwell_i        Vector con el número de cuadro en los que termina la pausa
%   .mov            Vector con duración en número de cuadros del movimiento
%   .mov_i          Vector con el número de cuadro en los que termina un
%                   movimiento
%   .vector         Vector con pausas(0)/movimientos(1) para cada cuadro del
%                   video analizado
function [ mov_dwell_array ] = mov_dwell_analysis( rho, movs, stims, fps )
    %Configuración
    max_anorm_length=3;
    mov_threshold=10;

        mov_dwell_array.mov=[];
        mov_dwell_array.dwell=[];
        mov_dwell_array.mov_i=[];
        mov_dwell_array.dwell_i=[];


        %Convierte información de tiempo a cuadros
        taps=ceil(movs*fps);
        stims=ceil(stims*fps);
        vel=rho;

        %Analizar movimiento entre el primero y el último tap
        vel_cut=vel(taps(1):taps(end));
        mov_dwell_array(trial).vel_cut=vel_cut;
        a_taps=taps-(taps(1));
        a_stims=stims-(taps(1));

        %Convierte vector rho en 0/1 para pausa/movimiento
        vel_cut=vel_cut>mov_threshold;
        last_state=1;

        c=0;
        first=1;
        vel_proc=[];


        for idx=1:length(vel_cut)
           %Cambia el estado actual si el nuevo estado es estable
           if(last_state==vel_cut(idx))
               vel_proc(idx)=vel_cut(idx);
               new_state=last_state;
           else
               lastIdx=idx+max_anorm_length;
               if(lastIdx>length(vel_cut))
                   lastIdx=length(vel_cut);
               end

               sum_states=sum(vel_cut(idx:lastIdx));
               if(sum_states>2)
                   %Movimiento estable
                   vel_proc(idx)=1;
                   new_state=1;
               else
                   %Pausa estable
                   vel_proc(idx)=0;
                   new_state=0;
               end
           end
           if(new_state==last_state)
               c=c+1;
           else
               %Eliminamos primer movimiento y primera pausa
               if(first<=2)
                   first=first+1;
               else
                   if(last_state==1)
                        mov_dwell_array.mov(end+1)=c;
                        mov_dwell_array.mov_i(end+1)=idx;
```

```
                    else
                        mov_dwell_array.dwell(end+1)=c;
                        mov_dwell_array.dwell_i(end+1)=idx;
                    end
                end
                c=0;
            end
            last_state=new_state;

        end
        mov_dwell_array.vector=vel_proc;

    end

end
```

Código 15 Función mov_dwell_analysis

Analiza el vector de movimiento obtenido con el algoritmo de flujo óptico para establecer un vector de movimiento/pausa

Simulaciones

Para investigar como las propiedades del patrón de actividad neuronal afectaba la generación de las trayectorias poblacionales. Generamos 5 repeticiones de las simulaciones de actividad neuronal para cada intervalo blanco. El periodo de activación de cada neurona de manera individual se construyó como la suma de 20 funciones gama aleatorias. El periodo de activación fue constante para todas las neuronas en una simulación, pero varió con el intervalo blanco: 197, 205, 213, 233 y 257ms de duración de la activación para los intervalos blancos de 450, 550, 650, 850 y 1000ms respectivamente. El tiempo de activación inicial para cada neurona fue ajustado para que la tasa de activación poblacional siguiera una función gaussiana con el fin de producir un patrón de “moving bump”. El número de neuronas en la simulación se incrementó de acuerdo al intervalo blanco (450ms, 108 neuronas; 550ms, 120 neuronas; 650 ms, 130 neuronas; 850ms, 170 neuronas; 1000ms, 182 neuronas). Las neuronas se agregaron de manera aleatoria en la porción intermedia del “moving bump” (ver Código 16).

```
%Función Simulation
% Simula la actividad de una población de neuronas cuya actividad genera un "moving
% bump" durante el tiempo entre taps simulados. La actividad de cada
% neurona es la suma de 20 funciones gama y el paso de activación entre
% neuronas sigue una función gausiana.
%Entrada:
% repeticiones      número de repeticiones a simular
%
%Salida:
% TTSimulRate       Actividad simulada de la población neuronal para cada
%                   intervalo y repetición
% TapTimes          Tiempos en los que ocurren los taps simulados
function [TTSimulRate, TapTimes]=Simulation(repeticiones)

%Configuración de intervalos, secuencias y repeticiones a simular
TDurations = 5;
TSerialOrder  = 3;
TTrials = repeticiones;

for numSim=1:5

    Totalcells =  [108   120   130   170   182];

    %Intervalos teóricos
```

```
    ActivationDuration = [450 550 650 850 1000];

    %Tasa de disparo máxima
    numspikes = [40 40 40 40 40];

    %Número de funciones gamma
    TotalGammas = 20;

    %Número de puntos a seleccionar para escalar las activaciones para cada
    %duración
    TotalActivation = 10000;%total number of ponit to pick and to the time scalling of the
activations for each duration

    JumpingFactor = [39 39 39 39 39];

    xrate_act=1;

    clear TDischargeCells;
    for trial = 1: TTrials
        for Serial_order = 1:TSerialOrder
            for cellidx = 1:Totalcells(5)
                coefGamaA = (rand(TotalGammas,1)*180)+10;
                coefGamaB = (rand(TotalGammas,1)*200)+50;

                x = 1:1:TotalActivation;
                Ytotal = zeros(1,TotalActivation);
                Ytotalf = zeros(1,TotalActivation);
                xTotal = 1:1:TotalActivation;

                for fun = 1:TotalGammas
                    ytem = gampdf(x,coefGamaA(fun),coefGamaB(fun));
                    nn = numel(ytem);
                    Ytotalf(1:nn) = Ytotalf(1:nn) + ytem;
                end
                maxY = max(Ytotalf);

                for Duration = 1:TDurations
                    convertion = numspikes(Duration)/maxY;
                    Ytotal = Ytotalf * convertion;

                    yPartial                                                                    =
Ytotal(1:JumpingFactor(Duration)+round(rand(1)*5):TotalActivation);%random cte 2 change 5
                    xPartial = 1:1:numel(yPartial);

TDischargeCells{Serial_order}{Duration}{trial}(cellidx,1:numel(yPartial)) = yPartial;

                end
            end
        end
    end

    TotalActivation = 4200;
    Ytotal = zeros(1,TotalActivation);
    xTotal = 1:1:TotalActivation;


    m=[0.0320   0.0290   0.0270   0.0270   0.0250];
    b=[6.7000    6.9000    7.1000    8.1000    8.5000];
    XChangeRate=[7.35 8.2 9.3 10 11] %multi neurons

    %Retraso inicial
    InitialLag = [430 430 430 430 430];

    loopincrement = [100 100 100 100 100];

    for trial = 1: TTrials
        for Duration = 1:TDurations

            ZRate = zeros(Totalcells(5),TotalActivation);
            nn = 1;
            nnF = InitialLag(Duration);
```

```
            temxstim = 0;
            temtapp = 450;
            figure(Duration);
            whitebg([1 1 1])
            temTapStim=[];
            for Serial_order = 1:TSerialOrder
                Ratetem=[];


                Ratetem                                                                                    =
normpdf(1:1:Totalcells(Duration),Totalcells(Duration)/2.2,Totalcells(Duration)/6);

                maxY = max(Ratetem);
                convertion = XChangeRate(Duration)/maxY;
                Ratetem = Ratetem * convertion;

                for cellidx = 1:Totalcells(Duration)

                    nn = round(nnF);
                    Ycell = zeros(1,TotalActivation);
                    temy = TDischargeCells{Serial_order}{Duration}{trial}(cellidx,:);
                    ny = numel(temy);
                    Ycell(1,nn:nn+ny-1) = temy;
                    ZRate(cellidx,:) = ZRate(cellidx,:)+Ycell(1:length(ZRate(cellidx,:)));

                    nnF=nnF+(Ratetem(cellidx));

                end
                nnF = nnF+loopincrement(Duration);

                xtim = ([temxstim temxstim]);
                ystim = ([-Totalcells(Duration) 0]);

                temxstim = temxstim+ActivationDuration(Duration);

                temTapStim(1,Serial_order) = temtapp;
                temtapp = temtapp+ActivationDuration(Duration);
            end

            temTapStim(1,Serial_order+1) = temtapp;
            xtim = ([temxstim temxstim]);
            ystim = ([-Totalcells(Duration) 0]);

            x = -500:TotalActivation-501;
            y = 0:-1:-Totalcells(5)+1;
            [X,Y] = meshgrid(x,y);
            Z = ZRate;
            TTSimulRate{Duration,trial} = ZRate;
            TapTimes{Duration} = temTapStim;

        end
    end

end
```

Código 16 Función Simulation

Simula la actividad de una población de neuronas cuya actividad genera un "moving bump" durante un intervalo de tiempo entre taps simulados. La actividad de cada neurona es la suma de 20 funciones gama y el paso de activación entre neuronas sigue una función gaussiana.

Resultados

Comportamiento

En la sección del comportamiento se describe las características del comportamiento de dos monos durante una tarea de sincronización (ST) y de tiempo de reacción (SRTT). Además, uno de los monos realizó una tarea de sincronización visual a un ritmo variable (TCST). Estas mismas tareas fueron realizadas por un grupo de 20 humanos. El objetivo de esta batería de tareas fue comparar las capacidades de sincronización de los monos y los humanos. En estudios anteriores de nuestro laboratorio, ya se han reportado comparaciones del comportamiento de monos y humanos durante diversas tareas de producción de intervalos (Zarco et al., 2009). Sin embargo, hasta ahora no se tenían reportes de que los monos pudieran adaptar sus movimientos rítmicos de manera dinámica a un metrónomo con cambios de *tempo*, tal como en la TCST.

Una vez que el comportamiento de los monos durante las tareas fue estable, realizamos registros extracelulares en la MPC de los monos mientras realizaban las tareas. Más adelante, en la sección de análisis de la dinámica poblacional, se presenta el estudio de un conjunto limitado de los registros obtenidos en uno de los monos durante las tareas de ST y SRTT.

Tarea de sincronización

El mono inició la tarea poniendo su mano libre en un sensor, donde la tuvo que mantener al menos por dos estímulos (fase de percepción del ritmo), para después presionar un botón en respuesta a un estímulo isócrono (fase de sincronización). Comparamos el comportamiento de participantes humanos y dos monos en esta tarea. Una ANOVA de medidas repetidas sobre el error constante con la modalidad del metrónomo (auditivo y visual) y la duración del intervalo instruido (450 u 850 ms) como factores dentro de grupos y la especie como el factor entre grupos, no reveló efectos principales significativos para el intervalo instruido y la modalidad y una interacción significativa para la interacción especie-modalidad ($F(1,20) = 10.097$, $P = 0.0047$). Este resultado indica, que aun cuando ambas especies producen intervalos precisos con errores cercanos a cero, hay diferencias en el error constante entre especies y modalidad.

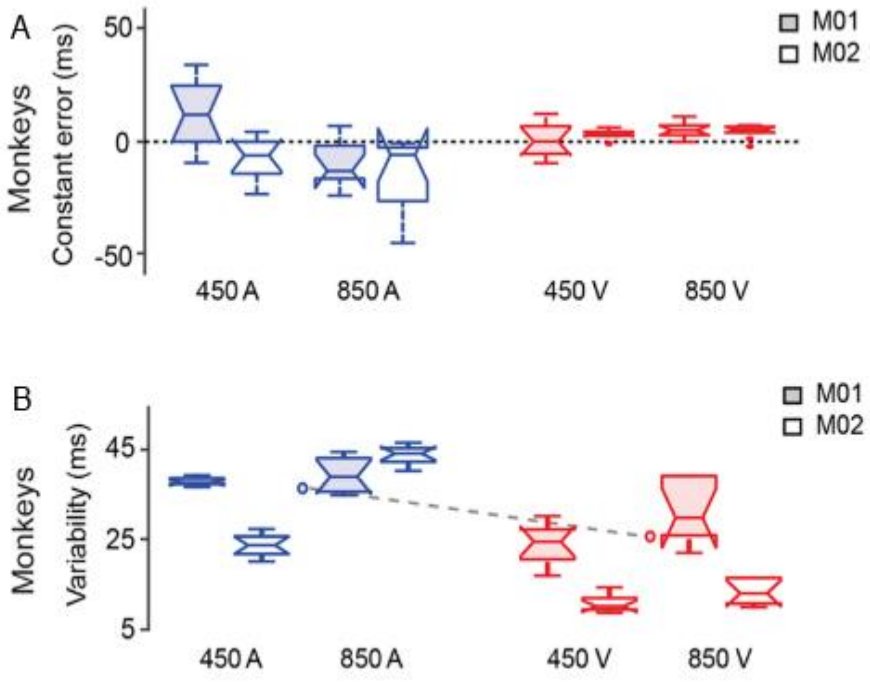

Figura 9 Comportamiento de los monos durante tarea de sincronización (ST)

***A**, Error constante para cada intervalo instruido y modalidad del metrónomo. (A: auditivo, azul, V: visual, rojo). Cada caja muestra la mediana (línea central) y los percentiles 25 (límite inferior) y 75 (límite superior). Los valores dentro de ± 2.7 desviaciones estándar están indicados por una línea punteada y los valores extremos por asteriscos. Los extremos de la muesca corresponden a $q2 – 1.57(q3 – q1)/(n)^{1/2}$ and $q2 + 1.57(q3 – q1)/(n)^{1/2}$,donde q2 es la mediana (percentil 50), q1 y q3 son los percentiles 25 y 75 respectivamente, y n es el número de observaciones. **B**, Variabilidad de los intervalos producidos. La variabilidad temporal media para cada modalidad está indicada por puntos unidos por una línea punteada. Mismo código de color que (A).*

[Tomado y modificado de Gámez et al., 2018]

Una ANOVA de medidas repetidas sobre la variabilidad temporal con factores similares a la ANOVA sobre el error constante, mostró efectos principales significativos del intervalo ($F(1,20) = 24.581$, $P < 0.0001$) y la modalidad ($F(1,20) = 12.877$, $P < 0.0018$). La interacción especie-modalidad ($F(1,20)=44.592$, $P<0.0001$) también fue estadísticamente significativa. Una prueba post hoc HSD de Tukey mostró una variabilidad temporal significativamente mayor en la modalidad auditiva en monos que en humanos. Estos resultados indican que la precisión temporal presentó un sesgo a los metrónomos visuales en monos y un sesgo a los metrónomos auditivos en humanos, mientras que ambas especies de primates presentan una mayor variabilidad para intervalos largos. Es importante mencionar que el nivel de precisión temporal en los monos, en especial el mono M02, fue alta (Figura 9), probablemente debido al alto nivel de entrenamiento de los monos para estas tareas.

La Figura 10 muestra las distribuciones y la resultante media (R) de las asincronías expresadas como fases relativas del círculo unitario en el mono M01 (Figura 10Figura 9A) y el mono M02 (Figura 10B)

para las duraciones de los intervalos instruidos y modalidades. Encontramos que *R*, una medida de la consistencia en la sincronización, fue cercana a uno para todas las especies, modalidad e intervalos instruidos con una distribución unimodal significativa para todas las condiciones (Rayleigh's test, P < 0.0001). Las asincronías medias circulares de los participantes humanos fueron estadísticamente menores a cero para ambas modalidades e intervalos (*t-test* circular de una muestra, P < 0.05), particularmente en la modalidad auditiva, de manera consistente con la literatura (Patel, Iversen, Chen, & Repp, 2005; BrunoH. Repp & Penel, 2004). En cambio, las asincronías de los monos fueron estadísticamente mayores a cero en ambas modalidades y todos los intervalos (*t-test* circular de una muestra, P<0.05), además de que para el intervalo de 450ms de modalidad visual el mono M01 respondió en anti fase con el estímulo.

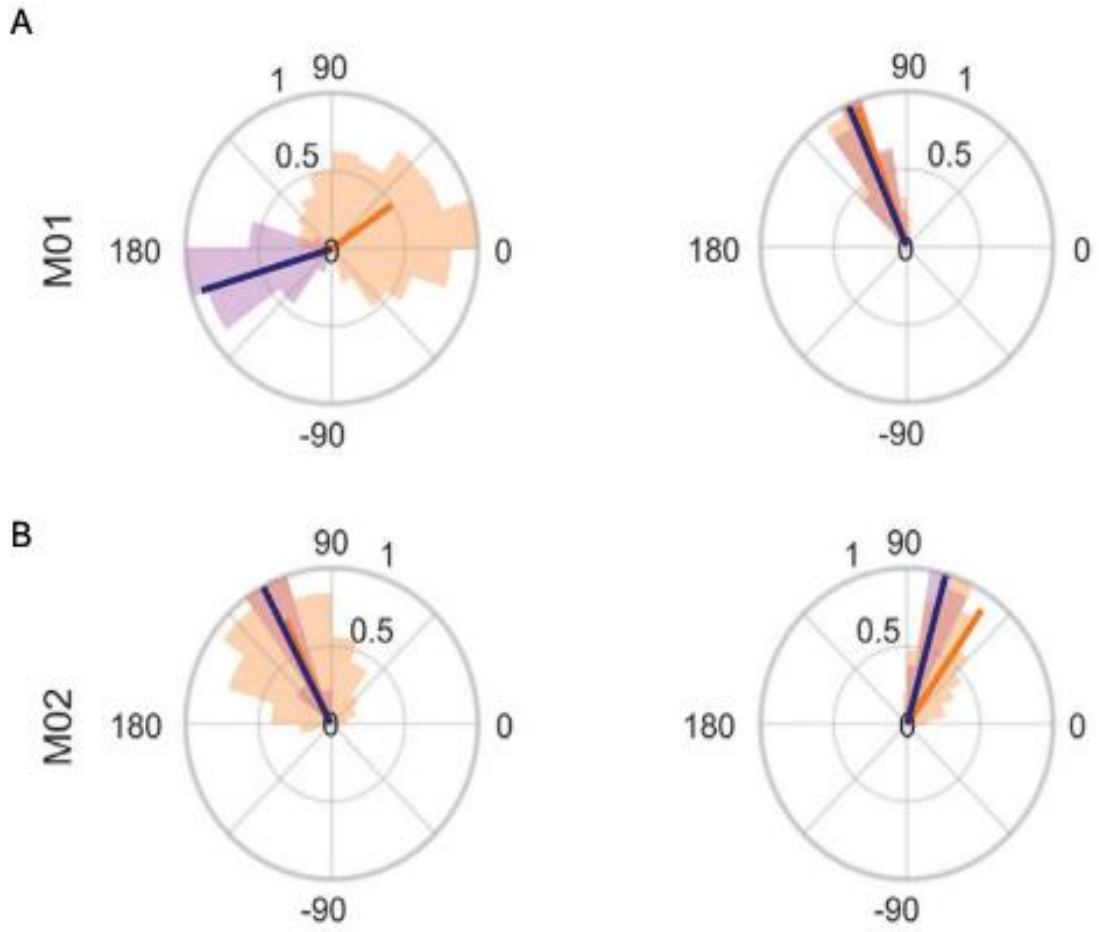

Figura 10 Asincronías in la tarea de ST.

***A**, Histograma circular de las asincronías del mono M01 para cada intervalo (izquierda: 450ms, derecha: 850ms) y la modalidad del metrónomo (auditivo, naranja; visual, azul). Las asincronías se expresan como valores de fase relativos, donde 0° indican que el botón se presionó al mismo tiempo que el estímulo y 180° indica que el botón se presionó en medio del intervalo instruido. Los valores negativos indican que el botón se presionó antes que el estímulo ocurriera, mientras que valores positivos indican que el botón se presionó después del estímulo. **B**, Histograma circulares de las asincronías del mono M02. Mismo formato que A.*

[Tomado y modificado de Gámez et al., 2018]

La Figura 10 muestra una gran diferencia en el comportamiento entre los monos M01 y M02 en el intervalo de 450ms para la modalidad auditiva. Las asincronías de M01 fueron cercanas a 0, mientras que las de M02 fueron cercanas a 90°.

Los humanos mostraron asincronías negativas y un sesgo para la condición auditiva, mientras que los monos mostraron asincronías positivas y un sesgo para los metrónomos visuales. La ANOVA de medidas repetidas correspondiente reveló efectos principales para modalidad ($F(1,38) = 75.332$, $P < 0.001$) y especie ($F(1,38) = 457.251$, $P < 0.001$), así como interacciones significativas especie-intervalo ($F(1,38)=16.446$, $P<0.001$) y especie-modalidad ($F(1,38) = 4.482$, $P = 0.041$). El análisis *post hoc* HSD de Tukey confirmó que las asincronías en humanos fueron estadísticamente más pequeñas que en monos, con asincronías negativas más grandes para la condición auditiva en humanos ($P<0.0001$).

Comparado con las asincronías de monos de 300ms que se reportaron en la tarea de SCT anteriormente (Zarco et al., 2009), las asincronías en la tarea ST fueron alrededor de 50 ms más cortas en M01 y 150 ms menores en el M02. Esta observación sugiere que el periodo de percepción rítmica y la inclusión de las asincronías en las reglas para otorgar la recompensa resultaron en una reducción en la magnitud de las asincronías.

Tarea de tiempo de reacción

Durante la tarea de tiempo de reacción (SRTT) los sujetos debían presionar un botón en respuesta de cinco estímulos visuales que se presentaron en una secuencia separados por un intervalo inter-estímulo aleatorio (elegido de manera aleatoria entre 450, 550, 650, 750, 850 y 950 ms), impidiendo que los sujetos pudieran predecir cuándo se presentaría el siguiente estímulo. El tiempo de reacción (media± SEM) de M01 fue de 441 ± 2.6ms y de 385±2ms para los intervalos de 450 y 850 ms respectivamente. Los tiempos de reacción de M02 fueron de 262 ± 3 ms y de 238 ± 1.6 ms para los intervalos de 450 y 850 ms respectivamente. Una ANOVA de los intervalos entre el estímulo y el tap (llamadas asincronías en la tarea de ST y tiempos de reacción en la tarea SRTT) mostró efectos principales significativos de la tarea ($F(1,2396) = 1633.45$, $P < 0.0001$), el intervalo blanco ($F(1,2396) = 11.21$, $P < 0.001$) y la interacción tarea-intervalo blanco ($F(1,2396) = 99.32$, $P < 0.01$). Una prueba *post hoc* HSD de Tukey mostró diferencias significativas entre todas las combinaciones de tareas e intervalos blancos. Por lo tanto, aun cuando los monos no presentaron asincronías negativas, sus respuestas durante la ST fueron más cortas que los tiempos de reacción de la SRTT, apoyando la hipótesis de que los monos utilizan un mecanismo de predicción temporal durante la ST.

Comportamiento predictivo de los humanos y monos durante el TCST

El paradigma del TCST requería que el mono sincronizara sus movimientos con una secuencia de 15 estímulos que contenía cambios acelerando o desacelerando el metrónomo (Fig 1D). La media (media ± DS) de las asincronías para los participantes humanos fue de –37 ± 8 ms (para la aceleración) y –21 ± 8 ms (para la desaceleración), mientras que para el mono fueron 171 ± 2 ms

(para la aceleración) y 172 ± 2 ms (para la desaceleración). Calculamos el promedio de las asincronías relativas para el M02 (ver Figura 11). Las asincronías relativas se definen como la resta de las asincronías menos el promedio de las primeras cinco asincronías, lo que permite eliminar diferencias entre ensayos y resaltar los cambios en las asincronías durante el ensayo. El M02 muestra un proceso de adaptación de las fase de sus *taps* durante la TCST, de manera similar a lo reportado en humanos (B. H. Repp & Keller, 2004).

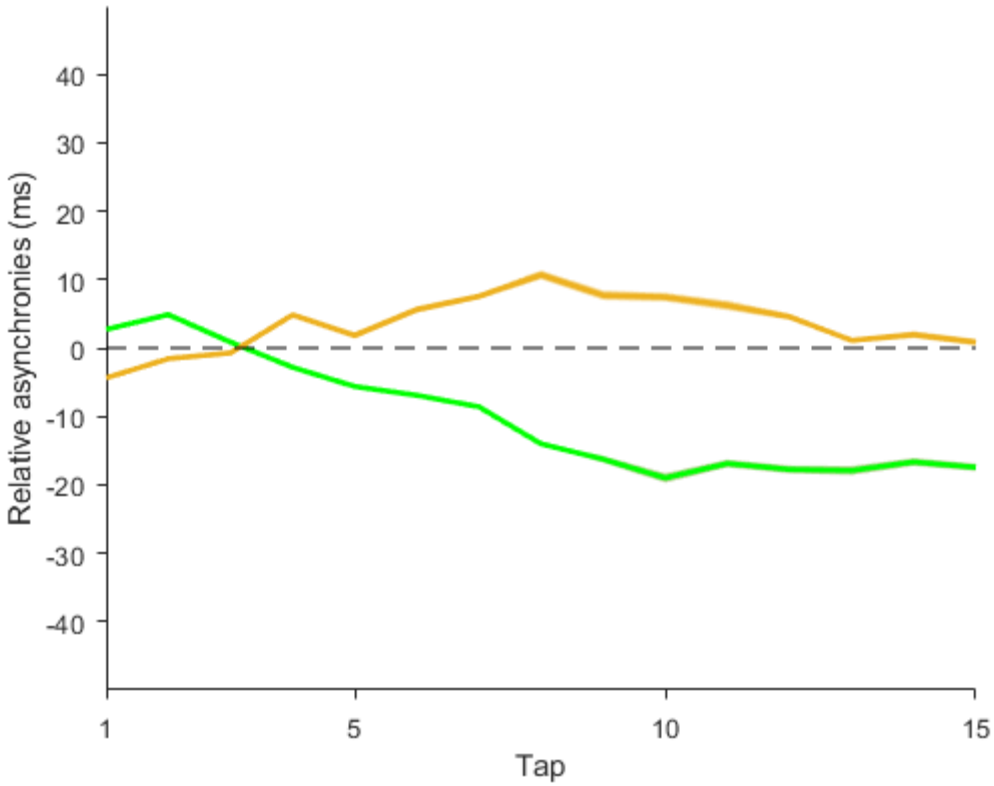

Figura 11 Asincronías relativas del mono M02 durante la TCST

Asincronías relativas (media ± error estándar) del M02 durante la TCST para la desaceleración (naranja) y aceleración (verde).

Se calculó el índice predictivo (PI), el cual refleja el grado en el que los participantes produjeron intervalos entre *taps* que se adelantaban o retrasaban a los intervalos de presentación entre estímulos en las secuencias de ritmos dinámicos (Pecenka & Keller, 2011). Valores menores a 1 reflejan una tendencia a seguir al metrónomo, mientras que valores mayores a 1 sugieren una tendencia a predecir los cambios temporales en la secuencia de estímulos. La Figura 12B muestra que para el mono en ambas condiciones el valor de PI fue mayor a 1. Esto sugiere la existencia de una habilidad compartida con los humanos para el comportamiento predictivo. Un *t-test* de una muestra confirmó que PI fue significativamente mayor a 1 en la aceleración ($t(19)=392.66$, $P<0.0001$) y en la desaceleración ($t(19)=159.48$, $P<0.0001$) en humanos, así como en la aceleración ($t(7) = 585.89$, $P < 0.0001$) y desaceleración ($t(7) = 400.55$, $P < 0.0001$) en M02. Además, una ANOVA

de dos vías mostró efectos principales significativos de la modalidad ($F(1,52) = 117.41$, $P < 0.0001$) y la interacción especie-modalidad ($F(1,52) = 7.75$, $P < 0.01$). Una prueba *post hoc* HSD de Tukey reveló diferencias significativas entre especies para la condición de desaceleración y que ambas especies fueron mejores prediciendo las aceleraciones en el ritmo que las desaceleraciones.

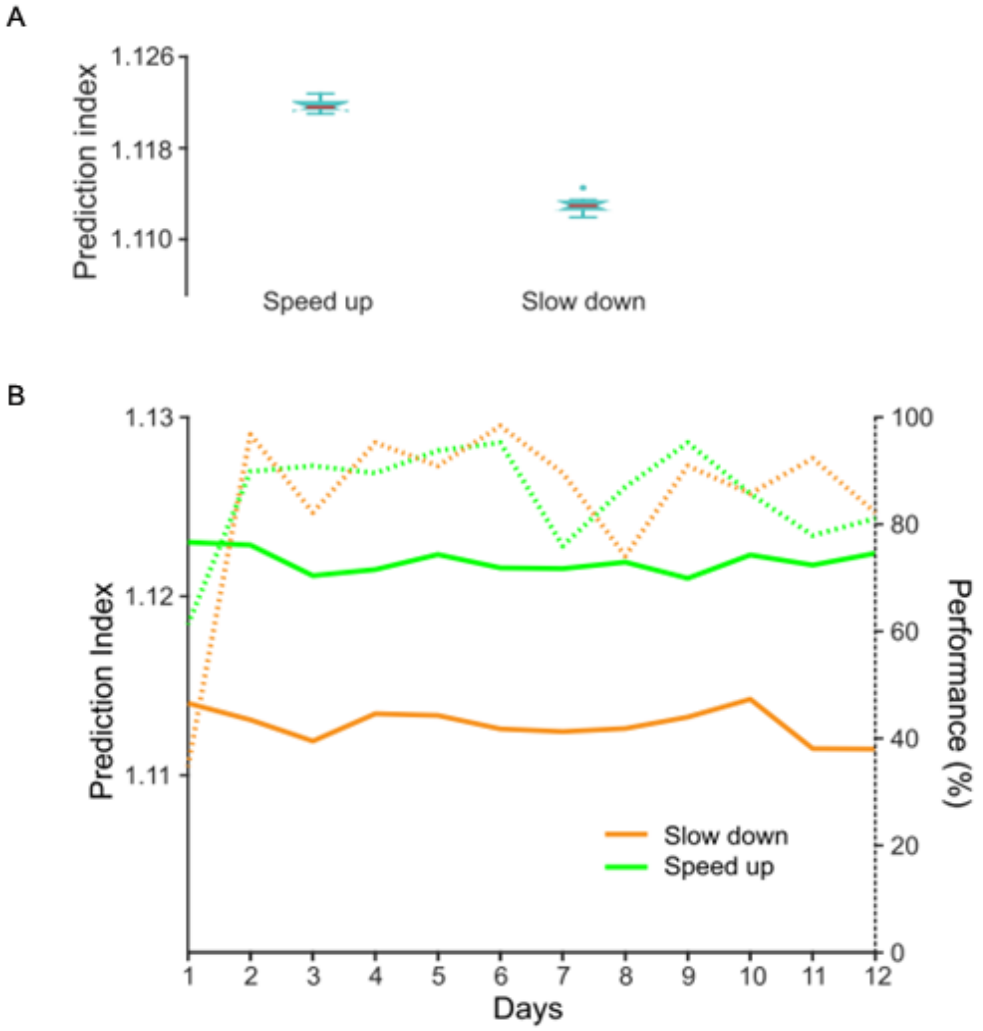

Figura 12. Desempeño del mono M02 durante la tarea de ritmo dinámico (TCST)

***A**, Índice de predicción para el mono M02 en las condiciones de desaceleración y aceleración. Cada caja muestra la mediana (línea roja central) y los intercuartiles 25 (límite inferior) y 75 (límite superior). Se hace notar que el índice para el mono es predictivo.**B**,Evolución del PI (línea solida) a través de los días para ambas condiciones de la TCST (verde, aceleración; naranja, desaceleración), así como porcentaje de ensayos correctos durante los mismos días (línea punteada, mismo código de color que PI).*

[Tomado y modificado de Gámez et al., 2018]

Vale la pena mencionar que el mono M02 fue capaz de realizar la tarea TCST desde el primer día de pruebas. La Figura 12B muestra que en el primer día el performance fue menor al 60%, dado que el mono se estaba ajustando a una duración de 15 taps en lugar de los 6 de las otras tareas. Sin

embargo, de los días 2 al 12, el animal realizó la TCST con un porcentaje de aciertos arriba del 75% y un PI mayor a 1.

Comparación del comportamiento de los monos durante las tareas de ST y SRTT

La tarea SRTT involucró estímulos similares, movimientos y una estructura secuencial similar a las tareas de ST y SCT. Sin embargo, debido a que los estímulos tienen un intervalo inter-estímulo aleatorio, no es posible la temporalización rítmica. Al comparar la SRTT con la ST, los tiempos de reacción fueron significativamente mayores para la SRTT que en la ST (media ± DS: 263 ± 37ms en la ST y 381 ± 46ms en la SRTT; efecto principal de ANOVA en la tarea: $F(1, 718) = 1443.93$, $p < 0.0001$). Estos resultados indican que aun cuando los monos presentan asincronías positivas durante las tareas de sincronización rítmica, cuentan con un mecanismo predictivo que les permite tener tiempo de reacción menores que en el caso de una tarea de tiempo de reacción.

Análisis poblacional de la actividad neuronal

Utilizando una base de datos de registros en la MPC de dos monos (M01 y M03) mientras realizaban la tarea de SCT, además de los registros obtenidos del M01 mientras realizaba las tareas de ST y SRTT realizamos una serie de análisis de la dinámica poblacional en el contexto de los sistemas dinámicos. En las siguientes secciones se presentan los resultados obtenidos.

Trayectorias neuronales

Se caracterizó la dinámica de los patrones de respuesta de 1477 células en la MPC de dos monos registradas durante la ejecución de la SCT, proyectando la actividad de la población neuronal en un espacio con un número reducido de dimensiones a través del Análisis de Componentes Principales (PCA, ver Métodos). Los resultados mostraron trayectorias altamente estereotípicas con una fuerte periodicidad en los primeros tres componentes principales (PCs) (ver Figura 13A-D). De hecho, la actividad proyectada sobre el plano definido por PC2 y PC3 mostró una órbita cíclica para cada intervalo producido (ver Figura 13C,D). Cada ciclo de la trayectoria correspondió a las variaciones periódicas de la actividad de la red durante la producción de una secuencia de intervalos rítmicos de la SCT. Las trayectorias circulares en el plano PC2/PC3 mostraron una tendencia a iniciar en la misma posición en el espacio-fase después de cada *tap*, sugiriendo la existencia de un punto disparador del movimiento en una localización particular en la trayectoria para todas las duraciones. Desde esta área común en el espacio-fase, los intervalos largos produjeron trayectorias más largas, con un incremento monotónico en el radio de la trayectoria como función del intervalo blanco tanto para SC como para CC (Figura 13E). Sin embargo, las modulaciones en la amplitud dependiente del intervalo no fueron acompañadas por modulaciones en las velocidades lineales de las trayectorias periódicas, pues la velocidad se mantuvo constante para las diferentes duraciones (Figura 13F).

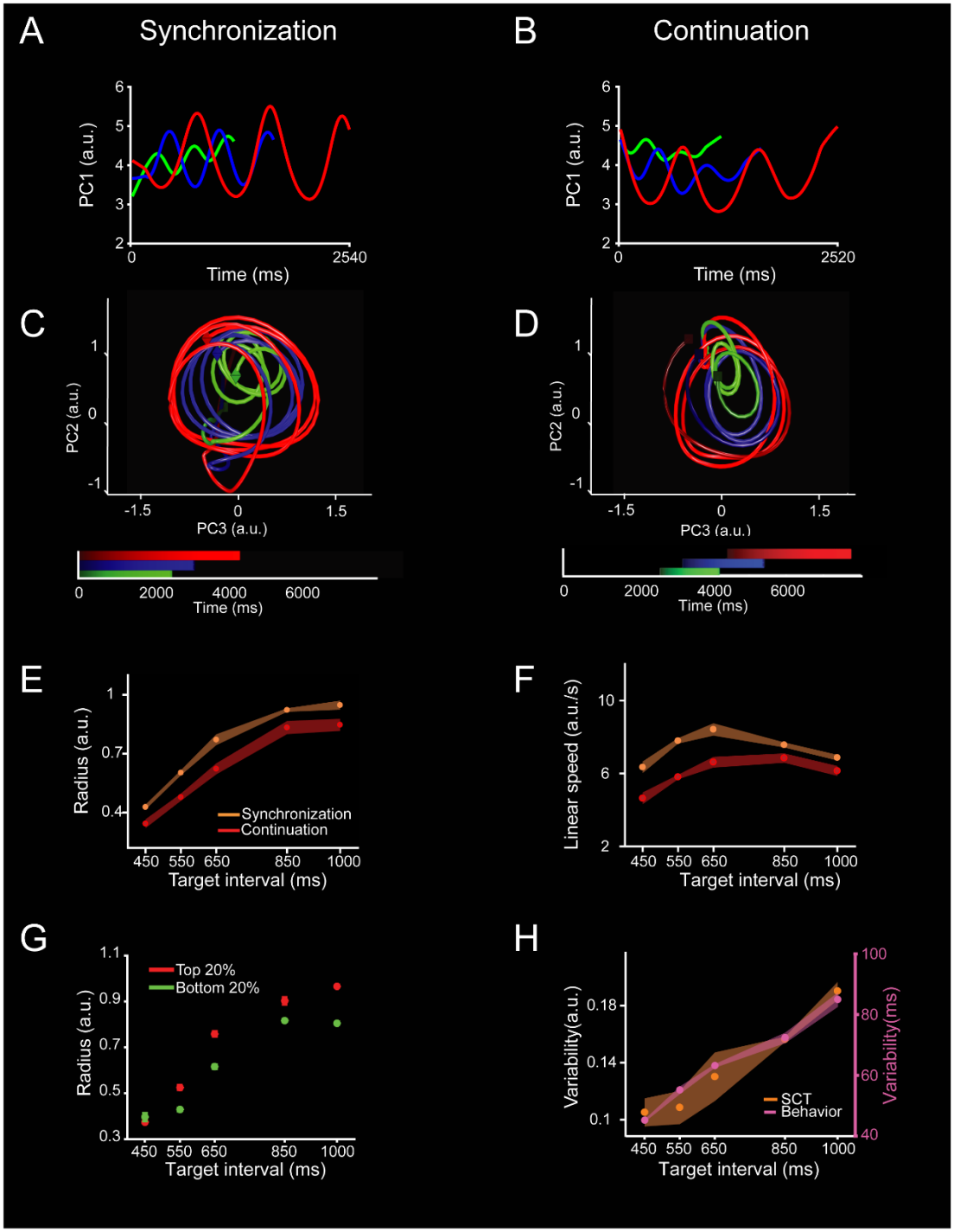

Figura 13 Trayectorias de las poblaciones neuronales durante la tarea de SCT y sus propiedades oscilatorias dinámicas

***A, C**, Proyección de la actividad neuronal en la MPC (1477 neuronas) durante las fases de sincronización de la SCT en el primer (A) o segundo y tercer componente principal(C). Cada punto en la trayectoria representa el estado de la red neuronal en un momento particular. La trayectoria completa un ciclo oscilatorio en cada intervalo producido durante las fases de sincronización (SC) y continuación (CC) del SCT. El intervalo blanco en milisegundos está codificado en el color de la trayectoria (450, verde; 650, azul; 1000, rojo). La progresión del color para cada intervalo blanco corresponde al tiempo transcurrido. Un cubo marca el inicio de cada trayectoria, mientras que un octaedro marca el fin. **B, D,** Proyecciones de la actividad neuronal durante la fase de continuación (CC) de la SCT en el primer (B) o el segundo y tercer (D) componente principal. El código de color es similar que en (A). **E**, incremento lineal de los radios en las trayectorias oscilatorias durante*

SC (rojo, media ± DS, pendiente=0.0009, constante=0.0679, R^2=0.9, p=0.01) y CC (naranja, media *± DS, pendiente =0.0009, constante=-0.0296, R^2=0.9, p < 0.01) como función del intervalo blanco.* ***F****, Velocidad lineal de las trayectorias neuronales durante la SC (naranja, media±DS, pendiente=0.0001, constante = 7.322, R^2=0.0007, p=0.896) y CC (roja, media±DS, pendiente=0.002, constante = 4.049, R^2=0.354, p = 0.002) como función del intervalo blanco (ANOVA efecto principal intervalo, F(4,39)=92.15,p<0.0001; efecto principal condición, F(1,39)=381.46, p<0.0001; interacción intervalo x condición, F(4, 39) = 15.15, p < 0.0001). La velocidad lineal fue similar (SC) o mostró un pequeño incremento (CC) con el intervalo blanco.* ***G****, El radio de las trayectorias neuronales para los 20% mayores (rojo, pendiente=0.0011, constante = -0.035, R^2=0.7, p< 0.0001) y menores 20% (verde, pendiente=0.00088, constante = -0.009, R^2=0.75, p< 0.0001) intervalos producidos para todos los intervalos blancos. Se hace notar que en aquellos intervalos en los cuales los monos solían producir duraciones inter-taps más cortas, el radio de las trayectorias era más pequeño y viceversa (ANOVA efecto principal intervalo, F(4,40)=155.7,p<0.0001; efecto principal población, F(1,40)=33.3, p<0.0001; interacción intervalo x población, F(4, 40) = 3.98, p = 0.008).* ***H****, variabilidad (SD) de las trayectorias neuronales rotacionales (naranja, media±DS, datos normalizados pendiente =0.0019, constante = -1.02, R^2=0.94, p= 0.005) y los intervalos producidos por el mono (magenta, media±DS, datos normalizados pendiente=0.005, constante = -0.721, R^2=0.98, p= 0.0008) como función del intervalo blanco. El incremento de Weber en la variabilidad de los taps no tuvo una diferencia estadísticamente significativa con el incremento en la variabilidad de las trayectorias neuronales para los intervalos blancos (datos normalizados, pendiente t-test = 0.86, p = 0.42; constante t-test =1.36, p = 0.22).*

[Tomado y modificado de Gámez et al., 2019]

De hecho, contrario al escalamiento temporal, donde hay un decremento de la velocidad lineal como una función del intervalo y donde las trayectorias neuronales siguen el mismo recorrido con una distancia similar para diferentes duraciones (Remington, Narain, Hosseini, & Jazayeri, 2018; Wang, Narain, Hosseini, & Jazayeri, 2018), encontramos que la temporización rítmica durante la SCT se representa como un incremento en el radio de la dinámica del estado de la red neuronal.

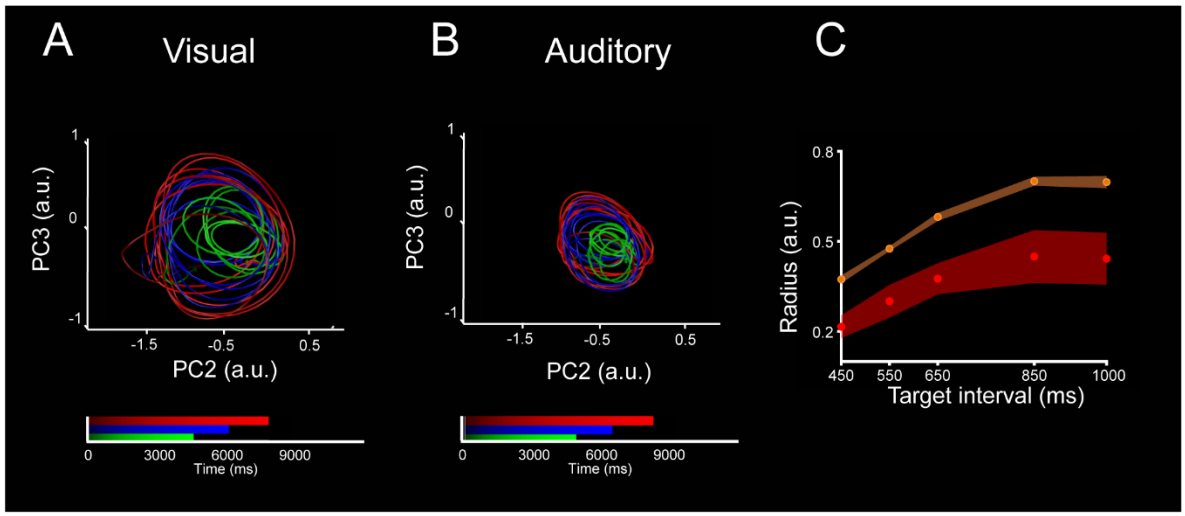

Figura 14 Trayectorias de las poblaciones neuronales durante la tarea de SCT para la modalidad auditiva y visual

A*, Proyección de la actividad neuronal en la MPC (1477 neuronas) durante la SCT con un metrónomo visual sobre el plano formado por el segundo y el tercer componente principales. El intervalo blanco en milisegundos está codificado en el color de la trayectoria (450, verde; 650, azul; 1000, rojo).* ***B****, Similar a A, para un metrónomo auditivo.* ***C****, incremento lineal de los radios en las trayectorias oscilatorias durante STC para la modalidad visual* (naranja, media *± DS, pendiente =0.0006, constante=0.144, R^2=0.89, p < 0.05) y auditiva* (roja, media *± DS, pendiente =0.00041, constante=0.068, R^2=0.86, p < 0.05). Los radios de las trayectorias auditivas fueron significativamente más pequeños (ANOVA efecto principal intervalo, F(4,40)=62.24,p<0.0001; efecto principal modalidad, F(1,40)=233.81, p<0.0001; interacción intervalo x modalidad, F(4, 40) = 2.05, p = 0.106).*

Para probar la relación entre los radios de la curvatura de las trayectorias del estado neuronal y el comportamiento de los monos durante la SC y CC, separamos los intervalos producidos en dos grupos: aquellos en los que los monos produjeron un intervalo inter-tap que fue más corto que el percentil 20% menor y aquellos en los que el intervalo inter-tap estuvo arriba del percentil 80% mayor (Crowe et al., 2014). En aquellos intervalos en los que los monos produjeron duraciones más cortas el radio de las trayectorias fue más pequeño y al contrario para las duraciones producidas más largas (Figura 13G).

Otra propiedad importante de los radios de las trayectorias neuronales fue que su variabilidad (desviación estándar de los radios de las trayectorias) siguió el mismo incremento lineal en función del intervalo blanco tal como el comportamiento del mono (Figura 13H). Esta relación lineal entre la variabilidad temporal y la duración del intervalo, conocida como la propiedad escalar de la temporización de intervalos, ha sido ampliamente reportada en la literatura de la medición temporal (Gibbon, 1977). Los resultados de este trabajo sugieren que esta variabilidad tiene un sustrato neuronal en el radio del estado dinámico de las trayectorias rotatorias de la población neuronal en el MPC durante ambas condiciones de la SCT.

Estas propiedades de las trayectorias neuronales se mantienen sin importar la modalidad del metrónomo (ver Figura 14). Proyectamos los datos de la SCT de la modalidad auditiva en el espacio fase generado por los coeficientes de PCA obtenidos con los datos de la tarea de SCT de la modalidad visual. En ambos casos se generaron orbitas circulares, cuyo radio se moduló con el intervalo blanco. Sin embargo, los radios de las trayectorias auditivas fueron menores que los de las visuales. Esto resultados sugieren que la población neuronal que mide el tiempo en la MPC durante la SCT es parcialmente la misma para ambas modalidades.

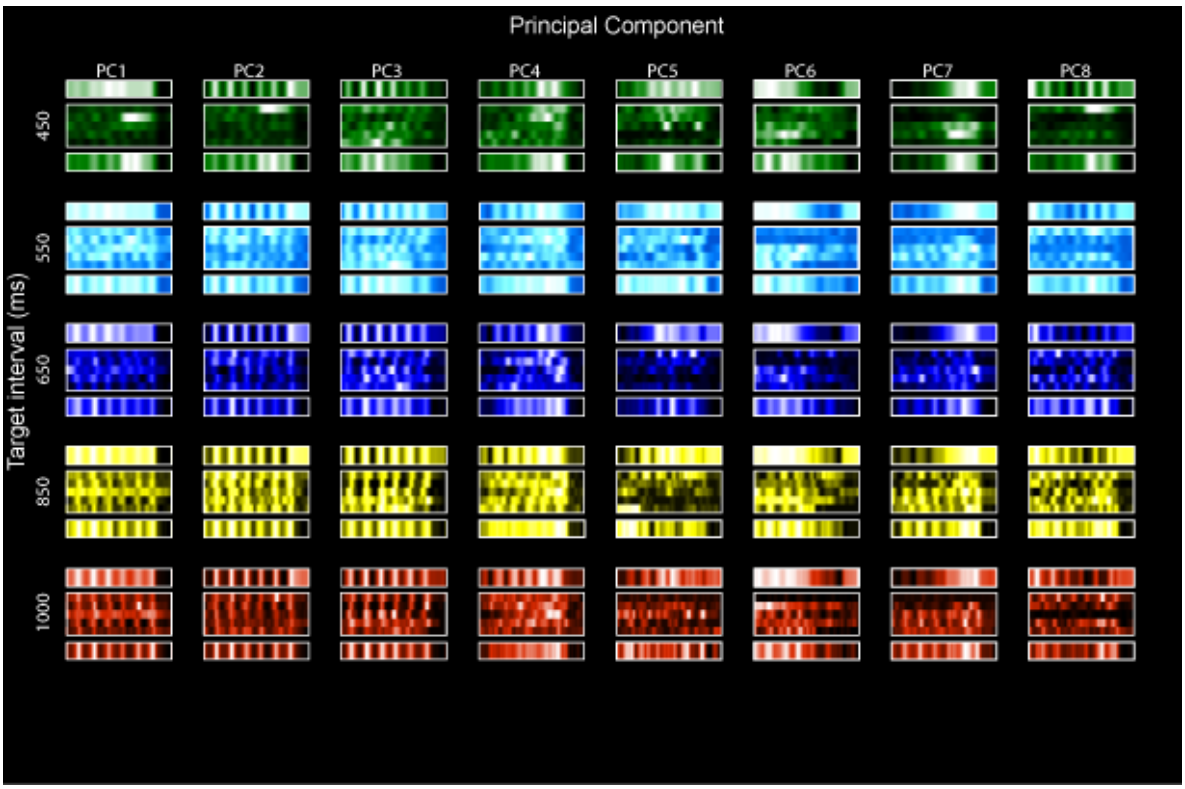

Figura 15 Perfiles de activación neuronal para los primeros 8 PC durante la SCT

Cada renglón está asociado con un intervalo blanco. Las columnas representan los primeros 8 componentes principales. Para cada combinación de intervalo blanco y PC se muestran tres series de tiempo en dentro de un rectángulo: arriba, patrón del PC; en medio, patrones de actividad de las cinco neuronas que más contribuyen a ese PC en particular; abajo, suma aritmética de la actividad de las cinco neuronas mostradas en medio.

Los perfiles de activación de las neuronas que más participan en un PC son similares a la actividad proyectada en el PC (ver Figura 15). Esto podría significar que el análisis de PCA está sesgado a una subpoblación de neuronas con una actividad altamente correlacionada, o que la actividad de estas neuronas está reflejando la actividad poblacional del resto de las células de manera similar a un componente principal.

Finalmente, es importante mencionar que todas las propiedades descritas de las trayectorias neuronales se presentan en los datos aun cuando se utilicen diferentes procedimientos para calcular los PCs (Ver Figura 16).

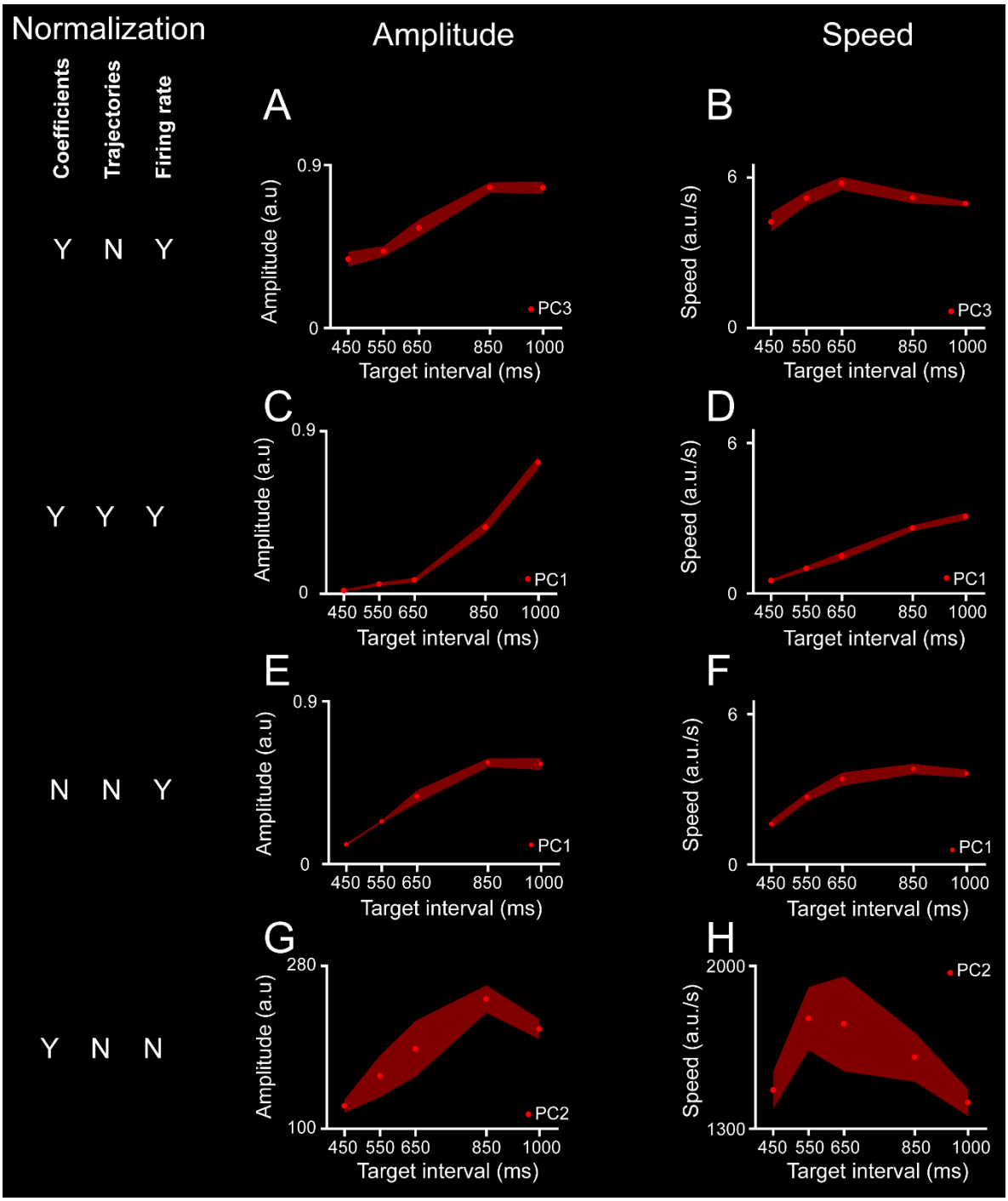

Figura 16 Efecto de la normalización del tiempo y la tasa de disparo en la amplitud y velocidad de las trayectorias neuronales

Se usaron diferentes combinaciones de normalización del tiempo y la tasa de disparo de los datos neuronales para calcular los coeficientes del PCA con los que se generaron trayectorias neuronales. Se realizó un ajusto de una función senoidal en cada uno de los primeros 10 PCs y se midió su amplitud y velocidad. Para cada posible combinación de normalizaciones, se encontró al menos uno de los primeros tres PCs presentó un ajuste robusto de la función senoidal y que fue acompañado por un incremento en la media y la variabilidad del radio de la trayectoria y una velocidad invariante para los diferentes intervalos blancos. Se muestra un CP para cada combinación de normalizaciones (ver A, C, E y G). (A-F) fueron generados

usando la tasa de disparo normalizada para calcular las trayectorias. La columna de la izquierda corresponde a la amplitud del CP y la de la derecha a la velocidad lineal del CP.

***A,B**, corresponden a datos donde los coeficientes se calcularon sobre datos normalizados en el tiempo, pero las trayectorias se calcularon con el tiempo original, que es el método utilizado en este trabajo para la tarea de SCT. (A) La amplitud del PC incrementó con el intervalo blanco: PC3, pendiente= 0.00081, constante = 0.011, R^2=0.899, p< 0.0001, ANOVA de efecto principal de intervalo blanco, F(4,20)=128.69,p<0.0001. (B) Velocidad lineal de los datos proyectados en el PC es similar para todos los intervalos blancos: PC3, regresión lineal no significativa, R^2=0.07, p=0.201, ANOVA de efecto principal de intervalo blanco, F(4,20)=22.12,p<0.0001.*

***C, D**, los coeficientes y las trayectorias calculados usando datos con el tiempo normalizado. (C) PC1, pendiente= 0.0012, constante = -0.651, R^2=0.902, p< 0.0001, ANOVA de efecto principal del intervalo blanco, F(4,20)=875.21,p<0.0001. (D) PC1, pendiente= 0.0048, constante = -1.638, R^2=0.98, p<0.0001, ANOVA del efecto principal del intervalo blanco, F(4,20)=390.94,p<0.0001.*

***E,F**, los coeficientes y las trayectorias son calculados usando datos sin normalizar en el tiempo. (E) PC1, pendiente= 0.00084, constante = -0.225, R^2=0.899, p< 0.0001, ANOVA de efecto principal del intervalo blanco, F(4,20)=332.76, p<0.0001. (F) PC1, pendiente= 0.0034, constante = 0.641, R^2=0.686, p<0.0001, ANOVA del efecto principal del intervalo blanco, F(4,20)=100.04, p<0.0001.*

***G, H**, lo mismo que (A, B) pero usando los datos de la actividad neuronal con la tasa de disparo sin normalizar para calcular las trayectorias. (G) PC2, pendiente= 0.175, constante = 62.162, R^2=0.625, p< 0.0001, ANOVA de efecto principal del intervalo blanco, F(4,20)=27.58,p<0.0001. (H) PC2, regresión lineal no significativa, R^2=0.089, p=0.145, ANOVA de efecto principal del intervalo blanco, F(4,20)=8.18, p<0.001.*

[Tomado y modificado de Gámez et al., 2019]

Demixed PCA

La dinámica en la actividad población del MPC durante la SCT también fue caracterizada usando el método de *demixed PCA* (dPCA, Figura 17). Este método descompone las dependencias de la actividad neuronal poblacional en los parámetros de la tarea en lugar de la varianza total explicada. El primer dPC (dPC1) mostró una estructura altamente periódica con un valor mínimo alrededor del tiempo de inicio de cada intervalo producido para la secuencia de la SCT, de manera similar a los resultados obtenidos con las trayectorias generadas usando PCA (Figura 17C, D). Además, el dPC1 mostró un fuerte cambio en la amplitud con el intervalo blanco. Dado que se usó información neuronal normalizada en el tiempo como entrada del análisis de dPCA, todos los ensayos tuvieron la misma longitud sin importar el intervalo blanco. Bajo estas condiciones, un mecanismo de escalamiento temporal debió producir trayectorias similares al ser proyectadas usando dPCA para todos los intervalos blancos. En cambio, se observó una modulación de la amplitud dependiente del tiempo. Para comparar ambos métodos de reducción dimensional, se calculó la distancia bin a bin entre la trayectoria de 450ms y los otros cuatro intervalos blancos (Figura 17F) usando las trayectorias de los PCs (Figura 17D) y del dPC1 (Figura 17E). Los perfiles de distancia resultantes son muy similares entre ambos métodos, con una estructura periódica cuya amplitud media y variabilidad incrementaron como función del intervalo blanco (Figura 17G, H). Por lo tanto, los resultados obtenidos por otro método como el dPCA, corroboraron la existencia de una estructura periódica en la dinámica de estado neuronal y un mecanismo de temporización rítmica basado en la modulación de la amplitud de las trayectorias poblacionales durante la SCT.

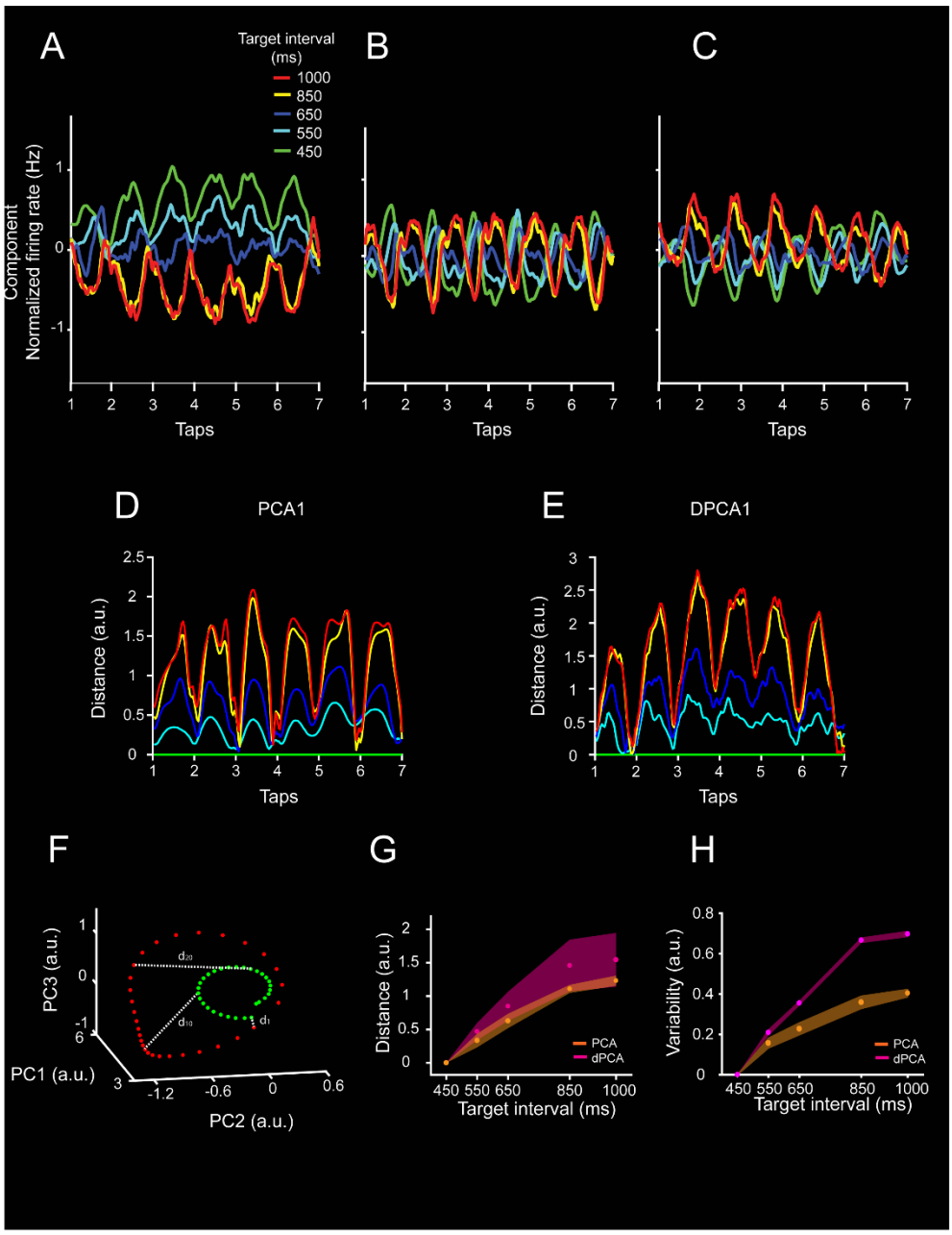

Figura 17 Demixed PCA aplicado a la actividad poblacional neuronal durante la SCT

***A,B,C**, Primeros tres componentes del demixed PCA de la actividad neuronal. Juntos explican el 10.8% de la varianza en los datos. El color denota el intervalo blanco en milisegundos (ver recuadro en (A)). Es importante notar que las trayectorias neuronales muestran actividad oscilatoria y su amplitud varía con el intervalo blanco. **D,E**, Distancia euclidiana entre el primer PC de un intervalo blanco de 450ms y el primer PC de cada intervalo blanco en el tiempo para (D) PCA normalizado en el tiempo y (E) dPCA. El intervalo blanco está codificado en el color de los datos como en (A). Una prueba Kolmogorov-Smirnov de dos muestras sobre las distribuciones de distancias de PCA y dPCA no mostró diferencias significativas ($p < 0.05$) para los intervalos blancos. **F**, Diagrama de cálculo de la distancia. Se muestra las trayectorias binarizadas de dos taps consecutivos para dos intervalos blancos (verde, 450ms; rojo, 1000ms). La trayectoria del intervalo blanco de 450ms se usa como referencia para el cálculo de las distancias. La distancia euclidiana entre cada bin de la secuencia se calcula entre la trayectoria del intervalo blanco de referencia y las trayectorias de los otros intervalos blancos. Ambos análisis*

poblacionales PCA y dPCA, generaron señales poblacionales con características similares. Por lo que tanto una actividad oscilatoria, la modulación de la amplitud con el intervalo blanco y un punto de intersección para las trayectorias de los diferentes intervalos blancos alrededor del tiempo del movimiento son características de la actividad neuronal poblacional sin importar el algoritmo de reducción dimensional usado. ***G,*** *Distancia euclidiana media entre taps (media±DS) del intervalo blanco de 450ms y cada intervalo blanco para el PCA (naranja) y el dPCA (magenta). Hubo una diferencia no significativa entre las pendientes del PCA y el dPCA (prueba de pendientes t-test = 1.97, p = 0.0539).* ***H****, Variabilidad de la distancia entre 450ms y cada intervalo blanco para el PCA (naranja) y el dPCA (magenta). La variabilidad incrementó de manera monotónica como una función del intervalo blanco para ambos análisis.*

[Tomado y modificado de Gámez et al., 2019]

Comparación de las trayectorias entre la tarea de sincronización y la tarea de tiempo de reacción

Los análisis descritos anteriormente fueron hechos en neuronas registradas a través de diferentes sesiones. Por lo tanto, las trayectorias neuronales también fueron estudiadas en neuronas registradas de manera simultánea mientras el mono M01 realizaba la tarea de sincronización (ST, Figura 6B) y una tarea de tiempo de reacción (SRTT, Figura 6C). Como en la SCT, la actividad proyectada usando PCA durante la ST mostró estados dinámicos periódicos (Figura 18A; Figura 19A), mientras que las trayectorias neuronales para la SRTT no fueron periódicas (Figura 18B; Figura 19B). De hecho, el análisis del MSE del ajuste de una función senoidal normalizada al primer PC mostró que el ajuste fue estadísticamente más robusto para ST que para SRTT (Figura 18C). Al igual que en la tarea de SCT, los radios de las trayectorias neuronales proyectadas en el plano PC1-PC2 durante la ST demostraron un incremento significativo tanto en el radio medio (Figura 18D, púrpura) y la variabilidad (Figura 18E), pero la velocidad lineal fue constante (Figura 18F) como función del intervalo blanco.

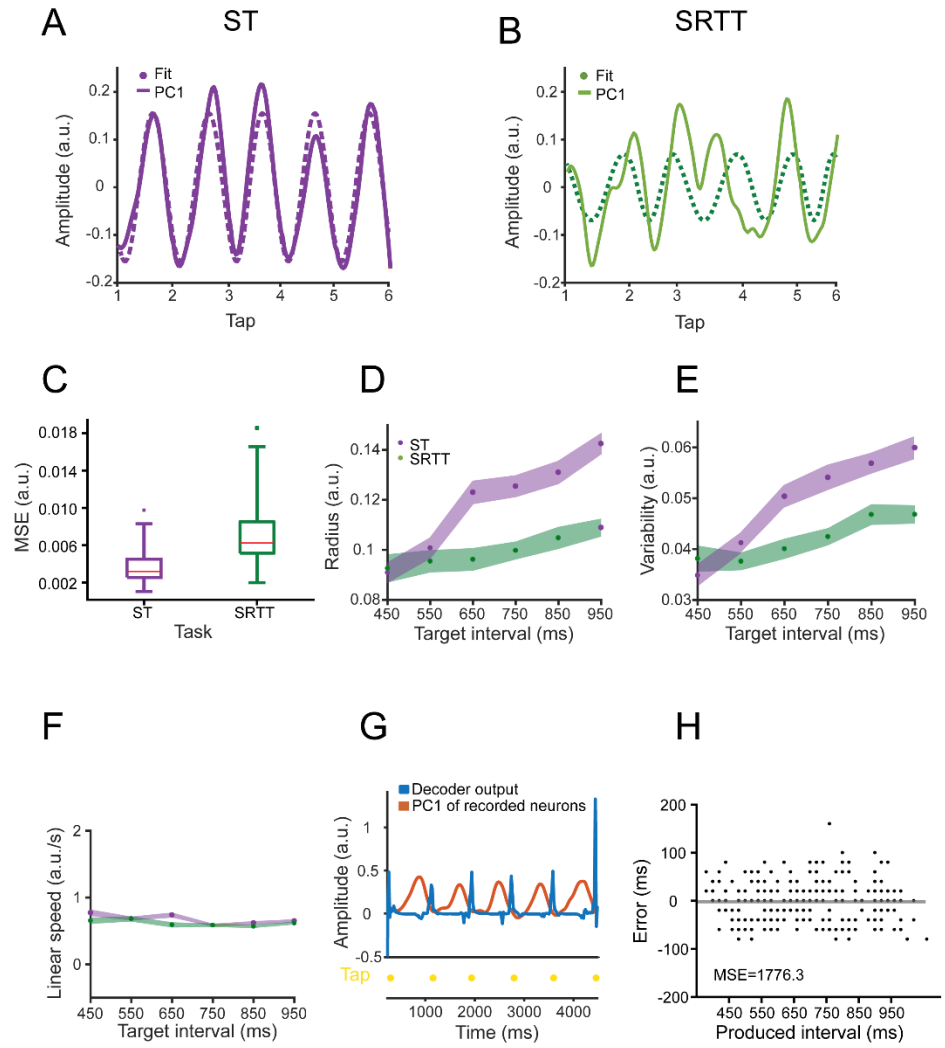

Figura 18 Comparación entre las trayectorias de neuronas registradas de manera simultánea para las tareas de ST y SRTT

A, *Actividad neuronal proyectada en el PC1 (línea solida, eliminando la tendencia lineal en los datos) y su ajuste senoidal correspondiente (línea punteada) durante un ensayo de ST para el intervalo blanco de 650ms.* ***B****, Similar a (A) para SRTT. Nótese que la fuerte estructura periódica de la trayectoria neuronal de la ST se pierde durante la SRTT en la misma población de células.* ***C****, Error medio cuadrado (MSE) de los ajustes senoidales durante ST (púrpura) es significativamente más pequeño que durante SRTT (verde; 60 ensayos, t-test pareado= -6.78, p < 0.0001).* ***D****, Radios de la trayectorias neuronales durante ST (purpura, pendiente=0.000087, constante = 0.055, R^2=0.619, p<0.0001) y SRTT (verde, regresión lineal no significativa, R^2=0.0172 y p=0.489) como función del intervalo blanco.* ***E****, Variabilidad de las trayectorias neuronales durante ST (púrpura, pendiente= 0.000037, constante = 0.028, R^2=0.368, p< 0.0001) y SRTT (verde, regresión lineal no significativa, R^2=0.0005 y p= 0.903) para los intervalos blancos.* ***F****, Velocidad lineal de las trayectorias neuronales durante el ST (púrpura, media±DS, pendiente=0.0001, constante = 7.322, R^2=0.0007, p=0.896) y SRTT (verde, media±DS, pendiente=0.002, constante = 4.049, R^2=0.354, p = 0.002) no cambio como función del intervalo blanco.* ***G****. Salida de la red neuronal con retraso temporal (TDNN, en azul) entrenada para decodificar la duración de los intervalos producidos basada en el PC1 de las trayectorias neuronales (naranja) durante un intervalo blanco de 850ms. Los tiempos en que se presionó el botón se muestran en amarillo.* ***H****, Error de la TDNN, definido como la diferencia entre el intervalo producido y decodificado para cada intervalo blanco. La TDNN predijo de manera precisa el comportamiento del mono ensayo por ensayo (la media decodificada no fue estadísticamente diferente de 0, t-test = -0.5228, p = 0.6).*

[Tomado y modificado de Gámez et al., 2019]

En cambio, el radio y la variabilidad de las trayectorias durante la SRTT sólo mostró cambios pequeños para los diferentes intervalos blancos, con un ajuste lineal no significativo para los tres parámetros como función del intervalo blanco (Figura 18D, E y F en verde). Esta diferencia sugiere que los movimientos rítmicos durante la sincronización con un metrónomo dependen de la amplitud de la dinámica cíclica de la actividad poblacional y que el cambio de un comportamiento predictivo al reactivo durante la SRTT impide la organización de trayectorias periódicas poblacionales de estado.

La simultaneidad de los registros durante la ST (Mendoza et al., 2016) permitió la decodificación de los intervalos producidos ensayo por ensayo. Usando una red neuronal de retraso temporal (TDNN, Figura 18G), se encontró que un lector ideal de las trayectorias neuronales podría predecir de manera precisa los tiempos de *taps* durante la ST en el 86% de los intervalos producidos. De hecho, la predicción de la decodificación fue mejor que el porcentaje actual de ensayos correctos de esta tarea (Figura 18H), apoyando la idea de que las trayectorias neuronales pueden predecir de manera robusta los movimientos rítmicos.

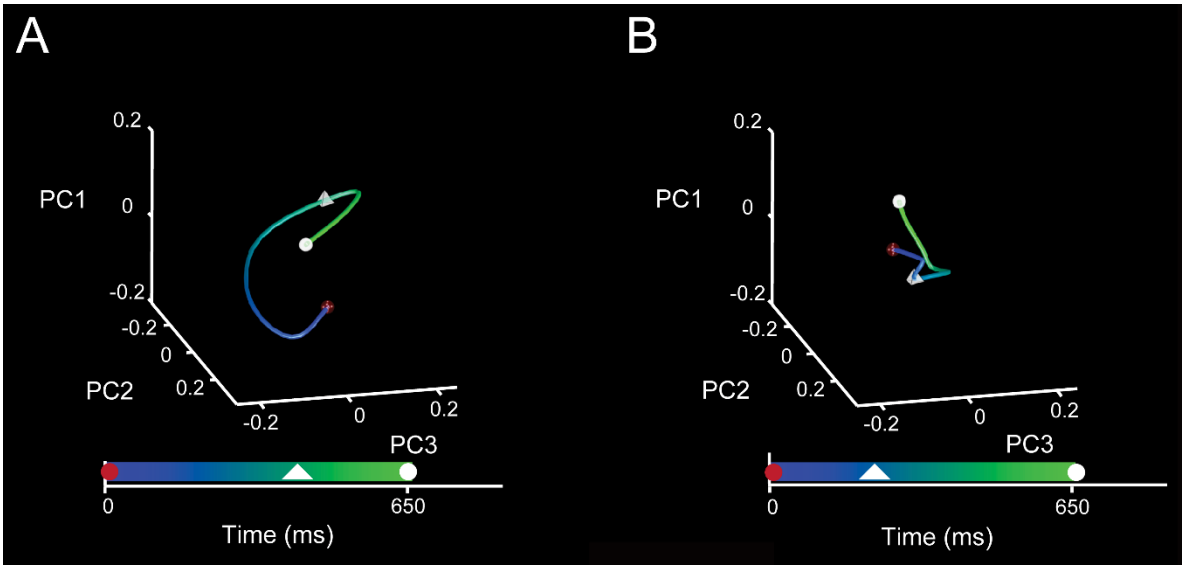

Figura 19 Trayectorias neuronales durante las tareas de ST y SRTT usando datos de neuronas registradas de manera simultánea.

A, B, Trayectorias neuronales proyectadas en los primeros tres PCs de un intervalo único de 650ms para ST (A) y SRTT (B). El tiempo transcurrido se muestra como una variación en el color de la trayectoria. Los taps anterior y siguiente están marcados por una esfera roja y blanca respectivamente. Los estímulos se muestran como una pirámide blanca.

[Tomado y modificado de Gámez et al., 2019]

Análisis de la cinemática y su relación con las trayectorias neuronales

La naturaleza cíclica y continua de las trayectorias neuronales durante la ST y la SCT contrasta con la cinemática del movimiento (Figura 20A,C-D), que se caracteriza por movimientos estereotípicos separados por periodos de pausa, siendo estos últimos los que modulan su duración como función del intervalo blanco (Figura 20E, Donnet et al., 2014; Gámez et al., 2018).

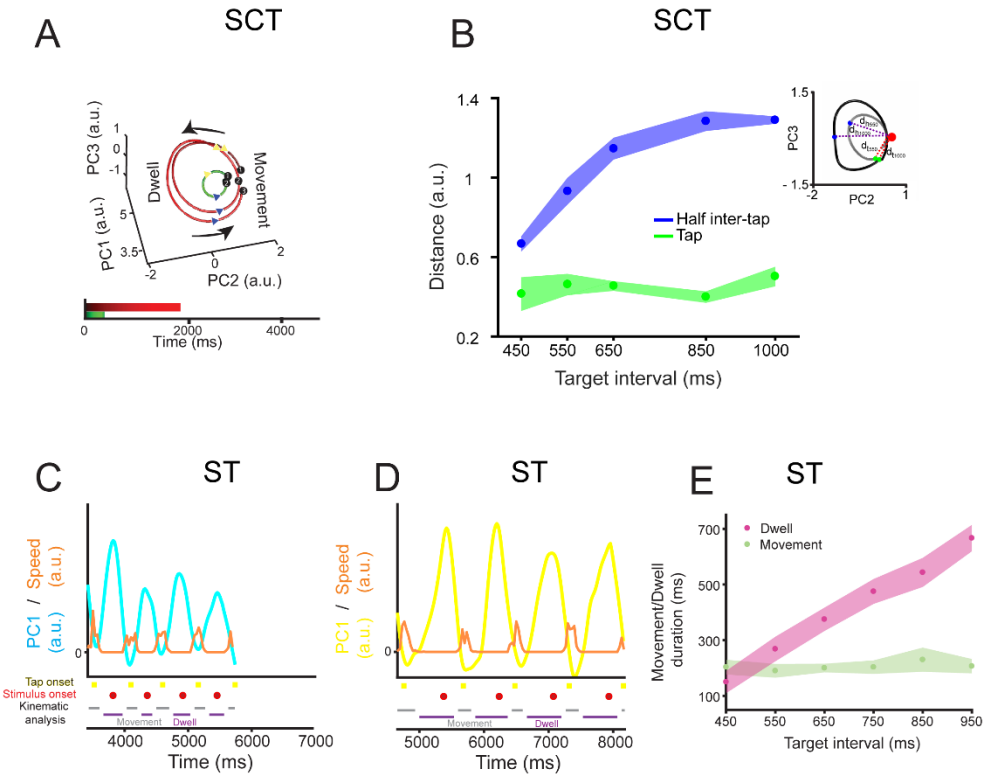

Figura 20 Las trayectorias neuronales no siguen la cinemática del movimiento rítmico de tapping

***A**, El diagrama de las trayectorias rotacionales de la actividad neuronal del SCT durante tres intervalos entre taps: un intervalo de 450ms (verde) y dos intervalos consecutivos de 1000ms (rojo). Cada tap está numerado y proyectado en la trayectoria como un círculo blanco. Un triángulo azul marca el inicio, mientras que un triángulo amarillo marca el fin del tiempo de movimiento. Los monos produjeron movimientos fásicos estereotípicos mientras controlaban el tiempo de descanso entre taps durante la SCT (Donnet et al., 2014). **B**, Distancia euclidiana entre un punto ancla (rojo) y la posición de cada tap (verde, media±DS, pendiente= 0.00007, R^2=0.0633, p=0.225), o a la mitad de la posición del intervalo entre-tap en las trayectorias neuronales (azul, media±DS, pendiente=-0.001, R^2=0.801, p<0.0001) para los intervalos blancos de la condición de sincronización (SC). Una ANOVA de dos vías encontró efectos principales significativos para la posición ($F(1,40) = 1855.72$, $p < 0.0001$), intervalo blanco ($F(4,40) = 77$, $p < 0.0001$) y su interacción ($F(4,40)=63.68$, $p<0.0001$). Una prueba post hoc HSD de Tukey mostró que las distancias del punto ancla a la posición del tap y a la mitad del intervalo entre taps fueron estadísticamente diferentes ($p<0.05$). A diferencia, la distancia del tap al punto ancla para los intervalos blancos no fueron estadísticamente significativas. En el recuadro, esquema del cálculo de la distancia, la esfera roja marca el punto ancla, se muestran dos trayectorias del intervalo entre-taps de ejemplo para los intervalos de 550ms (gris claro) y 1000ms (gris obscuro). La esfera verde marca la posición del tap y la esfera azul marca la posición de la mitad del intervalo entre-taps. Por lo tanto, las trayectorias neuronales convergen en un atractor alrededor del tiempo del tap, para después divergir a la mitad del intervalo entre-taps. Es de hacer notar que estos resultados sugieren la existencia de trayectorias circulares tangentes que convergen en una zona de intersección cerca del momento en el que se presiona el botón, aun cuando su amplitud cambia como función del intervalo. **C**, la velocidad del movimiento de tapping (línea naranja) del*

segundo al sexto tap del ST y la información neuronal proyectada en el PC1 para 26 neuronas registradas de manera simultánea durante un ensayo con un intervalo blanco de 550ms. Los taps se representaron como cuadros amarillos y los estímulos como círculos rojos. ***D****, similar a (C) para un ensayo de un intervalo blanco de 850ms (la información neuronal proyectada en el PC1 se muestra como un trazo amarillo). E, Media ± DS de la duración del movimiento (verde) y la pausa entre los movimientos (magenta) para los distintos intervalos blancos, calculados del perfil de velocidad de los movimientos de presión del botón. Una ANOVA de dos vías mostró efectos principales significativos en el estado cinemático (duración del movimiento/pausa, F(1,228) =1850,61, p < 0.0001), intervalo blanco (F(5,228) = 272.72, p < 0.0001) y su interacción (F(5,228)=236.18, p<0.0001). Una prueba post hoc HSD de Tukey mostró que la duración de la pausa para los diferentes intervalos blanco fue estadísticamente diferente (p<0.05). Por lo tanto, el mono moduló la duración de la pausa entre taps para temporalizar correctamente su comportamiento, mientras que el movimiento de tapping fue fásico y estereotípico para los diferentes intervalos blancos.*

[Tomado y modificado de Gámez et al., 2019]

Estas observaciones sugieren que durante los movimientos rítmicos un mecanismo de temporalización explícito en la MPC mide el tiempo de la pausa poniendo en movimiento un cambio continuo y periódico en el estado de la población neuronal. De acuerdo a este esquema, el comando motor asociado al tapping es iniciado una vez que las trayectorias de estado se encuentran en cierta área del espacio-fase que corresponden al punto de intersección entre las trayectorias circulares tangentes cuyos radios se incrementan con el intervalo medido. Para probar esta hipótesis, se calculó la distancia entre un punto en el espacio de estado y la posición de los taps en la trayectoria neuronal, encontrando una distancia similar para todos los intervalos blancos (Figura 20B, ver recuadro). Además, la distancia entre el mismo punto y la posición de la trayectoria a la mitad del intervalo entre dos taps se incrementó en función del intervalo blanco (Figura 20B). Estos resultados apoyan la idea de que las trayectorias neuronales codifican el tiempo de la pausa entre los taps en su radio y disparan el movimiento estereotípico asociado a los taps cuando la dinámica neuronal alcanza un punto en el espacio-estado (ver Figura 21).

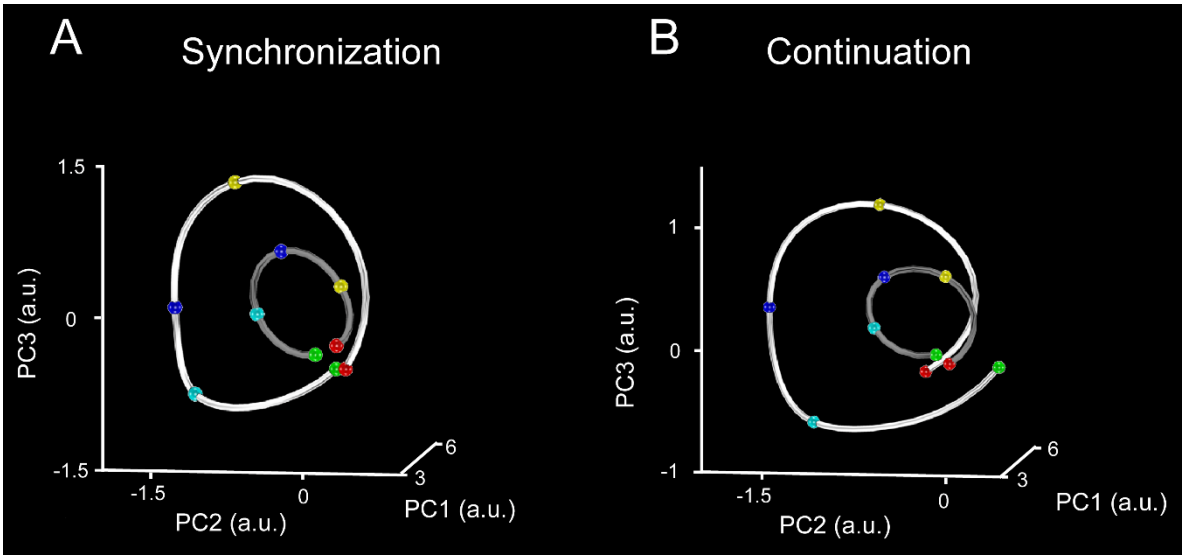

Figura 21 Progreso de las trayectorias neuronales durante la tarea de SCT

***A,B**, Un ciclo de las trayectorias neuronales para el segundo intervalo producido de la SC (A) y CC (B), durante un ensayo cuyo intervalo blanco fue de 450ms (gris obscuro) y 1000ms (gris claro). La progresión de la trayectoria se marca con esferas de colores: tap anterior (verde), primer cuarto del periodo entre taps (cian), segundo cuarto o mitad del intervalo (azul), tercer cuarto (amarillo) y el siguiente tap (rojo). Por lo tanto, las trayectorias siguen orbitas con diferentes radios que incrementan de acuerdo al intervalo blanco.*

[Tomado y modificado de Gámez et al., 2019]

Información temporal distribuida de la señal poblacional

Se determinó que es posible extraer información sobre el intervalo blanco a partir de la dinámica poblacional neuronal y como esta información es modulada por el tamaño de la población neuronal usada para calcular las trayectorias. Con este objetivo, primero se separó cada segmento entre taps de la actividad proyectada en una sola dimensión (PC) de acuerdo al intervalo blanco de la SCT (450, 550,…,1000ms; ver recuadro en Figura 22A). Posteriormente, con el fin de capturar la forma del segmento de la trayectoria como una coordenada tridimensional, se aplicó nuevamente un PCA (PCA') y se mantuvo el valor de los primeros 3 componentes principales. Como resultado, se obtuvo una nube de punto en tres dimensiones donde cada punto representa un segmento de trayectoria asociado a un intervalo producido particular (Figura 22A). Se entrenaron máquinas de vectores de soporte (SVM) para clasificar la nube de puntos para las cinco duraciones de la SCT. Se repitió el entrenamiento de los SVM diez veces y se usó validación cruzada de 5 separaciones para evaluar el comportamiento de los clasificadores. Por otro lado, cada neurona se ordenó de acuerdo a la magnitud del peso de los PCs originales. Las neuronas con la participación más grande para un PC se fueron eliminando en pasos de diez por ciento del tamaño de la población original y se calculó la segunda capa de PCA' en las nuevas trayectorias. Finalmente, la clasificación por SVM se llevó a cabo en los datos del PCA' de segunda capa para diferentes tamaños poblacionales (ver Figura 22).

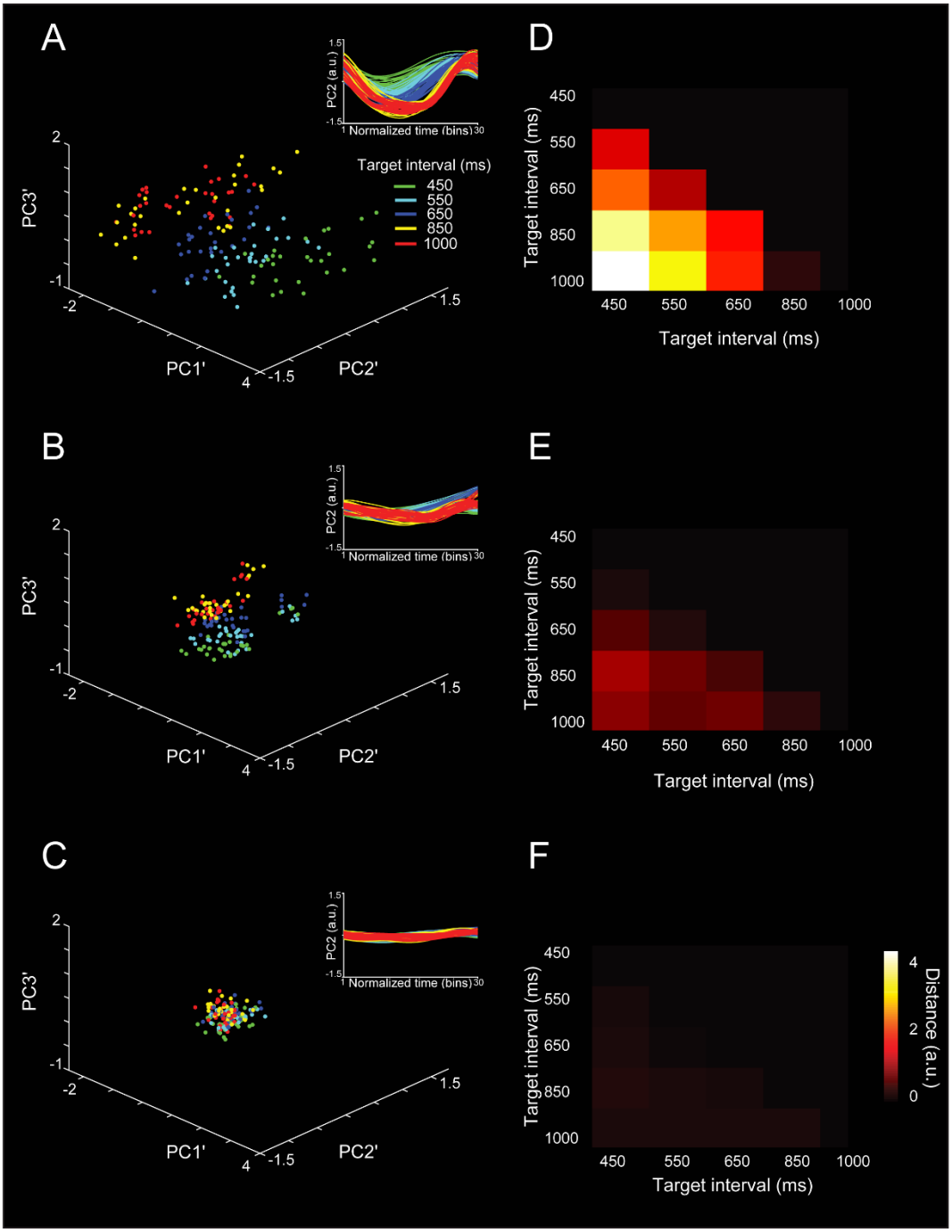

Figura 22 Robustez del clasificador para los intervalos blancos de SCT usando segmentos de las trayectorias neuronales de PCA entre taps con diferentes tamaños de poblaciones neuronales.

***A-C**, Proyección de los tres PCs del PCA de segunda capa aplicada a cada uno de los seis segmentos entre taps de la trayectoria y las cinco repeticiones (ver recuadro), para (A) 100, (B) 50 y (C) 1% de la población neuronal. El color del intervalo blanco se muestra en el recuadro de (A). D-F, Distancias entre los centroides de las nubes de puntos de los datos proyectados para los intervalos blancos para (D) 100, (E) 50 y (F) 1% de la población neuronal.*

[Tomado y modificado de Gámez et al., 2019]

Hubo una disminución asintótica en el performance del clasificador con la reducción del tamaño de la población neuronal (Figura 23A). sin embargo, aún con poblaciones pequeñas (15 células totales) el clasificador fue capaz de extraer información de los intervalos blancos arriba del azar. Estos resultados apoyan la idea de que la estructura temporal del comportamiento rítmico depende de un código poblacional neuronal que está distribuido en la MPC, contrariamente a que se deba a la actividad de un número pequeño de neuronas altamente correlacionadas (ver Figura 15).

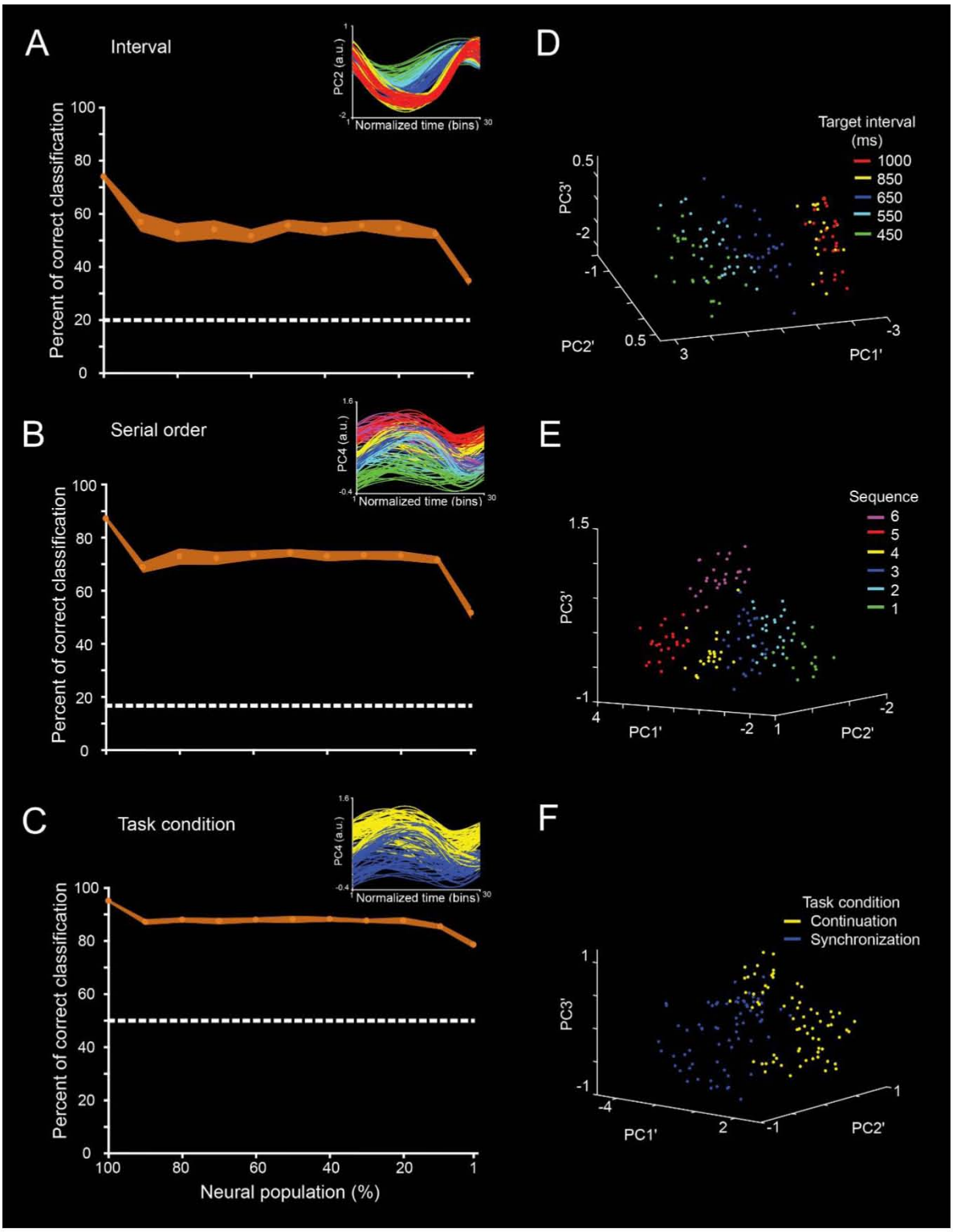

Figura 23 Robustez del clasificador de trayectorias para diferentes tamaños de poblaciones neuronales.

***A-C**, Comportamiento de la máquina de vectores de soporte (media ± DS del porcentaje correcto de clasificaciones) para clasificar los intervalos blancos (A, 5 intervalos instruidos), orden serial (B, 6 órdenes secuenciales) y condición (C, sincronización o continuación) durante la tarea de SCT basado en la trayectoria neuronal calculada con poblaciones de diferentes tamaños. El tamaño de la población inicial fue de 1477 neuronas. La línea punteada corresponde al nivel del*

azar. Las neuronas con la mayor participación para un CP fueron eliminadas en pasos de 10 por ciento de la población original, hasta alcanzar un tamaño del 1% de la población. El recuadro muestra los segmentos originales de las trayectorias normalizadas en el tiempo del PC usado para generar la segunda capa de PCA'. En A el PC seleccionado, por permitir una mejor clasificación del intervalo, fue el PC2, mientras que en B y C el PC seleccionado para secuencia y condición fue el PC4. ***D-E****, nube de puntos en un espacio tridimensional para el PCA' de segunda capa para los intervalos blancos. El código de color se representa en el recuadro. Es de hacer notar que el porcentaje de clasificación correcta disminuyó como una función del tamaño de la población, sin embargo, la clasificación siempre se mantuvo por arriba del nivel del azar aún para grupos pequeños de neuronas. [El inciso A y D fueron tomados de Gámez et al., 2019].*

Patrones temporales de activación neuronal

Los resultados de la sección revelaron una representación distribuida de la temporalización del tapping en la población neuronal de la MPC. Sin embargo, una pregunta importante es que aspecto de la actividad cambiante en el tiempo define los cambios en la amplitud de las trayectorias neuronales como función de la duración medida. Observaciones anteriores (Crowe et al., 2014; Hugo Merchant, Pérez, et al., 2015b) apoyan la hipótesis de que los patrones de actividad neuronal podrían estar directamente relacionados con las características que codifican la temporalización en las trayectorias neuronales durante la SCT. Para probar esta idea, se caracterizaron las propiedades de los "moving bumps" neuronales (Crowe et al., 2014; Hardy & Buonomano, 2018; Knudsen, Powers, & Moxon, 2014) durante esta tarea. Se llevaron a cabo simulaciones para determinar qué características principales de los "moving bumps" estaban relacionadas a los cambios observados en los radios y la variabilidad como función de la duración en las trayectorias neuronales.

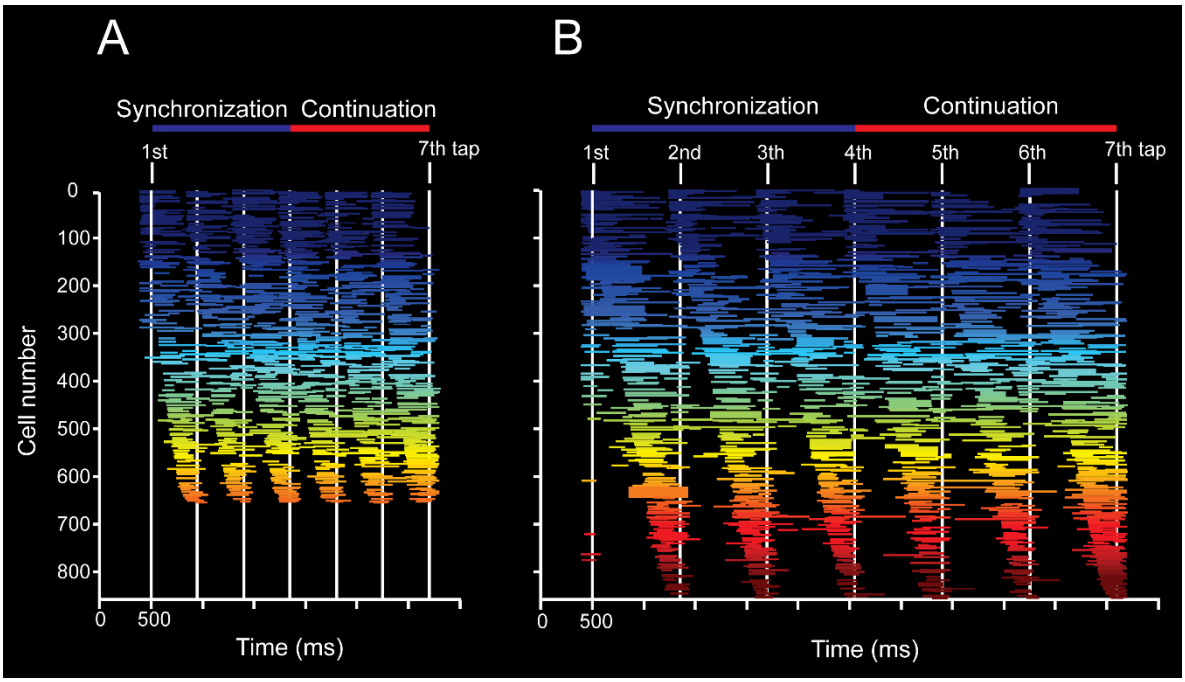

Figura 24 Patrones de actividad de las poblaciones neuronales en la MPC

A,B*, periodos de activación neuronal, ordenados por el tiempo medio del pico de actividad, durante una tarea de SCT para los intervalos blancos de (A) 450 y (B) 850ms. Cada línea horizontal corresponde al inicio y la duración de los periodos significativos de activación de una célula de acuerdo al análisis de tren de eventos de Poisson. El análisis de tren de eventos*

de Poisson se llevó a cabo sobre la tasa de disparo de las células warped a los tiempos de tapping (siete líneas blancas verticales; Hugo Merchant, Pérez, et al., 2015b; Perez et al., 2013). Hágase notar que el número de células con periodos de activación significativos es mayor para intervalos más largos.

[Tomado y modificado de Gámez et al., 2019]

Una proporción substancial de las neuronas del MPC durante la SCT mostraron un patrón progresivo de activación en la población neuronal, que consistió en el inicio gradual de la respuesta de células individuales para un intervalo producido. Este patrón de activación inició antes del tap, migró durante la temporalización del intervalo y terminó después del tap siguiente (ver Figura 24). Además, un perfil de activación similar se repitió de manera cíclica para los tres intervalos del SC y los tres intervalos del CC (ver Figura 24A,B) (Crowe et al., 2014; Hugo Merchant, Pérez, et al., 2015b). Estos resultados sugieren que la temporización rítmica puede ser codificada en la activación secuencial de poblaciones neuronales (Mello, Soares, & Paton, 2015). Una pregunta importante es qué parámetros de los perfiles de activación neuronales codifican el intervalo blanco y la condición de la SCT. El número de neuronas involucradas en estos patrones de activación (ver Figura 24A,B, Figura 25C), así como las duración de los periodos de activación (ver Figura 25D) se incrementaron en función del intervalo blanco. Durante la SC hubo un mayor número de células activas, mientras que durante la CC el periodo de activación de las células fue mayor. Sin embargo, el lapso de reclutamiento neuronal, definido como el tiempo entre la activación de neuronas que se activaron de manera consecutiva (ver Figura 25E), así como la tasa de disparo de las células (ver Figura 25F) no mostraron cambios estadísticamente significativos para los diferentes intervalos blancos ni condición de la tarea. Estos resultado sugieren que tanto el tamaño de los circuitos involucrados en medir el paso del tiempo, así como la duración de sus periodos de activación son señales que codifican el paso del tiempo en la MPC, sugiriendo la existencia de un delicado balance entre estas dos medidas para generar los perfiles de activación progresivos de las neuronas cuando se realizan movimientos siguiendo un metrónomo o una señal rítmica generada de manera interna (ver Figura 25C,D)

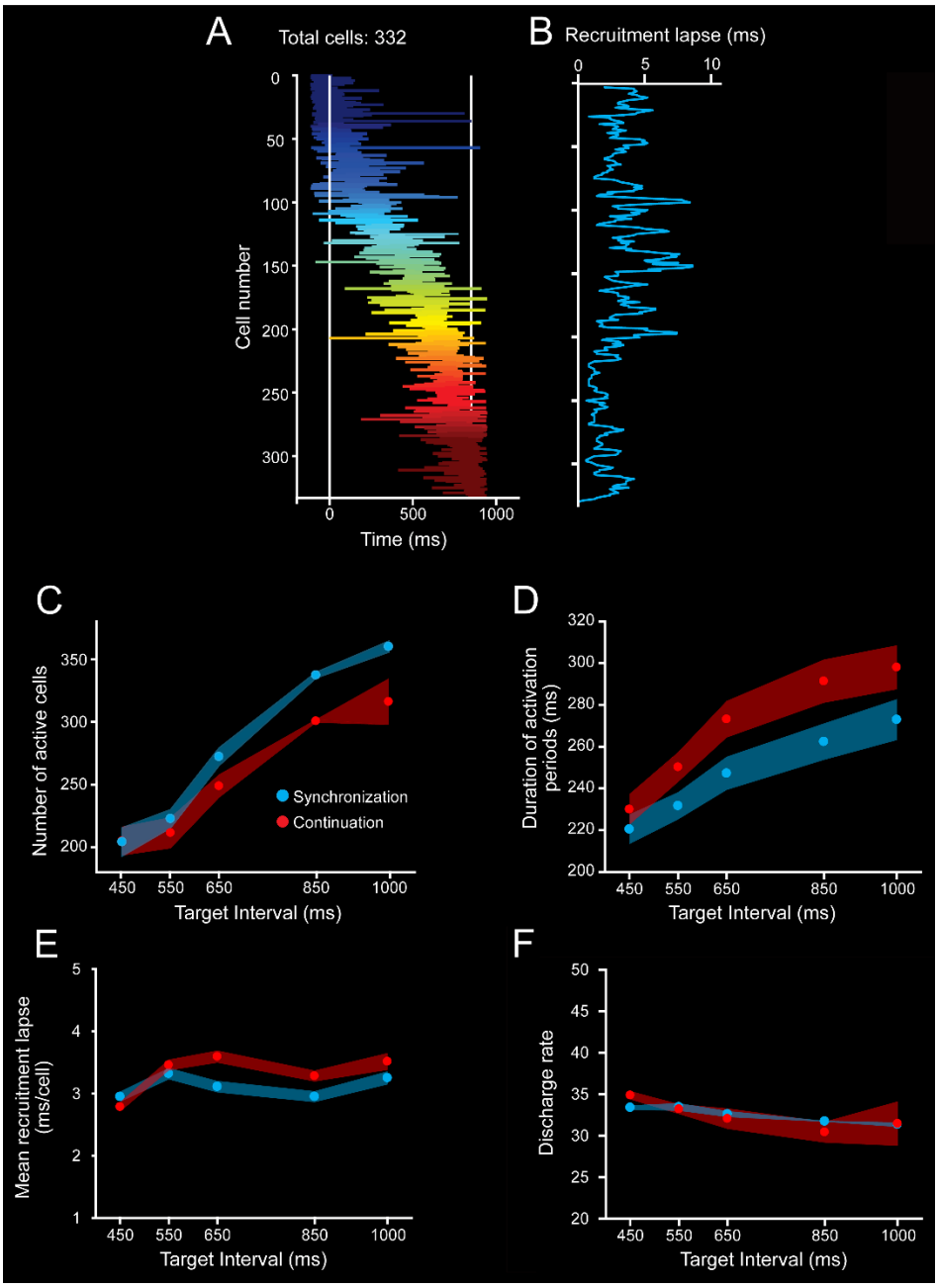

Figura 25 Desarrollo temporal de patrones de activación

***A**, Periodos de activación neuronal para el segundo Intervalo producido (las líneas verticales blancas representan al segundo y tercer tap) durante el SC para el intervalo blanco de 850ms. Las líneas horizontales de cada renglón corresponden al inicio y duración de los periodos de activación detectados por el análisis de trenes de eventos de Poisson. Las células se ordenaron de acuerdo al tiempo del pico de actividad. **B**, el lapso de reclutamiento como una función del número de célula. El lapso de reclutamiento se calculó como la diferencia en el tiempo del pico de actividad entre dos neuronas contiguas en la avalancha neuronal. El lapso promedio de activación (± SEM) fue de 2.98 ± 0.08 ms. **C**, número de células con periodos de activación significativos para los intervalos blancos de SC (rojo) y CC (azul). Las avalanchas de intervalos más largos reclutan más células. (ANOVA efecto principal del intervalo blanco, $F(4,20)=21.1, p<0.0001$; efecto principal de la condición de la tarea, $F(1,20)=6.2, p<0.02$; interacción intervalo x condición, $F(4, 20) = 0.71, p = 0.594$). **D**, Duración de los periodos de activación durante el SC (rojo) y CC (azul) se incrementó como función del intervalo blanco. (ANOVA efecto principal del intervalo blanco, $F(4,20)=18.9, p<0.0001$; efecto principal de la condición de la tarea, $F(1,20)=26.7, p<0.0001$; interacción intervalo x condición, $F(4, 20) = 1.3, p = 0.268$). E, El lapso de reclutamiento promedio*

durante SC (rojo) y CC (azul) no cambió como función del intervalo blanco (ANOVA efecto principal del intervalo blanco, F(4,20)=2.7,p=0.06; efecto principal de la condición de la tarea, F(1,20)=3.4, p=0.08; interacción de intervalo x condición, F(4, 20) = 0.79, p = 0.55). F, La tasa de descarga durante los periodos de activación en SC (rojo) y CC (azul) no variaron con el intervalo blanco (ANOVA efecto principal del intervalo blanco, F(4,20)=2.2,p=0.06; efecto principal de la condición de la tarea, F(1,20)=0.86, p=0.35; interacción intervalo x condición, F(4, 20) = 0.92, p = 0.45).

[Tomado y modificado de Gámez et al., 2019]

Simulaciones de trayectorias neuronales

Se realizaron simulaciones de los patrones de actividad poblacional con diferentes perfiles de respuesta y se evaluaron sus efectos al proyectarlos en un espacio de PCA. Primero, se generaron patrones de unidades individuales complejos, heterogéneos y que se escalaban en el tiempo, produciendo periodos de activación con la misma variación en el tiempo de la actividad pero con diferentes duraciones (ver Figura 26A, ver métodos; Wang et al., 2018). Posteriormente, se simularon patrones de secuencias de activación poblacionales para tres intervalos consecutivos, imitando dos características claves de las respuestas poblacionales en la MPC: la activación gradual de células individuales que iniciaban antes del *tap* anterior, migraban durante, y terminaban después del intervalo producido, con un reclutamiento constante de neuronas en el tiempo, así como la repetición cíclica de este perfil de respuesta para tres intervalos consecutivos (ver Figura 26C,D). Además, la Figura 27A muestra que las neuronas se agregaron de manera aleatoria en la porción intermedia de los “moving bumps” simulados al ir incrementando el número total de células. La proyección de las cascadas simuladas en el espacio de PCA generó órbitas (ver Figura 26B), cuyos radios y variabilidad incrementaron, pero su velocidad lineal fue similar para los diferentes intervalos blancos, tal como se observó en las respuestas neuronales reales. Estas propiedades solo se mantuvieron cuando las simulaciones de las secuencias de activación neuronales incluyeron un incremento tanto en el número de neuronas, así como en la duración de los periodos de activación en función del intervalo blanco (ver Figura 26 E,F).

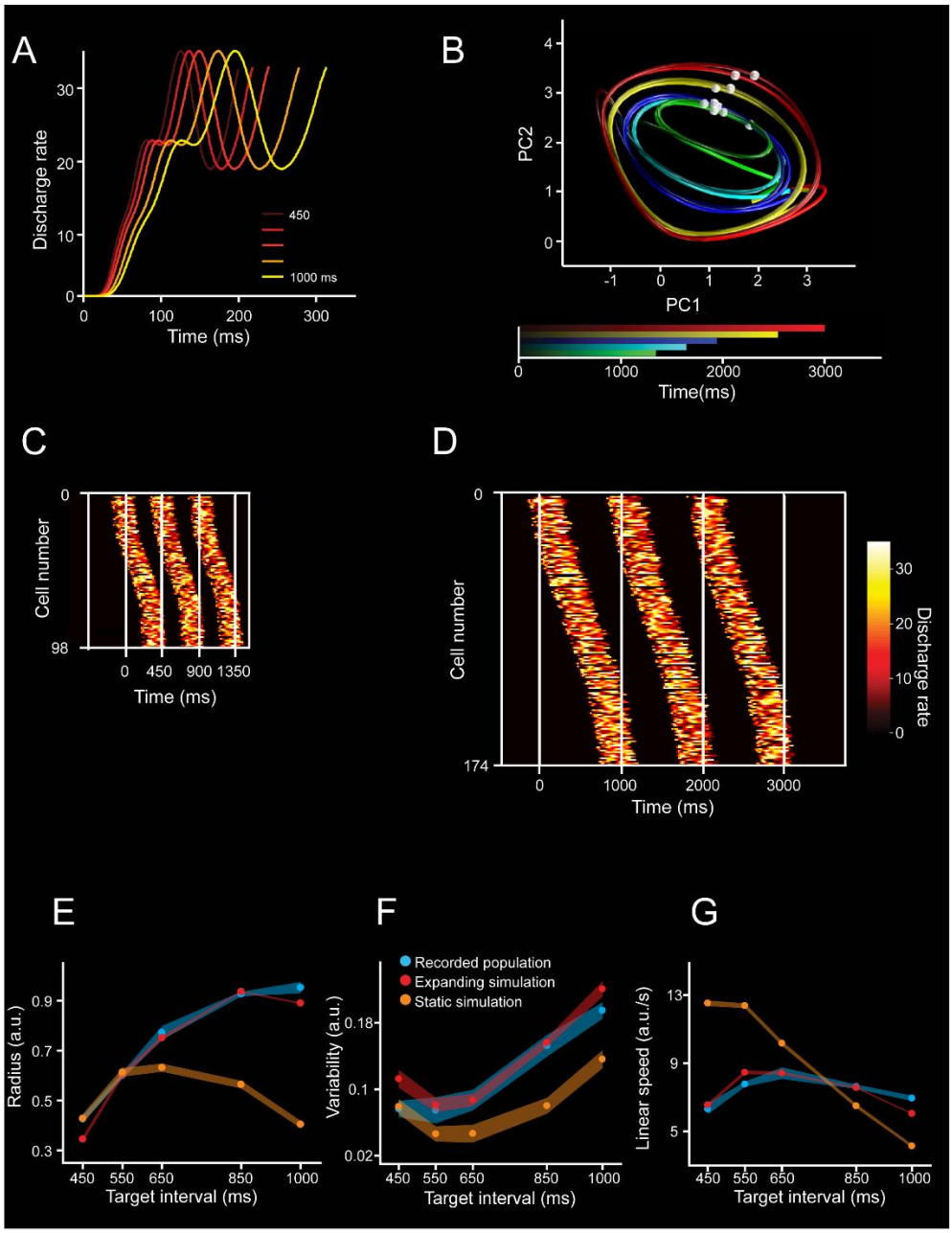

Figura 26 Simulaciones de los "moving bumps" y las trayectorias neuronales

***A**, Perfil de activación de una neurona simulada durante el periodo de activación escalado para las cinco duraciones simuladas. **B**, Trayectorias neuronales generadas de la actividad poblacional de las simulaciones de los "moving bumps". El número de neuronas y sus periodos de activación se modificó para cada intervalo blanco. El intervalo blanco simulado se codifica en el color de la trayectoria. El segundo y tercer tap simulados están marcados como esferas blancas en cada trayectoria. **C,D**, Perfiles de activación de neuronas para tres intervalos simulados consecutivos con una duración de 450ms (C) y de 1000ms(D). Las líneas blancas verticales corresponden a los eventos de los taps definiendo los intervalos. Los perfiles de activación siguen una forma gaussiana del reclutamiento neuronal, con bajas tasas de activación en los extremos (cerca de cada tap). El número de neuronas y la duración de los periodos de activación se incrementaron como función del intervalo blanco simulado. **E,F,G**, Radios (E), variabilidad (F) y velocidad lineal (F) de las trayectorias neuronales generadas a partir de las simulaciones. Datos de la actividad neuronal simulada con un número creciente de neuronas y periodos de activación (rojo), duración estática de los periodos de activación y número de neuronas (naranja) y de la población neuronal registrada durante la SCT (azul) para los intervalos blancos. Es de hacer notar que una constante se*

agregó a los datos de ambas simulaciones en los gráficos. E, Radios para las simulaciones con parámetros variables (rojo, media±DS, pendiente=0.0009, R^2=0.811, p<0.0001), simulación con parámetros constantes (naranja, media±DS, regresión lineal no significativa, pendiente=-0.0001, R^2=0.811, p=0.214) y actividad neuronal (azul, media±DS, pendiente=0.0009, R^2=0.897, p<0.0001). Las pendientes de los radios, variabilidad y velocidad lineal no fueron estadísticamente diferentes entre las simulaciones con los parámetros variables y las trayectorias neuronales registradas (pendiente del radio t-test = 0.15, p = 0.878; pendiente de la variabilidad t-test = 0.25, p = 0.803; pendiente de la velocidad lineal t-test = 1.8, p = 0.077). Sin embargo, las pendientes entre las simulaciones con parámetros constantes y las trayectorias neuronales mostraron diferencias estadísticamente significativas (pendiente del radio t-test = 9.13, p < 0.0001; pendiente de la variabilidad t-test = 3.73, p < 0.001; pendiente de la velocidad lineal t-test = 17.71, p < 0.0001).

[Tomado y modificado de Gámez et al., 2019]

Las simulaciones con valores constantes en ambos parámetros generaron trayectorias neuronales con radios o variabilidad similares para las diferentes duraciones de los intervalos, así como una reducción en la velocidad lineal, lo que sería consistente con el escalamiento temporal (Figura 26E-G, Figura 27B-E). Además, escalar únicamente la duración de la respuesta no reprodujo los cambios observados en el radio y la variabilidad para las diferentes duraciones en las trayectorias de estado (Figura 27D-E). Estos resultados indican que, además de una relación cercana entre las propiedades de los patrones neuronales secuenciales de activación y las trayectorias neuronales cíclicas durante el *tapping* rítmico, un incremento en el número de neuronas que participan en los patrones de activación poblacionales es fundamental para reproducir las dos características que dependen de la duración del intervalo temporizado en las trayectorias poblacionales neuronales: el incremento de la magnitud y la variabilidad de los radios como función del intervalo blanco. En la Figura 28 se muestran las trayectorias generadas con la actividad de una subpoblación de neuronas que mostraron al menos 15 periodos de activación, seleccionada de las 1477 neuronas registradas. El aumento significativo en la varianza explicada al aplicar PCA a esta subpoblación apoya la hipótesis de que es la actividad secuencial de los “moving bump” el origen de las órbitas periódicas de la dinámica poblacional, así como de su radio, variabilidad y velocidad lineal.

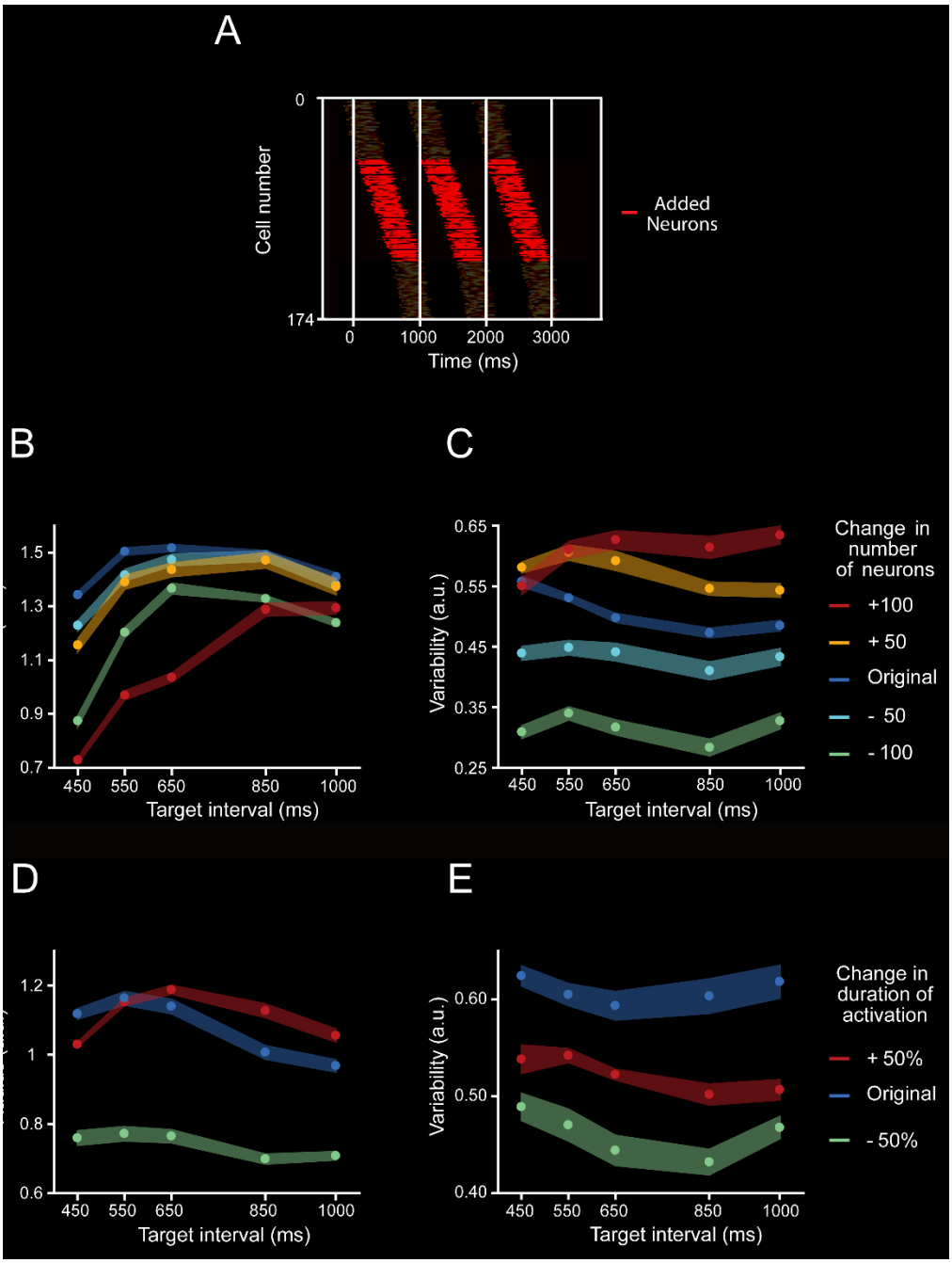

Figura 27 Efecto de los parámetros de las simulaciones de los moving bumps

***A**, Posición temporal de los periodos de activación de las neuronas que se agregan a una simulación para un ensayo de un intervalo blanco de 1000ms (rojo) a diferencia de la posición de los periodos de activación las neuronas que también participan en un ensayo de 450ms (negro). **B,C**, Radio (B) y variabilidad (C) de las trayectorias de PCA generadas de simulaciones de "moving bumps" cuando el número de neuronas se modifica en un número constante aumentando o disminuyendo el tamaño de la población original cuyo tamaño cambia como función del intervalo blanco. Una ANOVA de dos vías en los radios mostró un efecto principal significativo para el número de neuronas ($F(4,100) = 10544.2$, $p < 0.0001$), intervalo blanco ($F(4,100) = 4013.12$, $p < 0.0001$) así como su interacción ($F(16,100) = 25.8$, $p < 0.0001$). Una prueba post hoc HSD de Tukey mostró diferencias significativas para los radios de todas las simulaciones con diferente número de neuronas y para todos los intervalos blancos ($p < 0.05$). Además, una ANOVA de dos vías de la variabilidad mostró efectos principales significativos para el número de neuronas ($F(4,100) = 2421.8$, $p < 0.0001$), intervalo blanco ($F(4,100) = 3476.91$, $p < 0.0001$)*

y su interacción (F(16,100)=22.53, p<0.0001). Una prueba post hoc HSD de Tukey mostró diferencias significativas para la variabilidad en todas las simulaciones con diferente número de neuronas (p<0.05). ***D,E****, Radio (D) y variabilidad (E) de las trayectorias generada de los "moving bumps" neuronales donde la duración de los periodos de activación fue la mitad (cortos, amarillo) o el doble (largos, rojo) que la duración escalada original (azul) como función del intervalo blanco (ver Figura 26).Una ANOVA de dos vías sobre la variabilidad mostró efectos principales significativos para la duración de la activación (F(2,60) =3081.54, p < 0.0001), el intervalo blanco (F(4,60) =2801.16, p < 0.0001) y la interacción de ambos (F(8,60)=211.34, p<0.0001). Una prueba post hoc HSD de Tukey mostró diferencias significativas para todas las simulaciones con diferentes duraciones de activación (p<0.05). Además, una ANOVA de dos vías sobre la variabilidad mostró efectos principales significativos para la duración de la activación (F(2,60) =1227.53, p < 0.0001), intervalo blanco(F(4,60) =257.49, p < 0.0001) y su interacción (F(8,60)=24.87 p<0.0001). Una prueba post hoc HSD de Tukey mostró diferencias significativas para todas las simulaciones con diferentes duraciones de activación (p<0.05). Por lo tanto, el número de neuronas y la duración de la activación en los "moving bumps" generan cambios en el radio y la variabilidad de las trayectorias neuronales simuladas.*

[Tomado y modificado de Gámez et al., 2019]

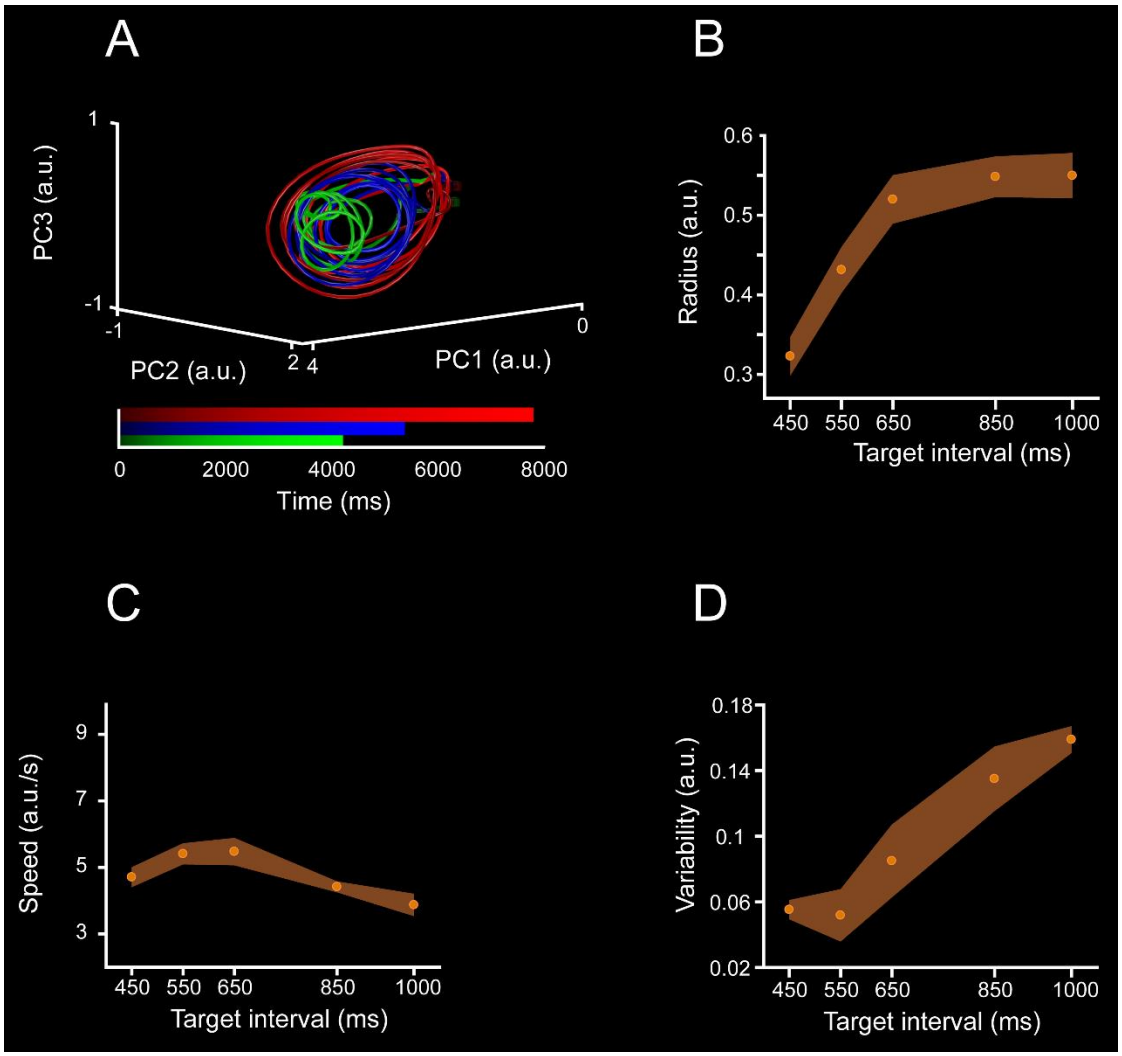

Figura 28 Trayectorias poblacionales neuronales durante la tarea de SCT de una subpoblación con actividad relacionada a la tarea

El análisis de PCA se aplicó sobre la actividad de 104 neuronas que mostraron al menos 15 periodos de activación en el análisis de tren de eventos de Poisson para los cinco intervalos blancos y los 6 elementos de orden serial de la SCT. Los primeros 3 PCs explicaron el 32.5 por ciento de la varianza total. ***A****, Proyección de la actividad neuronal durante la SC y CC de la SCT en los primeros PCs. La trayectoria completa un ciclo en cada intervalo producido durante las fases de sincronización y continuación de la SCT. El color de la trayectoria indica el intervalo blanco (450, verde; 650, azul; 1000, rojo). La progresión de color para cada intervalo blanco corresponde con el tiempo transcurrido. Un cubo marca el inicio de cada trayectoria, mientras que un octaedro marca el final.* ***B****, Radio de las trayectorias circulares durante la SC y CC (media±DS, pendiente=0.0003, constante = 0.2, R^2=0.7, p<0.0001) como función del intervalo blanco.* ***C****, Velocidad lineal de las trayectorias circulares durante la SC y CC (media±DS, pendiente=-0.002, constante = 6.3, R^2=0.4.2, p = 0.001) como función del intervalo blanco.* ***D****, Variabilidad de las trayectorias neuronales (media±DS, pendiente de datos normalizados=0.0002, constante = -0.05, R^2=0.87, p< 0.0001) como función del intervalo blanco.*

[Tomado y modificado de Gámez et al., 2019]

Discusión

Los resultados del presente estudio se pueden agrupar en dos temas principales: la capacidad de los monos para la reproducción de ritmos y el análisis de la dinámica poblacional neuronal en la MPC de los monos durante la producción rítmica.

Comportamiento

La producción rítmica en los humanos alcanza una complejidad sin igual en el reino animal. Se han realizado una gran cantidad de estudios en humanos de los diferentes aspectos que componen la percepción y reproducción rítmica (Cook, Rouse, Wilson, & Reichmuth, 2013; Hasegawa, Okanoya, Hasegawa, & Seki, 2011; Lewis et al., 2004; BrunoH. Repp & Penel, 2004; Thaut et al., 1998). Hace unos años se empezaron a utilizar a los monos Rhesus como modelo para el estudio de la producción rítmica (Zarco et al., 2009). Sin embargo, no se conocen los límites de las capacidades de sincronización rítmica en los monos. Se ha demostrado que los monos comparten diversas características de la producción de intervalos con los humanos. Sin embargo, a diferencia de los humanos, los monos no realizan el comportamiento de sincronización a un metrónomo de manera espontánea. Se requiere de un entrenamiento intenso, guiado por el reforzamiento de la recompensa, para que los monos alcancen los parámetros de comportamiento que se presentan en este trabajo. La expectativa de los monos por recibir recompensa se incrementa con el transcurso del ensayo, por lo que al inicio del entrenamiento muestran una preferencia por realizar ensayos de intervalos blancos cortos. Es por esto, que en la tarea de SCT se utilizaron recompensas cuya magnitud aumentaba de acuerdo a la duración del intervalo blanco. Sin embargo, en las tareas de ST y SRTT no se moduló la magnitud de la recompensa con el intervalo blanco. Pese a lo anterior, los monos lograron aprender a realizarlas de manera consistente después de un arduo entrenamiento.

Una de las diferencias reportadas entre el comportamiento de los humanos y los monos, durante la sincronización a metrónomos, es que los monos presentan asincronías positivas durante este tipo de tareas (Zarco et al., 2009). En este trabajo también encontramos que los monos presentaron asincronías positivas durante la sincronización a metrónomos visuales y auditivos. Sin embargo, las asincronías reportadas fueron en promedio 100ms menores que lo reportado por Zarco et al., 2009. Esta diferencia parece tener su origen en el esquema de entrenamiento. Debido a que para las tareas de ST y TCST se incluyó el valor de la asincronía como parte de las reglas para recompensar el comportamiento del mono. De tal manera, que los monos no recibían recompensa si presentaban asincronías mayores a un umbral, mientras que si el promedio de sus asincronías en un ensayo era menor que otro umbral recibían doble recompensa. Estos umbrales se ajustaron de manera individual para cada mono, de tal manera que recibiera recompensa en alrededor del 70% de los ensayos y recibieran doble recompensa en un 20% de ensayos. Aun cuando la reducción de las asincronías fue limitada estas tareas, en nuestro laboratorio se entrenó a otro mono con una serie de reglas que relacionaban el tiempo de aparición de los estímulos con el movimiento del *tap* del

mono. En este entrenamiento el mono aprendió a realizar sus movimientos con asincronías negativas (Gámez et al., 2018). De igual manera, otro grupo entrenó a varios monos Rhesus en una tarea de sincronización, donde los monos tenían que generar sácadas en sincronía con un metrónomo visual (Takeya, Kameda, Patel, & Tanaka, 2017). Ellos utilizaron un paradigma de entrenamiento donde se le daba recompensa al mono de manera inmediata cada vez que realizara sacadas con asincronías de menos del 20% del tiempo de aparición del estímulo guía. Los monos mostraron asincronías alrededor del tiempo del estímulo, incluyendo asincronías negativas. La sincronización a un metrónomo no es un comportamiento espontáneo en los monos, a diferencia de los humanos. No obstante, los monos pueden ser entrenados a sincronizarse a un metrónomo presentando asincronías negativas, siempre que se incluyan reglas con este fin en la recompensa del animal.

Reproduciendo reportes anteriores, encontramos que los monos siguen la propiedad escalar tanto para metrónomos de modalidad visual, así como auditiva (Zarco et al., 2009). A diferencia de los humanos, los monos mostraron una preferencia por los metrónomos visuales, que se observa en una menor variabilidad en los intervalos producidos y asincronías. La razón de esta discrepancia es motivo de investigación actualmente. Se cree que la diferencia pueda residir en la fuerza de las conexiones que llevan información auditiva de las regiones temporales a las frontales (Patel, 2014). Por ejemplo, se ha comprobado que el fascículo arcuato, el cual se ha relacionado con la transmisión de información auditiva en el habla, está más desarrollado en humanos que en monos (Rilling et al., 2008). Sin embargo, si asumimos que esta diferencia afecta el funcionamiento de la MPC, no es del todo claro el mecanismo por el que la sincronización a los ritmos auditivos podría verse afectada. En primer lugar, la falta de una vía con menos relevos podría afectar la latencia con la que la información auditiva se encuentra disponible en la MPC. Sin embargo, la latencia de la actividad de neuronas con respuestas motoras asociadas a estímulos auditivos en monos es menor que la asociada a estímulos visuales (J Tanji & Kurata, 1982). En segunda instancia, podría afectar la cantidad de información que alcanza la MPC, pero la mayor parte de las neuronas en esta área con respuestas sensoriales son bimodales a estímulos visuales y auditivos (J Tanji & Kurata, 1982). Asimismo, de aquellas neuronas que son unimodales, hay una mayor cantidad que son responsivas a estímulos acústicos que visuales (J Tanji & Kurata, 1982). Por otro lado, generamos trayectorias neuronales similares para la tarea de SCT para ambas modalidades, por lo que la población de neuronas de la PMC tiene información temporal similar para metrónomos de ambas modalidades. Otra posibilidad es que la información auditiva que llega por otras vías indirectas, disponibles en el cerebro del mono, tiene que seguir diferentes vías con diferente número de relevos, por lo que llega con diversas latencias a la PMC, lo que dificulta su procesamiento coherente. Finalmente, una última posibilidad podría ser que la causa de esta discrepancia se encuentre en algún otro nodo relacionado con el procesamiento auditivo y las respuestas motoras y no directamente en la MPC.

La tarea de TCST buscar evidenciar los mecanismos de adaptación a los cambios dinámicos en los ritmos. Se ha reportado que, durante esta tarea, los humanos presentan dos procesos de adaptación. Por un lado, adaptan el periodo del intervalo producido, y por otro la fase de los movimientos de sincronización (B. H. Repp & Keller, 2004). Durante la TCST, el mono presentó un comportamiento con un índice de predicción mayor a 1 y una autocorrelación negativa del lag-1 en la serie de tiempo, lo que soporta la noción de que los monos tienen un mecanismo de corrección del periodo. Por otro lado, el patrón de adaptación que presentaron sus asincronías relativas revela

que los monos también poseen un mecanismo de adaptación de la fase de sus *taps*. Es interesante que el patrón de adaptación es diferente para la modalidad de aceleración que para la desaceleración. En el primero, las asincronías tienen un incremento en su magnitud relacionado al cambio en el ritmo del metrónomo, que durante la progresión del ensayo regresa a un valor similar al inicial. Por otro lado, durante los ensayos de desaceleración, el mono reduce sus asincronías de manera lineal desde el inicio del ensayo hasta el final del cambio en el metrónomo. Esta diferencia podría estar relacionada con las reglas de recompensa nuevamente, pues si el mono incrementa mucho sus asincronías no recibe recompensa, por lo que intenta compensar el incremento que sufre durante al inicio de la aceleración del ritmo. Mientras que, durante la desaceleración, el mono aumenta la probabilidad de recibir doble recompensa al disminuir lo más posible sus asincronías.

Este conjunto de resultados establece que las habilidades a la sincronización de ritmos en los monos son superiores a lo que se creía hasta el momento. Cabe resaltar, que los mecanismos de sincronización de ritmos de los macacos no son tan restringidos como se creía previamente. Por lo tanto, el mono mostró contar con mecanismos que le permiten ajustar la fase y la frecuencia de sus movimientos. Gracias a los cuales, puede sincronizarse, además de a ritmos regulares, a variaciones dinámicas en la regularidad del ritmo.

Dinámica poblacional

La actividad de poblaciones neuronales proyectadas en un plano utilizando PCA, generó trayectorias estereotípicas en orbitas periódicas, donde el radio de estas orbitas estuvo relacionado con la duración del intervalo producido. Las trayectorias neuronales no estuvieron relacionadas con la cinemática estereotípica de los movimientos fásicos que realizan los monos durante la ST. Por el contrario, estuvieron asociadas a la medición del tiempo de la pausa entre movimientos (Sophie Donnet et al., 2014). La variabilidad de estas trayectorias mostró estar correlacionadas con la variabilidad del comportamiento del mono, pudiendo ser el sustrato neuronal de esta. Mientras tanto, el análisis de dPCA también produjo trayectorias con una modulación en su amplitud como función del intervalo blanco durante la SCT y la ST. Además, al cambiar de una tarea de *tapping* rítmico, donde el mono podía predecir el siguiente estímulo, a una tarea de tiempo de reacción SRTT, el sistema dinámico de la actividad neuronal se comporta diferente y presenta una desorganización en la periodicidad de las trayectorias neuronales, así como una pérdida de la relación en el radio de las trayectorias con el intervalo producido.

Secuencias de activación

La dinámica de las respuestas neuronales individuales en la MPC fue rica y heterogénea. Se encontró que la codificación de la información temporal se distribuye entre la población neuronal. Donde un grupo significativo de neuronas presentó un patrón de activación secuencial o “moving bump” durante cada intervalo producido. Este tipo de perfil de activación secuencial de grupos neuronales se ha encontrado en diversas partes del cerebro y se ha relacionado con una serie de comportamientos incluyendo memoria espacial en el hipocampo (Pastalkova, Itskov, Amarasingham, & Buzsaki, 2008) y PPC (Harvey et al., 2012); así como en tareas de medición del

tiempo en el estriado (Mello et al., 2015), hipocampo (MacDonald, Lepage, Eden, & Eichenbaum, 2011), MPC (Crowe et al., 2014; Hugo Merchant, Pérez, et al., 2015a) y corteza prefrontal (Bakhurin et al., 2017). Lo que sugiere, que este patrón de "*moving bump"* es parte de un diccionario de respuestas poblacionales que utiliza el cerebro para cuantificar el desarrollo de un proceso que transcurre en el tiempo o en el espacio. En ambos trabajos, Mello et al., 2015 y Bakhurin et al., 2017, encontraron "moving bumps" en poblaciones neuronales del estriado de roedores asociado a la medición de intervalos temporales. Mientras que Bakhurin et al., 2017, encontraron que la variabilidad de la respuesta del ratón se relacionaba con la velocidad de activación del patrón secuencial neuronal. Sin embargo, Mello et al., 2015, encontraron que el incremento en la variabilidad en las respuestas de las ratas a los intervalos más largos probablemente estaba asociado a un aumento en el periodo de las neuronas en función de su pico de latencia, así como a un decremento de la densidad de neuronas que tenían un pico en su actividad conforme transcurría el tiempo. En ambos trabajos, el tamaño de la población neuronal que participó en la secuencia de activación se mantuvo fijo para todos los intervalos. En contraste, en este trabajo encontramos que la longitud del periodo de activación de las neuronas en la MPC se incrementó en función del intervalo blanco, pero no varió con el tiempo transcurrido. De igual manera, encontramos que el número de neuronas que participaron en los patrones de activación secuencial se incrementaba con la duración del intervalo. El reclutamiento de diferentes grupos neuronales en función de la longitud del intervalo producido, podría estar asociado al mapa cronotópico en la MPC encontrado por Protopapa et al., 2019, donde por medio de fMRI en humanos encontraron una distribución cronotópica antero-posterior a lo largo de la PMC, en la cual grupos de neuronas asociadas a intervalos más cortos mostraron una mayor actividad diferencial en la parte anterior de esta área.

Trayectorias neuronales

La proyección de la actividad neuronal en un plano fase, formado por los componentes principales dos y tres, reveló un sistema dinámico con diversas órbitas periódicas tangentes. Donde cada intervalo blanco estuvo asociado a una órbita correspondiente. El intervalo blanco, indicado por el metrónomo durante la fase de percepción al inicio de cada ensayo, fue el parámetro inicial que llevaba la dinámica del sistema a la órbita correspondiente, donde permanecía hasta que el mono recibía recompensa (sólo se analizaron ensayos correctos). El intervalo blanco no modificó la velocidad a la que viajan las trayectorias neuronales periódicas en el espacio fase. La información neuronal proyectada en cada uno de estos dos componentes principales oscila durante los ensayos de las tareas de sincronización. Las señales oscilatorias en el componente principal dos y tres tienen una diferencia de fase de $\pi/2$ entre ellas. Anteriormente, se ha encontrado una dinámica rotacional similar en la actividad poblacional neuronal durante diversos movimientos rítmicos (Churchland et al., 2012). Sin embargo, la actividad rotacional que encontramos está relacionada a la medición del tiempo durante las pausas entre los movimientos fásicos de *tapping*. Una dinámica rotacional en el espacio fase no solo requiere de respuestas multifásicas, estos patrones de respuesta deben tener una diferencia de fase de $\pi/2$. Es gracias a esta diferencia de fase, que el comportamiento del sistema dinámico en el plano fase es una órbita estable. El comando motor de *tapping* se dispara cuando la órbita alcanza un área específica en el plano fase, la cual corresponde con el punto de intersección entre las trayectorias circulares tangentes. Estos resultados contrastan con las

trayectorias neuronales en las áreas frontales mediales durante la reproducción de un intervalo único (Remington et al., 2018; Wang et al., 2018), donde la posición inicial de las trayectorias neuronales paralelas era establecida por la entrada inicial y la velocidad de las trayectorias estaba modulada por la duración del intervalo a reproducir.

La simplicidad de las trayectorias neuronales se contrapone con la complejidad de las respuestas únicas de las neuronas que se encuentran en la MPC (Mendoza et al., 2018; Hugo Merchant, Pérez, et al., 2013; Hugo Merchant et al., 2011; Perez et al., 2013). La actividad poblacional en la MPC cumple con las tres características que propone Pandarinath et al., 2018, para que las respuestas poblacionales se puedan analizar desde el paradigma de los sistemas dinámicos: primera, la instrucción del intervalo blanco es el parámetro inicial que determina la órbita en la que oscilara el sistema; segunda, la actividad poblacional de las neuronas tiene una dinámica interna que se manifiesta durante la pausa en el movimiento del mono, y que por lo tanto no depende únicamente de las entradas y salidas del sistema; tercera, el sistema sigue diferentes trayectorias que no se superponen. Además, son estas características las que permiten que la actividad poblacional pueda ser usada como un reloj durante la producción de intervalos rítmicos (Karmarkar & Buonomano, 2007).

La recompensa juega un papel fundamental en el comportamiento del mono durante las tareas de sincronización. Además, se ha reportado que en la MPC existen neuronas que predicen el tiempo en el que se recibirá la recompensa. Estas neuronas muestran un incremento abrupto en su actividad un par de cientos de milisegundos antes del tiempo en el que se espera la recompensa y cesan completamente su actividad una vez que se recibe la misma (Campos, Breznen, Bernheim, & Andersen, 2005). También se ha reportado que existe un grupo de neuronas en la MPC que codifican la magnitud de la recompensa recibida en su tasa de disparo (Scangos, Aronberg, & Stuphorn, 2013). Nosotros observamos un incremento en la tasa de disparo de algunas neuronas que parece correlacionar con el tiempo en que se presenta la recompensa. Sin embargo, el incremento de la magnitud de la recompensa durante la SCT no es el origen del aumento de la amplitud de las trayectorias con el intervalo blanco reportado en este trabajo. Dado que, durante la tarea de ST, la amplitud de las trayectorias también muestra una correlación con el intervalo blanco, aun cuando no se moduló la cantidad de recompensa que recibían los monos con este intervalo.

Por otro lado, la variabilidad en el radio de las trayectorias neuronales se incrementó como función del intervalo blanco durante las tareas de SCT y ST, pero se mantuvo similar durante la SRTT, donde el mono sólo puede realizar movimientos de manera reactiva, sin poder predecir el momento en el que ocurrirá el siguiente estímulo o *tap*. Por lo tanto, a diferencia de Mello et al., 2015 y Bakhurin et al., 2017, estos resultados sugieren que la variabilidad en la dinámica poblacional oscilatoria en la MPC es un correlato neuronal factible de la propiedad escalar durante el *tapping* rítmico.

Un clasificador, basado en máquinas de vector de soporte, fue capaz de catalogar segmentos de las trayectorias neuronales de un componente principal único, con respecto al intervalo blanco, secuencia y condición del ensayo asociado a ellos. Además, una red neuronal artificial decodificó el momento en el que el mono realizó los *taps* y el intervalo que produjo, a partir de la información poblacional proyectada en un componente principal. La MPC tiene neuronas que multiplexan la información temporal y secuencial de la tarea de SCT en sus funciones de sintonización (Hugo Merchant, Pérez, et al., 2013). En este trabajo encontramos que la dinámica poblacional, además

de contener información del intervalo generado, también representa información de la secuencia y la fase de la tarea. De manera similar a lo reportado anteriormente (Mante et al., 2013), diferentes parámetros de la tarea estuvieron representados en diferentes dimensiones del espacio de PCA. Además, la información de estos parámetros se encuentra distribuida entre la población neuronal (Kobak et al., 2016). Estos resultados apoyan los modelos donde una compleja y rica dinámica neuronal, permite simplificar el diseño de circuitos neuronales locales, de tal manera que extraer los parámetros de una tarea se convierte en un problema de clasificación. Donde un grupo de neuronas son capaces de extraer estos parámetros al decodificar la información contenida en las respuestas neuronales complejas (Rigotti et al., 2013). Por otro lado, encontramos que las trayectorias neuronales tienen características semejantes tanto para la modalidad visual como la auditiva. En ambas modalidades, la dinámica poblacional representa el intervalo temporal medido en el radio de sus órbitas. Sin embargo, los radios tienen una menor magnitud para la modalidad auditiva que para la visual. Esto sugiere que la población de neuronas que representan el tiempo en su dinámica de actividad es parcialmente la misma sin importar la modalidad. La mayoría de las neuronas cuya actividad se correlaciona con un estímulo en la MPC, responden tanto a estímulos visuales como auditivos (J Tanji & Kurata, 1982), lo que apoyaría la existencia de un circuito temporal común para ambas modalidades.

Encontramos neuronas cuya actividad se asemeja al componente principal en el que más participan. Esto podría significar dos cosas, es posible que estas neuronas sesgan el PCA, de tal manera que el componente principal en realidad sólo está representando una pequeña población de neuronas con actividad altamente correlacionada. Por otro lado, es posible que estas neuronas estén decodificando la actividad poblacional utilizando una regla de aprendizaje que converge al componente principal, tal como propuso en un modelo teórico Oja, 1982a. El hecho de que al eliminar las neuronas que más contribuyen a un componente principal, la información proyectada en el componente sigue teniendo información temporal, apoya esta última opción y demuestra que la información está distribuida entre la población neuronal.

Finalmente, utilizando simulaciones encontramos que un patrón de actividad neuronal secuencial o "*moving bump*" genera órbitas estables al proyectar su actividad en un plano fase. Donde, el número de neuronas y la longitud de su periodo de activación determina el radio de las órbitas, así como su variabilidad. Además, para que las trayectorias circulares sean tangentes entre ellas, las neuronas deben tener una posición relativa parecida dentro de la secuencia de activación, de manera similar a lo observado en el estriado de la rata (Mello et al., 2015). De tal manera, que las neuronas que se incorporan a intervalos de mayor duración deben estar localizadas en la parte media de la secuencia de activación (Crowe, Zarco, Bartolo, & Merchant, 2014b). Estos resultados no solo replican observaciones empíricas, también soportan la idea de que las propiedades de los "moving bumps", en especial el número de neuronas participantes, pueden modular los radios y la variabilidad de las trayectorias neuronales durante la tarea de SCT.

Reloj poblacional en la MPC

La MPC es un nodo crucial de la producción de ritmos dentro del circuito cortico-ganglios basales-tálamo (Bartolo, Prado, & Merchant, 2014; Hugo Merchant, Zarco, & Prado, 2008; Schubotz et al.,

2000). La dinámica poblacional en forma de trayectorias neuronales que generan órbitas tangentes las cuales viajan a una velocidad constante y donde su radio está asociado a la longitud del intervalo temporal medido es consistente con la existencia de un reloj poblacional. Además, entre las diferentes órbitas tangentes, existe un punto común en el espacio fase relacionado con el momento donde se dispara el comando motor, sugiriendo que es la MPC el área encargada de temporalizar los movimientos rítmicos. En el estudio de Halsband et al., 1993, pacientes con lesiones en la MPC presentaron dificultades para reproducir ritmos de memoria. Sin embargo, se reportó que sí fueron capaces de reproducir secuencias rítmicas siguiendo un metrónomo auditivo. Desafortunadamente, en ese estudio no se reportaron las asincronías para ninguna de las tareas, pero los tiempos de reacción se vieron fuertemente afectados en los pacientes. Lo que sugiere, que los pacientes cambiaron de estrategia para resolver la reproducción rítmica en presencia de un metrónomo: es posible que, en lugar de anticipar la presentación de los estímulos, reaccionaron a ellos de manera similar a una tarea de SRTT. Este experimento apoyaría nuestros resultados y la conclusión de que la MPC se comporta como un reloj, generando las señales motoras en los tiempos precisos durante la sincronización rítmica.

Conclusiones

El tiempo es fundamental para la producción y coordinación de las acciones motoras, entre las que se encuentra la producción rítmica. Sin embargo, todavía no se conoce completamente los mecanismos neuronales que permiten la medición del tiempo en la escala de los cientos de milisegundos. En este trabajo entrenamos dos monos en una tarea de sincronización y de tiempo de reacción. Uno de los monos también fue entrenado en una tarea donde el ritmo del metrónomo cambia durante el transcurso del ensayo. Una vez que los monos tuvieron un comportamiento estable se realizaron registros extracelulares en la MPC de ambos monos utilizando un sistema con 64 sitios de registro. Posteriormente, se analizaron estos datos y los de una base de datos adquirida con anterioridad de dos monos realizando una tarea de sincronización-continuación. Utilizando un marco de referencia de sistemas dinámicos se obtuvieron las siguientes conclusiones:

- Los monos son capaces de generalizar sus habilidades de reproducción de ritmos isócronos para sincronizarse a ritmos dinámicos que tienen aceleraciones y desaceleraciones. Además, el mono presentó un comportamiento predictivo a los cambios en el ritmo del metrónomo. Por lo tanto, la capacidad rítmica de los monos es mayor que la reportada anteriormente.

- La dinámica poblacional de neuronas en la MPC presentó las siguientes características:
    - La proyección de la actividad neuronal durante una tarea de SCT en un plano fase generó trayectorias circulares tangentes. Estas trayectorias viajaron a una velocidad constante y presentaron orbitas con diferentes radios correlacionados con el intervalo producido.

    - La variabilidad de las trayectorias neuronales presentó la propiedad escalar durante las tareas de SCT y ST. Lo que sugiere que esta puede ser el sustrato de la propiedad escalar durante la producción rítmica.

    - Las trayectorias circulares se generan por un perfil de activación secuencial de grupos de neuronas o "*moving bumps*". Donde, el radio y la variabilidad de las trayectorias depende del número de neuronas y la longitud de su periodo de activación.

    - Se puede decodificar el tiempo de los movimientos realizados por los monos a partir de las trayectorias neuronales. Además, diferentes componentes principales contienen información de los parámetros de la tarea: intervalo blanco, secuencia y fase.

    - Las trayectorias neuronales no dependen de la modalidad del metrónomo.

En conclusión, el mecanismo de medición del tiempo en la generación de ritmos está basado en cambios en el radio de la dinámica de estado poblacional de neuronas en la MPC, donde intervalos más largos siguen una órbita con un radio mayor a una velocidad constante. Siendo la variabilidad de estas trayectorias el posible sustrato de la propiedad escalar durante la producción rítmica.

Referencias

Akkal, D., Dum, R. P., & Strick, P. L. (2007). Supplementary Motor Area and Presupplementary Motor Area : Targets of Basal Ganglia and Cerebellar Output. *The Journal of Neuroscience*, *27*(40), 10659-10673. https://doi.org/10.1523/JNEUROSCI.3134-07.2007

Bakhurin, K. I., Goudar, V., Shobe, J. L., Claar, L. D., Buonomano, D. V., & Masmanidis, S. C. (2017). Differential Encoding of Time by Prefrontal and Striatal Network Dynamics. *The Journal of Neuroscience*, *37*(4), 854-870. https://doi.org/10.1523/JNEUROSCI.1789-16.2016

Bartolo, R., Prado, L., & Merchant, H. (2014). Information Processing in the Primate Basal Ganglia during Sensory-Guided and Internally Driven Rhythmic Tapping. *Journal of Neuroscience*, *34*(11), 3910-3923. https://doi.org/10.1523/JNEUROSCI.2679-13.2014

Belmalih, A., Borra, E., Contini, M., Gerbella, M., Rozzi, S., & Luppino, G. (2009). Multimodal architectonic subdivision of the rostral part (area F5) of the macaque ventral premotor cortex. *The Journal of Comparative Neurology*, *512*(2), 183-217. https://doi.org/10.1002/cne.21892

Binder, J. R., Frost, J. A., Hammeke, T. A., Cox, R. W., Rao, S. M., & Prieto, T. (1997). Human Brain Language Areas Identified by Functional Magnetic Resonance Imaging. *The Journal of Neuroscience*, *17*(1), 353-362. https://doi.org/10.1523/JNEUROSCI.17-01-00353.1997

Boeing, G. (2016). Visual Analysis of Nonlinear Dynamical Systems: Chaos, Fractals, Self-Similarity and the Limits of Prediction. *Systems*, *4*(4), 37. https://doi.org/10.3390/systems4040037

Breakspear, M. (2017). Dynamic models of large-scale brain activity. *Nature Neuroscience*, *20*(3), 340-352. https://doi.org/10.1038/nn.4497

Buhusi, C. V., & Meck, W. H. (2005). What makes us tick? Functional and neural mechanisms of interval timing. *Nature reviews. Neuroscience*, *6*(10), 755-765. https://doi.org/10.1038/nrn1764

Buonomano, D. V., & Laje, R. (2010). Population clocks: motor timing with neural dynamics. *Trends in cognitive sciences*, *14*(12), 520-527. https://doi.org/10.1016/j.tics.2010.09.002

Buonomano, D. V., & Mauk, M. D. (1994). Neural Network Model of the Cerebellum: Temporal Discrimination and the Timing of Motor Responses. *Neural Computation*, *6*(1), 38-55. https://doi.org/10.1162/neco.1994.6.1.38

Burnod, Y., Baraduc, P., Battaglia-Mayer, A., Guigon, E., Koechlin, E., Ferraina, S., … Caminiti, R. (1999). Parieto-frontal coding of reaching: an integrated framework. *Experimental Brain Research*, *129*(3), 0325-0346. https://doi.org/10.1007/s002210050902

Campos, M., Breznen, B., Bernheim, K., & Andersen, R. A. (2005). Supplementary Motor Area Encodes Reward Expectancy in Eye-Movement Tasks. *Journal of Neurophysiology*, *94*(2), 1325-1335. https://doi.org/10.1152/jn.00022.2005

Cheney, P. D. (1985). Role of Cerebral Cortex in Voluntary Movements. *Physical Therapy*, *65*(5), 624-635. https://doi.org/10.1093/ptj/65.5.624

Chouinard, P. A., & Paus, T. (2006). The Primary Motor and Premotor Areas of the Human Cerebral Cortex. *The Neuroscientist*, *12*(2), 143-152. https://doi.org/10.1177/1073858405284255

Churchland, M. M., Cunningham, J. P., Kaufman, M. T., Foster, J. D., Nuyujukian, P., Ryu, S. I., & Shenoy, K. V. (2012). Neural population dynamics during reaching. *Nature*, *487*(7405), 51-56. https://doi.org/10.1038/nature11129

Cisek, P., & Kalaska, J. F. (2004). Neural correlates of mental rehearsal in dorsal premotor cortex. *Nature*, *431*(7011), 993-996. https://doi.org/10.1038/nature03005

Cook, P., Rouse, A., Wilson, M., & Reichmuth, C. (2013). A California sea lion (Zalophus californianus) can keep the beat: Motor entrainment to rhythmic auditory stimuli in a non vocal mimic. *Journal of Comparative Psychology*, *127*(4), 412-427. https://doi.org/10.1037/a0032345

Cortes, C., & Vapnik, V. (1995). Support-vector networks. *Machine Learning*, *20*(3), 273-297. https://doi.org/10.1007/BF00994018

Coull, J., & Nobre, A. (2008). Dissociating explicit timing from temporal expectation with fMRI. *Current Opinion in Neurobiology*, *18*(2), 137-144. https://doi.org/10.1016/j.conb.2008.07.011

Coull, J. T., Cheng, R.-K., & Meck, W. H. (2011). Neuroanatomical and Neurochemical Substrates of Timing. *Neuropsychopharmacology*, *36*(1), 3-25. https://doi.org/10.1038/npp.2010.113

Coull, J. T., Vidal, F., Nazarian, B., & Macar, F. (2004). Functional anatomy of the attentional modulation of time estimation. *Science (New York, N.Y.)*, *303*(5663), 1506-1508. https://doi.org/10.1126/science.1091573

Cross, E. S., Hamilton, A. F. de C., & Grafton, S. T. (2006). Building a motor simulation de novo: Observation of dance by dancers. *NeuroImage*, *31*(3), 1257-1267. https://doi.org/10.1016/j.neuroimage.2006.01.033

Crowe, D. A., Zarco, W., Bartolo, R., & Merchant, H. (2014). Dynamic Representation of the Temporal and Sequential Structure of Rhythmic Movements in the Primate Medial Premotor Cortex. *Journal of Neuroscience*, *34*(36), 11972-11983. https://doi.org/10.1523/JNEUROSCI.2177-14.2014

Cunningham, J. P., & Yu, B. M. (2014). Dimensionality reduction for large-scale neural recordings. *Nature Neuroscience*, *17*(11), 1500-1509. https://doi.org/10.1038/nn.3776

Decety, J., Philippon, B., & Ingvar, D. H. (1988). rCBF landscapes during motor performance and motor ideation of a graphic gesture. *European Archives of Psychiatry and Neurological Sciences*, *238*(1), 33-38. https://doi.org/10.1007/BF00381078

Donnet, S., Bartolo, R., Fernandes, J. M., Cunha, J. P. S., Prado, L., & Merchant, H. (2014). Monkeys time their pauses of movement and not their movement-kinematics during a synchronization-continuation rhythmic task. *Journal of Neurophysiology*, *111*(10), 2138-2149. https://doi.org/10.1152/jn.00802.2013

Durstewitz, D. (2003). Self-Organizing Neural Integrator Predicts Interval Times through Climbing Activity. *The Journal of Neuroscience*, *23*(12), 5342-5353. https://doi.org/10.1523/JNEUROSCI.23-12-05342.2003

Ferrari, P. F., Gerbella, M., Coudé, G., & Rozzi, S. (2017). Two different mirror neuron networks: The sensorimotor (hand) and limbic (face) pathways. *Neuroscience*, *358*, 300-315. https://doi.org/10.1016/j.neuroscience.2017.06.052

Feudel, U., Physics, T., & Systems, C. (2008). *COMPLEX DYNAMICS IN MULTISTABLE SYSTEMS*. 20.

Fogassi, L., Gallese, V., Fadiga, L., Luppino, G., Matelli, M., & Rizzolatti, G. (1996). Coding of peripersonal space in inferior premotor cortex (area F4). *Journal of Neurophysiology*, *76*(1), 141-157. https://doi.org/10.1152/jn.1996.76.1.141

Fritsch, G., & Hitzig, E. (2009). Electric excitability of the cerebrum (Über die elektrische Erregbarkeit des Grosshirns). *Epilepsy & Behavior*, *15*(2), 123-130. https://doi.org/10.1016/j.yebeh.2009.03.001

Gámez, J., Mendoza, G., Prado, L., Betancourt, A., & Merchant, H. (2019). The amplitude in periodic neural state trajectories underlies the tempo of rhythmic tapping. *PLOS Biology*, *17*(4). https://doi.org/10.1371/journal.pbio.3000054

Gámez, J., Yc, K., Ayala, Y. A., Dotov, D., Prado, L., & Merchant, H. (2018). Predictive rhythmic tapping to isochronous and tempo changing metronomes in the nonhuman primate: Predictive and tempo changing tapping in monkeys. *Annals of the New York Academy of Sciences*, *1423*(1), 396-414. https://doi.org/10.1111/nyas.13671

Gentilucci, M., Fogassi, L., Luppino, G., Matelli, M., Camarda, R., & Rizzolatti, G. (1988). Functional organization of inferior area 6 in the macaque monkey. *Exp Brain Res.*, *71*(3), 491-507.

Geyer, S., Matelli, M., Luppino, G., & Zilles, K. (2000). Functional neuroanatomy of the primate isocortical motor system. *Anatomy and Embryology*, *202*(6), 443-474. https://doi.org/10.1007/s004290000127

Geyer, Stefan, Luppino, G., & Rozzi, S. (2012). Motor Cortex. En *The Human Nervous System* (pp. 1012-1035). https://doi.org/10.1016/B978-0-12-374236-0.10027-6

Gibbon, J. (1977). Scalar expectancy theory and Weber's law in animal timing. *Psychol. Rev.*, *84*, 279-325.

Gibbon, J., Malapani, C., Dale, C. L., & Gallistel, C. R. (1997). Toward a neurobiology of temporal cognition: Advances and challenges. *Current Opinion in Neurobiology*, *7*(2), 170-184. https://doi.org/10.1016/S0959-4388(97)80005-0

Gillette, Martha U. (1991). SCN electrophysiology in vitro: rhythmic activity and endogenous clock properties. En Klein, D.C., Moore, R.Y., & Reppert, M., *Suprachiasmatic Nucleus: The Mind's Clock* (pp. 125-143). New York, NY: Oxford University Press.

Goldberg, J. M., & Brown, P. B. (1969). Response of binaural neurons of dog superior olivary complex to dichotic tonal stimuli: some physiological mechanisms of sound localization. *Journal of Neurophysiology*, *32*(4), 613-636. https://doi.org/10.1152/jn.1969.32.4.613

Gouvêa, T. S., Monteiro, T., Motiwala, A., Soares, S., Machens, C., & Paton, J. J. (2015). Striatal dynamics explain duration judgments. *eLife*, *4*(December2015), 1-14. https://doi.org/10.7554/eLife.11386

Grillner, S., & Robertson, B. (2015). The basal ganglia downstream control of brainstem motor centres—an evolutionarily conserved strategy. *Current Opinion in Neurobiology*, *33*, 47-52. https://doi.org/10.1016/j.conb.2015.01.019

Grothe, B., Pecka, M., & McAlpine, D. (2010). Mechanisms of Sound Localization in Mammals. *Physiological Reviews*, *90*(3), 983-1012. https://doi.org/10.1152/physrev.00026.2009

Halsband, U., Tanji, J., & Freund, H.-J. (1993). The role of premotor cortex and the supplementary motor area in the temporal control of movement in man. *Brain*, *116*, 243-266. https://doi.org/DOI: 10.1093/brain/116.1.243

Hardy, N. F., & Buonomano, D. V. (2018). Encoding Time in Feedforward Trajectories of a Recurrent Neural Network Model. *Neural Computation*, *30*(2), 378-396. https://doi.org/10.1162/neco_a_01041

Harvey, C. D., Coen, P., & Tank, D. W. (2012). Choice-specific sequences in parietal cortex during a virtual-navigation decision task. *Nature*, *484*(7392), 62-68. https://doi.org/10.1038/nature10918

Hasegawa, A., Okanoya, K., Hasegawa, T., & Seki, Y. (2011). Rhythmic synchronization tapping to an audio-visual metronome in budgerigars. *Scientific Reports*, *1*, 1-8. https://doi.org/10.1038/srep00120

Hatsopoulos, N. G. (2010). Columnar organization in the motor cortex. *Cortex*, *46*(2), 270-271. https://doi.org/10.1016/j.cortex.2008.07.005

He, S., Dum, R., & Strick, P. (1993). Topographic organization of corticospinal projections from the frontal lobe: motor areas on the lateral surface of the hemisphere. *The Journal of Neuroscience*, *13*(3), 952-980. https://doi.org/10.1523/JNEUROSCI.13-03-00952.1993

Hubel, D. H., & Wiesel, T. N. (1959). Receptive fields of single neurones in the cat's striate cortex. *The Journal of Physiology*, *148*(3), 574-591. https://doi.org/10.1113/jphysiol.1959.sp006308

Huerta, M. F., & Kaas, J. H. (1990). Supplementary eye field as defined by intracortical microstimulation: Connections in macaques. *The Journal of Comparative Neurology*, *293*(2), 299-330. https://doi.org/10.1002/cne.902930211

Ivry, Richard B. (1996). The representation of temporal information in perception and motor control. *Current Opinion in Neurobiology*, *6*(6), 851-857.

Izhikevich, E. M. (2007). *Dynamical systems in neuroscience: the geometry of excitability and bursting*. Cambridge, Mass: MIT Press.

Jeannerod, M., Arbib, M. A., Rizzolatti, G., & Sakata, H. (1995). Grasping objects: the cortical of visuomotor transformation. *Trends in Neurosciences*, *18*(7), 314-320. https://doi.org/10.1016/0166-2236(95)93921-J

Johnson, P. B., Ferraina, S., Bianchi, L., & Caminiti, R. (1996). Cortical Networks for Visual Reaching: Physiological and Anatomical Organization of Frontal and Parietal Lobe Arm Regions. *Cerebral Cortex*, *6*(2), 102-119. https://doi.org/10.1093/cercor/6.2.102

Jürgens, U. (1984). The efferent and afferent connections of the supplementary motor area. *Brain Research*, *300*(1), 63-81. https://doi.org/10.1016/0006-8993(84)91341-6

Kandel, E. R., Schwartz, J. H., & Jessell, T. M. (Eds.). (1991). *Principles of Neural Science* (Third). New York: Elsevier.

Karmarkar, U. R., & Buonomano, D. V. (2007). Timing in the absence of clocks: encoding time in neural network states. *Neuron*, *53*(3), 427-438. https://doi.org/10.1016/j.neuron.2007.01.006

Knudsen, E. B., Powers, M. E., & Moxon, K. A. (2014). Dissociating Movement from Movement Timing in the Rat Primary Motor Cortex. *Journal of Neuroscience*, *34*(47), 15576-15586. https://doi.org/10.1523/JNEUROSCI.1816-14.2014

Kobak, D., Brendel, W., Constantinidis, C., Feierstein, C. E., Kepecs, A., Mainen, Z. F., … Machens, C. K. (2016). Demixed principal component analysis of neural population data. *eLife*, *5*(APRIL2016), 1-36. https://doi.org/10.7554/eLife.10989

Kurata, K., & Hoshi, E. (2002). Movement-Related Neuronal Activity Reflecting the Transformation of Coordinates in the Ventral Premotor Cortex of Monkeys. *Journal of Neurophysiology*, *88*(6), 3118-3132. https://doi.org/10.1152/jn.00070.2002

Laplane, D., Talairach, J., Meininger, V., Bancaud, J., & Orgogozo, J. M. (1977). Clinical consequences of corticectomies involving the supplementary motor area in man. *Journal of the Neurological Sciences*, *34*(3), 301-314. https://doi.org/10.1016/0022-510X(77)90148-4

Large, E. W., & Snyder, J. S. (2009). Pulse and meter as neural resonance. *Annals of the New York Academy of Sciences*, *1169*, 46-57. https://doi.org/10.1111/j.1749-6632.2009.04550.x

Lemon, Roger. (1988). The output map of the primate motor cortex. *Trends in Neurosciences*, *11*(11), 501-506. https://doi.org/10.1016/0166-2236(88)90012-4

Lewis, P. A., Wing, A. M., Pope, P. A., Praamstra, P., & Miall, R. C. (2004). Brain activity correlates differentially with increasing temporal complexity of rhythms during initialisation, synchronisation, and continuation phases of paced finger tapping. *Neuropsychologia*, *42*(10), 1301-1312. https://doi.org/10.1016/j.neuropsychologia.2004.03.001

Lima, C. F., Krishnan, S., & Scott, S. K. (2016). Roles of Supplementary Motor Areas in Auditory Processing and Auditory Imagery. *Trends in Neurosciences*, *39*(8), 527-542. https://doi.org/10.1016/j.tins.2016.06.003

Luppino, G., Matelli, M., Camarda, R. M., Gallese, V., & Rizzolatti, G. (1991). Multiple representations of body movements in mesial area 6 and the adjacent cingulate cortex: An intracortical microstimulation study in the macaque monkey. *The Journal of Comparative Neurology*, *311*(4), 463-482. https://doi.org/10.1002/cne.903110403

Luppino, G., Murata, A., Govoni, P., & Matelli, M. (1999). Largely segregated parietofrontal connections linking rostral intraparietal cortex (areas AIP and VIP) and the ventral premotor cortex (areas F5 and F4). *Experimental Brain Research*, *128*(1-2), 181-187. https://doi.org/10.1007/s002210050833

Luppino, G., & Rizzolatti, G. (2000). The Organization of the Frontal Motor Cortex. *News in physiological sciences : an international journal of physiology produced jointly by the International Union of Physiological Sciences and the American Physiological Society*, *15*(October), 219-224.

Luppino, Giuseppe, Matelli, M., Camarda, R., & Rizzolatti, G. (1993). Corticocortical connections of area F3 (SMA-proper) and area F6 (pre-SMA) in the macaque monkey. *The Journal of Comparative Neurology*, *338*(1), 114-140. https://doi.org/10.1002/cne.903380109

Luppino, Giuseppe, Rozzi, S., Calzavara, R., & Matelli, M. (2003). Prefrontal and agranular cingulate projections to the dorsal premotor areas F2 and F7 in the macaque monkey: Prefrontal and cingulate projections to PMd. *European Journal of Neuroscience*, *17*(3), 559-578. https://doi.org/10.1046/j.1460-9568.2003.02476.x

Luzardo, A., Ludvig, E. A., & Rivest, F. (2013). An adaptive drift-diffusion model of interval timing dynamics. *Behavioural Processes*, *95*, 90-99. https://doi.org/10.1016/j.beproc.2013.02.003

Macar, Françoise, Coull, J., & Vidal, F. (2006). The supplementary motor area in motor and perceptual time processing: fMRI studies. *Cognitive Processing*, *7*(2), 89-94. https://doi.org/10.1007/s10339-005-0025-7

Macar, F., Lejeune, H., Bonnet, M., Ferrara, A., Pouthas, V., Vidal, F., & Maquet, P. (2002). Activation of the supplementary motor area and of attentional networks during temporal processing. *Experimental Brain Research*, *142*(4), 475-485. https://doi.org/10.1007/s00221-001-0953-0

MacDonald, C. J., Lepage, K. Q., Eden, U. T., & Eichenbaum, H. (2011). Hippocampal «time cells» bridge the gap in memory for discontiguous events. *Neuron*, *71*(4), 737-749. https://doi.org/10.1016/j.neuron.2011.07.012

Machens, C. K., Romo, R., & Brody, C. D. (2005). Flexible Control of Mutual Inhibition: A Neural Model of Two-Interval Discrimination. *Science*, *307*(5712), 1121-1124. https://doi.org/10.1126/science.1104171

Mante, V., Sussillo, D., Shenoy, K. V., & Newsome, W. T. (2013). Context-dependent computation by recurrent dynamics in prefrontal cortex. *Nature*, *503*(7474), 78-84. https://doi.org/10.1038/nature12742

Massion, J. (1992). Movement, posture and equilibrium: Interaction and coordination. *Progress in Neurobiology*, *38*(1), 35-56. https://doi.org/10.1016/0301-0082(92)90034-C

Matelli, M., Govoni, P., Galletti, C., Kutz, D. F., & Luppino, G. (1998). Superior area 6 afferents from the superior parietal lobule in the macaque monkey. *THE JOURNAL OF COMPARATIVE NEUROLOGY*, *402*, 327-352.

Matelli, M., & Luppino, G. (1996). Thalamic input to mesial and superior area 6 in the macaque monkey. *THE JOURNAL OF COMPARATIVE NEUROLOGY*, *372*, 59-87.

Matsuzaka, Y., & Tanji, J. (1996). Changing directions of forthcoming arm movements: neuronal activity in the presupplementary and supplementary motor area of monkey cerebral cortex. *Journal of Neurophysiology*, *76*(4), 2327-2342. https://doi.org/10.1152/jn.1996.76.4.2327

Meck, W. H. (1996). Neuropharmacology of timing and time perception. *Cognitive Brain Research*, *3*, 227-242.

Mello, G. B. M., Soares, S., & Paton, J. J. (2015). A Scalable Population Code for Time in the Striatum. *Current Biology*, *25*(9), 1113-1122. https://doi.org/10.1016/j.cub.2015.02.036

Mendoza, G., Méndez, J. C., Pérez, O., Prado, L., & Merchant, H. (2018). Neural basis for categorical boundaries in the primate pre-SMA during relative categorization of time intervals. *Nature Communications*, *9*(1). https://doi.org/10.1038/s41467-018-03482-8

Mendoza, G., & Merchant, H. (2014). Motor system evolution and the emergence of high cognitive functions. *Progress in Neurobiology*, *122*, 73-93. https://doi.org/10.1016/j.pneurobio.2014.09.001

Mendoza, G., Peyrache, A., Gámez, J., Prado, L., Buzsáki, G., & Merchant, H. (2016). Recording extracellular neural activity in the behaving monkey using a semi-chronic and high-density electrode system. *Journal of neurophysiology*, *116*, 563-574. https://doi.org/10.1152/jn.00116.2016

Merchant, H., Battaglia-Mayer, A., & Georgopoulos, A. P. (2001). Effects of Optic Flow in Motor Cortex and Area 7a. *Journal of Neurophysiology*, *86*(4), 1937-1954. https://doi.org/10.1152/jn.2001.86.4.1937

Merchant, Hugo. (2014). *Neurobiology of Interval Timing*.

Merchant, Hugo, & Averbeck, B. B. (2017). The Computational and Neural Basis of Rhythmic Timing in Medial Premotor Cortex. *The Journal of Neuroscience*, *37*(17), 4552-4564. https://doi.org/10.1523/JNEUROSCI.0367-17.2017

Merchant, Hugo, & Bartolo, R. (2018). Primate beta oscillations and rhythmic behaviors. *Journal of Neural Transmission*, *125*(3), 461-470. https://doi.org/10.1007/s00702-017-1716-9

Merchant, Hugo, & Georgopoulos, A. P. (2006). Neurophysiology of Perceptual and Motor Aspects of Interception. *Journal of Neurophysiology*, *95*(1), 1-13. https://doi.org/10.1152/jn.00422.2005

Merchant, Hugo, Grahn, J., Trainor, L., Rohrmeier, M., & Fitch, W. T. (2015). Finding the beat: a neural perspective across humans and non-human primates. *Philosophical transactions of the Royal Society of London. Series B, Biological sciences*, *370*, 20140093. https://doi.org/10.1098/rstb.2014.0093

Merchant, Hugo, Harrington, D. L., & Meck, W. H. (2013a). Neural basis of the perception and estimation of time. *Annual review of neuroscience*, *36*, 313-336. https://doi.org/10.1146/annurev-neuro-062012-170349

Merchant, Hugo, Harrington, D. L., & Meck, W. H. (2013b). Neural basis of the perception and estimation of time. *Annual review of neuroscience*, *36*, 313-336. https://doi.org/10.1146/annurev-neuro-062012-170349

Merchant, Hugo, Pérez, O., Bartolo, R., Méndez, J. C., Mendoza, G., Gámez, J., … Prado, L. (2015a). Sensorimotor neural dynamics during isochronous tapping in the medial premotor cortex of the macaque. *European Journal of Neuroscience*, *41*(5), 586-602. https://doi.org/10.1111/ejn.12811

Merchant, Hugo, Pérez, O., Bartolo, R., Méndez, J. C., Mendoza, G., Gámez, J., … Prado, L. (2015b). Sensorimotor neural dynamics during isochronous tapping in the medial premotor cortex of the macaque. *European Journal of Neuroscience*, *41*(5), 586-602. https://doi.org/10.1111/ejn.12811

Merchant, Hugo, Pérez, O., Zarco, W., & Gámez, J. (2013). Interval tuning in the primate medial premotor cortex as a general timing mechanism. *The Journal of neuroscience : the official journal of the Society for Neuroscience*, *33*(21), 9082-9096. https://doi.org/10.1523/JNEUROSCI.5513-12.2013

Merchant, Hugo, Zarco, W., Pérez, O., Prado, L., & Bartolo, R. (2011). Measuring time with different neural chronometers during a synchronization-continuation task. *Proceedings of the National Academy of Sciences of the United States of America*, *108*(49), 19784-19789. https://doi.org/10.1073/pnas.1112933108

Merchant, Hugo, Zarco, W., & Prado, L. (2008). Do we have a common mechanism for measuring time in the hundreds of millisecond range? Evidence from multiple-interval timing tasks. *Journal of neurophysiology*, *99*(2), 939-949. https://doi.org/10.1152/jn.01225.2007

Mesulam, M.-M., Hoesen, G. W. V., Pandya, D. N., & Geschwind, N. (1977). LIMBIC AND SENSORY CONNECTIONS OF THE INFERIOR PARIETAL LOBULE (AREA PG) IN THE RHESUS MONKEY: A STUDY WITH A NEW METHOD FOR HORSERADISH PEROXIDASE HtSTOCHEMISTRY. *Brain Research*, *136*, 393-414.

Mills, P. F., van der Steen, M. C. (Marieke), Schultz, B. G., & Keller, P. E. (2015). Individual Differences in Temporal Anticipation and Adaptation During Sensorimotor Synchronization. *Timing & Time Perception*, *3*(1-2), 13-31. https://doi.org/10.1163/22134468-03002040

Mita, A., Mushiake, H., Shima, K., Matsuzaka, Y., & Tanji, J. (2009). Interval time coding by neurons in the presupplementary and supplementary motor areas. *Nature Neuroscience*, *12*(4), 502-507. https://doi.org/10.1038/nn.2272

Mountcastle, V. B. (1957). MODALITY AND TOPOGRAPHIC PROPERTIES OF SINGLE NEURONS OF CAT'S SOMATIC SENSORY CORTEX. *Journal of Neurophysiology*, *20*(4), 408-434. https://doi.org/10.1152/jn.1957.20.4.408

Murray, J. M., & Escola, G. S. (2017). Learning multiple variable-speed sequences in striatum via cortical tutoring. *eLife*, *6*, 1-24. https://doi.org/10.7554/eLife.26084

Mushiake, H., Inase, M., & Tanji, J. (1991). Neuronal activity in the primate premotor, supplementary, and precentral motor cortex during visually guided and internally determined sequential movements. *Journal of Neurophysiology*, *66*(3), 705-718. https://doi.org/10.1152/jn.1991.66.3.705

Nachev, P., Kennard, C., & Husain, M. (2008). Functional role of the supplementary and pre-supplementary motor areas. *Nature Reviews Neuroscience*, *9*(11), 856-869. https://doi.org/10.1038/nrn2478

Narayanan, N. S. (2016). Ramping activity is a cortical mechanism of temporal control of action. *Current Opinion in Behavioral Sciences*, *8*, 226-230. https://doi.org/10.1016/j.cobeha.2016.02.017

Oja, E. (1982a). Simplified neuron model as a principal component analyzer. *Journal of Mathematical Biology*, *15*(3), 267-273. https://doi.org/10.1007/BF00275687

Oja, E. (1982b). Simplified neuron model as a principal component analyzer. *Journal of Mathematical Biology*, *15*(3), 267-273. https://doi.org/10.1007/BF00275687

Pandarinath, C., Ames, K. C., Russo, A. A., Farshchian, A., Miller, L. E., Dyer, E. L., & Kao, J. C. (2018). Latent Factors and Dynamics in Motor Cortex and Their Application to Brain–Machine Interfaces. *The Journal of Neuroscience*, *38*(44), 9390-9401. https://doi.org/10.1523/JNEUROSCI.1669-18.2018

Pastalkova, E., Itskov, V., Amarasingham, A., & Buzsaki, G. (2008). Internally Generated Cell Assembly Sequences in the Rat Hippocampus. *Science*, *321*(5894), 1322-1327. https://doi.org/10.1126/science.1159775

Patel, A. D. (2014). The Evolutionary Biology of Musical Rhythm: Was Darwin Wrong? *PLoS Biology*, *12*(3), e1001821. https://doi.org/10.1371/journal.pbio.1001821

Patel, A. D., Iversen, J. R., Chen, Y., & Repp, B. H. (2005). The influence of metricality and modality on synchronization with a beat. *Experimental Brain Research*, *163*(2), 226-238. https://doi.org/10.1007/s00221-004-2159-8

Pecenka, N., & Keller, P. E. (2011). The role of temporal prediction abilities in interpersonal sensorimotor synchronization. *Experimental Brain Research*, *211*(3-4), 505-515. https://doi.org/10.1007/s00221-011-2616-0

Penfield, W., & Rasmussen, T. (1950). *The cerebral cortex of man: a clinical study of localization of function*. Recuperado de https://books.google.com.mx/books?id=gtlNAAAAMAAJ

Penfield, Wilder, & Boldrey, E. (1937). SOMATIC MOTOR AND SENSORY REPRESENTATION IN THE CEREBRAL CORTEX OF MAN AS STUDIED BY ELECTRICAL STIMULATION. *Brain*, *60*(4), 389-443. https://doi.org/10.1093/brain/60.4.389

Perez, O., Kass, R. E., & Merchant, H. (2013). Trial time warping to discriminate stimulus-related from movement-related neural activity. *Journal of Neuroscience Methods*, *212*(2), 203-210. https://doi.org/10.1016/j.jneumeth.2012.10.019

Petit, L., Courtney, S. M., Ungerleider, L. G., & Haxby, J. V. (1998). Sustained Activity in the Medial Wall during Working Memory Delays. *The Journal of Neuroscience*, *18*(22), 9429-9437. https://doi.org/10.1523/JNEUROSCI.18-22-09429.1998

Phillips-Silver, J., & Keller, P. E. (2012). Searching for Roots of Entrainment and Joint Action in Early Musical Interactions. *Frontiers in Human Neuroscience*, *6*. https://doi.org/10.3389/fnhum.2012.00026

Protopapa, F., Hayashi, M. J., Kulashekhar, S., van der Zwaag, W., Battistella, G., Murray, M. M., … Bueti, D. (2019). Chronotopic maps in human supplementary motor area. *PLOS Biology*, *17*(3), e3000026. https://doi.org/10.1371/journal.pbio.3000026

Raos, V., Franchi, G., Gallese, V., & Fogassi, L. (2003). Somatotopic Organization of the Lateral Part of Area F2 (Dorsal Premotor Cortex) of the Macaque Monkey. *Journal of Neurophysiology*, *89*(3), 1503-1518. https://doi.org/10.1152/jn.00661.2002

Raos, V., Umiltá, M.-A., Gallese, V., & Fogassi, L. (2004). Functional Properties of Grasping-Related Neurons in the Dorsal Premotor Area F2 of the Macaque Monkey. *Journal of Neurophysiology*, *92*(4), 1990-2002. https://doi.org/10.1152/jn.00154.2004

Remington, E. D., Narain, D., Hosseini, E. A., & Jazayeri, M. (2018). Flexible Sensorimotor Computations through Rapid Reconfiguration of Cortical Dynamics. *Neuron*, *98*(5), 1005-1019.e5. https://doi.org/10.1016/j.neuron.2018.05.020

Repp, B. H. (2005). Sensorimotor synchronization: A review of the tapping literature. *Psychonomic Bulletin & Review*, *12*(6), 969-992. https://doi.org/10.3758/BF03206433

Repp, B. H., & Keller, P. E. (2004). Adaptation to tempo changes in sensorimotor synchronization: Effects of intention, attention, and awareness. *The Quarterly Journal of Experimental Psychology Section A*, *57*(3), 499-521. https://doi.org/10.1080/02724980343000369

Repp, B. H., & Su, Y.-H. (2013). Sensorimotor synchronization: A review of recent research (2006–2012). *Psychonomic Bulletin & Review*, *20*(3), 403-452. https://doi.org/10.3758/s13423-012-0371-2

Repp, BrunoH., & Penel, A. (2004). Rhythmic movement is attracted more strongly to auditory than to visual rhythms. *Psychological Research Psychologische Forschung*, *68*(4). https://doi.org/10.1007/s00426-003-0143-8

Reppert, S. M., & Weaver, D. R. (2002). Coordination of circadian timing in mammals. *Nature*, *418*(6901), 935-941. https://doi.org/10.1038/nature00965

Reutimann, J. (2004). Climbing Neuronal Activity as an Event-Based Cortical Representation of Time. *Journal of Neuroscience*, *24*(13), 3295-3303. https://doi.org/10.1523/JNEUROSCI.4098-03.2004

Rigotti, M., Barak, O., Warden, M. R., Wang, X.-J., Daw, N. D., Miller, E. K., & Fusi, S. (2013). The importance of mixed selectivity in complex cognitive tasks. *Nature*, *497*(7451), 585-590. https://doi.org/10.1038/nature12160

Rilling, J. K., Glasser, M. F., Preuss, T. M., Ma, X., Zhao, T., Hu, X., & Behrens, T. E. J. (2008). The evolution of the arcuate fasciculus revealed with comparative DTI. *Nature Neuroscience*, *11*(4), 426-428. https://doi.org/10.1038/nn2072

Rizzolatti, G, Camarda, R., Fogassi, L., Gentilucci, M., Luppino, G., & Matelli, M. (1988). Functional organization of inferior area 6 in the macaque monkey, II. Area F5 and the control of distal movements. *Exp Brain Res.*, *71*, 491-507.

Rizzolatti, Giacomo, & Craighero, L. (2004). THE MIRROR-NEURON SYSTEM. *Annual Review of Neuroscience*, *27*(1), 169-192. https://doi.org/10.1146/annurev.neuro.27.070203.144230

Rizzolatti, Giacomo, Fadiga, L., Gallese, V., & Fogassi, L. (1996). Premotor cortex and the recognition of motor actions. *Cognitive Brain Research*, *3*(2), 131-141. https://doi.org/10.1016/0926-6410(95)00038-0

Rizzolatti, Giacomo, Fogassi, L., & Gallese, V. (2001). Neurophysiological mechanisms underlying the understanding and imitation of action. *Nature Reviews Neuroscience*, *2*(9), 661-670. https://doi.org/10.1038/35090060

Rizzolatti, Giacomo, Fogassi, L., & Gallese, V. (2002). Motor and cognitive functions of the ventral premotor cortex. *Current Opinion in Neurobiology*, *12*(2), 149-154. https://doi.org/10.1016/S0959-4388(02)00308-2

Rosenberg-Katz, K., Jamshy, S., Singer, N., Podlipsky, I., Kipervasser, S., Andelman, F., … Hendler, T. (2012). Enhanced functional synchronization of medial and lateral PFC underlies internally-guided action planning. *Frontiers in Human Neuroscience*, *6*. https://doi.org/10.3389/fnhum.2012.00079

Rossi-Pool, R., Zainos, A., Alvarez, M., Zizumbo, J., Vergara, J., & Romo, R. (2017). Decoding a Decision Process in the Neuronal Population of Dorsal Premotor Cortex. *Neuron*, *96*(6), 1432-1446.e7. https://doi.org/10.1016/j.neuron.2017.11.023

Sadtler, P. T., Quick, K. M., Golub, M. D., Chase, S. M., Ryu, S. I., Tyler-Kabara, E. C., … Batista, A. P. (2014). Neural constraints on learning. *Nature*, *512*(7515), 423-426. https://doi.org/10.1038/nature13665

Sakai, K., Hikosaka, O., Miyauchi, S., Takino, R., Sasaki, Y., & Pütz, B. (1998). Transition of brain activation from frontal to parietal areas in visuomotor sequence learning. *The Journal of neuroscience : the official journal of the Society for Neuroscience*, *18*(5), 1827-1840. https://doi.org/10.1523/JNEUROSCI.4564-05.2006

Salinas, E., & Sejnowski, T. J. (2001). Correlated neuronal activity and the flow of neural information. *Nature Reviews Neuroscience*, *2*(8), 539-550. https://doi.org/10.1038/35086012

Sanger, T. D. (1989). Optimal unsupervised learning in a single-layer network. *Neural Networks*, *2*, 459-473.

Scangos, K. W., Aronberg, R., & Stuphorn, V. (2013). Performance monitoring by presupplementary and supplementary motor area during an arm movement countermanding task. *Journal of Neurophysiology*, *109*(7), 1928-1939. https://doi.org/10.1152/jn.00688.2012

Schibler, U., & Sassone-Corsi, P. (2002). A Web of Circadian Pacemakers. *Cell*, *111*(7), 919-922. https://doi.org/10.1016/S0092-8674(02)01225-4

Schieber, M. H. (2001). Constraints on Somatotopic Organization in the Primary Motor Cortex. *Journal of Neurophysiology*, *86*(5), 2125-2143. https://doi.org/10.1152/jn.2001.86.5.2125

Schoner, G., & Kelso, J. (1988). Dynamic pattern generation in behavioral and neural systems. *Science*, *239*(4847), 1513-1520. https://doi.org/10.1126/science.3281253

Schubotz, R. I., Friederici, a D., & von Cramon, D. Y. (2000). Time perception and motor timing: a common cortical and subcortical basis revealed by fMRI. *NeuroImage*, *11*(1), 1-12. https://doi.org/10.1006/nimg.1999.0514

Shenoy, K. V., Sahani, M., & Churchland, M. M. (2013). Cortical Control of Arm Movements: A Dynamical Systems Perspective. *Annual Review of Neuroscience*, *36*(1), 337-359. https://doi.org/10.1146/annurev-neuro-062111-150509

Shima, K., Mushiake, H., Saito, N., & Tanji, J. (1996). Role for cells in the presupplementary motor area in updating motor plans. *Proceedings of the National Academy of Sciences*, *93*(16), 8694-8698. https://doi.org/10.1073/pnas.93.16.8694

Simen, P., Balci, F., deSouza, L., Cohen, J. D., & Holmes, P. (2011). A Model of Interval Timing by Neural Integration. *Journal of Neuroscience*, *31*(25), 9238-9253. https://doi.org/10.1523/JNEUROSCI.3121-10.2011

Stephan, K. M., Fink, G. R., Passingham, R. E., Silbersweig, D., Ceballos-Baumann, A. O., Frith, C. D., & Frackowiak, R. S. (1995). Functional anatomy of the mental representation of upper extremity movements in healthy subjects. *Journal of Neurophysiology*, *73*(1), 373-386. https://doi.org/10.1152/jn.1995.73.1.373

Stuphorn, V., Brown, J. W., & Schall, J. D. (2010). Role of Supplementary Eye Field in Saccade Initiation: Executive, Not Direct, Control. *Journal of Neurophysiology*, *103*(2), 801-816. https://doi.org/10.1152/jn.00221.2009

Takeya, R., Kameda, M., Patel, A. D., & Tanaka, M. (2017). Predictive and tempo-flexible synchronization to a visual metronome in monkeys. *Scientific Reports*, *7*(1), 1-12. https://doi.org/10.1038/s41598-017-06417-3

Tanji, J, & Kurata, K. (1982). Comparison of movement-related activity in two cortical motor areas of primates. *Journal of Neurophysiology*, *48*(3), 633-653. https://doi.org/10.1152/jn.1982.48.3.633

Tanji, Jun. (1994). The supplementary motor area in the cerebral cortex. *Neuroscience Research*, *19*(3), 251-268. https://doi.org/10.1016/0168-0102(94)90038-8

Tanji, Jun, & Shima, K. (1994). Role for supplementary motor area cells in planning several movements ahead. *Nature*, *371*(6496), 413-416. https://doi.org/10.1038/371413a0

Thaut, M. H., Miller, R. A., & Schauer, L. M. (1998). Multiple synchronization strategies in rhythmic sensorimotor tasks: phase vs period correction. *Biological Cybernetics*, *79*(3), 241-250. https://doi.org/10.1007/s004220050474

Theys, T., Pani, P., van Loon, J., Goffin, J., & Janssen, P. (2012). Selectivity for Three-Dimensional Shape and Grasping-Related Activity in the Macaque Ventral Premotor Cortex. *Journal of Neuroscience*, *32*(35), 12038-12050. https://doi.org/10.1523/JNEUROSCI.1790-12.2012

Tipping, M. E., & Bishop, C. M. (1999). Probabilistic Principal Component Analysis. *J. R. Statist. Soc.B*, *61*, 12.

van der Steen, M. C. (Marieke), & Keller, P. E. (2013). The ADaptation and Anticipation Model (ADAM) of sensorimotor synchronization. *Frontiers in Human Neuroscience*, *7*. https://doi.org/10.3389/fnhum.2013.00253

Wang, J., Narain, D., Hosseini, E. A., & Jazayeri, M. (2018). Flexible timing by temporal scaling of cortical responses. *Nature Neuroscience*, *21*(1), 102-110. https://doi.org/10.1038/s41593-017-0028-6

Wilson, S. M., Saygin, A. P., Sereno, M. I., & Iacoboni, M. (2004). Listening to speech activates motor areas involved in speech production. *Nature neuroscience*, *7*(7), 701-702. https://doi.org/10.1038/nn1263

Woolsey, C. N., Settlage, P. H., Meyer, D. R., Sencer, W., Pinto Hamuy, T., & Travis, A. M. (1952). Patterns of localization in precentral and «supplementary» motor areas and their relation to the concept of a premotor area. *Research Publications - Association for Research in Nervous and Mental Disease*, *30*, 238-264.

Zarco, W., Merchant, H., Prado, L., & Mendez, J. C. (2009). Subsecond timing in primates: comparison of interval production between human subjects and rhesus monkeys. *Journal of neurophysiology*, *102*(6), 3191-3202. https://doi.org/10.1152/jn.00066.2009

Zatorre, R. J., & Binder, J. R. (2000). Functional and Structural Imaging of the Human Auditory System. En *Brain Mapping: The Systems* (pp. 365-402). https://doi.org/10.1016/B978-012692545-6/50014-3

Zatorre, R. J., Chen, J. L., & Penhune, V. B. (2007). When the brain plays music: auditory-motor interactions in music perception and production. *Nature reviews. Neuroscience*, *8*(7), 547-558. https://doi.org/10.1038/nrn2152

Zhou, Z., Chen, Y., Ding, M., Wright, P., Lu, Z., & Liu, Y. (2009). Analyzing brain networks with PCA and conditional Granger causality. *Human Brain Mapping*, *30*(7), 2197-2206. https://doi.org/10.1002/hbm.20661

Publicaciones

PLOS BIOLOGY

RESEARCH ARTICLE

The amplitude in periodic neural state trajectories underlies the tempo of rhythmic tapping

Jorge Gámez, Germán Mendoza, Luis Prado, Abraham Betancourt, Hugo Merchant*

Instituto de Neurobiología, Universidad Nacional Autónoma de México, Campus Juriquilla, Querétaro, México

* hugomerchant@unam.mx

OPEN ACCESS

Citation: Gámez J, Mendoza G, Prado L, Betancourt A, Merchant H (2019) The amplitude in periodic neural state trajectories underlies the tempo of rhythmic tapping. PLoS Biol 17(4): e3000054. https://doi.org/10.1371/journal.pbio.3000054

Academic Editor: Robert Zatorre, McGill University, CANADA

Received: September 13, 2018

Accepted: March 19, 2019

Published: April 8, 2019

Data Availability Statement: All underlying experimental data used in this study have been deposited in G-Node (https://doid.gin.g-node.org/d315b3db0cee15869b3d9ed164f88cfa/).

Funding: This work was funded by Consejo Nacional de Ciencia y Tecnologia #236836 and #196, https://www.conacyt.gob.mx/, and Programa de Apoyo a Proyectos de Investigación e Innovación Tecnológica #IN202317, http://dgapa.unam.mx/index.php/impulso-a-la-investigacion/papiit. The funders had no role in study design,

Abstract

Our motor commands can be exquisitely timed according to the demands of the environment, and the ability to generate rhythms of different tempos is a hallmark of musical cognition. Yet, the neuronal underpinnings behind rhythmic tapping remain elusive. Here, we found that the activity of hundreds of primate medial premotor cortices (MPCs; pre-supplementary motor area [preSMA] and supplementary motor area [SMA]) neurons show a strong periodic pattern that becomes evident when their responses are projected into a state space using dimensionality reduction analysis. We show that different tapping tempos are encoded by circular trajectories that travelled at a constant speed but with different radii, and that this neuronal code is highly resilient to the number of participating neurons. Crucially, the changes in the amplitude of the oscillatory dynamics in neuronal state space are a signature of duration encoding during rhythmic timing, regardless of whether it is guided by an external metronome or is internally controlled and is not the result of repetitive motor commands. This dynamic state signal predicted the duration of the rhythmically produced intervals on a trial-by-trial basis. Furthermore, the increase in variability of the neural trajectories accounted for the scalar property, a hallmark feature of temporal processing across tasks and species. Finally, we found that the interval-dependent increments in the radius of periodic neural trajectories are the result of a larger number of neurons engaged in the production of longer intervals. Our results support the notion that rhythmic timing during tapping behaviors is encoded in the radial curvature of periodic MPC neural population trajectories.

Author summary

The ability to extract the regular pulse in music and to respond in synchrony to this pulse is called beat synchronization and is a natural human behavior exhibited during dancing and musical ensemble playing. A part of the brain called the medial premotor cortex has been associated with rhythmic entrainment, and yet the neural basis of this complex behavior is still far from known. In this work, we recorded the neuronal activity from the medial premotor cortices of macaques trained to tap rhythmically to the frequency of a

data collection and analysis, decision to publish, or preparation of the manuscript.

Competing interests: The authors have declared that no competing interests exist.

Abbreviations: a.u., arbitrary unit; CC, continuation condition; DAT, Dynamic Attending Theory; dPCA, demixed PCA; EEG, electroencephalogram; MPC, medial premotor cortex; MSE, mean square error; PC, principal component; PCA, principal component analysis; preSMA, pre-supplementary motor area; SC, synchronization condition; SCT, synchronization-continuation task; SI, surprise index; SMA, supplementary motor area; SRTT, serial reaction time task; ST, synchronization task; SVM, support vector machine; TDNN, time-delay neural network; TIND, target interval normalized data; UTND, unit time normalized data.

metronome. Using principal component analysis, we projected the time-varying activity of hundreds of neurons into a low-dimensional space. The projected activity of the neural population generated a circular trajectory for every interval produced in the sequence, which travelled at a constant speed but with different radii for different tapping tempos. In addition, the increase in amplitude and variability of the neural trajectories accounted for the scalar property of timing, a generalized feature of temporal processing across tasks and species and which defines a linear relationship between the variability of temporal performance and interval duration.

Introduction

Precise timing is a fundamental requisite for a select group of complex actions such as the execution and appreciation of music and dance [1]. In these behaviors, the perception of time intervals is facilitated by the presence of a regular beat in the rhythmic sequence, and individual intervals are encoded relative to this pulse or beat. This is called beat-based timing and serves as a framework for rhythmic entrainment, in which subjects perform movements synchronized to music [2–4]. Most of occidental music is organized by a quasi-isochronous pulse and frequently also in a metrical hierarchy, in which the beats of one level are typically spaced at two or three times those of a faster level (i.e., the tempo of one level is 1/2 [march meter] or 1/3 [waltz meter] that of the other), and humans can typically synchronize at more than one level of the metrical hierarchy [5,6]. Rhythmic tapping to an isochronous metronome is the simplest case of beat entrainment [7] and has been thoroughly studied in humans [8,9]. In contrast to the large human flexibility to perceive and entrain to complex beats in music, non-human primates can perceive [10–13] and synchronize to simple isochronous beats [14–16]. On the other hand, other sets of behaviors, such as the interception of a moving target or the production of a single interval, seem to depend on a duration-based timing mechanism, in which the absolute duration of individual time intervals is encoded discretely, like a stopwatch [2,17]. Functional imaging and behavioral studies have suggested the existence of a partially segregated timing neural substrate, with the cerebellum as a key structure for duration-based timing, the basal ganglia as main nuclei for beat-based timing, and medial premotor cortices (MPCs; which include the pre-supplementary motor area [preSMA] and supplementary motor area [SMA]) as a potential master clock for both timing mechanisms [7,18–20]. Yet, the neural substrate for absolute timing, and especially for beat perception and rhythmic entrainment, is still largely unknown.

Recent advances on the neurophysiology of absolute timing during single interval reproduction tasks suggest that time is represented in the structured patterns of activation of cell populations in timing areas such as the MPC and the neostriatum [21–24]. Rather than being quantified in the instantaneous activity of single cells that accumulate elapsed time or encode the time remaining for an action [25–27], the duration of produced intervals depends on the speed at which the neural population response changes. This implies that the activation profiles are compressed for short and elongated for long intervals due to temporal scaling on the activity of the same population of cells [23,24].

On the other hand, MPC neurons are tuned to the duration and ordinal sequence of rhythmic movements produced either in synchrony with a metronome or guided by an endogenous tempo (synchronization-continuation task [SCT]) [4,21]. Remarkably, the time-varying profile of activation of these interval-specific neural circuits forms a moving bump, which is defined as a sequential pattern of responses in which the cells are activated consecutively within a

produced interval. The moving bump repeats itself on each produced interval of the tapping sequence [4,21,28]. Nevertheless, single MPC cells multiplex the interval, the serial order, and task phase of the SCT, showing complex and heterogenous time-varying profiles of activation that make it difficult to understand the neural population mechanisms behind rhythmic tapping. A successful approach to determine the latent task variables in cell populations is to project high-dimensional individual neural activity into a low-dimensional topological space, in order to generate a robust and stable manifold [29]. Recent studies have reconstructed key hidden task parameters in the neural state population dynamics [30–32]. Thus, the combined use of high-density single unit recordings with dimensional reduction methods have revealed basic organizing principles at the level of the population dynamics, which seem to be extremely complex at the level of individual neurons [29,33].

Here, we investigated the population dynamics of hundreds of MPC neurons in monkeys performing two isochronous tapping tasks, testing whether low-dimensional state network trajectories can act as a neural clock during rhythmic tapping. Using dimensional reduction analysis, we found highly stereotyped neural trajectories that had two main properties during the SCT. First, the three first principal components showed a periodic path for each produced interval. Notably, these oscillatory state trajectories did not overlap across durations, a signature of temporal scaling; instead, they showed a linear increase in their radius and a constant linear speed as a function of the target interval during metronome guidance (synchronization condition [SC]), as well as during internally controlled rhythmic tapping (continuation condition [CC]). Second, the intertrial variability of the trajectories' radial magnitude also increased as a function of the interval, accounting for a key feature of timing behavior: the scalar property, which states that the variability of produced or estimated intervals increases linearly as a function of interval duration. These properties were highly resilient to the number of participating neurons and were replicated using simultaneously recorded cells during synchronized tapping, but not during a serial reaction time-control task that precluded rhythmic prediction. Finally, we found a tight correlation between the interval-associated changes in trajectory amplitude and variability during SCT, the number of neurons involved in the sequential transient activation patterns, and the duration of the neural activation periods within these moving bumps. Indeed, moving bumps simulations revealed that scaling the duration of the transient period of activity and increasing the number of neurons participating in the evolving patterns produced an increase in the radius and the variability of the corresponding neural trajectories, replicating the empirical findings. These results suggest that rhythmic timing depends on the radial amplitude of periodic state population trajectories in MPC, which in turn depend on the number of neurons involved and the duration of these cells' activation periods within moving bumps.

Results

Rhythmic tapping behavior

We trained two monkeys (M01 and M02) in the SCT. M01 was also trained in two additional tapping tasks: the synchronization task (ST) and the serial reaction time task (SRTT). During SCT, the animals tapped on a push button in synchronization with a rhythmic metronome for four times, thus producing three intervals (SC phase), followed by three internally generated intervals (CC phase; Fig 1A). In the ST, the monkey produced five intervals guided by a metronome, similarly to the SC of SCT (Fig 1B). During the SRTT, the animal pressed the button in response to five brief visual stimuli presented in a sequence but separated by a random interstimulus interval, precluding the prediction of the next stimulus-response loop (Fig 1C). Thus, during SCT and ST, the animals entrained their rhythmic movements to a sensory

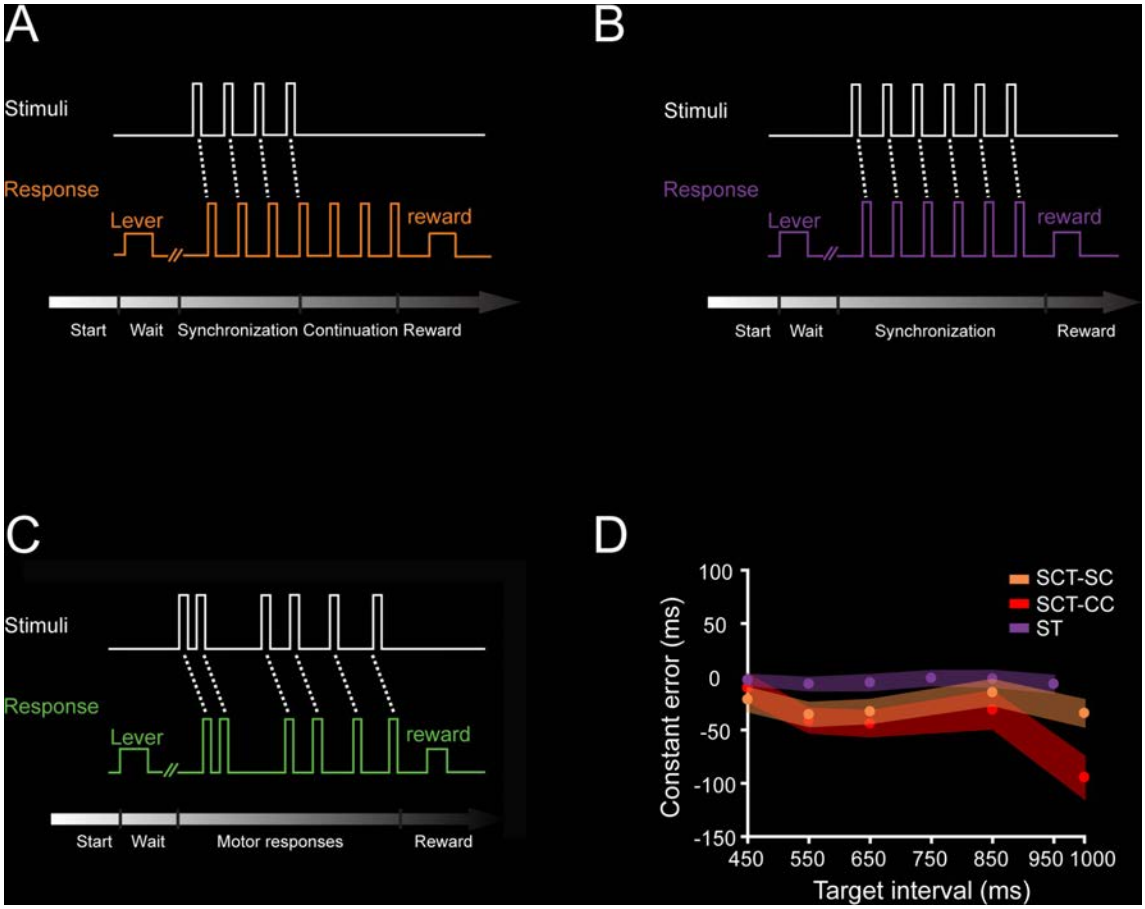

Fig 1. Tasks. A. SCT. The trial started when the monkey placed his hand on a lever for a variable delay. Then, a visual metronome was presented, and the monkey tapped on a button to produce three intervals of a specific duration following the isochronous stimuli (synchronization phase), after which the animal had to maintain the tapping rate to produce three additional intervals without the metronome (continuation phase). Correct trials were rewarded with an amount of juice that was proportional to the trial length. The instructed target intervals were 450, 550, 650, 850, and 1,000 ms. **B**. ST. Similar to the synchronization phase of the SCT, the animal had to produce five intervals guided by a visual metronome. The instructed intervals were 450, 550, 650, 750, 850, and 950 ms. **C**. SRTT. As in ST, the trial started when the monkey placed its hand on a lever for a variable delay. However, in this task, the monkey tapped the button after six stimuli separated by a random interstimulus interval, precluding the temporalization of the tapping behavior. **D.** Constant error (mean ± SD/2) as a function of target interval during the SC (orange) and CC (red) of the SCT (ANOVA main effect interval, $F(4, 1{,}112) = 61.01$, $p < 0.0001$; main effect task condition, $F(1, 1{,}112) = 43.16$, $p < 0.0001$; interval × condition interaction, $F(4, 1{,}112) = 17.66$, $p < 0.0001$), and the ST (purple) as a function of target interval (ANOVA for 450, 550, 650, and 850 target intervals between SC of the SCT and the ST, main effect interval, $F(3, 631) = 4.18$, $p < 0.01$; main effect condition, $F(1, 631) = 202.16$, $p < 0.0001$; nonsignificant interval × condition interaction, $F(3, 631) = 2.46$, $p = 0.06$). Underlying data are available in https://doid.gin.g-node.org/d315b3db0cee15869b3d9ed164f88cfa/. CC, continuation condition; SC, synchronization condition; SCT, synchronization-continuation task; SRTT, serial reaction time task; ST, synchronization task.

https://doi.org/10.1371/journal.pbio.3000054.g001

metronome, while in the CC of SCT, this was done to an internal representation of the same rhythm. The asynchronies in the SC of SCT were (mean ± SD: 288.7 ± 70 ms). On the other hand, the SRTT involved similar stimuli, tapping behavior, and sequential structure, but no predictive rhythmic timing was possible. Expectedly, the reaction times were significantly larger in the SRTT than the asynchronies in the ST (mean ± SD: 263 ± 37 ms in the ST and 381 ± 46 ms in the SRTT; ANOVA main effect of task: $F(1, 718) = 1443.93$, $p < 0.0001$). The constant error, a measure of timing accuracy that corresponds to the difference between the produced and the instructed interval, was slightly negative during SCT and ST, indicating that the monkeys were able to properly produce the intervals with a small underestimation across

target durations (Fig 1D). Finally, the temporal variability (a measure of timing precision) during the SCT and ST are depicted in Fig 2H and Fig 4E, respectively.

Neural state trajectories

We characterized the dynamics of the evolving response patterns using the projection of the neural population time-varying activity onto a low-dimensional state space using principal component analysis (PCA) on a population of 1,477 MPC cells recorded during SCT (see Materials and methods, recording locations in S1 Fig). The results showed highly stereotyped trajectories with a strong periodicity in the first three principal components (PCs) (Fig 2A–2D). Indeed, PC2 and PC3 showed together a cyclic path for each produced interval (Fig 2C and 2D). Each loop in the trajectory corresponded to the periodic network state variation during the production of the rhythmic tapping sequence of the SCT. The circular trajectories in the plane exhibited the tendency to start at the same position in the phase-space after each tap, suggesting the existence of a movement-triggering point at a particular location in the population trajectory across durations (see below). Crucially, from this common phase-space location, longer intervals produced larger state trajectory loops, with a monotonic increase in the trajectory radius as a function of target interval during both the SC and CC (Fig 2E). However, the observed interval-dependent modulations in curvilinear amplitude were not accompanied by modulations of the linear speeds of the periodic neural trajectories, as these remained constant across durations (Fig 2F). The same properties were observed in PC1 and when the PCA is computed from a subpopulation of neurons whose activity was task related (see S2 Fig). Hence, contrary to a prototypical temporal scaling, in which there is a decrease in linear speed as a function of interval and similar trajectory paths and traversed distances for different durations [24,34], the present results show that rhythmic timing during the SCT is represented as an increase in curvature radii in the neural network state dynamics.

To test the relationship between the radius of the curvature in the neural-state trajectories and the monkeys' behavior during SC and CC, we split the produced intervals into two groups: those in which the monkeys produced an inter-tap time that was below the 20th percentile, and those with inter-tap times above the 80th percentile [21]. Strikingly, on those intervals in which the monkeys tended to produce shorter inter-tap durations, the state trajectory radius was smaller, and vice versa (Fig 2G).

Another important property of the curvilinear radii in the PCA neural trajectories was that their variability (SD of the trajectory radii) followed the same linear increase as a function of target interval observed in the monkeys' behavior (Fig 2H). This linear relation between temporal variability and interval duration, known as scalar property of interval timing, has been widely reported in the timing literature, and our findings suggest that it depends on the radius of the rotatory dynamical state of MPC neural populations during both SCT conditions. It is important to mention that all the described properties in the neural trajectories are resilient on the methods used to compute the PCs (see S3 Fig).

The dynamics in the MPC population activity during the SCT was also characterized using demixed PCA (dPCA; Fig 3, see Materials and methods). This method not only captures most of the variance in the neural data but, most importantly, also decomposes the dependencies of the neural population activity into latent components associated with task parameters [30]. In contrast, PCA only focuses on the total variance explained using orthogonal decomposition. The first dPCA (dPCA1) showed a strong periodic structure with a minimum value around the beginning of each produced interval in the SCT sequence, similar to the findings from the PCA neural trajectories (Fig 2C and 2D). In addition, the dPCA1 showed a strong change in amplitude with target duration (Fig 3A). Because we used time-normalized neural data as

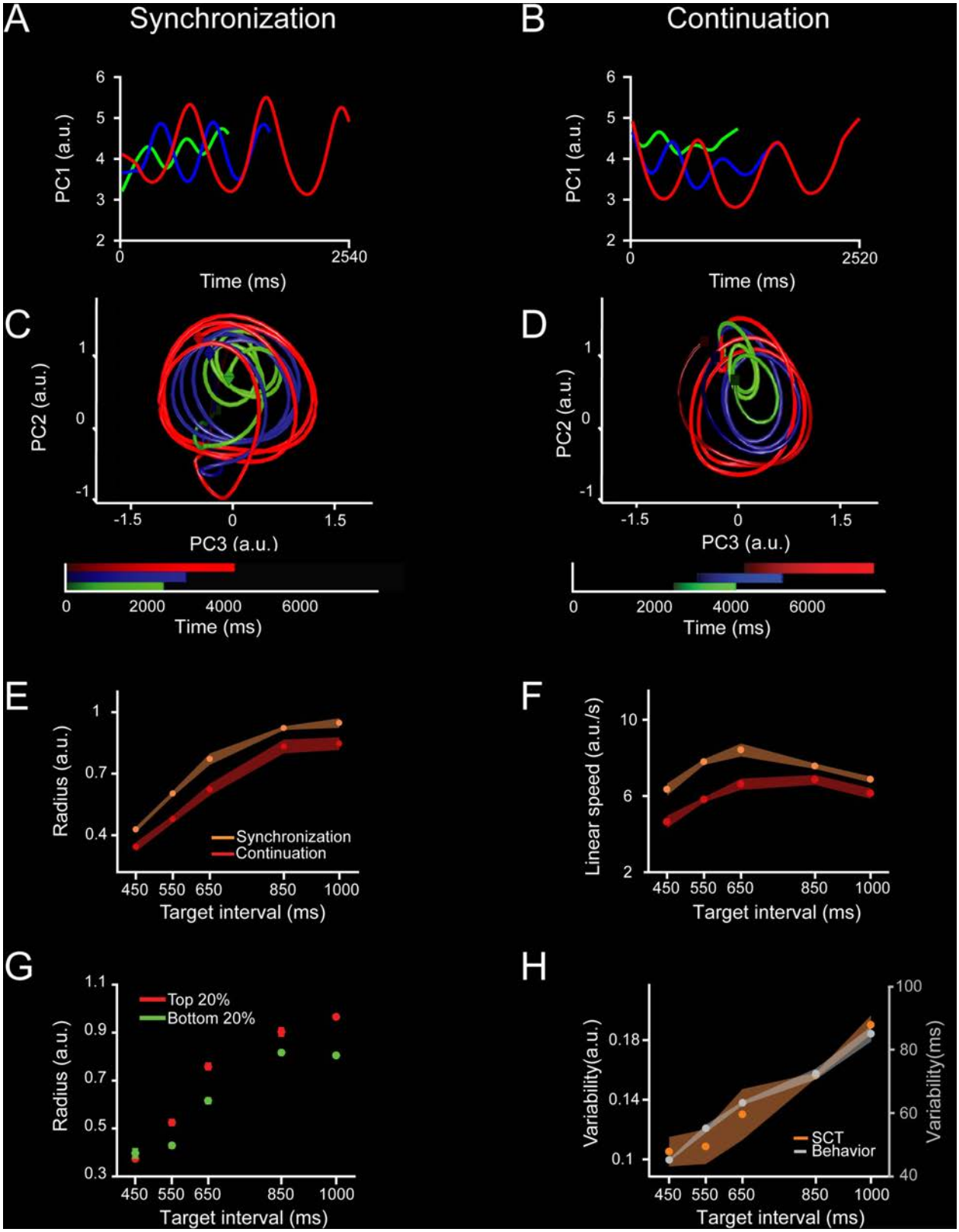

Fig 2. Neural population trajectories during SCT and their oscillatory dynamic properties. A, C. Projection of the neural activity in the MPC (1,477 neurons) during the SC of the SCT onto the first (**A**) or second and third PCs (**C**). The first three PCs explained the 10.7%, 3.8%, and 2.3% of

the total variance. Each point in the trajectory represents the neural network state at a particular moment. The trajectory completes an oscillatory cycle on every produced interval during the synchronization and continuation phases of the SCT. Target interval in milliseconds is color coded (450, green; 650, blue; 1,000, red). Color progression within each target interval corresponds to the elapsed time. A cube indicates the beginning of each trajectory, while an octahedron indicates the end. **B, D**. Projection of the neural activity during CC of the SCT onto the first (**B**) or the second and third (**D**) PC. Color code is the same as (**A**). **E**. Monotonic increase of the radii in the oscillatory neural trajectories during SC (orange, mean ± SD, slope = 0.0009, constant = 0.0679, $R^2 = 0.9$, $p = 0.01$) and CC (red, mean ± SD, slope = 0.0009, constant = −0.0296, $R^2 = 0.9$, $p < 0.01$) as a function of target interval. **F**. Linear speed of neural trajectories during SC (orange, mean ± SD, slope = 0.0001, constant = 7.322, $R^2 = 0.0007$, $p = 0.896$) and CC (red, mean ± SD, slope = 0.002, constant = 4.049, $R^2 = 0.354$, $p = 0.002$) as a function of target interval (ANOVA main effect interval, $F(4, 39) = 92.15$, $p < 0.0001$; main effect condition, $F(1,39) = 381.46$, $p < 0.0001$; interval × condition interaction, $F(4, 39) = 15.15$, $p < 0.0001$). The linear speed was similar (SC) or showed a slight increase (CC) with the target interval. **G.** Neural trajectory radii for the top 20% (red, slope = 0.0011, constant = −0.035, $R^2 = 0.7$, $p < 0.0001$) and bottom 20% (green, slope = 0.00088, constant = −0.009, $R^2 = 0.75$, $p < 0.0001$) inter-tap intervals across target intervals. Note that on those intervals in which the monkeys tended to produce shorter inter-tap durations, the state trajectory radius was smaller, and vice versa (ANOVA main effect interval, $F(4, 40) = 155.7$, $p < 0.0001$; main effect population, $F(1, 40) = 33.3$, $p < 0.0001$; interval × population interaction, $F(4, 40) = 3.98$, $p = 0.008$). **H**. Variability (SD) of SCT rotational neural trajectories (orange, mean ± SD, normalized data slope = 0.0019, constant = −1.02, $R^2 = 0.94$, $p = 0.005$) and the monkeys' produced intervals (gray, mean ± SD, normalized data slope = 0.005, constant = −0.721, $R^2 = 0.98$, $p = 0.0008$) as a function of target interval. The Weber increase in tapping variability was not statistically different from the increase in the variability of neural trajectories across target intervals (normalized data, slope t test = 0.86, $p = 0.42$; constant t test = 1.36, $p = 0.22$). Underlying data are available in https://doid.gin.g-node.org/d315b3db0cee15869b3d9ed164f88cfa/. a.u., arbitrary unit; CC, continuation condition; MPC, medial premotor cortex; PC, principal component; SC, synchronization condition; SCT, synchronization-continuation task.

https://doi.org/10.1371/journal.pbio.3000054.g002

input to the dPCA, all trials had the same length regardless of the target interval. In this scenario, a scaling mechanism should have produced similar dPCAs across durations. Instead, we observed a time-dependent modulation in dPCA1 amplitude. In order to compare the two methods for dimensional reduction, we computed the bin-by-bin distance between the 450-ms and the other four target intervals (Fig 3D) using the PCAs (Fig 3B) and dPCA1 (Fig 3C). The resulting distance profiles are very similar between methods, with a periodic structure whose amplitude mean and variability increased as a function of the target interval (Fig 3E and 3F). Thus, with a separate set of assumptions, the dPCA corroborates the existence of both the periodic structure of the neural state dynamics and a beat-based timing mechanism based on the amplitude modulation of the rotatory population trajectories during SCT.

The analyses described above were done on neurons recorded throughout different sessions. Thus, as a next step we determine the neural state trajectories on simultaneously recorded cells while monkey M01 performed an ST (Fig 1B) and an SRTT (Fig 1C). This strategy not only allows us to validate the data of the SCT on the ST but also permits us to determine population dynamics on a trial-by-trial basis. As in the SCT, the PCA-projected activity during the ST showed periodic state dynamics (Fig 4A; S4A Fig), whereas the SRTT neural trajectories were not as periodic (Fig 4B; S4B Fig). In fact, the fitting of a normalized sinusoidal function on the first PC was statistically more robust for ST than SRTT (in terms of mean square error [MSE]: Fig 4C), even when the length of the inter-tap PCA-projected activity was matched between different produced intervals (see Materials and methods). Again, the radius of the neural trajectories during the ST showed a significant increase in both mean radius (Fig 4D, purple) and variability (Fig 4E), but a constant linear speed (Fig 4F), as a function of the target interval, reproducing the findings in SCT. In contrast, the radius and variability of the trajectories during SRTT showed small changes across target intervals, with a nonsignificant linear fit as a function of target interval for the three parameters (Fig 4D, 4E and 4F, green). This phenomenological comparison suggests that rhythmic tapping to a metronome depends on the amplitude of the cyclic dynamics of population activity and that the shift from a predictive to a reactive behavior during SRTT precludes the organization of periodic population state trajectories.

The simultaneity of the recordings during ST [35] allowed for the decoding of the produced intervals on a trial-by-trial basis. Using a time-delay neural network (TDNN; see Materials and methods) (Fig 4G), we found that an ideal reader of the neural trajectories could predict

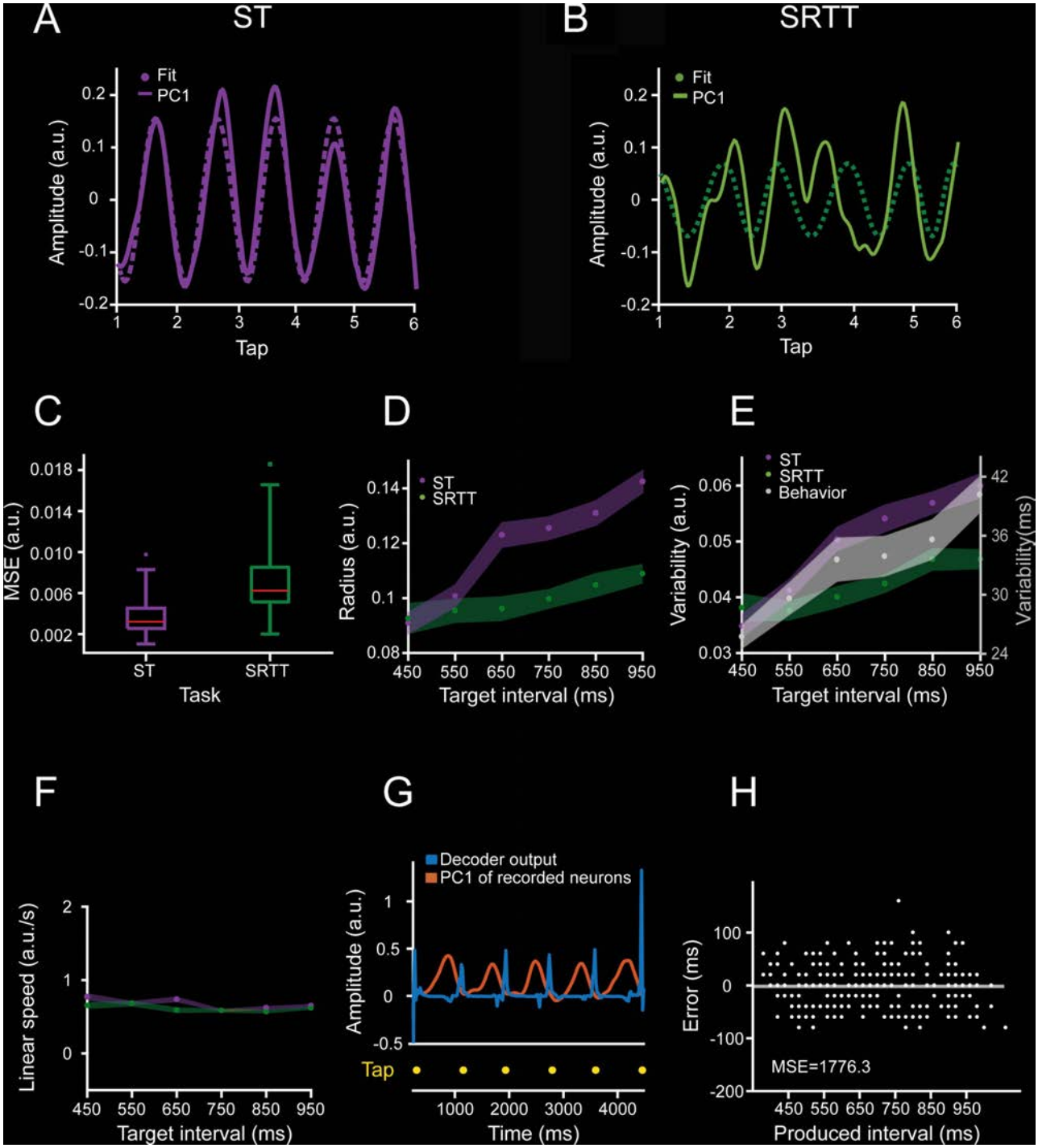

Fig 4. Comparison of ST and SRTT trajectories in simultaneously recorded neurons. A. Neural activity data projected on the PC1 (solid line, linearly detrended) and the correspondent sinusoidal fit (dotted line) during a trial of ST for the target interval of 650 ms. **B**. Similar to **(A)** for SRTT. Note that the strong periodic structure of the ST neural trajectory is lost during SRTT for the same population of cells. **C**. The MSE of the sinusoidal fits during ST (purple) is significantly smaller than during SRTT (green; 60 trials, two-sample t test = −6.78, $p < 0.0001$). **D**. Radii of the neural trajectories during ST (purple, slope = 0.000087, constant = 0.055, $R^2 = 0.619$, $p < 0.0001$) and SRTT (green, nonsignificant linear regression, $R^2 = 0.0172$ and $p = 0.489$) as a function of target interval. **E.** Variability of the neural trajectories during ST (purple, data slope = 0.000037, constant = 0.028, $R^2 = 0.368$, $p < 0.0001$), SRTT (green, nonsignificant linear regression, $R^2 = 0.0005$ and $p = 0.903$), and temporal variability of the monkeys' produced intervals (gray, mean ± SD/2, data slope = 0.0009, constant = −0.003, $R^2 = 0.999$, $p < 0.0001$) across target intervals during ST. **F.** Linear speed of neural trajectories during ST (purple, mean ± SD, slope = 0.0001, constant = 7.322, $R^2 = 0.0007$, $p = 0.896$) and SRTT (green, mean ± SD, slope = 0.002, constant = 4.049, $R^2 = 0.354$, $p = 0.002$) did not change as a function of target interval. **G.** Output of the time-delay neural network (TDNN, in blue)

trained to decode the duration of produced intervals based on the PC1 neural trajectories (orange) during a target interval of 850 ms. Tapping times are shown in yellow. **H.** TDNN error, defined as the difference between the produced and the decoded interval, as a function of produced interval. TDNN predicted accurately the performance of the monkey on a trial-by-trial basis (the decoded mean was not statistically different from 0, t test = −0.5228, $p = 0.6$). Underlying data are available in https://doid.gin.g-node.org/d315b3db0cee15869b3d9ed164f88cfa/. a.u., arbitrary unit; MSE, mean square error; PC, principal component; SRTT, serial reaction time task; ST, synchronization task; TDNN, time-delay neural network.

https://doi.org/10.1371/journal.pbio.3000054.g004

accurately the tapping times during ST on 86% of the produced intervals. Indeed, the decoding accuracy was better than the actual percent of correct trials in this demanding task (Fig 4H), supporting the notion that the neural trajectories can robustly predict the rhythmic tapping behavior.

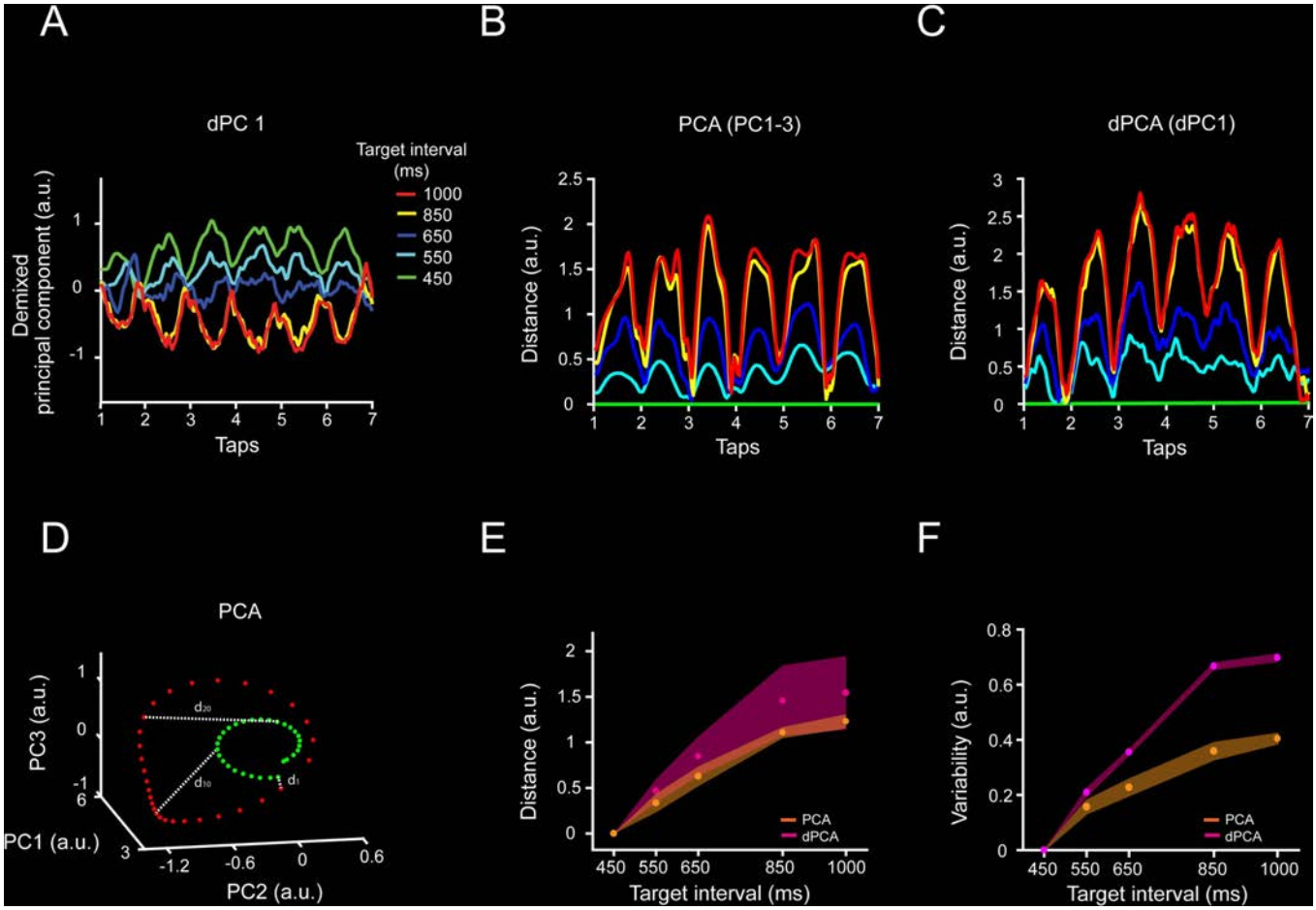

Fig 3. dPCA applied to neural population activity during SCT. A, dPC1 of the dPCA of the neural activity associated with the target interval (explains 7.8% of the total variance). Target interval in milliseconds is color coded (see inset **A**). The neural trajectories show oscillatory activity, and their amplitude varies across target intervals. **B,C.** Euclidean distance between the first PC of the 450-ms target interval and the first PC of each target interval across time for (**B**) time-normalized PCA and (**C**) dPCA. Target interval is color coded as in (**A**). Two-sample Kolmogorov–Smirnov test on the distributions of PCA and dPCA distances showed nonsignificant differences ($p < 0.05$) across target intervals. **D.** Distance calculation diagram for PCA data. The inter-tap trajectories for two target intervals are shown (green, 450 ms; red, 1,000 ms). The 450-ms target interval trajectory is used as the reference for distance calculation. The Euclidean distance between each sequential bin is calculated among the reference interval and the other target intervals trajectories. Both population analyses, PCA and dPCA, produced population signals with similar characteristics. Thus, oscillatory activity, modulation of the amplitude with the target interval, and an intersection close to the tap time are characteristics of the underlying neural population activity, irrespective of the dimension reduction algorithm. **E.** Mean inter-tap Euclidean distance (mean ± SD) between the 450-ms and each target interval for the PCA data using PC1–3, (orange) and dPCA using dPC1 (magenta). There was no significant difference between the slopes of PCA and dPCA (slope t test = 1.97, $p = 0.0539$) **F.** Variability of the distance between the 450-ms and each target interval for the PCA (orange) and dPCA (magenta). The variability increased monotonically as a function of the target interval for both analyses. Underlying data are available in https://doid.gin.g-node.org/d315b3db0cee15869b3d9ed164f88cfa/. a.u., arbitrary unit; dPCA, demixed PCA; PC, principal component; PCA, principal component analysis; SCT, synchronization-continuation task.

https://doi.org/10.1371/journal.pbio.3000054.g003

The population state dynamics are not related to the tapping kinematics

The cyclic and smooth nature of the neural trajectories during ST and SCT sharply contrast with the kinematics of movement (Fig 5A, 5C and 5D), which is characterized by stereotypic tapping movements separated by a dwell period that increased as a function of the target interval (Fig 5E; [16,37]). These observations suggest that during rhythmic tapping, an explicit timing mechanism in MPC keeps track of the dwell time by setting in motion a continuous and periodic change in the neural population state. According to this scheme, the tapping command is triggered once the state trajectories get to a specific position in the phase-space that corresponds to the intersection point between the tangent circular paths whose radii increase with the tapping tempo. To test the hypothesis, we computed the distance between a point in state space and the position of the taps in the neural trajectory and found a similar distance across target intervals (Fig 5B, see inset). In addition, the distance between the same point and half inter-tap position increased as a function of target interval (Fig 5B). Therefore, these results support the idea that the neural trajectories behave as tangent circles and encode the dwell time between taps in the PC amplitude and trigger the stereotypic tapping movements once the neural dynamics reach a point in state space (S5 Fig).

Distributed nature of the trajectories' timing information

We determined whether we could extract information about the target interval from the neural population dynamics, and how this information was modulated by the size of the neural population used to compute the trajectories. To this end, we first segregated each segment of the single-dimension trajectory according to the SCT target interval (450, 550, . . . 1,000 ms; see insets in Fig 6A). Then, to capture the shape of the trajectory segments as a single three-dimensional coordinate, we applied a second-layer PCA (PCA′) and kept the first three PCs. As a result, we obtained a dot cloud in 3D, in which each point represents a particular produced interval trajectory segment (Fig 6A). We trained support vector machines (SVMs) to classify the cloud of points for the five target intervals of the SCT. We trained the SVM ten times and used 5-fold cross-validation to evaluate the performance of the classifier. On the other hand, each neuron was sorted according to the weight magnitude of the original PCAs. The neurons with the largest PC participation were removed in steps of 10% from the original population size, and the second-layer PCAs were computed on the new trajectories. Finally, the SVM was carried out on the second-layer PCAs for different population sizes (see Fig 6). There was an asymptotic decline in the classifier performance with the removal of a larger percentage of the neural population (Fig 7A). However, even with very small populations (total cells: 15), the classifier was able to extract all SCT target intervals above chance. These results are in line with the idea that the temporal structure of rhythmic behavior depends on a neural population code that is distributed within MPC.

Neural population trajectories and evolving activation patterns

The results of the previous section revealed a distributed representation of tapping tempo across MPC cell populations. However, a critical question is what aspects of the time-varying activity defined the changes in amplitude in the neural trajectories as a function of the timed duration [28]. Based on our previous observations [4,21], we hypothesized that the evolving patterns of neural activity could be directly linked with the time-encoding features of the neural trajectories during the SCT. Consequently, to test this idea we first characterized the properties of neuronal moving bumps [21,23,36] during this task. With this information we carried out simulations to determine whether the key features of the moving bumps were linked to the

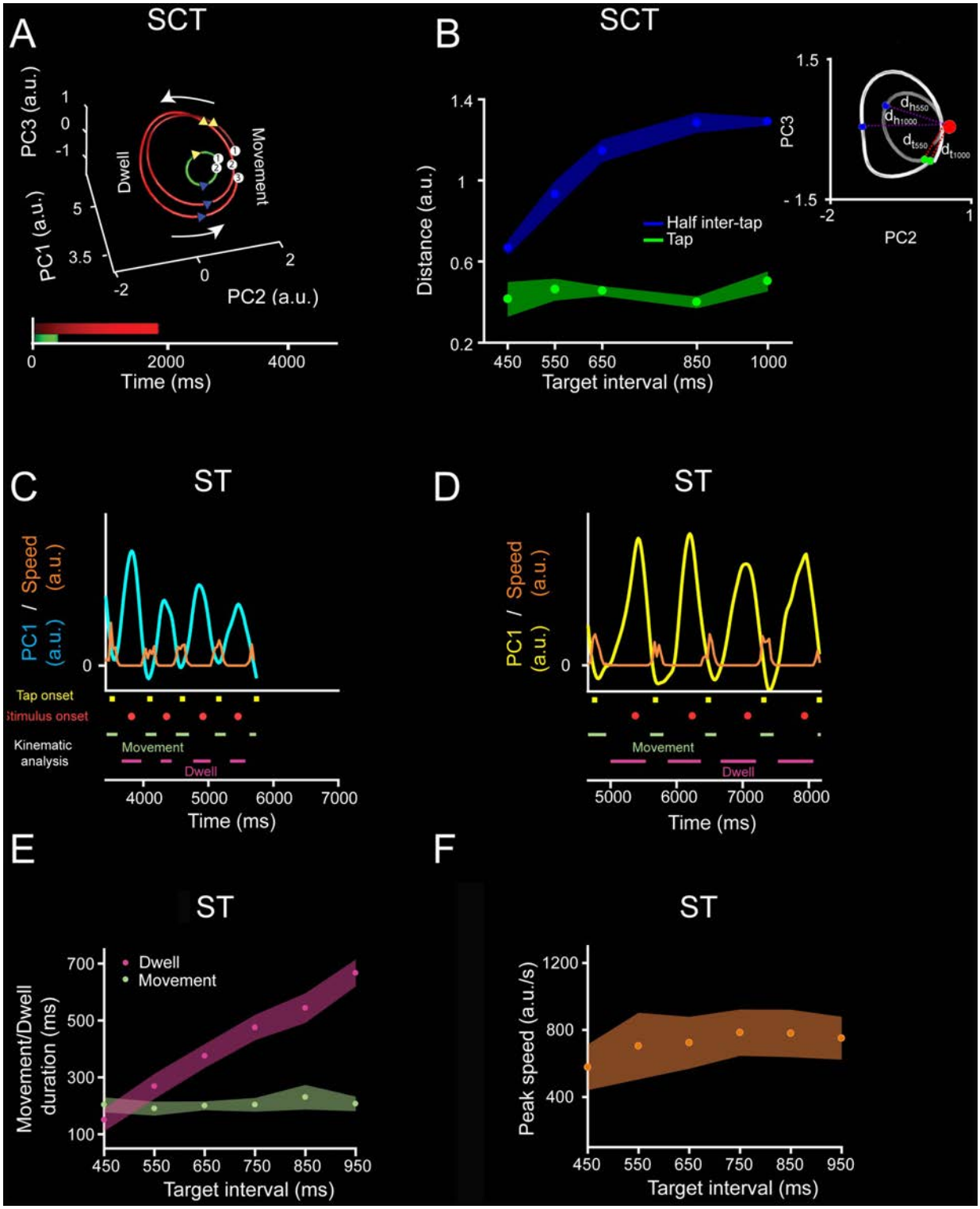

Fig 5. Neural trajectories do not follow the tapping kinematics. A. Diagram of the rotational trajectory of the SCT neural activity during three inter-tap intervals: one 450-ms interval (green) and two 1,000-ms intervals (red). Each tap is numbered and projected in the trajectory as a white circle. A blue triangle marks the beginning, whereas a yellow triangle marks the end of the movement time. The monkeys produced phasic stereotypic movements whilst timing the dwell between taps during SCT [37]. **B.** Euclidean distance (d_t, see inset) between an anchor point (red) and the position of each tap (green, mean ± SD, slope = 0.00007, $R^2 = 0.0633$, p = 0.225), or half of the inter-tap interval position on the neural trajectories (blue, mean ± SD, slope = −0.001, $R^2 = 0.801$, $p < 0.0001$) across target intervals for SC. A two-way ANOVA detected significant main

effects on position ($F(1, 40) = 1855.72$, $p < 0.0001$), target interval ($F(4, 40) = 77$, $p < 0.0001$) and their interaction ($F(4, 40) = 63.68$, $p < 0.0001$). Tukey HSD post hoc test showed that the distances of the anchor point to tap and half inter-tap positions were significantly different ($p < 0.05$). In contrast, the anchor to tap distances across target intervals were not statistically different. Inset: scheme of the distance calculation; red sphere marks the anchor point and two-sample inter-tap trajectories for 550 ms (dark gray) and 1,000 ms (light gray) are shown. The green sphere marks the tap position and the blue sphere marks the half inter-tap position. Thus, the neural trajectories converge on an attractor around the tap time, to later diverge at half the inter-tap interval. Note that these results suggest the existence of tangent circular trajectories that converge in an intersection zone close to the tapping moment, although their amplitude changed as a function of interval. **C**. Speed of the tapping movement (orange trace) from the second to the sixth tap of ST, and the PC1 projected neural information (cyan) for 26 simultaneously recorded neurons during a trial with a target interval of 550 ms. Taps were represented as yellow squares and stimuli as red circles. Movement and dwell times are depicted in green and magenta, respectively. **D**. Similar to (**C**) during an 850-ms target interval (PC1 projected neural information as a yellow trace). **E.** Mean ± SD of the duration of the movement (green) and the dwell between movements (magenta) across target intervals, computed from the speed profile of the tapping movements. A two-way ANOVA showed significant main effects on kinematic state (movement/dwell duration, $F(1, 228) = 1,850.61$, $p < 0.0001$), target interval ($F(5, 228) = 272.72$, $p < 0.0001$), and their interaction ($F(5, 228) = 236.18$, $p < 0.0001$). Tukey HSD post hoc test showed that dwell durations across intervals were significantly different ($p < 0.05$). Therefore, the monkey modulated the dwell duration to successfully temporalize her behavior, while the down-push-up sequence of the tapping movement was phasic and stereotypic across target intervals. **F.** Mean ± SD of the peak speed during the tapping movement as a function of the target interval during ST (ANOVA main effect interval, $F(5, 114) = 5.13$, $p < 0.001$). The Tukey HSD post hoc test showed that only the peak speed of the 450-ms target interval trials were significantly different from the 650-, 750-, 850-, and 950-ms trials ($p < 0.05$). Underlying data are available in https://doid.gin.g-node.org/d315b3db0cee15869b3d9ed164f88cfa/. a.u., arbitrary unit; d_h, Euclidean distance of the anchor point to the half inter-tap position; d_t, Euclidean distance from the anchor point to the tap position; HSD, honestly significant difference; PC, principal component; SCT, synchronization-continuation task; ST, synchronization task.

https://doi.org/10.1371/journal.pbio.3000054.g005

observed changes in curvature radius and variability as a function of duration in the neural state trajectories.

As expected, a substantial proportion of MPC cells during the SCT showed a progressive pattern of activation in the neuronal population, consisting of a gradual response onset of single cells within a produced interval (Fig 8, see Materials and methods). This activation pattern started before a tap, migrated during the timed interval, and finished after the next tap (Fig 8). In addition, a similar response profile was repeated in a cyclical manner for the three intervals of SC and the three intervals of CC (Fig 8A and 8B) [4,21]. These findings suggest that rhythmic timing can be encoded in the sequential activation of neural populations [23]. A central question is what parameters of the neuronal response profiles are encoding the target interval and the SCT condition. Remarkably, the number of neurons involved in these evolving activation patterns (Fig 8A and 8B, Fig 9C), as well as the duration of neural activation periods (Fig 9D), increased as a function of the target interval. SC showed a larger number of active cells, whereas CC showed a longer activation period. In contrast, the neural recruitment lapse, namely the time between pairs of consecutively activated cells (Fig 9E), and the cells' discharge rate (Fig 9F) did not show statistically significant changes across target intervals and task phases. These results suggest that both the size of the circuits involved in measuring the passage of time and the duration of their activation times are core time-encoding signals in MPC, and suggest the existence of a delicate balance between these two measures to produce the progressive activation profiles of neurons when tapping to a metronome or an internally generated rhythmic signal (Fig 9C and 9D).

Next, we simulated evolving patterns of population activity with different response profiles and evaluated their translation onto PCA state space. First, we generated activity patterns on individual units that were complex, heterogenous, and that scaled in time, producing activation periods with the same time-varying activity but different durations (Fig 10A, see Materials and methods) [24]. Then, we simulated population cascade patterns for three consecutive intervals, emulating two key features on the MPC population responses: a gradual response onset of single cells that started before, migrated within, and finished after the end of an interval, with a constant overall recruitment of cells over time; and the cyclical repetition of this response profile for the three intervals (Fig 10C and 10D). In addition, Fig 11A shows that neurons were added randomly in the intermediate portion of the simulated moving bumps when

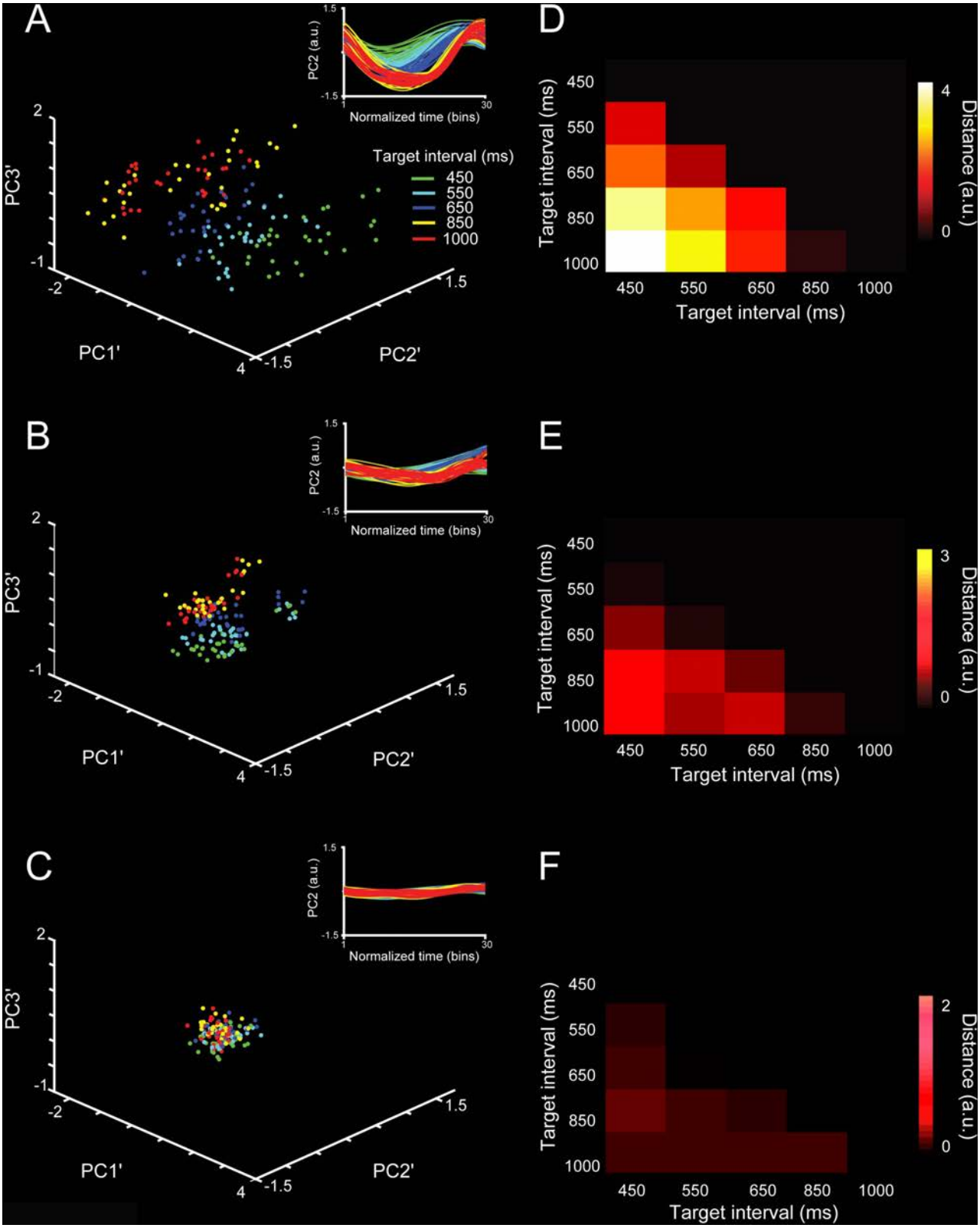

Fig 6. Robustness in the classifier for SCT target interval using segments of the PCA neural trajectory between taps with different neural population sizes. A-C. Three principal components projection of the second-layer PCA′ applied to each of the six inter-tap neural trajectory segments and the five trial repetitions (see inset) for (**A**) 100%, (**B**) 50%, and (**C**) 1% of the neural population. Each dot in the second-layer PCA′ corresponds to

an inter-tap trajectory segment. Target interval color in the inset in (**A**). **D-F.** Distances between cluster centroids of data projection across target intervals for (**D**) 100%, (**E**) 50%, and (**F**) 1% of the neural population. Underlying data are available in https://doid.gin.g-node.org/d315b3db0cee15869b3d9ed164f88cfa/. a.u., arbitrary unit; PC, principal component; PCA, principal component analysis; SCT, synchronization-continuation task.

https://doi.org/10.1371/journal.pbio.3000054.g006

increasing the total number of neurons. The projection of the simulated cascades onto PCA space produced oscillatory trajectories (Fig 10B), whose radii and variability increased but the linear speed was similar with the target interval, as seen in the actual population responses. Importantly, these properties were only followed when the simulated neural cascades included an increase in both the number of neurons and the duration of the activation periods as a function of target interval (Fig 10E and 10F). Simulations with constant values in both parameters produced PCA trajectories with similar radii or variability across interval durations, and a decrease in speed with target interval consistent with the notion of temporal scaling (Fig 10E–10G, Fig 11B–11E). Furthermore, the scaling of the response duration alone did not reproduce the observed changes in radii and variability across durations in the state trajectories (Fig 11D–11E). These findings indicate not only a close relation between the properties of the sequential neural patterns of activation and the neural state trajectories during rhythmic tapping, but also suggest that an increment in the number of neurons engaged in the evolving patterns of population activity is fundamental to reproducing the two critical duration-dependent features of the PCA neural population trajectories: the increase in the magnitude and variability of the radii as a function of target interval.

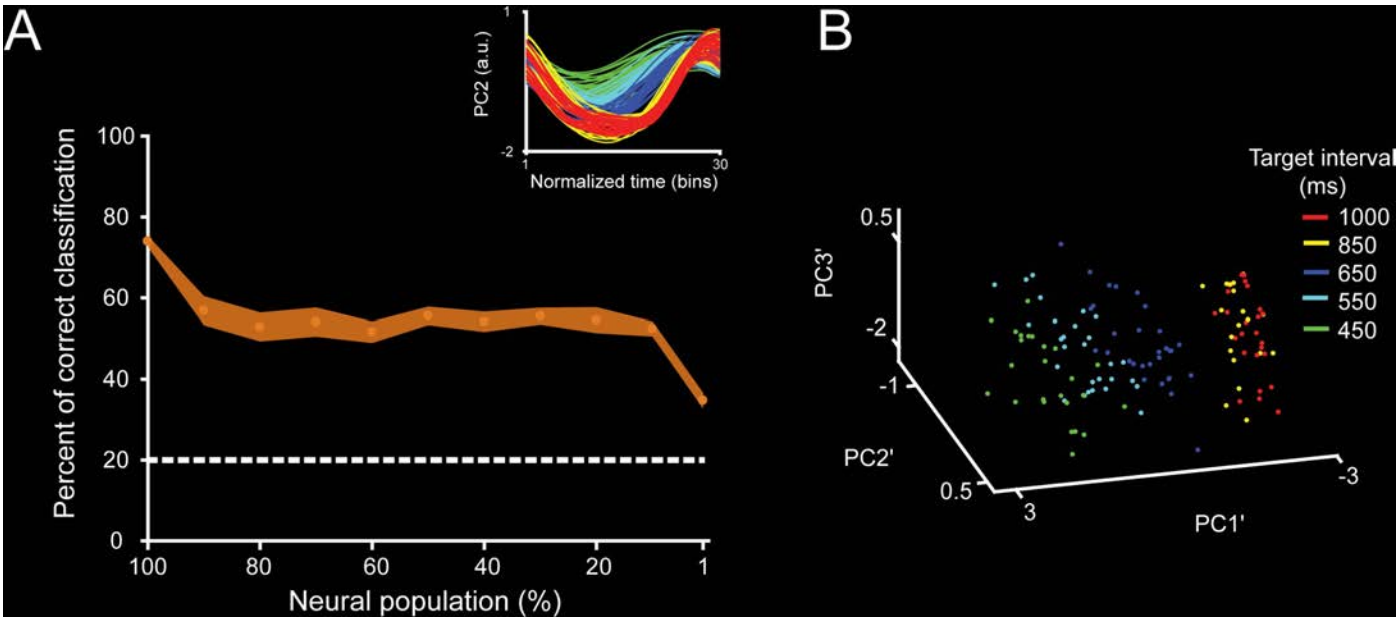

Fig 7. Trajectory classifier robustness across neural population sizes during SCT. A. SVM classifier performance (mean ± SD of percent of correct classifications) for target interval (five instructed intervals) during the SCT task based on the neural trajectory computed from different population sizes. The total initial population size was of 1,477 neurons. Dotted lines correspond to random level. The neurons with the largest PC participation were removed in steps of 10% of the original population size, until reaching 1% of the original population. Inset shows the original time-normalized neural trajectory PC used to generate the second-layer PCA′. **B**. Point cloud in 3D for the second-layer PCAs' for target interval. See color code in the inset. Note that the percentage of correct classification decreased as a function of the population size; however, the classification was above chance even for the trajectories based on small cell ensembles. Underlying data are available in https://doid.gin.g-node.org/d315b3db0cee15869b3d9ed164f88cfa/. a.u., arbitrary unit; PC, principal components; PCA, principal component analysis; SCT, synchronization-continuation task; SVM, support vector machine.

https://doi.org/10.1371/journal.pbio.3000054.g007

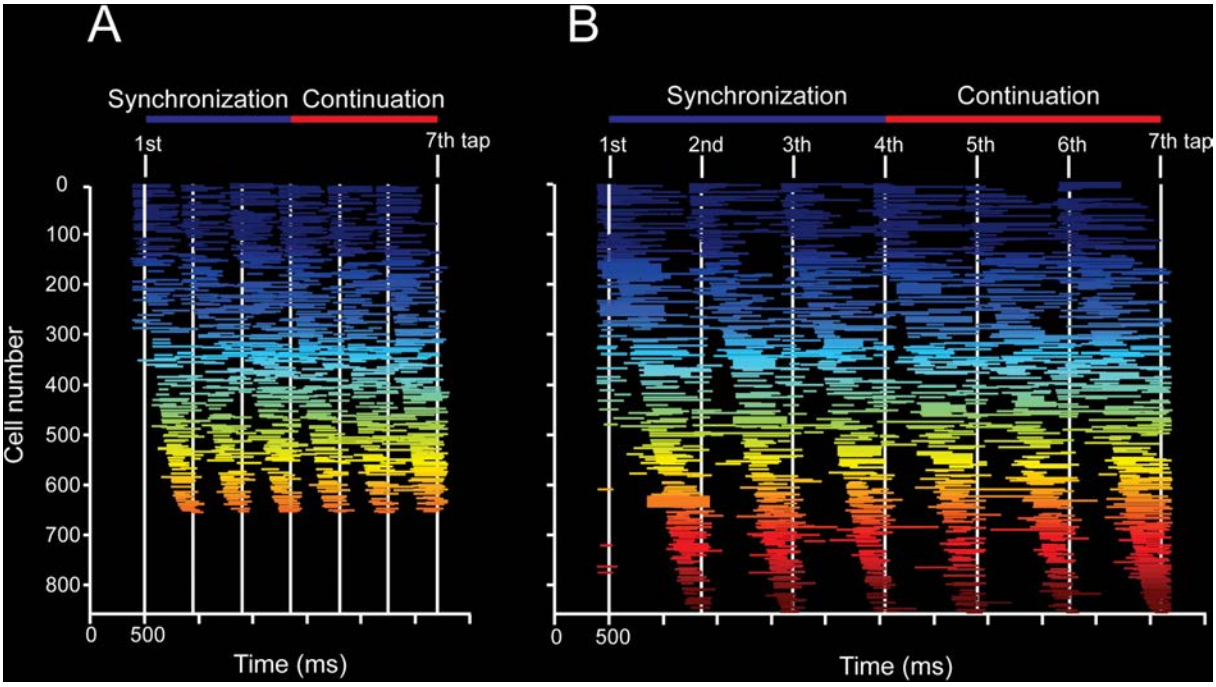

Fig 8. Overall patterns of activity in cell populations. A,B. Neural activation periods, sorted by their mean peak activation time, during the SCT task for the target intervals of 450 (A) and 850 (B) ms. Each horizontal line corresponds to the onset and duration of the significant activation period of a cell according to the Poisson-train analysis (see Materials and methods). The Poisson-train analysis was carried out on the discharge rate of cells that was warped in relation to the tapping times (seven white vertical lines [4,73]). Note that the number of cells with significant activation periods is larger for the longer target interval. Underlying data are available in https://doid.gin.g-node.org/d315b3db0cee15869b3d9ed164f88cfa/. SCT, synchronization-continuation task.

https://doi.org/10.1371/journal.pbio.3000054.g008

Discussion

The present study supports four conclusions. First, the time-varying discharge rate of MPC cells shows a strong periodic organization when projected onto a two-dimensional state space, generating a circular neural trajectory during each produced interval. The amplitude of this trajectory increases with target duration and is closely related to the rhythmic tapping during the SCT and ST, but not during the reactive tapping of SRTT. Second, the scalar property, a hallmark of timing behavior, was accounted for by the variability of the curvilinear radii in the PCA neural trajectories. Third, the population dynamics for simultaneously recorded MPC cell populations during ST contained information to accurately decode the tapping times on a trial-by-trial basis. Last, there is a strong correlation between the interval-associated changes in radial magnitude and variability of the periodic neural trajectories during SCT and the number of neurons involved in the sequential activation patterns, as well as the duration of their transient periods of activation within these moving bumps.

Rhythmic timing and the amplitude of neural state trajectories

The network state trajectories showed the following properties: they were simple, periodic, exhibited an amplitude modulation according to the timed duration, and were different from the stereotypic kinematics of the phasic tapping movements and the timing control of the dwell between movements in this task [16,37]. Notably, the increases in trajectory amplitude as a function of target interval were observed during the two rhythmic tapping tasks, reproduced with dPCA, and closely related with the monkeys' produced intervals during SCT and

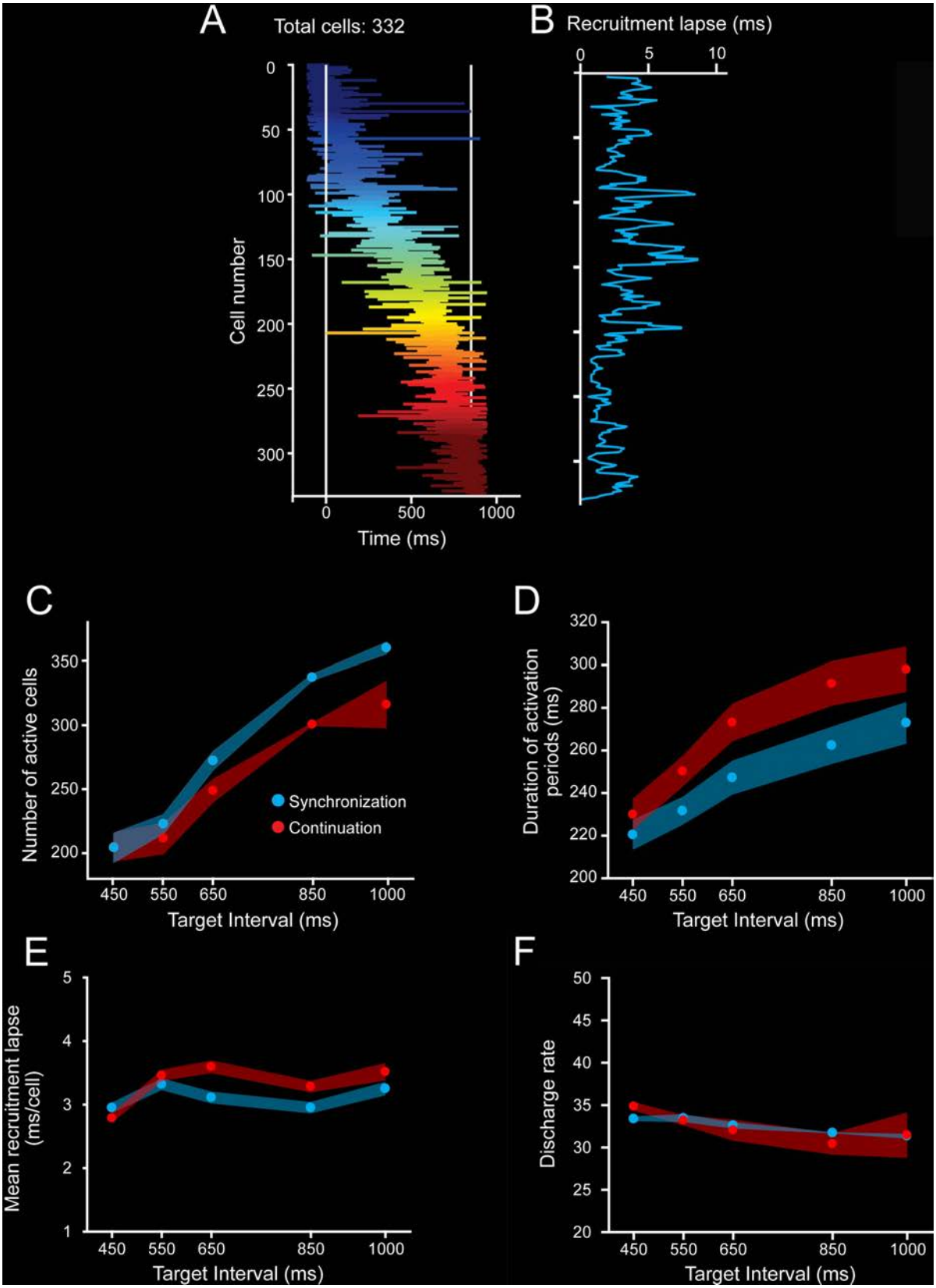
A
Total cells: 332
Cell number
Time (ms)
B
Recruitment lapse (ms)
C
Number of active cells
Synchronization
Continuation
Target Interval (ms)
D
Duration of activation periods (ms)
Target Interval (ms)
E
Mean recruitment lapse (ms/cell)
Target Interval (ms)
F
Discharge rate
Target Interval (ms)

Fig 9. Evolving patterns of activation. A. Neural activation periods for the second produced interval (second and third taps as white vertical lines) during SC for the target interval of 850 ms. The horizontal lines of each row correspond to the onset and extent of the activation periods detected by the Poisson-train analysis. Cells were sorted by their time of peak activity. **B.** Recruitment lapse as a function of cell number. The activation lapse was the difference in the time of peak activity between contiguous cells in the neural avalanche. The mean activation lapse (±SEM) was 2.98 ± 0.08 ms. **C.** Number of cells with significant activation periods across target intervals for SC (blue) and CC (red). Avalanches for longer intervals recruited more cells (ANOVA main effect target interval, $F(4, 20) = 21.1$, $p < 0.0001$; main effect task condition, $F(1, 20) = 6.2$, $p < 0.02$; interval × condition interaction, $F(4, 20) = 0.71$, $p = 0.594$). **D.** Duration of the activation periods during the SC (blue) and CC (red) increased as a function of target intervals. (ANOVA main effect target interval, $F(4, 20) = 18.9$, $p < 0.0001$; main effect task condition, $F(1, 20) = 26.7$, $p < 0.0001$; interval × condition interaction, $F(4, 20) = 1.3$, $p = 0.268$). **E.** Mean neural recruitment lapse during SC (blue) and CC (red) did not change as a function of target interval (ANOVA main effect target interval, $F(4, 20) = 2.7$, $p = 0.06$; main effect task condition, $F(1, 20) = 3.4$, $p = 0.08$; interval × condition interaction, $F(4, 20) = 0.79$, $p = 0.55$). **F.** The discharge rate during activation periods in SC (blue) and CC (red) did not vary across target intervals (ANOVA main effect target interval, $F(4, 20) = 2.2$, $p = 0.06$; main effect task condition, $F(1, 20) = 0.86$, $p = 0.35$; interval × condition interaction, $F(4, 20) = 0.92$, $p = 0.45$). Underlying data are available in https://doid.gin.g-node.org/d315b3db0cee15869b3d9ed164f88cfa/. CC, continuation condition; SC, synchronization condition.

https://doi.org/10.1371/journal.pbio.3000054.g009

ST. Furthermore, the switch from predictive rhythmic tapping to a reaction time task (SRTT) produced a profound disorganization in the periodicity of neural trajectories, accompanied by no changes in radial amplitude. In contrast with the temporal scaling model [24], we found that the neural trajectories do not scale in time, because they present a time-related amplitude modulation with similar linear speed profiles across durations. In line with our observations, neural-network simulations of complex sensorimotor patterns showed that temporal scaling of input stimuli produced curvilinear trajectories that increased in radii for longer intervals [38]. Hence, amplitude modulations in neural population trajectories can be associated with rhythmic timing [39] or complex temporal processing [38].

We found a strong correlation between the duration of the produced intervals and the curvilinear amplitude of the MPC neural trajectories during the SCT and ST, and, due to the simultaneity of the recordings in the latter task, we decoded accurately the produced durations on a trial-by-trial basis. In addition, the cyclic and smooth nature of the neural trajectories during ST and SCT sharply contrasts with the tapping kinematics, which are characterized by stereotypic tapping movements separated by a dwell period that increases with the timed interval [16,37]. Previous studies have demonstrated that cell populations in premotor and motor cortical areas show rotatory non-muscle-like trajectories that reflect the internal dynamics needed for controlling reaching and cycling [40,41]. Under this scenario, we found evidence supporting the notion that the periodic MPC trajectories during rhythmic tapping encode the dwell between taps in their curvilinear radii and that the tapping command is triggered whenever the trajectory reaches a specific phase-space, which corresponds to the intersection point between the tangent circular paths. This dynamical geometry contrasts with the neural trajectories of medial frontal areas during a single interval reproduction task [34]. In this interval-based paradigm, the state trajectories not only evolve at different speeds but also generate parallel paths for different timed intervals, depending on the initial conditions of the neural population dynamics [34]. Thus, the present data are consistent with the notion that timing is encoded in a neural population clock [28,42–45] and puts forward the hypothesis that temporal processing during the entrainment to an isochronous metronome depends on the amplitude of tangent circular trajectories in MPC populations. Under this scenario, temporal processing is governed by MPC neural population clocks that switch from temporal scaling of their state dynamics during interval timing to amplitude modulation in their tangent circular trajectories during rhythmic timing. Importantly, because MPC is part of both the cortico-basal ganglia and the cortico-cerebellar circuits, it can play an important role in both interval and rhythmic timing and can act as a synergistic context-dependent element within the two core timing systems, as suggested previously [46–49].

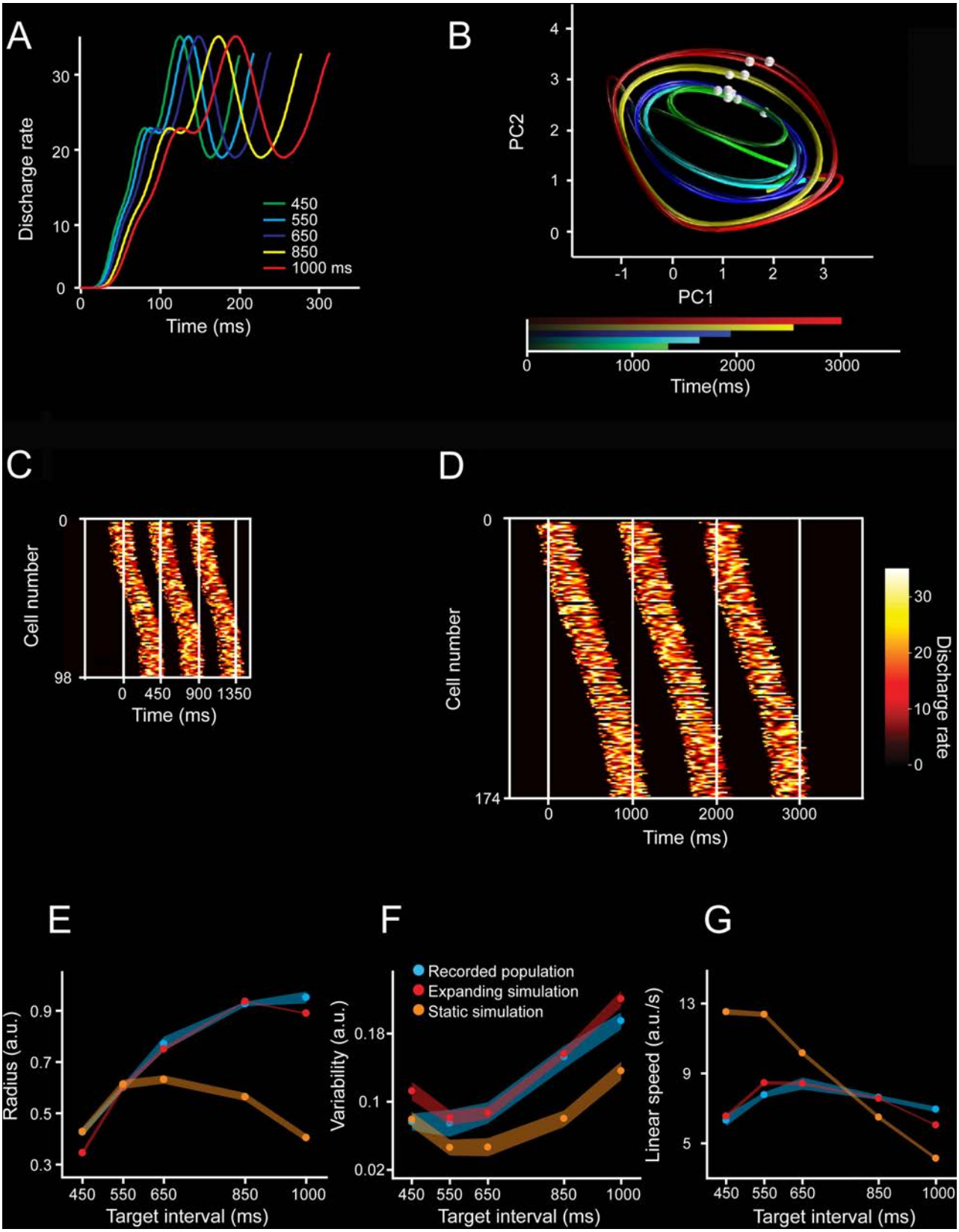
A
Discharge rate
Time (ms)
450
550
650
850
1000 ms
B
PC2
PC1
Time(ms)
C
Cell number
Time (ms)
D
Cell number
Time (ms)
Discharge rate
E
Radius (a.u.)
Target interval (ms)
F
Recorded population
Expanding simulation
Static simulation
Variability (a.u.)
Target interval (ms)
G
Linear speed (a.u./s)
Target interval (ms)

Fig 10. Simulations of moving bumps and neural trajectories. A. Activity profile of one simulated neuron during its activation period is scaled for the five simulated durations. **B**. Neural trajectories generated from the population activity of moving bumps simulations. The number of neurons and activation periods varied across intervals (see Materials and methods). The simulated interval is color coded. Second and third simulated taps are marked as white spheres on each trajectory. **C,D**. Activation profiles of neurons for three consecutive simulated intervals with durations of 450 ms (C) and 1,000 ms (D). The white vertical lines correspond to the tap events defining the intervals. The activation profiles follow a Gaussian shape of cell recruitment, with slow activation rates at the tails (close to each tap). The number of neurons and the duration of the activation periods increased as a function of simulated interval. **E,F,G.** Radii (E), variability (F), and linear speed (G) of the neural trajectories generated from simulations. Data from the simulated neural activity with growing numbers of neurons and activation periods (expanding simulation: red), constant duration of activation periods and constant number of neurons (static simulation: orange), and from the actual recorded population during SCT (blue) across target intervals. Note that a constant was added to both simulation data in graphs. (E) Radii for simulation with expanding parameters (red, mean ± SD, slope = 0.0009, $R^2 = 0.811$, $p < 0.0001$), simulation with static parameters (orange, mean ± SD, nonsignificant linear regression, slope = −0.0001, $R^2 = 0.811$, $p = 0.214$), and actual neural activity (blue, mean ± SD, slope = 0.0009, $R^2 = 0.897$, $p < 0.0001$). The slopes of the radius, variability, and linear speed were not statistically different between the simulations with expanding parameters and the actual neuronal trajectories (radius slope t test = 0.15, $p = 0.878$; variability slope t test = 0.25, $p = 0.803$; linear speed slope t test = 1.8, $p = 0.077$). However, the slopes between the simulations with constant parameters and neuronal trajectories showed statistically significant differences (radius slope t test = 9.13, $p < 0.0001$; variability slope t test = 3.73, $p < 0.001$; linear speed slope t test = 17.71, $p < 0.0001$). Underlying data are available in https://doid.gin.g-node.org/d315b3db0cee15869b3d9ed164f88cfa/. a.u., arbitrary unit; PC, principal component; SCT, synchronization-continuation task.

https://doi.org/10.1371/journal.pbio.3000054.g010

Beat perception in humans is shaped by the temporal structure of extrinsic musical sound and by the metrical interpretation that defines where a subject hears the beat. Thus, the perception of a beat and the corresponding movement entrainment depend on a mental interpretation of the metrics of music. The Dynamic Attending Theory (DAT) is one of the most successful hypotheses to explain these phenomena. According to DAT, it is possible to match the tapping movements to a beat during rhythmic entrainment because the periodic dynamics of music drive our attention [50,51], allowing the prediction of the next pulse in the rhythmic auditory sequence. The DAT suggests that attention is a dynamic process that can be successfully modeled by internal self-sustained oscillations in the auditory system [52,53]. These internal oscillations generate periodic shifts in attention to the most salient events in the sound signal (the pulse that constructs an isochronous sequence in the musical stream), so that the brain generates rhythmic expectations that correspond to the subjective interpretation of the beat. Indeed, electroencephalogram recordings in auditory areas of humans have shown that the brain oscillates at both the exogenous frequency of stimuli and at the metric interpretation of the beat, providing strong support for DAT [54]. In addition, the perception of an inferred musical beat in humans strongly engages the motor system, including the basal ganglia and the MPC [55,56], supporting the notion that rhythmic perception and entrainment depend on a dynamic interaction between the auditory and motor systems in the brain [15,43,57]. Consequently, the present findings add important elements to these ideas, namely, neural populations in the motor system show cyclic dynamics whose period is tightly associated with the tempo of the isochronous metronome, even when the metronome is turned off and the monkeys continue tapping with the same tempo. Hence, in accordance with DAT, the MPC neural trajectories act as a neural oscillator, with a period similar to the tapping tempo during both the sensory cued and the internally driven rhythmic tapping. Furthermore, in agreement with the audiomotor hypothesis for beat perception and entrainment, our data suggest that preSMA and SMA generate a periodic and predictive neural population signal that not only times the inter-tap dwell and triggers the rhythmic tapping movement, but also may help the sensory system to expect a specific temporal structure on the metronome [57,58]. However, a couple of cautionary notes are in place here. First, monkeys can perceive and predictively synchronize to isochronous metronomes [11,16,59]. We still do not know what the metrical hierarchy is that monkeys can perceive and entrain to [11], but, definitively, nonhuman primates do not have the flexibility to predictively perceive and entrain to a pulse across the range of tempi and meters observed in humans [6]. Hence, our present data may generalize only to isochronous rhythmic timing in humans. Second, monkeys show a bias to synchronize to visual rather than

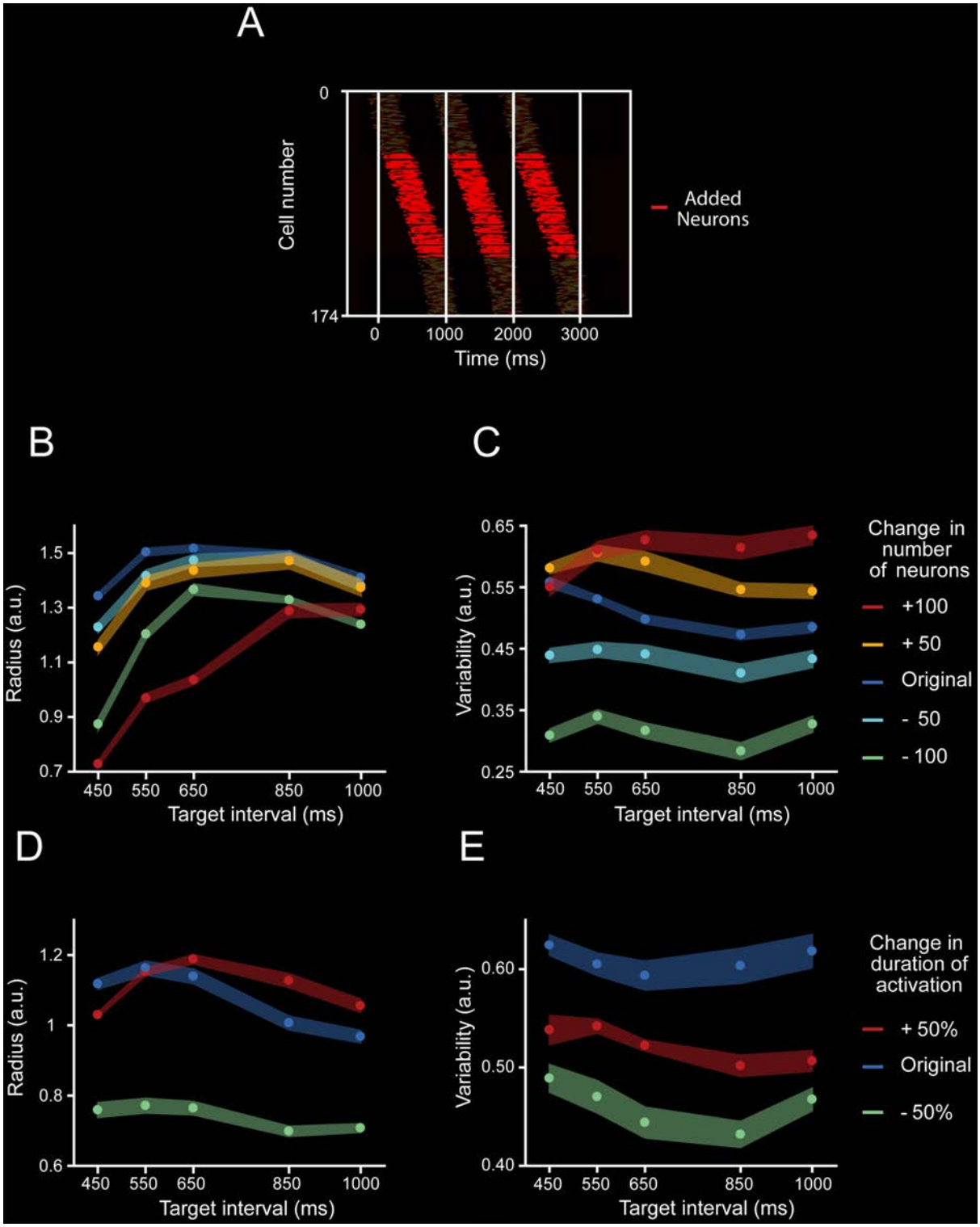

Fig 11. Moving bump simulation parameters. A. Temporal positions of the activation periods of the neurons that were included to the simulation of the 1,000-ms target interval trial (red), in addition to the position of the activation periods of neurons that also participated in the 450-ms simulation (shaded). **B,C.** Radius (B) and variability (C) of PCA trajectories generated from moving bump simulations when the number of neurons was modified by a constant number (−100, green; −50, cyan; +50, yellow; and +100, red) from the original number of neurons (208 neurons for 450-ms target interval, 220 neurons for 550-ms target interval, 230 neurons for 650-ms target interval, 270 neurons for 850-ms target interval, and 282 neurons for 1,000-ms target interval; blue) while the activation period was kept constant at 257 ms across

target intervals. A two-way ANOVA on the radius showed significant main effects for number of neurons ($F(4, 100) = 10{,}544.2$, $p < 0.0001$), target interval ($F(4, 100) = 4{,}013.12$, $p < 0.0001$), and their interaction ($F(16, 100) = 25.8$, $p < 0.0001$). Tukey HSD post hoc test showed significant differences for the radii of all simulations with different numbers of neurons and for all target intervals ($p < 0.05$). Additionally, A two-way ANOVA on the variability showed significant main effects for number of neurons ($F(4, 100) = 2{,}421.8$, $p < 0.0001$), target interval ($F(4, 100) = 3{,}476.91$, $p < 0.0001$), and their interaction ($F(16, 100) = 22.53$, $p < 0.0001$). Tukey HSD post hoc test showed significant differences for the variability of all simulations with different numbers of neurons ($p < 0.05$). **D,E.** Radius (D) and variability (E) of the trajectories generated from neural moving bumps in which the duration of the activation periods was reduced by 50% (short, green) or increased by 50% (long, red) of the original scaled duration (197 ms for 450-ms target interval, 205 ms for 550-ms target interval, 213 ms for 650-ms target interval, 233 ms for 850-ms target interval, and 257 ms for 1,000-ms target interval; blue) while the number of neurons was kept constant at 130 across target intervals. A two-way ANOVA on the variability showed significant main effects for activation duration ($F(2, 60) = 3{,}081.54$, $p < 0.0001$), target interval ($F(4, 60) = 2{,}801.16$, $p < 0.0001$), and their interaction ($F(8, 60) = 211.34$, $p < 0.0001$). Tukey HSD post hoc test showed significant differences for all simulations with different activation durations ($p < 0.05$). In addition, a two-way ANOVA on the variability showed significant main effects for activation duration ($F(2, 60) = 1{,}227.53$, $p < 0.0001$), target interval ($F(4, 60) = 257.49$, $p < 0.0001$), and their interaction ($F(8, 60) = 24.87$, $p < 0.0001$). Tukey HSD post hoc test showed significant differences for all simulations with different activation durations ($p < 0.05$). Thus, the number of neurons and the activation duration within moving bumps produce large changes in the radius and variability of the simulated neural trajectories. a.u., arbitrary unit; HSD, honestly significant difference; PCA, principal component analysis.

https://doi.org/10.1371/journal.pbio.3000054.g011

auditory metronomes [16], whereas humans have a strong entrainment bias towards auditory sequences, including music [1,14]. It has been suggested that the connections between the dorsal auditory regions and the motor planning areas via parietal cortex are stronger in humans than in nonhuman primates, conferring the latter their larger ability for beat perception and entrainment [15,57]. Therefore, it is quite possible that the neural state dynamics in the audiomotor system of the *Homo sapiens* are more flexible and complex than what we report here.

The scalar property of timing and the state dynamics variability

The scalar property states that temporal variability increases linearly as a function of timed duration [60]. This hallmark feature of temporal processing has been documented across many timing tasks and species [20,60–63]. Several computational models based on neural population time representations have been implemented to describe this property, including drift diffusion [64,65] and recurrent networks [36,66]. Here, we found that the variability in the radii of neural trajectories increased as a function of target interval during SCT and ST, but remained similar during the SRTT, a task that precludes time prediction while preserving the sensory and tapping components. Therefore, these results suggest that the amplitude of the MPC state-network trajectories is a feasible neural correlate of the scalar property during rhythmic tapping.

The relation between neural trajectories and moving bumps during rhythmic tapping

The dynamics of coordinated neural population activity define the evolution of the network state trajectories, which in turn have revealed functional principles in a variety of behaviors that are not evident at the single cell level [24,30,32,67]. Notably, the tapping tempo is strongly mapped in the neural trajectories and is encoded in a distributed fashion, not dependent on a particular response profile of individual neurons. Within this neural population framework, we found large groups of neurons that showed sequential transient activation patterns that traversed each produced interval during the SCT. Previous studies have reported moving bumps as a timing mechanism in parietal cortex [68], MPC [4,21], the basal ganglia [23,69,70], and hippocampus [71,72]. For example, the bump activity in the rat striatum during a peak interval task moved progressively slower as the timed interval progressed, providing a functional basis for the decrease in the animals' timing accuracy as the length of the timed interval increased [23]. In contrast, during the SCT we found that the rate of engagement of the neurons within

moving bumps was constant and was accompanied by an increase in the number of neurons participating in the evolving patterns of population activity. Thus, an optimal reader could estimate the tempo of rhythmic tapping based on two signals: the location of the activity within a bump, in which longer intervals engaged moving bumps composed of a larger number of neurons, and the resetting between consecutive evolving activation patterns [65]. Strikingly, our simulations revealed a tight relation between the scaling of the duration of the transient period of activity, the increase in the number of neurons within moving bumps, and the increase in radius and variability of the corresponding neural trajectories. The simulations also suggest that neurons have the same relative position within a moving bump independently of the timed interval, as seen previously in the rat striatum [23]. Consequently, the increase in neural population size for longer intervals implies incorporation of new cells at intermediate locations within the moving bump [21]. These results not only replicate our empirical observations but also support the notion that the properties of moving bumps, especially the number of participating neurons, can shape the curvilinear amplitude and the corresponding variability in neural state trajectories during SCT.

Conclusions

Overall, these findings support the notion that the rhythmic timing mechanism is based on the changes in curvature radii of the neural population state dynamics in MPC, with slower tempos encoded in larger traversed distances in the tangent periodic neural trajectories, and suggest that the variability in these neural trajectories is a feasible neural substrate of the scalar property during rhythmic tapping.

Materials and methods

Ethics statement

All the animal care, housing, and experimental procedures (protocol 090.A INB) were approved by the Ethics in Research Committee of the Universidad Nacional Autónoma de México and conformed to the principles outlined in the Guide for Care and Use of Laboratory Animals (NIH, publication number 85–23, revised 1985).

Subjects

Two monkeys (M01 and M02, *Macaca mulatta*, both males, 5–7 kg BW) were trained to tap on a push button in SCT, ST, and SRTT. The monkeys were monitored daily by the researchers and the animal care staff to check their conditions of health and welfare.

Tasks

SCT. The SCT has been described before [14]. Briefly, the monkeys were trained to push a button each time stimuli with a constant interstimulus interval were presented. This resulted in a stimulus-movement cycle (Fig 1A). After four consecutive synchronized movements, the stimuli were eliminated, and the monkeys had to continue tapping with the same interval for three additional intervals. Monkeys received a reward (drops of juice) if each of the intervals produced had an error $<30\%$ of the target interval. The daily performance of the monkeys was $>70\%$ of correct trials. The amount of juice was proportional to the trial length. Trials were separated by a variable intertrial interval (1.2–4 s). The target intervals, defined by visual stimuli (red square with a side length of 5 cm, presented for 33 ms), were 450, 550, 650, 850, and 1,000 ms. The target intervals were chosen pseudorandomly within a repetition. Five repetitions were collected for each target interval.

ST. This task was similar to the synchronization phase of the SCT [16]. The subject had to push a button with a stimulus. Six stimuli with a constant interstimulus were presented (red square with a side length of 5 cm, shown for 33 ms). Thus, the metronome was always present during the task. The target intervals were 450, 550, 650, 750, 850, and 950 ms. Five repetitions were collected for each target interval.

SRTT. This task is also described elsewhere [14]. Monkeys were required to push a button each time a stimulus was presented, but in this case the interstimulus interval within a trial was random (picking randomly from the same 450, 550, 650, 750, 850, or 950 ms), precluding the explicit temporalization of tapping (Fig 1B). Monkeys received a reward if the response time to each of the five stimuli was within a window of 200 to 500 ms. The intertrial interval was as ST. Visual (white square with a side length of 5 cm, presented for 33 ms) stimuli were used, and five repetitions were collected.

Neural recordings

For the SCT, the extracellular recordings were obtained from the MPC of the monkeys using a system with 7 or 16 independently movable microelectrodes (1–3 MΩ, Uwe Thomas Recording, Germany, S3). Only correct trials were analyzed. All isolated neurons were recorded regardless of their activity during the task, and the recording sites changed from session to session. At each site, raw extracellular membrane potentials were sampled at 40 kHz. Single-unit activity was extracted from these records using the Plexon offline sorter (Plexon, Dallas, TX). Using the seven-electrode system, the number of simultaneously recorded cells ranged from 5 to 14 cells, whereas with the 16-electrode system the number ranged from 10 to 35 cells during a recording session. In the present paper we analyzed the activity of 1,477 (1,074 of Monkey 1 and 403 of Monkey 2) MPC neurons in both monkeys. The functional properties of some of these cells (1,083 neurons) have been reported previously [20,21,25]. In addition, using a semichronic, high-density electrode system [35], 26 and 41 MPC cells were recorded simultaneously while Monkey 1 was performing the ST and SRTT tasks. All the isolated neurons were recorded regardless of their activity during the SCT, ST, and SRTT, and the recording sites changed from session to session.

Neural activation periods

We used the Poisson-train analysis to identify the cell activation periods within each interval defined by two subsequent taps. This analysis determines how improbable it is that the number of action potentials within a specific condition (i.e., target interval and ordinal sequence) was a chance occurrence. For this purpose, the actual number of spikes within a time window was compared with the number of spikes predicted by the Poisson distribution derived from the mean discharge rate during the entire recording of the cell. The measure of improbability was the surprise index (*SI*), defined as follows:

$$SI = -logP$$

where P was defined by the Poisson equation:

$$P = e^{-rT} \sum_{i=n}^{\infty} \frac{(rT)^i}{i!}$$

where P is the probability that, given the average discharge rate r, the spike train for a produced interval T contains n or more spikes in a trial. Thus, a large *SI* indicates a low probability that a specific elevation in activity was a chance occurrence. This analysis assumes that an activation

period is statistically different from the average discharge rate *r*, considering that the firing of the cell is following a nonhomogenous Poisson process (see also [73]). The detection of activation periods above randomness has been described previously [4,74]. Importantly, the Poisson-train analysis provided the response-onset latency and the activation period for each cell and for each combination of target interval/serial order.

Neural trajectories

Event time normalization and binarization. We developed a time-normalization algorithm to align the neural data from different tapping times of different recording sessions in the same relative time framework. For each neuron, we calculated the produced interval (time between two taps). Then, we subtracted the time of the second tap of a produced interval in the task sequence from all spike and stimulus times ($event_{times}$) and divided them by the produced interval. The tapping times acquired values of minus one and zero, and all the other $event_{times}$ were normalized between these two values. Finally, we added the tap sequence number. Thus, all the normalized values for movement, sensory, and spike events acquired values between zero and seven in an SCT trial, as follows:

$$time\_normalized\_event = \frac{(event\_time - tap\_time)}{produced\_interval} + tap\_sequence$$

Therefore, the time range of events between the first and the last tap of the normalized data of a trial (unit time normalized data [UTND]) was the same regardless of the target interval. In addition to the trial relative time framework, we also used the target interval normalized data (TIND), which corresponds to the UTND multiplied by the target interval. This time-normalization procedure was not necessary for simultaneously recorded data.

Trial binarization. For UTND, TIND, and simultaneously recorded data, we divided the neural data in bins by calculating the discharge rate on consecutive windows of 0.02 units. For UTND, we always got 50 bins between each pair of taps across target intervals, whereas for TIND and the simultaneously recorded data, this number depended on the target interval of the trial. For example, the total number of bins was 23 and 50 for trials with the 450- and 1,000-ms intervals, respectively. The binned data of each neuron were divided by the maximum discharge rate of that particular neuron across all repetitions and target intervals of the SCT. We did not use this time-normalization algorithm on the ST and SRTT data.

Principal component coefficients matrix. Given a linear transformation of a matrix **X** into a matrix **Y**, such that each dimension of **Y** explains variance of the original data **X** in descending order, PCA can be described as the search for matrix **P** that transforms **X** into **Y**, as follows:

$$Y = PX$$

Hence, we first calculated the matrix **P** using a matrix **X** that includes all trials and target interval combinations for the visual SCT of our UTND cell population. Using this **P** on other data guarantees that the same transformation is applied to different neural activity sets. Therefore, using the UTND framework we avoided over- or underrepresentation of the information for different target intervals, due to the constant total number of bins across conditions.

Generating neural trajectories

The TIND information for every trial of all neurons constituted the columns of the **X'** matrix. The principal component coefficients matrix **P** were multiplied by the **X'** matrix to transform the neural data into the space of the original **Y**. Using the same transformation matrix for each

trial allowed the comparison of trajectories for different trials and tasks. A locally weighted scatterplot smoothing function was applied to the columns of the **Y** matrix. The first three dimensions of **Y** were used to generate graphical three-dimensional trajectories, while the first eight dimensions, which explained at least 1% of the variance, were used for the other analysis.

Trajectory radius and variability

The first three PCs explained 10.7%, 3.8%, and 2.3% of the total variance. These three first PCs produced highly stereotyped trajectories with a strong periodicity. In addition, the PC2 and PC3 showed a strong oscillatory structure with a phase difference of π/2 radians during SCT. For these two PCs, we calculated the centroids of the segments of trajectories between adjacent taps. We measured the radius of the 2D trajectory segment as the mean of the Euclidean distances between the centroid and each point in the trajectory segment. The variability of the trajectory was calculated as the standard deviation of the Euclidean distances between the centroid and each point in the trajectory segment across the six serial order elements (three of the SC and three of the CC) for each target interval. Accordingly, the temporal variability of the behavior for each target interval was computed as the standard deviation of the produced intervals within a trial, namely the across-six-serial-order elements of the SCT.

Neural trajectory decoder

We trained a TDNN [75] to decode the produced intervals from the first PC of the simultaneously recorded neural activity during ST. The TDNN architecture had an input layer with 20 time delays and one hidden 10-unit layer. The output layer consisted of a single unit that was trained to generate a value of 1 when a tap occurred, or 0 otherwise. We trained the network using a Bayesian regularization backpropagation algorithm that minimized the mean squared error of the output. The tap time was defined as the time of the peak of the neural network output higher than a threshold of 0.12. We considered a correctly decoded interval when the decoded and the produced taps times' difference was less than 60 ms. We used 5-fold cross-validation to evaluate the performance of the neural network.

dPCA

The dPCA method finds separate decoder (**F**) and encoder (**D**) matrices for each task parameter ($\emptyset$) by minimizing the loss function,

$$L_{dPCA} = \sum_{\emptyset} \|X_{\emptyset} - F_{\emptyset} D_{\emptyset} X\|^2$$

where **X** is a linear decomposition of the data matrix, which contains the instantaneous firing rate of the recorded neurons, into parameter-specific averages:

$$X = \sum_{\emptyset} X_{\emptyset} + X_{noise}$$

The decoder and encoder axes permit us to reduce the data into a few components capturing the majority of the variance of the data dependent on each task parameter [30].

We used the TIND resampled to 30 bins for all target intervals as the input data to the dPCA, and the target interval as the marginalization parameter. Therefore, the length of all the trials for all target intervals was the same. We calculated the bin-by-bin Euclidean distance between the 450-ms first PC and all the target intervals using the PCA and dPCA analyses.

SVM classifier

We were interested in studying the relation between the neural trajectory dynamics and the instructed interval of the SCT (450 ms, 550 ms, . . . 1,000 ms). Therefore, we first normalized the length of each segment of the first eight PCs of the neural trajectory associated with a produced interval (the time between two taps) to 30 bins (see inset, Fig 7A). This step was necessary to avoid a bias associated with the length of the segment. Then, we applied a second-layer PCA′ to each of the original neural trajectory segments for each PC independently. We kept the first three PCs, as they explained 96% of the variance. As a result, a point in a new three-dimensional coordinate for each 30-bin trajectory segment was obtained (see Fig 7B). In order to assess which PC had more information about each of the SCT parameters, we carried out a classification procedure for each PC using an SVM algorithm [76]. Each classifier was retrained 10 times, and we used 5-fold cross-validation to evaluate the performance of the classifier. Thus, we identified the PC with more information for each SCT parameter and called it best-PC.

Additionally, we were interested in studying how the size of the neural population used to generate the PCA affected the information contained in the trajectory. We sorted each neuron according to the magnitude of the PCA weights for the best-PC. We iteratively removed the activity of 10% of the neurons with the largest PCA weights for the best-PC until reaching 1% (15 total neurons). Finally, for each population size, we computed the second-layer PCAs on the new trajectories and the corresponding SVM classification.

Oscillatory activity analysis

To characterize the phase, frequency, and amplitude of the neural trajectories, we calculated a series of nonlinear regression models over the residuals of linear regressions on the first PC projected data. Each inter-tap segment of the projected data was resampled to 30 bins and time normalized to 1 s before calculating the regressions. The general function of the nonlinear models was as follows:

$$PC = a * sine(2\pi * t + c) + d$$

where t is time. In addition, the parameter a is the amplitude of the oscillatory function, c the phase offset, and d is a constant. For each trial of both tasks (ST and SRTT), we calculated the MSE.

Movement kinematics

We applied the Lucas-Kanade optic flow method to measure the monkey's arm speed during the ST. This method calculates a flow field from the intensity changes between two consecutive video frames. The analyzed video was recorded with a Microsoft Kinect for Windows camera with a 640 × 480 resolution. The optic flow method was applied to a smaller area of 141 × 141 pixels from the original video that contained the monkey's arm during the whole trial, and no other moving objects. The arm's movement velocity vector was calculated across all frames as the magnitude of the sum of all the individual flow fields vectors whose magnitude was larger than a predefined threshold. The velocity vector was calculated from the first to the last tap on each correct trial. We reported the speed as the magnitude of the velocity vector. Posteriorly, the kinematic state of the arm was tagged as movement when the velocity vector was larger than a threshold or dwell otherwise. The tagging algorithm considered a change on the kinematic state when the new state lasted longer than three consecutive frames.

Moving bumps simulations

In order to investigate how the properties of the pattern of neuronal activation affected the generation of population neuronal trajectories, we generated five repetitions of simulations of neuronal activity for each target interval. The individual neuronal activation period was composed of the sum of 20 random gamma functions. The activation period was constant for all the neurons on one simulation, but varied with the target interval: 197-, 205-, 213-, 233-, and 257-ms activation durations for 450-, 550-, 650-, 850-, 1,000-ms target intervals, respectively. The initial activation time for each neuron was adjusted so that the population activation rate followed a Gaussian function as to produce a moving bump pattern. The number of neurons in the simulation was incremented according to the target interval (450 ms, 108 neurons; 550 ms, 120 neurons; 650 ms, 130 neurons; 850 ms, 170 neurons; 1,000 ms, 182 neurons). Fig 11A shows neurons were added randomly in the intermediate portion of the moving bumps.

Supporting information

S1 Fig. Location of the silicon shank for the MPC recordings in Monkey 1 during the ST. MRI cortical surface reconstruction of the macaque brain and the recording position of the Buszaki-64 silicon shank over MPC. The green line corresponds to the anterior-posterior location of the spur of the arcuate sulcus that divides preSMA from SMA. The silicon shank was implanted according to this landmark, so that four more anterior shanks were located in pre-SMA and other four posterior shanks in SMA. For the recording locations of MPC in Monkeys 1 and 2 during SCT, see Fig 1B of Merchant and colleagues, 2011. AS, arcuate sulcus; CS, central sulcus; IPS, intraparietal sulcus; MPC, medial premotor cortex; preSMA, pre-supplementary motor cortex; PS, principal sulcus; SMA, presupplementary motor cortex proper; ST, synchronization task.
(TIF)

S2 Fig. Neural population trajectories during SCT from a subpopulation of cells with task-related activity. The PCA was performed on the time-varying activity of 104 cells that showed at least 15 activation periods on the Poisson-train analysis across the five target durations and six serial order elements of the SCT. The first three PCs explained 32.5% of the total variance. **A.** Projection of the neural activity during the SC and CC of SCT onto the first three PCs. The trajectory completes an oscillatory cycle on every produced interval during the synchronization and continuation phases of the SCT. Target interval in milliseconds is color coded (450, green; 650, blue; 1,000, red). Color progression within each target interval corresponds to the elapsed time. A cube indicates the beginning of each trajectory, while an octahedron indicates the end. **B.** Linear increase of the radii in the oscillatory neural trajectories during SC and CC (mean ± SD, slope = 0.0003, constant = 0.2, $R^2 = 0.7$, $p < 0.0001$) as a function of target interval. **C**. Linear speed of neural trajectories during SC and CC (mean ± SD, slope = −0.002, constant = 6.3, $R^2 = 0.42$, $p = 0.001$) as a function of target interval. **D**. Variability of neural trajectories (mean ± SD, normalized data slope = 0.0002, constant = −0.05, $R^2 = 0.87$, $p < 0.0001$) as a function of target interval. Underlying data are available in https://doid.gin.g-node.org/d315b3db0cee15869b3d9ed164f88cfa/. CC, continuation condition; PC, principal component; PCA, principal component analysis; SC, synchronization condition; SCT, synchronization-continuation task.
(TIF)

S3 Fig. Effect of timing and firing rate normalization on the amplitude and speed of neural trajectories. We used different combinations of the time and firing rate normalization of the neural data in order to calculate the PCA coefficients and then the neural trajectories. We

fitted a sine function on each of the first 10 PCs and measured their amplitude and speed. For all the possible normalization combinations, we found at least one of the first three PCs that showed a robust fit of the sine function that was accompanied by a monotonic increase in the mean and the variability of the trajectory radius and a similar speed across target intervals. Here, we show only one PC for each normalization combination (see **A, C, E, G**). **(A-F)** These were generated using normalized firing rate data to calculate the trajectories. The left row corresponds to PC radial amplitude and the right row to the PC linear speed. **A,B.** Coefficients computed with time normalized but trajectories calculated on actual time bins, as presented across this paper for SCT. (**A**) PC amplitude increased with target interval: PC3, data slope = 0.00081, constant = 0.011, $R^2 = 0.899$, $p < 0.0001$, ANOVA main effect target interval, $F(4, 20) = 128.69$, $p < 0.0001$. (**B**) PC linear speed is similar across target intervals: PC3, nonsignificant linear regression, $R^2 = 0.07$, $p = 0.201$, ANOVA main effect target interval, $F(4, 20) = 22.12$, $p < 0.0001$.
C,D. Coefficients and trajectories are computed using time-normalized data. (**C**) PC1, data slope = 0.0012, constant = −0.651, $R^2 = 0.902$, $p < 0.0001$, ANOVA main effect target interval, $F(4, 20) = 875.21$, $p < 0.0001$. (**D**) PC1, data slope = 0.0048, constant = −1.638, $R^2 = 0.98$, $p < 0.0001$, ANOVA main effect target interval, $F(4, 20) = 390.94$, $p < 0.0001$. **E,F**. Coefficients and trajectories are computed using actual time data. (**E**) PC1, data slope = 0.00084, constant = −0.225, $R^2 = 0.899$, $p < 0.0001$, ANOVA main effect target interval, $F(4, 20) = 332.76$, $p < 0.0001$. (**F**) PC1, data slope = 0.0034, constant = 0.641, $R^2 = 0.686$, $p < 0.0001$, ANOVA main effect target interval, $F(4, 20) = 100.04$, $p < 0.0001$. **G,H**. Same as **(A,B)** but using non-normalized firing rate data to calculate the trajectories. (**G**) PC2, data slope = 0.175, constant = 62.162, $R^2 = 0.625$, $p < 0.0001$, ANOVA main effect target interval, $F(4, 20) = 27.58$, $p < 0.0001$. (**H**) PC2, nonsignificant linear regression, $R^2 = 0.089$, $p = 0.145$, ANOVA main effect target interval, $F(4, 20) = 8.18$, $p < 0.001$. Underlying data are available in https://doid.gin.g-node.org/d315b3db0cee15869b3d9ed164f88cfa/. PC, principal component; PCA, principal component analysis; SCT, synchronization-continuation task.
(TIF)

S4 Fig. State trajectories during ST and SRTT using simultaneously recorded neurons. A, B. Three-dimensional neural dynamics trajectory of 650-ms single ST (A) and SRTT (B) intervals. Elapsed time is color coded. The previous and the next taps are marked as red and white spheres, respectively. The stimuli are marked as a white pyramid. Underlying data are available in https://doid.gin.g-node.org/d315b3db0cee15869b3d9ed164f88cfa/. SRTT, serial reaction time task; ST, synchronization task.
(TIF)

S5 Fig. State trajectory progress during SCT. A,B. One trajectory loop for the second produced interval of the (A) SC and (B) CC, during 450-ms (dark gray) and a 1,000-ms (light gray) target intervals. Trajectory progression marked as colored spheres is as follows: previous tap (green), first inter-tap quarter (cyan), second inter-tap quarter/half interval (blue), third inter-tap quarter (yellow), and next tap (red). Therefore, the neural trajectories follow circular paths with different radii that increase according to the target interval, but with similar speed profiles. Underlying data are available in https://doid.gin.g-node.org/d315b3db0cee15869b3d9ed164f88cfa/. CC, continuation condition; SC, synchronization condition; SCT, synchronization-continuation task.
(TIF)

Acknowledgments

We thank Victor de LaFuente, Ranulfo Romo, and Roman Rossi for their fruitful comments on the manuscript. We also thank Raul Paulín for his technical assistance. Jorge Gámez is a doctoral student from Programa de Doctorado en Ciencias Biomédicas, Universidad Nacional Autónoma de México (UNAM), and received fellowship 339118 from CONACYT.

Author Contributions

Conceptualization: Jorge Gámez, Hugo Merchant.

Data curation: Jorge Gámez, Abraham Betancourt, Hugo Merchant.

Formal analysis: Jorge Gámez, Abraham Betancourt, Hugo Merchant.

Funding acquisition: Hugo Merchant.

Investigation: Jorge Gámez, Germán Mendoza, Luis Prado, Hugo Merchant.

Methodology: Jorge Gámez, Germán Mendoza, Luis Prado, Hugo Merchant.

Project administration: Luis Prado.

Software: Jorge Gámez, Abraham Betancourt, Hugo Merchant.

Supervision: Germán Mendoza, Luis Prado, Hugo Merchant.

Validation: Hugo Merchant.

Visualization: Hugo Merchant.

Writing – original draft: Jorge Gámez, Hugo Merchant.

Writing – review & editing: Jorge Gámez, Germán Mendoza.

References

1. Patel AD. The Evolutionary Biology of Musical Rhythm: Was Darwin Wrong? PLoS Biol. 2014; 12(3): 1–6. https://doi.org/10.1371/journal.pbio.1001821 PMID: 24667562
2. Teki S, Grube M, Kumar S, Griffiths TD. Distinct neural substrates of duration-based and beat-based auditory timing. J Neurosci. 2011; 31(10): 3805–3812. https://doi.org/10.1523/JNEUROSCI.5561-10.2011 PMID: 21389235
3. Grahn JA. Neuroscientific Investigations of Musical Rhythm: Recent Advances and Future Challenges. Contemp Music Rev. 2009; 28(3): 251–277. https://doi.org/10.1080/07494460903404360
4. Merchant H, Pérez O, Bartolo R, Méndez JC, Mendoza G, Gámez J, et al. Sensorimotor neural dynamics during isochronous tapping in the medial premotor cortex of the macaque. Eur J Neurosci. 2015; 41(5): 586–602. https://doi.org/10.1111/ejn.12811 PMID: 25728178
5. Phillips-Silver J, Trainor LJ. Hearing what the body feels: Auditory encoding of rhythmic movement. Cognition. 2007; 105(3): 533–546. https://doi.org/10.1016/j.cognition.2006.11.006 PMID: 17196580
6. Fitch WT. Rhythmic cognition in humans and animals: distinguishing meter and pulse perception. Front Syst Neurosci. 2013; 7: 68. https://doi.org/10.3389/fnsys.2013.00068 PMID: 24198765
7. Merchant H, Grahn J, Trainor L, Rohrmeier M, Fitch WT. Finding the beat: a neural perspective across humans and non-human primates. Philos Trans R Soc Lond B Biol Sci. 2015; 370(1664): 20140093. https://doi.org/10.1098/rstb.2014.0093 PMID: 25646516
8. Repp BH. Sensorimotor synchronization: A review of the tapping literature. Psychon Bull Rev. 2005; 12(6): 969–992. https://doi.org/10.3758/BF03206433 PMID: 16615317
9. Repp BH, Su Y-H. Sensorimotor synchronization: A review of recent research (2006–2012). Psychon Bull Rev. 2013; 20(3): 403–452. https://doi.org/10.3758/s13423-012-0371-2 PMID: 23397235
10. Honing H, Merchant H, Háden GP, Prado L, Bartolo R. Rhesus Monkeys (Macaca mulatta) Detect Rhythmic Groups in Music, but Not the Beat. PLoS ONE. 2012; 7(12): e51369. https://doi.org/10.1371/journal.pone.0051369 PMID: 23251509

11. Honing H, Bouwer FL, Prado L, Merchant H. Rhesus Monkeys (Macaca mulatta) Sense Isochrony in Rhythm, but Not the Beat: Additional Support for the Gradual Audiomotor Evolution Hypothesis. Front. Neurosci. 2018; 12: 475. https://doi.org/10.3389/fnins.2018.00475 PMID: 30061809
12. Hoeschele M, Merchant H, Kikuchi Y, Hattori Y, ten Cate C. Searching for the origins of musicality across species. Philos Trans R Soc Lond B Biol Sci. 2015; 370(1664): 20140094. https://doi.org/10.1098/rstb.2014.0094 PMID: 25646517
13. Ayala YA, Lehmann A, Merchant H. Monkeys share the neurophysiological basis for encoding sound periodicities captured by the frequency- following response with humans. Sci Rep. 2017; 7(1): 16687. https://doi.org/10.1038/s41598-017-16774-8 PMID: 29192170
14. Zarco W, Merchant H, Prado L, Mendez JC. Subsecond timing in primates: comparison of interval production between human subjects and rhesus monkeys. J Neurophysiol. 2009; 102(6): 3191–3202. https://doi.org/10.1152/jn.00066.2009 PMID: 19812296
15. Merchant H, Honing H. Are non-human primates capable of rhythmic entrainment? Evidence for the gradual audiomotor evolution hypothesis. Front Neurosci. 2014; 7: 274. https://doi.org/10.3389/fnins.2013.00274 PMID: 24478618
16. Gámez J, Yc K, Ayala YA, Dotov D, Prado L, Merchant H. Predictive rhythmic tapping to isochronous and tempo changing metronomes in the nonhuman primate. Ann N Y Acad Sci. 2018; 1–20. https://doi.org/10.1111/nyas.13671 PMID: 29707785
17. Merchant H, Georgopoulos AP. Neurophysiology of Perceptual and Motor Aspects of Interception. J Neurophysiol. 2006; 95(1): 1–13. https://doi.org/10.1152/jn.00422.2005 PMID: 16339504
18. Kotz SAE, Schwartze M. Differential Input of the Supplementary Motor Area to a Dedicated Temporal Processing Network: Functional and Clinical Implications. Front Integr Neurosci. 2011; 5: 86. https://doi.org/10.3389/fnint.2011.00086 PMID: 22363269
19. Merchant H, Harrington DL, Meck WH. Neural Basis of the Perception and Estimation of Time. Annu Rev Neurosci. 2013; 36: 313–336. https://doi.org/10.1146/annurev-neuro-062012-170349 PMID: 23725000
20. Merchant H, Pérez O, Zarco W, Gámez J. Interval tuning in the primate medial premotor cortex as a general timing mechanism. J Neurosci. 2013; 33(21): 9082–9096. https://doi.org/10.1523/JNEUROSCI.5513-12.2013 PMID: 23699519
21. Crowe DA, Zarco W, Bartolo R, Merchant H. Dynamic Representation of the Temporal and Sequential Structure of Rhythmic Movements in the Primate Medial Premotor Cortex. J Neurosci. 2014; 34(36): 11972–11983. https://doi.org/10.1523/JNEUROSCI.2177-14.2014 PMID: 25186744
22. Bartolo R, Prado L, Merchant H. Information Processing in the Primate Basal Ganglia during Sensory-Guided and Internally Driven Rhythmic Tapping. J Neurosci. 2014; 34(11): 3910–3923. https://doi.org/10.1523/JNEUROSCI.2679-13.2014 PMID: 24623769
23. Mello GBM, Soares S, Paton JJ. A Scalable Population Code for Time in the Striatum. Curr Biol. 2015; 25(9): 1113–1122. https://doi.org/10.1016/j.cub.2015.02.036 PMID: 25913405
24. Wang J, Narain D, Hosseini EA, Jazayeri M. Flexible timing by temporal scaling of cortical responses. Nat Neurosci. 2018; 21(1): 102–110. https://doi.org/10.1038/s41593-017-0028-6 PMID: 29203897
25. Merchant H, Zarco W, Pérez O, Prado L, Bartolo R. Measuring time with different neural chronometers during a synchronization-continuation task. Proc Natl Acad Sci U S A. 2011; 108(49): 19784–19789. https://doi.org/10.1073/pnas.1112933108 PMID: 22106292
26. Knudsen EB, Powers ME, Moxon KA. Dissociating Movement from Movement Timing in the Rat Primary Motor Cortex. J Neurosci. 2014; 34(47): 15576–15586. https://doi.org/10.1523/JNEUROSCI.1816-14.2014 PMID: 25411486
27. Jazayeri M, Shadlen MN. A Neural Mechanism for Sensing and Reproducing a Time Interval. Curr Biol. 2015; 25(20): 2599–2609. https://doi.org/10.1016/j.cub.2015.08.038 PMID: 26455307
28. Merchant H, Bartolo R. Primate beta oscillations and rhythmic behaviors. J Neural Transm. 2018; 125 (3): 461–470. https://doi.org/10.1007/s00702-017-1716-9 PMID: 28364174
29. Cunningham JP, Yu BM. Dimensionality reduction for large-scale neural recordings. Nat Neurosci. 2014; 17(11): 1500–1509. https://doi.org/10.1038/nn.3776 PMID: 25151264
30. Kobak D, Brendel W, Constantinidis C, Feierstein CE, Kepecs A, Mainen ZF, et al. Demixed principal component analysis of neural population data. Elife. 2016; 5: 1–36. https://doi.org/10.7554/eLife.10989 PMID: 27067378
31. Murray JM, Escola GS. Learning multiple variable-speed sequences in striatum via cortical tutoring. Elife. 2017; 6: 1–24. https://doi.org/10.7554/eLife.26084 PMID: 28481200
32. Rossi-Pool R, Zainos A, Alvarez M, Zizumbo J, Vergara J, Romo R. Decoding a Decision Process in the Neuronal Population of Dorsal Premotor Cortex. Neuron. 2017; 96(6): 1432—1446.e7. https://doi.org/10.1016/j.neuron.2017.11.023 PMID: 29224726

33. Shenoy K V, Sahani M, Churchland MM. Cortical control of arm movements: a dynamical systems perspective. Annu Rev Neurosci. 2013; 36: 337–359. https://doi.org/10.1146/annurev-neuro-062111-150509 PMID: 23725001

34. Remington ED, Narain D, Hosseini EA, Jazayeri M. Flexible Sensorimotor Computations through Rapid Reconfiguration of Cortical Dynamics. Neuron. 2018; 98(5): 1005–1019.e5. https://doi.org/10.1016/j.neuron.2018.05.020 PMID: 29879384

35. Mendoza G, Peyrache A, Gámez J, Prado L, Buzsáki G, Merchant H. Recording extracellular neural activity in the behaving monkey using a semichronic and high-density electrode system. J Neurophysiol. 2016; 116(2): 563–574. https://doi.org/10.1152/jn.00116.2016 PMID: 27169505

36. Hardy NF, Buonomano D V. Encoding Time in Feedforward Trajectories of a Recurrent Neural Network Model. Neural Comput. 2018; 30(2): 378–396. https://doi.org/10.1162/neco_a_01041 PMID: 29162002

37. Donnet S, Bartolo R, Fernandes JM, Cunha JPS, Prado L, Merchant H. Monkeys time their pauses of movement and not their movement-kinematics during a synchronization-continuation rhythmic task. J Neurophysiol. 2014; 111(10): 2138–2149. https://doi.org/10.1152/jn.00802.2013 PMID: 24572098

38. Goudar V, Buonomano D V. Encoding sensory and motor patterns as time-invariant trajectories in recurrent neural networks. Elife. 2018; 7: 1–28. https://doi.org/10.7554/eLife.31134 PMID: 29537963

39. Mendoza G, Merchant H. Motor system evolution and the emergence of high cognitive functions. Prog Neurobiol. 2014; 122: 73–93. https://doi.org/10.1016/j.pneurobio.2014.09.001 PMID: 25224031

40. Russo AA, Bittner SR, Perkins SM, Seely JS, London BM, Lara AH, et al. Motor Cortex Embeds Muscle-like Commands in an Untangled Population Response. Neuron. 2018; 97(4): 953—966.e8. https://doi.org/10.1016/j.neuron.2018.01.004 PMID: 29398358

41. Churchland MM, Cunningham JP, Kaufman MT, Foster JD, Nuyujukian P, Ryu SI, et al. Neural population dynamics during reaching. Nature. 2012; 487(7405): 51–56. https://doi.org/10.1038/nature11129 PMID: 22722855

42. Karmarkar UR, Buonomano D V. Timing in the absence of clocks: encoding time in neural network states. Neuron. 2007; 53(3): 427–438. https://doi.org/10.1016/j.neuron.2007.01.006 PMID: 17270738

43. Merchant H, Yarrow K. How the motor system both encodes and influences our sense of time. Curr Opin Behav Sci. 2016; 8: 22–27. https://doi.org/10.1016/j.cobeha.2016.01.006

44. Paton JJ, Buonomano D V. The Neural Basis of Timing: Distributed Mechanisms for Diverse Functions. Neuron. 2018; 98(4): 687–705. https://doi.org/10.1016/j.neuron.2018.03.045 PMID: 29772201

45. Merchant H, Bartolo R, Pérez O, Méndez JC, Mendoza G, Gámez J, et al. Neurophysiology of Timing in the Hundreds of Milliseconds: Multiple Layers of Neuronal Clocks in the Medial Premotor Areas. Adv Exp Med Biol. 2014; 829: 143–154. https://doi.org/10.1007/978-1-4939-1782-2_8 PMID: 25358709

46. Teki S, Grube M, Griffiths T. A Unified Model of Time Perception Accounts for Duration-Based and Beat-Based Timing Mechanisms. Front Integr Neurosci. 2012; 5: 90. https://doi.org/10.3389/fnint.2011.00090 PMID: 22319477

47. Schwartze M, Kotz SA. A dual-pathway neural architecture for specific temporal prediction. Neurosci Biobehav Rev. 2013; 37(10 Pt 2): 2587–2596. https://doi.org/10.1016/j.neubiorev.2013.08.005 PMID: 23994272

48. Allman MJ, Teki S, Griffiths TD, Meck WH. Properties of the Internal Clock: First- and Second-Order Principles of Subjective Time. Annu Rev Psychol. 2014; 65: 743–771. https://doi.org/10.1146/annurev-psych-010213-115117 PMID: 24050187

49. Bartolo R, Merchant H. β Oscillations Are Linked to the Initiation of Sensory-Cued Movement Sequences and the Internal Guidance of Regular Tapping in the Monkey. J Neurosci. 2015; 35(11): 4635–4640. https://doi.org/10.1523/JNEUROSCI.4570-14.2015 PMID: 25788680

50. Jones MR, Boltz M. Dynamic attending and responses to time. Psychol Rev. 1989; 96(3): 459–491. PMID: 2756068

51. Large EW, Jones MR. The dynamics of attending: How people track time-varying events. Psychol Rev. 1999; 106(1): 119–159. https://doi.org/10.1037/0033-295X.106.1.119

52. Fujioka T, Trainor LJ, Large EW, Ross B. Internalized Timing of Isochronous Sounds Is Represented in Neuromagnetic Beta Oscillations. J Neurosci. 2012; 32(5): 1791–1802. https://doi.org/10.1523/JNEUROSCI.4107-11.2012 PMID: 22302818

53. Iversen JR, Repp BH, Patel AD. Top-down control of rhythm perception modulates early auditory responses. Ann N Y Acad Sci. 2009; 1169: 58–73. https://doi.org/10.1111/j.1749-6632.2009.04579.x PMID: 19673755

54. Nozaradan S, Peretz I, Missal M, Mouraux A. Tagging the Neuronal Entrainment to Beat and Meter. J Neurosci. 2011; 31(28): 10234–10240. https://doi.org/10.1523/JNEUROSCI.0411-11.2011 PMID: 21753000

55. Chen JL, Penhune VB, Zatorre RJ. Moving on Time: Brain Network for Auditory-Motor Synchronization is Modulated by Rhythm Complexity and Musical Training. J Cogn Neurosci. 2008; 20(2): 226–239. https://doi.org/10.1162/jocn.2008.20018 PMID: 18275331

56. Grahn JA, Rowe JB. Feeling the Beat: Premotor and Striatal Interactions in Musicians and Nonmusicians during Beat Perception. J Neurosci. 2009; 29(23): 7540–7548. https://doi.org/10.1523/JNEUROSCI.2018-08.2009 PMID: 19515922

57. Patel AD, Iversen JR. The evolutionary neuroscience of musical beat perception: the Action Simulation for Auditory Prediction (ASAP) hypothesis. Front Syst Neurosci. 2014; 8: 57. https://doi.org/10.3389/fnsys.2014.00057 PMID: 24860439

58. Honing H, Merchant H. Differences in auditory timing between human and nonhuman primates. Behav Brain Sci. 2014; 37(6): 557–558. https://doi.org/10.1017/S0140525X13004056 PMID: 25514947

59. Cadena-Valencia J, García-Garibay O, Merchant H, Jazayeri M, De Lafuente V. Entrainment and maintenance of an internal metronome in supplementary motor area. Elife. 2018; 7. https://doi.org/10.7554/eLife.38983 PMID: 30346275

60. Gibbon J, Malapani C, Dale CL, Gallistel CR. Toward a neurobiology of temporal cognition: Advances and challenges. Curr Opin Neurobiol. 1997; 7(2): 170–184. https://doi.org/10.1016/S0959-4388(97)80005-0 PMID: 9142762

61. Merchant H, Zarco W, Prado L. Do we have a common mechanism for measuring time in the hundreds of millisecond range? Evidence from multiple-interval timing tasks. J Neurophysiol. 2008; 99(2): 939–949. https://doi.org/10.1152/jn.01225.2007 PMID: 18094101

62. García-Garibay O, Cadena-Valencia J, Merchant H, de Lafuente V. Monkeys Share the Human Ability to Internally Maintain a Temporal Rhythm. Front Psychol. 2016; 7: 1–12. https://doi.org/10.3389/fpsyg.2016.01971 PMID: 28066294

63. Mendez JC, Prado L, Mendoza G, Merchant H. Temporal and Spatial Categorization in Human and Non-Human Primates. Front Integr Neurosci. 2011; 5: 1–10. https://doi.org/10.3389/fnint.2011.00050 PMID: 21927599

64. Simen P, Balci F, DeSouza L, Cohen JD, Holmes P. A Model of Interval Timing by Neural Integration. J Neurosci. 2011; 31(25): 9238–9253. https://doi.org/10.1523/JNEUROSCI.3121-10.2011 PMID: 21697374

65. Merchant H, Averbeck BB. The Computational and Neural Basis of Rhythmic Timing in Medial Premotor Cortex. J Neurosci. 2017; 37(17): 4552–4564. https://doi.org/10.1523/JNEUROSCI.0367-17.2017 PMID: 28336572

66. Pérez O, Merchant H. The synaptic properties of cells define the hallmarks of interval timing in a recurrent neural network. J Neurosci. 2018; 38(17): 4186–4199. https://doi.org/10.1523/JNEUROSCI.2651-17.2018 PMID: 29615484

67. Kaufman MT, Churchland MM, Ryu SI, Shenoy K V. Cortical activity in the null space: permitting preparation without movement. Nat Neurosci. 2014; 17(3): 440–448. https://doi.org/10.1038/nn.3643 PMID: 24487233

68. Crowe DA, Averbeck BB, Chafee M V. Rapid Sequences of Population Activity Patterns Dynamically Encode Task-Critical Spatial Information in Parietal Cortex. J Neurosci. 2010; 30(35): 11640–11653. https://doi.org/10.1523/JNEUROSCI.0954-10.2010 PMID: 20810885

69. Jin DZ, Fujii N, Graybiel AM. Neural representation of time in cortico-basal ganglia circuits. Proc Natl Acad Sci. 2009; 106(45): 19156–19161. https://doi.org/10.1073/pnas.0909881106 PMID: 19850874

70. Gouvêa TS, Monteiro T, Motiwala A, Soares S, Machens C, Paton JJ. Striatal dynamics explain duration judgments. Elife. 2015; 4: 1–14. https://doi.org/10.7554/eLife.11386 PMID: 26641377

71. Pastalkova E, Itskov V, Amarasingham A, Buzsaki G. Internally Generated Cell Assembly Sequences in the Rat Hippocampus. Science. 2008; 321(5894): 1322–1327. https://doi.org/10.1126/science.1159775 PMID: 18772431

72. MacDonald CJ, Lepage KQ, Eden UT, Eichenbaum H. Hippocampal "time cells" bridge the gap in memory for discontiguous events. Neuron. 2011; 71(4): 737–749. https://doi.org/10.1016/j.neuron.2011.07.012 PMID: 21867888

73. Perez O, Kass RE, Merchant H. Trial time warping to discriminate stimulus-related from movement-related neural activity. J Neurosci Methods. 2013; 212(2): 203–210. https://doi.org/10.1016/j.jneumeth.2012.10.019 PMID: 23147009

74. Merchant H, Battaglia-mayer A, Georgopoulos AP. Effects of optic flow in motor cortex and area 7a. J Neurophysiol. 2001; 86(4): 1937–54. https://doi.org/10.1152/jn.2001.86.4.1937 PMID: 11600652

75. Waibel A, Hanazawa T, Hinton G, Shikano K, Lang KJ. Phoneme recognition using time-delay neural networks. IEEE Trans Acoust. 1989; 37(3): 328–339. https://doi.org/10.1109/29.21701

76. Cortes C, Vapnik V. Support-vector networks. Mach Learn. 1995; 20(3): 273–297. https://doi.org/10.1007/BF00994018

ANNALS OF THE NEW YORK ACADEMY OF SCIENCES
Special Issue: *The Neurosciences and Music VI*
ORIGINAL ARTICLE

Predictive rhythmic tapping to isochronous and tempo changing metronomes in the nonhuman primate

Jorge Gámez, Karyna Yc, Yaneri A. Ayala, Dobromir Dotov, Luis Prado, and Hugo Merchant

Instituto de Neurobiología, UNAM, Campus Juriquilla, Querétaro, Mexico

Address for correspondence: Dr. Hugo Merchant, Instituto de Neurobiología, UNAM, Campus Juriquilla, Boulevard Juriquilla No. 3001, 76230 QRO, México. hugomerchant@unam.mx

Beat entrainment is the ability to entrain one's movements to a perceived periodic stimulus, such as a metronome or a pulse in music. Humans have a capacity to predictively respond to a periodic pulse and to dynamically adjust their movement timing to match the varying music tempos. Previous studies have shown that monkeys share some of the human capabilities for rhythmic entrainment, such as tapping regularly at the period of isochronous stimuli. However, it is still unknown whether monkeys can predictively entrain to dynamic tempo changes like humans. To address this question, we trained monkeys in three tapping tasks and compared their rhythmic entrainment abilities with those of humans. We found that, when immediate feedback about the timing of each movement is provided, monkeys can predictively entrain to an isochronous beat, generating tapping movements in anticipation of the metronome pulse. This ability also generalized to a novel untrained tempo. Notably, macaques can modify their tapping tempo by predicting the beat changes of accelerating and decelerating visual metronomes in a manner similar to humans. Our findings support the notion that nonhuman primates share with humans the ability of temporal anticipation during tapping to isochronous and smoothly changing sequences of stimuli.

Keywords: beat entrainment; predictive timing; rhythm perception and production; synchronization task; monkey

Introduction

Rhythmic entrainment is the ability to synchronize movements of different body parts to the regular pulse or beat of music and permits synchronous responding to this pulse during dancing and musical ensemble playing.[1–4] This ability is foundational to music cognition where individuals are required to coordinate their movements with extreme temporal precision and yet remain flexible to the changes in the beat of music.[5]

Humans are extremely sensitive to auditory regularities and are able to entrain to auditory beats across a 250–2000 ms range.[1] Furthermore, sensorimotor synchronization performance to an auditory metronome is more precise than synchronization to a visual metronome with the same timing characteristics.[6,7] Two major mechanisms determine sensorimotor synchronization: temporal anticipation and adaptation.[5,8–10] Temporal anticipation is a predictive process where neuronal mechanisms extract prospective information from the regularity of rhythmic patterns of an incoming stimulus in order to plan and coordinate movements.[8,10] In contrast, adaptive timing is a reactive process where retrospective information[5] is used to generate error corrections, allowing performers to respond to stimulus timing variations by adjusting their movement timing. Therefore, beat entrainment is a dynamic process where predicting the temporal structure of the stimulus and maintaining an online evaluation of sensorimotor asynchronies to update motor plans provide a robust response to ongoing changes in the pulse of music.

The spread of capacities for beat perception and entrainment among different animal species is still largely unknown. The "vocal learning and rhythmic synchronization" (VLRS) hypothesis proposes that predictive and tempo-flexible entrainment to an auditory beat is restricted to vocal-learning species[11–15] and resulted from the specialization of

doi: 10.1111/nyas.13671

auditory and motor neural circuitry for vocal learning or vocal motor control.[12,16] The stronger coupling between audiomotor areas would also explain the auditory superiority in beat entrainment in humans.[16–19] However, a recent study showed that a California sea lion, a poor vocal learner, can entrain its head bobbing to complex musical stimuli and generalize this skill to a range of novel tempos, challenging the VLRS hypothesis.[20,21]

Across nonhuman primates, the nonvocal learner animals closest to humans, rhesus monkeys are able to detect the regularity of an isochronous visual or auditory metronome on the range of hundreds of milliseconds and reproduce its periodicity by tapping regularly.[4,22] Regular tapping intervals were produced by monkeys both during metronome-guided and internally driven phases of the classic synchronization–continuation task (SCT).[23] These monkeys produce isochronous rhythmic movements by varying the dwell time between movements and not the movement duration,[24] as also observed in humans.[25] Nevertheless, the taps of macaques typically occur about 300 ms after stimulus onset, whereas humans show negative asynchronies (NAs), moving slightly ahead of the beat.[1,22] Even though positive, the asynchronies in monkeys are shorter than reaction times in a control task with random interstimulus intervals, suggesting that these monkeys have temporal prediction capabilities.[26] It is important to consider that, in the study by Zarco and colleagues,[22] the reward contingencies were focused on the produced interval durations and not on the asynchronies. Indeed, a recent study demonstrated that macaques are capable of predictively synchronizing their eye movements with an isochronous visual beat when the rewards arrived on every predictive synchronized saccade.[27] Nevertheless, macaques are less sensitive than humans in detecting hierarchical metric structures with complex patterns of auditory beats.[28,29] Accordingly, the gradual audio-motor evolution (GAE) hypothesis[29] suggests that beat perception and entrainment have emerged gradually in the primate order. It also suggests that humans fully share single-interval timing with other primates,[22,30,31] while only partially sharing the ability for rhythmic entrainment with an isochronous metronome.[30,32] Crucially, it is still unknown whether monkeys can predictively entrain to dynamic tempo changes.

In the present study, we designed three tapping experiments to test the flexibility and predictive nature of rhythmic entrainment in monkeys and compared their performance to humans' performance (see Figs. 1–5). We found that monkeys can achieve human-level NA if two conditions are satisfied: asynchronies are part of the reward contingencies, and tap-by-tap feedback about entrainment performance is provided. This ability generalized to a novel untrained tempo. However, in contrast to humans' auditory bias, monkeys show a preference for and are more precise with visual metronomes. Notably, rhesus monkeys can adjust on-line their tapping tempo by predicting the speeding up or slowing down of dynamic visual metronomes, as observed in humans.

Materials and methods

Human participants

Twenty human participants (9 females and 11 males), mean (SD) age of 28.5 (3.2) years, (range: 24–34 years) were tested in this study. They were right-handed,[33] had normal or corrected to normal vision, and were naive about the task and purpose of the experiment. Each subject volunteered and gave informed consent, which complied with the Declaration of Helsinki and was approved by the National University of Mexico Institutional Review Board.

Monkeys

Three monkeys (*Macaca mulatta* 4.5–7 kg, referred to as M01, M02, and M03) were used. M01 was male, and M02 and M03 were females. The age of the monkeys was 9, 7, and 6 years, respectively. M01 and M03 were left-handed, and M02 was right-handed based on a conventional dexterity monkey test.[34] All animal experimental procedures were approved by the National University of Mexico Institutional Animal Care and Use Committee and conformed to the principles outlined in the Guide for Care and Use of Laboratory Animals (NIH, publication number 85-23, revised 1985).

Apparatus

Synchronization task and tempo-changing synchronization task. Human participants were seated comfortably in a chair facing a computer screen (refresh rate 60 Hz, Dell Optiplex 19") in a quiet experimental room and tapped a push button (4 cm diameter, #7717, Dassel MN, sampled at 1000 Hz). Responses were recorded on a

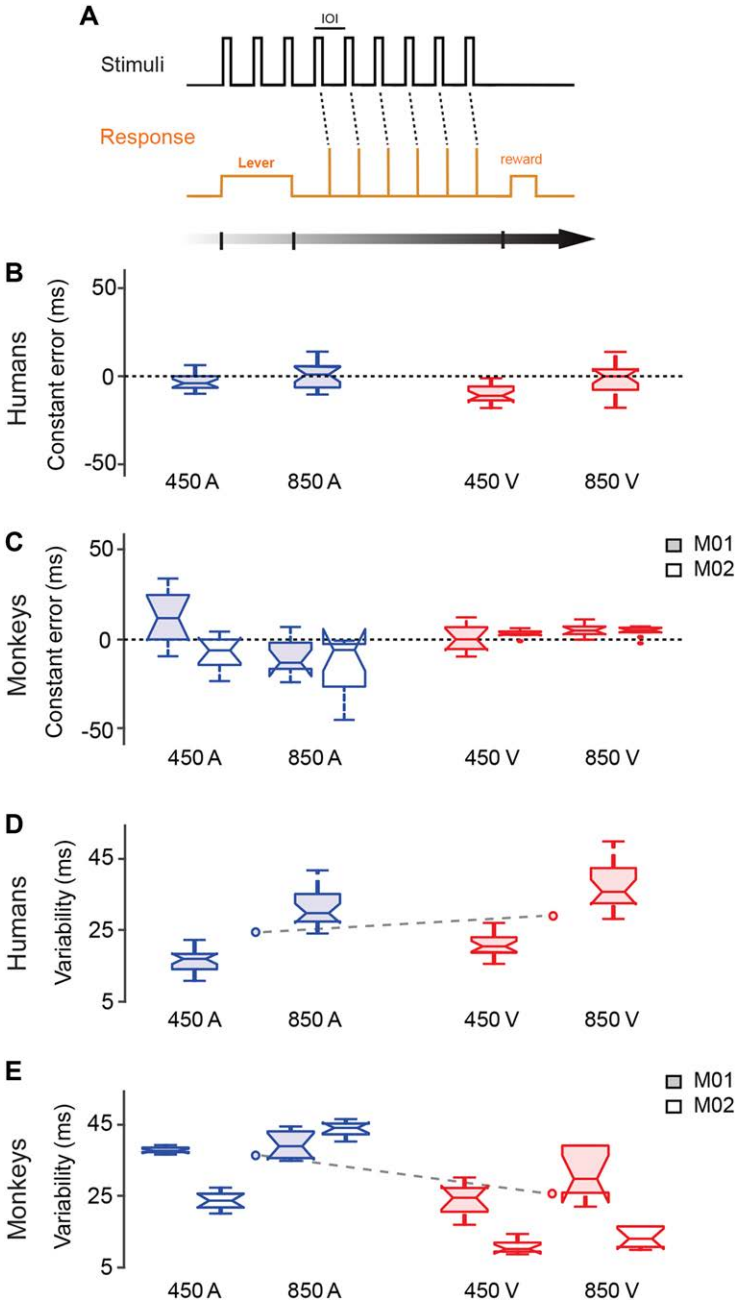

Figure 1. Human and monkey performance in the synchronization task (ST). (A) Schematic representation of the ST. Subjects held a lever while a visual or auditory isochronous metronome was presented. After the third stimulus, subjects started to tap on a button to produce five intervals following the metronome. The stimulus inter-onset interval (IOI) of the metronome corresponded to the instructed interval, 450 or 850 milliseconds. (B) and (C) Constant error of human participants and monkeys for each instructed interval and metronome modality (A: auditory, blue, V: visual, red), respectively. Each box plot shows the median (central line) and the 25th (bottom edge) and 75th percentiles (top edge). Values within ± 2.7 standard deviations are indicated by the dashed lines and outlier values are showed by asterisks. The notch extremes correspond to $q2 - 1.57(q3 - q1)/sqrt(n)$ and $q2 + 1.57(q3 - q1)/sqrt(n)$, where $q2$ is the median (50th percentile), $q1$ and $q3$ are the 25th and 75th percentiles, respectively, and n is the number of observations. (D) and (E) Variability of the produced intervals by human participants and monkeys, respectively. Mean temporal variability for each modality is indicated by dots joined by a dashed line. Same color code as (B) and (C).

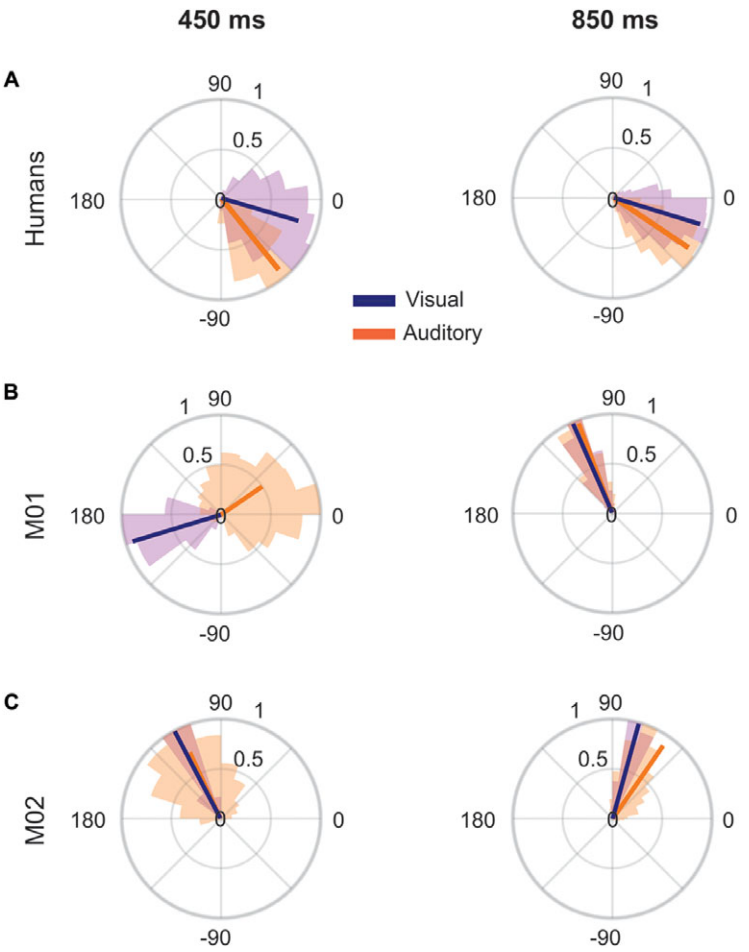

Figure 2. Human and monkey asynchronies in the ST. (A) Circular histograms of the asynchronies of human participants for each interval (right: 450 ms, left: 850 ms) and metronome modality (auditory, visual). Asynchronies expressed as relative phase values, where 0° indicates taps occurring at the same time than stimuli and 180° indicates taps occurring in the middle of the instructed interval. Negative values indicate taps occurring before stimuli, while positive values are taps occurring after stimuli. (B) and (C) Circular histograms of the asynchronies of monkeys M01 and M02, respectively. Same format as (A).

custom-made button box with millisecond accuracy. Pushing the button produced an approximately 50 dB SPL sound. Monkeys M01 and M02 were seated in a primate chair in a sound-attenuated room facing a computer screen during the synchronization task (ST). Monkey M02 performed the additional tempo-changing synchronization task (TCST). The animals tapped on the same type of push button with one hand, whereas their opposite arms were comfortably restrained during the task. The monkeys started each trial by placing their hands on a horizontal infrared key placed next to the push-button (see Supplementary Video S1, online only). Behavioral responses were acquired using a real-time processor (Tucker-Davis Technologies RZ2). The stimulus presentation was computer controlled by a custom-made Psychtoolbox program (MathWorks, Natick, MA, Version 7.3.0.267). Auditory stimuli arrived through noise-canceling headphones (Sony, MDR-NC50) for humans and two equidistant front speakers for monkeys. The monitor was 57 cm from the eyes in both species.

Synchronization task with feedback. Monkey M03 performed the task seated in a primate chair in a sound-attenuated room facing a computer screen (HP 7540, 17", refresh rate of 60 Hz) at a distance of 60 cm with two equidistant front speakers at

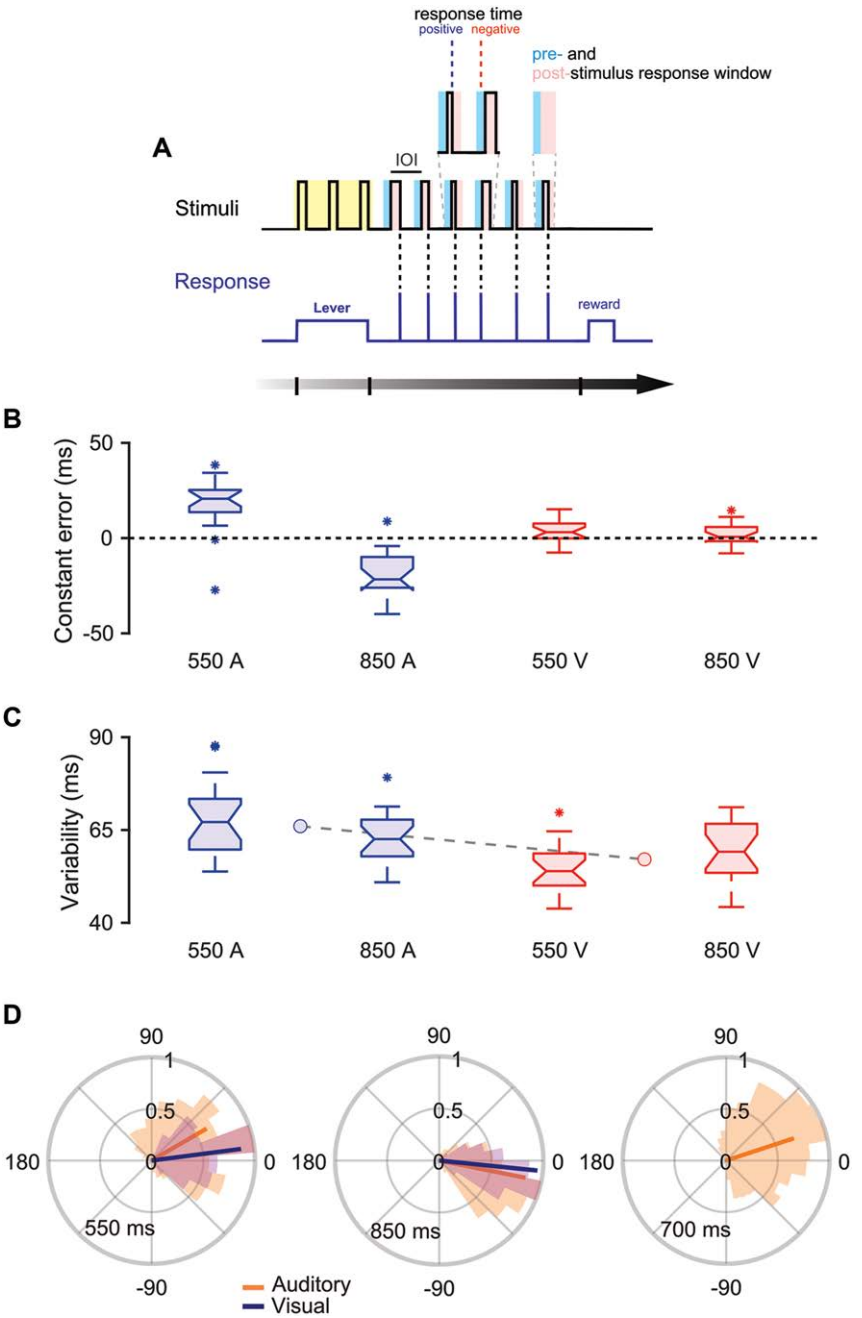

Figure 3. Monkey performance in the synchronization task with feedback (STF). (A) Monkey held a lever for 1.9 s while a yellow box was displayed and three visual or auditory stimuli were presented. Afterward, the monkey produced five intervals following the metronome by crossing an optical sensor with its hand. The stimulus inter-onset interval (IOI) corresponded to the instructed interval, 550 or 850 ms. The monkey could respond before (prestimulus) or after stimulus onset (poststimulus window, inset). When the response arrived after the stimulus onset (positive response time, inset), the stimulus lasted until the movement occurred. When the response arrived before the stimulus onset (negative-response time), then the stimulus lasted 50 ms. (B) and (C) Constant error and temporal variability for each instructed interval and metronome modality, respectively. Same format as Figure 1B and D. (D) Circular histograms of asynchronies. Same format as Figure 2A.

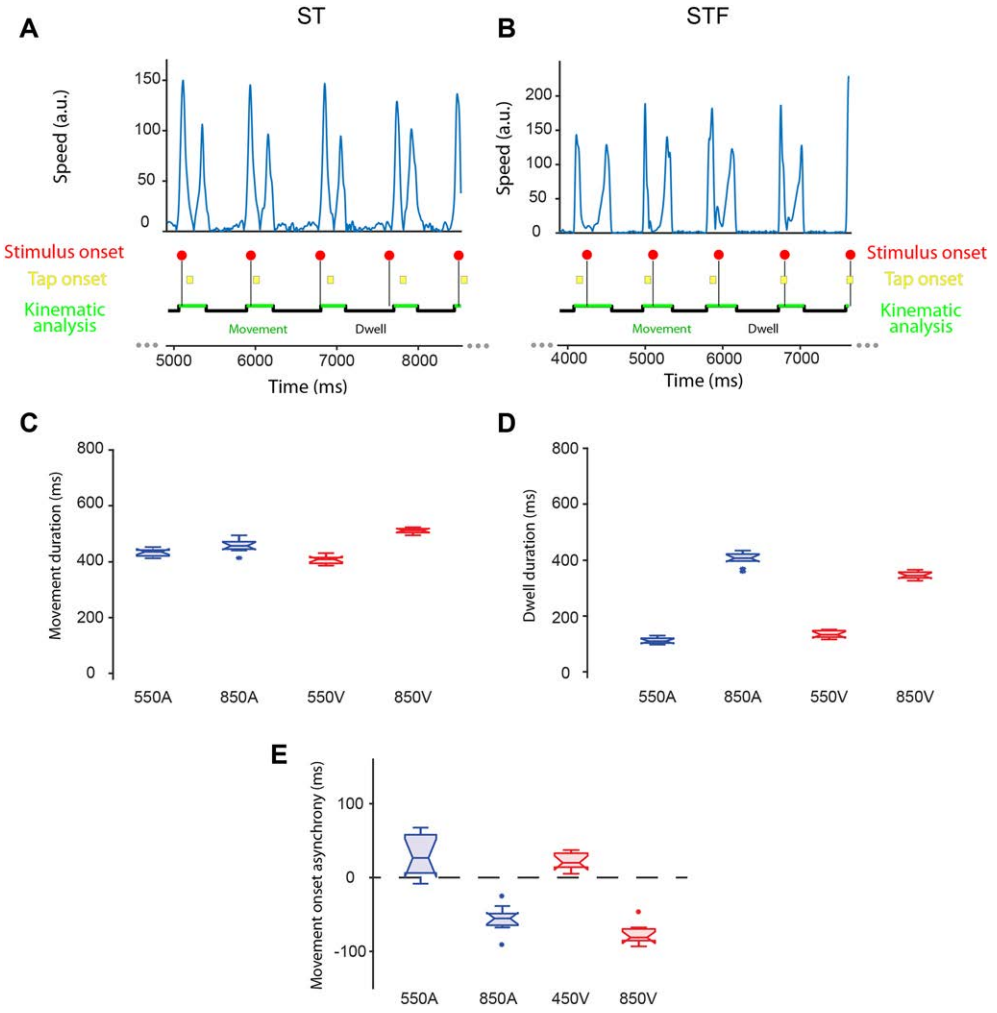

Figure 4. Movement kinematics during ST and STF. (A) and (B) Speed profile of the hand movement (blue trace) during the tapping stage of an 850-ms auditory representative trial during ST (M02) and STF (M03). The kinematic analysis comprehends the lapse time from the second to the sixth tap. The stimuli occurrence is represented as red dots, and the taps are represented as yellow squares. Both monkeys produced highly stereotypical tapping movements, alternating between movement (green trace) and dwell states (black trace). (C and D) Box plots for the movement (C) and dwell (D) times during STF across each interval and modality (A: auditory, blue, V: visual, red). (E) Movement onset asynchrony, defined as the time between a stimulus and the movement onset determined from the hand kinematics, for different tempos and modalities during STF. Same color code as (C) and (D).

50 cm. Behavioral responses were acquired using a Blackrock-Microsystem signal processor, and stimulus presentation was computer controlled by a custom made Psychotoolbox program (MathWorks, Version 9.1.0.441655). Instead of tapping a button, this monkey performed a phasic forward–backward movement over a noise-free acrylic platform. The main purpose of this setup was to record phasic movements without a sound-generating push button. Movement triggered an infrared optical sensor (Balluf BOS 11K, response time $\leq$1 ms) located at the front-right side of the platform. A groove over the platform surface indicated the position of the sensor in the anterior–posterior axis (see Supplementary Video S2, online only).

Task 1: synchronization task: human participants and monkeys

Subjects were trained to attend to a sequence of brief stimuli with a constant interstimulus interval

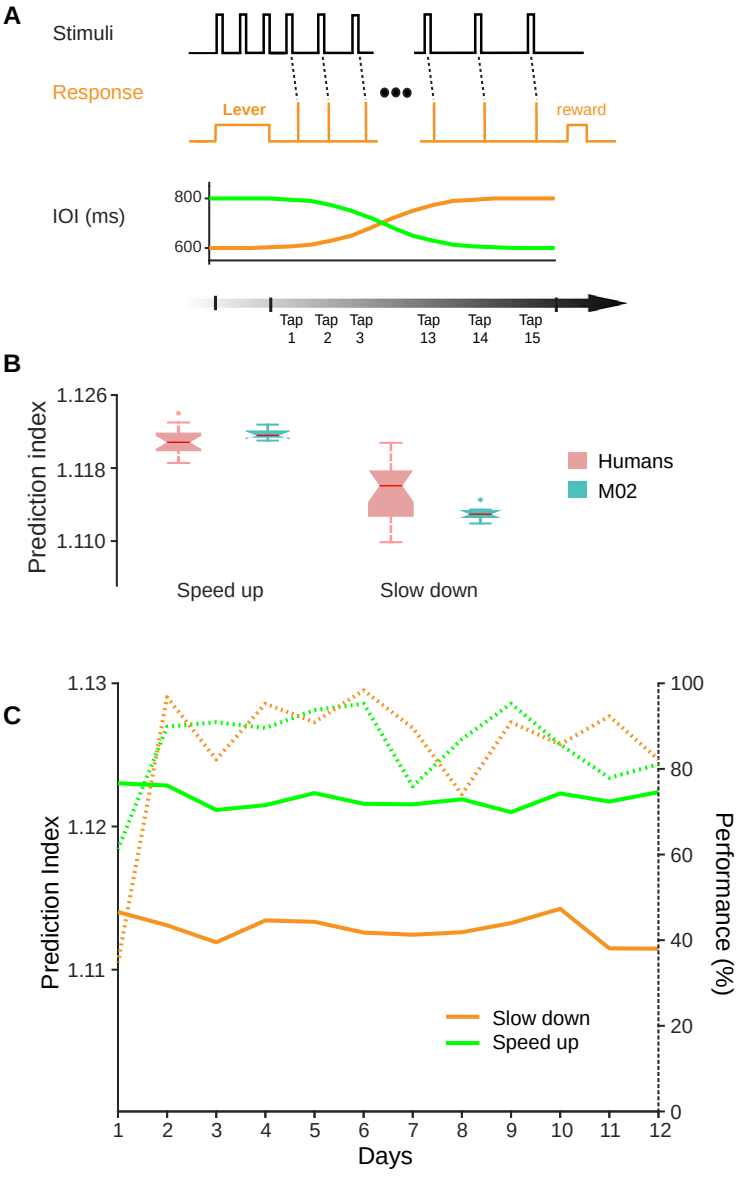

Figure 5. Tapping performance of human participants and monkey M02 during the tempo-changing synchronization task (TCST). (A) During the TCST, subjects were required to produce 15 taps in time with a sequence of visual stimuli that contained tempo changes. The stimulus inter-onset interval (IOI) followed a decreasing (speed up, 800–600 ms IOIs, green line) or increasing (slow down, 600–800 ms IOIs, magenta line) sigmoid function. (B) Prediction index for human participants and monkey M02 in slow down and speed up conditions. Each box plot shows the median (red central line) and 25th (bottom edge) and 75th interquartiles (top edge). Note that indices for both species are predictive.

and push a button in synchrony with the latter six of them (Fig. 1A). At the beginning of a trial, participants held a lever and attended to two or three stimuli, after which they started to move, the goal being to produce six taps in synchrony with the six remaining metronome pulses. Monkeys received a reward (fruit juice) if two conditions were satisfied: the produced intervals were not different by more than 18% of the instructed interval, and all asynchronies between stimuli and taps were less than a given threshold (250 ms in monkey 1 and 200 ms in monkey 2) (see Supplementary Video S1, online

only). A message stating whether the trial was correct or incorrect was displayed on the screen as feedback for humans. Trials were separated by a variable intertrial interval (1.2–4 seconds). The interonset intervals (IOIs, 450 or 850 ms) for the visual (red square with a side length of 5 cm, presented for 33 ms) or auditory (white noise with a 33 ms duration) metronomes were presented in blocks of 20 trials. The order of the four interval/modality combinations was random across days. In contrast with the SCT used previously,[22,35] the ST did not include a continuation phase and instead contained a perceptual entrainment phase comprising three pulses with no tapping at the beginning of each trial. In addition, the reward contingencies in the ST included an error threshold for both interval duration and stimulus–tap asynchrony, while the SCT only contained a threshold for interval duration.

Task 2: synchronization task with feedback: monkey

This task was designed to provide performance feedback to the monkeys (Fig. 3A). As in the ST, the trial began with perceptual entrainment for three stimuli (50 ms each) while the animal (monkey M03) held a lever. The three stimuli were presented at the center of a yellow box (10.5 × 10.5 cm) that indicated the time to hold the lever. Next, M03 triggered an infrared optical switch by performing fast forward–backward movements in response to the six stimuli of the metronome. The forward–backward movement was spontaneously exhibited by the monkey, and no noise was produced from the hand displacement. The IOI was constant, but the duration of the pulse varied according to the current stimulus–movement asynchrony of the monkey (see Supplementary Video S2, online only). In particular, the stimulus lasted 50 ms for NA (i.e., hand movement occurred before the stimulus onset). Otherwise, the stimulus was present until the movement occurred within a window of 50 ms after onset of the stimuli. The rationale for this was to provide tap-by-tap feedback within ongoing performance where longer stimulus duration corresponded to longer asynchronies. The monkey received a reward when the stimulus–movement asynchronies were between –100 and 200 ms for the visual metronome and –150 and 280 ms for the auditory metronome. If the monkey did not catch a given stimulus within the specified response window, the trial was aborted. The instructed intervals were 550 and 850 ms, presented pseudorandomly within a block of auditory (550 Hz, 80–85 dB SPL) or visual metronomes (red square with a 4.5 cm side).

Task 3: tempo-changing synchronization task: human participants and monkey

This task required the subjects to tap in time with a sequence of visual stimuli that contained tempo changes. A trial consisted of a 15-tap sequence where the IOIs of the visual metronome (green square with a side length of 5 cm, presented for 33 ms) followed a sigmoidal function in a decreasing (tempo speeding up, 800–600 ms IOIs) or increasing (tempo slowing down, 600–800 ms IOIs) direction. The function is:

$$y = 0.200\left(\frac{1}{1+e^{1.5(t-4)}}\right)d + I$$

where y is the instructed interval, t is the overall elapsed trial time, d is 1 for slowing down and –1 for speeding up, and I is the initial interval (800 ms for speeding up and 600 ms for slowing down). Trials were blocked per accelerating or decelerating condition, each block consisting of 60 trials, and block order was random across days. Trials were separated by a variable intertrial interval (1.2–4 seconds). The trial started with a perceptual entrainment phase where the participant needed to hold a lever for three stimuli before starting to tap. The requirements for correct trial were to produce intervals within an error of 35% of the instructed interval and with asynchronies below 250 milliseconds.

Procedure

Human participants performed the three tasks (ST visual, ST auditory, and TCST) in random order in three sessions. Twenty trials per session were collected during the ST for each marker modality, while 60 trails for each condition were collected for the TCST for each participant. Before data collection in each task, practice trials were given until the participants acknowledged that they understood the tasks and were comfortable with their performance.

Monkeys were trained following operant conditioning techniques. They received normal food rations but were water-deprived except for the juice drops obtained during the training and testing sessions. The animals worked 6 days/week, 3 h/day on average and performed around 300 correct trials per day, with a total liquid intake of 120–220 mL. Weight was strictly controlled by giving

supplementary fluids to the monkeys when they lost more than 20% of their initial weight. Twenty blocks, of 10 trials per block, were collected for each instructed interval and modality during the ST and synchronization task with feedback (STF). Eight blocks of 60 trials were collected on M02 during the TCST on the speeding up and slowing down conditions.

Table S1 (online only) indicates the tasks performed by each monkey and human participants, as well as the tasks using auditory and visual or purely visual metronomes.

ST monkey training

Monkeys M01 and M02 were initially trained with a visual metronome for 5 months. First, the monkeys received a reward whenever they held their hand on the lever for a few seconds. Afterward, they learned to push a button after holding the lever. Finally, they learned to hold the lever and push the button once a visual stimulus was presented. This first phase lasted 2 weeks for M01 and 3 weeks for M02. Throughout the following 3 weeks, the monkeys were presented only with isochronous stimuli with an instructed interval of 850 ms, while the number of stimuli was increased gradually until the monkeys could complete six taps without error. After the monkeys reached 60% performance per session, a new instructed interval was presented until they had learned six instructed intervals: 450, 550, 650, 750, 850, and 950 milliseconds. Initially, an asynchrony window of –100 to 350 ms was used, but it was adjusted individually for each monkey during training to keep a 60% performance. After the behavior of the monkeys was stable for all intervals, they were trained to wait with their hand on the lever for three stimuli at the beginning of the trial. Afterward, the monkeys were trained using an auditory metronome. M01 achieved stable performance in the auditory condition after 21 weeks and M02 after 35 weeks. It is important to point out that both monkeys initially paid no attention to the auditory metronome, and it took several weeks for them to start exhibiting isochronous tapping driven by auditory stimuli.

STF monkey training

Monkey M03 was initially trained with a visual metronome for 8 months. During the initial 3 weeks, the animal learned to hold the lever for increasing periods of time while the three stimuli for perceptual entrainment were presented. Then, the animal learned to respond to the fourth stimulus of the metronome by crossing the sensor with her hand. Subsequently, during the following 6 weeks, the number of stimuli displayed was increased up to six, and the allowed asynchronies were progressively reduced. Importantly, since the beginning of training, the duration of the visual stimulus was contingent on the monkey's asynchrony. This meant that the animal learned to "catch" the stimuli before they disappeared. The catching time window was equal to the positive asynchrony duration (e.g., 200 ms). The initial instructed interval was 450 ms, since the monkey comfortably produced intervals with this duration. In the next 10 weeks, a long interval of 850 ms and intermediate interval of 650 ms were randomly mixed with the 450 ms interval within a block of 20 trials. Finally, in the last 14 weeks, the remaining intervals of 550 and 750 were introduced, and trials from all duration conditions were presented in random order. At this point, the allowed asynchrony window was set to –100 to 200 ms. Once the monkey achieved stable performance of 60% correct trials over 200–300 total trials in a training day, we introduced the auditory metronome condition using a larger response window of –150 to 280 ms (the animal found it more difficult to synchronize to the auditory metronome). Thus, M03 first learned to perform the auditory STF with 550-ms interval (initial 12 weeks), then 850-ms interval, followed by 650- and 750-ms intervals (last 8 weeks). It took 8 months total for M03 to learn all the aspects of the task with a visual metronome and 5 months to perform the STF with an auditory metronome. As in the previous task, monkey M03 had a great difficulty using auditory stimuli to drive its temporal behavior.

No need of training in TCST

Once monkey M02 reached stable performance in ST, we tested her in TCST. Interestingly, she was able to perform the new task without further training, even if the trials lasted 15 taps before reward, twice more than in ST trials.

Analysis

ST and STF. Performance measures during the ST and STF tasks included constant error, temporal variability, and asynchronies. Constant error was the difference between produced and instructed intervals. The temporal variability per individual,

interval duration, and modality was defined as the standard deviation of the five produced intervals within a trial for all trials in a block. Asynchronies were the time difference between tap onset and stimulus onset. The first tap was removed from the analysis for the estimation of all three synchronization measures.

Standard statistical techniques (repeated-measures analysis of variance (ANOVA)) were used for data analysis of constant error, temporal variability, and asynchronies. In most cases, the between-subjects factor was species and the within-subjects factors included stimulus modality and interval duration. The Greenhouse–Geisser test in the repeated-measures ANOVAs was used to correct probability levels from deviations in sphericity (Mauchly test).

Asynchronies were expressed as phases relative to the beat onset times over the instructed interval. In particular, the asynchronies (a_i) in milliseconds were converted from milliseconds to angular units (θ_i) in radians with the equation $\theta_i = (2\pi \times a_i)/T_i$, where T_i was the target interval. We used circular statistics[69] to summarize the distribution of relative phases on the unit circle by means of the mean resultant vector. The mean resultant vector is defined by two parameters: length R (dimensionless from 0 to 1) and angle (radians from 0 to 2π). Length of 1 in the mean resultant indicates identical phases (perfect overlap on the unit circle), whereas a length of 0 indicates phases (and therefore asynchronies) distributed uniformly along the whole stimulus IOI. Vector angle of 0 indicates zero mean relative phase, and therefore perfect temporal alignment between tap and stimulus, while positive and negative angles indicate that the tap followed (positive asynchronies) or preceded (NAs) the stimulus, respectively. The Rayleigh test is a statistical test for unimodality of the phases, with a null hypothesis of a uniform distribution, and thus evaluates whether phases tended to be consistent, that is, whether each tap arrived at the same asynchrony before or after the stimuli.

Routines for MATLAB (MathWorks, Version 9.1.0.441655) and the SPSS (version 19, SPSS Inc., Chicago, IL, 2003) were used for all statistical analyses. The level of statistical significance to reject the null hypothesis was $\alpha = 0.05$.

TCST. Human participants and monkey M02 were tested in TCST where the stimulus tempo increased or decreased in blocks of trials (Fig. 5A). We calculated the prediction index (PI)[36] per subject and condition to measure individual anticipatory ability—whether subjects anticipated the sequence of gradual tempo changes or tracked tempo changes reactively. To this end, the cross-correlations between inter-tap intervals (ITIs) and the stimulus IOIs were calculated (the first and last two taps from the sequence of stimuli–taps were eliminated because there were no changes in tempo in these elements of the metronome). The lag-0 cross-correlation between ITIs and the IOIs is high when an individual anticipates the tempo changes, while the lag-1 cross-correlation is high when changes in ITIs arrive one step later as a reaction to tempo changes. The PI is the ratio of lag-0 cross-correlation over lag-1 cross-correlation and reflects whether an individual is mainly predicting (ratio >1) or tracking (ratio <1) ongoing tempo changes.[36]

Movement kinematics. We determined the onset and duration of hand movements with respect to the onset of the stimuli in M02 during the ST and in M03 during STF. Hand motion was segmented into dwell and moving parts using an optic flow method to extract hand velocity from a video recording. Each monkey's tapping was highly stereotypical, passing through fixed resting and target positions and following a near-linear path.[37,38] A high-speed camera (Basler acA750, Basler AG) positioned orthogonally to the hand's plane of motion recorded video frames (640×480 pixels) at 250 frames per second. We tracked the movement of the objects in an area of 320×240 pixels of the original frame (see Supplementary Videos S1 and S2, online only). No other moving objects entered the view, because the lens had a narrow field and close focus capturing only the working surface. The velocity field between successive video frames was estimated with the Lucas–Kanade method for optic flow between two brightness arrays, a standard algorithm in computational vision for tracking moving objects and estimating heading direction.[39] To get an approximation of hand velocity in the camera's frame of reference, we averaged each velocity field to a single 2D vector per time point and smoothed the resulting time series (10-point moving average window). A speed profile through time was generated from the velocity field, and the recording of button presses

was synchronized with the video to identify tapping. Then, we identified the periods in which the speed exceeded a pre-established threshold. These peaks were assigned to the nearest tap. The resulting motion onset and offset time points were used to calculate the movement and dwell durations within each ITI. There was no hand motion during the dwell intervals and, as Figure 4A shows, speed profiles had the double-bell–shaped profiles expected from reaching to tap a button in ST, as described previously in the SCT. The speed profiles during STF presented a similar double-bell shape, but with a less phasic change between the forward and backward motion alternation. It should be noted that the stimulus tended to occur earlier during the STF than the ST.

Results

Rhythmic performance in ST (Figs. 1 and 2) and STF (Fig. 3) across durations and modalities in both primate species was characterized using constant error (the difference between produced and instructed intervals), temporal variability (SD of produced intervals), and mean asynchronies (the time difference between stimulus onset and tap onset) (see Methods).

Human and monkey ST performance

Supplementary Video S1 (online only) shows the performance of M02 in a prototypic ST trial. The monkey started by placing her free hand on the key, kept it there for two stimuli (beat perception phase), and then tapped a push button in response to the isochronous stimuli (synchronization phase, five produced intervals). We compared the performance of human participants and two monkeys in this task, using the same hardware and software across species and task conditions.

A repeated-measures ANOVA on constant error, with metronome modality (auditory and visual) and instructed interval duration (450 or 850 ms) as within-subject factors and species as between-subject factor, revealed no significant main effects for instructed interval and modality and a significant species-modality interaction ($F(1,20) = 10.097$, $P = 0.0047$) (Fig. 1B and C). This indicates that, even when both species accurately produced intervals with errors close to zero, there were differences in constant error between species and modality.

The same repeated-measures ANOVA on temporal variability showed significant main effects of interval ($F(1,20) = 24.581$, $P < 0.0001$) and modality ($F(1,20) = 12.877$, $P < 0.0018$). The species–modality interaction ($F(1,20) = 44.592$, $P < 0.0001$) was also statistically significant (Fig. 1D and E). A Tukey honest significant difference (HSD) *post hoc* test showed a significantly larger temporal variability in the auditory modality in monkeys than humans. These results indicate that timing precision showed a bias toward visual metronomes in monkeys and a bias toward auditory metronomes in human participants, while in both primate species there was an increase in temporal variability for longer intervals. It is worth mentioning that the level of tapping precision in monkeys, especially M02, was quite high (Figs. 1E, 2B, and C), probably due to the high training level of the monkeys in the task.

Figure 2 shows the distributions (and mean resultant R) of asynchronies expressed as relative phases on the unit circle in humans (Fig. 2A), monkey M01 (Fig. 2B), and monkey M02 (Fig. 2C) across instructed durations and sensory modalities. We found that R, the measure of synchronization consistency, was close to one across species, modalities, and instructed intervals with a significant unimodal distribution across all conditions (Rayleigh's test, $P < 0.0001$). The mean circular asynchronies of human participants were statistically negative (statistically smaller than 0, for both modalities and intervals, one-sample circular t-tests, $P < 0.05$), particularly in the auditory modality (Table S2, online only), consistent with the literature.[6,7] In contrast, asynchronies in monkeys were statistically positive (statistically larger than 0, both modalities and intervals, one-sample circular t-test, $P < 0.05$) (Table S2, online only), and, for the 450 ms interval of the visual condition, M01 responded in antiphase with the stimuli. These findings suggest that monkeys need additional feedback about asynchrony to produce NAs in ST. This idea was tested in task STF.

Figure 2 reveals a large performance difference between monkeys M01 and M02 in the 450 ms interval of the auditory condition. M01's asynchronies were close to 0, whereas M02's were close to 90°. We do not have an explanation for these individual differences. Speculatively, the discrepancy could be the result of idiosyncratic individual strategies due to the challenging nature of task ST in the short-interval auditory condition.

Table 1 shows the mean asynchronies in milliseconds for human participants and monkeys across conditions of ST. Humans show NAs and a bias for the auditory condition, whereas monkeys show positive asynchronies and a bias for visual metronomes. The corresponding repeated-measures ANOVA revealed main effects for modality ($F(1,38) = 75.332$, $P < 0.001$) and species ($F(1,38) = 457.251$, $P < 0.001$), as well as significant species–interval ($F(1,38) = 16.446$, $P < 0.001$) and species–modality interactions ($F(1,38) = 4.482$, $P = 0.041$). The Tukey HSD *post hoc* analysis confirmed that asynchronies in humans were statistically smaller than in monkeys, with larger NAs for the auditory condition in humans ($P < 0.0001$).

Compared with the asynchronies of about 300 ms found in task SCT of our previous study (See Fig. 2 in Ref. 22), asynchronies in the current ST task were about 50 ms less in M01 and 150 ms less in M02. This qualitative observation suggests that the additional beat perception period and inclusion of asynchronies in the reward contingencies resulted in superior performance in the form of reduced asynchronies.

Further evidence for an enhanced ST performance was obtained from the reaction times recorded in a serial reaction-time task (SRTT), where animals pressed the push button in response to five brief visual stimuli presented in a sequence, but separated by a random IOI (i.e., 450, 550, 650, 750, 850 or 950 ms, picked randomly), precluding the possibility for predicting stimulus times. The reaction time (mean ± SEM) of M01 was 441 ± 2.6 ms and 385 ± 2 ms for intervals 450 and 850 ms, respectively. M02's reaction time was 262 ± 3 ms and 238 ± 1.6 ms for intervals 450 and 850 ms, respectively. An ANOVA on stimulus–tap intervals (called asynchronies in task ST and reaction times in task SRTT) revealed significant main effects of task ($F(1,2396) = 1633.45$, $P < 0.0001$), target interval ($F(1,2396) = 11.21$, $P < 0.001$), and task–target interval interaction ($F(1,2396) = 99.32$, $P < 0.01$). A Tukey HSD *post hoc* test showed significant differences between all combinations of tasks and target intervals. In consequence, although monkeys did not exhibit NAs, their tapping responses in ST were shorter than reaction times in SRTT, supporting the hypothesis that monkeys took advantage of a time prediction mechanism in ST.

Monkey STF performance

Constant error (Fig. 3B) showed no significant main effects of instructed interval and modality, but there was a significant modality–interval interaction ($F(1,19) = 67.907$, $P < 0.0001$). A Tukey HSD p*ost hoc* test showed no difference between 550 and 850 ms intervals in the visual modality ($P = 0.293$). On the contrary, constant error in the auditory modality was larger in the 550 than the 50 ms interval ($P < 0.0001$). Similarly, there were no significant main effects of modality and instructed interval for temporal variability (Fig. 3C), but there was a significant modality–interval interaction ($F(1,19) = 9.026$, $P = 0.007$). Temporal variability in the auditory was larger than in visual modality for the 550-ms interval ($P = 0.0001$), and the same but marginal trend ($P = 0.075$) was found for the 850-ms interval. In general, monkey M03 was quite accurate, producing intervals close to the instructed interval, especially with visual metronomes, while its timing precision was greater during the visual than during the auditory metronome condition (Supplementary Video S2, online only).

Synchronization consistency R was close to 1 for both modalities and instructed intervals, with a significant unimodal distribution across all conditions (Rayleigh's test, $P < 0.0001$, Fig. 3D). Importantly, the mean circular asynchronies were statistically lower than 0 (negative) for the 850-ms interval of both modalities and statistically larger

Table 1. Mean and standard deviation of asynchronies in the ST

	Auditory				Visual			
	450		850		450		850	
Species	Mean (ms)	SD (ms)	Mean (ms)	SD (ms)	Mean (ms)	SD (ms)	Mean (ms)	SD (ms)
Human	−46.61	72.98	−75.92	53.49	−10.32	43.75	−38.96	43.30
M01	66.38	87.74	262.98	39.32	249.04	27.82	265.05	25.55
M02	139.52	57.28	125.27	64.92	147.42	12.02	176.94	20.56

than 0 (positive) for the 550-ms interval of both modalities (one-sample circular *t*-tests, $P < 0.05$, Table S2, online only, Fig. 3D).

M03's asynchronies (mean ± SD) in the visual condition were 11.33 ± 22.92 and –13.42 ± 18.23 ms for the 550- and 850-ms intervals, respectively. In the auditory condition, the asynchronies were 50.36 ± 22.92 ms and –22.27 ± 11.11 ms for the 550- and 850-ms intervals, respectively. The repeated-measures ANOVA showed a significant main effect of interval ($F(1,19) = 174.01$, $P < 0.0001$), modality ($F(1,19) = 18.63$, $P = 0.0004$), and interval–modality interaction ($F(1,19) = 32.50$, $P < 0.0001$). The Tukey HSD *post hoc* analysis revealed that M03 performed smaller asynchronies in the visual than auditory modality for the 550-ms interval ($P < 0.001$), while the asynchronies in the auditory modality were similar for the 850-ms interval ($P = 0.0504$).

Monkey M03 showed NAs during the STF performance; however, a key question was whether her asynchronies were similar to those measured in humans. For this purpose, we compared the asynchronies in milliseconds between human participants and M03 (humans in ST and M03 in STF) in the 850-ms interval across modalities. The repeated-measure ANOVA revealed significant main effects of modality ($F(1,38) = 20.54$, $P < 0.001$) and species ($F(1,38) = 15.038$, $P < 0.001$) and a significant modality–species interaction ($F(1,38) = 7.73$, $P = 0.008$). *Post hoc* Tukey HSD showed that the NAs of human participants were more negative than in the monkey, with a bias toward auditory metronomes ($P < 0.05$).

Critically, we also tested whether the predictive tapping of M03 could generalize to a novel IOI of 700 ms with an auditory metronome during three test sessions. The monkey was never exposed to a metronome with a tempo of 700 ms. Her performance was comparable to trained tempos (Fig. 3D), with a consistency metric R of 0.69 and a significant synchronization test (Rayleigh's test, $P < 0.0001$). A repeated-measure ANOVA revealed that the asynchronies were different across the three intervals ($F(1,28) = 86.94$, $P < 0.001$). The *post hoc* Tukey HSD showed that the mean asynchrony of 33.43 ± 16.50 ms for the 700 ms was significantly higher than in trained intervals of 550 ($P = 0.026$) and statistically lower than in 850 ms ($P < 0.001$) (Fig. 3D).

Finally, to measure error correction in beat entrainment, we took the autocorrelation of the series of four successive intervals in STF. Mean autocorrelation across trials was negative in both the 550- and 850-ms instructed intervals and both metronome modalities (Table S3, online only). The autocorrelation was more negative in visual than auditory. These results support the notion that the monkey entrained to the isochronous beat during the STF using an error-correction mechanism.

Taken together, these findings indicate that monkey M03 was able to entrain to the beat and to perform predictive movements with NAs and an error-correction mechanism when tap-by-tap feedback was provided. This predictive behavior generalized to a novel tempo in the auditory metronome condition. In addition, results are consistent with ST in that sensorimotor synchronization was more precise with a visual than an auditory metronome.

Kinematics of monkey movements during ST and STF

We used a high-speed camera to determine the movement onset, as well as the duration of both the movements and the dwell time between movements, in monkeys M02 during ST and M03 during STF (see Methods; Fig. 4). The movement speed profile was computed from the changes in hand position overtime using an optic-flow algorithm (see Supplementary Videos S1 and S2, online only). We set a speed threshold to identify: (1) the movement onset, corresponding to the time at which the speed profile crossed the threshold upward; (2) the movement offset that was equal to the time where the speed profile crossed the threshold downward; and (3) the dwell time as the interval between the offset and onset of consecutive movements (Fig. 4A and B). Monkeys showed a phasic stereotypic movement to push the button during ST (Fig. 4A) or to perform the forward–backward movement over the platform during STF (Fig. 4B). In both tasks, the speed profile increased abruptly at the beginning of the movement, showed two bell-shaped speed kinematics divided by a low-speed point associated with the button press (Fig. 4A) or the change in movement direction over the platform (from forward to backward; Fig. 4B), and showed a sharp decrease close to zero at the end of the movement. The

movement offset was followed by a dwell time with low speed, where the animals waited to produce the next stereotypic movement in the isochronous sequence. Thus, for each trial, we identified four movement and four dwell times.

We focused our analysis on STF, since the kinematics was similar during ST. A repeated-measures ANOVA on movement time of M03 during STF showed a significant main effect of interval ($F(1,9) = 526.867$, $P < 0.0001$) and modality ($F(1,9) = 10.959$, $P = 0.0091$), as well as a significant interval–modality interaction ($F(1,9) = 150.628$, $P < 0.0001$). Although the changes in movement time were below 50 ms across conditions, the *post hoc* Tukey HSD showed significant differences between intervals and modalities. These results suggest a small modulation on the stereotypy of movements across tempos and modalities during the STF (Fig. 4C).

The dwell time repeated-measures ANOVA showed a significant main effect of interval ($F(1,9) = 4199.319$, $P < 0.0001$) and modality ($F(1,9) = 19.112$, $P = 0.0018$), and a significant interval–modality interaction ($F(1,9) = 63.082$, $P < 0.0001$). The *post hoc* Tukey HSD showed a large increase in dwell time between the intervals of 550 and 850 ms for both modalities ($P < 0.0001$). These findings support the notion that monkey M03 used an explicit timing mechanism to control the dwell between movements during the STF (Fig. 4D).

Importantly, the movement onset asynchrony (MOA), which is the time between the stimulus and the movement onset, showed negative values, especially in the 850-ms interval, for both modalities (Fig. 4E). Table S4 (online only) shows that MOAs were slightly more negative than the asynchronies associated with the activation of the infrared optical sensor. The repeated-measures ANOVA using MOA showed a significant main effect of interval ($F(1,9) = 233.961$, $P < 0.0001$) and modality ($F(1,9) = 11.383$, $P = 0.0082$), with no significant interval–modality interaction ($F(1,9) = 1.274$, $P = 0.2882$).

Human and monkey predictive behavior in TCST

We recorded the tapping performance of human participants and monkey M02 during the TCST. This paradigm required participants to synchronize their tapping with a sequence of 15 stimuli that contained tempo changes in the form of stimulus-onset asynchronies (IOIs) that were speeding up or slowing down (Fig. 5A). The mean (mean ± SD) asynchronies for human participants were –37 ± 8 ms (speed up) and –21 ± 8 ms (speed down), whereas for the monkey they were 171 ± 2 ms (speed up) and 172 ± 2 ms (speed down). We computed the PI, which reflects the degree to which participants produced ITIs that led or lagged behind the IOIs in tempo-changing sequences.[40] Values less than 1 reflect a tendency to track the pacing signal, while values greater than 1 suggest a tendency to predict the temporal changes in the stimuli sequence. Figure 5B shows that, in both species and both conditions, PI was above 1, indicative of a shared skill for predictive behavior. A one-sample *t*-test confirmed that PI was significantly greater than 1 in speed up ($t(19) = 392.66$, $P < 0.0001$) and slow down ($t(19) = 159.48$, $P < 0.0001$) in human participants, and also in speed up ($t(7) = 585.89$, $P < 0.0001$) and slow down ($t(7) = 400.55$, $P < 0.0001$) in M02. Additionally, a two-way ANOVA revealed significant main effects of modality ($F(1,52) = 117.41$, $P < 0.0001$) and species–modality interaction ($F(1,52) = 7.75$, $P < 0.01$). Tukey HSD *post hoc* tests showed significant differences between species for the decelerating condition and that both species were better at predicting accelerating than decelerating changes in tempo.

It is worth mentioning that monkey M02 was able to perform TCST from the first days of testing. Figure 5C shows that, in the first day, the performance was below 60%, since the monkey was adjusting to the new length of 15 taps instead of six taps. However, from days 2 to 12, the animal performed the TCST with a percent of correct above 75% and a PI above 1.

Discussion

The present study supports four conclusions. First, monkeys can predictively entrain to an isochronous beat, generating tapping movements before a metronome when two conditions are met: the asynchronies are part of the reward contingencies, and a tap-by-tap performance feedback is provided (Fig. 3). Second, that predictive tapping to an auditory metronome can generalize to a novel untrained tempo. Third, as expected, monkeys exhibit a preference for visual metronomes and humans for auditory ones (Figs. 1–3). Finally, macaques can

dynamically and predictively adjust their tapping tempo to match tempo changes in visual metronomes, with parameters comparable to those observed in humans (Fig. 5).

Previously, we found that, in SCT, monkeys produced intervals with a period similar to the IOI of the metronome and then maintained the tapping tempo without the entraining sensory signal.[22] We also showed that, in SCT, the monkeys used an explicit timing mechanism, controlling their ITI dwell time and producing stereotypic tapping movements,[24] as observed in the present kinematic results. In fact, the SCT dwell variability increased as a function of the interval following the scalar property of explicit timing observed in many tasks.[41,42] However, the fact that the macaques' asynchronies were lagging by 300 ms was interpreted as a sign that monkeys could not predict and instead were reacting to the metronome.[12,27] The present STF results suggest that monkeys possess strong tapping predictive abilities and can produce NAs when the proper training and task conditions are provided. Incorporating a perceptual entrainment phase before tapping and a reward contingency for the magnitude of the asynchronies reduced asynchronies by about 50 ms in M01 and 150 ms in M02, compared with asynchronies of about 300 ms observed previously in SCT (fig. 2 in Ref. 22). In addition, the present ST asynchronies were shorter than pure reaction times, suggesting some level of timing prediction. However, what switched asynchronies from positive to negative values was the fact that, in the STF, the stimulus IOI was constant, but the duration of the metronome's stimuli was not fixed and varied according to the stimulus–movement asynchronies of the monkey. In this context, the stimulus offset gave the monkey immediate feedback about its performance within the metronome sequence. A similar approach was followed in the study by Takeya and colleagues,[27] where monkeys synchronized their saccadic movements to an isochronous visual metronome when an immediate reward was given within each step of the sequence, providing feedback to the monkeys about their performance within a trial. Furthermore, the negative lag-1 autocorrelation of the ITI time series supports the notion that the monkey also used an online error correction mechanism in STF, where timing of a tap depended inversely on the duration of the preceding produced interval. Negative lag-1 autocorrelations are typical in tapping sensorimotor STs in humans.[1,23] Another study showed that macaques can internally follow a visual isochronous beat for a range from three to six intervals as accurately as human participants when a two-choice response is presented to them.[43] Therefore, monkeys are capable of isochronous beat entrainment when the proper training and feedback is given to them, highlighting the importance of the training strategy, the reward contingencies, and the performance feedback given to the animals, as discussed by Wilson and Cook.[20,21] An important conclusion, therefore, is that these constraints need to be taken into consideration when designing experimental paradigms with the aim to reveal deeper capacities of nonhuman primates and the evolutionary origins of beat perception and entrainment.[44]

The GAE hypothesis suggests that beat-based timing is gradually developed in primates, peaking in humans but present with limited properties in other nonhuman primates, while humans share single-interval timing with all nonhuman primates and related species.[26,29] The present findings suggest that monkeys can predictively entrain to an isochronous metronome (Fig. 3) and, more importantly, can dynamically adapt their tapping tempo to a rhythmic but accelerating or decelerating metronome (Fig. 5). These findings set the limits in the beat-entrainment abilities of monkeys quite above the reactive hypothesis previously suggested[12] and emphasize that the beat-based mechanisms of macaques are not as restricted, as previously thought. Thus, it is crucial that future experiments focus on finding the limits in entrainment capabilities of monkeys, using gradually more complex levels of metrical periodicity in their stimuli, such as rhythms based on nonisochronous temporal patterns or based on grouping of events at slower temporal scales.[45,46] In addition, the comparison of beat-entrainment abilities between human and nonhuman primates can be complemented with noninvasive electrophysiological experiments that allow the investigation of the neural correlates of beat perception, a precondition for rhythmic entrainment.[47–50] Indeed, we have studied the encoding of auditory periodicity through scalp-recorded evoked potentials while awake monkeys passively listened to periodic auditory stimuli with different levels of metrical hierarchy.[28,51] We demonstrated that macaques share with humans

the neurophysiological mechanisms to represent fast acoustic periodicities[51] by exhibiting a human-homologous frequency-following response (FFR).[49] Important for the present discussion is the fact that human participants that can entrain with high precision to an external beat also show larger intertrial consistency of the FFR potential,[52–54] suggesting a partial overlap between auditory circuits underlying the FFR and neural circuits involved in beat entrainment. In addition, monkeys can also detect stimulus omissions occurring in an isochronous auditory pattern exhibiting a mismatch negativity (MMN) potential[28] (i.e., a differential cortical brain signal to a deviant event, embedded in a stream of repeated standard events).[50] On the contrary, this MMN potential is not observed when an omission occurred in complex accented beat locations.[28] Taken together, the behavioral and electrophysiological results collected support the GAE hypothesis by showing that monkeys possess the neural machinery to perceive acoustic regularities and furthermore to entrain to isochronous beats.

We found that a rhesus monkey can transfer entrainment in the STF to a novel tempo (in this case 700 ms) without additional training. This is similar to the findings of Takeya *et al.*,[27] who found that monkeys could generalize the predictive synchronization of eye movements with metronomic visual stimuli to untrained tempi. However, they tested three untrained IOIs, whereas we used only one. Additionally, we observed that another monkey was able to generalize its tapping behavior from isochronous entrainment (ST) to a situation that demanded the dynamic adjustment of the tapping tempo according to an accelerating or decelerating sequence of stimuli (TCST). This is a remarkable finding because the monkey not only was required to make nine more taps than her standard ST but also showed the capability to adjust her tapping tempo to accelerating and decelerating metronomes. Therefore, the monkey showed a hallmark of human beat entrainment: a form of temporal anticipation that allows entraining not only to regular pulses but also to changes of this regularity.

After months of training, it was evident that the precision of monkeys in the ST and the STF was biased toward visual metronomes (Figs. 1–3). In contrast, adult humans do not need special training to perceive and entrain to the pulse of musical rhythms; the latter appears to be a robust, ubiquitous, and intuitive behavior. Furthermore, beat entrainment in humans is more accurate and precise with auditory than visual metronomes.[6,7] In this respect, the GAE also suggests that beat-based timing in humans is a neurocognitive phenomenon that depends on a dynamic interaction between auditory and motor systems in the brain.[19,29,55] The idea is that the bidirectional bottom-up and top-down interactions between the auditory and motor areas in the brain, including the motor cortico–basal ganglia–thalamo-cortical circuit, is quite developed and efficient in humans.[16,19,29,55,56] The present results suggest that the audiomotor system in monkeys is not as developed as in humans, confirming the previously reported structural differences between primate species.[18,57] Parts of the audiomotor circuit, including areas such as the putamen in the basal ganglia or the parietal cortex, also process information from the dorsal stream of visual processing.[58–60] Therefore, we suggest an additional notion of the GAE: the areas involved in the strong visuomotor coupling of monkeys partially overlap with the beat-entrainment audiomotor system, conferring the predictive and flexible entrainment abilities of monkeys, especially with visual stimuli.

Neurophysiological studies in monkeys performing an SCT support the notion that monkeys can perceive and respond predictively to isochronous auditory and visual metronomes. Cells with ramping activity in the MPC showed a cyclic interaction across the task sequence between cells that represented the elapsed time from the last movement and cells encoding the time remaining for an action.[61,62] In addition, cells in the MPC and the putamen are tuned to the interval and/or the serial-order structure of the SCT.[63,64] This neural signal is dynamic—the tuned cells showed a consecutive onset/offset of activity across discrete neural ensembles, generating a rapid succession of activation patterns between the two taps defining a produced interval.[65,66] This chain of activation profiles occurred cyclically across the sequential structure of the SCT,[65] but not during a serial reaction control task where the random IOIs did not afford synchronization behavior and required the animals to respond reactively instead of predictively to each stimulus.[63,65]

A warping analysis determined whether medial premotor cortex (MPC) cell activity is

statistically aligned to sensory or motor events in the synchronization phase of SCT.[67] A large proportion of cells were classified as sensory or motor according to this analysis.[68] Furthermore, two types of sensory cells were identified: one cell population with short response-onset latencies to the previous stimulus and another that was probably predicting the occurrence of the next stimuli. These cells were called sensory-driven and stimulus-predicting neurons, respectively.[68] Notably, sensory-driven neurons were more abundant for visual than auditory metronomes, giving a neurophysiological foundation to the observed visual bias of the present study. In contrast, stimulus-predicting neurons were bimodal and showed similar response profiles across serial-order elements.[68] A population of simultaneously recorded MPC cells contains information about the duration of produced intervals about 300 ms before the tap, on a trial-by-trial basis.[69,70] Hence, the primate supplementary/pre-supplementary motor areas and putamen possess a complex neurophysiological machinery to represent different sensorimotor aspects of time prediction in SCT and control rhythmic tapping behavior.[66]

In summary, the findings of the present study show for the first time that monkeys possess an anticipatory mechanism to predictively entrain to an isochronous beat and change their tapping tempo during accelerating and decelerating sequences of visual stimuli. These abilities, extensively documented in humans,[1,5,66] allow for a high degree of accuracy and precision during rhythmic entrainment in both primate species. Indeed, predictive and tempo-changing aspects of beat entrainment constitute high-level cognitive computations that transform rhythm perception into action. Therefore, our results establish that the limits of sensorimotor synchronization in nonhuman primates are not only beyond the level of mere reaction, but also that they have complex anticipatory mechanisms that confers on them the ability to dynamically change the timing of their rhythmic entrainment. Furthermore, our study opens new venues to understand the neurophysiological mechanisms underlying tempo changing during rhythm perception and production in behaving monkeys.

Acknowledgments

We thank Pavel Rueda for his advice on the high-speed camera. We also thank Raúl Paulín for his technical assistance and the graduate program in biomedical sciences of the Universidad Nacional Autónoma de México. Supported by CONACYT: 236836, CONACYT: 196, and PAPIIT: IN202317 grants to H.M., and DGAPA-UNAM postdoctoral fellowships to Y.A.A. and D.D. J.G. is a doctoral student from Programa de Doctorado en Ciencias Biomédicas, Universidad Nacional Autónoma de México (UNAM) and received Fellowship 339118 from CONACYT. J.G. and K.Y. performed the ST and TCST experiments. Y.A.A. and L.P. performed the STF experiments. J.G., Y.A.A., D.D., and H.M. wrote the manuscript. J.G., D.D., and H.M. designed and implemented analytic tools. H.M. designed the study.

Supporting information

Additional supporting information may be found in the online version of this article.

Table S1. Tasks performed by each subject. The musical note and the square indicate auditory and visual metronomes, respectively.

Table S2. Angle of the asynchronies' mean resultant in degrees (radians in parenthesis) across species, modalities, and instructed durations.

Table S3. Autocorrelation of the series of produced intervals at lag 1 across trials in the STF task.

Table S4. Mean and standard deviation of the movement onset asynchrony (MOA) and stimulus-tap asynchronies of the monkey M03 in the STF task.

Supplementary Videos S1

Supplementary Videos S2

Competing interests

The authors declare no competing interests.

References

1. Repp, B.H. 2005. Sensorimotor synchronization: a review of the tapping literature. *Psychon. Bull. Rev.* **12:** 969–992.
2. Repp, B.H. & Y.H. Su. 2013. Sensorimotor synchronization: a review of recent research (2006–2012). *Psychon. Bull. Rev.* **20:** 403–452.
3. Phillips-Silver, J. & P.E. Keller. 2012. Searching for roots of entrainment and joint action in early musical interactions. *Front. Hum. Neurosci.* **6:** 26.
4. Merchant, H., J. Grahn & L. Trainor, *et al.* 2015. Finding the beat: a neural perspective across humans and nonhuman primates. *Philos. Trans. R. Soc. Lond. B Biol. Sci.* **370:** 20140093.

5. Mills, P.F., M.C. van der Steen, B.G. Schultz, *et al.* 2015. Individual differences in temporal anticipation and adaptation during sensorimotor synchronization. *Timing Time Percept.* **3:** 13–31.
6. Repp, B.H. & A. Penel. 2004. Rhythmic movement is attracted more strongly to auditory than to visual rhythms. *Psychol. Res.* **68:** 252–270.
7. Patel, A.D., J.R. Iversen, Y. Chen, *et al.* 2005. The influence of metricality and modality on synchronization with a beat. *Exp. Brain Res.* **163:** 226–238.
8. Keller, P.E. 2008. Joint action in music performance. In *Enacting Intersubjectivity: A Cognitive and Social Perspective on the Study of Interactions.* F. Morganti, F.A. Carassa & G. Riva, Eds.: 205–221. IOS Press.
9. Keller, P.E. 2014. Ensemble performance: interpersonal alignment of musical expression. In *Expressiveness in Music Performance: Empirical Approaches across Styles and Cultures.* D. Fabian, R. Timmers & E. Schubert, Eds.: 260–282. Oxford University Press.
10. van der Steen, M.C. & P.E. Keller. 2013. The ADaptation and Anticipation Model (ADAM) of sensorimotor synchronization. *Front. Hum. Neurosci.* **7:** 253.
11. Patel, A.D. 2006. Musical rhythm, linguistic rhythm, and human evolution. *Music Percept.* **24:** 99–104.
12. Patel, A.D. 2014. The evolutionary biology of musical rhythm: was Darwin wrong? *PLoS Biol.* **12:** e1001821.
13. Hasegawa, A., K. Okanoya, T. Hasegawa, *et al.* 2011. Rhythmic synchronization tapping to an audio-visual metronome in budgerigars. *Sci. Rep.* **1:** 120.
14. Schachner, A., T.F. Brady, I.M. Pepperberg, *et al.* 2009. Spontaneous motor entrainment to music in multiple vocal mimicking species. *Curr. Biol.* **19:** 831–836.
15. Schachner, A. 2010. Auditory-motor entrainment in vocal mimicking species: additional ontogenetic and phylogenetic factors. *Commun. Integr. Biol.* **3:** 290–293.
16. Patel, A.D. & J.R. Iversen. 2014. The evolutionary neuroscience of musical beat perception: the Action Simulation for Auditory Prediction (ASAP) hypothesis. *Front. Syst. Neurosci.* **8:** 57.
17. Grahn, J.A. & M. Brett. 2007. Rhythm and beat perception in motor areas of the brain. *J. Cogn. Neurosci.* **19:** 893–906.
18. Mendoza, G. & H. Merchant. 2014. Motor system evolution and the emergence of high cognitive functions. *Prog. Neurobiol.* **122:** 73–93.
19. Merchant, H. & K. Yarrow. 2016. How the motor system both encodes and influences our sense of time. *Curr. Opin. Behav. Sci.* **8:** 22–27.
20. Cook, P., A. Rouse, M. Wilson, *et al.* 2013. A California sea lion (*Zalophus californianus*) can keep the beat: motor entrainment to rhythmic auditory stimuli in a non vocal mimic. *J. Comp. Psychol.* **127:** 412–427
21. Wilson, M. & P.F. Cook. 2016. Rhythmic entrainment: why humans want to, fireflies can't help it, pet birds try, and sea lions have to be bribed. *Psychon. Bull. Rev.* **23:** 1647–1659.
22. Zarco, W., H. Merchant, L. Prado, *et al.* 2009. Subsecond timing in primates: comparison of interval production between human subjects and rhesus monkeys. *J. Neurophysiol.* **102:** 3191–3202.
23. Wing, A.M. 2002. Voluntary timing and brain function: an information processing approach. *Brain Cogn.* **48:** 7–30.
24. Donnet, S., R. Bartolo, J.M. Fernandes, *et al.* 2014. Monkeys time their pauses of movement and not their movement-kinematics during a synchronization-continuation rhythmic task. *J. Neurophysiol.* **111:** 2138–2149.
25. Doumas, M. & A.M. Wing. 2007. Timing and trajectory in rhythm production. *J. Exp. Psychol. Hum. Percept. Perform.* **33:** 442–455.
26. Honing, H. & H. Merchant. 2014. Differences in auditory timing between human and nonhuman primates. *Behav. Brain Sci.* **37:** 557–558; discussion 577–604.
27. Takeya, R., M. Kameda, A.D. Patel, *et al.* 2017. Predictive and tempo-flexible synchronization to a visual metronome in monkeys. *Sci. Rep.* **7:** 6127.
28. Honing, H., H. Merchant, G.P. Haden, *et al.* 2012. Rhesus monkeys (*Macaca mulatta*) detect rhythmic groups in music, but not the beat. *PLoS One* **7:** e51369.
29. Merchant, H. & H. Honing. 2014. Are non-human primates capable of rhythmic entrainment? Evidence for the gradual audiomotor evolution hypothesis. *Front. Neurosci.* **7:** 274.
30. Mendez, J.C., L. Prado, G. Mendoza, *et al.* 2011. Temporal and spatial categorization in human and non-human primates. *Front. Integr. Neurosci.* **5:** 50.
31. Merchant, H., A. Battaglia-Mayer & A.P. Georgopoulos. 2003. Interception of real and apparent motion targets: psychophysics in humans and monkeys. *Exp. Brain Res.* **152:** 106–112.
32. Fitch, W.T. 2013. Rhythmic cognition in humans and animals: distinguishing meter and pulse perception. *Front. Syst. Neurosci.* **7:** 68.
33. Oldfield, R.C. 1971. The assessment and analysis of handedness: the Edinburgh inventory. *Neuropsychologia* **9:** 97–113.
34. Cole, J. 1957. Laterality in the use of the hand, foot, and eye in monkeys. *J. Comp. Physiol. Psychol.* **50:** 296–299.
35. Merchant, H., R. Bartolo, O. Pérez, *et al.* 2014. Neurophysiology of timing in the hundreds of milliseconds: multiple layers of neuronal clocks in the medial premotor areas. *Adv. Exp. Med. Biol.* **829:** 143–154.
36. Nozaradan, S., I. Peretz & P.E. Keller. 2016. Individual differences in rhythmic cortical entrainment correlate with predictive behavior in sensorimotor synchronization. *Sci. Rep.* **6:** 20612.
37. Morasso, P. 1981. Spatial control of arm movements. *Exp. Brain Res.* **42:** 223–227.
38. Wolpert, D., K. Pearson & C. Ghez. 2013. The organization and planning of movement. In *Principles of Neural Science.* Z.R. Kandel, J.H. Schwartz, T.M. Jessell, *et al.*, Eds.: 743–767. McGraw-Hill.
39. Barron, J.L., D.J. Fleet & S.S. Beauchemin. 1994. Performance of optical flow techniques. *Int. J. Comput. Vis.* **12:** 43–77.
40. Pecenka, N. & P.E. Keller. 2011. The role of temporal prediction abilities in interpersonal sensorimotor synchronization. *Exp. Brain Res.* **211:** 505–515.
41. Merchant, H., W. Zarco & L. Prado. 2008. Do we have a common mechanism for measuring time in the hundreds of millisecond range? Evidence from multiple-interval timing tasks. *J. Neurophysiol.* **99:** 939–949.

42. Merchant, H., W. Zarco, R. Bartolo, *et al.* 2008. The context of temporal processing is represented in the multidimensional relationships between timing tasks. *PLoS One* **3:** e3169.
43. Garcia-Garibay, O., J. Cadena-Valencia, H. Merchant, *et al.* 2016. Monkeys share the human ability to internally maintain a temporal rhythm. *Front. Psychol.* **7:** 1971.
44. Hoeschele, M., H. Merchant, Y. Kikuchi, *et al.* 2015. Searching for the origins of musicality across species. *Philos. Trans. R. Soc. Lond. B Biol. Sci.* **370:** 20140094.
45. Schwartze, M. & S.A. Kotz. 2015. The timing of regular sequences: production, perception, and covariation. *J. Cogn. Neurosci.* **27:** 1697–1707.
46. Nozaradan, S., M. Schwartze, C. Obermeier, *et al.* 2017. Specific contributions of basal ganglia and cerebellum to the neural tracking of rhythm. *Cortex* **95:** 156–168.
47. Nozaradan, S. 2014. Exploring how musical rhythm entrains brain activity with electroencephalogram frequency-tagging. *Philos. Trans. R. Soc. Lond. B Biol. Sci.* **369:** 20130393.
48. Nozaradan, S., I. Peretz, M. Missal, *et al.* 2011. Tagging the neuronal entrainment to beat and meter. *J. Neurosci.* **31:** 10234–10240.
49. Kraus, N., S.S. Anderson & T. White-Schwoch. 2017. The frequency-following response: a window into human communication. In *The Frequency-Following Response*. N. Kraus, S. Anderson, T. White-Schwoch, *et al.*, Eds.: 1–15. Springer-Nature.
50. Naatanen, R., P. Paavilainen, T. Rinne, *et al.* 2007.The mismatch negativity (MMN) in basic research of central auditory processing: a review. *Clin. Neurophysiol.* **118:** 2544–2590.
51. Ayala, Y.A., A. Lehmann & H. Merchant. 2017. Monkeys share the neurophysiological basis for encoding sound periodicities captured by the frequency-following response with humans. *Sci. Rep.* **7:** 16687.
52. Tierney, A. & N. Kraus. 2013. The ability to move to a beat is linked to the consistency of neural responses to sound. *J. Neurosci.* **33:** 14981–14988.
53. Tierney, A. & N. Kraus. 2016. Getting back on the beat: links between auditory-motor integration and precise auditory processing at fast time scales. *Eur. J. Neurosci.* **43:** 782–791.
54. Tierney, A., T. White-Schwoch, J. MacLean & N. Kraus. 2017. Individual differences in rhythm skills: links with neural consistency and linguistic ability. *J. Cogn. Neurosci.* **29:** 855–868.
55. Morillon, B., C.E. Schroeder & V. Wyart. 2014. Motor contributions to the temporal precision of auditory attention. *Nat. Commun.* **5:** 5255.
56. Merchant, H. & V. de Lafuente. 2014. Introduction to the neurobiology of interval timing. *Adv. Exp. Med. Biol.* **829:** 1–13.
57. Rilling, J.K., M.F. Glasser, T.M. Preuss, *et al.* 2008. The evolution of the arcuate fasciculus revealed with comparative DTI. *Nat. Neurosci.* **11:** 426–428.
58. Kimura, M. 1992. Behavioral modulation of sensory responses of primate putamen neurons. *Brain Res.* **578:** 204–214.
59. Merchant, H., A. Battaglia-Mayer & A.P. Georgopoulos. 2001. Effects of optic flow in motor cortex and area 7a. *J. Neurophysiol.* **86:** 1937–1954.
60. Merchant, H., A. Battaglia-Mayer & A.P. Georgopoulos. 2004. Neural responses during interception of real and apparent circularly moving stimuli in motor cortex and area 7a. *Cereb. Cortex* **14:** 314–331.
61. Merchant, H., W. Zarco, O. Perez, *et al.* 2011. Measuring time with different neural chronometers during a synchronization-continuation task. *Proc. Natl. Acad. Sci. USA* **108:** 19784–19789.
62. Merchant, H., D.L. Harrington & W.H. Meck. 2013. Neural basis of the perception and estimation of time. *Annu. Rev. Neurosci.* **36:** 313–336.
63. Merchant, H., O. Perez, W. Zarco, *et al.* 2013. Interval tuning in the primate medial premotor cortex as a general timing mechanism. *J. Neurosci.* **33:** 9082–9096.
64. Bartolo, R., L. Prado & H. Merchant. 2014. Information processing in the primate basal ganglia during sensory-guided and internally driven rhythmic tapping. *J. Neurosci.* **34:** 3910–3923.
65. Crowe, D.A., W. Zarco, R. Bartolo, *et al.* 2014. Dynamic representation of the temporal and sequential structure of rhythmic movements in the primate medial premotor cortex. *J. Neurosci.* **34:** 11972–11983.
66. Merchant, H. & R. Bartolo. 2018. Primate beta oscillations and rhythmic behaviors. *J. Neural Transm.* **125:** 461–470.
67. Perez, O., R.E. Kass & H. Merchant. 2013. Trial time warping to discriminate stimulus-related from movement-related neural activity. *J. Neurosci. Methods* **212:** 203–210.
68. Merchant, H., O. Pérez, R. Bartolo, *et al.* 2015. Sensorimotor neural dynamics during isochronous tapping in the medial premotor cortex of the macaque. *Eur. J. Neurosci.* **41:** 586–602.
69. Merchant, H. & B.B. Averbeck. 2017. The computational and neural basis of rhythmic timing in medial premotor cortex. *J. Neurosci.* **37:** 4552–4564.
70. Iversen, J.R., A.D. Patel, B. Nicodemus & K. Emmorey. 2015. Synchronization to auditory and visual rhythms in hearing and deaf individuals. *Cognition.* **134:** 232–244.

Graphical Abstract & Image

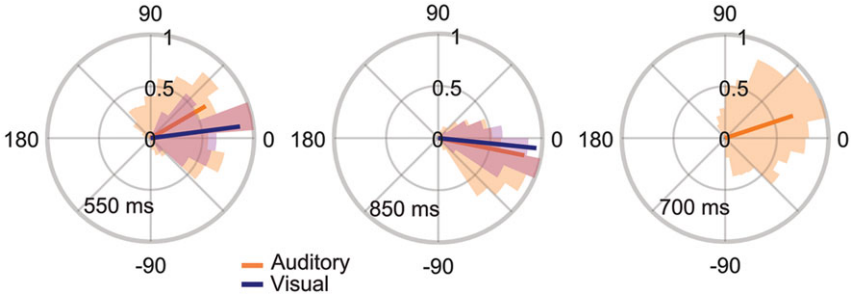

Previous studies have shown that monkeys share some of the human capabilities for rhythmic entrainment, such as tapping regularly at the period of isochronous stimuli. However, it is still unknown whether monkeys can predictively entrain to dynamic tempo changes. To address this question, we trained monkeys in three tapping tasks and compared their rhythmic entrainment abilities with those of humans.

J Neurophysiol 116: 563–574, 2016.
First published May 11, 2016; doi:10.1152/jn.00116.2016.

Recording extracellular neural activity in the behaving monkey using a semichronic and high-density electrode system

Germán Mendoza,[1] Adrien Peyrache,[2] Jorge Gámez,[1] Luis Prado,[1] György Buzsáki,[2] and Hugo Merchant[1]

[1]*Instituto de Neurobiología, National Autonomous University of Mexico, Querétaro, México; and* [2]*The Neuroscience Institute, School of Medicine and Center for Neural Science, New York University, New York, New York*

Submitted 8 February 2016; accepted in final form 4 May 2016

Mendoza G, Peyrache A, Gámez J, Prado L, Buzsáki G, Merchant H. Recording extracellular neural activity in the behaving monkey using a semichronic and high-density electrode system. *J Neurophysiol* 116: 563–574, 2016. First published May 11, 2016; doi:10.1152/jn.00116.2016.—We describe a technique to semichronically record the cortical extracellular neural activity in the behaving monkey employing commercial high-density electrodes. After the design and construction of low cost microdrives that allow varying the depth of the recording locations after the implantation surgery, we recorded the extracellular unit activity from pools of neurons at different depths in the presupplementary motor cortex (pre-SMA) of a rhesus monkey trained in a tapping task. The collected data were processed to classify cells as putative pyramidal cells or interneurons on the basis of their waveform features. We also demonstrate that short time cross-correlogram occasionally yields unit pairs with high short latency (<5 ms), narrow bin (<3 ms) peaks, indicative of monosynaptic spike transmission from pre- to postsynaptic neurons. These methods have been verified extensively in rodents. Finally, we observed that the pattern of population activity was repetitive over distinct trials of the tapping task. These results show that the semichronic technique is a viable option for the large-scale parallel recording of local circuit activity at different depths in the cortex of the macaque monkey and other large species.

monkey; silicon shanks; population dynamics; pyramidal interneurons; multielectrodes

NEW & NOTEWORTHY

This paper demonstrates high-density, chronic recordings of single units at different depths in behaving monkeys, which have been achieved until now only in rodents. We also show how two, and potentially many, silicon probes can be implanted effectively and at low cost in primates. Using different analytical tools on simultaneously recorded cells, we were able to identify inhibitory and principal cells, so that functionally connected cortical assemblies can be studied during task performance.

BRAIN FUNCTION IS THE RESULT of the structured interaction of groups of neurons forming functional networks in time and space (Mountcastle 1995; Buzsáki 2010). Recording of the extracellular activity of few neurons during different conditions or tasks has been a useful tool for the study of neuronal function in distinct brain areas (Mountcastle et al. 1969, 1975; Andersen et al. 1985; Georgopoulos et al. 1986; Schultz and Romo 1992; Lebedev et al. 2000). In those studies, the limited number of simultaneously recorded neurons and the variability of the neuronal responses as a function of the task parameters impose the necessity of collecting many trials under the same condition to determine the statistics of the neural response (Brown et al. 2004). This experimental strategy, however, results in a limited description of the functional properties of single cells, neural populations, and the dynamic interactions of different types of neurons (i.e., pyramidal vs. fast spiking interneurons [FS]) forming anatomic-functional networks (Merchant et al. 2012). In contrast, the brain processes information on a trial-by-trial basis exploiting the population activity to represent different behavioral parameters (Quian Quiroga and Panzeri 2009). Thus the comprehension of the mechanisms that make brain function possible requires the simultaneous sampling of the activity of representatively large groups of neurons (Brown et al. 2004; Buzsáki et al. 2015; Nicolelis and Lebedev 2009). Recent technological innovations have allowed the simultaneous recording of large number of neurons in several cortical and subcortical regions of the brain of awake, behaviorally trained rodents and nonhuman primates (Berényi et al. 2014; Dotson et al. 2015; Fraser and Schwartz 2012; Hatsopoulos and Donoghue 2009; Schwarz et al. 2014; Vandecasteele et al. 2012). Such methods and their combination with optogenetic tools have result in a better understanding of the brain function (Buzsáki et al. 2015; Wu et al. 2013, 2015). In spite of such progress, large-scale recordings are still technically challenging and have not been generalized across animal models, and each method has its own pros-and-cons. For example, a widely used method for chronic multiple recordings in human and nonhuman primates is the Utah array that has a 10-by-10 matrix arrangement (Schmidt et al. 1993). However, this FDA-approved recording system can only explore the functional properties of cell populations in the exposed flat part of the cortical gyri, with a maximum depth of 3 mm, and with no option to modify the recording location once placed. Furthermore, the 100 electrodes, each with a width of 80 μm can have a deleterious effect on the horizontal connections of the cortical tissue and its normal functioning (Ward et al. 2009).

The aim of the present study was to adapt a technique developed recently for the large-scale recording of extracellular activity in behaving rodents (Vandecasteele et al. 2012) to neural recordings in the behaving monkey. Nonhuman primates have been useful animal models for cognitive neuroscience for long time (Evarts 1968; Mountcastle et al. 1969) due to the similarity of their neuroanatomy and body plan to that of

Address for reprint requests and other correspondence: H. Merchant, Instituto de Neurobiología, UNAM, Campus Juriquilla, Querétaro, 76230, México (e-mail: hugomerchant@unam.mx).

humans and the possibility to train them in a variety of complex motor, perceptual, and cognitive tasks not available in other animal models (Averbeck et al. 2002; Crowe et al. 2004; Merchant et al, 2004a,b, 2011a; Chafee et al. 2007; Mendez et al. 2011). We employed commercial micromachined electrode arrays (NeuroNexus; http://www.neuronexus.com) for high-density recording of neuronal activity in the presupplementary motor cortex (pre-SMA) of a rhesus monkey working in a tapping task, which has been a backbone paradigm in the study of the neural basis of beat perception and entrainment (Zarco et al. 2009; Merchant et al. 2011b, 2015a). To achieve this, we developed a compact, low-cost microdrive, robust enough for semichronic recordings in the monkey. The technique allowed the recording of extracellular activity of local populations of neurons at different cortical depths during several weeks. Interestingly, we observed that the population activity was repetitive over distinct trials of the tapping task. Moreover, it was possible to identify monosynaptic connections between neurons and to classify them as putative pyramidal or interneurons. Such information was employed for the description of the functional connectivity in local circuits (Barthó et al. 2004). These results show that our method is a viable option for the chronic recording of local circuit activity in the cortex of the monkey and other large species. Current experiments employing this technique in our laboratory will provide new insights on the neurophysiology of explicit time processing by nonhuman primates.

MATERIALS AND METHODS

System description. We adapted the technique employed by Buzsáki and coworkers for semichronic recordings in rodents (Berényi et al. 2014; Vandecastele et al. 2012) to similar recordings in the behaving monkey. We used the Buzsaki64-Z64 probe manufactured by NeuroNexus (http://www.neuronexus.com). Nevertheless, other probes with similar structural characteristics can be employed (for an extensive comparison of the performance of several commercial probes chronically implanted in rodents review the work of Ward et al. 2009). The probe consists of eight silicon shanks separated from each other by 200 μm each with eight recording sites located at intervals of 20 μm in the vertical axis (Fig. 1*A*). The probe was connected to a microdrive that allowed the control of the movement of the probe in the dorso-ventral axis. Our microdrive consists of a body, a shuttle, and a basis (Fig. 1*B*). For the construction of the body and the shuttle electrical bakelite circuit board and board-to-board connectors (gold plated, pitch spacing: 2.54 mm; Smatec; www.samtec.com) were employed. The probe was fastened to the microdrive shuttle with dental acrylic. In addition, a brass screw (00–90 $\times$ 1; Fasteners & Metal Products; www.fastmetalproducts.com) attached to the body of the microdrive, went through the shuttle giving mobility to the probe. One turn of the screw corresponded to 280 μm. The probe, microdrive, and recording

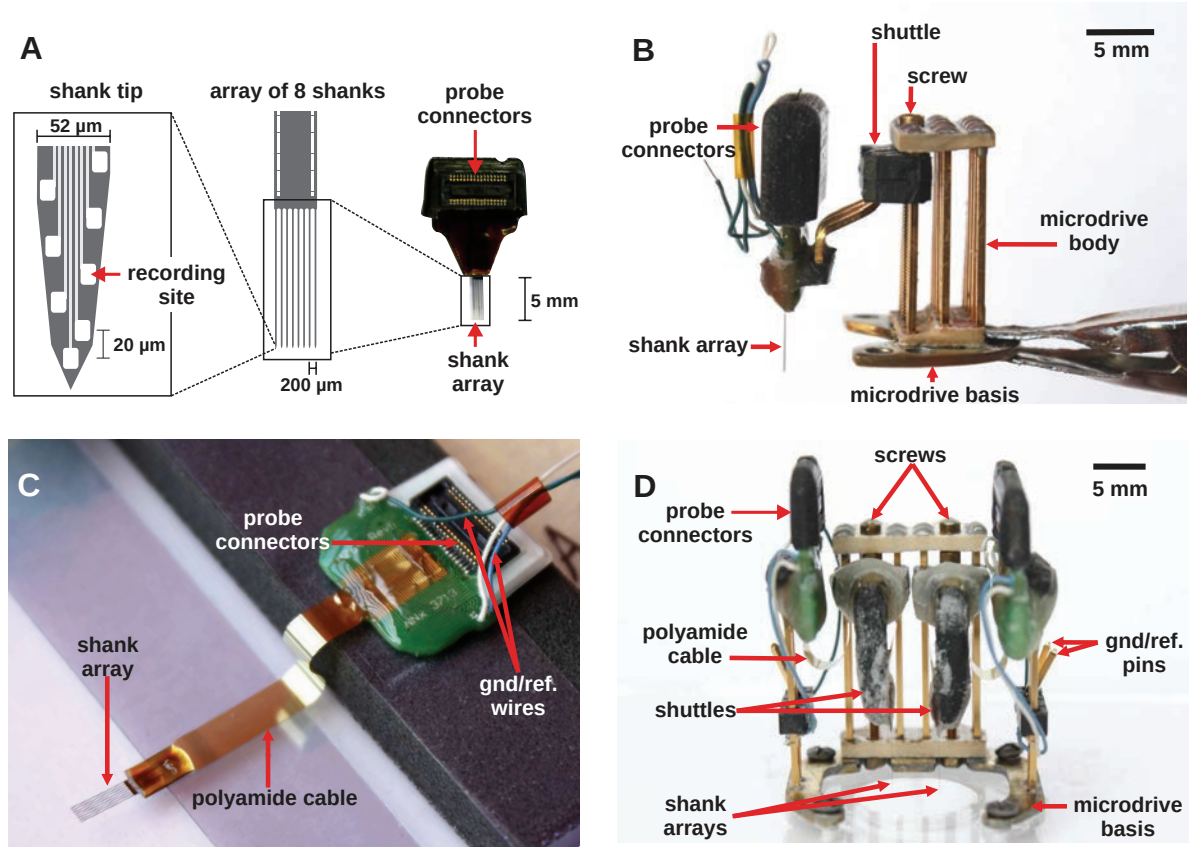

Fig. 1. Electrode and microdrive details. *A*: schematic drawing (*left* and *middle*) and view (*right*) of the Buzsáki64 shank array mounted with high-density connectors manufactured by NeuroNexus. The arrangement of the recording sites at the tip of 1 shank (*left*), the array of 8 shanks (*middle*), and the shanks mounted on commercial connectors (*right*) are shown. *B*: probe shown in *A* (*right*) is mounted in our custom-made microdrive. The movement resolution of the screw is 280 μm per turn. *C*: 1 shank array similar to that shown in *A* (*left* and *middle*) is mounted with a polyamide cable and high-density connectors (NeuroNexus). *D*: double microdrive holds two 64 recording site probes with polyamide extensions. This microdrive allows moving independently each probe. Note that the probe connectors are mounted on "towers" separated from the body of the microdrive and that the 2 towers and the microdrive are mounted on the same brass basis.

Table 1. *Neural recordings using one of two 64-channel silicon probes in the supplementary motor cortex of a monkey performing a synchronization tapping task*

	Single Probe	Double Probe
Recording days	74	72
Recording sessions	62	51
Maximum depth, mm	4.125	5.12
Total recorded neurons	1,905	3,862

connectors were covered by a protective aluminum/stainless steel case when the monkey was not in a recording session (see Fig. 3*G*).

It is possible to modify the basic structure of the microdrive to meet the needs of a particular experiment. The micromanipulator can be redesigned to accommodate different number of probes, different electrode configurations, recording locations, and recording depths. Importantly, these adaptations can be done in the laboratory employing commonly available tools and materials. For example, Fig. 1*D* shows a modification of the microdrive described above (Fig. 1*B*). The microdrive consists of two Buzsaki64-HZ64 probes glued to two shuttles mounted in the same body (Fig. 1*D*). Each shuttle is totally independent and is moved by a single screw. The microdrive allows the independent insertion and movement of the two probes in the same or in closely adjacent cortical areas. The two shank arrays were mounted 4 mm apart, but different distances can be achieved. Furthermore, the microdrive, the probe connectors, and the reference and ground connectors were attached in the same platform, conforming a single mechanically robust module. This design results in compact implants (see Fig. 4*C*) and reduces substantially the time required for implanting the probes and the overall surgery duration. A critical aspect for long-term recordings (up to 74 days so far, see Table 1) is the utilization of probes that includes a polyamide cable that connects the shank array with the probe connector (Fig. 1*C*). The polyamide cable and the use of the 64-channel ZIP-Clip connector (Tucker-Davis-Technologies; http://www.tdt.com) permit the easy day-by-day connection of the headstages without transferring force to the implanted electrodes and the surrounding tissue.

Preparing the shanks for the implantation. Before surgery, it was important that the headstages and the ZIP-Clip probe connector mate smoothly, avoiding excessive force to connect them. When this condition was not met, we employed a scalpel to cut small amounts of the probe connector until an easy mating was achieved. Next, the probe recording sites were cleaned in a solution of 4% of Conrad detergent (Conrad 70; Decond) in distilled water at 63°C during 2 h. Subsequently, the detergent was removed by the repeated immersion of the silicon shanks in distilled water (Vandecastele et al. 2012). Just before surgery, the probes as well as the microdrive were disinfected with 70% alcohol. In our experience, this method effectively avoided implant infections. Alternatively, sterilization can be achieved with oxide ethylene gas (Oliveira and Dimitrov 2008).

Surgical procedures. All the animal care, housing, and experimental procedures were approved by the National University of Mexico Institutional Animal Care and Use Committee and conformed to the principles outlined in the *Guide for the Care and Use of Laboratory Animals* (National Institutes of Health, Publication No. 85-23, revised 1985). One male rhesus monkey (8.5 kg) was subjected to two implantation procedures separated by 10 mo. In the first procedure, one 64-channel probe was implanted in the right pre-SMA, whereas in the second two probes were simultaneously implanted in the left and right pre-SMA.

Skullcap construction. The monkey was anesthetized initially with an intramuscular dose of ketamine (7 mg/kg)-xylazine (0.6 mg/kg), then underwent endotracheal intubation for sevofluorane anesthesia, and mounted on the stereotaxic apparatus. After preparing the skull vertex area (see Oliveira and Dimitrov 2008), we localized the stereotaxic coordinates of the recording sites based on structural MRI (high-resolution T1-weighted gradient echo sequence, TR = 20 ms, TE = 6.9 ms, flip angle = 25°, matrix = 240 × 108, slices = 80, resolution = 1.0 mm × 1.0 mm × 1.0, on a 3.0 T Philips MRI Scanner; Merchant et al. 2011b). Subsequently, we attached to the cranium the reference and ground screws/wires, as well as the titanium posts for head fixation and the securing screws (Fig. 2*A*). The securing screws and the basis of the titanium posts were covered with dental acrylic. Once the dental acrylic was hardening but still malleable, we built a flat acrylic platform (4.5 cm of diameter) around the recording site for the future fixation of the microdrive and the protective case (Fig. 2*B*). The reference and ground gold pins should protrude 7 mm over the implant surface (Fig. 2, *C* and *D*). After the dental acrylic was cured, antibiotic ointment was applied on the

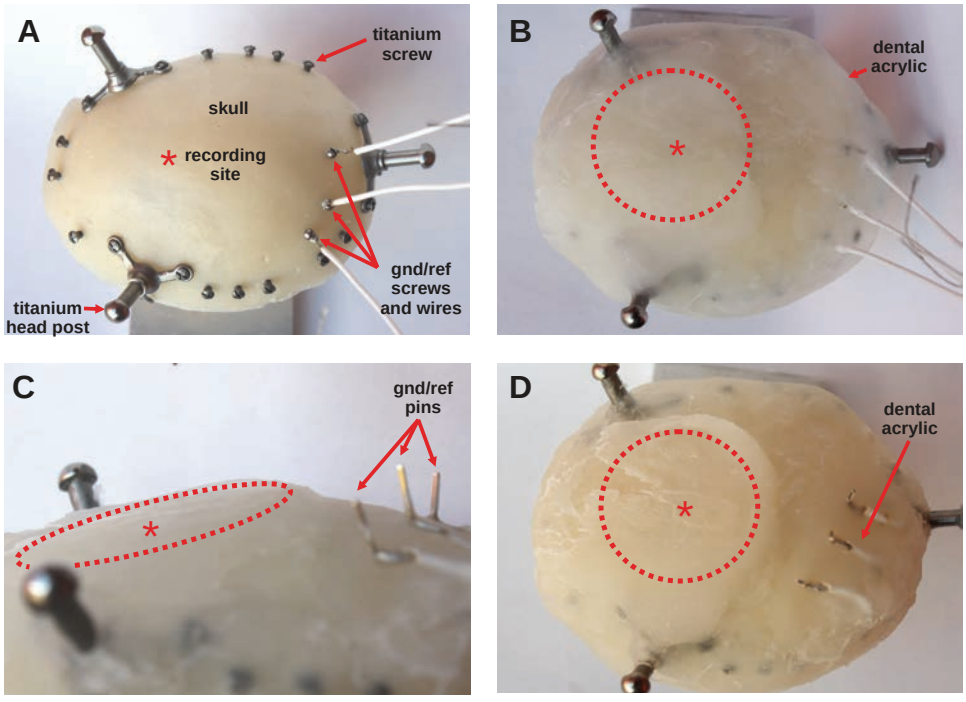

Fig. 2. Surgery procedures: skullcap construction. Note that the pictures correspond to a mock surgery. *A*: titanium posts, the titanium screws, and the ground and reference screws/wires were fixed to the previously prepared cranium. *B*: dental acrylic was employed to cover the cranium, post basis, screws and wires. A flat area (dotted circle) for mounting the microdrive was formed above the implantation site (red asterisk). *C*: note the ground and reference wires/pins emerging over the surface of the implant. *D*: wires and the base of the ground/reference pins were covered with dental acrylic.

wounds. The monkey was retired from stereotaxic frame and allowed to recover in a quiet room. Broad spectrum antibiotics (Enrofloxacin, 5 mg·kg^{-1}·day^{-1}) and analgesics (Ketorolac, 0.75 mg·kg^{-1}·6 h^{-1} or Tramadol, 50–100 mg/4–6 h) were administered intramuscularly the day of the surgery and in two subsequent days.

Probe implantation. The monkey was retrained in tapping task (Zarco et al. 2009; Merchant and Honing 2014) with its head fixed in the head-holding device. Then, a second surgery was performed to implant the shank array. Anesthetic and aseptic methods were the same to those of the first surgery. First, with the monkey fixed on the stereotaxic frame, a craniotomy was drilled through the acrylic skull cap and skull in the previously identified stereotaxic coordinates (Fig. 3*A*). Next, the dura matter at the insertion point was opened employing a miniature surgical blade or a hook (Vandecasteele et al. 2012). The microdrive was mounted in a stereotaxic tower for the positioning of the shanks (see Vandecasteele et al. 2012). Once the shanks were aligned with the penetration site, the microdrive was attached to the head cap by means of titanium screws and dental acrylic (Figs. 3*B* and 4*B*). Notably, the alignment of the shank array and the craniotomy and dura dissection point must be verified before fixing the microdrive in place. Once the microdrive was firmly attached to the skullcap, the stainless steel ring was mounted employing titanium screws and dental acrylic (Figs. 3*C* and 4*C*). We moved the microdrive screw to penetrate the shanks into the cortex under microscope assistance. We did not see brain dimpling during electrode insertion. Instead, the shanks may be bent due to their thin section (15-μm width) and

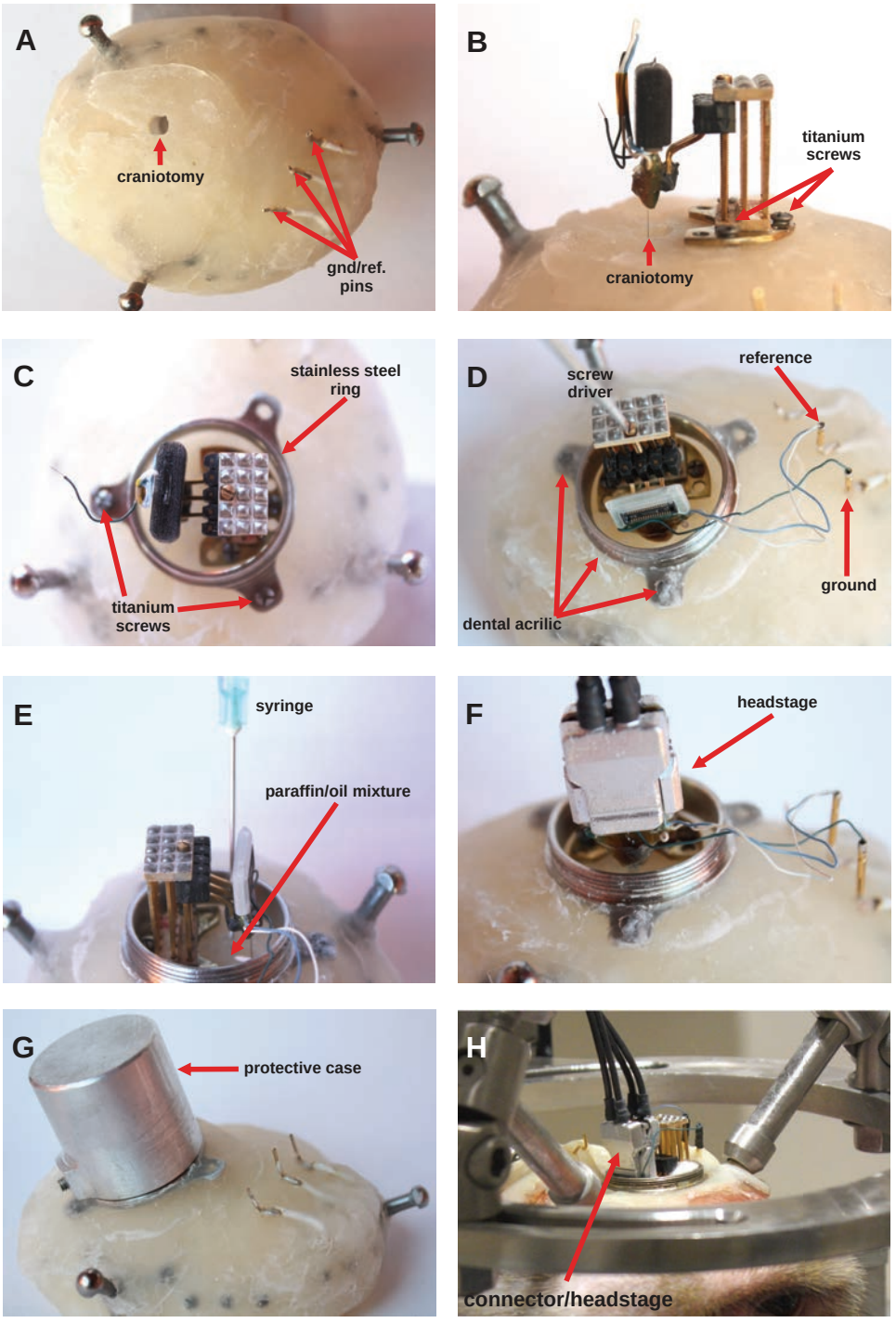

Fig. 3. Microdrive implantation. Note that the pictures correspond to a simulated surgery. *A*: craniotomy was drilled through the skull cap/scull over the implantation site. *B*: after opening the dura mater the microdrive was mounted in place by mean of titanium screws and dental acrylic. *C*: stainless steel ring is fixed to the skullcap. *D*: under microscope assistance, the electrodes were lowered until implanted in the cortex. *E*: warm mixture of paraffin/mineral oil was employed to seal the craniotomy. *F*: headstage and reference/ground wires were connected to corroborate the presence of neural activity. *G*: finally, all connectors were removed and the protective case mounted. *H*: behaving monkey. During neural recordings, the head of the monkey was fixed with a standard head holder.

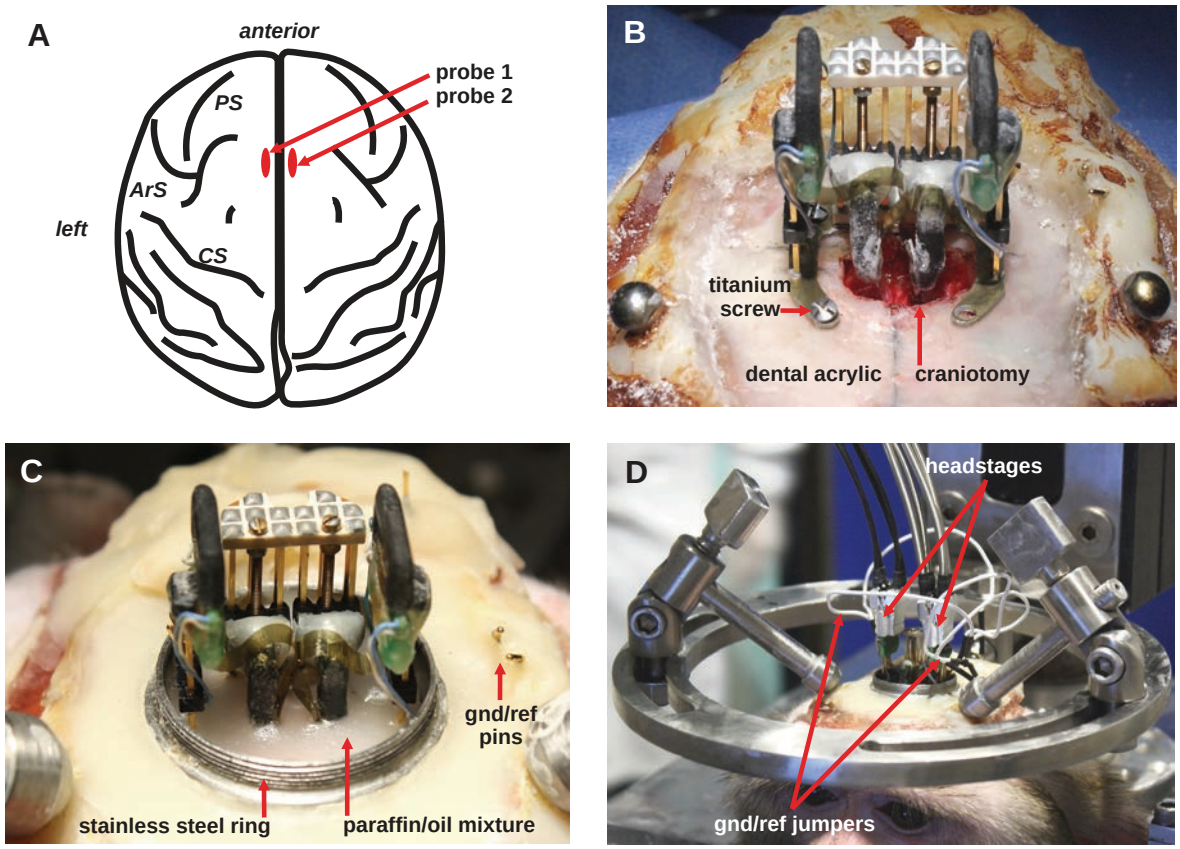

Fig. 4. Double microdrive implantation. *A*: drawing of the dorsal aspect of the monkey's brain indicating the approximate sites of implantation (red ovals). PS, principal sulcus; ArS, arcuate sulcus; CS, central sulcus. *B*: close-up of the craniotomy and the mounted microdrive. Before implanting the shanks, the microdrive was attached securely in place by mean of titanium screws and dental acrylic. *C*: after probe implantation, a mixture of wax and mineral oil serves to seal the craniotomy. Note the ground and reference pins, previously implanted, protruding from the skullcap. *D*: the behaving monkey. During neural recordings, the head of the monkey was fixed using a standard head holder. Headstages and ground and reference jumpers are visible.

flexibility. Consequently, care must be taken to avoid bending shanks excessively, because they can brake (Fig. 3*D*, Vandecasteele et al. 2012). If the shanks bent, they were pulled-up and then the penetration was tried again until the recording sites were inserted in the superficial layers of the cortex. Once the electrodes were implanted, the craniotomy was closed with a warm mixture of paraffin/mineral oil applied with a sterile syringe (Figs. 3*F* and 4*C*). After the presence of neural activity was verified, the aluminum case was placed to protect the probes, microdrive, and connectors (Fig. 3*G*). Antibiotic and analgesics were administered as in the first surgery.

Implant maintenance. After the implantation surgery care was taken to maintain the microdrive and the probe connectors clean from the cerebrospinal fluid and other debris that leaked from the craniotomy. Daily cleaning of the paraffin seal, the microdrive, and the probe connectors with sterile cotton swabs prevented implant infections and diminished recording artifacts that can result from humid probe connectors. Persistent humidity was eliminated with compressed air. Especially dirty connectors were cleaned with the point of a sterile syringe needle or with a sterile miniature brush under a surgical microscope view.

Signal acquisition. The neural data of 64 or 128 channels were acquired, amplified, and digitized using a PZ2 preamplifier (Tucker-Davis Technologies; http://www.tdt.com) at 24,414 Hz. The signal was transmitted to a RZ2 base station through fiber optic for online processing.

Spike detection and discrimination. Raw recording traces were high-pass filtered at 800 Hz and action potential candidates were selected as any events larger than seven standard deviations above baseline on at least one of the channels from the electrode group (the 8 channels of a given shank on the silicon probe). Spike sorting was then performed semiautomatically, using KlustaKwik (Harris et al. 2000; available at: http://klusta-team.github.io/klustakwik/) after dimensionality reduction of the waveforms using standard principal component analysis (3 components per channel typically explaining almost all the variance). This was followed by the manual adjustment of the waveform clusters using the software Klusters (Hazan et al. 2006). In 1 session, up to 64 isolated single neurons were detected (average of 27 cells per recording, range: 9–64 cells, for 4 analyzed recording sessions).

Identification of monosynaptic connections. Pairwise cross-correlations between all possible pairs of simultaneously recorded neurons were calculated using the discharge rate of cells in 0.5-ms bins. Cross-correlograms were smoothed with a 5-ms standard deviation Gaussian kernel (which is equivalent to a jittering of the spikes from the 2 neurons). At each time bin, the interval of confidence of the smoothed cross-correlogram was evaluated as the 99.9th percentile of a Poisson process defined by the rate resulting from the smoothing procedure (Stark and Abeles 2005). A putative excitatory or inhibitory connection was considered when any two consecutive bins of the original cross-correlogram exceeded the interval of confidence between 0 and 8 ms. The cross-correlograms were then manually examined to remove any spurious connections.

RESULTS

System description. We customized the large-scale system used to record from multiple single units in behaving rodents to use the same methodological and analytical framework in

monkeys performing different paradigms. We used the Buzsaki64-Z64, which consists of eight silicon shanks each with eighth staggered recording sites separated vertically by 20 μm (Fig. 1*A*). Furthermore, we modified the system to allow the independent recording of two separate but adjacent cortical areas with two probes. Each probe was coupled to a microdrive that allowed the independent control of the recording position in dorso-ventral axis (Fig. 4). With this system, we had the possibility to perform large-scale recordings in deep cortical areas in the profound gyri (up to 5 mm) for more than 10 consecutive weeks (see Table 1). Figure 5*A* shows the wide-band signal of the eight recording sites of one of the inserted shanks in the supplementary motor cortex of a rhesus monkey. The same neuron could be recorded in different recording sites of one shank, as illustrated in Fig. 5*B*, where the raster of seven spikes of the corresponding action potentials on the Fig. 5*A* is shown with the same color code. Thus the voltage profile of spikes across the recording sites in a probe provided an approximate location of the cell body of the recorded neuron (Csicsvari et al. 2003).

Unit clustering. Spike detection, feature extraction, and spike discrimination using clustering methods was performed semiautomatically with the open-source software KlustaKwik (Harris et al. 2000). Spike clusters were manually adjusted and eventually followed standard quality criteria such as low level of refractory period contamination. Figure 6*A* shows the spike clusters of the seven cells depicted in Fig. 5 using the same color code. These clusters are displayed along the first principal components of spike waveforms extracted from the sixth and seventh recording sites. In addition, Fig. 6*B* illustrates the mean ($\pm$SD) of the waveform of the seven-clustered cells (spk1-spk7, same color code) across the eight neighboring recording sites (RS1-RS8) of one silicon probe. The analysis of the auto- and cross-correlograms depicted in Fig. 6*C* also provided valuable information for the spike discrimination process. The diagonal of auto/cross-correlogram matrix (Fig. 6*C*) corresponds the auto-correlograms for the same seven cells (in color code Fig. 6, *A* and *B*). These auto-correlograms showed an absence of spikes at short intervals ($<$2 ms) corresponding to the refractory period of the neurons and thus indicating that the recording of each of the seven spikes was made from a single independent cell. Furthermore, asymmetric peaks in the cross-correlograms can indicate that the decreasing amplitude of the spikes within a burst produced by a single cell has been classified as a separate cluster (Harris et al. 2000). However, Fig. 6*C* shows that all cross-correlograms (gray) were symmetric, supporting the notion of robust spike discrimination.

Large-scale recording from multiple single units in the behaving monkey. A monkey was trained to synchronize its hand taps to a button with a sequence of pacing isochronous visual stimuli. The animal developed a timing behavior that was built from the predictive rhythmic structure of the task (Merchant et al. 2008, 2013). Interestingly, the silicon probe recordings during task execution showed that the periodic taping of the monkey was associated with a repetitive pattern of activation of multiple single cells. Figure 7*A* shows the simultaneous recording of 64 cells that were sorted by their response onset latency. It is evident that the neurons show many cycles of activations and that the phase of this activations changed systematically across the neuronal population, forming a neural avalanche of activation on every task trial. The repetitive pattern of activity could be clearly observed by projecting the ensemble profile of activation overtime onto the first two principal components. As seen on Fig. 7*B*, the population activity is, in this principal component subspace, rotating cyclically along a low-dimensional trajectory. Indeed, the trial-by-trial analysis of the population neural trajectories, depicted in Fig. 7*C*, shows a stereotypic behavior where the neural dynamics start in the middle lower part of the principal component analysis (PCA) subspace (dark blue) and then rotates counterclockwise to finally return around the initial starting point (yellow colors). Interestingly, the cyclical trajectories are similar for trials where the monkey produced intervals with different durations, suggesting a relative rather than an abso-

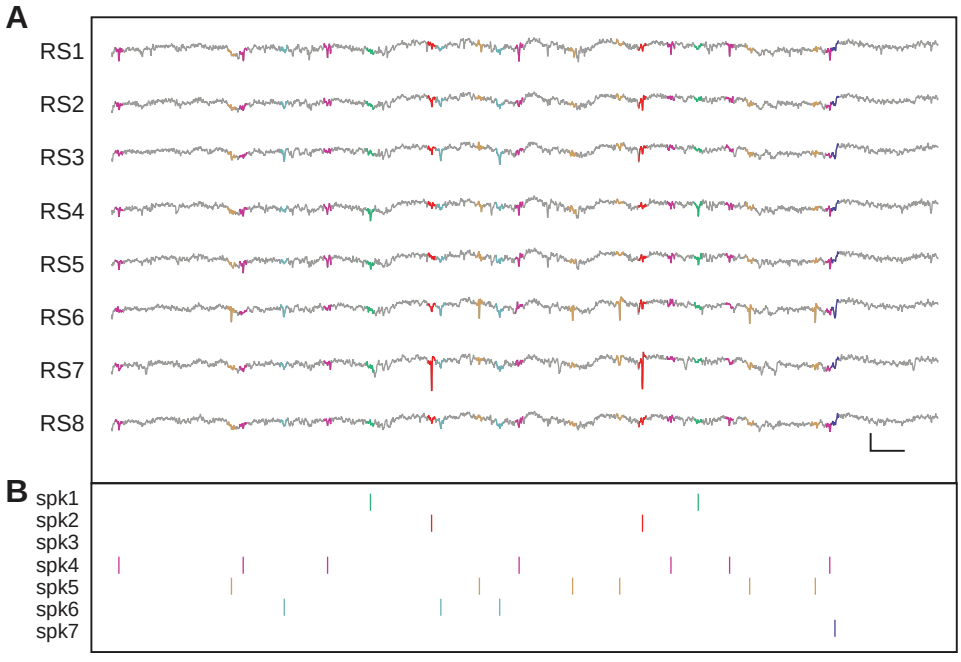

Fig. 5. Recording of large ensembles of pre-supplementary motor cortex (pre-SMA) cells using a 64-channel silicon probe in a monkey performing the tapping task. *A*: broadband recording traces from 8 neighboring recording sites (RS1-RS8) in one of the shanks. Extracellular waveforms of 7 clustered neurons (spk1-spk7) are superimposed on the traces using the same color code of the spike-discrimination clustering in Fig. 6. Calibration: vertical: 500 μV; horizontal :10 ms. *B*: raster plot of the activity of the seven cells in *A* using the time stamps and the color code in *A*. Note that some spikes are present in many of the 8 recording sites.

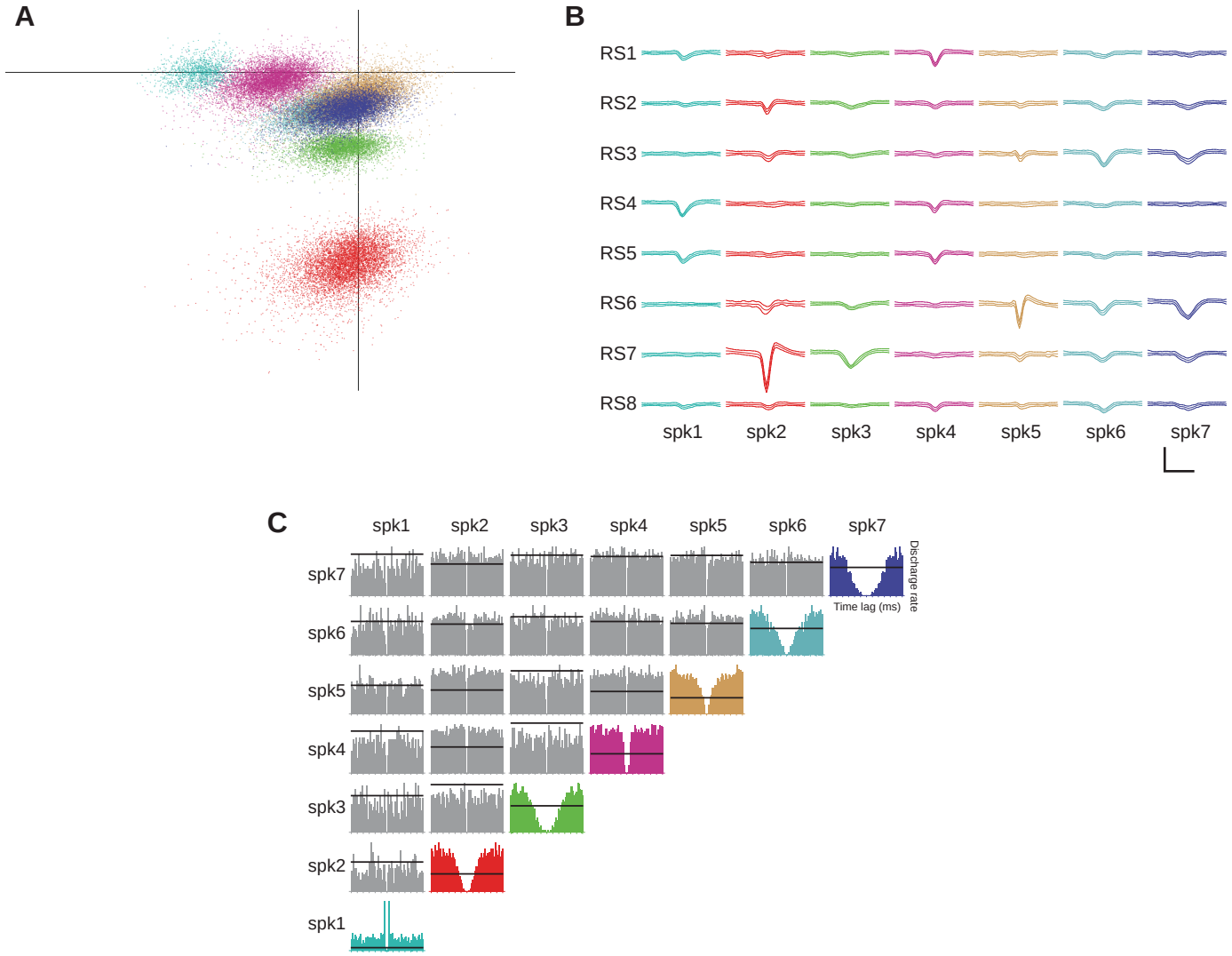

Fig. 6. Semiautomatic spike discrimination of the cells. *A*: spike clusters of the seven cells depicted in Fig. 5 (same color code) displayed along the first principal components of spike waveforms extracted from the 6th and 7th channel. *B*: waveforms (mean ± SD) of the 7-clustered cells (spk1-spk7) across the 8 neighboring recording sites (RS1-RS8) of 1 silicon probe. Same color code as in *A*. *C*: calibration: vertical 500 μV; horizontal 1.7 ms. Auto- and Cross-correlograms for all possible pairs of the seven neurons discriminated in *A*, displayed in a matricial arrangements where the diagonal in color (same color as in *A*) correspond to the auto-correlations, and the other elements (in gray) are the cross-correlations between different cell pairs. The horizontal line corresponds to a threshold of the 99.9th percentile of a Poisson process defined by the rate resulting from the smoothing procedure (see MATERIALS AND METHODS).

lute representation of the passage of time. A similar phenomenon was observed in single neuron and ensemble activity recorded in the primary motor and premotor cortices of monkeys producing self-timed hand movements (Lebedev et al. 2008). Furthermore, the population neural trajectories were similar in trials where the monkey did not tap and only perceived the sensory metronome (Fig. 7*C*, *trial 15*). These phenomena were already documented in a tapping task but using the activity of pre-SMA neurons recorded in many different sessions due to the small number of simultaneously recorded cells (Merchant et al. 2014a, 2015b; Crowe et al. 2014). Hence, the simultaneous recordings of hundreds of cells in a particular cortical area during complex cognitive tasks will allow the characterization of neural population codes that can be related with different parameters of behavior on a trial-by-trial basis.

Electrophysiological and functional identification of pyramidal and FS neurons. Units were classified as putative pyramidal cells and putative GABAergic interneurons on the basis of their waveform features. Putative pyramidal cells were characterized by broad waveforms whereas putative interneurons showed narrow spikes (Merchant et al. 2012). To separate between the two classes of cells, we used two waveform features: *1*) half-peak duration, which corresponds approximately to the time it takes for the membrane potential to repolarize *2*) the trough-to-peak duration. These two waveform features were clustered using an Expectation-Maximization method fitting the population with a mixture of two two-dimensional Gaussian distributions. Cluster identity of a cell was defined as a posterior probability >80% to one of the two clusters (Fig. 8*A*). This method successfully clustered almost all neurons (107/108), which showed clearly separated waveform shape (Fig. 8*B*). Narrow-spike neurons are likely FS (parvalbumin-expressing) interneurons (Royer et al. 2012). As expected, mean firing rates were twice as high for putative FS interneurons than for putative excitatory pyramidal neurons (Fig. 8*C*; $P < 10^{-4}$, Wilcoxon rank sum test). Many studies

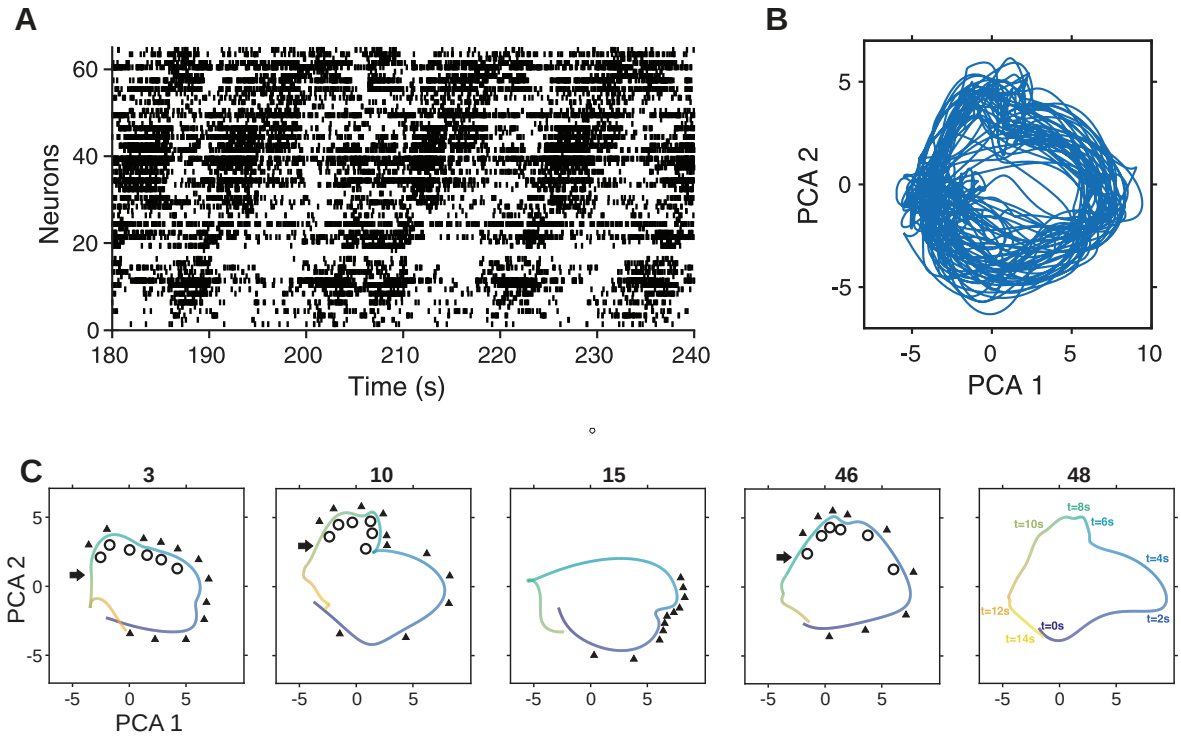

Fig. 7. *A*: raster plot of 64 simultaneously recorded neurons, sorted by their activation phase during the tapping task. *B*: projection of the neuronal data of the 64 cells onto its 1st 2 principal components revealed a highly constraint population dynamics during the task. *C*: neural trajectories of 5 of the trials in *B*, color coded for elapsed time since the beginning of the trial (see times on the *trial 48* on the *right*). The open circles depict the seven tapping times, whereas the close triangles the isochronous stimulus times. The rightward arrows illustrate the reward times. Note that the cyclical trajectories of the neural population are similar across trials, even when the monkey produced intervals with different durations (*trial 3* = 650 ms; 10 = 850 ms; 46 = 750 ms; 48 = 950 ms) or when the monkey perceived the sensory metronome but did not produced taps in synchrony with the stimuli (*trial 15*).

have shown that the electrophysiological signatures of extracellular action potentials and the spontaneous activity of the cells cannot be the only criteria to identify putative pyramidal vs. putative FS interneurons, due to the large amount of classification errors (Barthó et al. 2004; Merchant et al. 2008, 2012). Thus one of the large advantages of the silicon probe system used in the present study is its high recording density, which maximizes the possibility to find monosynaptic interactions between multiple pairs of neurons. Consequently, the cell types were further assessed by analyzing candidates of synaptic connection between cell pairs evidenced from their temporal cross-correlogram at millisecond time range (Barthó et al. 2004; Peyrache et al. 2012). Figure 8*D* shows an example of an excitatory postsynaptic effect of a broad waveform, putative pyramidal neuron onto a narrow-spike, putative FS cell. The average probability of connectivity is 1.45% (±1.25, SD), for a total number of eight excitatory connections.

DISCUSSION

The main novel contributions of our report are *1*) the development of a new compact, low-cost implantable microdrive and its corresponding protective device, both of them robust enough for semichronic recordings in the monkey and other large animals; *2*) the development of a new implantation technique that, in combination with our microdrive design, saves time during surgeries; *3*) these innovations allowed us to perform chronic high-density recordings of extracellular activity of local populations of neurons at different cortical depths during several weeks in the rhesus monkey, which to our knowledge has not previously accomplished; and *4*) the demonstration that advanced spike sorting and analytical techniques recently developed for chronic recordings in rodents can be also employed for the analysis of chronic recordings performed in larger animals such as the rhesus monkey.

Our method combines the flexibility of acute recordings, the advantages of chronic systems, the high spatial resolution, and the massive neurophysiological information generated by high-density silicon probes. These features provide our technique with several advantages over previous reported methods. First, in contrast to other chronic, high-density systems like the Utah array, our microdrive allows the movement of the electrode arrays at any time during different recording sessions. The arrays can be moved in the dorso-ventral axis to optimize the recording quality or to scan the properties of deep regions of the cortical tissue. Second, the micromanipulator can be redesigned to accommodate different number of probes, electrode configurations, recording locations, and recording depths. Most important, these adaptations can be done in the laboratory at a very low cost, employing commonly available tools and materials. Third, we employed NeuroNexus commercial probes, but any recording array with similar structural characteristics can be employed. Fourth, the microdrive, the probe connectors, and the reference and ground connectors are attached in the same platform and form a single mechanically robust module. This design results in compact implants and reduces substantially the time required for implanting the probes and the overall surgery duration. This is achieved because the spatial relation between the

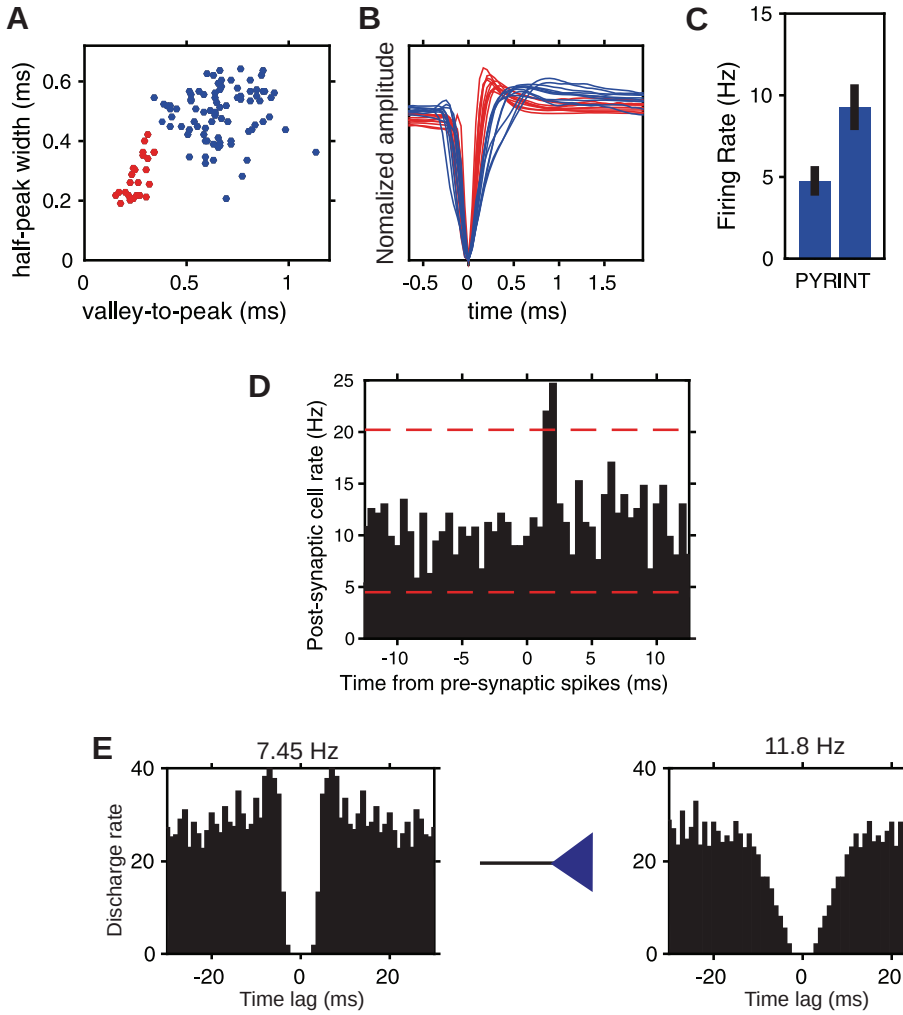

Fig. 8. Identification of putative excitatory pyramidal cells and inhibitory interneurons by clustering of extracellular waveform features. *A*: valley-to-peak vs. half-peak width values for putative pyramidal cells (blue) and interneurons (red). Data were fitted to a mixture of 2 Gaussian distributions. Cells were included in the cluster for which their posterior probability >90%. *B*: 10 superimposed example waveforms for each group. *C*: average firing rate for the 2 groups of cells (bars display SE). *D*: cross-correlogram between a pyramidal (reference spikes) and an interneuron (target spikes) showing a short latency, narrow peak indicative of a putative mono-synaptic excitatory connections. Red dotted lines indicate 99.9% interval of confidence obtained by jittering the spikes in 10-ms windows. *E*: auto-correlograms for the pyramidal (*left*) and the interneuron (*right*). The average firing rate is shown on *top*.

recording probes and all the required connectors is adjusted before surgery and all of them are implanted at the same time as a whole after opening the craniotomy. Fifth, the type of probe mounting and connector employed permits the fast and easy day-by-day connection of the head stages without transferring force to the implanted electrodes and the surrounding tissue. Sixth, our recording method can be combined with recently developed freely available spike sorting tools, which were specially designed for recordings with high-density electrode arrays (Rossant et al. 2016).

On the other hand, one disadvantage of our system is that it requires the daily cleaning of the microdrive and the probe connectors to maintain the aseptic conditions of the implant site. In our experience, daily cleaning of the paraffin seal, the microdrive, and the probe connectors prevented implant infections. This procedure also maintained the connectors clean and dry, which is a prerequisite to avoid recording artifacts. It is important to mention that these disadvantages are similar to those presented in classic acute recordings (Naselaris et al. 2005) and that the advantages of our method clearly overcome these drawbacks.

The use of silicon probes with multiple, staggered recording sites allowed the identification of distinct neuronal clusters in the pre-SMA of the behaving monkey that were reliably identified using standard semiautomatic clustering software. Thus, the voltage profile of spikes across the recording sites in a probe provided an approximate location of the cell body of the recorded neuron. Furthermore, we were able to record sixty-four cells simultaneously during the performance of a tapping task. Their activation profile showed many cycles of activations, where the response phase changed systematically across the neuronal population, forming periodic neural avalanches during task performance. In fact, at the population level, a cyclic and systematic trial-by-trial pattern of activation was observed when the ensemble response profile overtime was projected onto the first two principal components. Finally, using different electrophysiological signatures and the cross-correlograms of simultaneously recorded cells, we were able to identify inhibitory interneurons and principal cells in cortical networks. Thus the parallel recordings of neuronal activity allowed for the identification of anatomically and functionally connected assemblies.

Nonhuman primates and in particular rhesus monkeys have been a fundamental animal model in cognitive neuroscience for almost 50 yr (Evarts 1968; Mountcastle et al. 1969; Lin et al. 2014). Neurophysiological studies in different brain areas while monkeys perform a variety of perceptual (Britten et al. 1992; Romo and Salinas 2003), memory- or rule-based (Miller 2000; Tomita et al. 1999), spatial and temporal cognition (Georgopoulos et al. 1994; Chafee et al. 2007; Seo et al. 2012,

2014, Merchant et al. 2013; Jazayeri and Shadlen 2015), numerosity (Nieder and Miller 2003), and fine voluntary motor control tasks (Schwartz 1994; Kraskov et al. 2009; Churchland et al. 2012) are the pillars of system neuroscience. Thus despite the world-wide pressure to abandon this model, macaques are still a valuable and necessary model for the study of high cognitive processes at the single cell and neural population levels, due to the similarity of their neuroanatomy and general body plan to those of humans, and the possibility to train them in a variety of complex paradigms not available in other animal models. Nevertheless, many monkey neurophysiologist are still using the single electrode approach to study the neural underpinnings of cognition, with a total disregard on how large ensembles of cells interact to process and transfer information between and within brain areas (see Merchant et al. 2014b; Crowe et al. 2013 for some exceptions) and how the anatomy of neural circuits define high-order brain operations. In contrast, different large-scale recording methods have been developed in behaving rodents with enormous success. In particular, the use of silicon-probes for high-density recordings of local circuits in behaving rats and mice has opened the possibility for the systematic study of hundreds of simultaneously recorded neurons, the identification of the electroanatomic boundaries of layers and regions in the hippocampus and neocortex, the construction of circuit diagrams of functional connections (excitatory or inhibitory) among neurons in real anatomic space (Buzsaki 2004; Berenyi et al. 2014), and the investigation of the circuit operations and behavior-dependent interactions between and within brain areas (Berenyi et al. 2014; Fujisawa et al. 2008). Furthermore, the large-scale recordings of neuronal spiking with silicon probes can be combined with the optogenetic manipulation of the activity of diverse neuronal phenotypes to determine the causal role of different circuit components and brain areas on the organization of behavior (Buzsáki et al. 2015). Consequently, the purpose of this study was to adapt the large-scale recording system of behaving rodents to use the same methodological and analytical framework in monkeys executing different paradigms. We were not only successful to record neural activity for many weeks from different depths of pre-SMA in a monkey but also managed to redesign the recording system and the micromanipulators to accommodate different number of probes, different electrode configurations, recording placements, and recording depths. Such versatility could be useful for the dense recording of multiple interconnected areas during the execution of particular tasks. A promising avenue to identify functional circuits across cortical areas in the monkey is the use of electrical microstimulation of key cortical or subcortical nodes and to measure the induced changes in functional magnetic resonance imaging to evaluate the functional activity resulting from the stimulation of interconnected regions (Tolias et al. 2005; Moeller et al. 2008; Petkov et al. 2015) or optogenetic stimulation of neurons (Wu et al. 2013, 2015). Thus, once the interconnected voxels are identified in a specific macaque, the employment of the semichronic system described here will allow the study of the critical processing nodes linked to a high order behavior with all the mentioned methodological strengths that have the high-density recordings with silicon probes.

The geometrically precise distribution of the eight recording sites across eight silicon shanks allowed for robust spike discrimination using semiautomatic clustering software, since the signal coming from one neuron can be recorded in adjacent recording sites. The semiautomatic process consisted of an automatic classification program that uses the information of all recording sites, followed by examination and reassignment by a human operator. Therefore, the semiautomatic spike sorting is considerably faster than the manual method, is free from the subjective bias and the experience level of the experimenter, and shows lower error rates in spike discrimination (Harris et al. 2000). In addition, the two-dimensional recording arrangement of the silicon probes permit the determination of the "center of mass," i.e., the approximate two-dimensional position of cell bodies of the putative single neurons with respect to the electrode layout (Csicsvari et al. 2003). This is the first step for the partial circuit reconstruction based on physiological interactions. Second, the dense recording distribution maximizes the probabilities to find monosynaptic excitatory and inhibitory interactions between pairs of cells, which are characterized by large peaks or troughs at short-latency time lags in the cross-correlograms. With spatially closely recorded neurons, it is possible to determine the monosynaptic connections between cells. Third, with the use of the spike duration and the spontaneous discharge rate of the cells, it is possible to identify putative pyramidal, with long duration action potentials and low discharge rate, and putative FS interneurons, with narrow action potentials and high discharge rate (Merchant et al. 2008). This information can complement the partial circuit reconstruction based on determination of the monosynaptic connections. Finally, dynamics in the interactions between cellular elements of the partially reconstructed network can be determined as a function of different task epochs and the value of the independent parameters of a specific behavioral paradigm (Fujisawa et al. 2008). Indeed, graph theory is a promising tool to identify how the reconstructed small circuit interactions change as a function of behavior (Carrillo-Reid et al. 2011).

In summary, large-scale recordings of single units with silicone-probe systems allow for a detailed study of the neural correlates of complex behaviors in the behaving monkey at many levels of neural processing: single cells, cell populations, the interaction between different cell types and their position across layers and cortical columns, functional circuits, as well as the interplay between encoding of behavioral parameters in the action potentials with the dynamic oscillations in different frequency bands on the surrounding cerebral tissue.

ACKNOWLEDGMENTS

We thank Raul Paulín for technical assistance.

GRANTS

This study was supported by CONACYT Grants 236836, PAPIIT: IN201214-25 (to H. Merchant), CONACYT Scholarship 164310 (to G. Mendoza), and National Institutes of Health Grants NS-34994, MH-54671, and NS-074015 (to G. Buzsáki).

DISCLOSURES

No conflicts of interest, financial or otherwise, are declared by the author(s).

AUTHOR CONTRIBUTIONS

G.M., G.B., and H.M. conception and design of research; G.M., J.G., L.P., and H.M. performed experiments; G.M., A.P., and L.P. analyzed data; G.M.,

A.P., J.G., G.B., and H.M. interpreted results of experiments; G.M., A.P., J.G., and H.M. prepared figures; G.M., A.P., G.B., and H.M. drafted manuscript; G.M., A.P., J.G., L.P., G.B., and H.M. edited and revised manuscript; G.M., A.P., J.G., L.P., G.B., and H.M. approved final version of manuscript.

REFERENCES

Andersen RA, Essick GK, Siegel RM. Encoding of spatial location by posterior parietal neurons. *Science* 230: 456–458, 1985.

Averbeck BB, Chafee MV, Crowe DA, Georgopoulos AP. Parallel processing of serial movements in prefrontal cortex. *Proc Natl Acad Sci USA* 99: 13172–13177, 2002.

Barthó P, Hirase H, Monconduit L, Zugaro M, Harris KD, Buzsáki G. Characterization of neocortical principal cells and interneurons by network interactions and extracellular features. *J Neurophysiol* 92: 600–608, 2004.

Berényi A, Somogyvári Z, Nagy AJ, Roux L, Long JD, Fujisawa S, Stark E, Leonardo A, Harris TD, Buzsáki G. Large-scale, high-density (up to 512 channels) recording of local circuits in behaving animals. *J Neurophysiol* 111: 1132–1149, 2014.

Britten KH, Shadlen MN, Newsome WT, Movshon JA. The analysis of visual motion: a comparison of neuronal and psychophysical performance. *J Neurosci* 12: 4745–4765, 1992.

Brown EN, Kass RE, Mitra PP. Multiple neural spike train data analysis: state-of-the-art and future challenges. *Nat Neurosci* 7: 456–461, 2004.

Buzsáki G. Large-scale recording of neuronal ensembles. *Nat Neurosci* 7: 446–451, 2004.

Buzsáki G. Neural syntax: cell assemblies, synapsembles, readers. *Neuron* 68: 362–385, 2010.

Buzsáki G, Stark E, Berényi A, Khodagholy D, Kipke DR, Yoon E, Wise KD. Tools for probing local circuits: high-density silicon probes combined with optogenetics. *Neuron* 86: 92–105, 2015.

Carrillo-Reid L, Hernández-López S, Tapia D, Galarraga E, Bargas J. Dopaminergic modulation of the striatal microcircuit: receptor-specific configuration of cell assemblies. *J Neurosci* 31: 14972–14983, 2011.

Chafee MV, Averbeck BB, Crowe DA. Representing spatial relationships in posterior parietal cortex: single neurons code object-referenced position. *Cereb Cortex* 17: 2914–2932, 2007.

Churchland MM, Cunningham JP, Kaufman MT, Foster JD, Nuyujukian P, Ryu SI, Shenoy KV. Neural population dynamics during reaching. *Nature* 487: 51–56, 2012.

Crowe DA, Chafee MV, Averbeck BB, Georgopoulos AP. Neural activity in primate parietal area 7a related to spatial analysis of visual mazes. *Cereb Cortex* 14: 23–34, 2004.

Crowe DA, Goodwin SJ, Blackman RK, Sakellaridi S, Sponheim SR, MacDonald AW 3rd, Chafee MV. Prefrontal neurons transmit signals to parietal neurons that reflect executive control of cognition. *Nat Neurosci* 16: 1484–1491, 2013.

Crowe DA, Zarco W, Bartolo R, Merchant H. Dynamic representation of the temporal and sequential structure of rhythmic movements in the primate medial premotor cortex. *J Neurosci* 34: 11972–11983, 2014.

Csicsvari J, Henze DA, Jamieson B, Harris KD, Sirota A, Barthó P, Wise KD, Buzsáki G. Massively parallel recording of unit and local field potentials with silicon-based electrodes. *J Neurophysiol* 90: 1314–1323, 2003.

Dotson NM, Goodell B, Salazar RF, Hoffman SJ, Gray CM. Methods, caveats and the future of large-scale microelectrode recordings in the non-human primate. *Front Syst Neurosci* 9: 149, 2015.

Evarts EV. A technique for recording activity of subcortical neurons in moving animals. *Electroencephalogr Clin Neurophysiol* 24: 83–86, 1968.

Fraser GW, Schwartz AB. Recording from the same neurons chronically in motor cortex. *J Neurophysiol* 107: 1970–1978, 2012.

Fujisawa S, Amarasingham A, Harrison MT, Buzsáki G. Behavior-dependent short-term assembly dynamics in the medial prefrontal cortex. *Nat Neurosci* 11: 823–833, 2008.

Georgopoulos AP, Lurito JT, Petrides M, Schwartz AB, Massey JT. Mental rotation of the neuronal population vector. *Science* 243: 234–236, 1994.

Georgopoulos AP, Schwartz AB, Kettner RE. Neuronal population coding of movement direction. *Science* 233: 1416–1419, 1986.

Harris KD, Henze DA, Csicsvari J, Hirase H, Buzsáki G. Accuracy of tetrode spike separation as determined by simultaneous intracellular and extracellular measurements. *J Neurophysiol* 84: 401–414, 2000.

Hatsopoulos NG, Donoghue JP. The science of neural interface systems. *Annu Rev Neurosci* 32: 249–266, 2009.

Hazan L, Zugaro M, Buzsáki G. Klusters, NeuroScope, NDManager: a free software suite for neurophysiological data processing and visualization. *J Neurosci Methods* 155: 207–216, 2006.

Jazayeri M, Shadlen MN. A neural mechanism for sensing and reproducing a time interval. *Curr Biol* 25: 2599–2609, 2015.

Kraskov A, Dancause N, Quallo MM, Shepherd S, Lemon RN. Corticospinal neurons in macaque ventral premotor cortex with mirror properties: a potential mechanism for action suppression? *Neuron* 64: 922–930, 2009.

Lebedev MA, Mirabela G, Erchova I, Diamond ME. Experience-dependent plasticity of rat barrel cortex: redistribution of activity across barrel-columns. *Cereb Cortex* 10: 23–31, 2000.

Lebedev MA, O'Doherty JE, Nicolelis MA. Decoding of temporal intervals from cortical ensemble activity. *J Neurophysiol* 99: 166–186, 2008.

Lin CP, Chen YP, Hung CP. Tuning and spontaneous spike time synchrony share a common structure in macaque inferior temporal cortex. *J Neurophysiol* 112: 856–869, 2014.

Mendez JC, Prado L, Mendoza G, Merchant H. Temporal and spatial categorization in human and non-human primates. *Front Integr Neurosci* 5: 50, 2011.

Merchant H, Bartolo R, Pérez O, Méndez JC, Mendoza G, Gámez J, Yc K, Prado L. Neurophysiology of timing in the hundreds of milliseconds: multiple layers of neuronal clocks in the medial premotor areas. *Adv Exp Med Biol* 829: 143–154, 2014a.

Merchant H, Battaglia-Mayer A, Georgopoulos AP. Neural responses during interception of real and apparent circularly moving stimuli in motor cortex and area 7a. *Cereb Cortex* 14: 314–331, 2004a.

Merchant H, Crowe DA, Fortes AF, Georgopoulos AP. Cognitive modulation of local and callosal neural interactions in decision making. *Front Neurosci* 8: 245, 2014b.

Merchant H, Crowe DA, Robertson MS, Fortes AF, Georgopoulos AP. Top-down spatial categorization signal from prefrontal to posterior parietal cortex in the primate. *Front Syst Neurosci* 5: 69, 2011a.

Merchant H, de Lafuente V, Peña F, Larriva-Sahd J. Functional impact of interneuronal inhibition in the cerebral cortex of behaving animals. *Prog Neurobiol* 99: 163–178, 2012.

Merchant H, Fortes AF, Georgopoulos AP. Short-term memory effects on the representation of two-dimensional space in the rhesus monkey. *Anim Cogn* 7: 133–143, 2004b.

Merchant H, Grahn J, Trainor L, Rohrmeier M, Fitch WT. Finding the beat: a neural perspective across humans and non-human primates. *Philos Trans R Soc Lond B Biol Sci* 370: 20140093, 2015a.

Merchant H, Honing H. Are non-human primates capable of rhythmic entrainment? Evidence for the gradual audiomotor evolution hypothesis. *Front Neurosci* 7: 274, 2014.

Merchant H, Naselaris T, Georgopoulos AP. Dynamic sculpting of directional tuning in the primate motor cortex during three-dimensional reaching. *J Neurosci* 28: 9164–9172, 2008.

Merchant H, Pérez O, Bartolo R, Méndez JC, Mendoza G, Gámez J, Yc K, Prado L. Sensorimotor neural dynamics during isochronous tapping in the medial premotor cortex of the macaque. *Eur J Neurosci* 41: 586–602, 2015b.

Merchant H, Pérez O, Zarco W, Gámez J. Interval tuning in the primate medial premotor cortex as a general timing mechanism. *J Neurosci* 33: 9082–9096, 2013.

Merchant H, Zarco W, Perez O, Prado L, Bartolo R. Measuring time with multiple neural chronometers during a synchronization-continuation task. *Proc Natl Acad Sci USA* 108: 19784–19789, 2011b.

Miller EK. The prefontral cortex and cognitive control. *Nat Rev Neurosci* 1: 59–65, 2000.

Moeller S, Freiwald WA, Tsao DY. Patches with links: a unified system for processing faces in the macaque temporal lobe. *Science* 320: 1355–1359, 2008.

Mountcastle V. The evolution of ideas concerning the function of the neocortex. *Cereb Cortex* 5: 289–295, 1995.

Mountcastle VB, Lynch JC, Georgopoulos A, Sakata H, Acuna C. Posterior parietal association cortex of the monkey: command functions for operations within extrapersonal space. *J Neurophysiol* 38: 871–908, 1975.

Mountcastle VB, Talbot WH, Sakata H, Hyvarinen J. Cortical neuronal mechanisms in flutter-vibration studied in unanesthetized monkeys: Neuronal periodicity and frequency discrimination. *J Neurophysiol* 32: 452–484, 1969.

Narselaris T, Merchant H, Amirikian B, Georgopoulos AP. Spatial reconstruction of trajectories of an array of recording microelectrodes. *J Neurophysiol* 93: 2318–2330, 2005.

Nicolelis MA, Lebedev MA. Principles of neural ensemble physiology underlying the operation of brain-machine interfaces. *Nat Rev Neurosci* 10: 530–540, 2009.

Nieder A, Miller EK. Coding of cognitive magnitude: compressed scaling of numerical information in the primate prefrontal cortex. *Neuron* 37: 149–157, 2003.

Oliveira LM, Dimitrov D. Surgical techniques for chronic implantation of microwire arrays in rodents and primates. In: *Chapter 2. Frontiers in Neuroscience. Methods for Neural Ensemble Recordings* (2nd ed), edited by Nicolelis MA. Boca Raton, FL: CRC, 2008.

Petkov CI, Kikuchi Y, Milne AE, Mishkin M, Rauschecker JP, Logothetis NK. Different forms of effective connectivity in primate frontotemporal pathways. *Nat Commun* 6: 6000, 2015.

Peyrache A, Dehghani N, Eskandar EN, Madsen JR, Anderson WS, Donoghue JA, Hochberg LR, Halgren E, Cash SS, Destexhe A. Spatiotemporal dynamics of neocortical excitation and inhibition during human sleep. *Proc Natl Acad Sci USA* 109: 1731–1736, 2012.

Quian Quiroga RQ, Panzeri S. Extracting information from neuronal populations: information theory and decoding approaches. *Nat Rev Neurosci* 10: 173–185, 2009.

Romo R, Salinas E. Flutter discrimination: neural codes, perception, memory and decision making. *Nat Rev Neurosci* 4: 203–218, 2003.

Rossant C, Kadir SN, Goodman DF, Schulman J, Hunter ML, Saleem AB, Grosmark A, Belluscio M, Denfield GH, Ecker AS, Tolias AS, Solomon S, Buzsáki G, Carandini M, Harris KD. Spike sorting for large, dense electrode arrays. *Nat Neurosci* 19: 634–641, 2016.

Royer S, Zemelman BV, Losonczy A, Kim J, Chance F, Magee JC, Buzsáki G. Control of timing, rate and bursts of hippocampal place cells by dendritic and somatic inhibition. *Nat Neurosci* 15: 769–775, 2012.

Schmidt S, Horch K, Normann R. Biocompatibility of silicon-based electrode arrays implanted in feline cortical tissue. *J Biomed Mater Res* 27: 1393–1399, 1993.

Schultz W, Romo R. Role of primate basal ganglia and frontal cortex in the internal generation of movements. I. Preparatory activity in the anterior striatum. *Exp Brain Res* 91: 363–384, 1992.

Schwartz AB. Direct cortical representation of drawing. *Science* 265: 540–542, 1994.

Schwarz DA, Lebedev MA, Hanson TL, Dimitrov DF, Lehew G, Meloy J, Nicolelis MA. Chronic, wireless recordings of large-scale brain activity in freely moving rhesus monkeys. *Nat Methods* 11: 670–676, 2014.

Seo H, Cai X, Donahue CH, Lee D. Neural correlates of strategic reasoning during competitive games. *Science* 346: 340–343, 2014.

Seo M, Lee E, Averbeck BB. Action selection and action value in frontal-striatal circuits. *Neuron* 74: 947–960, 2012.

Stark E, Abeles M. Applying resampling methods to neurophysiological data. *J Neurosci Meth* 145: 133–144, 2005.

Tolias AS, Sultan F, Augath M, Oeltermann A, Tehovnik EJ, Schiller PH, Logothetis NK. Mapping cortical activity elicited with electrical microstimulation using FMRI in the macaque. *Neuron* 48: 901–911, 2005.

Tomita H, Ohbayashi M, Nakahara K, Hasegawa I, Miyashita Y. Top-down signal from prefrontal cortex in executive control of memory retrieval. *Nature* 401: 699–703, 1999.

Vandecasteele M, MS, Royer S, Belluscio M, Berényi A, Diba K, Fujisawa S, Grosmark A, Mao D, Mizuseki K, Patel J, Stark E, Sullivan D, Watson B, Buzsáki G. Large-scale recording of neurons by movable silicon probes in behaving rodents. *J Vis Exp* 61: e3568, 2012.

Ward MP, Rajdev P, Ellison C, Irazoqui PP. Toward a comparison of microelectrodes for acute and chronic recordings. *Brain Res* 1282: 183–200, 2009.

Wu F, Stark E, Im M, Cho IJ, Yoon ES, Buzsáki G, Wise KD, Yoon E. An implantable neural probe with monolithically integrated dielectric waveguide and recording electrodes for optogenetics applications. *J Neural Eng* 10: 056012, 2013.

Wu F, Stark E, Ku PC, Wise KD, Buzsáki G, Yoon E. Monolithically integrated μLEDs on silicon neural probes for high-resolution optogenetic studies in behaving animals. *Neuron* 88: 1136–1148, 2015.

Zarco W, Merchant H, Prado L, Mendez JC. Subsecond timing in primates: comparison of interval production between human subjects and rhesus monkeys. *J Neurophysiol* 102: 3191–3202, 2009.

EJN European Journal of Neuroscience

FENS Federation of European Neuroscience Societies

European Journal of Neuroscience, Vol. 41, pp. 586–602, 2015 doi:10.1111/ejn.12811

Sensorimotor neural dynamics during isochronous tapping in the medial premotor cortex of the macaque

Hugo Merchant, Oswaldo Pérez, Ramón Bartolo, Juan Carlos Méndez, Germán Mendoza, Jorge Gámez, Karyna Yc and Luis Prado

Instituto de Neurobiología, UNAM, Campus Juriquilla, Boulevard Juriquilla No. 3001, Querétaro, Qro. 76230, México

Keywords: medial premotor areas, rhesus monkeys, sensorimotor integration, timing mechanism

Abstract

We determined the response properties of neurons in the primate medial premotor cortex that were classified as sensory or motor during isochronous tapping to a visual or auditory metronome, using different target intervals and three sequential elements in the task. The cell classification was based on a warping transformation, which determined whether the cell activity was statistically aligned to sensory or motor events, finding a large proportion of cells classified as sensory or motor. Two distinctive clusters of sensory cells were observed, i.e. one cell population with short response-onset latencies to the previous stimulus, and another that was probably predicting the occurrence of the next stimuli. These cells were called sensory-driven and stimulus-predicting neurons, respectively. Sensory-driven neurons showed a clear bias towards the visual modality and were more responsive to the first stimulus, with a decrease in activity for the following sequential elements of the metronome. In contrast, stimulus-predicting neurons were bimodal and showed similar response profiles across serial-order elements. Motor cells showed a consecutive activity onset across discrete neural ensembles, generating a rapid succession of activation patterns between the two taps defining a produced interval. The cyclical configuration in activation profiles engaged more motor cells as the serial-order elements progressed across the task, and the rate of cell recruitment over time decreased as a function of the target interval. Our findings support the idea that motor cells were responsible for the rhythmic progression of taps in the task, gaining more importance as the trial advanced, while, simultaneously, the sensory-driven cells lost their functional impact.

Introduction

The quantification of the passage of time in the hundreds of milliseconds is a critical element for complex behaviors such as the performance of sports (Merchant & Georgopoulos, 2006; Merchant *et al.*, 2009), and the execution and appreciation of music (Janata & Grafton, 2003; Phillips-Silver & Trainor, 2005). Humans have the ability to quantify intervals, defined by different sensory modalities, in a variety of perceptual or motor activities (Merchant *et al.*, 2013a). Remarkably, the temporal precision increases as a function of the number of timed intervals in a sequence (Ivry & Hazeltine, 1995; Grondin, 2001; Merchant *et al.*, 2008a). This is particularly true during the execution of isochronous taps, where the interval-timing mechanism benefits from the predictive rhythmic structure of the cyclical behavior (Merchant *et al.*, 2008b). A large amount of evidence supports the existence of a partially distributed timing mechanism, integrated by core structures such as the motor cortico-thalamic-basal ganglia circuit, and areas that are selectively engaged by different behavioral contexts (Buhusi & Meck, 2005; Coull *et al.*, 2011; Merchant *et al.*, 2011a; Stauffer *et al.*, 2012; Merchant *et al.*, 2013a). For example, neurophysiological experiments in behaving monkeys have shown that neurons in the medial premotor cortex (MPC) (pre-supplementary motor area and supplementary motor area proper) are tuned to the duration of intervals during isochronic tapping (Merchant *et al.*, 2013b; Bartolo *et al.*, 2014). Thus, the fact that a subgroup of these interval-tuned neurons showed similar preferred intervals across modalities and during tasks involving the production of one or multiple intervals corroborates the hypothesis that the MPC is part of the core timing mechanism. Furthermore, a gain mechanism for the encoding of the total number of produced intervals in a sequence has been documented, where the discharge rate for the preferred interval of tuned cells increases for larger numbers of produced intervals (Merchant *et al.*, 2013b). Accordingly, functional imaging studies in humans showed that the execution of complex rhythmic sequences produces higher activity in the MPC than isochronous movements (Dhamala *et al.*, 2003; Bengtsson *et al.*, 2005).

The synchronisation-continuation task (SCT) has been a pivotal paradigm in the study of time production. In this task, subjects synchronise taps with pacing isochronous brief stimuli and then continue tapping at the instructed rate without the advantage of the sensory metronome (Wing, 2002). In order to synchronise their responses in the initial part of this task, subjects not only need to attend to the pacing stimuli and generate a predicted sequence of sensory events, but also to produce a predictive tapping behavior with a particular temporal and sequential structure. This phase of the task also requires the recognition and correction of errors between the incoming and predicted sensory events and the actual tapping sequence (Lewis *et al.*, 2004). The neural substrate of these

Correspondence: Dr Hugo Merchant, as above.
E-mail: hugomerchant@unam.mx

Received 25 August 2014, accepted 26 November 2014

processes is unknown. Therefore, the present article provides the first neurophysiological evidence in the MPC regarding the dynamic processing of sensory signals, sensorimotor transformations, and motor commands during isochronous tapping to a sensory metronome.

Materials and methods

General

All of the animal care, housing, and experimental procedures were approved by the National University of Mexico Institutional Animal Care and Use Committee and conformed to the principles outlined in the Guide for Care and Use of Laboratory Animals (NIH, publication number 85-23, revised 1985). The two monkeys (*Macaca mulatta*, both males, 5–7 kg body weight) were monitored daily by the researchers and the animal care staff to check their conditions of health and welfare.

Synchronisation-continuation task

The SCT has been described in detail previously (Zarco *et al.*, 2009; Merchant *et al.*, 2011a). Briefly, on each trial the monkey tapped a button seven times in succession, with the goal of maintaining a constant inter-tap interval across all taps. The first four taps were made synchronously with a repetitive cue stimulus (either a visual stimulus presented on a computer monitor or an auditory tone via speakers). The monkey then had to tap the button three more times with the same inter-tap duration but without sensory guidance (continuation phase) (Fig. 1A). Hence, this task had six serial-order elements, three in the synchronisation phase and three in the continuation phase. Five different target intervals were used: 450, 550, 650, 850, and 1000 ms. During the recording of each group of cells (one 'set'), the monkey performed five repetitions of each target interval (for a total of 25 trials), with durations randomly ordered within each repetition. Trials were separated by an inter-trial interval of 1.2–4 s.

Neural recordings

The extracellular activity of single neurons in the medial premotor areas was recorded using a system with seven independently movable microelectrodes (Merchant *et al.*, 2001) (1–3 MΩ, Uwe Thomas Recording, Germany). All of the isolated neurons were recorded regardless of their activity during the task, and the recording sites changed from session to session. At each site, raw extracellular membrane potentials were sampled at 40 kHz. Single-unit activity was extracted from these records using an off-line sorter (Plexon, Dallas, TX, USA). Structural magnetic resonance imaging (MRI) was used to localise the recording sites (Merchant *et al.*, 2011a). An initial ANOVA using the discharge rate during the key holding (control) period as dependent variable, and the recording time across all trials of the SCT as a factor was performed for each neuron to identify cells whose activity changed significantly during the recording. A significant variation of the baseline rate across trials was taken to indicate instability of the cell's task responsiveness, and therefore these cells were excluded from further analyses. It is important to clarify that the 1083 cell database used in the present article has

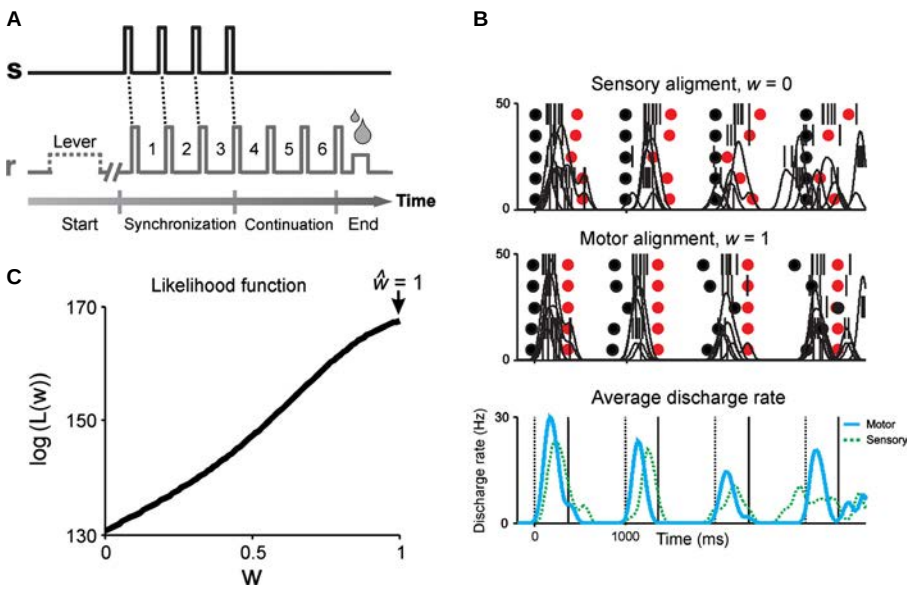

FIG. 1. Task and time-warping analysis. (A) The SCT. Monkeys were required to push a button (r, gray line) each time that stimuli with a constant inter-stimulus target interval (s, black line) were presented, which resulted in a stimulus–movement cycle. After four consecutive synchronised movements, the stimuli stopped, and the monkeys continued tapping with a similar target interval for three additional intervals. Hence, six inter-tap intervals were generated by the monkeys in each trial. The instructed durations, defined by brief auditory or visual stimuli, were 450, 550, 650, 850, and 1000 ms, and were chosen pseudo-randomly within a repetition. (B) The cell activity during the synchronisation of the SCT was used to determine whether the activity of the cell was better aligned to sensory or motor events using the time-warping analysis. Simulated spike trains of a motor cell during the synchronisation phase of the SCT are shown. Top: Raster plot of the simulated activity aligned to the stimulus presentations (black circles) with an inter-stimulus interval of 1000 ms, where every tick mark corresponds to a single spike time stamp and the spike density functions for each trial are shown as a black line. Middle: The same responses as shown at the top, but aligned to the button press (red circles) using the transformation in eqn 1. Bottom: The average spike density function (eqn 3) is shown for the sensory (continuous blue line) or motor (dotted green line) alignments. The black vertical dotted lines correspond to the stimulus time events, whereas the vertical continuous lines correspond to the warping motor events. (C) The logarithm of the homogeneity measure log($L(w)$), computed from eqn 5, is plotted as a function of the warping value. The larger warping value ($\hat{w}$) is equal to 1.

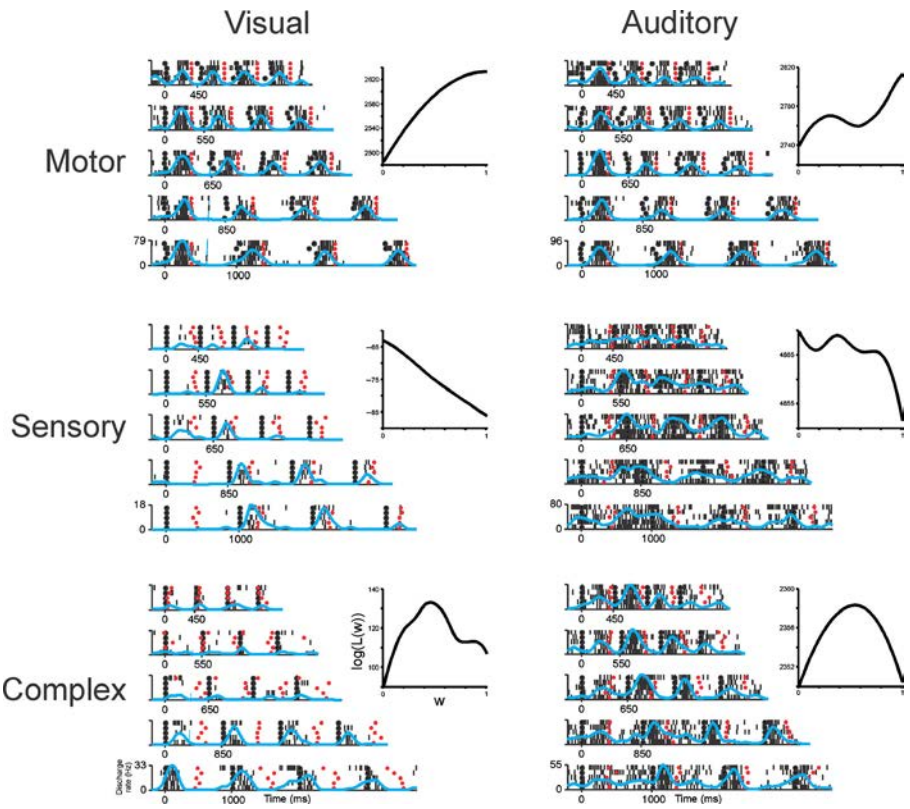

FIG. 2. The raster plots of the activity of cells classified in the time-warping analysis as motor (top), sensory (middle), or complex (bottom) for the visual and auditory conditions. Every tick mark corresponds to a single spike time stamp in a correct trial. The spike density function averages (blue line) are below each raster. The black circles represent the stimulus presentation and the red circles represent the button press. The five target intervals are shown. Motor cells are aligned to the button press, whereas sensory and complex cells are aligned to the stimuli. The insets show the logarithm of homogeneity measure log ($L(w)$) as a function of w. For each neuron, the larger warping value ($\hat{w}$) is equal to 1 for the motor, equal to 0 in the sensory, and close to 0.5 in the complex cells.

been analysed previously in other conceptual contexts (Merchant *et al.*, 2011a, 2013b).

Identification of recording locations

We determined the position of the recording sites relative to the brain sulci using structural MRI. Custom-made plastic tubes filled with an aqueous solution of vitamin E ran through the perimeter and center of the recording chamber and were employed as fiducial objects to localise the recording chamber relative to the anatomical landmarks in an MRI volume. Monkeys were sedated throughout the image-acquisition procedure using a mixture of ketamine (10 mg/kg) and xylazine (0.25 mg/kg), and placed in an MRI-compatible stereotaxic apparatus. The scan parameters were as follows: a high-resolution T1-weighted gradient echo sequence was acquired [repetition time (TR), 20 ms; echo time (TE), 6.9 ms; flip angle, 25°; matrix, 240 × 108; slices, 80; resolution, 1.0 × 1.0 × 1.0 mm; coronal slices, acquisition time, 5 min 24 s] with a 1.0 T Philips Intera MRI Scanner. Images were transferred to a workstation in the laboratory for further analysis using MRICRO[2] (Rorden *et al.*, 2007) and IMAGEJ (http://rsbweb.nih.gov/ij/; developed by Wayne Rasband, National Institutes of Health, Bethesda, MD, USA).

Once we identified the center of the recording chamber for the two monkeys in relation to the brain sulci, we placed the approximate recording locations inside the chamber, based on the location description for each recording penetration from our experimental protocols. Hence, considering this last point and the fact that the functional MRI resolution was 1 mm, it is important to emphasise that the reported recording locations (depicted in Fig. 3) are only approximations of the real recording locations.

Data analysis

Selection of significant cells

We selected for further analysis those cells whose firing rates were significantly related to either the serial order or target interval, using a two-way ANOVA that included as factors the serial order, target interval, and serial order × target interval interaction. Cells were included if their activity was significantly related to the serial order and/or target interval in this ANOVA at a threshold of $P < 0.05$. Of the 1083 cells, 607 and 540 cells met this inclusion criterion for the visual and auditory conditions, respectively, and were used in the subsequent analyses. It is important to emphasise that all of the analyses were carried out only during the synchronisation phase of the SCT.

Identification of sensory and motor neurons – time-warping analysis

We previously proposed a warping transformation (Perez *et al.*, 2013) to determine whether the activity of a cell was better aligned to sensory or motor events during the synchronisation phase of the SCT. We defined the time of sensory events as the instant in which

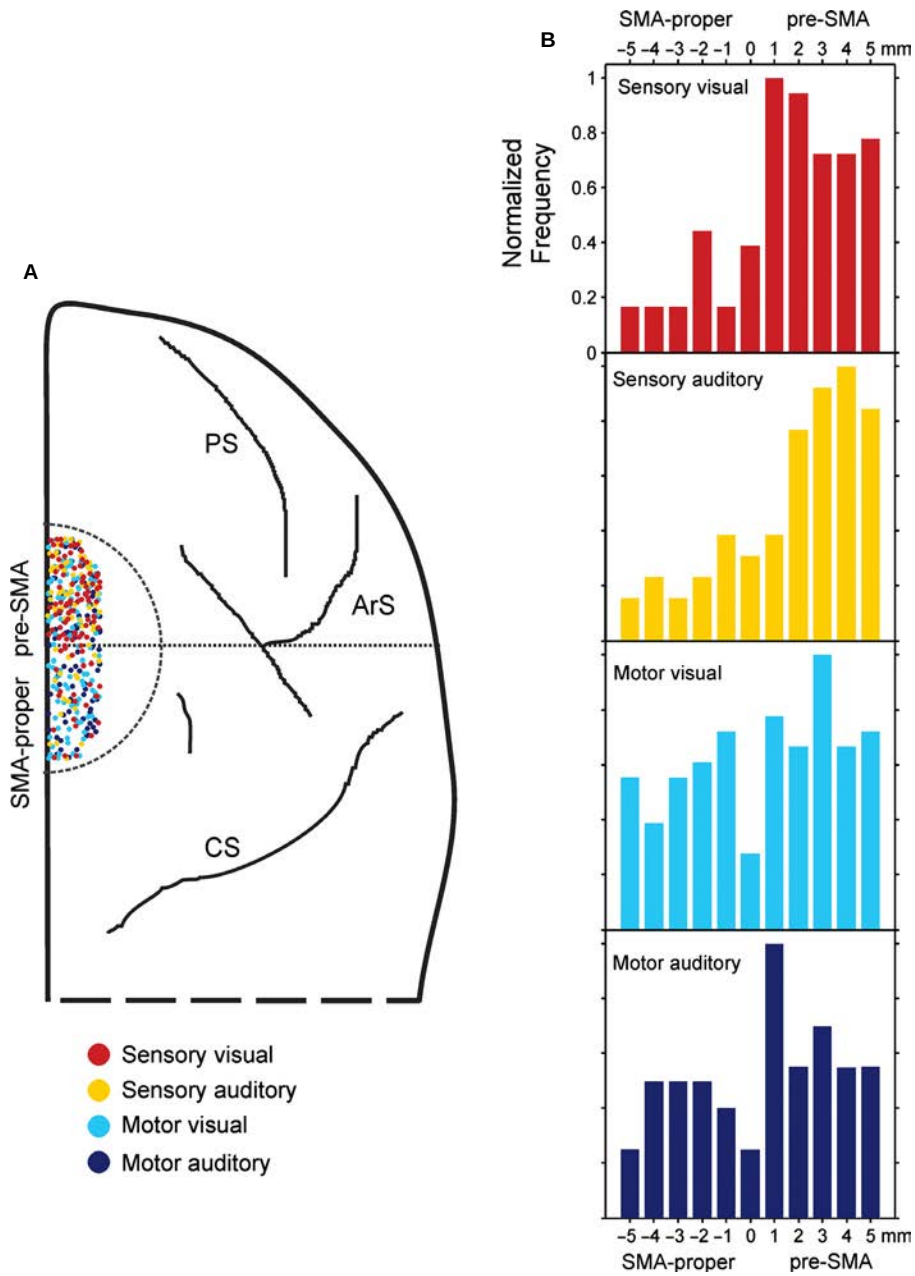

FIG. 3. Top view of the medial premotor areas and the location of different cell types. (A) MRI surface reconstruction of macaque brain and recording sites in the two monkeys. Colored dots correspond to the cell types as in the key below. PS, principal sulcus; ArS, arcuate sulcus; CS, central sulcus; surface bounded by a semicircle, recording area and MPC. The line dividing the circle corresponds to the hypothetical division between the SMA proper (caudal) and pre-SMA (rostral). (B) Frequency histograms of the distribution of the different cell types in the two medial premotor areas. The data from the two monkeys were similar and were pooled in this figure.

the auditory or visual stimulus was presented. The time of motor events was defined as the moment in which the monkey tapped on the button. The goal of this analysis was to find the cell alignment that produced the smallest inter-trial variability (Fig. 1B). The method had the following steps:

(1) The action potential times $\{t_{i,j}\}$ were initially aligned to the stimulus times $\{S_{i,1}, S_{i,2}, S_{i,3}, S_{i,4}\}$, where i corresponds to the trial repetition and j to the spike number. In addition, we defined the following transformation in order to align the action potential times $\{t_{i,j}\}$ to the motor events $\{M_{i,1}, M_{i,2}, M_{i,3}, M_{i,4}\}$

$$T_i(t) = \frac{L_{j+1} - L_j}{M_{i,j+1} - M_{i,j}}\left(t - M_{i,j}\right) + L_j \qquad (1)$$

when $M_{i,j} \le t \le M_{i,j+1}$ and $\{L_1, L_2, L_3, L_4\}$ were landmark references. L_1 was the average reaction time of the monkeys for the first stimulus during cell recordings, whereas L_2 to L_4 were defined as the target intervals (i.e. 450, 550, 650 ms, etc.). This transformation was performed for each trial across the five target intervals in the SCT.

(2) The warping transformation was

$$T_w^i(t) = wT_i(t) + (1-w)t \tag{2}$$

that depended on the parameter w. When $w = 0$ the responses were aligned to the sensory events S. When $w = 1$ the responses were aligned to the motor events M. w values between 0 and 1, in steps of 0.1, produced alignments between S and M events.

(3) The average spike density function $r_w(t)$ for every target interval across trials was computed using the following equation for a particular w.

$$r_w(t) = \frac{1}{N}\sum_{i=1}^{N}\sum_{j=1}^{n_i}\frac{1}{\sqrt{2\pi}\sigma}e^{-\frac{(t-T_w^i(t_{ij}))^2}{2\sigma^2}} \tag{3}$$

where n_i is the total number of action potentials in a trial i, N is the total number of trials, and the Gaussian kernel width σ =20 ms.

(4) The likelihood function representing the multi-trial response variability of a cell, for a particular w alignment, was calculated assuming that $D_i = \{t_{i,1}, t_{i,2}, \ldots, t_{i,n_i}\}$, the times of n_i spikes in trial i, is a non-homogeneous Poisson process with rate $r_w(t)$

$$L_i(w) = p(D_i|w) = e^{-\int_0^T r_w(t)dt}\prod_{j=1}^{n_i} r_w(t_{i,j}) \tag{4}$$

As the likelihood function represents the multi-trial response variability of a cell using the average spike density function, we used a leave-one-out cross-validation method to determine the variability of trial i from the average firing rate. Then, for every neuron, we computed the total probability that was the product of $L_i(w)$ for every trial i and for each of the five target intervals *Int*

$$L(w) = \prod_{Int}\prod_{i} L_i(w) \tag{5}$$

Finally, we found the w that maximised the function $L(w)$, which corresponds to the value that maximises the spike prediction accuracy across trials and was called the warping value ($\hat{w}$) (see Fig. 1C). Consequently, this measure is associated with the warping value that minimises the inter-trial variability of the cell activity.

Bayes factors

The warping transformation finds the best-fitting alignment of a cell. However, it is important to determine the probability of assigning a particular warping value to a sensory or motor alignment. Let D be the set of all spike times of a neuron across trials and target intervals. For cell i we have

$$\begin{aligned} p(D|sensory) &= L(0) \\ p(D|motor) &= L(1) \\ p(D|complex) &= \int_0^1 L(w)dw \end{aligned} \tag{6}$$

We then define the following Bayes factors

$$\gamma_1 = log_{10}\left(\frac{p(D|motor)}{p(D|sensory)}\right)$$

$$\gamma_2 = log_{10}\left(\frac{p(D|motor)}{p(D|complex)}\right)$$

$$\gamma_3 = log_{10}\left(\frac{p(D|sensory)}{p(D|complex)}\right) \tag{7}$$

These factors summarise the evidence provided by the data in favor of one category, i.e. motor (if $\gamma_1 > 0$ and $\gamma_2 > 0$), sensory (if $\gamma_1 < 0$ and $\gamma_3 > 0$), and complex (if $\gamma_2 < 0$ and $\gamma_3 < 0$). We classified the cells in three different categories based on this information as follows: motor neuron if $\gamma_1 > 1$ and $\gamma_2 > 1$, sensory neuron if $\gamma_1 < -1$ and $\gamma_3 > 1$, and complex neuron if $\gamma_2 < -1$ and $\gamma_3 < -1$. Cells that did not meet any of the criteria for classification were considered indeterminate. Therefore, the γ thresholds used in the present article (a value larger than 1) provide strong evidence in favor of a particular cell category, according to Kass & Raftery (1995). The warping analysis was performed independently for the cell recordings in the auditory and visual SCT conditions.

Identification of cell activation periods – Poisson-train analysis

For the cells classified as sensory or motor by the time-warping analysis, we used the Poisson-train analysis (Hanes *et al.*, 1995) to identify the periods of cell activation within each interval defined by two subsequent stimuli (sensory cells) or two subsequent taps (motor cells). This analysis determines how improbable it is that the number of action potentials within a specific condition (i.e. target interval and ordinal sequence) was a chance occurrence. For this purpose, the actual number of spikes within a time window was compared with the number of spikes predicted by the Poisson distribution derived from the mean discharge rate during the entire recording of the cell. The measure of improbability was the surprise index (*SI*) defined as

$$SI = -logP \tag{8}$$

where P was defined by the Poisson equation

$$P = e^{-rT}\sum_{i=n}^{\infty}\frac{(rT)^i}{i!} \tag{9}$$

and where P is the probability that, given the average discharge rate r, a spike train of a produced interval T contains n or more spikes in a trial. Thus, a large *SI* indicates a low probability that a specific elevation in activity was a chance occurrence (Merchant *et al.*, 2001). This analysis assumes that an activation period is statistically different from the average discharge rate r, considering that the firing of the cell is following a non-homogenous Poisson process (see also Perez *et al.*, 2013).

The spike-train analysis was applied grouping all trials of the three intervals of the synchronisation phase in the SCT (15 intervals, five duration × three intervals in the sequence). We used the algorithm (Hanes *et al.*, 1995) to detect activations above randomness, as described previously (Merchant *et al.*, 2001, 2013b). Briefly, the mean discharge rate (r) was computed for the entire recording session of the cell (i.e. the SCT in the auditory and visual conditions). The first two consecutive spikes that had a mean discharge rate greater than or equal to r were found, and the time between these two spikes was defined as the initial T value. The next spike was then identified and the inter-spike interval between this and the previous spike was added to T. The corresponding *SI* was calculated. This was repeated until the end of the spike train and the spike at the end of the interval T with the maximum *SI* was defined as the end of the burst. Next, the *SI* was calculated for the interval T from

the last to the first spike. The spikes from the beginning were then removed until the end of the spike train, computing the corresponding *SI* in each step. The spike at which *SI* was maximised was defined as the beginning of the burst. All produced intervals that showed a burst larger than 80 ms and an *SI* $P < 0.01$ were considered as having a significant activation. If this criterion was not fulfilled, it was assumed that there was no response for that target duration/ordinal sequence combination. Consequently, the Poisson-train analysis provides the response-onset latency and the extent of the activation period for each cell in a particular combination of target interval/serial order.

Normal distribution analysis

The time-varying changes in activation periods identified with the Poisson-train analysis showed a clear progressive pattern of responses in the motor cell population, where groups of neurons formed functional ensembles that encode information of the SCT during small time windows. The sequential patterns of activation of different neural ensembles showed different dynamics, with distinct rates of cell activation profiles across target intervals and serial order. Hence, we characterised the overall population change in activity as a function of time using an elliptical bivariate normal distribution illustrated in Fig. 9A and B. In this figure, the ellipse is centered at the *x*–*y* mean, where *x* is time aligned to the button press, and *y* is the order of the cells' activation. The activation order was computed by sorting (from minimum to maximum) the mean onset latency (across duration and serial order) of all of the cells with activation periods in the Poisson-train analysis. The lengths of the ellipse axes are proportional to the square root of the two eigenvalues of the *x*–*y* variance–covariance matrix. The two axes are orthogonal, and are equivalent to the variances along each axis (i.e. the larger axis corresponds to the axis of larger variance). We scaled the axis using the constant $x_p^2(\alpha)$, which corresponds to the upper (100α)th percentile of the Chi-squared distribution with *k* degrees of freedom. This leads to an ellipse that contains the $(1 - \alpha) \times 100\%$ of the distribution probability, where $\alpha = 0.8$ (Fig. 9A and B). Finally, the orientation of the ellipse was defined by the angle θ that was equal to the arctangent of the *x* and *y* elements of the eigenvector from the larger eigenvalue (Merchant *et al.*, 2004c). Importantly, this angle determines the rate of information flow in the cell population over time.

Results

Behavioral performance

The activity of MPC neurons was recorded in two monkeys during the performance of a SCT (Fig. 1A), where the animals tapped a button in time with four evenly-spaced visual or auditory stimuli (synchronisation phase) and then continued to tap three more times with same duration (continuation phase). Thus, the task had six serial-order elements, three for each phase. Five instructed inter-tap durations (target intervals) were used: 450, 550, 650, 850, and 1000 ms. Monkeys were able to accurately produce the instructed intervals, showing an average underestimation of ~50 ms across durations in the SCT (Merchant *et al.*, 2013b). The temporal variability of the monkeys' tapping performance (defined as the SD of the individual inter-response intervals) increased linearly as a function of duration. Hence, the monkeys showed appropriate temporal performance in the SCT (Zarco *et al.*, 2009; Merchant & Honing, 2014).

Time-warping analysis – classification of sensory and motor neurons

The main purpose of the present study was to determine the response profiles of cells classified as sensory or motor by the time-warping analysis during the synchronisation phase of the SCT. This phase of the task included a sequence of sensory and motor events. We developed a transformation that allowed us to align spike times to all of the push-button events in a trial (Perez *et al.*, 2013) (see Materials and methods). This transformation depends on a parameter *w* that can acquire values between 0 and 1. When $w = 0$, spikes are completely aligned to the stimuli, as the original data. An example of this alignment is shown for simulated spike trains in Fig. 1B top (black circles). Conversely, when $w = 1$, spike trains are aligned to the motor events, as shown in Fig. 1B middle (red circles). Obviously, when responses were given intermediate *w* values, they were aligned between sensory and motor events, and were considered complex cells. In order to find which *w* value was the best to minimise the inter-trial variability for a given cell, we used a homogeneity measure, *L*, whose value is inversely proportional to this variability. Figure 1B bottom shows that, when the spike times in the top panels are aligned to the motor event, the average spike density functions acquire larger values than when aligned to sensory events, which indicates that the cell responses show less inter-trial variability in the former alignment. In accordance with this, Fig. 1C shows the $log(L(w))$ as a function of *w* for simulated spike trains shown in Fig. 1B, where it can be seen that the highest probability is reached when $\hat{w} = 1$. This means that the best alignment for the activity of this simulated cell was to motor events.

We performed the time-warping analysis in 607 cells in the visual condition and 540 cells in the auditory condition of the SCT. These cells showed significant changes in their activity as a function of the serial order and/or target interval in a two-way ANOVA (see Materials and methods). Representative examples for cells classified by the time-warping analysis as sensory, motor, and complex for the auditory and visual conditions are depicted in Fig. 2.

In addition, $log(L(w))$ as a function of *w* are illustrated in Fig. 2 as an inset in each raster, where motor cells showed the highest probability at $\hat{w} = 1$, sensory cells at $\hat{w} = 0$, and complex cells at $\hat{w} \sim 0.5$. In order to determine how strong was the evidence in the *L* probabilities in favor of one of the response categories illustrated in Fig. 2, we used an additional analytical algorithm called the Bayes factors (γ) (described in eqn 6 and 7). Using the criteria provided by Kass & Raftery (1995) we classified each cell into the three categories using the following γ thresholds: motor when $\gamma_1 > 1$ and $\gamma_2 > 1$, sensory when $\gamma_1 < -1$ and $\gamma_3 > 1$, and complex when $\gamma_2 < -1$ and $\gamma_3 < -1$. Otherwise, the cells were categorised as indeterminate.

The results of the Bayes factors analysis on our database, depicted in Table 1, shows that most of the neurons [309/607 (51%) for the visual and 259/540 [48%] for the auditory condition] recorded in the MPC during the synchronisation phase of the SCT were classified as motor. Nevertheless, a large percentage of cells were also classified as sensory (see Table 1). These findings suggest that the medial premotor areas not only showed a motor response component, but they also processed the visual and auditory information used as a metronome in a rhythmic tapping task. Note, however, that the classification was performed using only the inter-trial cell response consistency to the stimuli or tap events. We did not identify the visual or auditory receptive fields of cells, nor the cells' responses induced by joint manipulation, muscle tapping, or cutaneous stimulation.

TABLE 1. Number (and percentage) of cells that were classified as motor, sensory, complex and undetermined based on their γ values

Cell type	Visual	Auditory
Sensory	185 (30.5)	137 (25.4)
Complex	9 (1.5)	19 (3.5)
Motor	309 (50.9)	259 (48)
Undetermined	104 (17.1)	125 (23.1)
Total	607 (100)	540 (100)

We determined the position of the recording sites along the medial premotor areas relative to the brain sulci, using structural MRI (see Materials and methods). This analysis was carried out in order to test whether the cells classified as sensory in the present study showed a bias towards the pre-SMA, whereas motor cells showed a bias towards the SMA proper, as classical neurophysiological studies have previously demonstrated (Matsuzaka *et al.*, 1992). The results are shown in Fig. 3, where it is evident that cells classified as sensory in the visual and auditory conditions were mainly located in the pre-SMA, with a significant difference in their spatial distribution between the SMA proper and pre-SMA [visual: χ^2 test (1) = 6.4, $P = 0.011$; auditory: χ^2 test (1) = 7.3, $P = 0.007$]. Nevertheless, the cells classified as motor also showed a slight location bias towards the pre-SMA, with marginal differences between the two medial premotor areas [visual: χ^2 test (2.8) = 2.9, $P = 0.09$; auditory: χ^2 test (1) = 2.99, $P = 0.084$]. It is important to emphasise that the recording locations shown in Fig. 3 are approximated maps with a coarse spatial resolution (see Materials and methods). The proper spatial reconstruction of microelectrode trajectories requires the use of electrolytic lesions or coating the electrodes with a fluorescent dye, followed by the use of anatomical techniques in the postmortem tissue that allow the localisation of the lesions or fluorescent tracks (Matsuzaka *et al.*, 1992; Merchant *et al.*, 1997; Naselaris *et al.*, 2005). Unfortunately, we were not able to perform either of these methods in the present study.

Poisson-train analysis – finding the response profile of each cell

The response profile of each cell with respect to the stimuli or tapping movements was determined using the Poisson-train analysis, on the cells classified as sensory or motor in the previous time-warping section. This analysis determines how improbable it is that the number of action potentials within a specific time interval is a chance occurrence. For this purpose, the actual number of spikes within a time interval was compared with the number of spikes predicted by the Poisson distribution derived from the mean discharge rate across all conditions (see Materials and methods). Thus, the Poisson-train analysis essentially finds the response-onset latency and the extent of the periods of activation within each interval defined by two subsequent stimuli (sensory cells) (see Fig. 4) or two subsequent taps (motor cells) during the synchronisation phase of the SCT. In order to determine activation periods before and after each event, the Poisson-train analysis was carried out at 100 ms before the first event (stimulus or tap) and at 100 ms after the second event. Figure 5A shows the activation profiles of all sensory cells in the visual condition, where each row is associated with one neuron and the onset and extent of each activation period are illustrated as a horizontal line for the second serial-order element of the synchronisation phase and the 850 ms target interval. The cells were ordered according to their mean response-onset latency to the previous stimulus across all target intervals and serial-order elements. The Poisson-train analysis is quite stringent and only cells with consistent responses show significant activation periods. Consequently, the number of sensory and motor cells with significant activation periods is smaller than the original cells from the time-warping analysis, as shown in Table 2. It is crucial to emphasise that some cells, particularly in the sensory population, showed significant activation periods during both the visual and auditory conditions (audio-visual cells in Table 2). This result suggests that there was a small partial overlap in the sensory cell population processing the two modalities.

Visual and auditory responses – sensory-driven and stimulus-predicting activity

It is evident that the group of cells at the top of Fig. 5A showed shorter onset latencies than the cell group at the bottom. We used a hierarchical clustering analysis on the response-onset latencies of all of the cells, using the data for the second serial-order element of the synchronisation phase of the target interval of 850 ms (see Merchant *et al.*, 2003; Merchant & Georgopoulos, 2006). The results, shown in the dendrogram of Fig. 5B, indicate the existence of two large cell clusters (similar clustering was obtained using the other target intervals and serial-order elements). However, the hierarchical clustering is a descriptive method and therefore we used an algorithm using the expectation-maximisation clustering method on the mean response-onset and response-offset latencies across conditions. The expectation-maximisation was performed iteratively to obtain the

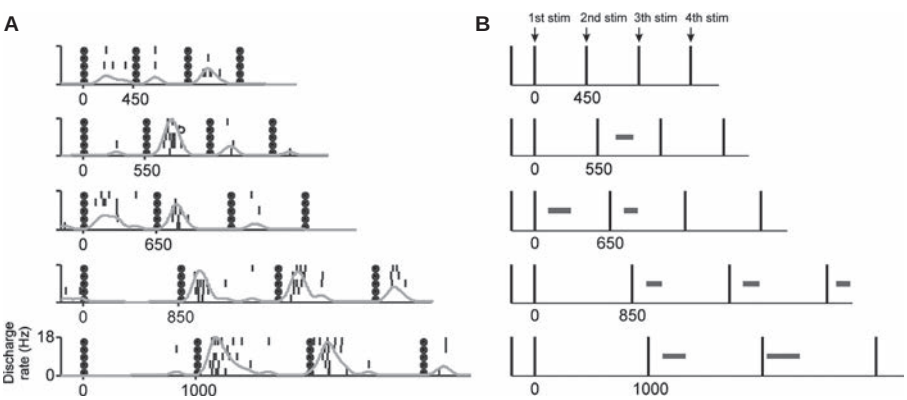

FIG. 4. Poisson-train analysis. (A) Raster plot of the activity of the cell shown in Fig. 2 and classified as sensory in the visual condition. Conventions as in Fig. 2. (B) Activation periods from the cell responses showed in A computed with the Poisson-train analysis.

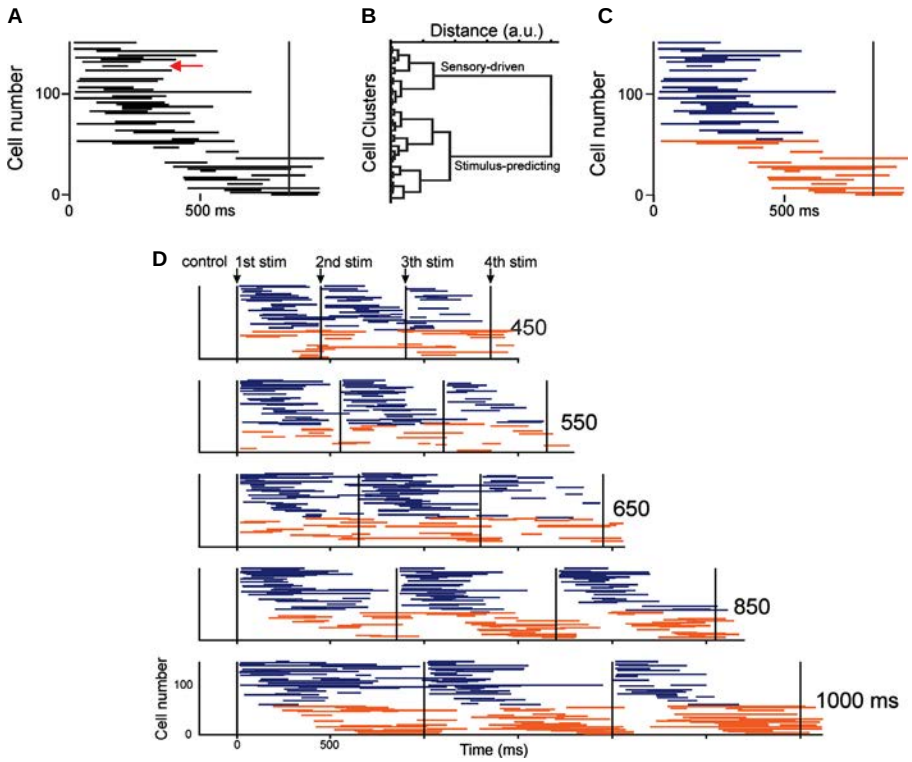

FIG. 5. Response profiles of sensory cells. (A) Response profiles for the cells with significant activation effects in the Poisson-train analysis. Each row is associated with one neuron and the onset and extent of each activation period are illustrated as a horizontal black line for the second serial-order element of the synchronisation phase and the 850 ms target interval. The red arrow is pointing at the visual sensory cell shown in the raster of Fig. 2. The black vertical lines correspond to the stimulus presentation. (B) Dendrogram of the hierarchical clustering using the response-onset latencies in A. The sensory-driven and stimulus-predicting large branches are specified. (C) The same activation profiles as in A are divided by the expectation-maximisation clustering results (see text for details). The blue color is for the sensory-driven cells and the orange for the stimulus-predicting cells. (D) Activation profiles of all of the sensory neurons across target intervals and serial-order elements of the synchronisation phase of the SCT in the visual condition. Again, the blue color is for the sensory-driven cells and the orange for the stimulus-predicting cells. a.u., arbitrary unit.

TABLE 2. Number of sensory and motor cells with consistent activation periods in the Poisson-train analysis

Cell type	Visual	Auditory	Audiovisual
Sensory	154	111	27
Motor	224	204	82

best clustering model using the Bayesian information criterion, testing different numbers of clusters and initial centroid and variance values. The best results were obtained with two clusters and the outcome is shown in Fig. 5C. One population of cells showed short response-onset latencies to the first stimulus (similar to the response to stimuli in sensory areas) and were therefore called sensory-driven neurons (Fig. 5C, blue). The other cell cluster was integrated by cells with long response onsets and with activity profiles that were probably predicting the occurrence of the next stimuli, instead of responding to the previous stimulus. This last group of cells was called stimulus-predicting neurons (Fig. 5C, orange).

We subsequently used the clustering outcome of Fig. 5C to identify the population response profile across all target intervals and serial-order elements. The results of this analysis are shown in Fig. 5D, where it is evident that the sensory-driven neurons showed similar activation profiles across target intervals and serial-order elements, whereas the stimulus-predicting neurons showed clear changes across target intervals. Interestingly, the sensory-driven neurons showed a significant decrease in the number of active cells as a function of the serial-order element [χ^2 test (2) = 12.1, $P = 0.002$], and a larger number of active cells in the visual than the auditory conditions [χ^2 test (1) = 9.9, $P = 0.002$] (see Fig. 6). In contrast, the number of active sensory-driven cells did not change as a function of target duration [χ^2 test (4) = 1.2, $P = 0.88$]. However, stimulus-predicting neurons did not show significant changes in the number of active cells as a function of the serial-order element [χ^2 test (2) = 0.7, $P = 0.7$], or between modalities [χ^2 test (1) = 0.99, $P = 0.32$], but showed a significant increase as a function of target duration [χ^2 test (4) = 23.1, $P < 0.0001$] (Fig. 6). These results suggest, first, that the sensory-driven neurons were more responsive to the first stimulus, and as the synchronisation phase was progressing to enter the internally-driven continuation phase, the cells were less engaged in responding to the incoming stimuli. On the contrary, the stimulus-predicting neurons were similarly engaged across serial-order elements. Second, sensory-driven neurons showed a clear bias toward the visual modality, in accordance with previous findings showing the bias of monkeys to process visual stimuli to guide their motor behavior (Zarco *et al.*, 2009; Nagasaka *et al.*, 2013; Honing & Merchant, 2014), whereas the number of activated stimulus-predicting neurons did not change across modalities. Finally, the target duration did not affect the number of active sensory-driven cells, but induced an increase in responding stimulus-predicting neurons, supporting the predictive nature of the latter group of cells, as there is an increase in expectation as time passes (Janssen & Shadlen, 2005).

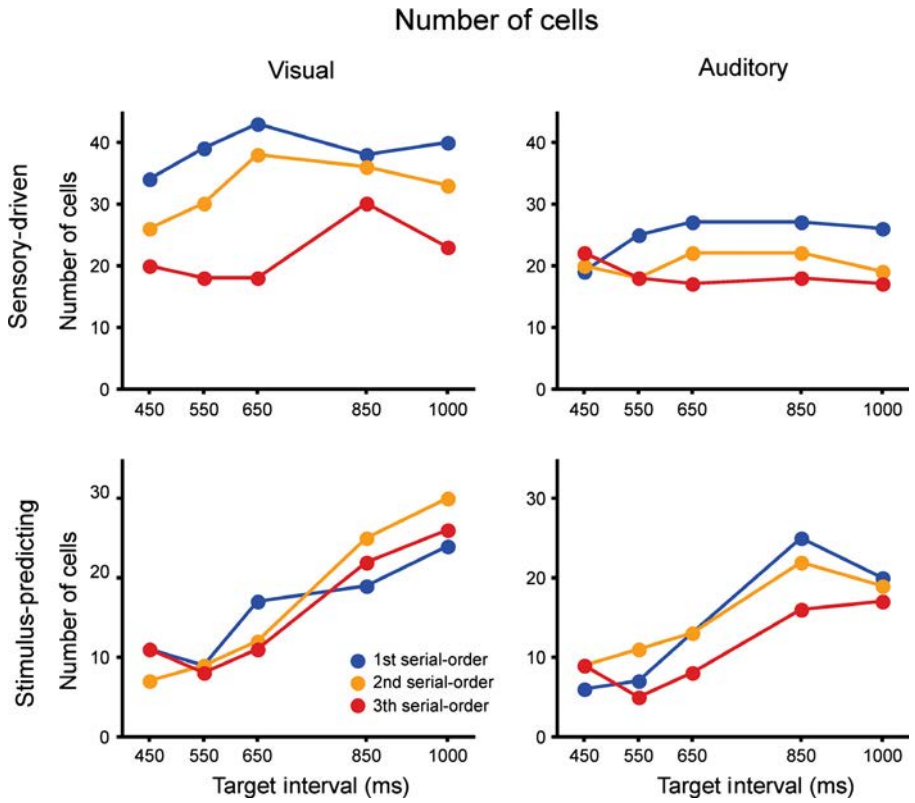

FIG. 6. Plots of the number of cells with significant effects in the Poisson-train analysis as a function of the target interval, and the serial-order element (color code in the inset), for the sensory-driven and stimulus-predicting cells, and for the visual and auditory conditions.

In addition, we performed an ANOVA where the target interval, serial order, and modality were the factors, and the dependent variable was the response-onset latencies with respect to the previous stimulus (Fig. 7). For the sensory-driven neurons, the ANOVA only showed a significant main effect for serial order ($F_{2,787} = 12.4$, $P < 0.0001$), with shorter latencies for the second and third elements of the serial order. It is notable that no differences were found in the response-onset latencies between modalities, indicating that the MPC has access to visual and auditory information at similar times from the presentation of a stimulus. The ANOVA for stimulus-predicting neurons showed significant main effects for serial order ($F_{2,398} = 4.63$, $P = 0.01$) (with shorter latencies for the second and third elements of serial order) and target interval ($F_{4,398} = 23.4.2$, $P < 0.0001$) (with a monotonic increment in onset latencies as a function of interval), but not modality ($F_{1,398} = 1.8$, $P = 0.18$). Finally, an additional ANOVA showed significant differences in response-onset latencies between sensory-driven and stimulus-predicting cells ($F_{1,1220} = 440$, $P < 0.0001$), where the former showed shorter response onsets.

We also analysed the response-onset latencies with respect to the next stimulus (Fig. 8). The results showed a significant strong linear increase in response latencies as a function of target interval for the sensory-driven cells ($F_{4,804} = 295.1$, $P < 0.0001$). This finding corroborates the idea that sensory-driven cells were tied to the previous stimulus with constant response-onset latencies to the previous stimulus and linearly varying latencies to the next stimulus as a function of target interval. In contrast, the response-onset latencies to the next stimulus showed a smaller increment as a function of target interval in stimulus-predicting cells. Although in this case the ANOVA also showed a significant main effect for target interval ($F_{4,415} = 30.7$, $P < 0.0001$), the slope of the linear regression between the response latencies to the next stimulus and the target interval was significantly larger in sensory-driven (mean slope 0.98, $R^2 = 0.61$) than in stimulus-predicting (mean slope 0.48, $R^2 = 0.2$) cells (Fig. 8) in an ANOVA analysis (see Zar, 1999) ($F_{1,702} = 17.5$, $P < 0.0001$). Therefore, the response onset of stimulus-predicting cells was probably dictated by an interaction between the duration of the activation profile associated with the increase in expectation as time passes, and the onset of the prediction process linked to the next stimulus presentation.

Overall, these analyses support the notion of two populations of sensory cells, one responding to the incoming sensory information when it is used to drive the periodic tapping of the monkeys, and another that predicts the appearance of the next stimulus in a rhythmic sequence of sensorimotor events.

Motor responses – a coordinated gradient of activation profiles

There was a gradual and dynamic profile in the onset–offset of the activation patterns of motor cells. Figure 9A shows the activation profiles with respect to movement taps for all motor cells in the visual condition for the second serial-order element and the 850 ms target duration. The response profiles were ordered according to their mean response-onset latencies from the previous tap times across all target intervals and serial-order elements. Thus, the cells in blue were active just before the first tap in that serial-order element and it seems that they pass the information to the cells in green, so that there is a gradient of cell activation throughout the interval, with the red cells being activated before and after the second tap. The activation gradients of motor cells are quite different from the two-cluster behavior of sensory cells. In fact, the best results of the expectation-maximisation clustering using the

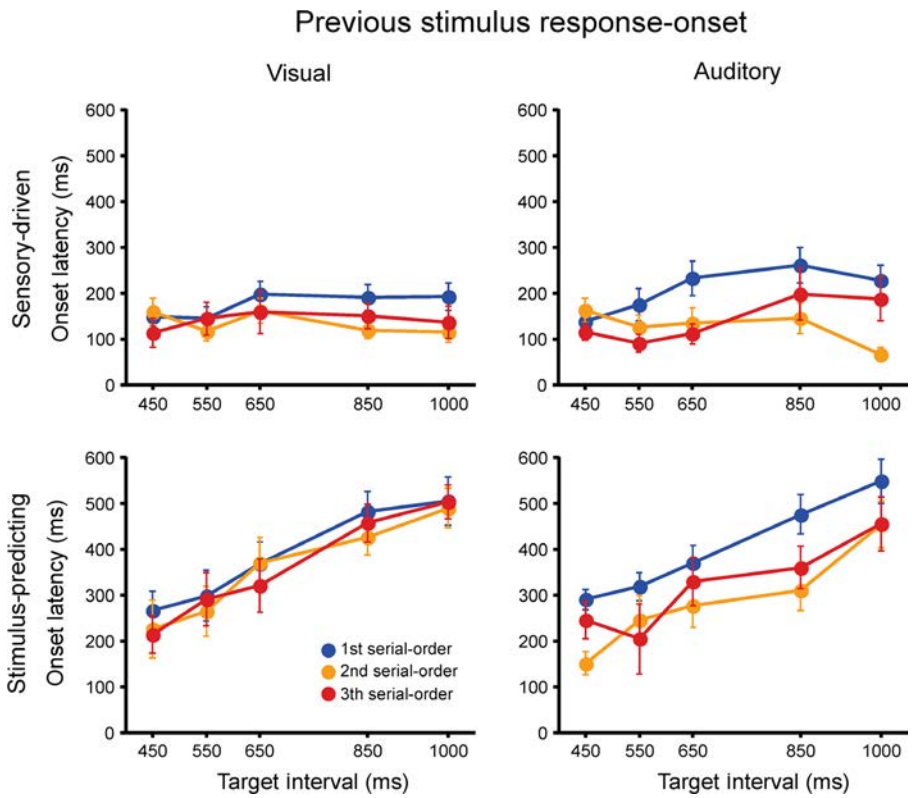

FIG. 7. Plots of the response-onset latency to the previous stimulus in cells with significant effects in the Poisson-train analysis as a function of the target interval, and the serial-order element (color code in the inset), for the sensory-driven and stimulus-predicting cells, and for the visual and auditory conditions.

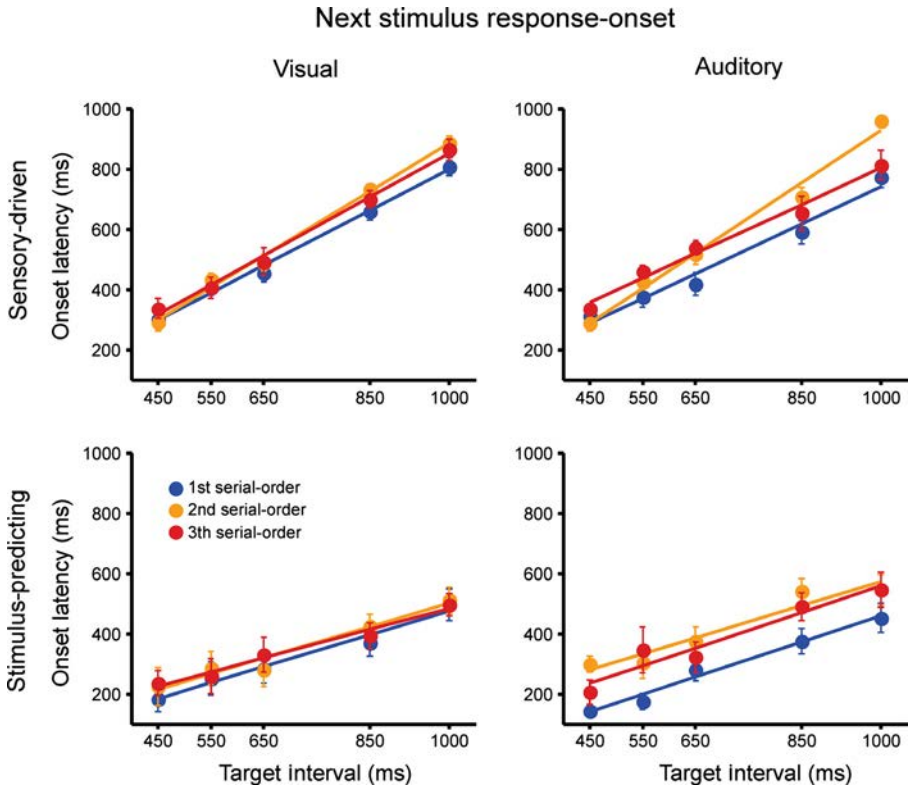

FIG. 8. Plots of the response-onset latency to the next stimulus in cells with significant effects in the Poisson-train analysis as a function of the target interval, and the serial-order element (color code in the inset), for the sensory-driven and stimulus-predicting cells, and for the visual and auditory conditions. Continuous colored lines correspond to the best linear regression model for the data of each serial-order element.

Bayesian information criterion were obtained with four clusters, suggesting the existence of a continuous pattern of activation profiles rather than two clusters as in the case of sensory cells. Hence, we used a two-dimensional normal distribution in order to characterise the cell activation gradients across all combinations of target intervals and the serial-order elements. From the normal distribution that has an elliptical shape (Fig. 9A), we can extract the important parameters associated with the larger ellipse diameter (called the normal distribution vector). These parameters are: δ, which is the vector length, θ, which is the vector angle, and τ, which is the latency to the vector's superior-left peak (Fig. 9B). These parameters define the dynamic pattern of activation profiles among conditions. Figure 9C shows the activation profiles of all of the motor neurons across target intervals and serial-order elements of the synchronisation phase of the SCT in the visual condition. This figure shows that the cells in blue were active just before the first tap of the corresponding serial-order element. The blue cells seem to pass the information to the green/yellow cells, forming a gradient of cell activation throughout the interval that ends with the red cells that were activated before and after the second tap of the corresponding serial-order element. These gradients are particularly evident for longer durations and the second and third serial-order elements of the SCT sequence. In addition, Fig. 9C shows that the two-dimensional normal distribution characterises properly the dynamic profile of activation of the motor cells across all of the target interval/serial-order element combinations. It also shows that the elliptical shape of these distributions changed with the experimental conditions. Indeed, the response-onset latencies of motor cells showed significant changes as a function of target interval ($F_{4,2782}$ = 35.5, $P < 0.0001$) and serial order ($F_{2,2782}$ = 6.6, P = 0.001), but were similar between modalities ($F_{1,2782}$ = 3.2, P = 0.074). In addition, motor cells showed significant main effects in their response duration for serial order ($F_{2,2782}$ = 34.1, $P < 0.0001$) and target interval ($F_{4,2156}$ = 13.3, $P < 0.0001$), and again were similar between modalities ($F_{1,2782}$ = 1.89, P = 6.66) (Fig. 11A). Finally, Fig. 9C depicts a cyclical configuration of these activation patterns, so that once a serial-order element is finished, a similar activation gradient starts again in the next element.

The cyclical configuration of the population activation patterns is more evident in Fig. 10A and B, where the normal distribution vectors were plotted as a function of target interval and serial-order element. Furthermore, the dotted lines in Fig. 10A and B exemplify a hypothetical connection between the last group of cells activated at the end of one serial-order element, and the first group of cells activated at the beginning of the next element. These hypothetical connections would be highly coordinated for target intervals above 550 ms, as the beginning and end of the normal distribution vectors overlapped with their corresponding initial and following taps. Conversely, the beginning of the normal distribution vectors for shorter durations start almost in the middle of each interval, reflecting a strong bias in the pattern of activation for the next tap (i.e. tap prediction). Accordingly, the length of the normal distribution vectors δ increased (Fig. 11B) and the peak latency τ decreased (Fig. 11C) as a function of the target duration and the serial order. It is of importance that the cyclical configuration of activation patterns showed a progressive and significant increase in the number of responding cells as the serial-order elements evolved [χ^2 test (2) = 6.2, P = 0.046] (Fig. 10C and D). In addition, there was a significant increase in the number of active motor cells as a function

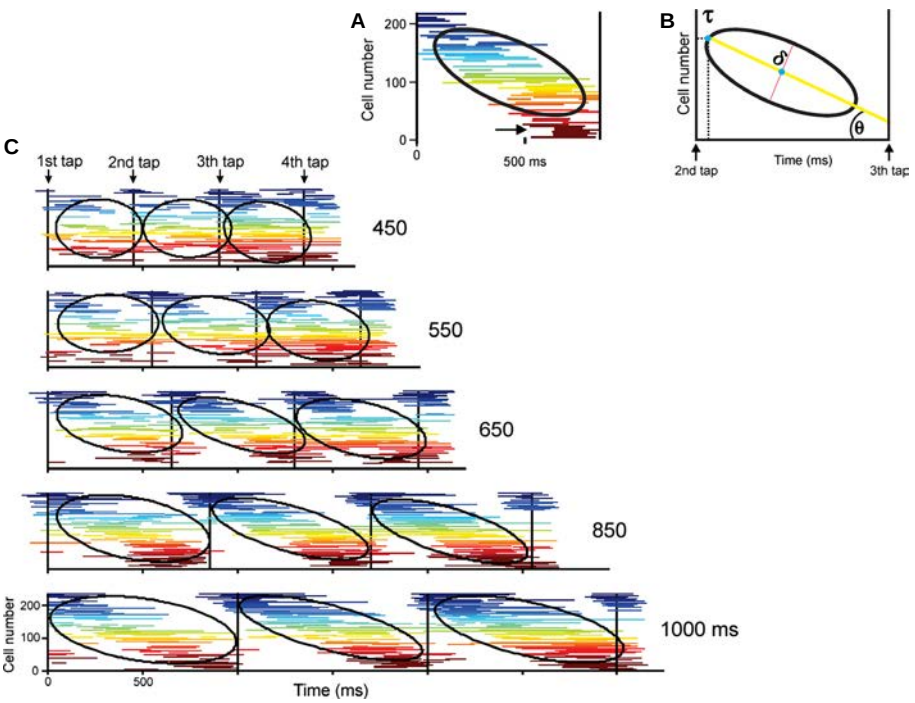

FIG. 9. Response profiles of motor cells. (A) Response profiles for the cells with significant activation effects in the Poisson-train analysis during the second serial-order element of the synchronisation phase and the 850 ms target interval. The black vertical lines correspond to the time of the taps. The black arrow points to the response-onset latency and the extent of the periods of activation for the visual motor cell shown in Fig. 2. The black ellipse is the normal distribution for the activity profiles of all cells. (B) Normal distribution parameters from the vector (normal distribution vector) associated with the larger ellipse diameter. δ, vector length; θ, vector angle; τ, latency to the vector's superior-left peak. (C) Activation profiles of all of the motor neurons across target intervals and serial-order elements of the synchronisation phase of the SCT in the visual condition. The color code used in the activation profiles of cells is to highlight the continuum in the response-onset latencies of motor cells.

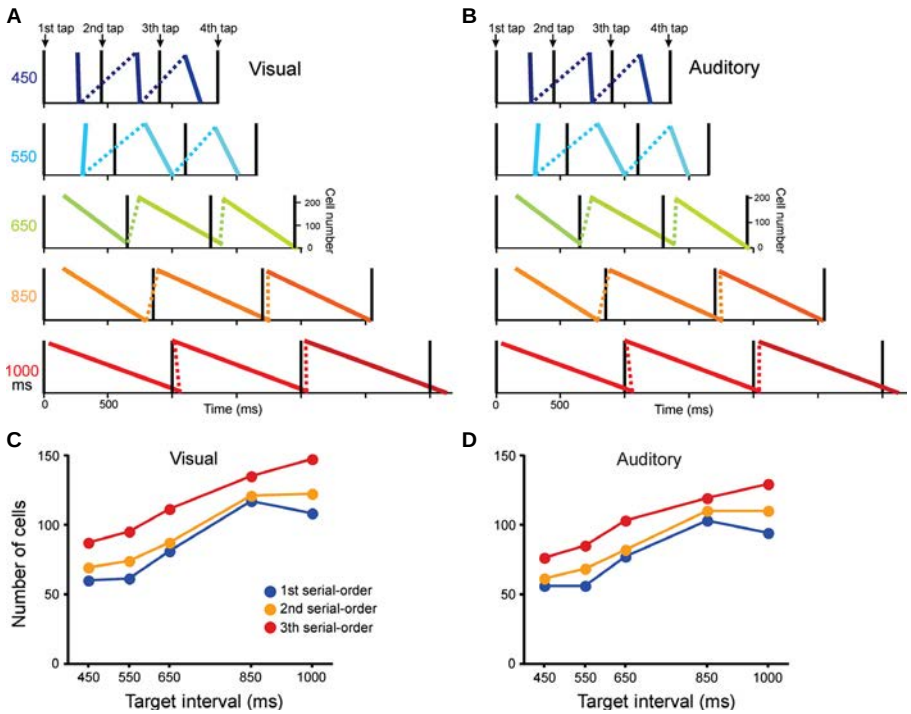

FIG. 10. Normal distribution vectors of motor cells across target intervals and serial-order elements for the visual (A) and auditory (B) conditions. Plots of the number of motor cells with significant effects in the Poisson-train analysis as a function of the target interval, and the serial-order element (color code in the inset) for the visual (C) and auditory (D) conditions.

of target interval [χ^2 test (4) = 21, $P < 0.0001$], and the number of active motor cells was similar between the visual and auditory conditions [χ^2 test (1) = 1.1, $P = 0.28$] (Fig. 10C and D). In sum, these findings support the idea that the cyclical configuration of the activation dynamics recruited more motor cells as the serial-order elements progressed across the synchronisation phase of the SCT.

The rate at which the cells were recruited over time is captured by the angle θ of the normal distribution vector (Fig. 9B), which makes this parameter a fundamental variable to study cell ensemble dynamics. The angle θ (Fig. 11D) showed a significant increase as a function of target interval (ANOVA on regression slopes, see Zar, 1999) for the visual ($F_{3,65026} = 58.3$, $P < 0.0001$) and auditory ($F_{3,59826} = 150.6$, $P < 0.0001$) conditions, and also as a function of serial order (visual: $F_{1,149226} = 410.1$, $P < 0.0001$; auditory: $F_{1,131635} = 173.2$, $P < 0.0001$), but was similar between modalities [t-test(575516) = 0.22, $P = 0.54$].

In conclusion, the cells classified as motor in the time-warping analysis show a cyclical configuration of activation gradients, where the number of recruited cells in these gradients increases as a function of the serial-order elements and the rate of cell engagement over time in the population dynamics decreases as a function of the target interval. The coordinated activation profiles of cell populations were similar between the modalities tested.

Sensory and motor cells encode temporal and sequential information

We performed a two-way ANOVA, where the target interval and the serial-order element of the SCT during the synchronisation phase were the factors and where the discharge rate of the sensory or motor cells was the dependent variable. Table 3 shows the number of cells with significant main effect or the interaction for target interval × serial order for all of the cell types studied in the present study. It is clear that sensory-driven, stimulus-predicting, and motor cells encoded the temporal and sequential information, as previously reported for cells multiplexing these parameters in their tuning functions (Merchant *et al.*, 2013b).

Discussion

We determined the response properties of MPC cells that were classified as sensory or motor during a task that involved isochronous tapping to a sensory metronome. The classification was based on a warping transformation (Perez *et al.*, 2013) that allowed us to statistically determine whether the activity of a cell was better aligned to sensory or motor events during the synchronisation phase of the SCT. We found that a large proportion of cells were categorised as either sensory or motor, suggesting that the medial premotor areas not only show a motor response component, but also process brief visual or auditory stimuli used as a metronome in a rhythmic tapping task. The recording location of both cell types was biased towards the pre-SMA, particularly for sensory cells. We then characterised the response-onset latency and the extent of the activation periods within each interval defined by two subsequent stimuli (sensory cells) or two subsequent taps (motor cells). Two distinctive clusters of sensory cells were observed, i.e. one cell population with short response-onset latencies to the previous stimulus (called sensory-driven neurons), and another that included cells with long response-onsets and with activity profiles that were probably predicting the occurrence of the next stimuli, instead of responding to the previous stimulus (called stimulus-predicting neurons). Sensory-driven neurons showed a clear bias towards the visual modality and were more responsive to the first stimulus, so that as the synchronisation phase progressed, the cells were less engaged in responding to the incoming stimuli. In contrast,

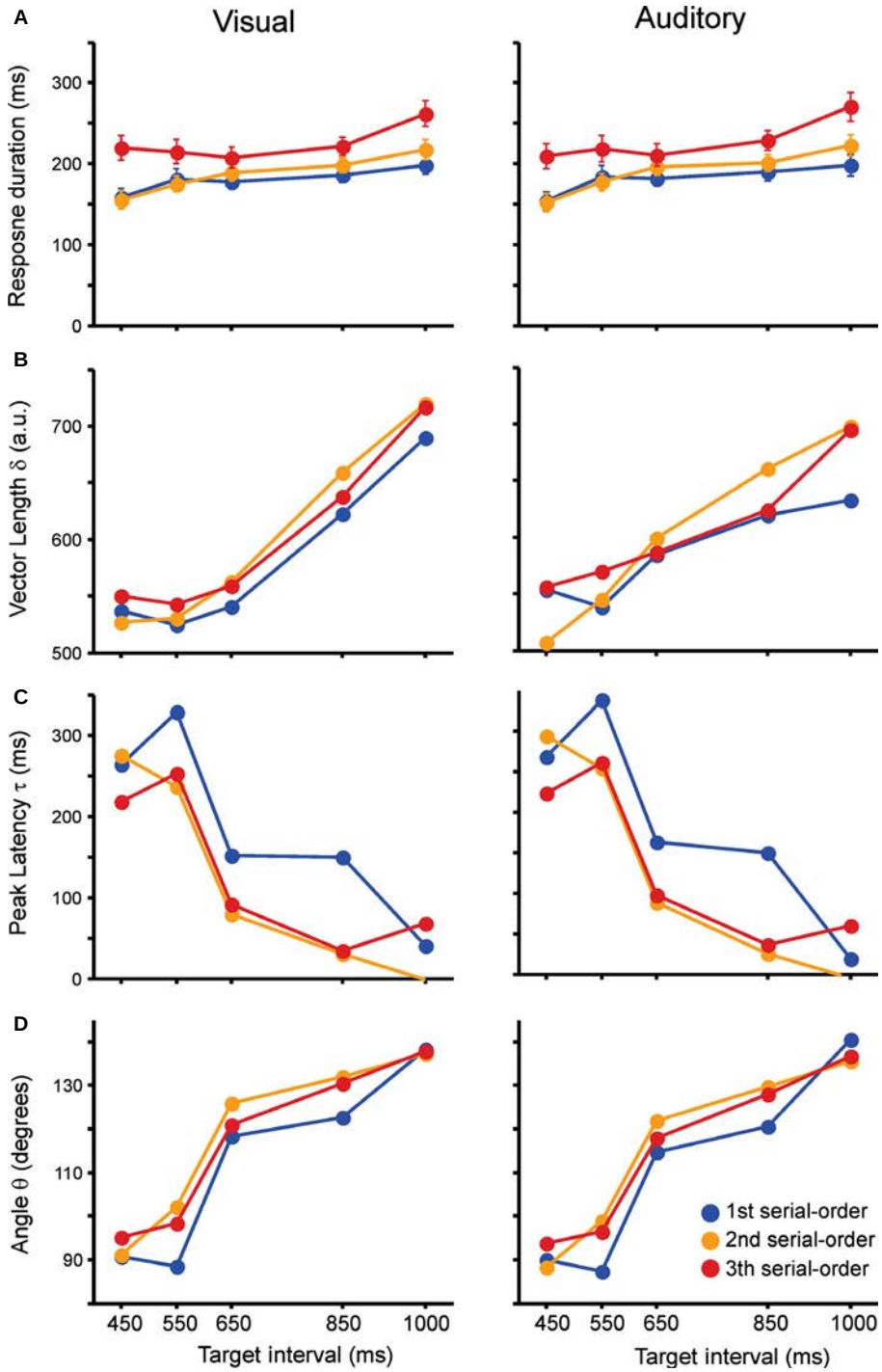

FIG. 11. (A) Plots of the response duration of the motor cells with significant effects in the Poisson-train analysis as a function of the target interval, and the serial-order element (color code in the inset). (B) Length δ of the normal distribution vectors of motor cells as a function of the target interval, and the serial-order element. (C) Peak latency τ of the normal distribution vectors of motor cells as a function of the target interval, and the serial-order element. (D) Angle θ of the normal distribution vectors of motor cells as a function of the target interval, and the serial-order element. Visual condition on the left, auditory condition on the right. a.u., arbitrary unit.

stimulus-predicting neurons were bimodal and showed similar response profiles across serial-order elements. However, the motor cells showed a consecutive onset in the activity of discrete neural ensembles, generating a rapid succession of neural events between the two taps defining a produced interval. This dynamic chain of neural events occurred for each element of the task synchronisation phase, resulting in a cyclical recruitment of similar activation profiles across the sequential structure of the isochronous tapping. However, the rate of cell recruitment over time in the population dynamics decreased and was more coordinated as a function of the target interval. In addition, the cyclical configuration in activation profiles engaged more motor cells as the serial-order elements progressed across the synchronisation phase of the SCT. These findings support the notion that motor cells are responsible for the rhythmic progression of movements

TABLE 3. Number of sensory and motor cells with responses that showed significant effects for target interval or serial order in a two-way ANOVA

Cell type	Interval	Serial order
Sensory-driven A	40	45
Sensory-driven V	64	74
Stimulus-predicting A	26	27
Stimulus-predicting V	35	44
Motor V	152	191
Motor A	127	148

A, auditory; V, visual condition.

in the task, gaining more importance as the trial evolves, whereas, simultaneously, the sensory-driven cells lose their functional influence.

The recording locations of both sensory and motor cells in the present study, according to our structural MRI reconstructions, were biased towards the pre-SMA particularly for the first type of cells. In contrast, Matsuzaka *et al.* (1992) demonstrated that the SMA proper is mainly responsible for: (i) evoked movements by intracortical microstimulation, (ii) passive somatosensory responses, and (iii) phasic premovement activity during a motor task, whereas the pre-SMA shows a strong a bias towards task-induced visual responses. Subsequent anatomical and neurophysiological studies have supported the existence of the two distinct medial premotor areas (i.e. Alexander & Crutcher, 1990; Luppino *et al.*, 1993). Although some of the cell responses described in the present study could be classified in terms of classic sensory or motor responses, many lines of evidence suggest that these cells are engaged in cognitive rather than traditional sensorimotor functions. First, a large proportion of our motor cells were recorded in the pre-SMA, suggesting that some of them may not show the motor properties described in previous articles (Matsuzaka *et al.*, 1992). Second, most of the sensory and motor cells encoded the duration and serial order of the intervals produced in the SCT (Table 3), suggesting their role in encoding cognitive parameters of the task. Third, there was a decrease in the number of engaged sensory-driven neurons as the serial-order elements progressed in the SCT, accompanied by a decrease in their response-onset latencies to the previous stimulus event. Hence, these were not classical sensory cells, and probably their sensory input arose from the posterior parietal cortex, which in turn could have been modulated centrally to prepare the circuit for the upcoming internally driven continuation phase of the task, as shown previously in other paradigms (Merchant *et al.*, 2011a; Crowe *et al.*, 2013). Finally, the responses of motor cells that were activated after the taps also showed a strong serial-order effect, where the number of active cells was larger for the second and third elements of the SCT sequence, which is not the behavior of cells with passive somatosensory responses (Romo *et al.*, 1997). We discuss these issues in the following paragraphs.

Rhythmic entrainment refers to the ability to align motor actions with an auditory beat, where a beat corresponds to the perceived pulse that marks equally spaced points in music or a sequence of auditory stimuli (Large & Palmer, 2002; Honing, 2012; Merchant & Honing, 2014). In humans, rhythmic entrainment is a common and widespread behavior that involves timed movements of different body parts (such as finger or foot taps, or body sway). Indeed, the majority of human listeners can easily synchronise (with no training) at rates that are integer multiples or fractions of the basic beat (Large & Jones, 1999). Thus, rhythmic entrainment is a fundamental element of music behavior and has a clear bias towards the auditory modality (Grondin *et al.*, 1996; Merchant *et al.*, 2008a; Grahn, 2012; Hove *et al.*, 2013a; Honing & Merchant, 2014); for a long time this was thought to be an exclusive trait of humans beings (Patel, 2014). The synchronisation phase of the SCT is the simplest case of rhythmic entrainment, as the beat is isochronous, and has been extensively used to study the neural underpinnings of rhythmic behavior. Humans differ substantially in their entrainment abilities from other primates (Merchant & Honing, 2014). Monkeys, for example, do not appear to spontaneously move to the beat of a musical rhythm. Nevertheless, monkeys are able to produce rhythmic movements with proper tempo matching during the SCT (which constitutes a simple isochronous challenge for humans). Indeed, monkeys produced isochronous rhythmic movements by temporalising the pause between movements and not the duration of their movement (Donnet *et al.*, 2014). These results indicate that monkeys use an explicit timing strategy to perform the SCT, where the timing mechanism controlled the duration of the movement pauses, which also triggered the execution of stereotyped pushing movements across each produced interval in the rhythmic sequence. However, macaques do not seem to have the refined prediction abilities of humans during rhythmic entrainment and show better performance in the SCT using visual rather than auditory cues, contrary to the auditory bias in humans (Honing & Merchant, 2014). The present results indicate a larger number of sensory-driven neurons responding to visual rather than auditory metronomes. Hence, the large visual input from the posterior parietal areas (particularly area PFG) to the MPC (Luppino *et al.*, 1993) can be used to generate an initial sensory signal in the motor system to generate subsequent predictive sensory signals. In contrast, the auditory information also coming from the posterior parietal areas seems to drive the activity of a smaller MPC cell network (Uhrig *et al.*, 2014), even if the response-onset latencies of sensory-driven neurons to stimuli of both modalities were similar. Consequently, this discrepancy could explain the monkeys' bias towards visual stimuli when driving their rhythmic behavior. In turn, we can speculate that the strong auditory input to the premotor system in humans (Hove *et al.*, 2013b), coming through a larger arcuate and superior longitudinal fasciculus than in monkeys (Rilling *et al.*, 2008), is a key element for the auditory bias in music behavior in *Homo sapiens* (Mendoza & Merchant, 2014). It is important to emphasise that neural responses in the MPC, similar to the reported sensory-driven neurons, have been recorded using visual, tactile, and auditory stimuli in tasks where a single stimulus cued a monkey motor response using a particular rule (Kurata & Tanji, 1985; Tanji & Kurata, 1985; Romo & Schultz, 1987; Romo *et al.*, 1993, 1997; Merchant *et al.*, 2001, 2004a). In contrast, when the same stimulus is presented in a passive context, the associated sensory responses are not observed (Tanji & Kurata, 1982; Kurata & Tanji, 1985). These findings suggest that the monkeys need to be focused on a task using the stimulus to drive their behavior in order to observe the sensory driven activity in the MPC. A note of precaution is in order here. Our time-warping method gives a statistical measure of the response alignment to sensory or motor events during a sensorimotor sequential task. Nevertheless, additional neurophysiological procedures are needed to define whether a cell classified as sensory with the warping method indeed has a sensory receptive field and encodes the physical properties of the incoming stimulus (Romo *et al.*, 1996; de Lafuente & Romo, 2006).

We can also speculate that, through the intensive training in the SCT (Zarco *et al.*, 2009), the initial sensory-driven responses of the MPC in the monkey may have been linked to neurons triggering the tapping behavior. This initial sensorimotor association started by sending a motor command in order to react to each stimulus, and

was then probably transformed to generate a predictive sensory signal in order to produce tapping responses closer to the stimulus onset. In fact, the time between the stimuli and the taps of trained monkeys in the SCT are shorter than their reaction times in a control task with random inter-stimulus intervals, suggesting that monkeys do have temporal prediction capabilities during the SCT (Zarco *et al.*, 2009). We suggest that the monkey prediction abilities in the SCT depend on the stimulus-predicting neurons found in the present study, which were bimodal and showed similar response profiles across serial-order elements. In previous studies we found that the motor system processes visual information of a moving target in a predictive fashion in order to trigger a single interception movement (Merchant *et al.*, 2004a,b; Merchant & Georgopoulos, 2006). Hence, the learning process of behaviors that need temporal prediction, such as target interception, collision avoidance, and rhythmic entrainment, probably generates sensory prediction signals in the motor cortical system (Merchant *et al.*, 2009, 2011a). It has been reported that human beta oscillations are crucial for predictive timing in auditory beat processing, and that beta oscillations involve top-down interactions between motor and auditory regions (Fujioka *et al.*, 2009, 2012). The beta signals tracked the tempo of the stimulus beat and predicted the onset of the following beat (Fujioka *et al.*, 2012). Furthermore, beta oscillations in the motor cortico-thalamic-basal ganglia circuit are involved in processing predictive temporal information during both the SCT (Bartolo *et al.*, 2014) and the presentation of auditory stimuli with complex metrics (Iversen *et al.*, 2009). Overall, these observations support the idea that the sensory prediction signals may not only interact with the neural apparatus present in the motor cortical system for the activation of predictive motor commands, but also generate top-down signals to sensory areas in order to efficiently process the incoming sensory information during rhythmic entrainment.

The cells classified as motor in the present study showed an organised and sequential onset in activity, so that the groups of active neurons changed dramatically within the two taps defining a produced interval. Hence, these neural responses are qualitatively different from the traditional movement preparation and execution signals in the motor and premotor areas of the cortex (Tanji & Evarts, 1976; Georgopoulos *et al.*, 1982, 2007; Tanji & Kurata, 1982; Wise, 1985; Naselaris *et al.*, 2006). Recently, we demonstrated that the MPC cells that encode the duration and the serial order in the SCT showed similar activation dynamics (Crowe *et al.*, 2014; Merchant *et al.*, 2015), suggesting that the motor cells of the present study constitute the main cell type reported in the previous article. In the present study, however, the dynamic chain of neural events occurred within each element of the task synchronisation phase, resulting in a cyclical recruitment of cell populations with similar activation profiles across the sequential structure of the task (Buonomano & Laje, 2010; Goel & Buonomano, 2014). This cyclical repetition of activation profiles within each produced interval can be the neural substrate for the rhythmic progression of movements during isochronous tapping to a sensory metronome. We suggest that the cyclical repetition of response profiles has an anatomofunctional substrate, where the neuronal ensembles are arranged in inter-connected modules, providing a strong synaptic drive to the next ensemble, and producing a recurring flow of information along a chain of neural ensembles (Gewaltig *et al.*, 2001). This hypothesis is supported by the recent observation that the magnitude of baseline activity correlations among cell pairs, which is an indirect measure of synaptic relations between the simultaneously recorded cells (de la Rocha *et al.*, 2007), shows a cyclical organisation along the elements of the SCT task sequence (Crowe *et al.*, 2014).

The rate of cell recruitment over time in the population dynamics decreased as a function of the target interval, again supporting the idea that the temporal structure of the SCT depends on these dynamic population code. Furthermore, we observed that the cyclical activation profiles engaged more motor cells as the serial-order elements progressed across the synchronisation phase of the SCT. This last finding corroborates the notion that the cells classified as motor in the present article could define the rhythmic evolution of movements in the task, gaining more importance as the trial progressed, whereas the sensory metronome was less important and the corresponding input from sensory-driven cells became less preponderant.

To finish, we also found that sensory-driven, stimulus-predicting, and motor cells encoded the temporal and sequential information, as previously reported for MPC cells multiplexing these parameters in their tuning functions (Merchant *et al.*, 2013b). Therefore, the dynamic response profiles of cells associated with the sensory, sensorimotor, and motor aspects of the synchronisation phase of the SCT include another dimension of neural processing, i.e. the duration and the element in the sequence that is being performed. We can infer that an intricate set of dynamic interactions between these cell types is needed in order to perform the isochronous tapping to a sensory metronome. The nature of these interactions, however, is out of the reach of the present article, as a large amount of simultaneously recorded cells is required to determine synaptic interactions and the dynamic transfer of information within and between neural circuits (Fujisawa *et al.*, 2008; Merchant *et al.*, 2011b, 2014; Berényi *et al.*, 2014). Thus, experiments using multiple chronic microelectrodes in animals performing the SCT are in progress.

Acknowledgements

This research was supported by CONACYT (151223) and PAPIIT (IN201214-25). We thank Victor de Lafuente for his fruitful comments on the manuscript. We also thank Raúl Paulín and Juan José Ortiz for their technical assistance. The authors declare no conflict of interest.

Abbreviations

MPC, medial premotor cortex; MRI, magnetic resonance imaging; preSMA, pre-supplementary motor area; SCT, synchronisation-continuation task; *SI*, surprise index; SMA, supplementary motor area proper.

References

Alexander, G.E. & Crutcher, M.D. (1990) Preparation for movement: neural representations of intended direction in three motor areas of the monkey. *J. Neurophysiol.*, **64**, 133–150.

Bartolo, R., Prado, L. & Merchant, H. (2014) Information processing in the primate basal ganglia during sensory guided and internally driven rhythmic tapping. *J. Neurosci.*, **34**, 3910–3923.

Bengtsson, S.L., Ehrsson, H.H., Forssberg, H. & Ullén, F. (2005) Effector-independent voluntary timing: behavioural and neuroimaging evidence. *Eur. J. Neurosci.*, **22**, 3255–3265.

Berényi, A., Somogyvári, Z., Nagy, A.J., Roux, L., Long, J.D., Fujisawa, S., Stark, E., Leonardo, A., Harris, T.D. & Buzsáki, G. (2014) Large-scale, high-density (up to 512 channels) recording of local circuits in behaving animals. *J. Neurophysiol.*, **111**, 1132–1149.

Buhusi, C.V. & Meck, W.H. (2005) What makes us tick? Functional and neural mechanisms of interval timing. *Nat. Rev. Neurosci.*, **6**, 755–765.

Buonomano, D.V. & Laje, R. (2010) Population clocks: motor timing with neural dynamics. *Trends Cogn. Sci.*, **14**, 520–527.

Coull, J.T., Cheng, R.K. & Meck, W.H. (2011) Neuroanatomical and neurochemical substrates of timing. *Neuropsychopharmacology*, **36**, 3–25.

Crowe, D.A., Goodwin, S.J., Blackman, R.K., Sakellaridi, S., Sponheim, S.R., MacDonald, A.W. III & Chafee, M.V. (2013) Prefrontal neurons transmit signals to parietal neurons that reflect executive control of cognition. *Nat. Neurosci.*, **16**, 1484–1491.

Crowe, D.A., Zarco, W., Bartolo, R. & Merchant, H. (2014) Dynamic representation of the temporal and sequential structure of rhythmic movements in the primate medial premotor cortex. *J. Neurosci.*, **34**, 12660–12671.
Dhamala, M., Pagnoni, G., Wiesenfeld, K., Zink, C.F., Martin, M. & Berns, G.S. (2003) Neural correlates of the complexity of rhythmic finger tapping. *NeuroImage*, **20**, 918–926.
Donnet, S., Bartolo, R., Fernandes, J.M., Cunha, J.P., Prado, L. & Merchant, H. (2014) Monkeys time their movement pauses and not their movement kinematics during a synchronization-continuation rhythmic task. *J. Neurophysiol.*, **111**, 2250–2257.
Fujioka, T., Trainor, L.J., Large, E.W. & Ross, B. (2009) Beta and gamma rhythms in human auditory cortex during musical beat processing. *Ann. NY Acad. Sci.*, **1169**, 89–92.
Fujioka, T., Trainor, L.J., Large, E.W. & Ross, B. (2012) Internalized timing of isochronous sounds is represented in neuromagnetic beta oscillations. *J. Neurosci.*, **32**, 1791–1802.
Fujisawa, S., Amarasingham, A., Harrison, M.T. & Buzsáki, G. (2008) Behavior-dependent short-term assembly dynamics in the medial prefrontal cortex. *Nat. Neurosci.*, **11**, 823–833.
Georgopoulos, A.P., Kalaska, J.F., Caminiti, R. & Massey, J.T. (1982) On the relations between the direction of two-dimensional arm movements and cell discharge in primate motor cortex. *J. Neurosci.*, **2**, 1527–1537.
Georgopoulos, A.P., Merchant, H., Naselaris, T. & Amirikian, B. (2007) Mapping of the preferred direction in the motor cortex. *Proc. Natl. Acad. Sci. USA*, **104**, 11068–11072.
Gewaltig, M.O., Diesmann, M. & Aertsen, A. (2001) Propagation of cortical synfire activity: survival probability in single trials and stability in the mean. *Neural Networks*, **14**, 657–673.
Goel, A. & Buonomano, D.V. (2014) Timing as an intrinsic property of neural networks: evidence from in vivo and in vitro experiments. *Philos. T. Roy. Soc. B.*, **369**, 20120460.
Grahn, J.A. (2012) See what I hear? Beat perception in auditory and visual rhythms. *Exp. Brain Res.*, **220**, 51–61.
Grondin, S. (2001) From physical time to the first and second moments of psychological time. *Psychol. Bull.*, **127**, 22–44.
Grondin, S., Ivry, R.B., Franz, E., Perreault, L. & Metthe, L. (1996) Markers' influence on the duration discrimination of intermodal intervals. *Percept. Psychophys.*, **58**, 424–433.
Hanes, D.P., Thompson, K.G. & Schall, J.D. (1995) Relationship of presaccadic activity in frontal eye field and supplementary eye field to saccade initiation in macaque: Poisson spike train analysis. *Exp. Brain Res.*, **103**, 85–96.
Honing, H. (2012) Without it no music: beat induction as a fundamental musical trait. *Ann. NY Acad. Sci.*, **1252**, 85–91.
Honing, H. & Merchant, H. (2014) Differences in auditory timing between human and non-human primates. *Behav. Brain Sci.* **37**.
Hove, M.J., Iversen, J.R., Zhang, A. & Repp, B.H. (2013a) Synchronization with competing visual and auditory rhythms: bouncing ball meets metronome. *Psychol. Res.*, **77**, 388–398.
Hove, M.J., Fairhurst, M.T., Kotz, S.A. & Keller, P.E. (2013b) Synchronizing with auditory and visual rhythms: an fMRI assessment of modality differences and modality appropriateness. *NeuroImage*, **67**, 313–321.
Iversen, J.R., Repp, B.H. & Patel, A.D. (2009) Top-down control of rhythm perception modulates early auditory responses. *Ann. NY Acad. Sci.*, **1169**, 58–73.
Ivry, R.B. & Hazeltine, R.E. (1995) Perception and production of temporal intervals across a range of durations: evidence of a common timing mechanism. *J. Exp. Psychol. Human.*, **21**, 3–18.
Janata, P. & Grafton, S.T. (2003) Swinging in the brain: shared neural substrates for behaviors related to sequencing and music. *Nat. Neurosci.*, **6**, 682–687.
Janssen, P. & Shadlen, M.N. (2005) A representation of the hazard rate of elapsed time in macaque area LIP. *Nat. Neurosci.*, **8**, 234–241.
Kass, R.E. & Raftery, A.E. (1995) Bayes factors. *J. Am. Stat. Assoc.*, **90**, 773–795.
Kurata, K. & Tanji, J. (1985) Contrasting neuronal activity in supplementary and precentral motor cortex of monkeys. II. Responses to movement triggering vs. nontriggering sensory signals. *J. Neurophysiol.*, **53**, 142–152.
de Lafuente, V. & Romo, R. (2006) Neural correlate of subjective sensory experience gradually builds up across cortical areas. *Proc. Natl. Acad. Sci. USA*, **103**, 14266–14271.
Large, E.W. & Jones, M.R. (1999) The dynamics of attending: how people track time-varying events. *Psychol. Rev.*, **106**, 119–159.
Large, E.W. & Palmer, C. (2002) Perceiving temporal regularity in music. *Cognitive Sci.*, **26**, 1–37.
Lewis, P.A., Wing, A.M., Pope, P.A., Praamstra, P. & Miall, R.C. (2004) Brain activity correlates differentially with increasing temporal complexity of rhythms during initialisation, synchronisation, and continuation phases of paced finger tapping. *Neuropsychologia*, **42**, 1301–1312.
Luppino, G., Matelli, M., Camarda, R. & Rizzolatti, G. (1993) Corticocortical connections of area F3 (SMA-proper) and area F6 (pre-SMA) in the macaque monkey. *J. Comp. Neurol.*, **338**, 114–140.
Matsuzaka, Y., Aizawa, H. & Tanji, J. (1992) A motor area rostral to the supplementary motor area (presupplementary motor area) in the monkey: neuronal activity during a learned motor task. *J. Neurophysiol.*, **68**, 653–662.
Mendoza, G. & Merchant, H. (2014) Motor system evolution and the emergence of high cognitive functions. *Prog. Neurobiol.*, **122**, 73–93.
Merchant, H. & Georgopoulos, A.P. (2006) Neurophysiology of perceptual and motor aspects of interception. *J. Neurophysiol.*, **95**, 1–13.
Merchant, H. & Honing, H. (2014) Are non-human primates capable of rhythmic entrainment? Evidence for the gradual audiomotor evolution hypothesis. *Front. Neurosci.*, **7**, 274.
Merchant, H., Zainos, A., Hernández, A., Salinas, E. & Romo, R. (1997) Functional properties of primate putamen neurons during the categorization of tactile stimuli. *J. Neurophysiol.*, **77**, 1132–1154.
Merchant, H., Battaglia-Mayer, A. & Georgopoulos, A.P. (2001) Effects of optic flow in motor cortex and area 7a. *J. Neurophysiol.*, **86**, 1937–1954.
Merchant, H., Battaglia-Mayer, A. & Georgopoulos, A.P. (2003) Functional organization of parietal neuronal responses to optic-flow stimuli. *J. Neurophysiol.*, **90**, 675–682.
Merchant, H., Battaglia-Mayer, A. & Georgopoulos, A.P. (2004a) Neural responses in motor cortex and area 7a to real and apparent motion. *Exp. Brain Res.*, **154**, 291–307.
Merchant, H., Battaglia-Mayer, A. & Georgopoulos, A.P. (2004b) Neural responses during interception of real and apparent circularly moving stimuli in motor cortex and area 7a. *Cereb. Cortex*, **14**, 314–331.
Merchant, H., Fortes, A.F. & Georgopoulos, A.P. (2004c) Short-term memory effects on the representation of two-dimensional space in the rhesus monkey. *Anim. Cogn.*, **7**, 133–143.
Merchant, H., Zarco, W. & Prado, L. (2008a) Do we have a common mechanism for measuring time in the hundreds of millisecond range? Evidence from multiple-interval timing tasks. *J. Neurophysiol.*, **99**, 939–949.
Merchant, H., Zarco, W., Bartolo, R. & Prado, L. (2008b) The context of temporal processing is represented in the multidimensional relationships between timing tasks. *PLoS One*, **3**, e3169: 1–9.
Merchant, H., Zarco, W., Prado, L. & Pérez, O. (2009) Behavioral and neurophysiological aspects of target interception. *Adv. Exp. Med. Biol.*, **629**, 201–220.
Merchant, H., Crowe, D.A., Robertson, M.S., Fortes, A.F. & Georgopoulos, A.P. (2011a) Top-down spatial categorization signal from prefrontal to posterior parietal cortex in the primate. *Front. Syst. Neurosci.*, **5**, 69.
Merchant, H., Zarco, W., Pérez, O., Prado, L. & Bartolo, R. (2011b) Measuring time with different neural chronometers during a synchronization-continuation task. *Proc. Natl. Acad. Sci. USA*, **108**, 19784–19789.
Merchant, H., Harrington, D. & Meck, W.H. (2013a) Neural basis of the perception and estimation of time. *Annu. Rev. Neurosci.*, **36**, 313–336.
Merchant, H., Pérez, O., Zarco, W. & Gámez, J. (2013b) Interval tuning in the primate medial premotor cortex as a general timing mechanism. *J. Neurosci.*, **33**, 9082–9096.
Merchant, H., Crowe, D.A., Fortes, A.F. & Georgopoulos, A.P. (2014) Cognitive modulation of local and callosal neural interactions in decision making. *Front. Neurosci.*, **8**, 245.
Merchant, H., Grahn, J., Trainer, L., Rohrmeier, M. & Fitch, TW. (2015) Finding the beat, a neuro-computational approach. *Philos. T. Roy. Soc. B.*, **370**.
Nagasaka, Y., Chao, Z.C., Hasegawa, N., Notoya, T. & Fujii, N. (2013) Spontaneous synchronization of arm motion between Japanese macaques. *Sci. Rep.*, **3**, 1151.
Naselaris, T., Merchant, H., Amirikian, B. & Georgopoulos, A.P. (2005) Spatial reconstruction of trajectories of an array of recording microelectrodes. *J. Neurophysiol.*, **93**, 2318–2330.
Naselaris, T., Merchant, H., Amirikian, B. & Georgopoulos, A.P. (2006) Large-scale organization of preferred directions in the motor cortex. II. Analysis of local distributions. *J. Neurophysiol.*, **96**, 3237–3247.
Patel, A.D. (2014) The evolutionary biology of musical rhythm: was darwin wrong? *PLoS Biol.*, **12**, e1001821.
Perez, O., Kass, R. & Merchant, H. (2013) Trial time warping to discriminate stimulus-related from movement-related neural activity. *J. Neurosci. Meth.*, **212**, 203–210.

Phillips-Silver, J. & Trainor, L.J. (2005) Feeling the beat: movement influences infant rhythm perception. *Science*, **308**, 1430.
Rilling, J.K., Glasser, M.F., Preuss, T.M., Ma, X., Zhao, T., Hu, X. & Behrens, T.E.J. (2008) The evolution of the arcuate fasciculus revealed with comparative DTI. *Nature*, **11**, 426–428.
de la Rocha, J., Doiron, B., Shea-Brown, E., Josić, K. & Reyes, A. (2007) Correlation between neural spike trains increases with firing rate. *Nature*, **448**, 802–806.
Romo, R. & Schultz, W. (1987) Neuronal activity preceding self-initiated or externally timed arm movements in area 6 of monkey cortex. *Exp. Brain Res.*, **67**, 656–662.
Romo, R., Ruiz, S., Crespo, P., Zainos, A. & Merchant, H. (1993) Representation of tactile signals in primate supplementary motor area. *J. Neurophysiol.*, **70**, 2690–2694.
Romo, R., Merchant, H., Zainos, A. & Hernández, A. (1996) Categorization of somaestetic stimuli: sensorimotor performance and neuronal activity in primary somatic sensory cortex of awake monkeys. *NeuroReport*, **7**, 1273–1279.
Romo, R., Merchant, H., Zainos, A. & Hernández, A. (1997) Categorical perception of somesthetic stimuli: psychophysical measurements correlated with neuronal events in primate medial premotor cortex. *Cereb. Cortex*, **7**, 317–326.
Rorden, C., Karnath, H.O. & Bonilha, L. (2007) Improving lesion-symptom mapping. *J. Cognitive Neurosci.*, **19**, 1081–1088.
Stauffer, C.C., Haldemann, J., Troche, S.J. & Rammsayer, T.H. (2012) Auditory and visual temporal sensitivity: evidence for a hierarchical structure of modality-specific and modality-independent levels of temporal information processing. *Psychol. Res.*, **76**, 20–31.
Tanji, J. & Evarts, E.V. (1976) Anticipatory activity of motor cortex neurons in relation to direction of an intended movement. *J. Neurophysiol.*, **39**, 1062–1068.
Tanji, J. & Kurata, K. (1982) Comparison of movement-related activity in two cortical motor areas of primates. *J. Neurophysiol.*, **48**, 633–653.
Tanji, J. & Kurata, K. (1985) Contrasting neuronal activity in supplementary and precentral motor cortex of monkeys. I. Responses to instructions determining motor responses to forthcoming signals of different modalities. *J. Neurophysiol.*, **53**, 129–141.
Uhrig, L., Dehaene, S. & Jarraya, B. (2014) A hierarchy of responses to auditory regularities in the macaque brain. *J. Neurosci.*, **34**, 1127–1132.
Wing, A.M. (2002) Voluntary timing and brain function: an information processing approach. *Brain Cognition*, **48**, 7–30.
Wise, S.P. (1985) The primate premotor cortex: past, present, and preparatory. *Annu. Rev. Neurosci.*, **8**, 1–19.
Zar, J.H. (1999) *Biostatistical Analysis*. Prentice Hall, New Jersey.
Zarco, W., Merchant, H., Prado, L. & Mendez, J.C. (2009) Subsecond timing in primates: comparison of interval production between human subjects and rhesus monkeys. *J. Neurophysiol.*, **102**, 3191–3202.

Neurophysiology of Timing in the Hundreds of Milliseconds: Multiple Layers of Neuronal Clocks in the Medial Premotor Areas

Hugo Merchant, Ramón Bartolo, Oswaldo Pérez, Juan Carlos Méndez, Germán Mendoza, Jorge Gámez, Karyna Yc, and Luis Prado

Abstract

The precise quantification of time in the subsecond scale is critical for many complex behaviors including music and dance appreciation/execution, speech comprehension/articulation, and the performance of many sports. Nevertheless, its neural underpinnings are largely unknown. Recent neurophysiological experiments from our laboratory have shown that the cell activity in the medial premotor areas (MPC) of macaques can represent different aspects of temporal processing during a synchronization-continuation tapping task (SCT). In this task the rhythmic behavior of monkeys was synchronized to a metronome of isochronous stimuli in the hundreds of milliseconds range (synchronization phase), followed by a period where animals internally temporalized their movements (continuation phase). Overall, we found that the time-keeping mechanism in MPC is governed by different layers of neural clocks. Close to the temporal control of movements are two separate populations of ramping cells that code for elapsed or remaining time for a tapping movement during the SCT. Thus, the sensorimotor loops engaged during the task may depend on the cyclic interplay between two neuronal chronometers that quantify in their instantaneous discharge rate the time passed and the remaining time for an action. In addition, we found MPC neurons that are tuned to the duration of produced intervals during the rhythmic task, showing an orderly variation in the average discharge rate as a function of duration. All the tested durations in the subsecond scale were represented in the preferred intervals of the cell population. Most of the interval-tuned cells were also tuned to the ordinal structure of the six intervals produced sequentially in the SCT. Hence, this next level of temporal processing may work as the notes of a musical score, providing information to the timing network about what duration and ordinal

H. Merchant (✉) • R. Bartolo • O. Pérez • J.C. Méndez • G. Mendoza • J. Gámez • K. Yc • L. Prado
Instituto de Neurobiología, UNAM,
Campus Juriquilla, Boulevard Juriquilla No. 3001,
Querétaro 76230, Mexico
e-mail: hugomerchant@unam.mx

H. Merchant and V. de Lafuente (eds.), *Neurobiology of Interval Timing*,
Advances in Experimental Medicine and Biology 829, DOI 10.1007/978-1-4939-1782-2_8,

element of the sequence are being executed. Finally, we describe how the timing circuit can use a dynamic neural representation of the passage of time and the context in which the intervals are executed by integrating the time-varying activity of populations of cells. These neural population clocks can be defined as distinct trajectories in the multidimensional cell response-space. We provide a hypothesis of how these different levels of neural clocks can interact to constitute a coherent timing machine that controls the rhythmic behavior during the SCT.

Keywords

Interval timing • Medial premotor areas • Interval tuning • Ramping activity • Network dynamics

Introduction

Time is a crucial variable in life and organisms have developed different mechanisms to quantify the passage of time along a wide range of durations. From microseconds to circadian rhythms, temporal information is used to organize behavior and specific brain mechanisms have been suggested for the measurement of different time scales. Indeed, the central nervous system does not have a time sensory organ; however, organisms are able to extract temporal information from stimuli of all sensory modalities and use it to generate timed behaviors. This chapter focuses on the neural underpinnings of interval timing in the hundreds of milliseconds, since it is a time scale involved in many complex behaviors such as the perception and production of speech [1, 2], the execution and appreciation of music and dance [3, 4], and the performance of a large variety of sports [5–7]. In music, for example, time comes in a variety of patterns which include isochronous sequences where temporal intervals are of a single constant duration or, more commonly, polyrhythmic sequences containing intervals of many durations. In addition, the ability to capture and interpret the beats in a rhythmic pattern allows people to move and dance in time to music [3]. Music and dance, then, are behaviors that depend on intricate loops of perception and action, where temporal processing can be engaged during the synchronization of movements with sensory information or during the internal generation of movement sequences [4]. In a simplified version of these activities, numerous studies have examined how subjects synchronize taps with rhythmic isochronous auditory stimuli and then continue tapping at the instructed rate without the advantage of the sensory metronome [8, 9]. Thus, the synchronization-continuation tapping task (SCT) has at least four main components, namely, a sensorimotor process during synchronization, an internal timing component during both synchronization and continuation, a cyclic element for repetitive interval production, and a working-memory component used during the continuation. The cyclic nature of this task implies that subjects must keep track of the time elapsed since the previous sensory and motor events as well as the time remaining until the next events [10].

The present manuscript describes the functional properties of neurons in the primate medial premotor cortex (MPC, i.e. supplementary motor area [SMA] and pre-supplementary motor area [preSMA]) during the execution of the SCT. We show how the single cell and population activity of this cortical area represents different aspects of the temporal processing involved in the execution of a rhythmic task that has been a backbone in the timing literature.

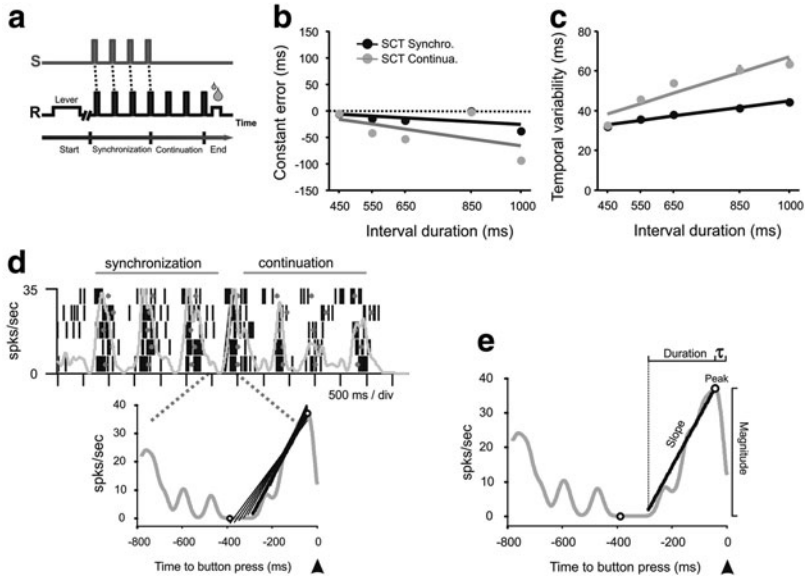

Fig. 1 (**a**) Sincronization-Continuation Task (SCT). Monkeys were required to push a button (R, *black line*) each time stimuli with a constant interstimulus interval (S, *gray line*) were presented, which resulted in a stimulus-movement cycle. After four consecutive synchronized movements, the stimuli stopped, and the monkeys continued tapping with a similar pacing for three additional intervals. The target intervals, defined by brief auditory or visual stimuli, were 450, 550, 650, 850, and 1,000 ms, and were chosen pseudo-randomly within a repetition. (**b**) Constant error (produced-target interval) during the performance of the SCT in the auditory interval marker condition. Monkeys slightly underestimated the interval durations during the synchronization (*black*) and continuation (*gray*) phases of SCT. The SEM is smaller than the dot diameter. (**c**) Temporal variability (i.e. the intertap SD) increased as a function of target interval during both phases of SCT. (**d**) Iterative algorithm used to find the best regression model to explain the increase or decrease of instantaneous activity over time with respect to a sensory or motor event. Top, raster plot and mean SDF (*gray function*) of a ramping cell aligned to the first tap of the continuation phase. The region indicated by the *dotted rectangle* is expanded below, where a series of linear regression functions are displayed, including the best model identified by the algorithm shown as the *thicker line*. (**e**) Parameters that were extracted from the linear regression model for the motor and relative-timing ramps. Modified from [10, 36]

Ramping Activity as an Instantaneous Timing Signal for Temporal Execution

We recorded the activity of MPC cells during a version of the SCT where monkeys were required to push a button each time stimuli with a constant interstimulus interval were presented, which resulted in a stimulus-movement cycle (Fig. 1a). After four consecutive synchronized movements, the stimuli stopped, and the monkeys continued tapping with the same interval for three additional intervals. Brief auditory or visual interval markers were used during the synchronization phase and the range of target intervals was from 450 to 1,000 ms [10, 11]. The monkeys were able to accurately produce the target intervals, showing an average underestimation of ~50 ms across interval durations during the synchronization and continuation phases of the SCT (Fig. 1b). In addition, we analyzed the temporal variability of the monkeys' tapping performance, which was defined as the SD of the individual inter-response intervals [12, 13]. Temporal variability increased linearly as a function of interval duration in both phases of SCT (Fig. 1c). These findings show that the monkeys had a remarkably accurate timing performance in this complex temporal tapping task. Furthermore, the data show a temporal variability that followed the scalar property of interval timing, a property that has been documented in many species and temporal tasks [14]. In a recent study, where the speed profile of

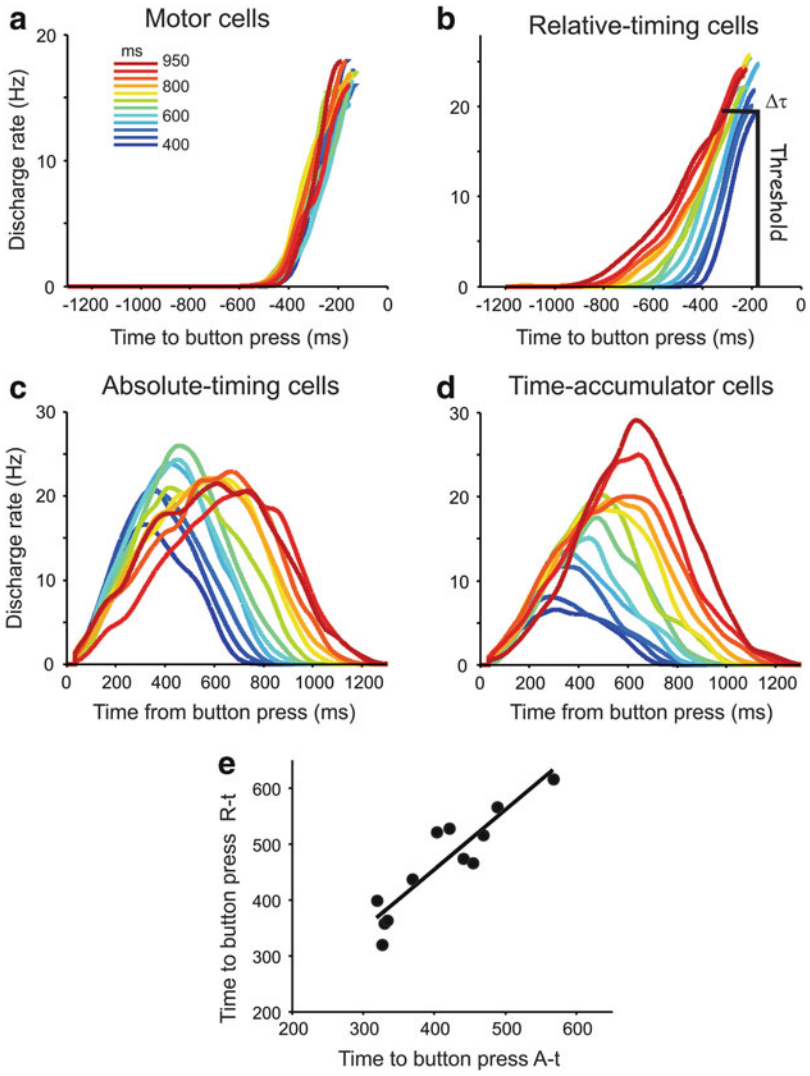

Fig. 2 Ramp population functions for motor (**a**), relative-timing (**b**), absolute-timing (**c**) and time-accumulator (**d**) cells. **a** and **b** are aligned to the next button press while **c** and **d** are aligned to the previous button press. The color code in the inset of A corresponds to the duration of the produced intervals during the SCT. (**e**) Time to button press of the ramp population functions at 14 Hz for absolute-timing (A-t) cells plotted against the time to button press associated with the ramp population functions at 7 Hz for relative-timing (R-t) cells. The ramp population functions are equal to the addition of the magnitudes of individual ramps over time. Modified from [10]

the tapping movements was computed using semiautomatic video tracking algorithms, we demonstrated that monkeys temporalize their movement-pauses and not their tapping movements during the SCT [15–17]. Macaques showed a strong ability to temporalize their movement-pauses for a wide range of intervals (450–1,000 ms), while their movements were similar across the duration of produced intervals, the sequential structure of the SCT, or the modality of the interval marker. These findings suggest that monkeys use an explicit timing strategy to perform the SCT, where the timing mechanism controlled the duration of the movement-pauses, while also triggered the execution of stereotyped pushing movements across each produced interval in the rhythmic sequence [15].

The extracellular activity of single neurons in the medial premotor areas was recorded during task performance using a system with seven independently movable microelectrodes (1–3 MΩ, Uwe Thomas Recording, Germany [10]). A large population of neurons showed ramping activity before or after the button press in the SCT (703 out of 1,083 recorded cells) [18]. Indeed, we developed a warping algorithm to determine whether the cells responses were aligned to the sensory or motor aspects of the

SCT, and we found that most MPC cells were aligned to the tapping movements instead of the stimuli used to drive the temporal behavior [18].

Next, an iterative algorithm was used to find the best regression model to explain the increase or decrease of instantaneous activity over time with respect to a sensory or motor event using the spike density function (SDF; Fig. 1d). With this method we defined for each ramp the following parameters: duration, slope, peak magnitude, and the time τ from the peak to the stimulus presentation or button press (Fig. 1e). Using this information, we classified different cell populations with ramping activity in four groups: motor, relative-timing, absolute-timing and time-accumulator [10]. For example, a large group of cells (n = 236) show ramps before the movement onset that are similar across produced durations and the sequential structure of the task, and therefore, are considered motor ramps (Fig. 2a). The inherent noise present in single temporal ramps, however, implies that the downstream reading neural node cannot rely on single cells to quantify the passage of time or produce accurately timed movements. Therefore, we propose a population code for encoding time during SCT, where the reading network adds the magnitudes of a population of individual ramps over time, resulting in a ramp population function [$R(t,I) = \frac{\sum_{n=1}^{N} r(t,I)}{N}$, where $r(t, I)$ corresponds to each individual ramp over time (t), from 1 to N total number of ramps of a cell type, and for a particular produced interval (I)]. Figure 2a shows the ramp population functions for the motor cells, where it is evident that the motor ramps are similar across the intervals produced by the monkeys during the SCT performance [10].

Interestingly, another cell population showed an increase in ramp duration but a decrease in slope as a function of the animals' produced duration, reaching a similar discharge magnitude at a specific time before the button press. These cells are called relative-timing cells, since their ramping profile could signal how much time is left for triggering the button press in the task sequence (n = 163 cells; Fig. 2b). Therefore, there is a population of MPC neurons that has the response properties to encode the time remaining for a motor event, and once the population reaches a firing magnitude threshold it could trigger the button press movements [10].

On the other hand, other groups of cells show a consistent increase followed by a decrease in their instantaneous discharge rate when their activity was aligned to the previous button press rather than to the next one (n = 304 neurons). In these absolute-timing cells the duration of the up-down profile of activation increases as a function of the produced interval (Fig. 2c), whereas in the time-accumulator cells there is an additional increase in the magnitude of the ramps' peak (Fig. 2d). Therefore, these cells could be representing the passage of time since the previous movement, using two different encoding strategies: one functioning as an accumulator of elapsed time where the peak magnitude and the duration of the activation period is directly associated with the time passed, and another where only the duration of the activation period is encoding the length of the time passed since the previous movement [10].

The rhythmic structure of the SCT may impose the need not only for the prediction of when to trigger the next tap to generate an interval, but also for the quantification of the time passed from the previous movement, in order to have cohesive timing mechanism to produce a repetitive tapping behavior. Indeed, the cells encoding elapsed (absolute-timing) and remaining time (relative-timing) showed some level of interaction during each cycle of time production in the SCT, supporting this notion [10] (Fig. 2e).

Cell activity changes associated with temporal information processing in behaving monkeys have been reported in the cerebellum [19], the basal ganglia [20], the thalamus [21], the posterior parietal cortex [22, 23], and the prefrontal cortex [24–27], as well as in the dorsal premotor cortex [28], motor cortex [29, 30], and the medial premotor areas MPC [10, 31]. These areas form different circuits that are linked to sensorimotor processing using the skeletomotor or oculomotor effector systems. Most of these studies have described climbing activity during different

timing contexts, which include discrimination of time, time estimation, single interval reproduction, and delay-related responses. Therefore, the increase or decrease in instantaneous activity as a function of the passage of time is a property present in many cortical and subcortical areas of the cortico-thalamic-basal ganglia circuit (CTBGc) that may be involved in different aspects of temporal processing in the hundreds of milliseconds scale. Indeed, recent studies have suggested the existence of a partially distributed timing mechanism, integrated by main core interconnected structures such as the CTBGc, and areas that are selectively engaged depending on the specific behavioral requirement of a task [12, 32, 33]. These task-dependent areas may interact with the core timing system to produce the characteristic pattern of performance variability in a paradigm and the set of intertask correlations described previously in psychophysical experiments [12].

The ubiquitous presence of cells' increments or decrements in discharge rate as a function of time across different timing tasks and areas of a potential core timing circuit suggests that ramping activity is a fundamental element of the timing mechanism. A key characteristic of ramping activity is their instantaneous nature and the fact that they normally peak at the time of an anticipated motor response. In the case of the SCT, the multiple neural chronometers must interact at some point in their ramping activity in order to define the rhythmic structure of the task. Thus, the tight interaction between the cells computing the elapsed time since the previous tap with the cells encoding the time remaining to the next tap generates a coordinated cycle of activation that ends with the triggering of a motor command, and the activation of motor cells involved in the execution of the tapping movement. Therefore, although the reported absolute-timing and the time-accumulator cells (Fig. 2c, d) are encoding the elapsed time since the previous motor event, it is evident that ramping cells are engrained in the temporal construction of motor intentions and actions [23, 34, 35]. This is a crucial point, since every timing task requires a movement, whether to express the perceptual decision in categorization or discrimination tasks or to produce accurately timed movements in tasks like SCT. Therefore, ramping activity may be part of the temporal apparatus that gates the motor responses to express a perceptual decision or produce a timed movement in a variety of behavioral contexts. An alternative possibility is that ramping activity reflects the accumulation of temporal information as described in the posterior parietal cortex [36, 37]. On the other hand, more abstract timing signals such as interval tuning, which are described below, can represent more cognitive elements of temporal processing.

Interval Tuning: An Abstract Signal of Temporal Cognition

Psychophysical studies on learning and generalization of time intervals give support to the notion that neurons in the timing circuit are tuned to specific interval durations, but can be activated in a modality- and context-independent fashion [38–40]. In addition, interval tuning has been suggested in conceptual papers [41]. In a recent paper, we described a graded modulation in the discharge rate of cells as a function of interval duration during the SCT in cells of MPC [42]. Figure 3a, b shows the profile of activation of a cell in the preSMA of a monkey performing this task. The neuron shows larger activity for the longest durations, with a preferred interval around 900 ms (Fig. 3c). In fact, a large population of MPC cells is tuned to different interval durations during the SCT, with a distribution of preferred intervals that covers all durations in the hundreds of milliseconds, although there was a bias towards long preferred intervals ($n = 487$ neurons; Fig. 3d). These observations suggest that the MPC contains a representation of interval duration, where different populations of interval-tuned cells are activated depending on the duration of the produced interval [42]. In addition, most of these cells also showed selectivity to the sequential organization of the task, a property that has been described in sequential motor tasks in MPC [43]. The cell in Fig. 3a, b

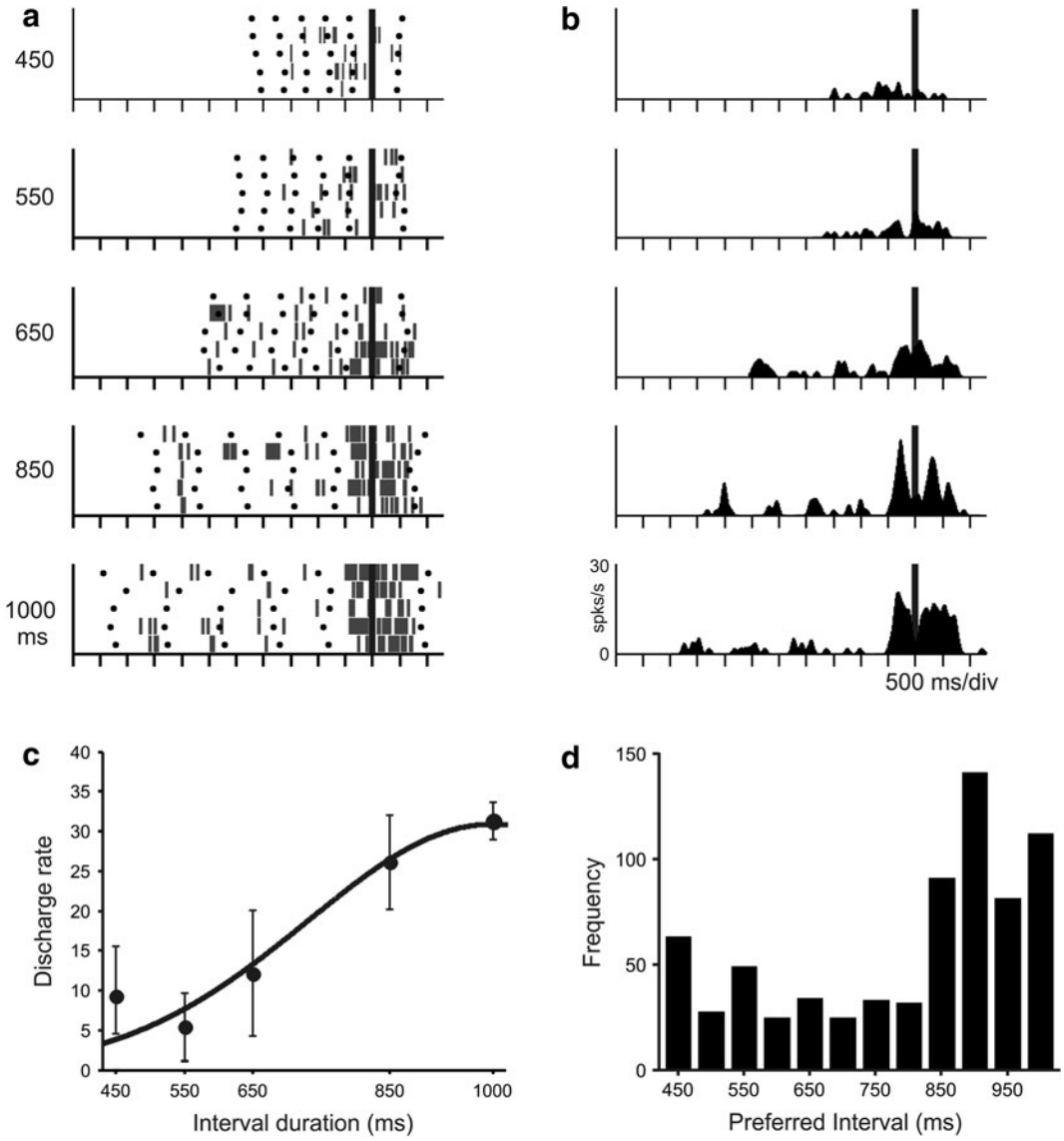

Fig. 3 Interval and ordinal-sequence tuning. (**a**) Responses of an interval-tuned cell with a long preferred interval and a sequential response to the last interval of the continuation phase during the SCT. Raster histogram aligned (*black line*) to the third tap of the continuation in the visual condition. (**b**) Average spike-density functions of the responses shown in **a**. (**c**) Tuning function for the same cell, where the mean (±SEM) of the discharge rate is plotted as a function of the target interval duration. The *continuous line* corresponds to the Gaussian fitting of the data. (**d**) Histograms of the preferred intervals in the visual marker condition for cells with significant interval tuning during the SCT. Modified from [36]

also shows an increase in activity during the last produced interval of the continuation phase of the task. Again, at the cell population level, all the possible preferred ordinal-sequences were covered (n = 426 neurons) [42]. These findings support the notion that MPC can multiplex interval duration with the number of elements in a sequence during the rhythmic tapping [42].

Cell tuning is an encoding mechanism used by the cerebral cortex to represent different sensory, motor, and cognitive features [44], which include the duration of the intervals, as reported here.

This signal must be integrated as a population code, where the cells can vote in favor of their preferred interval to generate a neural "tag" of the interval that is being executed during rhythmic tapping tasks. Interestingly, the cell tuning for duration is commonly accompanied by tuning to the ordinal structure of the SCT. Hence, the temporal and sequential information is multiplexed in a cell population signal that works as the notes of a musical score in order to define the duration of the produced interval and its position in the learned SCT sequence [10, 45].

As described above the elapsed or remaining time for a temporalized movement during the SCT is encoded in the ramping activity of MPC cells [10]. Relevant to the interval tuning phenomenon is the fact that one type of ramping cell shows a linear increase in its instantaneous discharge rate as a function of the elapsed time since a motor event, working as a time "accumulator". Here, we found that most of these time-accumulator cells were also significantly tuned to an interval, showing preferred intervals only for long durations. Therefore, a crucial question is what is the difference in functional impact between pure time-accumulator and pure interval-selective cells during the SCT? To try to answer this question we computed the Mutual Information (MI) between the spike density functions of the time-accumulator or the non-ramping interval-tuned cells and the target intervals using a sliding window for the auditory marker condition. The MI is a measure of the statistical dependency between the behavioral variable, in this case the target interval, and the neural activity. The MI of time-accumulator cells showed an up-down profile of activation with a MI maximum around the ramps' peak (Fig. 4a). In contrast, for interval-tuned cells that did not show a ramping profile in their instantaneous discharge rate, the MI was smaller but similar throughout the produced intervals (Fig. 4b). These findings support the notion that ramping cells are engrained in the dynamic construction of motor intentions and actions [10, 34, 46, 47]. On the other hand, interval tuning on the overall discharge rate may represent more cognitive aspects of temporal processing that are disengaged from the motor tapping output.

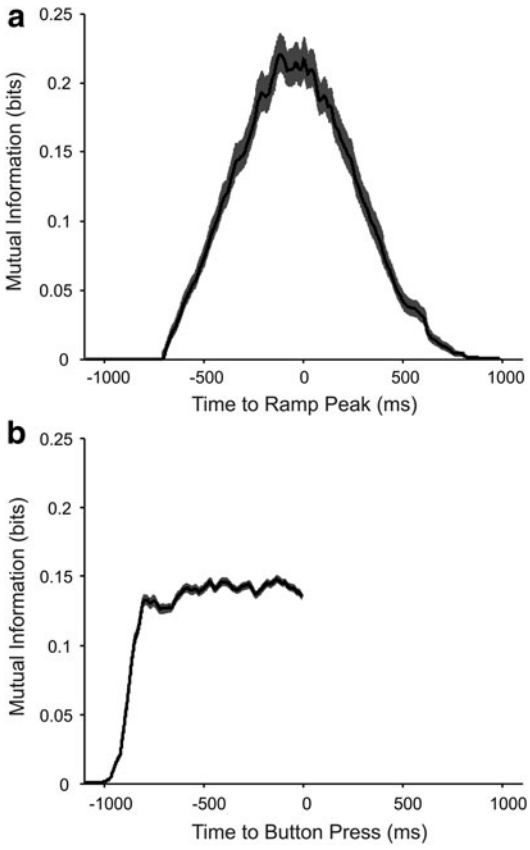

Fig. 4 Mutual Information for cells tuned to interval during the SCT. (**a**) Mean (*black*) and SEM (*gray*) of the mutual information as a function of time to ramp peak for the population of time-accumulator (n = 100) cells. (**b**) Mean (*black*) and SEM (*gray*) of the mutual information as a function of time to button press for the non-ramping duration-tuned (n = 304) cells

Neural Population Clocks in Behaving Primates: Temporal Processing in the Neural Dynamics

Time can be encoded in the unique temporal patterns of the integrated activity of groups of cells [47]. These cell populations should show time varying activity that is related to temporal processing. Different population clocks have been reported. For example, using a model of the activity of granule cells in the cerebellum, a

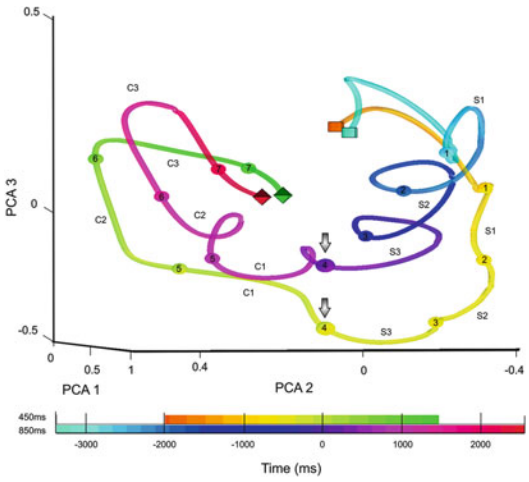

Fig. 5 Plot of the population dynamics of 549 cells during the SCT using the first three components of a Principal Component analysis on the time varying activity of the cells. The color code is associated to the passage of time for two network trajectories corresponding to 450 and 850 ms interval durations (see color codes at the *bottom*). The *cubes* correspond to the beginning of the trial, the *ellipses* to the median of the tapping movements (the tap ordinal number is inside), and the *diamonds* to the end of the trial. The trials are aligned to the fourth tapping movement as indicated by the *gray arrows*. S1–S3 correspond to the three synchronization intervals and C1–C3 to the three continuation intervals. Note the large difference in the network trajectories between interval durations and task phases. Unpublished observations

continuously changing population pattern can be read by Purkinje cells to tell time [48]. In addition, cell response simulations of recurrent cortical networks have been used to build population clocks that encode time in the context of temporal production [47] or perception [49]. In these models, time is implicitly encoded in the time-varying but repetitive state of the simulated networks.

Using the same logic, a clock population model was constructed using the task related activity of populations of MPC cells during the SCT. The history of the state of population responses can be depicted as an evolving trajectory in principal component space. Principal component analysis (PCA) is an analytical tool used to determine the most meaningful dimensions of a multidimensional dataset. Thus, Fig. 5 shows a 3D plot, using the first three PCAs, of the millisecond by millisecond change in the network state depicted here as a trajectory of the neural population during the six produced intervals of the SCT for a particular interval duration. Once the animal starts the tapping sequence in the task, the evolving trajectory of the population moves in a specific fashion to generate spirals for each of the produced intervals in the synchronization and continuation phases of the SCT (labeled as S1–S3 and C1–C3, respectively). Once the trial is finished (diamonds) the population returns to a state similar to the beginning (cubes) of the SCT. These trajectories of the recorded population are similar on different trials using the same interval, suggesting that the population clock reliably represents the passage of time. Indeed, there is a large difference in the population clock trajectories between interval durations (450 and 850 ms) and task phases. Hence, when reading the activity of task related cells, the next node of the core timing circuit can have access to information about the interval that is being produced and whether the subject is handling time in a sensory guided or an internally driven context.

Multiple Layers of Neuronal Clocks in the Medial Premotor Cortex

Our neurophysiological recordings in behaving animals indicate that MPC, an area of the core timing mechanism [32], uses multiple encoding strategies to represent different aspects of the temporal structure of the SCT. Ramping activity, the most reported timing signal in the literature, is close to the motor output and is used to trigger the multiple movements of the task sequence. Thus, the tight interaction between the cells computing the elapsed time since the previous tap with the cells encoding the time remaining to the next tap generates a coordinated cycle of activation that defines the rhythmic structure of the SCT. Figure 6 shows the ramping activity at the bottom of the encoding hierarchy of time during the SCT. We suggest that the ramps probably define the duration of each element of the rhythmic sequence, triggering the tapping

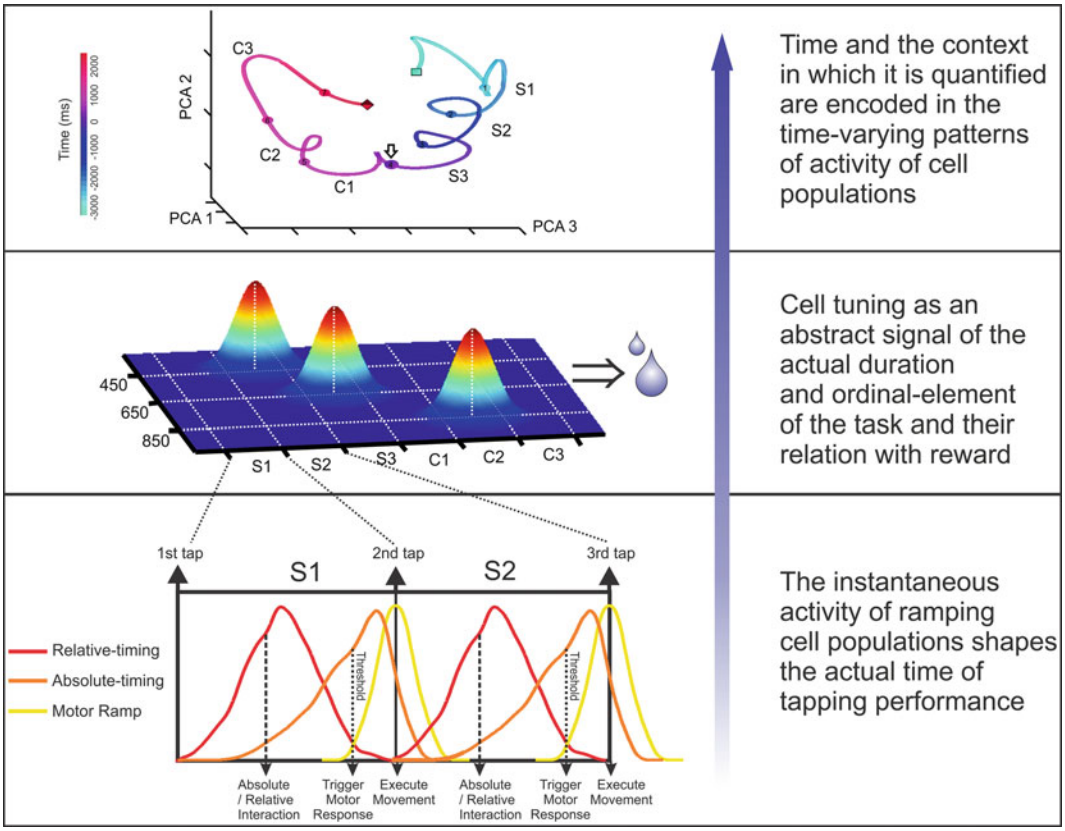

Fig. 6 A model of the interaction between the multiple layers of neuronal clocks in the medial premotor cortex. *Bottom*. Ramping activity defines the movement to movement temporal behavior of the animals during the SCT. *Middle*. Neuronal tuning to both duration and sequential order during the SCT as an abstract signal of what is the identity of the actually executed interval in an overlearned rhythmic task and its relation with the reward contingencies. *Top*. A population clock arises from the time-varying activity of a population of neurons dynamically interacting inside the MPC and across the core timing network

command that is probably generated in premotor areas and the primary motor cortex [34, 35]. Consequently, it is possible that the timing mechanism uses a temporal code in the form of ramp to encode timing actions [50, 51].

On top of these instantaneous signals we have neural tuning, which encodes the duration and the ordinal element of the six intervals produced sequentially during the SCT, as depicted in Fig. 6. This next level of temporal processing may work as the notes of a musical score, providing information to the timing network about what duration and ordinal element of the sequence is being executed. This information can be used to coordinate the networks that have been shaped by training to associate the temporal and ordinal structure of the SCT with the reward contingencies of our experiments [51].

Finally, the CNS uses dynamic neural representations of the passage of time and the context in which the intervals are executed by integrating the time-varying activity of populations of cells. Thus, the dynamics of the local cell ensemble and the overall flux of information in the core timing network can define the properties of the population clock observed in the MPC during the execution of the SCT. This integrated population signal is at the top of the hierarchy, since different nodes of the core timing network can: (1) read, (2) process, and (3) transmit the locally transformed population signal in a dynamic and reverberant fashion. This dynamic

and complex signal can encode the passage of time together with: (1) the history of the encoded interval in a rhythmic sequence, and (2) the context in which the intervals are produced, namely, using sensory cues or internal commands.

Acknowledgements We thank Raul Paulín, and Juan Jose Ortiz for their technical assistance. Supported by CONACYT: 151223, PAPIIT: IN200511.

References

1. Diehl RL, Lotto AJ, Holt LL. Speech perception. Annu Rev Psychol. 2004;55:149–79.
2. Shannon RV, et al. Speech recognition with primarily temporal cues. Science. 1995;270:303–4.
3. Phillips-Silver J, Trainor LJ. Feeling the beat: movement influences infant rhythm perception. Science. 2005;308:1430.
4. Janata P, Grafton ST. Swinging in the brain: shared neural substrates for behaviors related to sequencing and music. Nat Neurosci. 2003;6:682–7.
5. Tresilian JR. The accuracy of interceptive action in time and space. Exerc Sport Sci Rev. 2004;32:167–73.
6. Merchant H, Georgopoulos AP. Neurophysiology of perceptual and motor aspects of interception. J Neurophysiol. 2006;95:1–13.
7. Merchant H, Battaglia-Mayer A, Georgopoulos AP. Interception of real and apparent motion targets: psychophysics in humans and monkeys. Exp Brain Res. 2003;152:106–12.
8. Repp BH. Sensorimotor synchronization: a review of the tapping literature. Psychon Bull Rev. 2005;12:969–92.
9. Wing AM, Kristofferson AB. Response delays and the timing of discrete motor responses. Percept Psychophys. 1973;14:5–12.
10. Merchant H, Zarco W, Perez O, Prado L, Bartolo R. Measuring time with multiple neural chronometers during a synchronization-continuation task. Proc Natl Acad Sci U S A. 2011;108:19784–9.
11. Zarco W, Merchant H, Prado L, Mendez JC. Subsecond timing in primates: comparison of interval production between human subjects and rhesus monkeys. J Neurophysiol. 2009;102:3191–202.
12. Merchant H, Zarco W, Prado L. Do we have a common mechanism for measuring time in the hundreds of millisecond range? Evidence from multiple-interval timing tasks. J Neurophysiol. 2008;99:939–49.
13. Merchant H, Zarco W, Bartolo R, Prado L. The context of temporal processing is represented in the multidimensional relationships between timing tasks. PLoS One. 2008;3:e3169.
14. Gibbon J, Malapani C, Dale CL, Gallistel CR. Toward a neurobiology of temporal cognition: advances and challenges. Curr Opin Neurobiol. 1997;7:170–84.
15. Donnet S, Bartolo R, Fernandes JM, Cunha JP, Prado L, Merchant H. Monkeys time their movement pauses and not their movement kinematics during a synchronization-continuation rhythmic task. J Neurophysiol. 2014;111(6):2250–6.
16. Merchant H, Honing H. Are non-human primates capable of rhythmic entrainment? Evidence for the gradual audiomotor evolution hypothesis. Front Neurosci. 2014;7(274):1–8.
17. Honing H, Merchant H. Differences in auditory timing between human and non-human primates. Behav Brain Sci. 2014;37(5):473–474.
18. Perez O, Kass R, Merchant H. Trial time warping to discriminate stimulus-related from movement-related neural activity. J Neurosci Methods. 2013;212(2):203–10.
19. Perrett SP. Temporal discrimination in the cerebellar cortex during conditioned eyelid responses. Exp Brain Res. 1998;121:115–24.
20. Jin DZ, Fujii N, Graybiel AM. Neural representation of time in cortico-basal ganglia circuits. Proc Natl Acad Sci U S A. 2009;106:19156–61.
21. Tanaka M. Cognitive signals in the primate motor thalamus predict saccade timing. J Neurosci. 2007;27:12109–18.
22. Leon MI, Shadlen MN. Representation of time by neurons in the posterior parietal cortex of the macaque. Neuron. 2008;38:317–27.
23. Maimon G, Assad JA. A cognitive signal for the proactive timing of action in macaque LIP. Nat Neurosci. 2006;9:948–55.
24. Oshio K, Chiba A, Inase M. Temporal filtering by prefrontal neurons in duration discrimination. Eur J Neurosci. 2008;28:2333–43.
25. Brody CD, et al. Timing and neural encoding of somatosensory parametric working memory in macaque prefrontal cortex. Cereb Cortex. 2003;13:1196–207.
26. Sakurai Y, Takahashi S, Inoue M. Stimulus duration in working memory is represented by neuronal activity in the monkey prefrontal cortex. Eur J Neurosci. 2004;20:1069–80.
27. Genovesio A, Tsujimoto S, Wise SP. Feature- and order-based timing representations in the frontal cortex. Neuron. 2009;63:254–66.
28. Lucchetti C, Bon L. Time-modulated neuronal activity in the premotor cortex of macaque monkeys. Exp Brain Res. 2001;141:254–60.
29. Lebedev MA, O'Doherty JE, Nicolelis MA. Decoding of temporal intervals from cortical ensemble activity. J Neurophysiol. 2008;99:166–86.
30. Renoult L, Roux S, Riehle A. Time is a rubberband: neuronal activity in monkey motor cortex in relation to time estimation. Eur J Neurosci. 2006;23:3098–108.
31. Mita A, Mushiake H, Shima K, Matsuzaka Y, Tanji J. Interval time coding by neurons in the presupplementary and supplementary motor areas. Nat Neurosci. 2008;12:502–7.
32. Merchant H, Harrington D, Meck WH. Neural basis of the perception and estimation of time. Annu Rev Neurosci. 2013;36(1):313–36.

33. Merchant H, Bartolo R, Mendez JC, Perez O, Zarco W, Mendoza G. What can be inferred from multiple-task psychophysical studies about the mechanisms for temporal processing? Multidisciplinary aspects of time and time perception. In: Esposito A, Giagkou M, Cummins F, Papadelis G, Vatakis A, editors. Lecture notes in computer science. Berlin: Springer; 2011. p. 207–29.
34. Merchant H, Battaglia-Mayer A, Georgopoulos AP. Neural responses during interception of real and apparent circularly moving targets in motor cortex and area 7a. Cereb Cortex. 2004;14:314–31.
35. Merchant H, Perez O. Neurophysiology of interceptive behavior in the primate: encoding and decoding target parameters in the parietofrontal system. Coherent behavior in neural networks. In: Josic K, Matias M, Romo R, Rubin J, editors. Springer series in computational neuroscience, vol 3. New York: Springer; 2009. p. 191–206.
36. Janssen P, Shadlen MN. A representation of the hazard rate of elapsed time in macaque area LIP. Nat Neurosci. 2005;8:234–41.
37. Roitman JD, Shadlen N. Response of neurons in the lateral intraparietal area during a combined visual discrimination reaction time task. J Neurosci. 2002;22:9475–89.
38. Meegan DV, Aslin RN, Jacobs RA. Motor timing learned without motor training. Nat Neurosci. 2000;3:860–2.
39. Nagarajan SS, Blake DT, Wright BA, Byl N, Merzenich M. Practice-related improvements in somatosensory interval discrimination are temporally specific but generalize across skin location, hemisphere, and modality. J Neurosci. 1998;18:1559–70.
40. Bartolo R, Merchant H. Learning and generalization of time production in humans: rules of transfer across modalities and interval durations. Exp Brain Res. 2009;197:91–100.
41. Ivry RB. The representation of temporal information in perception and motor control. Curr Opin Neurobiol. 1996;6:851–7.
42. Merchant H, Pérez O, Zarco W, Gámez J. Interval tuning in the primate medial premotor cortex as a general timing mechanism. J Neurosci. 2013;33:9082–96.
43. Tanji J. Sequential organization of multiple movements: involvement of cortical motor areas. Annu Rev Neurosci. 2001;24:631–51.
44. Merchant H, de Lafuente V, Peña F, Larriva-Sahd J. Functional impact of interneuronal inhibition in the cerebral cortex of behaving animals. Prog Neurobiol. 2012;99(2):163–78.
45. Bartolo R, Prado L, Merchant H. Information processing in the primate basal ganglia during sensory guided and internally driven rhythmic tapping. J Neurosci. 2014;34(11):3910–3923.
46. Merchant H, Battaglia-Mayer A, Georgopoulos AP. Neurophysiology of the parieto-frontal system during target interception. Neurol Clin Neurophysiol. 2004;1(1):1–5.
47. Buonomano DV, Laje R. Population clocks: motor timing with neural dynamics. Trends Cogn Sci. 2010;14:520–7.
48. Medina JF, Garcia KS, Nores WL, Taylor NM, Mauk MD. Timing mechanisms in the cerebellum: testing predictions of a large-scale computer simulation. J Neurosci. 2000;20:5516–25.
49. Karmarkar UR, Buonomano DV. Timing in the absence of clocks: encoding time in neural network states. Neuron. 2007;53:427–38.
50. Zarco W, Merchant H. Neural temporal codes for representation of information in the nervous system. Cogn Critique. 2009;1(1):1–30.
51. Sohn JW, Lee D. Order-dependent modulation of directional signals in the supplementary and presupplementary motor areas. J Neurosci. 2007;27:13655–66.

Behavioral/Cognitive

Interval Tuning in the Primate Medial Premotor Cortex as a General Timing Mechanism

Hugo Merchant, Oswaldo Pérez, Wilbert Zarco, and Jorge Gámez
Instituto de Neurobiología, Universidad Nacional Autónoma de México, Campus Juriquilla, Quéretaro, México 76230

The precise quantification of time during motor performance is critical for many complex behaviors, including musical execution, speech articulation, and sports; however, its neural mechanisms are primarily unknown. We found that neurons in the medial premotor cortex (MPC) of behaving monkeys are tuned to the duration of produced intervals during rhythmic tapping tasks. Interval-tuned neurons showed similar preferred intervals across tapping behaviors that varied in the number of produced intervals and the modality used to drive temporal processing. In addition, we found that the same population of neurons is able to multiplex the ordinal structure of a sequence of rhythmic movements and a wide range of durations in the range of hundreds of milliseconds. Our results also revealed a possible gain mechanism for encoding the total number of intervals in a sequence of temporalized movements, where interval-tuned cells show a multiplicative effect of their activity for longer sequences of intervals. These data suggest that MPC is part of a core timing network that uses interval tuning as a signal to represent temporal processing in a variety of behavioral contexts where time is explicitly quantified.

Introduction

Temporal processing in the hundreds of milliseconds is a fundamental component of many complex behaviors, such as speech perception and articulation (Diehl et al., 2004), the execution and appreciation of music (Janata and Grafton, 2003), and sports performance (Merchant and Georgopoulos, 2006). Human subjects have the ability to quantify single or multiple intervals, defined by different sensory modalities, in a variety of perceptual or motor activities. Thus, a central question in timing research is whether a single neural mechanism is used for the measurement of time across different behaviors or if, on the contrary, multiple encoding strategies are used by the brain depending on the behavioral context in which time is processed (Merchant et al., 2013). Modeling studies have suggested that the representation of time is ubiquitous, arising from the intrinsic dynamics of nondedicated neural mechanisms (Karmarkar and Buonomano, 2007; Buonomano and Laje, 2010). In contrast, functional imaging studies using perceptual or motor tasks, with single or multiple time intervals and different sensory modalities used to define intervals, consistently found that structures such as the neostriatum and the supplementary motor areas, which are part of the cortico-basal ganglia-thalamocortical circuit (CBGT), are activated regardless of the nontiming factors involved in the task (Macar et al., 2006; Harrington et al., 2010). Furthermore, in accordance with recent neuroimaging studies (Bueti et al., 2008), psychophysical research using multiple timing tasks supports neither a common nor multiple context-dependent timing mechanisms (Merchant et al., 2008a,b). Therefore, a parsimonious hypothesis is that timing depends on the interplay between multipurpose timing structures such as CBGT and areas that are selectively engaged depending on the specific requirements of a task (Coull et al., 2011; Merchant et al., 2013).

Psychophysical studies on learning and generalization of time intervals give support to the notion that neurons in the timing circuit are tuned to specific intervals but can be activated in a modality- and context-independent fashion (Nagarajan et al., 1998; Meegan et al., 2000; Bartolo and Merchant, 2009). Therefore, the change in discharge rate as a function of duration could be a neural code used by the CBGT to represent the passage of time (Matell et al., 2003a), as it has been shown for spatial and numerical variables (Buhusi and Meck, 2005; Nieder et al., 2006). Nevertheless, it remains unknown whether cells in the core timing circuit are tuned to intervals and whether the CBGT encodes temporal information similarly across behavioral contexts, number of temporalized intervals, and sensory modalities. Consequently, in the present study we examined the response properties of medial premotor cortex (MPC) cells during the execution of two rhythmic tapping tasks where the intervals were defined by auditory or visual cues. The results showed that MPC cells are tuned to the duration of intervals during rhythmic tapping. Interestingly, the interval-tuned neurons showed similar preferred intervals (PIs) across modalities during single interval reproduction and synchronization–continuation tasks. These data suggest that MPC is part of a core timing circuit that uses interval tuning as a signal to represent temporal information in a variety of timing behaviors.

Received Nov. 28, 2012; revised April 8, 2013; accepted April 12, 2013.

Author contributions: H.M. designed research; H.M. and W.Z. performed research; O.P. contributed unpublished reagents/analytic tools; H.M., O.P., W.Z., and J.G. analyzed data; H.M. wrote the paper.

This work was supported by CONACYT Grant 151223 and PAPIIT Grant IN200511. We thank Bruno Averbeck, David Crowe, Victor de Lafuente, and Ranulfo Romo for fruitful comments on this manuscript. We also thank Luis Prado, Raul Paulín, and Juan Jose Ortiz for technical assistance.

Correspondence should be addressed to Dr. Hugo Merchant at the above address. E-mail: hugomerchant@unam.mx, merch006@umn.edu.

DOI:10.1523/JNEUROSCI.5513-12.2013

 0270-6474/13/339082-15$15.00/0

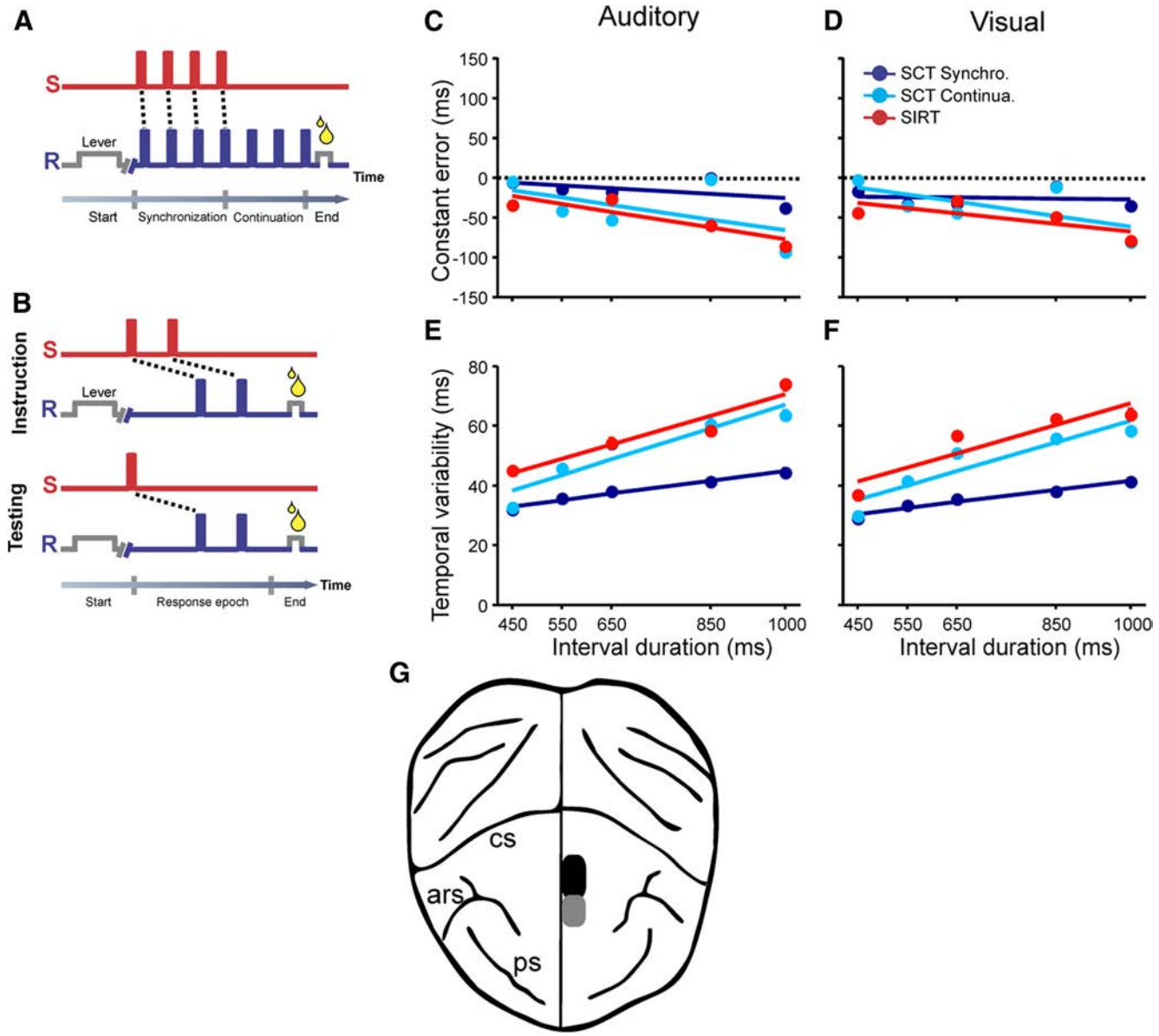

Figure 1. Tapping tasks, behavioral performance, and neural recordings. ***A***, SCT. Monkeys were required to push a button (R, blue line) each time stimuli with a constant interstimulus interval (S, red line) were presented, which resulted in a stimulus-movement cycle. After four consecutive synchronized movements, the stimuli stopped, and the monkeys continued tapping with a similar interval for three additional intervals. The target intervals, defined by brief auditory or visual stimuli, were 450, 550, 650, 850, and 1000 ms and were chosen pseudo-randomly within a repetition. ***B***, SIRT. For each interval, there were training and testing periods. In the training period, the target interval (450, 650, 850, or 1000 ms) was presented at the beginning of the trial. Then, the animal tapped twice on the button to produce the same interval. This was repeated for five training trials, after which the monkey entered the testing period, where he produced another 10 single intervals, each in response to the presentation of a single stimulus. ***C***, ***D***, Constant error (produced-target interval) during the performance of both tasks using auditory (***C***) and visual (***D***) interval markers. Monkeys slightly underestimated the intervals during the synchronization (Synchro; blue) and continuation (Continua; cyan) phases of SCT, as well as during the SIRT (red). The SEM is smaller than the dot diameter. ***E***, ***F***, Temporal variability increased as a function of target interval in the auditory (***E***) and visual (***F***) interval marker conditions, during both phases of SCT and during SIRT. ***G***, Location of the recording area in SMA (black oval) and pre-SMA (gray oval) in a top view of the monkey brain. cs, Central sulcus; ars, arcuate sulcus; ps, principal sulcus.

Materials and Methods

General

All the animal care, housing, and experimental procedures were approved by the National University of Mexico Institutional Animal Care and Use Committee and conformed to the principles outlined in the *Guide for the Care and Use of Laboratory Animals* (NIH, publication number 85-23, revised 1985). The two monkeys (*Macaca mulatta*, both males, 5–7 kg body weight) were monitored daily by the researchers and the animal care staff, and every second day by the veterinarian, to check the conditions of health and welfare. To ameliorate their condition of life, we routinely introduced in the home cage (1.3 m^3) environment toys (often containing items of food that they liked) to promote their exploratory behavior. The researcher that tested the animals spent half an hour interacting with the monkeys directly, giving, for example, new objects to manipulate.

Synchronization–continuation task. The synchronization–continuation task (SCT) used in this study has been described previously (Zarco et al., 2009; Merchant et al., 2011). Briefly, the monkeys were required to push a button each time stimuli with a constant interstimulus interval were presented, which resulted in a stimulus-movement cycle (Fig. 1*A*). After four consecutive synchronized movements, the stimuli were eliminated, and the monkeys continued tapping with the same interval for three additional intervals. To avoid a preference toward short intervals, the reward amount was adjusted as a function of target durations, with longer durations giving greater amounts of juice, as described previously (Zarco et al., 2009). Trials were separated by a variable intertrial interval

(1.2–4 s). The target intervals, defined by brief auditory (33 ms, 2000 Hz, 65 dB) or visual (4 cm side green square, 33 ms) stimuli, were 450, 550, 650, 850, and 1000 ms and were chosen pseudo-randomly within a repetition. Five repetitions were collected for each target interval and modality.

Single interval reproduction task. For each interval, there were training and testing periods (Fig. 1*B*). In the training, the target interval (450, 650, 850, or 1000 ms presented in blocks of trials) was presented at the beginning of the trial. Then, the monkey tapped twice on the push-button to reproduce this interval. After five training trials, the animal entered the testing period, where it reproduced another 10 single intervals with the same duration, each in response to a single stimulus that acted as a go signal. The duration of each interval was associated with a particular stimulus feature so that during the testing period, the go signal was a stimulus that had been linked to the production of a specific interval during the training period. Thus, a 4400 Hz tone or a blue square was associated with the reproduction of 450 ms, a 3000 Hz tone or green square with 650 ms, a 1000 Hz tone or cyan square with 850 ms, and a 650 Hz tone or yellow square with 1000 ms. The target intervals were chosen pseudo-randomly between blocks. A total of 60 trials (40 for the testing period) were collected. Monkeys were rewarded following the same rules described in the SCT (Zarco et al., 2009). Throughout the experiment, trials were separated by a variable 1.2–4 s intertrial interval.

Procedure. A block of tasks consisted in the random order execution of the four task combinations: SCT and single interval reproduction task (SIRT), with visual and auditory interval marker conditions. During each day of recordings, the animals performed between two and five blocks of tasks. The same monkeys used by Merchant et al. (2011) were used in the present study. It is important to emphasize that we used the same durations in the SCT and SIRT. These intervals correspond to the hundreds of milliseconds range, as in previous time perception experiments (Leon and Shadlen, 2003; Harrington et al., 2010), but not as in previous time production experiments where intervals in the seconds range were used (Rakitin et al., 1998; Mita et al., 2009). Therefore, in the present study, we were able to investigate the neural underpinnings of temporal processing in the hundreds of milliseconds range during the execution of rhythmic sequences that share many components of musical execution, as well as during the production of single intervals.

Neural recordings. The extracellular activity of single neurons in the medial premotor areas was recorded using a system with seven independently movable microelectrodes (1–3 MΩ; Uwe Thomas Recording) (Merchant et al., 2004). All the isolated neurons were recorded regardless of their activity during the task, and the recording sites changed from session to session. At each site, raw extracellular membrane potentials were sampled at 40 kHz. Single-unit activity was extracted from these records using the Plexon off-line sorter (Plexon). Structural magnetic resonance imaging was used to localize the recording sites (Merchant et al., 2011). Capillary tubes filled with vitamin-E oil were placed in the internal phase and on top of the 1.5 cm circular recording chambers and were used as markers to determine the anteroposterior and mediolateral location of the electrode penetrations (Fig. 1*G*).

Data analysis

General. Subroutines written in Matlab (version 7.6.0.324; Mathworks) and the SPSS statistical package (version 12, 2003; SPSS) were used for the statistical analyses. The level of statistical significance to reject the null hypothesis was $\alpha = 0.05$. An initial ANOVA was performed for each neuron to identify cells whose activity changed significantly during the recording session. Of a total of 1570 cells recorded in the MPC in both monkeys (1267 in monkey 1 and 303 in monkey 2), 993 did not show a statistically significant effect of recording time during the key hold control period and were analyzed further. In this study, we do not address functional differences between SMA versus pre-SMA, since similar neural signals were observed in both areas. All these neurons were recorded for 5 repetitions during the SCT and for 15 repetitions during the SIRT; however, for the latter only the 10 trials corresponding to the testing phase were analyzed in the present study.

Timing behavior. Two parameters were evaluated as a measure of subject performance: the variance and the constant error. The mean and SD of each intertap interval for each monkey were used to compute the constant error and the variance, respectively. This implies that for the SCT, the variance corresponded to a general measure of within- and between-trial variability without averaging across trials in the synchronization and continuation phases. In accordance, in the SIRT the variance corresponded to the between-trial variability, since only one interval per trial was produced. The constant error was defined as the difference between the mean of the produced intervals minus the target interval. In a previous study, we compared the performance of human subjects and three monkeys during the two tasks using auditory or visual interval markers (Zarco et al., 2009). The results showed that the time subestimation and the increase in temporal variability as a function of the interval were similar to the data shown in Figure 1*C–F* for the two monkeys performing the tasks during the electrophysiological recording sessions of the present paper.

Computing the discharge rate. The duration of target intervals varied systematically in the SCT and SIRT. Therefore, we could not use a fixed temporal window to compute the discharge rate of the cells, since it could artificially produce a bias in discharge rate toward shorter intervals. Instead, we used the Poisson train analysis (Hanes et al., 1995) to identify the periods of cell activation within each produced interval. This analysis determines how improbable it is that the number of action potentials within a specific condition (i.e., target interval and ordinal sequence) was a chance occurrence. For this purpose, the actual number of spikes within a time window was compared with the number of spikes predicted by the Poisson distribution derived from the mean discharge rate during the entire recording of the cell. The measure of improbability was the surprise index (*SI*) defined as follows:

$$SI = -\log P, \tag{1}$$

where P was defined by the following Poisson equation:

$$P = e^{-rT} \sum_{i=n}^{\infty} \frac{(rT)^i}{i!}, \tag{2}$$

where P is the probability that, given the average discharge rate r, a spike train of a produced interval T contains n or more spikes in a trial. Thus, a large *SI* indicates a low probability that a specific elevation in activity was a chance occurrence. This analysis assumes that an activation period is statistically different from the average discharge rate r, considering that the firing of the cell is following a nonhomogenous Poisson process (see also Perez et al., 2013).

The spike train analysis was applied for all trials of each produced interval in the SCT (30 produced intervals, 5 duration × 6 intervals in the sequence) and the SIRT (4 produced intervals, 4 durations × 1 interval in the sequence). We used the algorithm (Hanes et al., 1995) to detect activations above randomness, as follows. The mean discharge rate (r) was computed for the entire recording session of the cell (i.e., the four task combinations). The first two consecutive spikes that had a mean discharge rate greater or equal to r were found, and the time between these two spikes was defined as the initial T value. Then, the next spike was identified, and the interspike interval (ISI) between this and the previous spike was added to T. The corresponding *SI* was calculated. This was repeated until the end of the spike train, and the spike at the end of the interval T with the maximum *SI* was defined as the end of the burst. Next, the *SI* was calculated for the interval T from the last to the first spike. Then, the spikes from the beginning were removed until the end of the spike train, computing the corresponding *SI* in each step. The spike at which *SI* was maximized was defined as the beginning of the burst. All produced intervals that showed a burst larger than 80 ms and a $SI\ p < 0.05$ were considered as having a significant activation. If this criterion was not fulfilled, it was assumed that there was no response for that target duration/ordinal sequence combination. We found cases with more than one significant burst inside a produced interval, and in this situation we computed the average discharge rate for the two periods of activation.

Interval and sequence selectivity. We recorded 993 neurons during the performance of the four task combinations (see above). The activity of these cells was subjected to two initial analyses. The first one was per-

formed to determine the cells with significant differences in their response magnitude across durations, for each produced interval in the rhythmic sequence of the SCT, and for the single reproduced interval of the SIRT. The corresponding ANCOVA used the discharge rate computed from the Poisson train analysis as the dependent variable, the discharge rate during the key holding control epoch as the covariate, and the target interval as the factor. The second analysis was performed to determine the cells with significant changes in activity across duration, ordinal sequence, or both parameters during the SCT. This analysis consisted of a two-way ANOVA where the discharge rate computed from the Poisson train analysis was the dependent variable and the target interval (450,550, 650, 850, and 1000 ms) and the ordinal sequence (one to six produced intervals) were the factors.

Classification of ordinal sequence or task phase selectivity. Cells with significant ANOVA effects on Sequence or Interval × Sequence interaction were segregated in two functionally distinct cell populations, namely ordinal- or phase-selective neurons, using K-means clustering. This procedure partitioned neural responses into 13 clusters, where each cell was assigned to the cluster with the nearest mean (Johnson and Wichern, 1998). The initial means of the clusters were the following:

$$\mu_1 = (1,0,0,0,0,0)$$

$$\mu_2 = (0,1,0,0,0,0)$$

$$\mu_3 = (0,0,1,0,0,0)$$

$$\mu_4 = (0,0,0,1,0,0)$$

$$\mu_5 = (0,0,0,0,1,0)$$

$$\mu_6 = (0,0,0,0,0,1)$$

$$\mu_7 = (1,1,0,0,0,0)$$

$$\mu_8 = (0,1,1,0,0,0)$$

$$\mu_9 = (0,0,1,1,0,0)$$

$$\mu_{10} = (0,0,0,1,1,0)$$

$$\mu_{11} = (0,0,0,0,1,1)$$

$$\mu_{12} = (1,1,1,0,0,0)$$

$$\mu_{13} = (0,0,0,1,1,1)$$

where $\mu_1 - \mu_6$ correspond to the clusters that responded only to one element of the six interval sequence; $\mu_7 - \mu_{11}$ to the clusters that responded to two consecutive elements of the sequence; and μ_{12} and μ_{13} to the synchronization and continuation phase, respectively. The normalized discharge rate of the Poisson train analysis for each ordinal element, across durations and trials (a total of 30 trials for each ordinal element), was used as the dependent variable. A one-way multivariate ANOVA was performed using the normalized responses of cells across each ordinal element as dependent variables and the clustering results as factors. The results showed that the 13 clusters were significantly different from each other ($\chi^2_{(72)} = 3.61 \times 10^3$; $p < 0.00001$).

Gaussian regression. A Gaussian function was fitted to the cell activity in MPC to determine the tuning to duration. These fittings were performed only on the cells with a significant effect on the corresponding ANOVA (see above). The discharge rate computed from the Poisson train analysis for each produced interval during the SCT or the SIRT was treated as the dependent variable in a nonlinear regression where the target duration was used as independent variables in the following equation:

$$f(s) = he^{-\left(\frac{s-s_p}{k}\right)^2}, \quad (3)$$

where $f(s)$ corresponds to the discharge rate associated with a particular value of the independent variable s, h is the parameter of maximum height, and k is the parameter of dispersion. s_p corresponds to the preferred interval. The regression was performed for each of the six elements of the SCT sequence and for a single produce interval in the SIRT. The function was fitted using the least squares method following a genetic algorithm implemented in Matlab (version 7.3.0.267; Mathworks). A detailed analysis of the residuals was performed (Draper and Smith, 1981), and the R^2 was calculated. Furthermore, the significant level of the R^2 was assessed using a bootstrap technique as follows. First, the firing rate of the 25 total trials collected (five repetitions, five durations) was permuted to get five random mean firing rates. Second, a curve was fitted to these data, and the R^2 was computed. This procedure was repeated 1000 times, and the distribution of R^2 values was saved. Finally, if the R^2 of the original regression was larger than the value at 0.95 of the bootstrap R^2 distribution, the regression was considered significant (Merchant et al., 2008c). Nonsignificant ($p \geq 0.05$) or out-of-bounds fits were excluded from the results.

Tuning dispersion measure. We used the half-width dispersion, k_{50}, at the midpoint of the tuning magnitude as the consistent measure of tuning dispersion. The corresponding equation was as follows:

$$k_{50} = \sqrt{ln2k}. \quad (4)$$

Double-Gaussian regression. A double-Gaussian was fitted to the cell activity in MPC to determine produced duration and sequence-order tuning during the SCT using the following equation:

$$f(I,S) = he^{-\left(\frac{I-I_p}{k_I}\right)^2 - \left(\frac{S-S_p}{k_S}\right)^2}, \quad (5)$$

where h is the parameter of maximum height and k_I and k_S are the parameters of dispersion for interval and sequence, respectively. I_p and S_p correspond to the preferred interval and preferred sequence order, respectively. The significant level of the R^2 was assessed using the above bootstrap technique. Again, nonsignificant ($p \geq 0.05$) or out-of-bounds fits were excluded from the results.

Bayesian decoding. We used a Bayes analysis approach to address the following problem: given the firing rates of cell populations tuned to both the interval and the ordinal structure of the SCT, how can we optimally infer the sequential and temporal behavior of the animals in the task? The basic method assumes that we know the encoding functions $f_1(I,S)$, $f_2(I,S)$,… $f_N(I,S)$ are associated with the produced duration/sequence order for a population of n cells from Equation 5. Given the discharged rate (r, based on the Poisson train analysis), fired by the cells within a specific produced duration–sequence combination, the objective was to compute the decoded probability distribution for both task parameters, across trials with similar temporal behavior throughout the six produced intervals.

Let the vector $x = (I,S)$ be the duration–sequence combination and the vector $r = (r_1, r_2, \ldots, r_N)$ be the discharge rate of our recorded cells within this period. The reconstruction is based on the following standard Bayes equation for conditional probability:

$$p(x|r) = \frac{p(r|x)\,p(x)}{p(r)}. \quad (6)$$

The goal is to compute $p(x|r)$, that is the probability for the duration–sequence parameters to be at the value x, given the firing rates r. $p(x)$ is the duration–sequence probability, which was dependent on the overall distribution of the produced durations by the monkey and the constant sequential structure of the SCT. The probability $p(r)$ for the occurrence of the firing rate r is equal to the sum of the conditional probability $p(x|r)$ over all $p(x)$. Thus, the key step is to evaluate $p(x|r)$, which is the probability that the firing rate r occurred given that we know the duration–sequence combination x. It is intuitively clear that this probability is determined by the estimated firing rates from Equation 5. More precisely, if we assume that the cell activity has a Poisson distribution and that the different cells are statistically independent of one another, then we can obtain the following explicit expression:

$$p(r|x) = \prod_{i=1}^{N} \frac{f_i(x)T}{(r_iT)!} e^{-f_i(x)T}, \quad (7)$$

where $f_i(x)$ is the average predicted firing rate of cell i of a population of n cells, x is the duration–sequence parameter, and T is an arbitrary time window (500 ms in this case).

The Bayesian reconstruction method uses Equation 7 to compute the probability distribution $p(x|r)$ for the parameter's combination x given the firing rate r for all cells associated with that x. Then, once Equation 6 is solved, we consider the maximum value of the computed probability distribution as the decoded duration–sequence parameter (Merchant and Perez, 2009). In other words:

$$\hat{X}_{MAP} = \arg\max_x p(x|r) \quad (8)$$

To systematically decode both the duration of the produced intervals and the sequential order of the SCT, we used groups of trials to compute $p(x|r)$ where the temporal behavior on the monkeys was similar and where the activity of cells during this behavior was significantly tuned according to Equation 5. Hence, the SCT trials during cell recording were divided into four classes using the following procedure. First, the medians of the produced durations for each of the three intervals in the synchronization and the three intervals in the continuation phase were computed for the entire database. Then, each of the six consecutive intervals of a trial were called "short" or "long" if their value was below or above the median of the corresponding six distributions. Finally, the synchronization phase of a trial was classified as "preferential short" if two or three of its produced intervals were short, or as "preferential long" if two or three of its produced intervals were long. The same criteria were used for the continuation phase. Consequently, the four classes of trials were (1) synchronization short–continuation short, (2) synchronization short–continuation long, (3) synchronization long–continuation short, and (4) synchronization long–continuation long.

For each of the four classes, we performed 1000 decodifications using permuted populations of 200 trials to avoid a population-size effect in the reconstructed values. Since this decoding method used groups of trials with similar timing performance across neurons that were not necessarily recorded simultaneously, we also performed decoding with cross-validation to access possible overfittings. In this case, 1000 decodifications for each condition were performed using permuted populations of 150 cells (from the total number of neurons, namely 246 for visual and 216 for the auditory conditions) and a leaving-one-out cross-validation algorithm, with the purpose of sampling the reconstruction accuracy (variance and bias; Dayan and Abbott, 2001, their Eqs. 3.38 and 3.39) within the overall cell population. The results of the cross-validation method were very similar to the decoded values shown in Figure 5, indicating high correlation values between the two decoding measures (Auditory Duration: $r = 0.82$, $p < 0.0001$; Auditory Ordinal-Sequence: $r = 0.99$, $p < 0.0001$; Visual Duration: $r = 0.84$, $p < 0.0001$; Visual Ordinal-Sequence: $r = 0.98$, $p < 0.0001$). Therefore, the results showed in Figure 5 are not the result of data overfitting.

The bias between the decoded and the behavioral parameters, shown in Figure 6*C–F*, was evaluated using the standard methods (Johnson and Wichern, 1998). On the other hand, Figure 6 shows the mean and the two-dimensional variability of all decoded values. The two-dimensional variability was characterized using the bivariate normal distribution in the form of an ellipse. This ellipse is centered at the x–y (sequence–duration) mean, and the length of its axes is proportional to the square root of the two eigenvalues of the x–y variance–covariance matrix. The two axes are orthogonal and are equivalent to the variances along each axis (i.e., the larger axis corresponds to the axis of larger variance). We scaled the axis using the constant where there is the upper (100α)th percentile of the χ^2 distribution with k degrees of freedom. This leads to an ellipse that contains the $(1 - \alpha) \times 100\%$ of the distribution probability, where $\alpha = 0.69$ that corresponds to the SD of the distribution (Fig. 5). Finally, the orientation of the ellipse was defined by the angle θ that was equal to the arctangent of the x and y elements of the eigenvector from the larger eigenvalue (Johnson and Wichern, 1998).

Cell stability during the performance of the four tasks. We used previously validated criteria to assess the single-unit stability during the performance of the tasks by measuring the similarity of the average spike waveforms and the ISI histograms (ISIHs) (Dickey et al., 2009). For the case of the ISIH, we used a score that compares the overall shape of the ISIH for two tasks. The ISIH shape for each task was modeled using a mixture of three log-normal distributions, where each distribution can be considered as comprising a fast (centered on 2.5 ms), a medium (30 ms), and a slow (1 s) ISIH component. The mixture model was fitted using an expectation–maximization algorithm (Hastie et al., 2001). Hence, each ISIH was described by eight parameters: the mean and SDs of the three components and the mixing probabilities of the first two components (the last is not needed because the probabilities sum to 1). Then, the similarity score I between the ISIHs of two tasks was defined as follows:

$$I(A,B) = \sqrt{\sum_{i=1}^{8} \frac{(A_i - B_i)^2}{\sigma_i^2}}, \quad (9)$$

where A and B are the two sets of eight parameters and σ_i are the normalizing factors obtained from the variance of the eight parameters for a set of sample data. The data come from the ISIHs of the four tasks of the cell in Figure 7*A–D*. Therefore, a similarity score I close to zero indicates stability, whereas a high value indicates instability of the cell between the two tasks. The stability threshold used here was 10.5, which was reported previously as an appropriate value in chronic single-cell recordings (Dickey et al., 2009).

A total of 762 cells showed a similarity score I below the 10.5 threshold (Dickey et al., 2009) in at least two consecutive tasks and were considered stable between the task pairs with I scores below that threshold. Thus, the difference in preferred intervals across tasks was computed for a population of 668 neurons that showed both a significant Gaussian fitting for interval tuning and stable responses according to the similarity score I for pairs of consecutive tasks combinations.

Bootstrap for preferred intervals across tasks. We performed a bootstrap analysis to test whether the percentage of cells with similar preferred intervals (PI difference <150 ms) was above chance for different task pairs. We built 5000 bootstrap populations, by selecting randomly the PI of the cells within each task pair [i.e., auditory SCT (SCTa) vs visual SCT (SCTv)] and computed the PI difference for each randomly selected pairs. Then, we measured the percentage of cells with similar PIs (PI difference <150 ms) in tuning in these bootstrap populations and compared it with the original percentage of cells with similar PIs. We found that for all the task pairs [SCTa-SCTv, auditory SIRT (SIRTa)-visual SIRT (SIRTv), SCTa-SIRTa, and SCTv-SIRTv] the probability that the bootstrapped populations showed a similarity in PI between tasks that was equal or above the original PI similarity was always below $p = 0.05$.

Results

Behavioral performance

We investigated how MPC neurons encoded the temporal structure of different tapping behaviors that varied in the number of produced intervals and the modality used to drive temporal processing. We trained two monkeys in a SCT and a SIRT (Zarco et al., 2009). In the SCT, the monkeys were required to push a button each time stimuli with a constant interstimulus interval were presented, which resulted in a stimulus-movement cycle (Fig. 1*A*). After four consecutive synchronized movements, the stimuli stopped, and the monkeys continued tapping with the same interval for three additional intervals (Fig. 1*A*). SIRT started with training trials where the monkey tapped twice on a button to reproduce an instructed target interval, followed by testing trials where a go signal triggered the reproduction of the same interval (Fig. 1*B*). Brief auditory or visual interval markers were used during both tasks, and the range of target intervals was from 450 to 1000 ms. The monkeys were able to accurately produce the target intervals, showing an average underestimation of ~50 ms across durations and modalities, during the testing phase of SIRT and both task phases of the SCT (Fig. 1*C*,*D*). In addition, we analyzed the temporal variability of the monkeys' tapping perfor-

mance, which was defined as the SD of the individual interresponse intervals (Merchant et al., 2008a) (see Materials and Methods). Temporal variability increased linearly as a function of duration in SIRT and the synchronization and continuation phases of SCT (Fig. 1*E*,*F*). The timing behavior was similar for the auditory and visual interval marker conditions (Fig. 1*C–F*; *t* test for constant error and temporal variability, $p > 0.05$). These findings show that the monkeys had a remarkably accurate timing performance in complex temporal tapping tasks. Furthermore, the data show a temporal variability that followed the scalar property of interval timing, a property that has been documented in many species and temporal tasks (Gibbon et al., 1997).

Generalities on the neurophysiology of interval production

A large number of parameters were used in the present experimental design to test the existence of a single or multiple neural clocks in a cortical area that has been associated with temporal processing in functional imaging and neurophysiological studies (Mita et al., 2009; Wiener et al., 2010; Merchant et al., 2011). Our results indicated for the first time that cells in MPC were tuned to intervals in the hundreds of milliseconds range, showing an orderly variation in discharge rate as a function of the produced duration in the SIRT and SCT. Thus, the present study focuses on the comparison of the interval tuning properties of cells between tasks [which involve the time production of one (SIRT) or six intervals (SCT)] and the modality used to define the intervals (auditory vs visual). In the initial part, we describe the interval tuning properties of neurons during SCT and SIRT. Then, we describe strong interaction between the neural signals associated with the representation of the produced interval and the organization of sequential motor behavior during the SCT. Next, we determine the differences in preferred intervals across tasks and modalities, showing interval-tuning invariance in a large population of cells. Finally, we provide evidence for a possible gain mechanism for encoding the total number of intervals in a sequence of rhythmic movements.

Interval tuning in SCT and SIRT

We recorded from 993 randomly selected MPC cells that showed stable responses during the performance of the four task combinations (Fig. 1*G*). An initial analysis was performed to determine the cells with significant differences in their response magnitude across interval durations, for each produced interval in the rhythmic sequence of the SCT, and for the single reproduced interval of the SIRT. The corresponding ANCOVA used the discharge rate as the dependent variable, the discharge rate during the key holding control epoch as the covariate, and the target interval as the factor. It is important to emphasize that the duration of target intervals varied systematically in our tasks, and therefore we could not use a fixed temporal window to compute the discharge rate of the cells. As an alternative, we used the Poisson train analysis (see Materials and Methods) to identify the periods of cell activation within each produced interval. Table 1 shows the number of cells with a significant effect on interval duration in the ANCOVA for the four task combinations. It is evident that a large percentage of cells showed modulations in activity for different durations in the SCT and SIRT, with a small bias toward visual marker conditions in both tasks.

We fitted Gaussian functions to the discharge rate of cells as a function of interval on the cells with significant ANCOVA effects for Interval. Most of these cells showed significant Gaussian tuning (Table 1), and therefore they were considered interval-selective cells (Fig. 2). Figure 2, *A* and *B*, shows the raster of a cell tuned for a long duration during both the SCT and SIRT in the auditory interval maker condition. The preferred interval of the cell was around 880 ms in both tasks, as shown in Figure 2*C* for the respective Gaussian fittings.

Table 1. Number of neurons with a significant effect on target interval in the ANCOVA and a significant Gaussian fit for interval across the four task combinations

Task	ANCOVA	Gaussian fit
SCT auditory	521 (52.5)	440 (84.5)
SCT visual	570 (57.4)	487 (85.4)
SIRT auditory	304 (30.6)	229 (75.3)
SIRT visual	317 (31.9)	232 (73.2)

Numbers in parentheses correspond in the ANCOVA to the percentages from the 993 studied neurons and in the Gaussian fits to the percentages from the neurons with significant effects in the ANCOVA.

Although a wide range of preferred intervals was represented in the population of interval-selective cells, the distribution of preferred intervals showed a bias toward long intervals in the four task combinations (Fig. 2*D–G*). In addition, the half-height tuning dispersion was skewed toward low dispersions (see Fig. 2*H* for the SCT in the visual condition; the tuning dispersion for the other three task combinations is not depicted but showed a similar trend). The results suggest that MPC cells showed an orderly variation in discharge rate as a function of the produced duration in the SIRT and SCT for auditory and visual interval marker conditions, where all possible preferred intervals are represented in the cell population, even though there was a clear bias toward long durations.

Cell encoding for interval and ordinal sequence during the SCT

A large group of neurons during the SCT showed activity that varied significantly (two-way ANOVA) with the interval, the task sequence (six elements, three in the synchronization and three in the continuation phase), or both parameters during this task (Auditory = Interval, 475 of 993 cells; Sequence, 461; Interval × Sequence, 172; Visual = Interval, 494; Sequence: 511; Interval × Sequence, 237). These findings suggest that MPC shows strong neural signals for both the sequential and the temporal structure of the SCT. Therefore, the next step was to characterize the encoding properties of MPC neurons for these task parameters, focusing first on sequence, then on the interaction between ordinal sequence and duration.

Cells with significant ANOVA effects on Sequence or Interval × Sequence interaction were segregated in two functionally distinct cell populations according to their responses to the sequential order of the SCT using a clustering algorithm (see Materials and Methods). The first group may encode the ordinal structure of the task sequence, since these cells responded during one or two consecutive elements of the six interval sequence (Table 2; Fig. 3*A–C*). These cells were considered ordinal-selective cells, and they indicate that the well known ordinal sequential movement activity in MPC (Tanji, 2001) is also present during the execution of the SCT. In contrast, the second group consisted of cells that were active during the synchronization or continuation phase of the SCT (Table 2; Fig. 3*A*,*D*). This type of phase-selective response may be associated with the temporal information processing during sensory-guided (synchronization) or internally driven (continuation) cyclic movement production.

The interaction between the neural signals associated with the organization of sequential motor behavior and the representa-

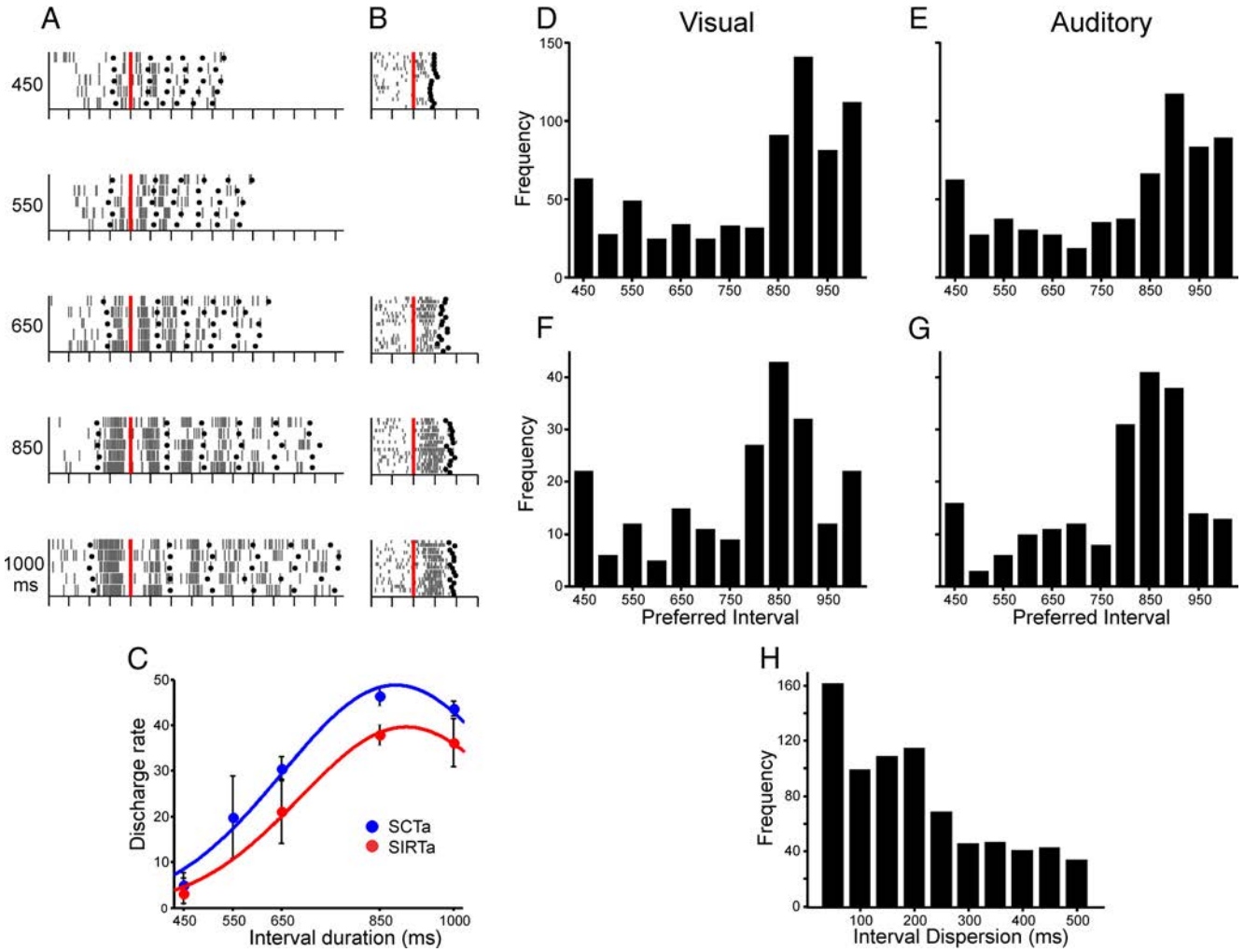

Figure 2. Cell tuning for interval during the SCT and SIRT. ***A***, Responses of an interval-tuned cell with a long preferred interval during the first two elements of the synchronization phase of the SCT in the auditory marker condition. The raster histogram is aligned (red line) to the second tap of the synchronization phase. Black dots correspond to tapping times. ***B***, Responses of the interval-tuned cell in ***A*** with a long preferred interval during the SIRT in the auditory condition. The raster histogram is aligned (red line) to the first tap. ***C***, Tuning functions for the cell in ***A*** and ***B***, where the mean ± SEM of the discharge rate is plotted as a function of the target interval. The continuous lines correspond to the significant Gaussian fits. SCTa, SCT auditory (blue line); SIRTa, SIRT auditory (red line). ***D***, Histogram of preferred intervals in the visual condition for cells with significant interval tuning during the SCT (median, 842.3 ms). ***E***, Histogram of preferred intervals for tuned cells during the SCT in the auditory condition (median, 835.7 ms). ***F***, Histogram of preferred intervals for tuned cells during the SIRT in the visual condition (median, 821.3 ms). ***G***, Histogram of preferred intervals for tuned cells during the SIRT in the auditory condition (median 808.5 ms). ***H***, Histogram of half-height tuning dispersion of the cells in ***D*** (median, 179.4 ms).

Table 2. Number of neurons whose responses were classified as sequence selective to one or two consecutive elements of the six-interval sequence or phase selective (synchronization or continuation) or were unclassified during the visual and auditory conditions of the SCT

	SCT visual	SCT auditory
Sequence 1	241	199
Sequence 2	185	193
Phase	81	51
Unclassified	42	52

tion of the actual produced interval during the SCT (Fig. 4) was described using double-Gaussian regressions on the ordinal-selective cells. In this case, however, we computed the regressions using the duration of the produced intervals during the task execution, instead of the target intervals with which the animals were instructed, to capture the relationship between neural activity and temporal performance (nevertheless, similar results were obtained with target interval as the independent variable). We found that 221 (56.4%, 221 of 392) of the ordinal-selective cells in the auditory condition and 250 (58.7%, 250 of 426) in the visual marker condition were significantly tuned to both variables during the SCT. Figure 4, *A* and *C*, shows the raster plots and double-tuning curve, respectively, for a cell with a short preferred interval and a preferred sequence order around the first continuation interval, whereas Figure 4, *B* and 4*D*, corresponds to a cell that was sharply double-tuned with a long preferred interval and a preferred sequence order around the second continuation interval. The density of preferred interval and preferred sequence order for all the significant double-tuned cells showed a bias toward longer durations, as well as a bias for the synchronization phase in the auditory condition (Fig. 4*F*) and a bias for the continuation phase in the visual condition (Fig. 4*E*). In addition, some cells in these distributions showed a preferred sequence order during the transition between phases (synchronization–continuation), which could imply that these cells could be phase transition detectors instead of sequence-selective cells. Nevertheless, all possible combinations of duration/sequence order were encoded in the population in both interval marker conditions. Figure 5 shows the χ^2 values between the predicted and the actual re-

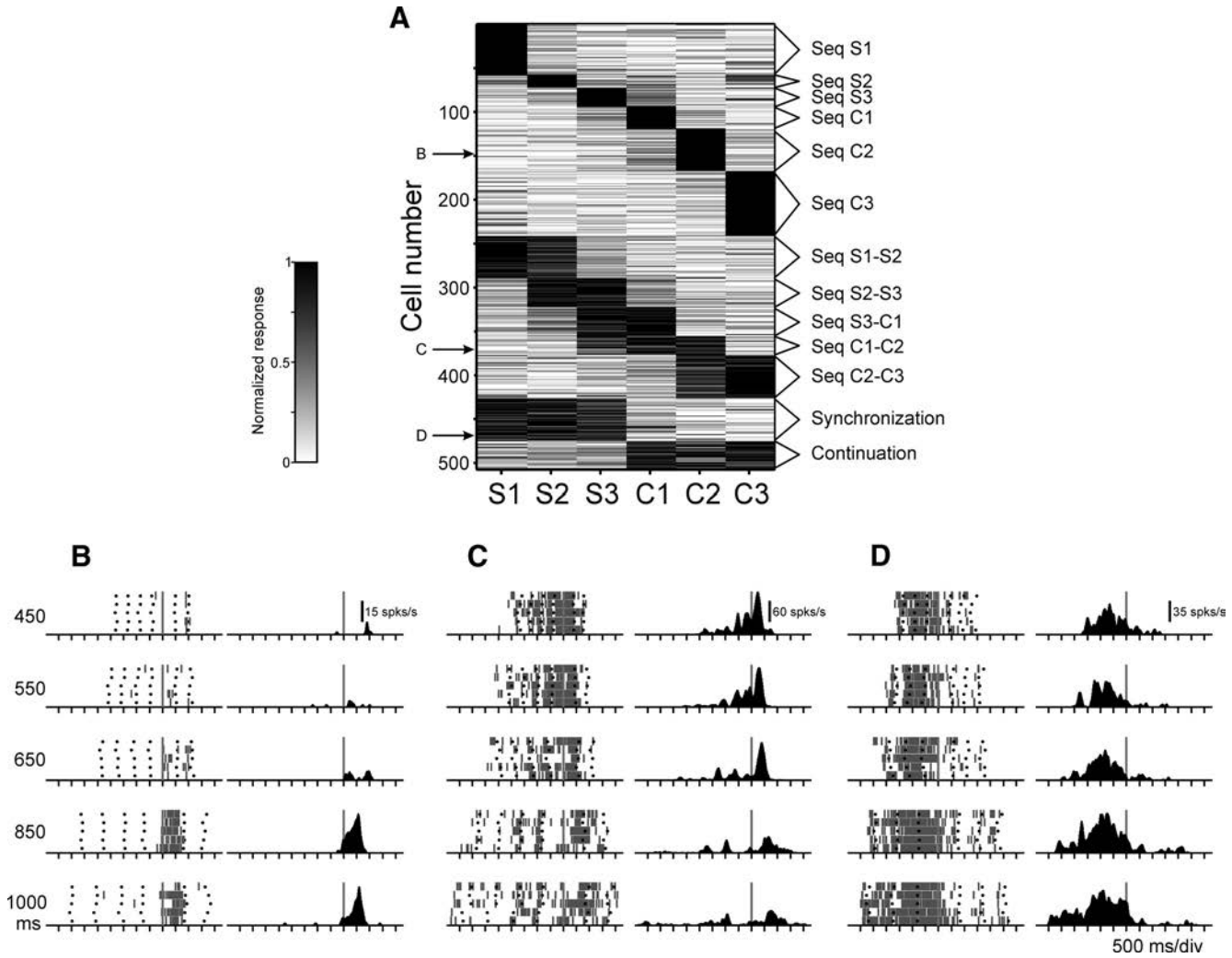

Figure 3. Cell selectivity to the sequential order and task phase during the SCT. ***A***, Normalized activity for a population of neurons with significant effects on sequence (Seq; ANOVA) that were classified as sequence selective to one, two, or three consecutive elements of the SCT using K-means clustering. Each row corresponds to one cell, and each column corresponds to one element of the SCT sequence. The letters with the arrows correspond to the raster of the cells below. ***B***, Responses of a cell with a preferred sequence order to the second continuation interval. This cell is also tuned to longer intervals. The raster histogram is aligned (gray line) to the first tap of the continuation phase. Black dots correspond to tapping times. The associated spike-density functions are shown to the right. ***C***, Cell that shows a selective response for the first and second intervals of the continuation phase, which also shows a preference for short intervals. The raster histogram is aligned to the first tap of the continuation phase. ***D***, Responses of a cell with selective activity during the synchronization phase of the SCT. The raster histogram is aligned to the last tap of the synchronization phase.

sponses of individual cells for the double-Gaussian against the single-Gaussian model for interval duration using the six elements of the SCT sequence. It is evident that most cells showed better fittings for the double-Gaussian function, in the visual (Fig. 5*A*) and auditory (Fig. 5*B*) conditions. Overall, these analyses suggest that the MPC shows a simultaneous representation of duration and sequential order during the execution of a rhythmic task such as the SCT.

It is important to mention that some cells that were phase selective on the cluster analysis were also significantly tuned to interval (Auditory: 23.5%, 12 of 51; Visual: 37%, 30 of 81; see Fig. 7*A*,*B*), suggesting that MPC can multiplex interval information with the number of elements in a sequence or with the context in which the tapping rhythms are generated (i.e., sensory driven or internally generated).

Decoding the temporal-sequential structure of the SCT

Once we determined the dependence of the neural responses on the ordinal sequence of the SCT and the durations produced by the monkeys during task execution, we used a Bayes analysis approach to address the inverse problem: given the firing rates of double-tuned cells, how can we optimally infer the sequential and temporal behavior of the animals in the task? Figure 6, *A* and *B*, shows the mean (black dots) and two-dimensional variance (ellipses) of the decoded values by populations of double-tuned cells recorded during trials with similar produced lengths (see Materials and Methods), for each target interval and across the six-interval sequence of the task, for the auditory and visual conditions. In addition, the colored squares in Figure 6, *A* and *B*, depict the mean ± SD of the produced intervals in the trials used for the decoding. The decoded values were accurate, particularly for the synchronization phase in the auditory condition and the continuation phase in the visual condition, across the five target durations (t tests between phases, $p < 0.05$). Furthermore, the decoding was more accurate for 650 and 850 ms. These findings, then, are in accordance with the bias in the distribution of preferred intervals and ordinal sequence shown in Figure 4, *E* and *F*. Thus, these results suggest that MPC shows a temporal process-

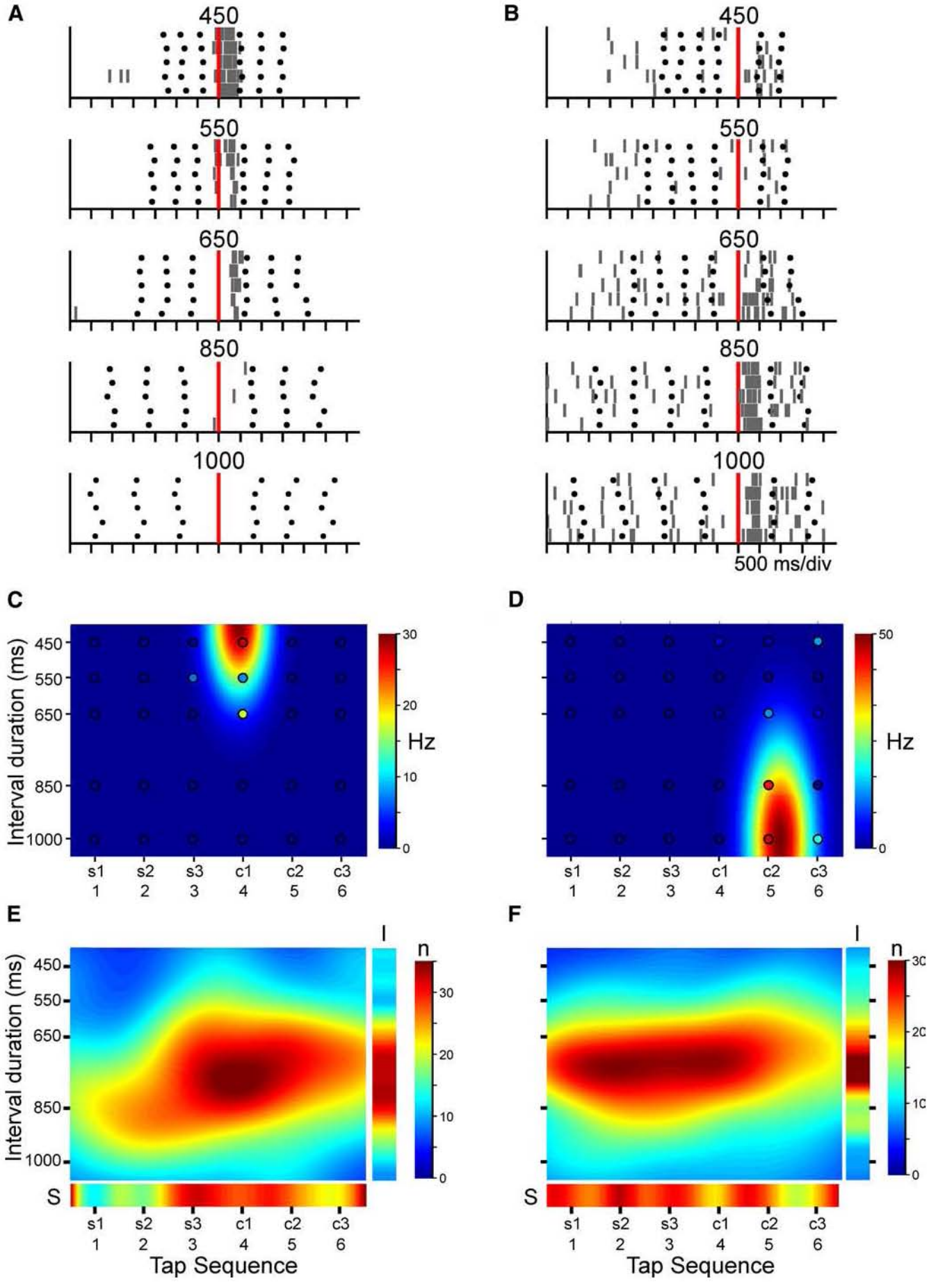
A
450
550
650
850
1000
B
450
550
650
850
1000
500 ms/div
C
Interval duration (ms)
450
550
650
850
1000
30
20
10
0
Hz
s1 1
s2 2
s3 3
c1 4
c2 5
c3 6
D
50
0
Hz
s1 1
s2 2
s3 3
c1 4
c2 5
c3 6
E
Interval duration (ms)
450
550
650
850
1000
I
n
30
20
10
0
S
s1 1
s2 2
s3 3
c1 4
c2 5
c3 6
Tap Sequence
F
I
n
S
s1 1
s2 2
s3 3
c1 4
c2 5
c3 6
Tap Sequence

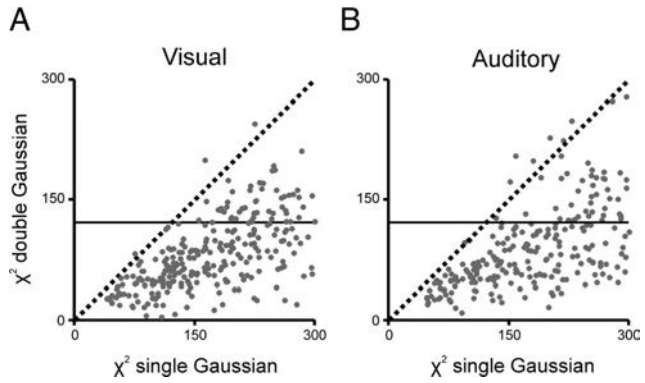

Figure 5. Comparison of χ^2 between single- and double-Gaussian fittings for cells with significant effects of duration in the ANCOVA for the visual (***A***) and auditory (***B***) conditions. $X^2 = \Sigma_i \frac{(O_i - E_i)^2}{E_i}$, where O_i is observed discharge rate and E_i is expected discharge rate for trial *i*. For single-Gaussian fittings, the discharge rate across trials and sequence order was the dependent variable, and target interval was the independent variable, using Equation 3. For the double-Gaussian fittings, the discharge rate computed for each interval and sequence order across trials was the dependent variable, and interval and sequence order were the independent variables, using Equation 5. In both fittings, we used 150 trials: 5 intervals × 6 sequence orders × 5 trials. The dotted line corresponds to the diagonal, and below the continuous horizontal, the cells showed a significant fitting on the χ^2 test ($p < 0.05$). It is evident that the double-Gaussian model showed smaller χ^2 and better fittings than the single-Gaussian model.

ing that depends on the modality of the interval markers used during the synchronization phase. Furthermore, the bias between the decoded and produced durations showed a pattern of overestimation for short durations and of underestimation for long intervals for both marker modalities, following the same trend of the monkey behavior (compare Figs. 1*C*,*D*, 6*C*,*D*). Figure 6*F* shows for the auditory marker condition a small underestimation for the decoded sequential-order values during the continuation, whereas Figure 6*E* shows a small overestimation between the decoded and sequential order values during the synchronization. Overall, the results suggest that cell populations in MPC have information to represent the sequential-order as well as the duration of intervals during rhythmic behavior. This neural population signal may correspond to a two-dimensional representation of the ordinal and temporal structure of movement sequences that could be present during music execution, for example.

Interval tuning in MPC across timing contexts

Next, we wanted to test whether a common timing mechanism or a set of context-dependent neural clocks could explain the behavior of interval-selective cells, comparing their tuning properties not only between the visual and auditory marker conditions, but also among the SCT and SIRT for the same set of intervals. Figure 7*A–D* shows the activity profiles of a cell that was tuned with preferred intervals around 850 ms during the SCT and SIRT for both interval marker modalities. The similarity in preferred intervals among tasks in this cell (Fig. 7*E*) supports the notion that interval tuning is a representation of time that may be used in a variety of behaviors and different sensory modalities. It is important to mention that the shapes of both the spike waveform (Fig. 7*A–D*, bottom insets) and the ISIHs of this cell were very similar between tasks, indicating that the recordings during the four tasks were stable and that the tuning properties across tasks belonged to the same cell (data not shown). Then, we compared the interval tuning properties of 668 cells across tasks. These cells were considered stable between tasks using various criteria, which included the average spike waveforms and the shape of the ISIHs, and were tuned to the interval in at least one pair of the four task combinations (see Materials and Methods) (Dickey et al., 2009). Interestingly, 61.8% (412 of 668) of the cells showed similar preferred intervals (with a difference below 150 ms) across the different combinations of tasks pairs (Fig. 7*F*; Table 3). Finally, Figure 7*G* shows the density of preferred intervals for cells that were interval selective for different combinations of task pairs. This graph shows that, although there was the bias toward long durations, there was a group of cells that showed a similar preferred interval across tasks, particularly for the shorter and longer preferred intervals.

We performed a more detailed analysis of the cells' tuning properties, using the cumulative distributions of the difference in preferred intervals for the same cells between specific tasks pairs, to determine whether the number of produced intervals (one for SIRT and six for SCT) and the modality of the interval marker produced systematic drifts in the cells' preferred intervals.

The results corroborate that more than half of the MPC cell population showed small differences in their preferred interval across behavioral contexts (Fig. 8*A*; Table 4). In addition, the cumulative distributions of the preferred interval differences between same tasks but different modalities (Fig. 8*A*, SCTa - SCTv in blue and SIRTa - SIRTv in red) were shifted to the left with respect to the distributions of different tasks but same modality (Fig. 8*A*, SCTa - SIRTa in green and SCTv - SIRTv in orange; Table 5). Finally, a bootstrap analysis showed that the similarity in preferred intervals (with a difference below 150 ms) across these tasks pairs was above chance ($p < 0.05$; see Materials and Methods).

To assess the similarities in cell responses between tasks pairs across all the tested durations and not only the preferred interval, we performed a linear regression using the discharge rates of the same cells across durations between different pairs of tasks. For example, Figure 8*C* shows a linear regression between the firing rates of the SIRT against the SCT for the cell depicted in Figure 2*A–C*. The resulting slope was close to unity (1.1); however, the constant was 5.8 Hz, suggesting that the response across duration was similar in the two tasks but scaled with larger responses in the SCT. When the regressions were performed between the same tasks but different modality (SCT-auditory vs SCT-visual and SIRT-auditory vs SIRT-visual), the slope distribution for the interval-selective cells was around one (Fig. 8*D*) and the constant distribution was centered on zero (Fig. 8*F*). These results support the notion that interval tuning was not strongly affected by the modality used to drive the temporal behavior. In contrast, the

←

Figure 4. Cell tuning to interval and sequential order during the SCT. ***A***, Responses of a double-tuned cell with a short preferred interval and a sharp preferred sequence order around the first continuation interval. The raster histogram is aligned (red line) to the first tap of the continuation phase. ***B***, Responses of a sharply double-tuned cell with a long preferred interval and a preferred sequence order around the second continuation interval. The raster is aligned (red line) to the second tap of the continuation phase. ***C***, ***D***, Double-Gaussian tuning functions for the cell responses depicted in ***A*** and ***B***, respectively. The dots correspond to the mean discharge rate for each duration–sequence order combination. The color code represents the discharge rate (hertz) of the cells. ***E***, ***F***, Distribution of the dual preferred interval/sequence order for the cell population with significant Gaussian fits in the visual and auditory marker conditions, respectively. S, Distribution of preferred ordinal sequence; I, distribution of preferred interval. The color code represents the number (n) of double-tuned cells in different duration and sequence order combinations.

regressions performed on the cell activity between same modality but different task (SIRT-auditory vs SCT-auditory and SIRT-visual vs SCT-visual), showed a slope distribution for the interval-selective cells that peaked at 1 but was skewed for larger values (Fig. 8*E*). These results suggest that the cells showed either a similar response profile between SCT and SIRT (slopes close to 1) or a rate of change in activity among durations that was larger for SCT than SIRT (slopes larger than 1). This last result provides evidence for tuning sharpening during the SCT for a subpopulation of MPC cells.

The fact that a large population of interval-tuned neurons showed similar preferred intervals and response profiles for the tested durations across the four task combination provides support to the hypothesis that MPC is part of a core timing mechanism that is engaged in multiple timing behaviors.

A gain mechanism to encode the number of produced intervals in a rhythmic sequence

The cells depicted in Figures 2*A–C* and 7*A–E* show another property of interval tuning in MPC, namely that although the preferred intervals of these cells were similar across tasks, the discharge rate at the preferred duration was larger in the SCT than the SIRT. Accordingly, at the population level we observed a significantly larger maximum discharge rate for cells with similar preferred intervals (<100 ms in PI difference) during the SCT with respect to SIRT, for both the visual and auditory conditions (Fig. 8*B*, Mann–Whitney *U* tests; Table 6). In addition, the constant of the linear regressions between same modality but different task (SIRT-auditory vs SCT-auditory and SIRT-visual vs SCT-visual), was shifted to the right (Fig. 8*G*). Hence, a large population of cells showed positive values in the constant or intercept of the regression, suggesting a coordinated increase in discharge rate for the SCT with respect of SIRT, as depicted in Figure 8*C*. These findings suggest the existence of a gain mechanism as the possible neural representation for the total number of produced intervals in a sequence, where the discharge rate of the tuned cells increases between one and six produced intervals, although the preferred intervals are similar across conditions.

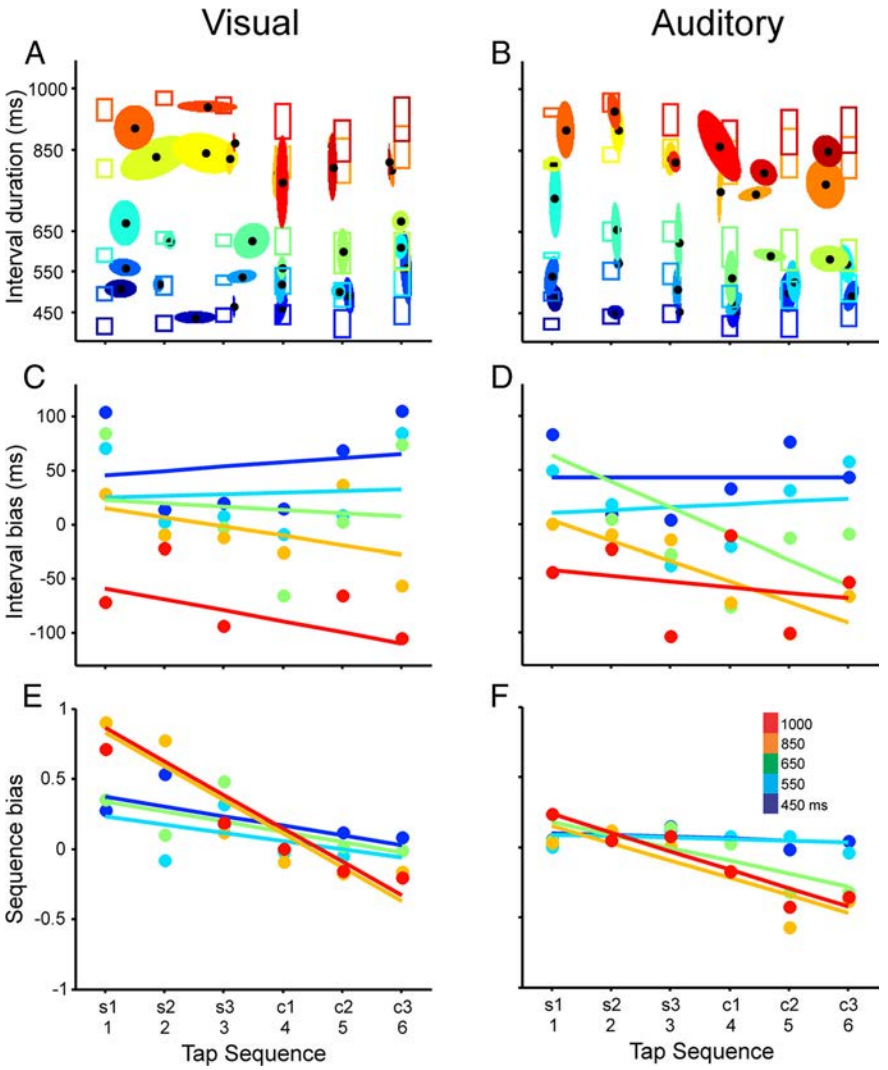

Figure 6. Decoding the sequential and temporal structure of the SCT. ***A***, ***B***, Bivariate normal distributions of the Bayesian decoded values for produced duration/ordinal sequence using the activity of double-tuned cell populations recorded during similar temporal behavior in the SCT. Each ellipse is centered at the *x–y* mean (sequence– duration; black dot), and the length of its axes is proportional to the total SD of the decoded values. The bottom and top of the color boxes correspond to the mean ± SD of the produced intervals on the trials used for decoding. The gradient in the color code changes as a function of sequence order and target interval, for both the decoding ellipses and the behavior boxes. ***C***, ***D***, Bias between the decoded and produced durations as a function of the tapping sequence across the five target intervals, using the color code shown in the inset in ***F***. ***E***, ***F***, Bias between the decoded and the actual sequential order as a function of the tapping sequence, across the five target intervals. The results for the visual (left) and auditory (right) marker conditions are shown.

Discussion

The present study describes the following functional properties in MPC cells: (1) cells in MPC are tuned to duration in different tapping tasks; (2) there was interval-tuning invariance across tasks (SCT and SIRT) and modalities in a large population of neurons; (3) during the SCT, a large cell population was tuned to both the sequential and temporal structure of the task; and (4) there is a possible gain mechanism for encoding the number of intervals in a sequence of temporalized movements. We discuss these results separately below.

This study gives, as far as we know, the first empirical evidence for duration tuning in the behaving monkey. The existence of interval tuning was inferred from learning and generalization studies of time intervals (Nagarajan et al., 1998; Meegan et al., 2000; Bartolo and Merchant, 2009; Heron et al., 2012) and has been suggested in conceptual papers (Ivry, 1996). These results suggest that the MPC contains a representation of interval, where different populations of interval-tuned cells are activated depending on the duration of the produced interval. Cell tuning is an encoding mechanism widely used in cortical cells to represent sensory, cognitive, and motor information (deCharms and Zador, 2000; Merchant et al., 2012). Studies of tuning have demonstrated that most cortical neurons carry information about a

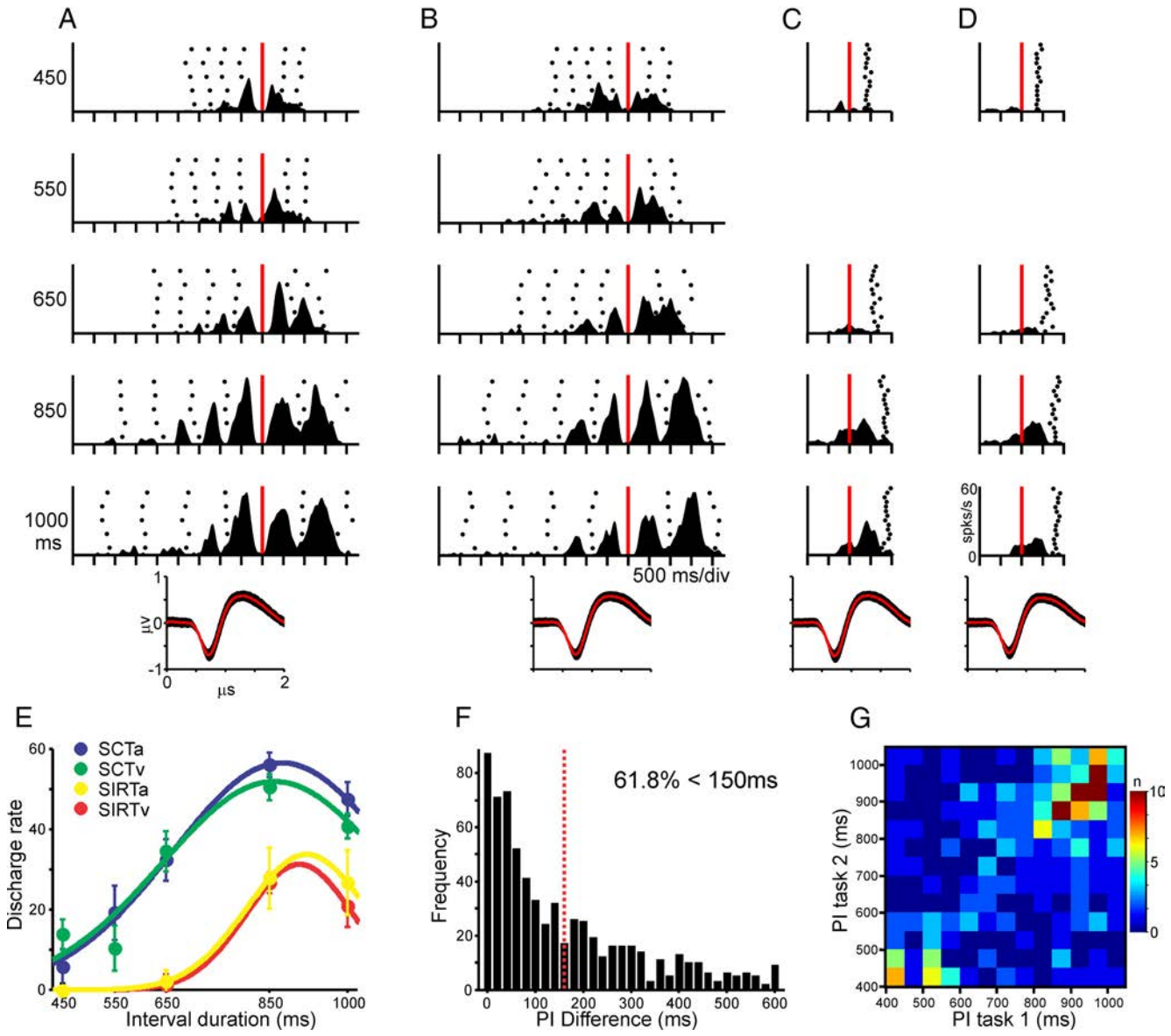

Figure 7. Interval tuning across tasks and sensory modalities. ***A–D***, Average spike-density functions of the responses of an interval-tuned cell with a long preferred interval across different temporal contexts. The mean (red curve) and SD (black area) of the action potential waveform during each task combination is shown at the bottom. ***A***, SCT in the auditory condition. ***B***, SCT in the visual condition. ***C***, SIRT in the auditory condition. ***D***, SIRT in the visual condition. In ***A*** and ***B***, the raster histograms are aligned (red line) to the first tap of the continuation phase, whereas in ***C*** and ***D***, they are aligned to the first tapping movement. ***E***, Tuning functions for the cell in ***A–D***, where the mean ± SEM of the discharge rate is plotted as a function of the target interval. The continuous lines correspond to the significant Gaussian fits. SCTa, Auditory SCT (blue); SCTv, visual SCT (green); SIRTa, auditory SIRT (yellow); SIRTv, visual SIRT (red). ***F***, Distribution of the PI difference for the cells tuned during different task pairs. The Dotted red line corresponds to the 150 ms PI difference. ***G***, Density plot of the PIs for the same cells between all possible combinations of task pairs (task 1 vs task 2). The color code represents the number (n) of cells with different PI combinations between tasks.

Table 3. Statistics of the distributions of preferred interval differences between the specified number of tasks

	Two	Three	Four
Number	272	100	16
Median	120.2	127.2	74.3
Mean	173.2	173.1	120.2
SD	164.1	161.4	126.8
% < 150 ms	57.7	56	69.8

limited range of values or a particular behavioral feature, with an orderly decrease in discharge rate around a preferred value (Merchant et al., 2012). Thus, interval timing, as in the case of numerosity and spatial magnitudes (Georgopoulos et al., 1986; Walsh, 2003; Buhusi and Meck, 2005; Nieder et al., 2006), is represented as an abstract quantity in MPC by a population of interval-tuned cells. The distribution of preferred intervals was skewed for intervals around 850 ms in the four task combinations, which could reflect that monkeys have a behavioral timing repertoire where this interval is prevalent. Indeed, we found that the constant error for this interval was close to zero across tasks. Additional experiments are needed to determine whether tuning to interval is an emergent property of MPC cells that depends on the local integration of graded inputs or is a distributed representation of time throughout the CBGT (Matell and Meck, 2004).

Importantly, the present findings indicate that a large population of tuned cells in MPC showed similar preferred intervals across tapping behaviors that varied in the number of produced intervals and the modality used to drive temporal processing.

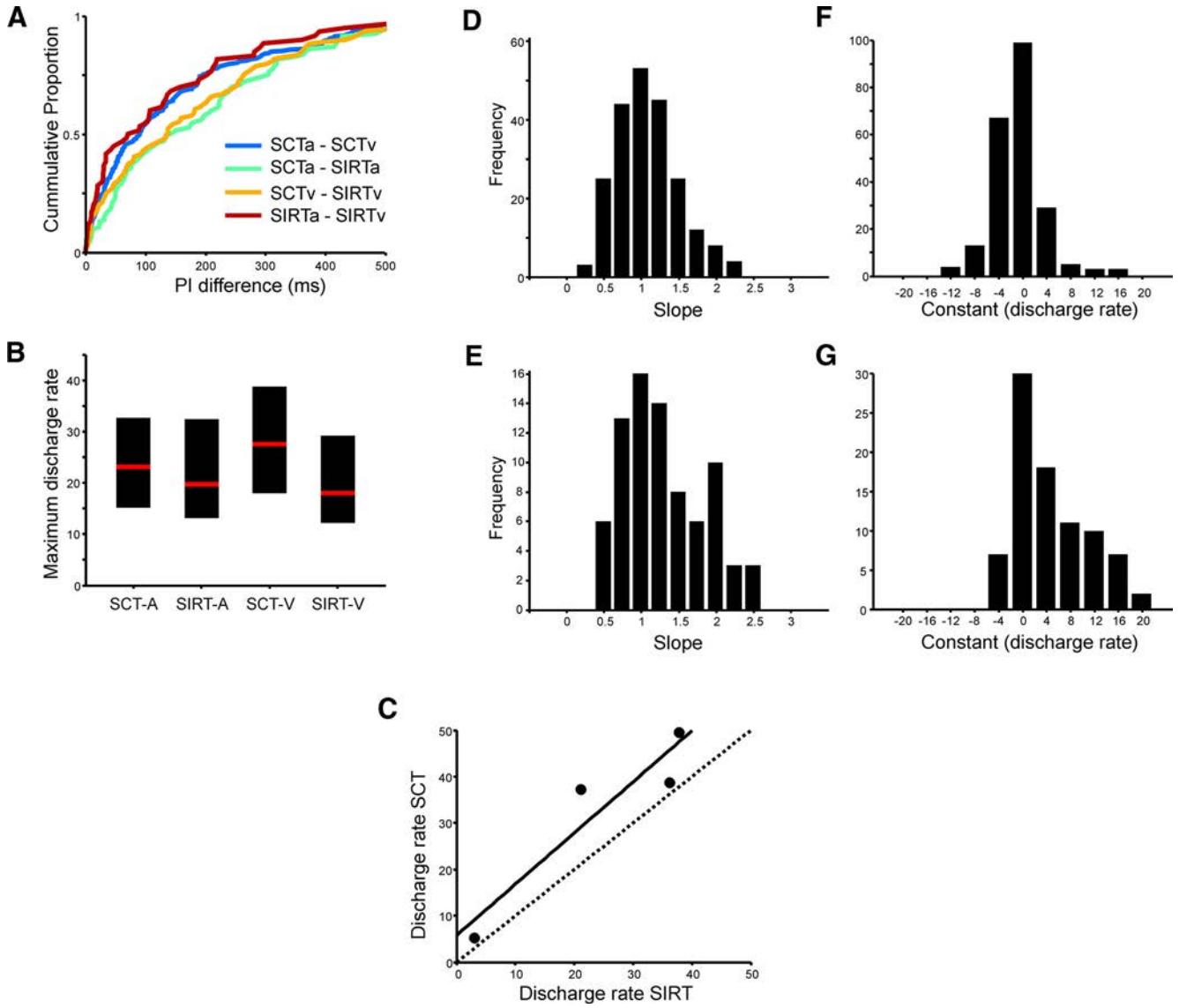

Figure 8. Gain mechanism for the number of produced intervals. ***A***, Cumulative distributions for the PI difference for tuned cells between specific task pairs. The color code for task pairs is given in the inset. ***B***, Interquartile ranges (black bars) and medians (red line within bars) of the maximum discharge rate of cells across the four task combinations. Only cells that were interval tuned in at least two tasks and showed a small difference (<100 ms) in their preferred interval across tasks were included in the analysis. ***C***, Discharge rates of the SIRT against the SCT of the cell in Figure 2*A–C*, where the dotted line is the diagonal and the black line is the predicted function of the corresponding linear regression. ***D***, ***E***, Histograms of the slope and constant of the significant linear regression models for single-cell discharge rates between same tasks but different modality [SCTa vs SCTv ($n = 200$) and SIRTa vs SIRTv ($n = 33$)]. ***F***, ***G***, Histograms of the slope and constant of the significant linear regression models for single-cell discharge rates between same modality but different task regressions [SIRTa vs SCTa ($n = 49$) and SIRTv vs SCTv ($n = 61$)]. SCTa, Auditory SCT; SCTv, visual SCT; SIRTa, auditory SIRT; SIRTv, visual SIRT.

Table 4. Statistics of the distributions of preferred interval differences between the specified tasks pairs

	SIRTa-SIRTv	SCTa-SCTv	SCTa-SIRTa	SCTv-SIRTv
Number	60	218	93	109
Median	78.7	89.2	143.5	136.8
Mean	132.7	143.1	187.5	178.1
SD	152.8	151.6	159.6	168.4
% < 150 ms	68.3	66	51.6	54.1

SCTa, SCT auditory; SCTv, SCT visual; SIRTa, SIRT auditory; SIRTv, SIRT visual.

Table 5. *p* values of the Kolmogorov–Smirnov tests between the distributions of preferred interval differences between the specified tasks pairs

	SCTa-SIRTa	SCTv-SIRTv	SIRTa-SIRTv
SCTa-SCTv	0.007	0.066	0.423
SCTa-SIRTa		0.471	0.007
SCTv-SIRTv			0.058

SCTa, SCT auditory; SCTv, SCT visual; SIRTa, SIRT auditory; SIRTv, SIRT visual.

Table 6. *p* values of the Mann–Whitney *U* tests between the intervals with the maximum discharge rates for the specified tasks

	SCTv	SIRTa
SCTa	0.08	0.03
SIRTv	0.0000001	0.201

SCTa, SCT auditory; SCTv, SCT visual; SIRTa, SIRT auditory; SIRTv, SIRT visual.

Hence, interval-tuning invariance across the four tested task combinations suggests that the medial premotor areas tag the timed durations as a context-independent neural signal. Tuning invariance to low-order parameters also has been observed in the upper hierarchies of processing in the visual and auditory sys-

tems, where there are cells that show selective responses to abstract features of complex stimuli (Sadagopan and Wang, 2008). For example, cells in the inferotemporal cortex show visual object-selective cells that exhibit tuning invariance to complex shapes (such as faces) submitted to translation, scale changes, and a limited rotation in depth (Logothetis and Sheinberg, 1996) and probably are associated with the perceptual recognition of objects. The interval-tuning invariance observed here supports the notion that the CNS needs a reliable representation of duration in different behavioral circumstances. Therefore, these findings are consistent with the existence of a core timing mechanism that is engaged in multiple timing behaviors and that includes the MPC (Merchant et al., 2008a, 2013; Harrington et al., 2010).

On the other hand, the ability to capture and interpret the beats in a rhythmic pattern allows people to move and dance in time to music (Phillips-Silver and Trainor, 2005). Thus, rhythmic behaviors depend on intricate loops of perception and action, where temporal processing can be engaged during the synchronization of movements with sensory information or during the internal generation of movement sequences (Janata and Grafton, 2003). The SCT has been an instrumental paradigm to study these processes, and a recent neurophysiological study has shown that sensorimotor loops engaged during this task may depend on the cyclic interplay between different neuronal chronometers in MPC that quantify in their instantaneous activity the time passed and the remaining time for an action (Merchant et al., 2011). The present findings suggest that MPC also uses interval tuning as an abstract representation of the passage of time. Interestingly, interval tuning during the SCT is multiplexed with the tuning to ordinal sequence in the same population of cells. Therefore, the brain might use a cell population signal that works as the notes of a musical score to represent both the duration of the produced interval and the rank order of the interval that is executed in the learned SCT sequence. Hence, not only is MPC involved in the independent encoding of the multiple movement sequences (Tanji and Shima, 1994; Shima and Tanji, 1998) or the timing of isolated movements (Mita et al., 2009) but there is also a two-dimensional representation of sequence order and timing in populations of MPC cells during rhythmic behaviors such as the SCT. It is important to mention that previous studies have shown that MPC neurons modulate their activity according to the number of remaining movements in a sequence to receive a reward, suggesting that they might encode the timing of reward (Sohn and Lee, 2007). Although it is possible that some of the sequence order signals reported here could be related to the time remaining to reward, the distribution of preferred ordinal sequence in the population is not biased toward the last elements of the sequence, particularly for the auditory marker condition (Fig. 4*E*), supporting the notion that the double-tuned cells were multiplexing ordinal and temporal structure of the SCT. Finally, the multiplexing of ordinal sequence and duration also may be a neural signal shared throughout the CBGT, since previous studies have described neural responses associated with interval duration and the organization of sequential motor behavior in the neostriatum (Kermadi and Joseph, 1995; Miyachi et al., 1997; Matell et al., 2003a,b; Jin et al., 2009; Bartolo et al., 2012).

Time-related cell responses have been reported in parietal (Leon and Shadlen, 2003) and prefrontal (Brody et al., 2003; Genovesio et al., 2009) cortex, putamen (Jin et al., 2009), thalamus (Tanaka, 2007), MPC (Mita et al., 2009; Merchant et al., 2011), and motor cortex (Lebedev et al., 2008). Hence, in agreement with the neuroimaging literature, these neurophysiological studies point to a highly distributed processing of temporal information by CBGT networks (Meck et al., 2008). Most of these studies report ramping activity during a variety of timing tasks. A fundamental characteristic of climbing activity is its instantaneous nature and the fact that it normally peaks at the time of an anticipated motor response, suggesting its involvement in the temporal construction of motor intentions and actions (Merchant et al., 2004; Maimon and Assad, 2006; Renoult et al., 2006). In contrast, the cells that are tuned to an interval may represent different aspects of temporal processing that can be dissociated from the motor response.

As a final point, the present results suggest the existence of a gain mechanism for encoding the total number of produced intervals in a sequence, where larger numbers of produced intervals were associated with a multiplicative response scaling across durations and the corresponding increase in discharge rate in the preferred interval of tuned cells. Psychophysical studies in both perceptual and production tasks have demonstrated that temporal variability decreases as a function of the number of intervals to be timed (Keele et al., 1989; Ivry and Hazeltine, 1995; Merchant et al., 2008a,b). Hence, the decrease in variability with the number of timed intervals could be the result of the increase in discharge rate in the preferred interval of MPC cells. Gain mechanisms have been described for the combination of retinal and gaze signals (Andersen et al., 1985) and for the representation of states of visual attention (Treue and Martinez Trujillo, 1999) and have been regarded as a major computational principle of nonlinear neuronal processing (Salinas and Thier, 2000). The MPC may use this gain principle to represent the total number of produced intervals in a sequence, while through tuning it can multiplex interval and ordinal sequence in a rhythmic paradigm. Needless to say, studies using different total numbers of intervals, instead of just one (SIRT) and six (SCT), are necessary to confirm this hypothesis.

References

Andersen RA, Essick GK, Siegel RM (1985) Encoding of spatial location by posterior parietal neurons. Science 230:456–458. CrossRef Medline

Bartolo R, Merchant H (2009) Learning and generalization of time production in humans: rules of transfer across modalities and interval durations. Exp Brain Res 197:91–100. CrossRef Medline

Bartolo R, Prado L, Merchant H (2012) The oscillatory activity of the primate putamen is associated with the temporal and sequential structure of a synchronization–continuation tapping task. Paper presented at 42nd Congress of the Society for Neuroscience, New Orleans, LA, October.

Brody CD, Hernández A, Zainos A, Romo R (2003) Timing and neural encoding of somatosensory parametric working memory in macaque prefrontal cortex. Cereb Cortex 13:1196–1207. CrossRef Medline

Bueti D, Walsh V, Frith C, Rees G (2008) Different brain circuits underlie motor and perceptual representations of temporal intervals. J Cogn Neurosci 20:204–214. CrossRef Medline

Buhusi CV, Meck WH (2005) What makes us tick? Functional and neural mechanisms of interval timing. Nat Rev Neurosci 6:755–765. CrossRef Medline

Buonomano DV, Laje R (2010) Population clocks: motor timing with neural dynamics. Trends Cogn Sci 14:520–527. CrossRef Medline

Coull JT, Cheng RK, Meck WH (2011) Neuroanatomical and neurochemical substrates of timing. Neuropsychopharmacology 36:3–25. CrossRef Medline

Dayan P, Abbott LF (2001) Theoretical neuroscience, computational and mathematical modeling of neural systems. London: MIT.

deCharms RC, Zador A (2000) Neural representation and the cortical code. Annu Rev Neurosci 23:613–647. CrossRef Medline

Dickey AS, Suminski A, Amit Y, Hatsopoulos NG (2009) Single-unit stability using chronically implanted multielectrode arrays. J Neurophysiol 102:1331–1339. CrossRef Medline

Diehl RL, Lotto AJ, Holt LL (2004) Speech perception. Annu Rev Psychol 55:149–179. CrossRef Medline

Draper NR, Smith H (1981) Applied regression analysis. New York: Wiley.

Genovesio A, Tsujimoto S, Wise SP (2009) Feature- and order-based timing representations in the frontal cortex. Neuron 63:254–266. CrossRef Medline

Georgopoulos AP, Schwartz AB, Kettner RE (1986) Neuronal population coding of movement direction. Science 233:1416–1419. CrossRef Medline

Gibbon J, Malapani C, Dale CL, Gallistel C (1997) Toward a neurobiology of temporal cognition: advances and challenges. Curr Opin Neurobiol 7:170–184. CrossRef Medline

Hanes DP, Thompson KG, Schall JD (1995) Relationship of presaccadic activity in frontal eye field and supplementary eye field to saccade initiation in macaque: Poisson spike train analysis. Exp Brain Res 103:85–96. Medline

Harrington DL, Zimbelman JL, Hinton SC, Rao SM (2010) Neural modulation of temporal encoding, maintenance, and decision processes. Cereb Cortex 20:1274–1285. CrossRef Medline

Hastie T, Tibshirani R, Friedman J (2001) The elements of statistical learning: data mining, inference, and prediction. New York: Springer.

Heron J, Aaen-Stockdale C, Hotchkiss J, Roach NW, McGraw PV, Whitaker D (2012) Duration channels mediate human time perception. Proc Biol Sci 279:690–698. CrossRef Medline

Ivry RB (1996) The representation of temporal information in perception and motor control. Curr Opin Neurobiol 6:851–857. CrossRef Medline

Ivry RB, Hazeltine RE (1995) Perception and production of temporal intervals across a range of durations: evidence of a common timing mechanism. J Exp Psychol Hum Perform 21:3–18. CrossRef Medline

Janata P, Grafton ST (2003) Swinging in the brain: shared neural substrates for behaviors related to sequencing and music. Nat Neurosci 6:682–687. CrossRef Medline

Jin DZ, Fujii N, Graybiel AM (2009) Neural representation of time in cortico-basal ganglia circuits. Proc Natl Acad Sci U S A 106:19156–19161. CrossRef Medline

Johnson RA, Wichern DW (1998) Applied multivariate statistical analysis. Upper Saddle River, NJ: Prentice Hall.

Karmarkar UR, Buonomano DV (2007) Timing in the absence of clocks: encoding time in neural network states. Neuron 53:427–438. CrossRef Medline

Keele S, Nicoletti R, Ivry R, Pokorny R (1989) Mechanisms of perceptual timing: beat-based or interval-based judgments? Psychol Res 50:251–256. CrossRef

Kermadi I, Joseph JP (1995) Activity in the caudate nucleus of monkey during spatial sequencing. J Neurophysiol 74:911–933. Medline

Lebedev MA, O'Doherty JE, Nicolelis MA (2008) Decoding of temporal intervals from cortical ensemble activity. J Neurophysiol 99:166–186. CrossRef Medline

Leon MI, Shadlen MN (2003) Representation of time by neurons in the posterior parietal cortex of the macaque. Neuron 38:317–327. CrossRef Medline

Logothetis NK, Sheinberg DL (1996) Visual object recognition. Annu Rev Neurosci 19:577–621. CrossRef Medline

Macar F, Coull J, Vidal F (2006) The supplementary motor area in motor and perceptual time processing: fMRI studies. Cogn Process 7:89–94. CrossRef Medline

Maimon G, Assad JA (2006) A cognitive signal for the proactive timing of action in macaque LIP. Nat Neurosci 9:948–955. CrossRef Medline

Matell MS, Meck WH (2004) Cortico-striatal circuits and interval timing: coincidence detection of oscillatory processes. Brain Res Cogn Brain Res 21:139–170. CrossRef Medline

Matell MS, Meck WH, Nicolelis MA (2003a) Interval timing and the encoding of signal duration by ensembles of cortical and striatal neurons. Behav Neurosci 117:760–773. CrossRef Medline

Matell MS, Meck WH, Nicolelis MAL (2003b) Integration of behavior and timing: anatomically separate systems or distributed processing? In: Functional and neural mechanisms of interval timing (Meck WH, ed), pp 371–392. Boca Raton, FL: CRC.

Meck WH, Penney TB, Pouthas V (2008) Cortico-striatal representation of time in animals and humans. Curr Opin Neurobiol 18:145–152. CrossRef Medline

Meegan DV, Aslin RN, Jacobs RA (2000) Motor timing learned without motor training. Nat Neurosci 3:860–862. CrossRef Medline

Merchant H, Georgopoulos AP (2006) Neurophysiology of perceptual and motor aspects of interception. J Neurophysiol 95:1–13. Medline

Merchant H, Perez O (2009) Neurophysiology of interceptive behavior in the primate: encoding and decoding target parameters in the parietofrontal system. In: Coherent behavior in neural networks (Josic K, Matias M, Romo R, Rubin J, eds), Springer Series in Computational Neuroscience, Vol 3, pp 191–206. New York: Springer.

Merchant H, Battaglia-Mayer A, Georgopoulos AP (2004) Neural responses during interception of real and apparent circularly moving stimuli in motor cortex and Area 7a. Cereb Cortex 14:314–331. CrossRef Medline

Merchant H, Zarco W, Prado L (2008a) Do we have a common mechanism for measuring time in the hundreds of millisecond range? Evidence from multiple-interval timing tasks. J Neurophysiol 99:939–949. CrossRef Medline

Merchant H, Zarco W, Bartolo R, Prado L (2008b) The context of temporal processing is represented in the multidimensional relationships between timing tasks. PloS One 3:e3169:1–9. CrossRef Medline

Merchant H, Naselaris T, Georgopoulos AP (2008c) Dynamic sculpting of directional tuning in the primate motor cortex during 3D reaching. J Neurosci 28:9164–9172. CrossRef Medline

Merchant H, Zarco W, PérezO, Prado L, Bartolo R (2011) Measuring time with different neural chronometers during a synchronization–continuation task. Proc Natl Acad Sci U S A 108:19784–19789. CrossRef Medline

Merchant H, de Lafuente V, Peña-Ortega F, Larriva-Sahd J (2012) Functional impact of interneuronal inhibition in the cerebral cortex of behaving animals. Prog Neurobiol 99:163–178. CrossRef Medline

Merchant H, Harrington D, Meck WH (2013) Neural basis of the perception and estimation of time. Annu Rev Neurosci, in press.

Mita A, Mushiake H, Shima K, Matsuzaka Y, Tanji J (2009) Interval time coding by neurons in the presupplementary and supplementary motor areas. Nat Neurosci 12:502–507. CrossRef Medline

Miyachi S, Hikosaka O, Miyashita K, Kárádi Z, Rand MK (1997) Differential roles of monkey striatum in learning of sequential hand movement. Exp Brain Res 115:1–5. CrossRef Medline

Nagarajan SS, Blake DT, Wright BA, Byl N, Merzenich MM (1998) Practice-related improvements in somatosensory interval discrimination are temporally specific but generalize across skin location, hemisphere, and modality. J Neurosci 18:1559–1570. Medline

Nieder A, Diester I, Tudusciuc O (2006) Temporal and spatial enumeration processes in the primate parietal cortex. Science 313:1431–1435. CrossRef Medline

Perez O, Kass RE, Merchant H (2013) Trial time warping to discriminate stimulus-related from movement-related neural activity. J Neurosci Methods 212:203–210. CrossRef Medline

Phillips-Silver J, Trainor LJ (2005) Feeling the beat: movement influences infant rhythm perception. Science 308:1430. CrossRef Medline

Rakitin BC, Gibbon J, Penney TB, Malapani C, Hinton SC, Meck WH (1998) Scalar expectancy theory and peak-interval timing in humans. J Exp Psychol Anim Behav Process 24:15–33. CrossRef Medline

Renoult L, Roux S, Riehle A (2006) Time is a rubberband: neuronal activity in monkey motor cortex in relation to time estimation. Eur J Neurosci 23:3098–3108. CrossRef Medline

Sadagopan S, Wang X (2008) Level invariant representation of sounds by populations of neurons in primary auditory cortex. J Neurosci 28:3415–3426. CrossRef Medline

Salinas E, Thier P (2000) Gain modulation: a major computational principle of the central nervous system. Neuron 27:15–21. CrossRef Medline

Shima K, Tanji J (1998) Both supplementary and presupplementary motor areas are crucial for the temporal organization of multiple movements. J Neurophysiol 80:3247–3260. Medline

Sohn JW, Lee D (2007) Order-dependent modulation of directional signals in the supplementary and presupplementary motor areas. J Neurosci 27:13655–13666. CrossRef Medline

Tanaka M (2007) Cognitive signals in the primate motor thalamus predict saccade timing. J Neurosci 27:12109–12118. CrossRef Medline

Tanji J (2001) Sequential organization of multiple movements: involvement of cortical motor areas. Annu Rev Neurosci 24:631–651. CrossRef Medline

Tanji J, Shima K (1994) Role for supplementary motor area cells in plan-

ning several movements ahead. Nature 371:413–416. CrossRef Medline

Treue S, Martínez Trujillo JC (1999) Feature-based attention influences motion processing gain in macaque visual cortex. Nature 399:575–579. CrossRef Medline

Walsh V (2003) A theory of magnitude: common cortical metrics of time, space and quantity. Trends Cogn Sci 7:483–488. CrossRef Medline

Wiener M, Turkeltaub P, Coslett HB (2010) The image of time: a voxel-wise meta-analysis. Neuroimage 49:1728–1740. CrossRef Medline

Zarco W, Merchant H, Prado L, Mendez JC (2009) Subsecond timing in primates: comparison of interval production between human subjects and rhesus monkeys. J Neurophysiol 102:3191–3202. CrossRef Medline